~

Modeling Fine Sediment Behavior in Gravel-Bed Rivers

Submitted by

Gabriele Johanna Lamparter

to the University of Exeter

as a thesis for the degree of Doctor of Philosophy in Geography

July 2014

I certify that all material in this thesis which is not my own work has been identified and that no material has previously been submitted and approved for the award of a degree by this or any other University.

Signature:

Date:

Abstract

Fine-grained sediment accumulation in the interstices of gravel beds is a key factor in degrading riverine habitats. However, interstitial deposits are highly dynamic and are not sufficiently understood. This work enhances the understanding of interstitial fine sediment deposition by investigating interstitial storage and ingress, flow, suspended sediment and gravel bed character. Furthermore, this work introduces a numerical suspended sediment deposition model with the power to predict patterns of interstitial ingress.

The investigation of interstitial deposition were carried out on two levels. Both data orginating from flume experiments and from three locations of the River Culm, Devon, UK was collected. The experimental data showed the significant influence of small scale variations in flow and bed character and their influence on interstitial ingress. The field investigation showed clear differences in interstitial fine-grained sediment for the different river reaches and an overall higher interstitial ingress compared to recent published data.

The numerical model development was realised in a two-step approach. First, the model was coded and calibrated for the flume scale processes and, second, an upscaled reach scale model was devolped for the field data. This reach scale suspended sediment deposition model included flow information, for which depth-averaged two dimensional hydrodynamic models were developed with the software Delft3D. The overall explanatory power of the model at this state is not satisfactory with regards to local deposition distribution. A separate chapter discusses the possible causes and implications of this short coming for further research from a data aquisition and modelling perspective.

Acknowledgement

Sitting here at the very end of far too many PhD years, I know I could not have done it without those people, who accompanied me on parts of my journey and more so those, who went all the way. These far too few sentences are the place to offer my deep gratitude for their often extensive and generous help.

I am very grateful for the general institutional help I received at the Exeter Geography Department, in particular from the laboratory and technical staff (Neville England, Susan Franklin, Jim Grapes). Also the equipment of the Archaeology Department made progress in my research much easier (a special thanks goes to Sean Goddard). Furthermore, this work would not have been possible without the access to the farmland of Mr Lewis, Mrs Dinsney and Mr Greed. The biggest institutional 'thank you' goes to the Agricultural Development and Advisory Service (ADAS) and Great Western Research. Their financial support by offering a full scholarship made this research project possible for me in the first place.

I am deeply indebted to my current boss, Gerhard Gerold, Head of the Landscape Ecology Department at Göttingen University. Hiring me for a major research project in Western Brazil knowing that I still have to finish my PhD on a different topic at a different institution and nonetheless having near endless patience and providing substantial support for my PhD is much more than I could have ever asked for.

My main supervisor, Andrew Nicholas, deserves the unconditional credit for bringing me to Exeter, for putting the finger on the weak spots of this work, for clarifying countless technical issues of numerical modelling and for reviewing so many draft chapters in an often far too early state. I am also very grateful for the thoughtful comments made by my second supervisor, Adrian Collins (University of Southampton/Rothamsted Research and formerly ADAS), in particular for his thorough and extensive input in the very final stages of this thesis. A 'thank you' for her input also goes to my third supervisor, Katerina Michaelides (University of Bristol).

At various times and in different ways different people offered advice, ideas, dis-

traction at the right time, information for and/or help with their hands, including but not limited to shovelling and cleaning gravel and criss-crossing the River Culm in waders carrying the all so important scientific equipment. These are in no particular order: Adrian Bayley, Victoria James, Andrew Williams, Kim Mack, Steven Haley, Alan Putock, Rebecca Rixon, Miriam Glendell, Michael and Suzanne Grenfell, Florence Ferretti, Barbora Tomisov, Anne Riering, Heide and Gottlieb Lamparter, Dorothea Weller, Christoph Schubert-Weller, Olivia and Joe Hall, Sylvia Lags and Claire Steer.

A special thanks goes to those who spent their often very limited free time on providing feedback on my drafts and helping me to combat all the confusing sentences, wrong prepositions and inconsistent wordings: Chris Hutton, Victoria James, Hannah Bevis, Nicolas Dietrich (plus an extra 'thanks' for reviewing my LaTeX and BibTeX code), Johanna Jäger, Holger Vogt-Altena and Anika Grübel.

Finally without the all-embracing support of Julian Weller, this PhD would not have been completed. Amongst many other things, he read more draft versions of this thesis than can possibly been healthy and never stopped encouraging and counselling me, while taking care of the many life chores and tasks, above all our three sons. Especially in the last five months, our life was anything but easy, dealing with my exhaustion and many hours of absence in the evenings and on weekends. Last, but not least, I want to say thank you to Linus, Floyd and Isaak, who showed support and ignorance in the right dose for their mother's PhD. You always took very good care of me by gently reminding me not to take academia too seriously after all.

Contents

List of Tables

List of Figures

Abbrevations

A area in [m^2]

a slope of linear regression model

ADV Acoustic Doppler Velocimeter

$Area$ area of the flume experimental channel in [m^2]

$area$ area of a single patch in the suspended sediment deposition model in [m^2]

$ave5$ velocity value set derived from averaging velocity measurements at 5 cm distanece to the bed

b intercept of linear regression model

C Suspended sediment concentration in [g/L]

C_0 Initial suspended sediment concentration of an experimental run

C_{end} Suspended sediment concentration at the end of an experimental runs

$Closs_i$ Suspended sediment concentration loss at time i in [g/L] $Closs = C_o - C_i$

$Closs`_i$ normalised concentration loss $\frac{C_0 - C_end}{C_0}$

C' Dimensionless suspended sediment concentration $C' = \frac{C}{C_0}$

c_{Chezy} bed roughness coefficient after Chezy

$c_{White-Colebrook}$ bed roughness coefficient after White-Colebrook dependent on k_s and local d

$^\circ C$ degree celsius

$\triangle$ Delta, distance between two points

$\triangle_\rho$ density difference between solid and fluid $\rho_s - \rho_f$

d water depth, in [m]

d_{mean} average water depth of a reach, in [m]

dep deposition as descriobed in the Krone formulation [kg]

dis interpolated values

dis_i position of interrpolated value

D_{50} mean percetile of a distribution, grain size of distribution with 50 % coarser and 50% finer material, accordingly other percentiles are defined, e.g. D_{80} is the grain size where 80 % of distribution is finer and 20 % is coarser

D37 gravel bed with a D_{50} of 37 mm

D48 gravel bed with a D_{50} of 48 mm

Dpot potential deposition Dpot=$\frac{\text{Closs}*Vol}{Area}$

DEM digital elevation model

$\delta\rho$ surplus density of solid submerged in fluid $\rho_s - \rho_f$

f_D Darcy-Weisback friction coefficient

GPS Global Positioning System

GSD Grain Size Distribution

H Height (above the river bed) [m]

h hour

IBL Initial Bed Level, in [m] AMSL, points representing river bed

κ Karman constant, used in bed shear stress calculations with a typically value of 0.41

k_s Strickler roughness coefficient

LM Linear Regression Model

log logarithmic profile method to establish bed shear stress

λ calibration coefficient of the Krone formulation for deposition

M number of grid cells in downstream direction

mod label for data originating from model output (either hydrodynamic or numeric deposition model)

$mean$ velocity value set calculated from averaging velocity measurements at 5, 10, 15 and 20 cm distanece to the bed

μ dynamic viscosity

ν kinetic viscosity $\frac{\mu}{\rho}; \mu = \nu$ for water at 20 $°C$

NS Nash-Sutcliffe Model Calibration Coefficient

NTU Nephelometric Turbidity Unit

N number of grid cells in cross-stream direction

n number of data points in a data set

n_{Ma} Mannings roughness coefficient

obs label for data observed in the field or flume experiment

P fraction within a grain size class

P^- fraction finer than a grain size class

P^+ fraction coarser than a grain size class

PBIAS percetual bias, stadrad error set into relation to the average of the observed value

phi grain size on the Wentworth scale (Wentworth, 1928)

p_{gsc} fraction of grain size class of total C

Q discharge in [m^3/s]

Q30 and , Q50,Q80, Q100, naming of experimetnal runs with a discharge of 30, 50, 80 or 100 L/s repectively

R_{hyd} hydraulic radius of an open channel in [m]

R particle radius in [m]

Re Reynolds number; dimensionless coefficient describing inertial forces; Re =

RINEX Receiver Independent Exchange Format, used for localisation data of GPS reference stations

RMA Reduced Major Axis, line with slope of the standart deviation of the y-axis values divided by the standart deviation of the x-axis values, crossing through the point with $x = \bar{x}$ and $y = \bar{y}$

RMS Root Mean Square

rpm round per minute

r Pearson coefficient

r^2 coefficient of determination

ρ_f density of fluid in[kg/m^3]

ρ_s density of solid in[kg/m^3]

S grain size of a distinct grain size class

S^- lower limit of a distinct grain size class

S^+ upper of a distinct grain size class

S1 naming of experimetnal runs from the first Series

S2 naming of experimetnal runs from the second Series

TR trapping rates of a single trap given in [kg/m^2]

S_{hyd} hydraulic slope

TR_{mean} averaged trapping rates of a flume experimetnal run [kg/m^2]

TR' normalised trapping rate $TR' = \frac{\text{TR}}{\text{Dpot}}$

TIN Triangulated Irregular Network

TKE Turbulent Kinetic Energy

Txyz Turbulent Kinetic Energy method using velocity fluctuations in all three vector directions

Tz Turbulent Kinetic Energy method using velocity fluctuations only in downstream vector direction z

τ_0 Shear stress above bed [Pa]

τ_{cr} Critical shear stress of sediment in water [Pa]

u-velocity cross-stream velocity vector

V Volt, unit of electric potential

Vol total water volume of the flume

v_{mag} velocity magnitude

v velocity

v-velocity downstream velocity vector

v^* bed shear velocity $v^* = \sqrt{\frac{\tau_0}{\rho_f}}$

v_{cr} critical velocity of sediment in water

w_s settling velocity

WL Water Level, in [m] AMSL, points representing water surface

x-velocity velocity vector in M direction of a model grid

$\bar{x}_{am}$ arithmetric mean after method of moments

$\bar{x}_{gm}$ geometric mean after method of moments

$\bar{x}_{gf}$ geometric mean after Folk and Ward method

y-velocity velocity vector in N direction of a model grid

z_0 critical height above river bed, where flow velocity approaches 0

Introduction

This work investigates the dynamics of fine sediment within gravel bed rivers, where 'dynamics' refers to processes relating to fine sediment being transported in suspension or deposited in a river. The special focus of this work is the deposition of fine sediment within the interstices of the gravel bed and its re-suspension into the water column. The relevance of this research focus stems from the fact that serious concerns are frequently raised by hydrologist and aquatic ecologist relating to the degrading effect of fine sediment in riverine ecosystems. The thesis analyses interstitial deposition both with flume experiments and at three locations in the upper, middle and lower reaches of the River Culm, Devon, UK. Based on the physical description of suspended sediment deposition after Krone (1962) in combination with the the flume and field data, a numerical suspended sediment deposition model is developed in order to understand in how far established physical equations of fine sediment deposition are valid for the complex environments of gravel beds and beyond to predict spacial and temporal variation of fine sediment in the gravel bed.

To address this research task, the thesis is structured as follows. Chapter 1 (Research topic and the current state of scientific knowledge) gives an overview of the literature on the relevance, quantity and the prediction of interstitial sediment as part of the fine sediment budget. It also analyses the state of the art in river related fine sediment research and shows where this work fits in and goes beyond the current state of research. Chapter 2 (Flume experiments) reports on the results of flume experiments conducted to quantify interstitial deposition in relation to flow, bed and suspended sediment properties. In Chapter 3 (Flume scale numerical de-

position model), the results of the experimental flume work are used to setup and calibrate a numerical model for predicting suspended sediment concentration loss and interstitial deposition. Chapter 4 (Fieldwork) reports on the fieldwork conducted to investigate interstitial deposition at three sites of the River Culm. The collected field data consist of direct measurement of suspended sediment and interstitial deposition and data are used to setup hydrodynamic models for the field reaches. The purpose of the hydrodynamic models is the investigation of flow conditions for various discharge conditions. The setup and calibration of the hydrodynamic models for all field study reaches is explained in Chapter 5 (Hydrodynamic models). Finally, Chapter 6 (Reach scale numerical deposition model) presents the numerical deposition model, based on the model in Chapter 3. The model is adapted for the application on reach scale. Direct field data and the results of hydrodynamic simulations are used to calibrate this model. It is further applied to investigate temporal and spatial patterns of interstitial deposition for a scenario period in the three study reaches. The thesis then finishes with Chapter 7 (Conclusion and outlook), which discusses the achievements and shortcomings of this research and provides suggestions for further advancement.

Chapter 1

Research topic and the current state of scientific knowledge

1.1 Fine sediment in gravel-bed rivers

Excess supply of fine sediment is one of the most critical factors causing water quality degradation in rivers (see for example Bilotta and Brazier, 2008). This work brings into focus the fine sediment budget of rivers with a gravel-sized, porous bed substrate. For the purpose of this research, fine sediment is defined as clay- to sand-sized particulate matter with the ability to be transported in the river as suspended sediment (similar to the definition in Wilkinson et al., 2009). Special attention is drawn to the fine sediment deposited within the interstices of the gravel framework.

The source of suspended fine sediment is typically soil erosion, delivering fine sediment as sheet and rill flow into the stream (see for example Summer et al., 1998; Carling et al., 2001). In the most basic assessment of sediment dynamics, the delivered sediment passes through the river network as suspended sediment and is destined for an ultimate sink beyond the river's mouth. A more detailed conceptualisation includes the fine sediment dynamics within the river network; floodplain deposition, bank erosion and the highly dynamic in-channel deposition in the inter-

stices of the gravel bed and its re-suspension.

The short lived, variable nature of in-channel sediment deposits provoke considerable challenges, when one is attempting to measure it as a part of the fine sediment budget. Many authors point out the importance of interstitial deposits and the dearth of studies covering it, amongst others Frostick et al. (1984a); Sear et al. (2008); Collins and Walling (2006, 2007b). The following two sections first show the ecological impact of fine sediment in gravel bed rivers and then give an overview of previous studies on this topic. The review of case studies focuses on the inclusion of in-channel fine sediment as a component of the catchment fine sediment budget. The fine sediment budget of the River Culm is introduced in more detail because it is the location of all field research for this particular study.

1.1.1 Ecological relevance

Naturally, gravel bed rivers are environments with low suspended load (Greig et al., 2005). Unfortunately for the majority of gravel bed rivers in the UK, this is not true anymore. The increased fine sediment input into the river systems is usually attributed to soil erosion through intensification in farming (Walling and Amos, 1999; Haygarth et al., 2006). According to Wood and Armitage (1997) more than 50 % of fine sediment in rivers is attributed to poorly managed arable land. Intensification of farming includes, amongst other things, the use of heavy machinery, the lack of sufficiently wide buffer zones around rivers, the use of autumn sown winter crops and a shift towards fodder maize production, which exposes large proportions of the soil area to rainsplash and runoff during the spring sowing period (see for example Greig et al., 2005; Bilotta and Brazier, 2008). Agricultural intensification in the UK is exemplified by looking at the following numbers. The UK's farmland increased from 65 % after World War II to 75 % today with a simultaneous increase in production of 400 % (Robinson and Sutherland, 2002). Recent studies put soil erosion from grass lands into focus. Traditionally, grass is seen as an effective protection against

soil loss. The research of Bilotta and Brazier (2008) suggests otherwise. Their lysimenter experimental data shows high subsurface sediment runoff predominantly in the colloidal grain size range from intact grass lands. Similar concerns are raised by Haygarth et al. (2006). This group of authors from different disciplines claim that there is a strong contribution of stock grazing areas to fine sediment erosion. Not only do they believe this is a major and so far overlooked part of the fine sediment budget but they claim further that soil eroded from pastures is high in organic content and highly loaded with nutrients (for example P) and contaminants (such as pathogens), resulting in severe ecological effects for the receiving rivers. Although finger printing research suggests that in the UK the dominant source of fine sediment in rivers are cultivated areas (e.g. Walling and Amos, 1999; Collins and Walling, 2007a) other sources such as roads, constructions, mining, channel incision and bank erosion due to reduced bank protection can as well be highly relevant (see for example Golosov et al., 2004; Nelson and Booth, 2002; Collins and Walling, 2004). Above the fact, that soil erosion from cultivated land is a problem it itself (degradation of agricultural areas, loss of soil quality) it causes severe further effects on its transport path into and through the river network. Here it affects for example human constructions (e.g. the reduction of reservoir volume through sedimentation) and - most relevant to this work - it causes severe degradation of the riverine ecosystem (Owens and Collins, 2006).

Bilotta and Brazier (2008) categorise the degrading effects of fine sediment on the riverine ecosystem in four groups: (1) Turbidity light depletion, (2) Nutrient and contaminant availability, (3) Abrasion and clogging of organs and (4) Clogging of gravel pores by interstitial fine sediment deposition. Suspended sediment in the water column is mainly responsible for the effects in group (1) to (3). The possible effects of fine suspended sediment range from eutrophication and oxygen depletion through nutrients (as for example demonstrated by Greig et al. (2005) in relation to N through the mechanism of nitrification) to long term health effects caused by persis-

tent contaminants (due to accumulation in the adipose tissue of mammals they can reach dangerous concentrations over time as described by Foster et al., 1995). After Walling et al. (2003) around 90 % of the nutrient and contaminant fluxes in rivers are associated with fine sediment smaller than 63 μm. However, the exact dynamics of nutrient and contaminant distribution and release are complex. On a basic level, more sediment increases the chance of nutrient and contaminant release into the river ecosystem. Horowitz (2005b) showed the difficulties to find correlations between the magnitude of discharge and suspended sediment with contaminant concentrations. His solution is the determination of averaged values for specific sites in the US, which then can be combined with the sediment loads on-site to investigate the total delivery of contaminants. More details can be found in work such as Reynoldson (1987); Meade (1988); Horowitz et al. (1990); Landrum and Robbins (1990); Foster et al. (1995); Wood and Armitage (1997); Walling and Ongley (1998); Fetter and Fetter Jr (1999); Relyea et al. (2000); Kersten and Smedes (2002); Greig et al. (2005); Horowitz (2005a); Leeks et al. (2005); Owens et al. (2005) and Bilotta and Brazier (2008). Effects of group (4), are dependent on the suspended sediment's interaction with the river bed, in the so called hyporheic zone. The hyporheic zone is defined as 'the water saturated interstices of river bed deposits' (Orghidan, 1959, 2010, first published in German and only recently translated into English). Orghidan (1959) was the first to stress the importance of the hypoheic zone as a habitat for a multitude of animal groups (such as coelenterates (hydra), nematodes, oligochaetes, crabs, copepods, ostracods, syncarids, isopods, amphipods, tardigrades, insect larva and fish). The above listed riverine animals depend - at least in one part of their life cycle - on the sheltered conditions within the porous substrate of the river bed. Physical pore clogging caused by interstitial fine sediment ingress reduces the amount of available habitat. Furthermore, the clogging of pores causes a decline in the exchange of oxygenated water, causing a shortage of vital oxygen (Sear et al., 2014). Early research on the ecological effects of fine sediment

in gravel-beds dates back to the 1980s. A group of North American researchers raised concern regarding reduced salmonid reproduction (amongst others Beschta and Jackson, 1979; Carling and Reader, 1982; Carling, 1984a; Frostick et al., 1984a; Diplas and Parker, 1985; Alonso et al., 1988; Chapman, 1988; Lisle, 1989; Lisle and Church, 2002). It became apparent that the decline of wild salmon populations is foremost an effect of a lower production in their freshwater stages (Acornley and Sear, 1999). Nowadays, ecological concern about pore clogging includes a broader range of animals and also focuses on the survival of invertebrates. Still, there is ongoing research into the survival of salmonid species. A special research focus is on the incubation of salmonid eggs as the most sensitive life cycle phase (Sear et al., 2014). Research on salmonid spawning is concentrated on riffle sub-environments - the salmonid spawning grounds in so called redds. Greig et al. (2007) sees oxygen as the key parameter influencing embryo survival, which is again governed by complex processes, such as the respiratory requirements of the egg and the exchange of oxygenated water. Although only the ingress of fine sediment into the gravel bed (relating to group (4) effects) is directly investigated in this research, interstitial fine sediment deposits are a readily available secondary source of suspended sediment during flood events (Owens et al., 2005) and can increase the suspended sediment concentration and therefore intensify the degradation effects (1) to (3) during flood runoff. Grain size distribution, timing, intensity and duration of the sediment load are crucial for the estimation of the fine sediment effects (Rempel et al., 2000; Relyea et al., 2000; Bilotta and Brazier, 2008). Independent of the exact focus of a single study on interstitial fine sediment, the severe consequences of a surplus of interstitial fine sediment for the ecosystem river are widely accepted. As Greig et al. (2005) concludes (for salmonids) 'a much more fundamental reduction in fine sediment input into rivers is necessary to sustain healthy conditions'. Therefore, a deeper understanding of the temporal and spatial variability of interstitial fine sediment storage potentially aids with the implementation of more effective preventive measures

for controlling sediment mobilisation and delivery to river systems.

1.1.2 Gravel bed rivers and fine sediment

Gravel bed rivers in a broad sense, are rivers with a gravel substrate. The natural channel substrate is always the result of the balance between sediment supply and sediment transport capacity. Gravel bed rivers develop, if the dominant flow regime causes fine sediment to be flushed through the river and coarser gravel material to remain within the river. One of the most used classifications for rivers was developed by the US Department of Agriculture, Forest Service after Rosgen (1994) (see Klingeman, 1998). In this classification, gravel bed rivers are class C rivers. Typically their slope is less than 2 % and their meandering channel flows in well-defined floodplains. Generally, they are located in broad valleys with terraces and old channels covered by alluvial soils. Channel substrate is a porous gravel, which is only transported at high discharge. The downstream structure of the channel is a repeating riffle-pool-bar sequence. Riffles are straight stretches with shallow fast flow and pools are located in the meander bends with deep and slow flow. Gravel bars are located at the inside of bends and middle of riffles. Bars are typically exposed during low flow (Rosgen, 1994; Knighton, 1998). This classification does not give consideration to the diverse nature of conditions within a gravel bed river. A more detailed classification of habitats within gravel bed rivers can be found in the work of Padmore et al. (1998). This classification, based on field studies in North-East England, identifies single morphological units and the associated biotopes for each of these units. The high variability in hydro-morphological units found in gravel bed rivers results in a high biodiversity, making gravel bed rivers a diverse field of interest from both a hydrological and a biological viewpoint. In the UK, gravel bed rivers (in the sense of class C after Rosgen, 1994) are located in areas with high rainfall and runoff. They are found in high numbers in the maritime influenced areas in the west and north of the UK (see river map in Holmes et al., 1998). In these areas, the most

intensive rainfalls are found in autumn and winter. In their natural state, gravel bed rivers have very low fine sediment yields and support an abundance of freshwater fish (Greig et al., 2005). However, today the suspended fine sediment concentrations in gravel bed rivers in the UK often give rise for concern. The combination of a winter season with high rainfall and low vegetation cover results in a predisposition for soil erosion, especially for catchments with a high proportion of grass and farmland (see Haygarth et al., 2006; Greig et al., 2005, 2007; Sear et al., 2008, 2014). This suggests the winter season to be especially vulnerable to the effects of fine sediment delivery to rivers and associated risk on ingress into the river bed.

Table 1.1 presents data from several studies on interstitial fine sediment in gravel bed rivers. These studies were chosen on the basis of the classification of the river, the methods used to measure interstitial sediment and preferably the same fine sediment unit, namely kg m^{-2}. The table includes two fundamentally different methods to measure interstitial sediment: a re-suspension method and a trap based method. The re-suspension method gives instantaneous estimates of fine sediment content in the upper layer of the bed (typically 5 to 10 cm), whereas the basket traps are installed with a fine sediment free gravel framework and subsequently measure ingress over the period of deployment in the river bed (a more detailed description of the two methods can be found in Section 4.4). Some studies with a different specification of the interstitial deposition (e.g. given as total loads) were included due to their location or their relevance for this research project. These are placed at the bottom of the table. All studies measure significant amounts of fine sediment in the river bed. In the River Wylye, fine sediment storage was calculated to account for 15 % of the fine sediment budget (Wilson et al., 2005). In the River Nadder, fine sediment deposition was found to clog 17 % of the pores, exceeding the 5 % threshold suggested by Sear et al. (2014) as a threshold for good salmonid egg survival. The results of Skalak and Pizzuto (2010) using mercury analysis in river bed cores, suggest fine sediment storage of 17 to 43 % of the annual yield within the river channel margins. However,

the listed values of interstitial storage and deposition need to be interpreted with great care. Obviously, the results of the re-suspension method cannot directly be compared to the result of basket trap based methods. Further concerns are raised due to the lack of standardisation within these methods and a limited understanding of spatial and temporal patterns. With regards to the application of basket traps, Zimmermann and Lapointe (2005) believe, that although most studies use traps of a similar design, there is still a lack of standardisation and different metrics are reported (e.g. depth of traps, fine grain size considered). This lack of standard makes the comparison between the findings reported by different studies almost impossible. The studies listed in Table 1.1 give isolated statements about the spatial and temporal distribution of interstitial fine sediment. Regarding their distribution along the river morphology, Walling et al. (2003) found that the majority of fine sediment in the channel is associated with deeper pool areas and river margins. Although the winter period is associated with the highest suspended load, little is known about the seasonal patterns of interstitial fine sediment. Data of Walling et al. (2003), Wilson et al. (2005) and Collins and Walling (2007b) are examples, which do not show clear seasonal patterns. Other studies present results of fine sediment deposited in channels for only one part of the year, such as Owens et al. (1999) who measured only in summer or Lambert and Walling (1987) with one measurement in November and one in May. Arguments are found for both higher deposition in summer and in winter. On the one hand, the higher suspended sediment concentration during winter promotes more in-channel deposition. On the other hand, during the summer the gravel bed is stable and sediment is richer in organic material forming lasting fine sediment deposits accumulating over the whole season. This means, the concrete linkage between suspended sediment runoff and infiltration into the gravel bed is not yet understood sufficiently to predict deposition. With measurements already being difficult, the calculation and prediction is connected with even more uncertainties. Therefore, further investigations are needed.

1.1.3 Selection of the study area

This research project was based at the University of Exeter. There are several gravel bed rivers in the surrounding area. The River Culm was chosen for the following reasons: (1) It encompasses different gravel bed specifications from the upper to the lower reaches. (2) It is easy to access (with the M5 motorway running along the valley). (3) A large volume of research has already been undertaken on the river. This facilitated both the access to data and farmers and their land. (4) The catchment receives intensive rainfalls. For example the town of Cullompton, which is located centrally in the River Culm catchment, receives an annual precipitation of 1036 mm and has an average temperature of 9.3 $^{\circ}$C (Metoffice, 2014). The precipitation is highest during winter with more than 100 mm per month from October to January. (5) The land use of the catchment is dominated by pasture and farmland (e.g. fodder maize) and high annual fine sediment yields have been recorded (Lambert and Walling, 1988). Information on suspended sediment yields for the River Culm is available from two monitoring stations, one in the middle (Woodmill) and one in the lower reaches (Rewe). After Walling and Bradley (1989), the total annual fine sediment yield at Woodmill was 11859 t and 8514 t at Rewe. Suspended sediment peaks can reach concentrations as high as 1000 mg L^{-1}. The suspended sediment load is the most important component of the catchment sediment budget, with 97 % of the total sediment budget being finer than 63 μm (Lambert and Walling, 1987). After Hardy et al. (2000), bankfull discharge of approximately 18 m^3 s^{-1} is exceeded around eight times a year with the maximum discharge up to 40 m^3 s^{-1}. The typical particle size of suspended sediment for samples collected at Rewe comprises 77 % of particles smaller than 2 μ m compared to 65% in Woodmill (Walling and Bradley, 1989). In both cases, this material is much finer than material found in floodplain traps in the same study with 43-55 % particles smaller than 2 μm (Walling and Bradley, 1989). Phillips and Walling (1999) conducted a study measuring the effective and absolute grain size distribution of re-suspended interstitial sediment smaller than 63 μm.

Source / study	**River**	**method**	**fine sed. size**	**in-bed max measured**	**fraction of total sediment yield**	**basin**	**yearly yield (additional comments)**
			μm	kg m^{-2}	%	km^{-2}	t
Frostick et al. (1984b)	Turkey br.	traps	$<$63	1.6			
Lambert and Walling (1988)	Exe	re-suspension	$<$63	0.4	1.6		
Walling et al. (1998)	Ouse	re-suspension	$<$150			3315	16076
	Wharfe					818	1866
Owens et al. (1999)	Tweed	re-suspension	$<$63	0.64			
	Teviot			1.12			
	Ettrick			0.54			
	sum				6.6	4380	66010
Walling and Amos (1999)	Piddle	re-suspension	2-120	5		63	(weekly deposit max 3.5 kg m^{-2})
Wilson et al. (2005)	Leadon	re-suspension / traps	$<$63	3 / 3.54	193.2 (1.5)*	293	12748
	Tone			1.28 / 2.54	0.9	84	7512
	Torridge			2.04 / 2.54	1.4	258	16929
	Wylye			2.05 / 1.65	15.9	443	1756
Collins and Walling (2006)	Frome	re-suspension	$<$63	2.3			total storage: 1700 (May'03)
Piddle				4.3			1400 (July'04)
Collins and Walling (2007b)	Frome	re-suspension	$<$63	0.53-1.49			
	Tadnoll Brook			0.41-0.74			
	Cerne			0.73-0.94			
	Hooke			0.55-2.63			
	Piddle			0.39-4.34			
	Bere Stream			1.67-1.08			
	Devils Brook			0.26-1.45			
Sear et al. (2014)	Tyne	traps		1.54			
Acornley and Sear (1999)	Test	traps	$<$250	0.65 kg m^{-2} d^{-2}		1250	14875
				% pores			
Heywood and Walling (2007)	Nadder	traps		17			
	Wylye			10			
	Avon			12			
	Bourne			15			
Phillips and Walling (1999)	Culm	traps		0.1 kg m^{-2} in 4 days		273	

Table 1.1: Results of studies measuring interstitial fine sediment. Listing the source of information, the study river, the method used to measure interstitial sediment, the mean measured interstitial sediment in kg m^{-2}, if available the percentage of the total annual fine sediment yield and the annual sediment yield of the catchment

The absolute D_{50} of suspended sediment during the winter season was 11 μm compared to 8 μm in summer. For the effective grain size distribution, the D_{50} was much higher for both seasons with higher values in summer of 92 μm compared to

55 μm in winter. Lambert and Walling (1987) measured the organic content of the suspended sediment during storm runoff and of the floodplain deposits at Woodmill and Rewe. Remarkably, all values were similar and ranged between 7.02 and 7.93 %. The interstitial sediment measured by Phillips and Walling (1999) puts the River Culm well within the range of UK rivers with potential problems due to interstitial fine sediment ingress (see Table 1.1).

1.2 Flow and sediment transport processes

The transition of sediment in transport into sediment in deposition or vice versa is foremost described empirically (Le Roux, 2005). Nevertheless, most descriptions include a theoretical framework, when relating sediment transport to key measurable parameters. Sediment transport is determined by factors connected to flow conditions and factors connected to critical sediment properties. Flow related factors include discharge (Q), hydraulic radius (R_{hyd}), hydraulic slope (S_{hyd}), mean velocity (v_{mean}) and the bed shear stress (τ_0). Critical sediment properties include the amount or concentration (C), grain size (D), sediment density (ρ_s), settling velocity (w_s) and critical shear stress (τ_{cr}) or critical velocity (v_{cr}). Sediment transport functions parameterise the framework for the key interactions between flow and sediment and deliver a basis for the analysis of transport, deposition and erosion of fine-grained sediment.

1.2.1 Flow equations

The most relevant flow conditions represented in equations for sediment transport are velocity and bed shear stress. In rivers, velocity and bed shear stress are foremost dependent on Q, R_{hyd}, S_{hyd} and hydraulic roughness (often named c). In hydrodynamic terms, the flow in rivers is referred to as flow in open channels. Typically, the complex flow in rivers is simplified, especially for smaller rivers by assuming a

steady, uniform flow (Dittrich, 1998). The most commonly used equations to describe a steady and uniform flow in open channels are the Manning equation, the Chezy equation and the Darcy-Weisbach equation, with the latter being very similar to the Chezy equation. All three describe the relationship of the mean velocity (v_{mean}) to R_{hyd} (which is a measure of river depth and width) and S_{hyd}. All three equations include a coefficient for bed roughness, which is dependent on many properties, including sinuosity. The fundamental difference between the Manning and both the Chezy and Darcy-Weisbach equations is the influence of R_{hyd} on the flow as shown in Equation 1.1 for Manning, in Equation 1.2 for Chezy and in Equation 1.3 for Darcy-Weisbach. In the Manning equation, R_{hyd} is included to the power of $\frac{2}{3}$, whereas the equations of Chezy and Darcy-Weisbach include it to the power of $\frac{1}{2}$.

$$v_{mean} = \frac{1}{n_{Ma}} R_{hyd}^{\frac{2}{3}} S_{hyd}^{\frac{1}{2}} \tag{1.1}$$

$$v_{mean} = c_{Chezy} (R_{hyd} S_{hyd})^{\frac{1}{2}} \tag{1.2}$$

$$v_{mean} = c_{Darcy-Weisbach} (R_{hyd} S_{hyd})^{\frac{1}{2}} \tag{1.3}$$

The coefficient n_{Ma} in the Manning equation is an index of the river roughness. Based on the river character, it can be estimated (a guideline to estimate n_{Ma} can for example be found in Arcement et al., 1984). Methods to define c_{Chezy} are based on experience and use for example Manning's n_{Ma} and water depth H. $c_{Darcy-Weisbach}$ is defined as shown in Equation 1.4.

$$c_{Darcy-Weisbach} = \sqrt{\frac{8g}{f}} \tag{1.4}$$

with g being the gravity acceleration, f being dependent on the hydraulic radius, velocity and two coefficients, h_f and the the Darcy-Weisbach friction factor L; f is given in Equation 1.5.

$$f = h_f \frac{4R_{hyd}}{L} \frac{2g}{v^2} \tag{1.5}$$

The knowledge about v_{mean} is not sufficient to predict the occurrence of sediment deposition and erosion. The decisive velocity for these processes is the velocity immediately adjacent to the river bed. Velocity in an open channel develops a velocity profile between the free flow at the surface (V) and no flow close to the river bed at height z_0. Under laminar flow conditions, the vertical profile of a river can be seen as many single flow layers, where one layer is slowed down by the layer below (internal friction is a tangential force described by the dynamic viscosity of the fluid μ). The tangential stress between two layers is proportional to the velocity gradient. The lowest layer, referred to as the boundary layer, experiences the highest friction due to the close proximity of the river bed (Gordon et al., 2004). Under laminar flow conditions, the friction or bed shear stress (τ) is described using Newton's law.

$$\tau = \mu \frac{\delta v}{\delta H} \tag{1.6}$$

Typically for turbulent flow, three zones are differentiated: the viscous sublayer or boundary layer at the boundary with the bed and an outer region close to the free surface with a turbulent zone as the intermediate transition. In the turbulent zone and the outer region the interaction between the layers is diffuse and caused by eddy mixing (Chanson, 2004). Hitherto such a velocity profile can only be described statistically. For turbulent conditions and depending on the boundary layer thickness (δ_l), the velocity in the water depth profile can be calculated with the Blasius equation, see Gordon et al. (2004).

$$v = V(\frac{2H}{\delta_l} \frac{H^2}{\delta_l^2}) \tag{1.7}$$

The thickness of the boundary layer δ_l is approximately $10\mu\rho_f^{-1}V^{-1}$ (Chanson, 2004, p. 170). Detailed explanations of the representation above can be found in text books on Hydrology, such as Chow (1964); Linsley Jr et al. (1975); Dyck and Peschke (1989).

The equations above describe calculations of flow velocity. However, many fac-

tors for sediment transport relate to the distribution of bed shear stress, not velocity. There are various methods to calculate bed shear stress from velocity. A standard method is to deduct bed shear stress from the vertical alligned velocity profile, as described above, using the logarithmic velocity law (Schlichting et al., 2000; Van Rijn, 1984a) shown in Equation 1.8.

$$\frac{v}{u^*} = \frac{1}{\kappa} ln(\frac{H}{z_0}) \tag{1.8}$$

Where u^* is the bed shear velocity, H the height above the river bed and z_0 is the roughness length where flow velocity reaches 0 and κ being the Karman constant, for which typically the value of 0.41 is used (for example Biron et al., 2004; Petrie et al., 2010). u^* can be transferred into τ_0 as shown in Equation 1.9.

$$u^* = \sqrt{\frac{\tau_0}{\rho_f}} \tag{1.9}$$

A fundamentally different approach is the Turbulent Kinetic Energy (TKE) method proposed by Soulsby (1983) and Kim et al. (2000), which is also evaluated in Biron et al. (2004). The TKE method calculates bed shear stress using the fluctuation of the velocity measurements closest to the river bed, see Equation 1.10.

$$\tau_0 = c_1 * [0.5 * \rho_f * (< x'^2 > + < y'^2 > + < z'^2 >)] \tag{1.10}$$

with c_1 being a proportionality constant of 0.19 and x', y' and z' the fluctuation of each velocity vector (Biron et al., 2004). The application of both methods is demonstrated in 2.2.2.

1.2.2 Sediment transport equations and properties

There are numerous sediment transport equations generally describing the relation of settling forces (such as w_s) to transport forces (such as τ_0). Transport equations

can be grouped into equations describing bed load transport (typically of gravel sized particles) and suspended sediment transport (typically clay- and silt-sized particles). However, a totally distinct differentiation between bed load and suspension can not be defined. Garde and Raju see suspended sediment transport as an 'advanced stage of bed load transport' (2000, p. 226). Typically, bed load is transported in saltation. With continuous higher bed shear stresses the finer particles loose contact with the river bed and enter a state of suspended transport at approximately the same speed as the flow.

Transport equations for both bed load and suspended transport are based on one or more of the following four core concepts. (1) The most fundamental concept is the **threshold theory**. It assumes that a particular value of a flow parameter defines the threshold between the states (deposition or transport) of the sediment. The threshold theory is based on the work of Hjulstrom (1935). He developed a diagram relating flow velocity to grain size and delineated sediment erosion, continuous transport and deposition. A similar curve on the basis of dimensionless shear stress was developed by Shields et al. (1936). Such a threshold value is called a critical value and is for sediment transport typically v_{cr} or τ_{cr}. (2) The transition of a grain from a steady position into motion is researched with the concept of **incipient motion**. Most of the numerous studies in this area relate to bed load transport (again see Buffington and Montgomery (1997) with the review of the results of almost 100 studies). Transport is defined by a certain fraction of the sediment reaching a state of motion. Incipient motion tries to account for the fact that at a certain threshold, not all available sediment grains simultaneously start to move. Although incipient motion mainly focuses on the detachment of sediment particles, it clearly shows the gradual nature of all thresholds. (3) Another concept acknowledging the gradual nature of sediment transport is the assumption that a certain flow condition has a defined capacity to transport sediment. **Sediment transport capacity** (STC) is the maximum sediment load, which can be carried by a certain discharge (Prosser et al., 2001).

(4) A further approach to describe the relationship of flow conditions to sediment properties for transport is the formulation of a **probability function**. With changing flow conditions, a continuously larger fraction of available fine sediment is changing from one to the other state, for example used in Benda and Dunne (1997).

Bed load transport is often used synonymously with incipient motion studies, which intends to define the critical value for erosion. The first transport equations were developed with the help of incipient motion studies. A prime example is the Einstein equation: Einstein and Shen (1964) developed a sediment transport function based on the results of flume studies of incipient motion with Φ as the intensity of the bed load transport , see Equation 1.11.

$$\Phi = \frac{q_b}{S_{hyd}}(\frac{\rho_f}{\rho_s - \rho_f})^{\frac{1}{2}}(\frac{1}{gD^3})^{\frac{1}{2}} \tag{1.11}$$

Where q_b is the rate of bed load transport, ρ_s the density of the sediment, g the gravitational constant and D the particle diameter. The intensity of the bed load transport is a function of flow ($\Phi = f(\psi_*)$), described by the Einstein flow function, which is given in Equation 1.12.

$$\psi_* = \zeta Y(\frac{\tau^2}{\tau_{cr}^2})\psi) \tag{1.12}$$

With ζ as a hiding factor (accounting for the fact, that larger grains prohibit the erosion of smaller grains hidden between these), Y accounting for the bed roughness and ψ as given in Equation 1.13

$$\psi = (\frac{\rho_s - \rho_f}{\rho_f}\frac{D_{35}}{R_{hyd}S_{hyd}}) \tag{1.13}$$

The idea of sediment transport being proportional to the difference between shear stress and critical shear stress can be found in numerous transport functions, both for bed load and for suspended sediment. Alternative frequently used equations are the bed load transport after Meyer-Peter and Mueller (1948) (reproduced from Chanson,

2004) shown in Equation 1.14

$$\frac{q_s}{\sqrt{(s-1)gD^3}} = 0.66 \tag{1.14}$$

or bed load transport after van Rijn (1984) which defines a statistical relationship between the particle parameter $D*$ and the transport stage parameter T including the dimensionless pick-up rate (Φ_p) by Einstein and Krone (1962), see Equation 1.15

$$\Phi_p = 0.00033D*^{0.3}\, T^{1.5} \tag{1.15}$$

The statistical relationship is based on experimental results with a relative standard error of 30 % associated with the equation. However, research of Reid and Frostick (1986) suggests a more complex relationship between flow forces and bed load transport. Using a continuous recording bed load sampler, their research shows a wave like nature of bed load transport. They found that the flow forces causing incipient motion are roughly five times higher compared to the flow forces still competent to transport gravel at the end of a bed load transport wave. The theory of bed framework dilation (based on the findings of Allan and Frostick, 1999) adds a further level of complexity is. A change of the bed morphology is normally attributed to bed load transport. However, Allan and Frostick (1999) described a mechanism of bed dilation with flow forces below the threshold of bed load transport. This mechanism was investigated further by several researchers (see Brasington et al., 2000; Middleton et al., 2000; Marquis and Roy, 2012, further described in Section 1.3.1). Marquis and Roy (2012) formulated a consistent theory. They applied three methods to measure bed load transport (with Digital Elevation Models (DEMs), tagged gravels and bed load traps). By comparing the results of the three methods they could show that mechanisms prior to the bed load transport cause bed contraction due to winnowing of fines and bed dilation due to fine infiltration into the gravel framework.

Suspended sediment transport is often parameterised by using critical values for deposition. Especially in the case of gravel bed rivers, interstitial deposits re-suspension can not be seen as the opposite mechanism to deposition. In gravel bed channels, re-suspension of fine interstitial material is not connected to fine sediment properties, but to the transport properties of the gravel bed, which forms the framework for the ingressed fine sediment (Klingeman, 1998, Ch. 25). Suspended sediment transport equations typically work with the concept of the concentration profile ($\frac{\delta C}{\delta H}$). The concentration at a specific height above the river bed (H) is constant, if the following equilibrium equation is true:

$$w_s C + \epsilon_s \frac{\delta C}{\delta H} = 0 \tag{1.16}$$

with ϵ_s as the sediment diffusion coefficient (upward force) and $\frac{\delta C}{\delta H}$ as the sediment concentration gradient (for example in Garde and Raju, 2000).

The Krone formulation for suspended sediment deposition (dep) uses the near bed concentration and describes its probability of deposition as a function of τ_0 and τ_{cr} (Krone, 1962), see Equation 1.17.

$$dep = \lambda w_s C(1 - \frac{\tau^2}{\tau_{cr}^2}) \tag{1.17}$$

with λ as an empirical coefficient, $w_s C$ as the maximum downward flux of sediment and $\frac{\tau^2}{\tau_{cr}^2}$ as the proportion of sediment remaining in suspension.

An alternative equation is given by Van Rijn (1984c) for the suspended sediment transport Z

$$Z = \frac{w_s}{\beta \kappa u*} \tag{1.18}$$

with β as a coefficient including diffusion, κ the Karman constant and $u*$ the shear velocity.

Because the suspended sediment in the water column is transported at the speed of flow, suspended sediment transport can also be described in hydrodynamic equa-

tions. Gailani et al. (1991, 1996) for example used a vertically integrated transport equation, similar to the conservation of mass equation for hydrodynamics in 2D flow

$$\frac{\delta(HC_k)}{\delta k} + \frac{\delta(UC_k)}{\delta x} + \frac{\delta(VC_k)}{\delta y} = D_h[\frac{\delta}{\delta x}(H\frac{\delta C_k}{\delta x}) + \frac{\delta}{\delta y}(H\frac{\delta C_k}{\delta y})] + Q_{s,k} \tag{1.19}$$

with u being velocity in x direction (downstream) and v velocity in y direction (cross-stream), H being water depth, C_k the concentration of the grain size class k, D_h the eddy diffusity. Gailani et al. (1991, 1996) applied this equation in a numerical model of interstitial fine sediment deposition (see SIDO model in Section 1.3.2). Lauck et al. (1993), who is working specifically with fine sediment intrusion into gravel beds, developed empirical descriptors of interstitial sedimentation quantified by coefficients determined in experiments. He calculates fine sediment deposition as suspended particles raining randomly into the pore space of a gravel bed and moving potentially deeper from one bed layer to the next based on likelihood descriptors.This deposition description of Lauck et al. (1993) was applied in the numerical model of Wooster et al. (2008) and Cui et al. (2008).

Settling velocity and critical shear stress are at the core of the description of a suspended sediment profile and many fine sediment transport functions. Ultimately, fine sediment settling velocity and critical shear stress for a certain particle can only be defined correctly with the help of laboratory studies. Nevertheless, many scientists have gone to great lengths to develop deterministic equations with the support of empirical data. These approaches to determine settling velocities and critical shear stress are briefly summarised in the following two sections.

Settling velocity: Some authors, e.g. Krishnappan (1994), believe measuring settling velocity directly is the only valid option, since every sediment exhibits different characteristics. This was, for example undertaken in many settling column based laboratory investigations which measure concentration decline and the grain size distribution of those particles retained in suspension over time (such as Owen, 1976;

Gibbs et al., 1971; Loch, 2001; Guo et al., 2009). The equation of Stokes (1851) is the first and still most widely used equation to define w_s in dependence on D (Equation 1.20).

$$w_s = \frac{D_s^2 g \rho}{c_1 \mu} \tag{1.20}$$

Where μ is the dynamic viscosity of water and c_1 a constant of typically 18. Stokes law is only applicable for small Reynolds numbers ($Re \leq 1$), which describes laminar flow conditions, where the influence of viscosity is dominant (Ferguson and Church, 2004), small particle sizes ($D \leq$100μm) prevail and for rigid spherical sediments (see Loch, 2001). Referring to Stokes law, many studies have produced data to verify, extend the range of and adapt the law for different applications. A good example for such an adaption is the work of Clift et al. (1978), who developed four separate equations for different grain size ranges relating w_s to D. Similar work was conducted by Le Roux (2005) who also aimed to verify and improve Stokes law. Le Roux (2005) assessment of data relating w_s to D resulted in three separate relationships for three grain size ranges. Gibbs et al. (1971) revisited Stokes law with their own experiments using exact spherical quartz grains between 1 - 6000 μm . The comparison with this data resulted in a slight alteration of Stokes settling curve with similar settling velocities for silt and fine sand but progressively smaller settling velocities for coarser sand and gravel. Another good example for the alteration of Stokes law is the settling velocity after van Rijn (1984). He divides settling velocity calculations into three grain size ranges: Using Stokes law for the smallest ($D \leq$100 μ), Zanke (1977) calculations for grain sizes between 100 - 1000 μm and his own equation for larger particles up to 2 mm. Cheng (1997) attempted to formulate a valid equation for w_s in dependence on D for a wide grain size range. He used dimensionless settling velocity (w_s*) and dimensionless grain sizes ($D*$) and compared them to his own as well as data from the literature. His core findings are characterised by Equation 1.21.

$$\frac{w_s D}{\mu} = (\sqrt{25 + 1.2D^2} - 5)^{\frac{3}{2}} \tag{1.21}$$

Equation 1.21 needs an iterative solution. A universal solution for the whole grain size range without an iterative determination was introduced by Ferguson and Church (2004). Instead of comparing w_s* to $D*$, they compared w_s* to the dimensionless viscosity ($\mu*$). Further, instead of developing several equations for different grain sizes, they chose two equations describing settling velocity for the limits of the grain size range. For small grain sizes (clay), this was Stokes law, which includes a strong influence of the dynamic viscosity. For coarse grain sizes (sand), where viscosity is subordinate, a drag coefficient based on the description of w_s was found to be most suitable ($w_s = \sqrt{\frac{4rgD}{3c_2}}$). If these two equations are converted into a dimensionless equation, they result in the lower limit $\frac{1}{w_s*} = c_1\mu*$ and in the upper limit $\frac{1}{w_s*} = (0.75c_2 - 2)^{\frac{1}{2}}$. The combination of both equations results in Equation 1.22.

$$w_s = \frac{(\rho_s - \rho_f)gD^2}{(c_1\mu*) + (c_2 0.75(\rho_s - \rho_f)gD^3)^{\frac{1}{2}}} \tag{1.22}$$

For small particles, the first part of the numerator supersedes the impact of the second and vice versa for large particles the second part of the numerator is dominant. For c_1 = 18 and c_2 = 1, the equation results in very good fits to the literature and the researchers' own data and it is superior, especially for larger particles, to Cheng's equation (1.21). Despite the great advantages of a universal equation, it is important to consider the significance of cohesive and non-cohesive fine sediment and their difference in the effective and absolute grain size distribution. The effective grain size is the actual particle size as aggregates and flocs being bound together by electromagnetic properties. Absolute grain size is the size of a single mineral component of the sediment after the removal of bonds and organic material. The divergence between the effective and absolute grain size is especially relevant for the cohesive clay fraction in aquatic systems, often referred to as mud (comprising clay minerals and organic compounds Berlamont et al., 1993). The effective grain size of cohesive sediment can be considerable larger than the absolute grain size measured with most standard methods. This difference has already been demonstrated by the large dis-

crepancy between absolute and effective grain size measured in the River Culm by Phillips and Walling (1999). Baugh and Manning (2007) showed that settling velocity is crucially different for fine non-cohesive and cohesive sediment. They developed empirical equations for w_s dependent on τ for micro and macro flocs. Predictions of deposition using these w_s values were superior to those using other values from the literature. This means if w_s is deduced from exiting equations in the international literature, it is important to understand which sediment was used for the empirical derivation of this equation.

Critical shear stress and critical velocity: In its simplest form, for any grain of a certain size and density, this critical force corresponds to an exact value. There are some suggestions, how that settling velocity can be directly related to τ_{cr} for suspended particle deposition. An example is the direct use of w_s as the threshold condition ($u* = w_s$, Le Roux, 2005) or by applying empirical equations ($\tau_{cr} = 1.24 w_s^{0.33}$ for w_s <0.1 m s^{-1}, Collins and Rigler, 1982). Nevertheless, no generally accepted easy solution is currently available. Despite these suggestions, most determinations of τ_{cr} are based on the original or modified Shields curve. Shields et al. (1936) developed a diagram with the dimensionless critical shear stress ($\tau_{cr}*$) on the y-axis and the dimensionless Reynolds number ($Re*$) on the x-axis and identified a critical area. This area was later characterised using a curve by Vanoni et al. (1964). $\tau_{cr}*$ and $Re*$ are given in Equations 1.23 and 1.24.

$$\tau_{cr}* = (\frac{\tau_{cr}}{\rho_s - \rho_f} g D_{50}) \tag{1.23}$$

$$Re* = u * \frac{D_{50}}{\mu} \tag{1.24}$$

Since then, many researchers have attempted to prove and refine the Shields curve. For example, Miller et al. (1977) attempted to extend the Shields curve by three orders of magnitude (from D = 0.0000001-0.01 m or 10-100,000 μm). He used a large

number of published equations and data from several studies which are all based on experiments in straight channel flumes. Despite this extensive data collection, he concluded that none of the existing threshold criteria are universally correct. In the review of Miller et al. (1977), the iterative threshold curves of Inman, Bangold and Lane are considered in the work at hand. Self et al. (1989) set up experiments to test τ_{cr} for erosion and deposition for non-cohesive and cohesive sediment. Self et al. (1989) found that τ_{cr} for deposition is mainly a function of grain size for both cohesive and none cohesive fine sediment. Further, he converted the established τ_{cr} for deposition into critical velocity and compared it to Hjulstrom (1935). His values are about three times higher than the original Hjulstrom (1935) values. The v_{cr} of erosion determined by Self et al. (1989) is of the same magnitude as the one defined by Hjulstrom (1935). However, Self et al. (1989) experiments show a constant value for v_{cr} for erosion for all cohesive particles $<$180 μm compared to a increase for finer particles stated in Hjulstrom (1935). A reason for this is probably the complex behaviour of sediment of different grain size mixtures.

In conclusion, for the application of any sediment transport function, it is crucial to consider the grain size distribution of the sediment and the changing critical values according to particle size evolution. Also, additional sediment properties, such as cohesion, need to be considered, for example in the calibration coefficient. The application of a sediment transport function for a specific case can only be assumed to be valid with individual calibration.

1.3 Models of fine-grained sediment dynamics

Models, in a broad sense, are simplified representations of objects found in the physical world. Models are generally used to exemplify a critical process of interest. In a model, the researcher specifies the key parameters of influence and monitors the

model's reaction to this certain set of conditions. The aim is to use the model as a stand-in for the real world to test an assumption or to assist extrapolation. In sediment transport research, two complementing kinds of models are used: physical models or experiments and numerical computer-based models. The main difference between a physical experiment and a numerical model is the way processes are presented. In physical experiments, natural processes take place in a scaled copy of the natural environment. This means that natural processes, such as flow, control the sensitivity of the model. In numerical models, the same process needs to be described as a mathematical function. The following sub-sections briefly review how scientists have tested and applied sediment transport functions in both physical and numerical models.

1.3.1 Physical models

Burt and Walling (1984) as well as Church (1984) see physical experiments as an image of the real world. The former describe the process of an ideal physical experiment by completing several steps starting with an experience and forming an image of the real world in your head. This can then be conceptualised and formulated in a hypothesis. The experimental design aims to produce data to test the hypothesis. These fundamental step should enable the researcher to develop laws and theories, which consequently give an explanation for the investigated system. Physical models connected with sediment transport are mainly devised and tested in experimental flumes. Flumes are artificial channels with the possibility to regulate flow, bed and sediment supply. Their advantage beyond the possibility to influence key parameters is their accessibility compared to the field.

The following section introduces flume experiments conducted to investigate processes in connection with fine sediment erosion, transport and ingress into the gravel bed. There are two fundamentally different kinds of flumes: Flumes either consist of a channel with an inflow and outflow or have an annular channel. Flumes of the first

category are often straight channels with pipe recirculated or constantly renewed water flow (for example used in Einstein and Krone, 1962; Petit, 1994; Sambrook Smith and Ferguson, 1996; Shvidchenko, 2000; Wooster et al., 2008; Ali et al., 2011). Annular flumes are typically circular (as for example used in Lau et al., 2001; Haralampides et al., 2003; Chan et al., 2006; Maa et al., 2008) but other shapes, for example racetrack shapes are known as well (as for example used in Hendriks et al., 2006). Typically, processes connected to gravel beds are investigated in straight channels, whereas processes connected to the deposition and erosion of fine sediment are often examined in annular flumes. The use of annular flumes is especially relevant for cohesive sediment transport investigation which often includes processes of a longer timescale. For example processes developing over hours, like floculation would be disturbed when passing through the recirculating pipe in a straight flume system.

Flume studies for the initial motion of gravel beds are at the foundation of bed load transport equations. For example the bed-load transport function of Einstein is based on a series of flume experiments with various gravel beds and flow velocities (Einstein and Shen, 1964). This was done in almost the same manner for the equation of Meyer-Peter and Mueller (1948). Beside the investigation of general flow-transport relationships, flume experiments help to understand more small scale factors influencing gravel movement. For example, Kirchner et al. (1990) studied the effect of local topographical structures, such as the exposure and friction angles of the single grains on the transportability of gravels. Not surprisingly, even whole PhD-research projects are devoted to flume experiments determining probability functions for gravel particle displacement (Shvidchenko, 2000) or the testing of transport formulations in the literature (Piedra, 2010). Another group of flume experiments is designed to test the influence of different grain size fractions on particle mobility. Petit (1994) performed flume experiments to investigate the influence of uniform and mixed gravel grain sizes on incipient motion. Curran (2007) studied different mixtures of sand and gravel. This work suggested that the amount of sand supply changes the mobility of

gravel beds. In her study, a higher proportion of sand resulted in a lower τ_{cr} for both gravel and sand. Sambrook Smith and Ferguson (1996) also used bimodal sediment of sand and gravel size to investigate the influence of slope on the size distribution of bed surface particles. This work showed a continuous fining of the bed surface with a lower slope.

Studies investigating fine sediment deposition and erosion are of special relevance for this research. The determination of thresholds for suspended sediment deposition under flow is generally based on flume experiments. These experiments are often orientated on the Hjulstrom diagram for critical velocities (Hjulstrom, 1939) or the Shields diagram of critical shear stress (Shields et al., 1936). A good example is the work of Vanoni who conducted detailed fine sediment deposition and erosion experiments in a flume and included a defined curve for the critical values instead of the original area in the Shields diagram (Vanoni et al., 1964). Self et al. (1989) undertook similar work in relation to Hjulstrom. The experiments of Self et al. (1989) were conducted with non-cohesive crushed quartz particles of $<$0.18 mm. The data showed that the two curves in the Hjulstrom diagram are only valid for cohesive sediment. Non-cohesive sediment of clay and silt size (like the one Self used) did not show a divergence between critical values for deposition and erosion. A study setting out to prove the validity of flume experiments for fine sediment transport is Pope et al. (2006). This study showed in an annular flume with various natural fine sediment that τ_{cr} for erosion (here established with the TKE method) is similar to those measured in the field. Therefore, annular flumes can be seen as an adequate tool to investigate τ_{cr} for fine sediment. Other studies set out to investigate the more complex nature of cohesive sediment. For example Krishnappan (1994) conducted cohesive fine sediment experiments in a rotating circular flume and defined mean critical values for deposition and erosion for a wide range of grain sizes on the basis of concentration and suspended sediment effective grain size distribution data. Subsequently, he summarised his results by using them to setup and calibrate a

mathematical model of sediment deposition (Krishnappan, 2006). Similar work was undertaken by Chan et al. (2006) as well resulting in a comprehensive data set of τ_{cr} for cohesive sediment. Maa et al. (2008) have a different focus. An annular flume was used, which results in a distribution of shear stress between the shorter inner and longer outer ring. The experiments showed different levels of sediment concentration loss and a varying width of the area of deposition for different shear stress distributions. Moreover, the experimental results could show that deposition of fine sediment is not affected by the flow depth, but only by the conditions directly above the deposition surface (sediment concentration and shear stress). Apart from the determination of critical values for fine sediment, flume experiments have, for example, been conducted to test the applicability of different methods. For example Hosseini et al. (2006) successfully applied an Acoustic Doppler Velocimeter (ADV) in an annular flume for velocity and synchronous C and D measurements for suspended sediment. With this technique, the settling velocities for different D can be estimated more easily.

A comparatively small number of flume experiments directly investigate the ingress of fine sediment into gravel beds. Einstein and Krone (1962) pioneered in this area. They investigated deposition of suspended sediment for different velocities above a gravel bed. Similar studies were conducted by Wooster et al. (2008) with large flume experiments testing bed load transport and fine sediment intrusion as a model for dam removal. Also Grams and Wilcock (2007) conducted flume experiments with an artificial, fixed and regular gravel bed to investigate sand intrusion under various flow conditions and feeding rates. Beschta and Jackson (1979) ran 21 flume experiments with a gravel bed and a constant sediment feeding rate of sand. They used two different sands, a coarse mixture with a D_{50} of 0.5 mm and a finer with 0.2 mm. The experiments showed a buildup of a seal for the coarser sand with the depth of the seal dependent on flow velocity. Higher flow velocities resulted in a deeper seal. This is probably due to the 'jiggling' of the gravel, which assists sand to intrude deeper

via kinematic sieving. Finer sand resulted in a bottom up infill of the gravel pores. Further research into the area of processes prior to the threshold of gravel entrainment was realised in the flume experiments with sand gravel mixtures of Allan and Frostick (1999). They used photographic analysis to investigate processes at three flow conditions (just above the thresholds of sand entrainment, just above the threshold of gravel entrainment and at conditions with flow forces considerably higher than both these thresholds). They found dilation of the gravel bed to take place just prior to its entrainment. In their work Allan and Frostick (1999) did not specify if dilation is connected to the process of fine infiltration in or winnowing from the gravel framework. A significant expansion of the gravel bed framework at forces below threshold of entrainment was verified in further experiments (Brasington et al., 2000; Middleton et al., 2000). Brasington et al. (2000) could show with extensive video analysis of laboratory flume experiments that dilation of the gravel bed results in a rapid infiltration of fines. However later work by Marquis and Roy (2012) (in a natural stream) could show that both winnowing and infiltration can result from bed dilation without bed entrainment. Above the experimental findings of physical models, many flume experiments are set up to deliver directly calibration data for numerical models. These are discussed in the context of the numerical model in the following subsection.

1.3.2 Numerical models

Due to progress over recent decades in computation, fluvial models are now able to enhance our ability to represent key fluvial processes (Peckham, 2003). Merritt et al. (2003) give an extensive review of existing computer software-based erosion and sediment transport models. This review distinguishes three main types of models: empirical, conceptual and physically-based. For most models, a clear allocation to one category is not possible since features of all three groups are commonly represented. In the main, sediment dynamic models are physically-based with empirical relationships used to present those areas of limited physical under-

standing or complex interdependencies. Independent of the type of model, sediment dynamic models include two fundamental parts: A component describing flow and, secondly, a component describing sediment behaviour. Other processes, e.g. the mobilisation and delivery of nutrients, can also be included. After Peckham (2003), for a physically-based model, the two fundamental components (flow and sediment behaviour) can be covered with four fundamental equations: A mass conservation equation, the definition of flow in the down slope direction, a flow resistance formulation and a sediment transport formulation. For many of the models considered here, the flow component is simulated with a hydrodynamic software tool (for example Delft3D or HEC-RAS in Bouma et al., 2007; Pattison et al., 2012, repectively) and the output of the hydrodynamic simulations is processed in a separate sediment transport component of the model. Both flow and sediment components need to be calibrated to adapt the model to each specific application. Typically, this is accomplished with the help of field data or data derived from physical experiments. A prime example is the work of Bouma et al. (2007) who investigated fine sediment deposition around epibenthic structures in maritime environments. The calibration data consisted of a range of direct field data, experimental data derived from artificial epibenthic structures made of bamboo sticks in the field and from a flume. The sediment transport component of a model can encompass the processes from source to sink, which comprise erosion, transport and deposition. Predominantly, these processes are seen as functions of the sediment grain size. Wilcock (1998) states that many sediment transport models define one representative grain size. However, in many cases, one grain size fails to represent the actual characteristics of transported sediment and, consequently the transport of the finer fraction is underestimated. This becomes especially clear when observing the fundamentally different modes of transport of clay particles in suspension and gravel grains in saltation. A fraction-by-fraction approach often fails due to the lack of local grain size distribution data. In his paper, Wilcock (1998) introduces a solution by representing

the sediment in two fractions smaller and larger than 2 mm. These two fractions are generally easy to identify in the field. He found that the two grain size ranges have fundamentally different thresholds for erosion and deposition. In addition, Wilcock (1998) could show that the proportions of the two fractions did influence the transportability of both fractions, similar to the bed experiments with sand and gravel conducted by Sambrook Smith and Ferguson (1996) and Curran (2007). Wilcock concluded that, up to a fine sediment content of 20 %, gravel is interlocked in the bed framework. For a fine sediment content higher than 40 %, the river bed can be seen as a fine sediment matrix with clasts of gravel. Accordingly, he found a steep decrease of critical shear stress of erosion for both fractions at the point where the gravel framework gets detached from itself, which is between 20 and 40 % fines content. Other authors; such as Gailani et al. (1991, 1996); applied three grain size classes for modelling sediment transport. In the model of Gailani et al. (1991, 1996), the flow component consists of a vertically integrated 2D flow and also includes the transport and deposition of suspended sediment using a conservation of momentum equation. The re-suspension of fine sediment is the sediment component of the model and is dependent on shear stress and a site specific calibration coefficient. Lopes and Lane (1988) introduced a model with simultaneous calculations of fine sediment entrainment (with a rain intensity and a shear stress based component) and deposition resulting in a net sediment flux into the river flow. Soil detachment parameters and coefficients for depositions were derived from physical experiments. Other models focus on one part of the sediment transport. For example, the PSYCHIC (Phosphorous and Sediment Yield CHaracterisation In Catchments) model is a soil erosion and sediment delivery model with an additional component for phosphorous mobilisation and release. PSYCHIC calculates sediment delivery to, but not routing through, the river channel (Collins et al., 2007; Davison et al., 2008; Collins et al., 2009a,b). At the other end, the model introduced in Benda and Dunne (1997) investigates the fate of large amounts of fine sediment introduced to a channel dur-

ing one event (for example a fire or landslide). They describe sediment transport as a probability function of the travel length of material of a single absolute grain size.

There is a range of fine sediment deposition models applied to other environments, predominantly marine estuary and lagoon environments or floodplain sedimentation (see for example Douillet et al., 2001; Hardy et al., 2000; Woodruff et al., 2001; Lumborg and Pejrup, 2005; Bouma et al., 2007; Baugh and Manning, 2007) Nicholas and Walling (1998); Hardy et al. (2000). These are all characterised by a slower and more uniform flow environment and are mainly concerned and calibrated with data of a much longer time frame (e.g. seasons, years or decades). Only very few models concentrate on fine sediment deposition in the interstices of the gravel bed with a high temporal and spatial reolution, the focus of this research. The best documented model is SIDO (Sediment Intrusion and Dissolved Oxygen transport), based on Gailani et al. (1991); Havis et al. (1993). SIDO was developed from the Salmon and Spawning Analysis Model (SSAM) and a HEC-6 model by Alonso et al. (1988) for the Tucannon River. SIDO is a physically-based numerical model, predicting sediment transport and intrusion and the consequences for salmonid egg-survival based on intragravel oxygen levels (as described in Section 1.1.1). Fine sediment deposition in SIDO arises only from the suspended sediment in the overlaying water column, it treats the river bed (representing the gravel matrix at reach scale plus redds) as a fixed structures and focuses on sediment $<$1 mm, which is summarised in one effective grain size for the complete sediment range. Infiltration of the suspended sediment into the gravel bed is based on the difference between local near bed and averaged suspended sediment concentration (Sear et al., 2014). Havis et al. (1993) reports an application of the model with calibration data including flow conditions above an artificial redd, measured sedimentation rates based on ingress into retrievable basket traps over the salmonid spwning season. Havis et al. (1993) shows that SIDO delivers good results for the fraction $<$63 μm.

SIDO was originally developed for North America. In recent years, a research

group at the University of Southampton adopted the model for UK rivers (Sear et al., 2014). The preliminary adaptation of SIDO for the UK was based on the recalibration of the hydrodynamic component of the model with data for three rivers with different flow regimes, for example the River Ithon, Wales (Pattison et al., 2012). Further calibration data was generated with the help of flume studies aimed to understand fine sediment deposition in salmonid redds. Sear et al. (2014) reports that the numerical model stability was improved by applying HECRAS to model the models stream hydrodynamic in daily time steps (Pattison et al., 2012). Pattison et al. (2012) applied the model to a 153 day period on the River Ithon with a high average discharge of 13.02 m^3 s^{-1} and above-average mean suspended sediment concentrations of 81 mg L^{-1}. Infiltration calibration data was based on investigations using five artificially constructed redds. Both the SIDO model and the experimental data showed a complete infill of the gravel pores during the period of deployment. This was accompanied by a drop in dissolved oxygen level and a reduction of interstitial flow to less than 20 % of the initial value. The application of the SIDO model to such an extreme infill period did result in a good model performance, but does not answer any questions about intermediate levels of sedimentation and concominant salmonid egg survival. The application of SIDO demonstrated in Sear et al. (2014) showed very good results for the accumulation of fine sediment in the artificial redd. Modelled sedimentation filled 7.5 % of the pore space compared to 8.3 % observed in the field. The modelling of oxygen levels was less successful. Factors changing oxygen levels represented in the model seemed to be outperformed by factors not included in the model. Sear et al. (2014) believe the reason for this is upwelling groundwater with a much lower O_2-saturation. Whereas these recent applications of SIDO in the UK show the potential of the model, the performance also underlines the importance of higher resolution data for sediment ingress and detailed assessment of epochs of potential egg lethality.

1.4 Aims and implementation of the research project

Suspended and interstitial fine sediment in the riverine environment is of high ecological relevance. Typically, degrading effects due to a surplus of fine sediment take place during short time periods and at specific locations. Yet, we know very little about the temporal and spatial distribution, especially of interstitial fine sediment. While a number of equations describing the process of fine sediment transport and deposition are published, their applicability specifically to the gravel bed environment is not yet sufficiently tested. Therefore, this study aims to collect a high resolution spatial and temporal data set of both interstitial fine sediment deposition and the environmental conditions controlling it (e.g. flow and suspended fine sediment dynamics). This data is then used to setup a numerical model based on established fine sediment deposition theory. The model serves two aims: First, it allows us to systematically investigate the applicability of the chosen fine sediment deposition equation in the gravel bed environment and, second, to predict amounts and variability of interstitial fine sediment.

With regard to interstitial fine sediment in natural gravel bed rivers, comparative measurements for different river reaches are only indirectly reported in the literature (for example for the River Frome and its tributaries by Collins and Walling, 2007b). Also, our understanding of seasonal and short term variability is very restricted. Therefore, the field work of this research project aims to answer the following questions:

a) Do the different reaches of a river (upper, middle and lower reaches) behave differently with regard to the amount and the timing of fine sediment storage and how is sediment deposition in the different reaches connected to the local hydrograph and suspended sediment concentrations?

b) Are there periods in the year with overall higher in-bed fine sediment storage?

c) How high is the variability within a river reach with regard to in-bed fine sedi-

ment storage?

d) How is the variability of in-bed fine sediment storage related to the bed framework grain size, bed morphology and local flow?

The research project identified the River Culm to be a suitable candidate for the fieldwork location, due to its reported high fine sediment transport and storage, its variable nature of the river from source to mouth, its accessibility and the existing infrastructure. In order to answer questions a and b, three locations along the River Culm are equipped with stage and turbidity probes. The gravel framework grain size is mapped in the three reaches (question d). Further, the fine sediment storage is sampled in regular intervals with the re-suspension method, similar to the *re-suspension* studies listed in Table 1.1. Beyond this general approach, a more detailed sampling of fine sediment ingress with retrievable basket traps (similar to the *trap* studies listed in Table 1.1) aims to investigate questions c and d. The detailed sampling is implemented during the winter flood season with the highest potential for soil erosion, the most dynamic sedimentological and hydrological events and the season of fish spawning. The majority of the retrievable basket traps is installed on riffles, because they are the most vital habitat (Sear, 1993; Wood and Armitage, 1999; Soulsby et al., 2001) and the area with the most intensive fine sediment ingress and re-suspension (Lisle and Hilton, 1992; Diplas, 1994; Sear et al., 2014). The traps are applied during several periods. For each period, the traps contain the same gravel and are placed at the same position in the river. Information on how far these environments are charged with interstitial sediment is particularly valuable for the interpretation of the potential environmental threats, especially in combination with the field suspended sediment and discharge records. In order to regionalise flow information from stage measurements for the whole river bed of the study reaches, auxiliary hydrodynamic models are set up. The hydrodynamic models base on a detailed differential GPS bed survey and are calibrated with distributed flow velocity and water level measurements.

The fine sediment ingress in the gravel framework is dependent on rapidly changing conditions. This means periods of continuous deposition are much shorter than the periods of trap application in the field. Direct flow measurements and short trap application periods in the field during floods with high suspended sediment loads are not feasible because the river is inaccessible during such events. Therefore, fine sediment ingress with a higher temporal resolution and conditions closer to the traps are investigated with identical retrievable basket traps in laboratory flume experiments. The flume experiments are designed to mimic conditions found in the field, also with regard to scale. Therefore, the gravel grain size distributions and bed height alterations are of a comparable magnitude than those found in the field. Besides, in a flume setup the number of influence factors can be reduced and single factors can be investigated by altering each factor individually (e.g. the grain size of the suspended sediment, the gravel framework grain size, the flow velocity and the bed morphology). The measurements in the flume allow us to answer and, ideally, quantify the relationships of the following questions:

e) What is the deposition behaviour of distinctly different suspended sediment mixtures (silt and sand) under different flow conditions?

f) How does fine sediment deposition change over time?

g) Does the bed framework grain size distribution change the suspended sediment deposition?

h) What is the local influence of bed morphology on local fine sediment ingress?

i) What is the influence of the fine sediment grain size distribution on deposition? Is the effective grain size distribution more meaningful for the interpretation of fine sediment ingress processes than the standard measured absolute grain size distribution?

The flume experiments compare the behaviour of two distinct fine sediment mixtures, two distinct flow velocities (question e) and two distinct bed grain size distribution of

an alternating bed (question g and h). During these experiments, flow conditions (velocity), suspended sediment distribution and its grain size distribution (question e) are measured in regular intervals. The traps are positioned at different positions of the bed morphology in pairs. The trap pairs are sealed off at different times during the experiments (question f). For each experimental run, the bed alteration and trap positions are replicated carefully to ensure matchable conditions.

Beyond the analysis of relationships in the field and the flume experiments, a numerical model based on the Krone (1962) formulation is developed and subsequently calibrated with flume and field data. The calibration procedure aims to answer the following questions:

j) Is an established fine sediment transport theory in combination with critical values from the literature an adequate tool to describe and predict fine sediment deposition in the flume environment?

k) Which parameters need to be adapted and extended in order to coherently explain the measured data?

l) Are relationships found in the flume environment also applicable to processes in the field?

m) What is a simple and feasible numerical representation of the fine sediment re-suspension?

o) Is the resulting model able to explain and predict spatial and temporal patterns of fine sediment ingress and storage coherently?

In order to answer question j and k, the model is calibrated with the available flume data and a wide range of literature data for critical values to establish suitable parameters determining deposition speed. A successful calibration indicates an accordance of the established deposition theory and the experimental findings. Second, the parameters performing best in the flume scale model are then used in an upscaled model application for the reach scale to answer question l. Also, a threshold

of re-suspension is introduced. This threshold is determined through the calibration of the reach scale model with field data and the results of the hydrodynamic models. The calibration of the upscaled model shows if the upscaling is legitimate and if a simple re-suspension threshold can be an adequate tool to describe the presumably complex mechanism of fine sediment re-mobilisation from the gravel framework (question m).

With regard to the structure of the thesis, flume and reach scale investigations are discussed in two separate parts. The first part consists of the description and discussion of the flume experiments (Chapter 2) and the flume scale numerical deposition model (Chapter 3). The second part consists of the description and discussion of the conducted fieldwork (Chapter 4), the setup and calibration of the auxiliary hydrodynamic models (Chapter 5) and finally the consolidation in the reach scale numerical deposition model (Chapter 6). The final Chapter 7 concludes in a discussion about the achievements and shortcomings of this research and especially the numerical model. Further, it makes suggestions for advanced research in the area of interstitial fine sediment dynamics.

Part I

Flume scale investigation

Aim of flume investigation

The investigation of processes connected to interstitial fine sediment deposition faces significant challenges regarding adequate measurement techniques, especially in the field. First, the timing of sampling is sensitive, since for example hydraulic conditions determining the fate of fine sediment are very variable, in particular close to the river bed. Additionally, measuring fine sediment quantities and characteristics is very complex and laborious. Sampling methods are prone to errors due to the transient nature of fine sediment in transport and deposition. In a field situation, the danger of access during flood events and the re-suspension of the deposited interstitial fine-grained sediment through the sampling procedure are just two examples. In this light, flume experiments are widely used because they allow us to control key parameters, to reduce complexity and to create an environment where measurements can be taken relatively easily compared to natural sites. However, flume experiments using fine sediment suspension in combination with gravel beds are sparse. Experiments either study the motion of gravel (e.g. Kirchner et al., 1990; Petit, 1994), intrusion of sand into gravel beds (e.g. Einstein, 1968; Beschta and Jackson, 1979; Self et al., 1989; Sambrook Smith and Ferguson, 1996) or investigate the silty fine sediment deposition onto a flat bed (e.g. Einstein and Krone, 1962; Lau and Krishnappan, 1992; Maa et al., 2008). Experiments measuring deposition of fine silty sediment into gravel beds are only indirectly mentioned in the literature for example in combination with the setup and calibration of the SIDO model (Alonso et al., 1988; Pattison et al., 2013; Sear et al., 2014). Therefore, aim of the experimental part of this work is to develop and implement flume experiments that investigate both, sand and silt intrusion into a gravel framework.

Paramount is the quantification of silty fine sediment intrusion into the gravel bed. In particular, the question is, what influence has the overall flow, the local flow (introduced by altering bed elevation), the grain size distribution of the suspended sediment and the grain size distribution of the gravel bed on the deposition behaviour. A

more detailed question of special interest is the definition of the grain size distribution of the suspended fine sediment. Either it is measured including all aggregates and flocs (effective) or aggregates and flocs are broken down in their mineral components (absolute grain size distribution) before measurement.

The investigation of fine sediment intrusion in gravel bed is concepualised with the use of the Krone formulation for fine sediment deposition (which was developed for flat beds). The setup and measurement routine of the experiments include all parameters of this equation. Beyond, the data gathered in the flume experiments will be used to setup a numerical model. This numerical model bases also on the Krone formulation and on the concept of patches which can be regarded as uniform regarding their fine sediment deposition behaviour. With regards to the structure, Chapter 2 outlines the relations that need to be quantified and summarises the setup, the implementation and the results of the flume experiments. Chapter 3 describes the setup and calibration of the flume scale numerical suspended sediment deposition model, calibrated with the data of the flume experiments.

Chapter 2

Flume experiments

This chapter reports on the flume experiments carried out to investigate interstitial deposition of suspended sediment. The experiments carried out in this study aim to represent a range of natural gravel beds, fine sediment (with focus on silty grain size ranges) and flow characteristics. The main objective of these experiments is to aid the understanding of the pathways of fine sediment using a mass balance framework that accounts for the input, transport and deposition of fine sediment under various environmental conditions. More specifically, the aim of this work is to quantify:

- Temporal changes in suspended sediment concentration during experiments and their dependence on the fine sediment grain size distribution, velocity and shear stress,
- spatial patterns of deposition and their dependencies on local bed properties and flow characteristics, caused by alterations in the river bed.

This chapter is divided into four sections. Section 2.1 presents the theoretical background, which supports the investigation. It formulates hypotheses regarding the relationships of key parameters and defines the variables measured during the experiments. Section 2.2 describes the experimental facility, in which the research is carried out, outlines the two series of experimental runs and explains the sampling conducted during the experiments. Section 2.3 presents the results of the flume

experiments with a focus on four areas: First, the quality and reproducibility of the experimental runs; second, the velocity and shear stress distribution; third, temporal changes in the sediment concentration and grain size distribution of suspended sediment during the course of the experiments; and fourth, amounts of fine sediment deposition. Section 2.4 then provides an overview of these results.

2.1 Deposition theory and hypotheses

Section 1.2.2 outlines several equations, which describe sediment transport, including the Krone formulation (1962) for suspended sediment deposition (dep). The Krone (1962) formulation is believed to include the main physical determinants driving fine-sediment deposition. Therefore, this equation is used as the base for a systematic interpretation of the data, also by means of a numerical model. It states that rise in suspended sediment concentration, settling velocity and also decline of flow velocity or bed shear stress all lead to an increase in suspended sediment deposition. The fine sediment deposition model for gravel beds developed in this research and discussed in more detail in Chapter 3. Consequently, the experiments need to investigate the parameters in the equation to deliver calibration data plus infromation that is typical for gravel beds (in this case the gravel grain size distribution). The Krone formulation is either used with regard to velocity, see Equation 2.1, or with regard to shear stress, see Equation 2.2 to describe the competence of the flow to transport sediment. λ is a calibration coefficient, C is the suspended sediment concentration in g L^{-1}, w_s is the settling velocity of the fine sediment in m s^{-1}, v is the flow velocity and v_{cr} is the critical velocity (both in m s^{-1}), τ_0 is the bed shear stress, and τ_{cr} is the critical shear stress (both in Pa).

$$dep = \lambda * C * w_s * (1 - (\frac{v}{v_{cr}})^2) \tag{2.1}$$

$$dep = \lambda * C * w_s * (1 - \frac{\tau_0}{\tau_{cr}}) \tag{2.2}$$

The key of the Krone formulation is that deposition shows a positive relationship with suspended sediment concentration and settling velocity. Additionally, deposition decreases when flow velocity or shear stress increases until velocity, or shear stress, is equal to a critical value and further deposition is impossible. Both critical values (v_{cr}, τ_{cr}) and w_s are related to the properties of the fine sediment (primarily the grain size). This implies that it is not sufficient to represent a fine sediment mixture with one value of v_{cr}, τ_{cr}, and w_s , where the sediment is composed of a range of grain sizes. Consequently, the Krone formulation should be applied to several distinct grain size classes with the total sediment concentration distributed between these classes. The Krone formulation does not include a separate quantification of fine sediment re-suspension. Net re-suspension of fine sediment from the bed is assumed to take place only when the gravel bed of the river is itself mobilised. The critical velocities and critical shear stresses to move the much larger gravel particles are not considered in the context of the flume experiments, since flow conditions were never sufficient to move the gravel bed.

In order to produce a comprehensive calibration data set in order to apply the Krone formulation to the gravel bed environment, the following components need to be investigated:

- Suspended sediment concentration (C), its distribution and development,
- grain size distribution of suspended and deposited sediment (because it is critical for w_s, v_{cr} and τ_{cr}),
- hydraulic conditions in the water column at different levels above the bed (in order to calculate the bed shear stress τ_0 as a function of the velocity gradients and to investigate the influence of average and near bed velocity - v)
- hydraulic conditions above alterations of the river bed (causing acceleration,

deceleration and flow with higher turbulence) and

- bed characteristics (gravel grain size and pore volume).

Independently of the applicability of the results as calibration data, the following hypotheses will be tested in the experiments:

1. Finer suspended sediment grain sizes, higher flow velocities and higher shear stresses each result in a more persistent and higher suspended sediment concentration.

2. A coarser suspended sediment distribution results in higher and faster deposition.

3. Bed areas with higher velocity and higher bed shear stress experience lower deposition, compared to areas with lower velocity, respectively bed shear stress.

4. The gravel bed grain size and structure and the resulting bed roughness has a significant influence on amounts and rates of deposition, i.e. rougher conditions result in lower deposition.

HIER: experiment is set up in such a way that a they vary inbetween each other by one variable. For example, same bed, same velocity, but once with silty fine sediment, once with sandy fine sediment. Allows for direct comparison, what the effect of grain size distribution on deposition is. Similar, identical setup, but variation of bed grain size, velocity,

2.2 Experimental setup

2.2.1 Experimental facilities

The experimental and analytical work was carried out at the facilities of the Geography Department of the University of Exeter between winter 2008 and spring 2010.

The following three paragraphs provide an overview of the available facilities used in the flume experiments.

Flume and Pump: The flume is an Armfield recirculating flume with a 10 m long, 0.6 m wide and 0.6 m high glass walled experimental channel. A sketch of the flume can be found in Figure 2.2. The flume is visually divided into eight segments by its metal framework, each segment being 1.25 m long. The experimental channel is elevated 1.2 m and can be tilted up to an angle of 15° but was used in a level position. Pumpage can be regulated using a wheel which allows the user to close or open the recirculating pipe while keeping the revolutions of the pump constant. The readout at the pump was in L s^{-1}. Pumpage resulting in a stable discharge (without occilations) in an empty flume ranged from 10 to ca 225 L s^{-1}. The flume already provides a sediment trap for coarse material at the end of the experimental channel before the inlet into the recirculating pipe in order to protect the pump from damaging particles. The manual of the manufacturer suggests the use of gravel no smaller than 20 mm in diameter, which is coarse compared to the sizes expected in natural gravel bed rivers. To address this issue, a custom made screen was fitted behind the sediment trap with a mesh diameter of 10 mm. Therefore, gravel no smaller than 11.3 mm could be used in the experiments. Later, the screen was replaced by a perforated sheet with round holes of 3.8 mm, allowing us the use of gravel as fine as 4 mm.

However, the screen caused several problems. For certain pumpage rates, an oscillation in the flume emerged. Testing showed that oscillations were especially problematic for a pumpage rate around 90 L s^{-1}. Consequently, this discharge was not applied in the flume experiments. Furthermore, a comb-like wall was added between the basin at the exit of the recirculating pipe and the upstream end of the experimental channel to equalise the flow coming out of the recirculating pipe, similar as in the experiments of Ghoshal et al. (2010). The aim was to aid the uniform distribution of the water flow.

Gravel bed: The flume's experimental channel was fitted with a minimum 18 cm deep gravel bed, which amounts to a volume of 1020 L. The gravel was cleaned prior to each experimental run outside the flume with a power hose and a custom made screen. The gravel was then mixed, loaded and distributed by hand. The gravel used for the experiments was a combination of gravel already available at the department, commercially acquired gravel and collected samples from the field. Apart from the latter, the entirety of the gravel had to be carefully selected, since river gravel in the river Culm is mainly flat and angular shaped. Therefore, the available gravel had to be sorted into gravel likely coming from a riverine source and gravel with a likely marine origin, which was subsequently excluded. In order to understand the influence of the grain size of the gravel framework on fine sediment deposition, two gravel grain size distributions were used in the experiments. With the available resources, it was possible to achieve the two grain size distributions of flat and angular gravel shown in Table 2.1: One comparatively coarse bed grain size distribution ($D_{50} = 48$ mm, from now on referred to as D48) and - after improving the screen at the outlet - a finer grain size distribution ($D_{50} =$37 mm, from now on referred to as D37).

size	**Wentworth scale**	**D48 bed D_{50}=48 mm**	**D37 bed D_{50}=37 mm**	**field average ($\geq$ 11.3 mm)**
mm	ϕ	**mass-%**	**mass-%**	**mass-%**
128-181	-7 to -8.5	0.51	0.35	0
90-128	-6.5 to -7	3.08	2.22	0.96 (1.18)
64-90	-6 to -6.5	24.98	17.97	7.66 (9.19)
45-64	-5.5 to -6	27.49	19.77	14.68 (17.97)
32-45	-5 to -5.5	21.18	18.68	18.23 (22.52)
23-32	-4.5 to -5	15.32	15.63	15.97 (19.96)
16-23	-4 to -4.5	2.25	7.61	11.32 (13.87)
11.3-16	-3.5 to -4	0	2.74	10.66
8-11.3	-3 to -3.5	0	2.10	4.17
4-8	-2 to -3	0	2.04	3.90
characteristic values				
total weight	kg	1557	2165	
total volume	L	1020	1155	
average density w. pores	kg L^{-1}	1.53	1.88	
measured pore volume	%	38.5	24.3	
average density no pores	kg L^{-1}	2.65	2.65	
average bed depth	m	0.18	0.20	
pore space	%	35	29	
D_{10}	mm	24	13	9 (15)
D_{50}	mm	48	37	26 (32)
D_{90}	mm	82	78	61 (64)

Table 2.1: Gravel grain size distributions and characteristic values for the two bed grain size distribution (referred to as D48 and D37) and the average of all field samples. Field values refer to a distribution including grains from 4 mm to 181 mm and in parentheses for a distribution only from 11.3 mm to 181 mm, reflecting the restrictions of the screen respectively the perforated sheet.

Both flume bed grain size distributions have a unimodal distribution. In comparison, the average grain size distribution based on field data taken from the River Culm is characterised by a larger fraction of finer grain size classes and a bimodal distribution. The gravel grain size distribution of the River Culm is discussed in detail in Section 4.3.

The literature suggests that a finer grain size distribution is associated with a larger pore volume (as for example in Haschenburger and Roest, 2009). However, the pore space of the experimental gravel bed, as listed in Table 2.1, has a larger pore volume for the D48 bed. These conflicting findings may be explained by the

lack of arrangement through flow. The flow velocities in the flume are not sufficient to create a water worked bed. This leads to an unnatural large pore space. The arrangement effect might not be as significant for the finer D37 mixture, which can fill the pores of the coarser particles. This assumption is supported by the fact that although the mass of the finer D37 bed exceeds that of the coarser D48 bed by 30 %, the gravel bed rises only by 2 cm which is approximately 11 %.

Fine sediment: In order to understand more about the intrusion of silty size suspended sediment into gravel beds, most experiments were run with fine sediment originating from a Cambisol from Devon. The soil was sieved through a 2 mm sieve before being soaked in 30 L of water for three days with regular mixing. The resulting sediment mixture was stirred well before decanting into ten beakers. At the beginning of each experimental run, the content of the ten beaker was then added at the downstream end of the experimental channel (see Figure 2.1b with beakers ready for pouring). The downstream end was chosen as the input point in order to achieve a thorough mixing of water and suspended sediment in the recirculating pipe before entering the experimental channel from the upstream end.

	size μm	**Cambisol mass-%**	**Initial susp. mass-%**
sand	$\geq$ 125	1.98	0.06
	63-125	3.44	0.04
silt	32-63	6.98	0.85
	16-32	13.92	8.22
	8-16	16.72	18.29
	4-8	18.78	23.29
clay	2-4	16.77	22.48
	1-2	10.46	13.67
colloidal	0.5-1	7.68	9.25
	0.25-0.5	2.95	3.49
	-0.25	0.30	0.40

Table 2.2: Fractions of the grain size distribution of Cambisol used as silty fine sediment and the average of initially suspended sample drawn at 15 cm height at the beginning of each experimental run, both measured absolute grain size with the Digi-Sizer

The grain size distribution of the silty fine sediment (Cambisol) shown in Table 2.2 (measured with the DigiSizer as later explained in Section 2.2.2) is the average of four samples with a standard deviation of 3.3 %. The grain size distribution of the initial suspended sediment sample is the average of all silty experimental runs with a mean standard deviation of all samples of 2.7 %. These numbers are visually represented in Figure 2.1. The grain size distribution of the soil sample is coarser than that of the initial suspended sediment sample. This is most likely due to a rapid loss of coarser grain sizes from the suspended load in the first few minutes after the sediment input and before the initial sample was drawn. This phenomenon is here after referred to as 'time lag' in the initial concentration measurement.

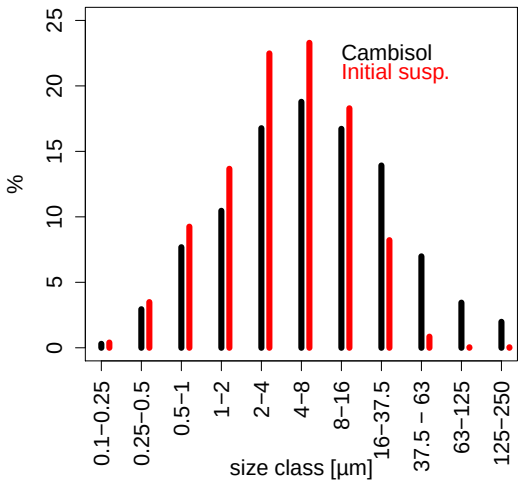

(a) Grain size distribution of silty fine sediment, for the Cambisol used as silty fine sediment and the average of initially suspended sample drawn at 15 cm height at the beginning of each experimental run, both measured absolute grain size with the DigiSizer.

(b) Beakers with silty fine sediment suspension ready to be poured at the downstream end of the experimental channel, screen visible on the right.

Figure 2.1: Silty fine sediment input procedure and grain size distribution.

Additionally, in a smaller number of experiments, a sandy fine sediment is used. The source of this was a commercially available sand, which was sieved to 63 to 500 μm and into subset of 63 to 250 μm and 250 to 500 μm. The sieved grain size

distribution of the whole sand as well as its finer and coarser subset can be seen in Table 2.3. For sieving, vibrating squared screens were used. In contrast to the silty fine sediment, the dry sand was added at the start of the experimental run at the beginning of the experimental channel.

μm	**sand 100-500 mass-%**	**fine sand 100-250 mass-%**	**coarse sand 250-500 mass-%**
63-90	3.21	8.41	
90-125	7.46	18.98	
125-181	10.32	27.13	
181-250	17.32	45.48	
250-375	47.54		78.53
375-500	14.15		21.47

Table 2.3: Grain size distribution of sand used as sandy fine sediment source measured by dry sieving through square holed sieves.

2.2.2 Methods and measurements

Velocity distribution

The source of flow information were velocity measurements taken with a Nortek Acoustic Doppler Velocimeter (ADV). Each value was the average of a two minute measurement. The ADV setup consisted of four heads, which were mounted on one vertical joist with 5 cm distance between each of the heads. The joist was mounted on top of the flume, reaching into the experimental channel. This setup could be moved with the help of a computer controlled motor on rails in both cross- and downstream directions with an accuracy of 1 mm and manually to different heights above the bed. The lowest safe measurement was at 5 cm above the bed, which resulted in measurements at 5, 10, 15 and 20 cm height above bed. For all runs, velocity measurements were taken in clear water, with the already laid out gravel bed and installed traps. This approach meant that measurements were taken prior to the fine sediment input, which was defined as the actual start of the experimental run. In

turbid conditions, the operation of the velocimeter includes the risk of driving into elevated bed areas. Therefore, repeat velocity measurements during experimental runs were only conducted for runs with a flat gravel bed. The computer controlled steerage ensured an exact replication of the measured cross- and downstream positions for all experimental runs. In the first part of the experimental runs, the velocity measurements were only operated directly above the traps. In later experimental runs, the sampling regime included detailed probing on three levels: (a) three lateral positions for each downstream position (each 10 cm from the side walls and one in the centre), (b) systematic scans every 62.5 cm downstream (at half segment distances) and (c) scans in the middle, beginning (5 cm into trap) and end (5 cm before end) of each trap. The measurements were corrected for errors, viewed, processed and exported with WinADV32. The results of repeated ADV scans are shown and discussed in Subsection 2.3.1.

Calculation of bed shear stress

There is a multitude of different methods to estimate shear stress from velocity measurements. In this study, two fundamentally different approaches are pursued. Both are introduced in 1.2.2: (a) a velocity profile method and (b) a turbulence based method. Method (a) deduces bed shear stress based on the logarithmic velocity profile from vertical aligned measurements, shown in Equation 2.3, where v^* is the bed shear velocity, H the height above the bed and z_0 is the roughness length where flow velocity reaches zero and κ being the Karman constant, for which typically the value 0.41 is used, see for example Biron et al. (2004); Petrie et al. (2010).

$$\frac{v}{v^*} = \frac{1}{\kappa} ln(\frac{H}{z_0}) \tag{2.3}$$

v^* can be transferred into bed shear stress (τ_0) as shown in Equation 2.4, with ρ_f being the fluid density.

$$v^* = \sqrt{\frac{\tau_0}{\rho_f}} \tag{2.4}$$

The first step for this method is to calculate the logarithmic height of the measurement points above the river bed. A linear model is fitted for logarithmic height versus velocity and is used to calculate velocity at z_0. This can be then converted first into $u*$ and consequently into τ_0 using Equation 2.4.

Method (b) is the Turbulent Kinetic Energy approach (TKE) after Soulsby (1983) and Kim et al. (2000), which is reviewed in Biron et al. (2004). The TKE method calculates τ_0 using the velocity fluctuation of the velocity measurements closest to the bed. The original method uses the fluctuation of all velocity vectors, x vertical orthogonal to flow, y horizontal orthogonal to main flow direction and z the main flow direction. This is shown in Equation 2.5 with c_1 being a proportionality constant of 0.19 and x', y' and z' the fluctuation of each velocity vector. This is given as the Root Mean Square (RMS) of the fluctuation around the mean velocity, which is equivalent to the standard deviation of each individual measurement (see WinADV32 manual p.23). Kim et al. (2000) developed and tested the slightly simpler method using only fluctuation information in downstream direction (z direction), which is shown in Equation 2.6 with a different proportionality constant c_2=0.9.

$$\tau_0 = c_1 * [0.5 * \rho_f * (< x'^2 > + < y'^2 > + < z'^2 >)] \tag{2.5}$$

$$\tau_0 = c_2 * [0.5 * \rho_f * (< z'^2 >)] \tag{2.6}$$

The validity of TKE established bed shear stress was proven by annular flume experiments of Pope et al. (2006). The two methods are later referred to as $Txyz$ and Tz.

Suspended fine sediment concentration

The main concentration information was based on two 0.5 L replica bottled samples drawn with a tube fixed to the glass channel wall at 15 cm above the gravel bed with a frequency of either 15 or 30 minutes. The sampling position in the experimental channel was directly at the inlet. This is based on the assumption that the suspended sediment with the highest degree of mixing comes directly out of the recirculating pipe. Additional control samples were taken from tubes fixed at the same height above the gravel bed at 5 and 9.25 m into the experimental channel. Furthermore, sampling tubes were attached to the ADV heads and fixed along the ADV connecting cables and led to the outside of the experimental channel. With these tubes, samples could be drawn at different heights to establish the concentration profile of the suspended sediment. Each of the 0.5 L bottled samples was filtered through a rinsed, dried (at 105° C) and pre-weighted glass fibre filter with the help of a vacuum pump. The filter water was collected and its volume recorded. The used filters were dried again at 105° C for 12 h and weighed. The concentration was calculated for each sample from filter weight difference and water volume. This method was very exact with a standard deviation of the concentration between replica bottled samples of less than 3 %.

Fine sediment grain size distribution

Fine sediment in suspension often consists of clay and organic rich material. These fine particles are often referred to as cohesive sediment. Their physio-chemical properties cause aggregation. Such particles results in much larger composite particles, which have a crucially different depositional behaviour compared to their disaggregated mineral components. The grain size distribution of aggregated particles is referred to as effective grain size, whereas the grain size of the disaggregated particles is defined as the absolute grain size of the sediment.

In order to measure both of the above silty sediment grain size distributions, two

different instrument were employed, the DigiSizer and the LISST-100. The following paragraphs describe the different size analysis methods of these instruments based on the manuals and the experience of the laboratory staff at the University of Exeter Geography Department.

DigiSizer: All absolute fine sediment grain size distribution measurements were carried out with a Saturn DigiSizer 5200 from Micrometrics. The DigiSizer uses a laser based size analysis, measuring grain size as a function of scattering angle and concentration as a function of obscurity in a range from 1 - 1000 μm. The DigiSizer measures absolute grain size distribution in three repetitions for each sample and offers a high rate of accuracy and reproducibility, in an acceptable time span of ca. 8 to 10 samples per hour. Additionally to the sampling itself, each sample needs a thorough preparation. The DigiSizer requires an organic free sample of 1-3 g of sediment. Therefore, large bottled samples with 10 L flume bulk water were drawn at two hour intervals. Bulk samples were split up into one litre samples to be centrifuged with a Thermo Scientific Haraeus Multifuge centrifuge holding four buckets each containing a one litre liquid sample. To achive complete deposition, the centrifuge had to run on 2500 rounds per minute (rpm) for 60 minutes. The supernatant was decanted and the deposit collected in smaller centrifuge tubes and centrifuged again at 2500 rpm for 60 minutes. Finally, the supernatant was decanted and the deposit rinsed into a small glass beaker. The first step in the oxidation of organic matter of the sample was to add 5 mL of 0.5 % hydrogen peroxide (H_2O_2). After two hours, another 5 mL H_2O_2 was added and left for consumption over night at room temperature with watch glass lids to avoid drying out. The second step was to heat the sample for approximately one day on hotplates, starting with 80° C rising slowly to 100° C. To avoid drying out, re-aggregation or destruction of the sample, deionised water was added regularly. Only when the supernatant was completely clear, the sample was centrifuged again at 2500 rpm for 60 minutes. After decanting, the deposit of each sample was flushed with 50 mL of 0.04 % sodium-hexametaphospahte

($(NaPO_3)_6$) into probe beakers, which were then placed on the horizontal rotating table of a Micrometrics MasterTech 052 autosampler. This autosampler has two advantages: First, it allows the sample to be drawn from a sampling head directly into the DigiSizer and changes automatically to the next sample; second, the sampling head was equipped with a mechanic stirrer and ultrasound to disperse the sample. To achieve an optimal output, the DigiSizer uses bubble free deionised water as a carrier fluid, which was prepared with a Micrometrics AquaPrep. The DigiSizer auto-dilutes the sample to an aimed obscurity of 15 %, accepting only measurements with an obscurity of 5 to 30 %. The results are three repetition distribution curves per sample with their average as the final result. The standard deviation between the repetitions of the samples measured for this work never exceeded 3.2 %.

LISST-100: LISST stands for Laser In-Situ Scattering and Transmissiometry. The LISST-100 instrument (produced by the company 'Sequoia') measures effective grain size distribution and volume concentration for grain sizes 1-500 μm, with a lower accuracy for larger particles. The principle of the LISST technique is the proportionality of the laser scatter angle to the particle size. A single laser beam with 6 mm diameter is emitted at one side of the u-shaped sample head and first checked by a reference detector, then attenuated and reflected in the 5 cm water column enclosed by the sample head to subsequently be collected by 32 detector rings on the other side of the sample head. Each of the 32 rings detects with a photo-diode a small range of logarithmically increasing scatter angles. The largest particles are measured with the innermost detector ring and the finest particles with the largest outer ring. The magnitude of scatter increases linearly with the number of particles. In addition, the transmitted beam hits a sensor behind the detector rings and its attenuation is a measure of the overall sediment concentration. The LISST-100 is a very effective and reasonably exact instrument for effective grain size distribution measurement. One of its restrictions is that it is only effective with an optical transmission of more than 30 %, which as a rule of thumb is less than 200 mg L^{-1}, see Berlamont et al. (1993).

Therefore, the probe could not be directly used in the flume, but a sample had to be extracted and diluted for measurement. For the measurement, the calibration chamber of the instrument was used. This chamber is a 4 L Plexiglas container with a circular opening at one side. The probe head can slide into the circular opening. To avoid settling during the measurement period of two minutes per sample (with one reading every second), the whole setup was elevated in order to mount a magnetic stirring device under the experimental chamber. The dilution rate was 1:3 with 1 L flume sample and 3 L deionised water. However, some settling occurred during the measurement period, which was obvious when looking at the recorded concentrations for each single reading. Therefore, only readings of grain size distributions with concentration of $>$95 % of the maximum concentration value were considered and consequently averaged. Nevertheless, the standard deviation of the D_{50} of the single readings compared to the average was 11.5 %. This means LISST-100 samples are connected to considerable more noise than DigiSizer readings. For more in-depth information on the LISST-100, see Agrawal and Pottsmith (2000) and Berlamont et al. (1993).

Fine sediment deposition

The deposition of fine sediment was measured with custom made sediment traps. These traps consisted of 0.2 m*0.18 m*0.3 m metal grid baskets with a wire diameter of 2 mm and grid height and width of 18 mm (covering an area of 0.054 m^2 and a volume of 0.010 m^3). These were filled with gravel and provided with a plastic sleeve. Figure 2.3a shows an empty trap with a folded sleeve prior to the installation in the flume and filling with bed gravel. The plastic sleeve was folded down leaving only two handles reaching the bed surface. For recovery, the sleeve was raised by pulling the two handles. The sleeve was long enough to fold over the top of the trap, therefore sealing it. With this procedure, traps recovered during experimental runs could be left in place until the end of the experimental run to minimise disturbance. Additionally,

tiles were used to secure the plastic sleeve safely on top of the trap. After each experimental run, the experimental channel was drained down to the bed surface, so the traps were still surrounded by water in order to achieve minimum leaking. Only then, the traps were removed from the flume. Gravel, grid basket and sleeve were thoroughly rinsed and the washing water was collected in the same bucket. The trap content was left to settle for two days and supernatant was removed with a siphon tube. The deposit at the bottom was then flushed into a shallow bowl and dried at 105° C and weight. A subsample of 5 g was used for further grain size distribution measurement in the DigiSizer. The weight of the fine sediment divided by the trap area of 0.054 m^2 is defined as the trapping rate (TR) and is given in kg m^{-2}.

2.2.3 Experimental parameters

The flume experiments consisted of 17 individual runs of which three are completely excluded from the results discussion and two are only partially valid due to irregularities in flow or fine sediment character. Consequently, Series 1 had three valid runs, Series 2 consisted of eleven valid runs of which seven were run with silty and four with sandy fine sediment. Each experimental run was operated under constant hydraulic conditions, hence there was no variation in discharge, flow velocity or bed structure. Series 1 was run with a flat bed. In Series 2, the area of the flume was divided into several patches with different bed elevations. For a schematic overview of the setup of the two series, see Figure 2.2.

The water volume for all experimental runs was fixed to 3750 L. This was measured by water input per time and controlled by calculating water volume in the actual flume experimental channel using water level and pore space calculations. The naming of the experimental runs is as follows: S1 (flat bed) and S2 (alternate bed elevation) stand for the two series, Q signifies the discharge and was followed by the discharge in L s^{-1} and D characterised the bed grain size distribution and is followed by the D_{50} in mm for Series 2 runs. In the case of sandy experimental runs, this is

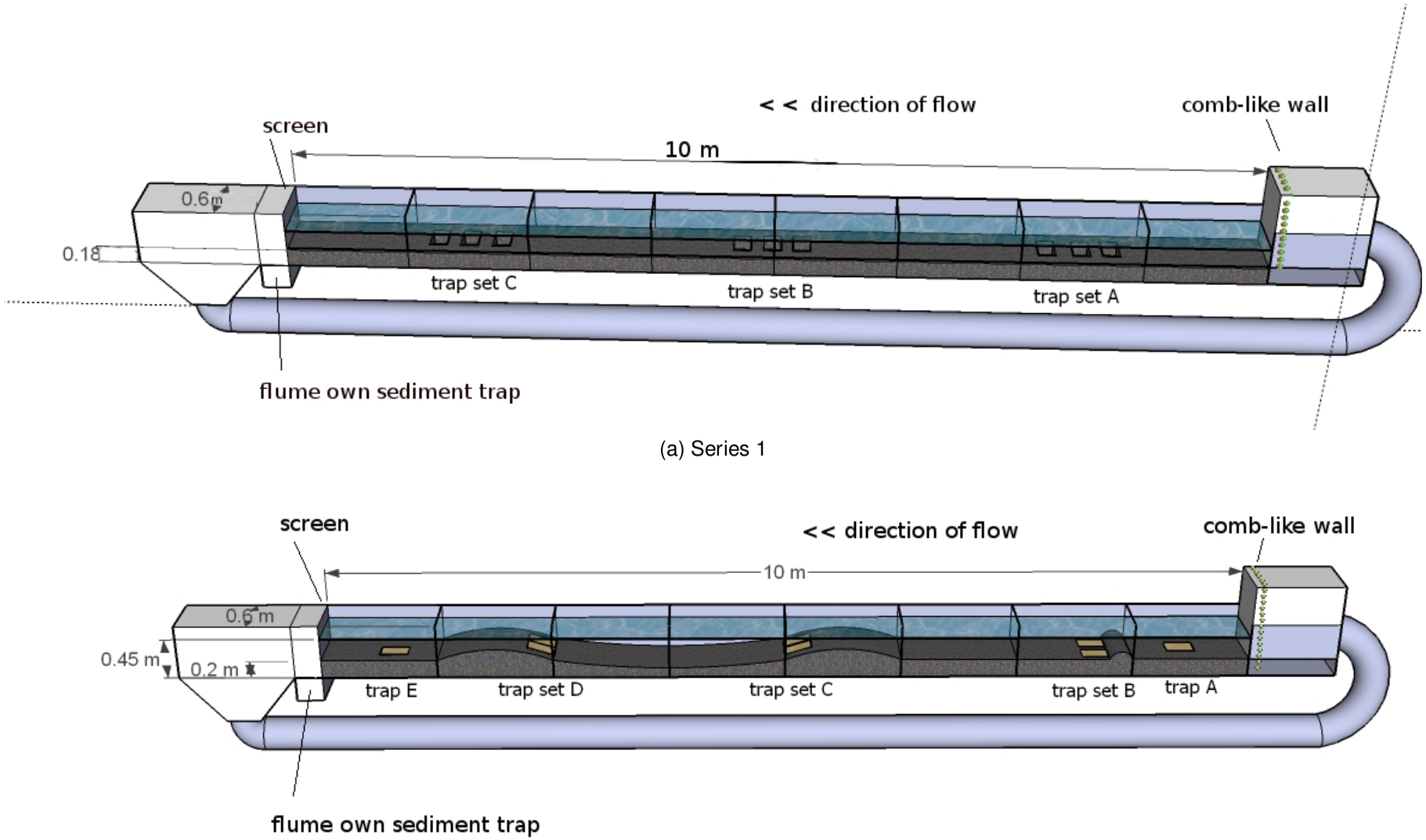

(a) Series 1

(b) Series 2

Figure 2.2: Schematic flume layout and trap positioning during flume runs in Series 1 and Series 2, flow direction from right to left, segmentation conforms with the metal framework of the flume, which was used for orientation during bed and trap positioning (own drawing).

then followed by -s. Finally, repeat experimental runs with identical setups are indicated by numbers (-1 or -2). The following two subsections describe in detail the experimental setup of each series and the single runs.

Series 1: This series was setup as a test series in order to identify practical problems. Therefore, of the five experimental runs only three were included in the result discussion. All experiments used suspended silty fine sediment from the described silty sediment, although with different amounts and successively longer soaking times (soaking times: S1Q80 8 h, S1Q50-1 24 h and S1Q50-1 for three full days). The bed was furbished with 9 sediment traps situated in triplets (A1 to A3, B1 to B3, C1 to C3). Traps with the same letter are of the same character. Traps with the same number were recovered at the same time in the experimental runs. It is important to mention that traps are named in downstream direction from 1 to 3, but recovered in opposite direction from 3 to 1 to limit disturbance of neighbouring traps as far as possible. Two of the valid experiments were run with a completely flat 18 cm deep D48 gravel bed, one experiment at 80, the other at 50 L s^{-1}. I order to test the range of influence of the gravel grain size distribution,the trap sets (A, B and C) varied insofar that each set contained a different gravel grain size distribution, which is listed in Table 2.4. The third valid experimental run of Series 1 operated at 50 L s^{-1} and had a gravel bed of D48 in bed and traps. Here the influence of bed alteration as tested. The general gravel bed height was 18 cm, but gravel between 3.75 m and 6.25 m in the experimental channel was cumulated to 28 cm, with gentle slopes reaching upstream towards 3 m and downstream to 7 m. The setup and trap positions of S1Q80 and S1Q50-1 are shown in Figure 2.2a. Velocity scans using an ADV (as described in 2.2.2) were conducted prior to each experimental run and for S1Q80 at three times during the experimental run (listed in Table 2.4). The defined combination of bed grain size distribution and discharge was referred to as an experimental setting. For Series 1, there were two experimental settings.

	Q L s^{-1}	v_{mean} m s^{-1}	duration h	variation	recovery at h	2x0.5L every x h	10L every xh	ADV at h
S1Q80	80	0.53	15	in trap GSD: A=D135, B=D48$_{pure}$, C=D48$_{mix}$	3,6,9	0.5	2	1.75,4.75,7.75
S1Q50-1	50	0.33	10	in trap GSD: A=D135, B=D48$_{pure}$, C=D48$_{mix}$	2,5,8	0.5	2	pre exp.
S1Q50-2	50	0.33	10	bed elevation	3,6,9	0.5	2	pre exp.

Table 2.4: Experimental parameters of flume experiments in Series 1 with constant discharge (Q) and resulting mean velocity in the experimental channel (v_{mean}) and the total duration of the experimental run. The character of the variation between traps is indicated. For trap sets with varied D_{50} D is followed by the D_{50} in mm. Subscripts for D48 indicate the nature, where mix stands for a distribution equivalent to the surrounding bed, opposed to $pure$ which includes material from only one grain size class, here 32-44 mm. Recovery indicates the time of trap sealing. 2x0.5 L gives the timing of 0.5 L bottled samples taken for concentration measurement and 10 L gives the frequency of 10 L samples drawn for grain size distribution measurements with the DigiSizer. Finally, ADV lists the frequency of velocity scans.

Series 2: Since the tests in Series 1 showed a clear influence of elevation patterns, but a marginal (disputable) influence of in trap gravel framework grain size distribution, all experiments in Series 2 were run with an uniform bed gravel distribution and and alternated bed elevation. Bed elevation patterns were designed to imitate rapid flow, decelerating and acceleration flow or as a reference to a natural river, riffle (A, B and E), end riffle (C) and end pool positions (D). The bed was replicated for each experiment using the flume construction framework, markers on the floor and glass wall of the experimental channel and wooden wedges to support the traps to keep them in the same place and angle. All experimental runs in Series 2 were furbished with eight traps (A, B1, B2, C1, C2, D1, D2, E). Trap A and trap E were setup at the beginning and end of the experimental channel in a flat bed resembling traps in Series 1. The B trap pair was positioned behind a 10 cm high obstacle aimed to cause disturbance of the flow. The C trap pair was positioned at the down-sloping side of a gravel accumulation with the trap surface tilting away from the flow. Trap pair D was positioned at the rising side of an identical gravel accumulation, tilted towards

the flow. The area between these two gravel accumulations had a shallower bed of 10 cm depth. The setup, including the trap positions, is shown in Figure 2.2b. The traps were recovered at different points in time. In general, experimental runs were run for 8 h and typically the recovery of traps B1 and C1 was after 2 h, A and E after 3 h, C1 and D1 after 5 h and eventually B2 and D2 after 8 h. Further, in order to amplify the effect of overall discharge in the experimental runs, the divergence between fast and flow discharge experiments was larger with 30 and 100 L s^{-1} pumpage. The variation between different runs followed a systematic matrix (shown in Table 2.5) with the variation in bed sediment, discharge and fine sediment character. The four combinations of discharge and bed grain size distribution are each referred to as one experimental setting.

	silty fine sediment		**sandy fine sediment**	
Q **= 30 L s^{-1}**	S2Q30D37	S2Q30D48-1 & 2	-	-
Q **= 100 L s^{-1}**	S2Q100D37	S2Q100D48-1 (-2&-3)	S2Q100D37-s-1 &-2	S2Q100D48-s-1 &-2
	fine bed (D37)	**coarse bed (D48)**	**fine bed (D37)**	**coarse bed (D48)**

Table 2.5: Matrix of experimental setup in Series 2, showing names of experimental runs with the variation of fine sediment (silty and sandy) in left and right column, variation of discharge (30 and 100 Ls^{-1}) at top and variation of bed grain size distribution for each split column at the bottom.

Table 2.6 gives the experimental parameters and specification of the measurement routine for the single experimental runs in Series 2. For all experimental runs in Series 2, ADV velocity measurements were carried out prior to the experimental runs. As a further differentiation for S2Q100D37-s, the sandy fine sediment was again split into two sub-ranges. One with sand $>$250 μm (used in S2Q100D37-s1) and one $<$250 μm (used in S2Q100D37-s2). This grain size distribution is shown in Table 2.3.

	Q	v_{mean}	dur	recovery at	2x0.5 every	10L every	D_{50}
	L s^{-1}	m s^{-1}	h	h	x h	x h	mm
silty							
S2Q30D48-1	30	0.2	8	2,3,5,8	0.5	hour[1]	48
S2Q30D48-2	30	0.2	5	2,3,5,8	0.5	-	48
S2Q30D37	30	0.2	8	2,3,5,8	0.5	0,1,3,4,6,8	37
S2Q100D48-1	100	0.67	8	2,3,5,8	0.5	hour	48
S2Q100D48-2	100	0.67	8	2,3,5,8	0.25	0,1,5,8	48
S2Q100D37	100	0.67	8	2,3,5,8	0.5 till 3h, then 1	0,1,3,4,6,8	37
sandy							
S2Q100D48-s-1	100	0.67	4	1,1.5,2.5,4	0.25	-	48
S2Q100D48-s-2	100	0.67	2	1,1.5,2	0.25	0,0.5,1	48
S2Q100D37-s-1	100	0.67	4	1,2,4	0.25	0,1	37
S2Q100D37-s-2	100	0.67	4	1,2,4	0.25	2	37

Table 2.6: Experimental parameters of experimental runs in Series 2 with constant Q and resulting (v_{mean}) and the total duration of the experimental run (dur). Recovery indicates the time of the trap sealing. 2x0.5 L gives the timing of 0.5 L bottled samples taken for concentration measurement and 10 L gives the frequency of 10 L samples drawn for grain size distribution measurements with the DigiSizer. Finally, D_{50} gives the 50 % percentile of the grain size distribution of the bed in mm.

2.3 Results of flume experiments

2.3.1 Standardisation

For a meaningful discussion of results, the standardisation of the experimental conditions for the different runs is important. For a direct comparison of the different experimental runs, the bed structure and flow patterns need to variate only in the way intended by the experimental setup. The first step of each experimental run was the replication of the bed structure. The replication was achieved with the help of markers and angled wood blocks. Besides, during the filling of the flume with gravel, the incoming bed material was thoroughly mixed. The bed setup was controlled by water depth measurements over each trap at two points. For Series 1 with a completely flat bed, the measurement was simple, since all traps were positioned directly on the channel floor and the gravel was filled around, lining up with the trap rim (see Figure 2.3b). For experimental runs in Series 1 the variation in bed elevation was

(a) Empty basket trap with folded sleeve before installing in the bed, wire with 2 mm diameter and 16 mm grid squares.

(b) Lateral view of the gravel bed with installed basket trap, rim aligned with the surface of the gravel bed.

Figure 2.3: Basket traps used for fine sediment deposition measurement.

less than 2 cm. In the case of Series 2, the bed structure was more complex. Figure 2.4a shows a not to scale sketch of the longitudinal cross-section through the experimental channel. For orientation purposes, a line is plotted at 20 cm giving the aimed plane for the flat bed areas in Series 2 D37. The overall variation is very small considering a grain size distribution with a D_{50} of 48 and 37 mm. Most variation is due to the change from a coarser to a finer gravel bed, which caused a general rise of the bed of ca. 2 cm. For both series, the standardisation of the bed is very satisfactory.

The second step of verifying the standardisation was to compare velocity profiles over replica traps and between experimental runs with identical setup and discharge. A picture of the ADV heads in the flume is shown in Figure 2.4b, showing the joist with the four vertically mounted ADV heads with 5 cm distance to the bed and to each other.

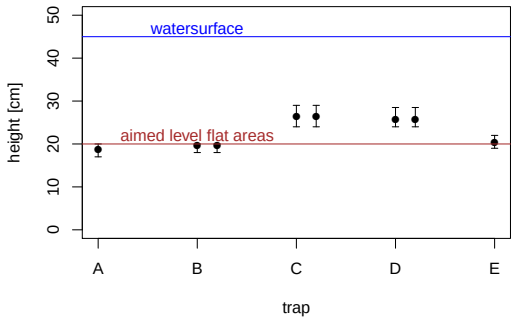

(a) Bed and resulting water depth variation in Series 2: Averaged bed elevation over traps (respectively trap pairs) for all experimental runs in Series 2 ordered in downstream direction with error bars showing the maximal and minimal value. The blue line indicates the water surface and the orange line the bed level for D37 flat areas.

(b) Lateral view into experimental channel during fill up for S2Q30D48-1 with ADV heads mounted at 5, 10, 15 and 20 cm above the bed. Further the picture shows the sampling tubes used for concentration measurement at different heights which were attached to each head.

Figure 2.4: Bed elevation and setup of ADV measurement heads.

The measured velocity magnitude for the three experimental runs in Series 1 are shown in Figure 2.5a, 2.5b and 2.5c. Repeated velocity measurement were only conducted in S1Q80 resulting in the display of error bars only for this experimental run. The error bars indicate the maximum and minimum measured value. The positions close to the bed displays the largest error bar, caused by disturbances during the trap recovery. Still, velocity variations were small over the whole period of this experimental run. Also, variation between replica traps is very small. For S1Q80, trap C3 is an outlier, with very high near bed velocities. This might have been a positioning effect of the gravel, since the bed elevation does not show any irregularities. This unexpected behaviour needs to be considered when discussing trapping rates.

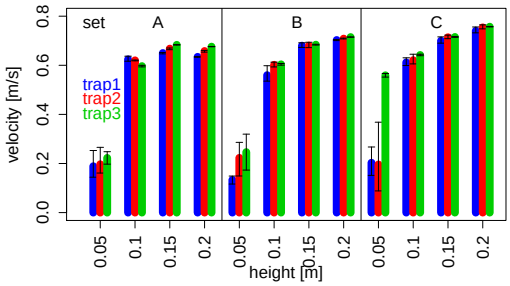

(a) Averaged velocities measured at 0, 3 and 6 h into the experimental run S1Q80. Errorbars showing the maximum and minimum of all values measured at this point

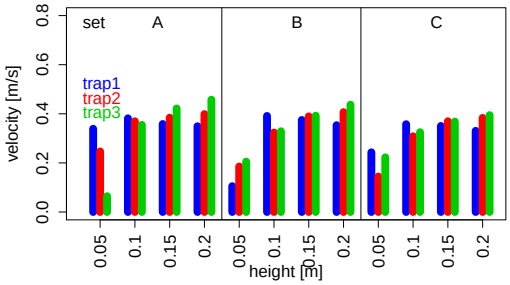

(b) Velocity measurement above the traps for S1Q50-1

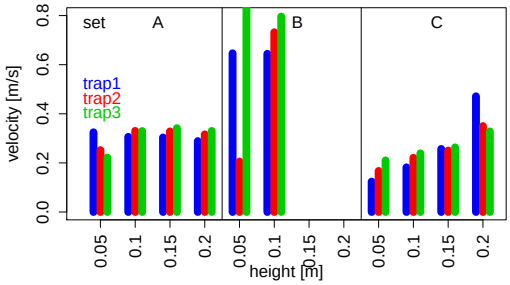

(c) Velocity measurement above the traps for S1Q50-2. Measurements at 15 and 20 cm above triplet B were not possible due to higher bed elevation and consequently shallower water depth

Figure 2.5: Velocity above replica traps in Series 1: velocity magnitude at 5, 10, 15 and 20 cm (as shown on x-axis) of trap triplets A, B and C. Different traps in triplet are represented by colour (trap 1 blue, trap 2 red, trap 3 green).

For Series 1 experimental runs with 50 L s^{-1} discharge, the velocity profile gradient was less steep (see Figure 2.5b and 2.5c). Traps A1 to A3 record the development of a typical velocity profile in both experimental runs with 50 L s^{-1} discharge. In trap A1, there is still a uniform velocity distribution for all four heights, A2 displays an intermediate velocity distribution. A3 has a fully developed velocity profile. The uniform velocities over A1 are the residues of the flow in the pipe and the effect of the comb-like structure. This phenomenon needs to be considered in the discussion of the trapping ratios, too. Apart from traps A1 and A2, the velocity pattern in S1Q50-1 (Figure 2.5b) are very similar for all traps. S1Q50-2 shows a similar effect for trap set A, very high and variable velocities over the elevated trap set B and a slowing of the

velocity in C, especially C1. The comparatively low velocities over C1 are the result of a shadowing effect of the bed elevation around trap set B.

Figure 2.6 plots the velocity distribution over the traps for the four experimental settings in Series 2 (see Table 2.5). Error bars indicate maximum and minimum measured values.

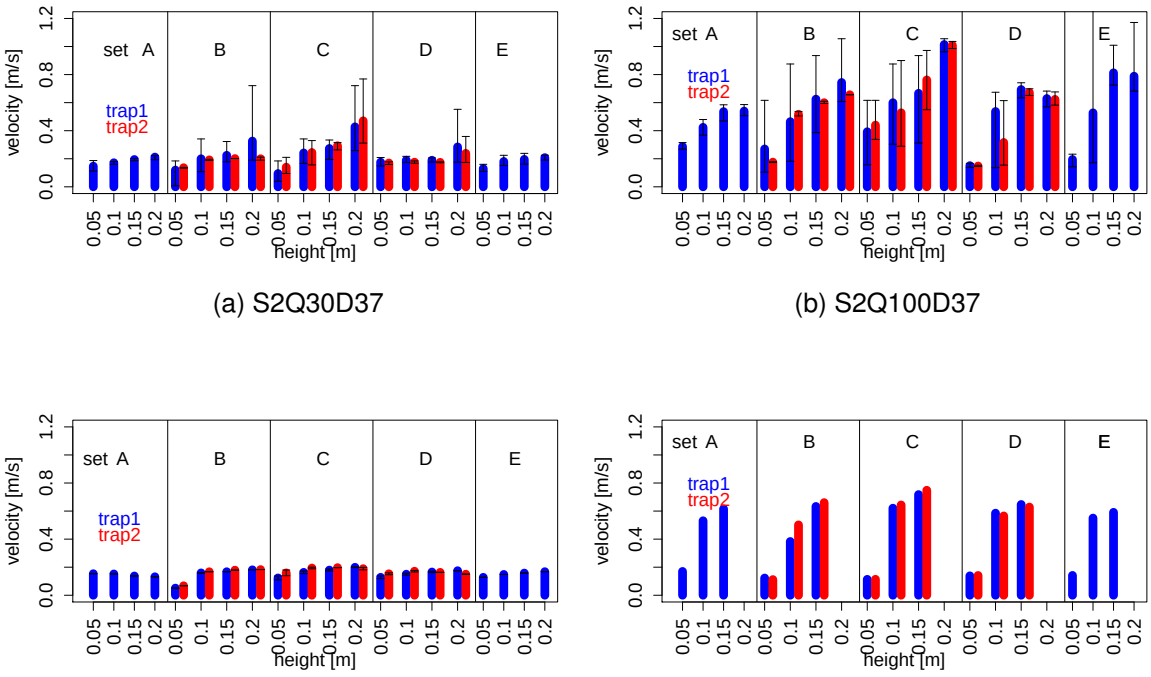

(a) S2Q30D37

(b) S2Q100D37

(c) S2Q30D48

(d) S2Q100D48, missing 0.2 m values due to ADV head failure

Figure 2.6: Velocity magnitudes in Series 2: at 5, 10, 15 and 20 m above the bed for the four experimental settings (Q30D37, Q100D37, Q30D48 and Q30D48) for all traps. For the trap pairs B, C and D, trap 1 is shown in blue and trap 2 in red. Values for various positions over the traps are averaged. Error bars give the maximum and minimum value measured at this position.

The range between minimum and maximum values for a discharge of 30 L s^{-1} was smaller than for 100 L s^{-1}. This is to be expected since higher velocities cause higher turbulence. The value range over trap pairs B, C and D was larger than the range over A and E. This difference is an intended variation, since B experienced turbulence caused by the upstream obstacle and C and D are positioned on rising respectively falling parts of the gravel bed, which are also a source of fluctuations.

Seemingly, the variations are larger for experimental runs with a finer bed grain size of D37. However, this is misleading because in experimental runs with D37, the ADV scanning was operated for three positions (front, middle and end of the trap). Consequently, more variation was measured resulting in more discrepancy between minimum and maximum values. All trap pairs show consistently similar average and magnitude of error bars. Overall, the velocity distribution for the D48 bed is not significantly different to the D37 bed. This was tested using a two sample Kolmogorov-Smirnov test, which resulted in a D-value of 3.8* 10^{-7} and a p-value of 0.873 (with D=0 and p=1 being a perfect fit).

2.3.2 Velocity and bed shear stress distribution

Figure 2.7 consists of three scatterplots comparing the three methods to establish τ_0. The bed shear stress range extends up to 10 Pa, but the main data concentrates around 1 Pa. Therefore, the axes were chosen to enable the illustration of the divergences. Comparing the log method to both TKE methods, the log method covers a much smaller range of values (in Figure 2.7a and 2.7b). This is caused by the considerable limitations of the log method in this flume setup. Due to the shallow water and the minimum distance of 5 cm between ADV heads, only four points were available to establish a profile. Furthermore, with a distance of 5 cm to the bed, the velocity in the boundary layer could not be fully measured. Therefore, the linear model of logarithmic depth and velocity exhibits small slopes. Consequently, a low bed shear stress is established. A further complication arises from the fact that the ADV head at 20 cm distance from the bed failed during Series 2 and therefore some experimental runs have only three points in the velocity profile. Hence, a large proportion of log method derived shear stress values plot around zero.

Concerning the two TKE based methods (shown in Figure 2.7c), there is no systematic divergence between the two. However, Biron et al. (2004) suggest that using only velocity fluctuations in z direction results in smoother and more reliable values.

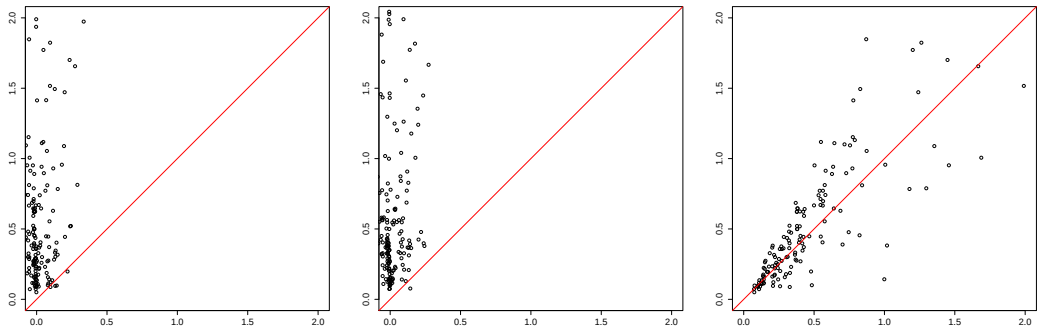

(a) x=log, y= Tz (b) x=log, y=$Txyz$ (c) x=Tz, y=$Txyz$

Figure 2.7: Comparative scatterplot of methods to derive bed shear stress values with three different methods, using kinetic turbulent energy with all velocity fluctuation ($Txyz$) and only downstream velocity fluctuation (Tz) and the logarithmic velocity profile method (log)

Additionally, Tz covers a larger range than $Txyz$ and therefore tends to emphasise the difference of flow pattern. Consequently, the values based on the Tz method are used for the further discussions in this chapter. The ultimate interest of this study is to understand interstitial deposition of suspended sediment. Therefore, it is central to understand the conditions above the traps (the actual points where deposition is measured) in relation to the range of flow conditions in the rest of the experimental channel. Ideally, uniform bed sections and discharge should result in identical velocity and bed shear stress. The following analysis aims to show the degree of uniformity within identical settings and the degree of divergence between different settings. For this purpose, ADV data was divided into four sub-datasets. The first set includes measurements at regular distances for the whole flume, the second set comprises data measured above the traps, the third set only includes data from the centre of the flume for both trap and non-trap positions and the fourth set comprises all measurements at 10 cm distance to the walls. The sub-datasets are referred to as 'flume', 'traps', 'centre' and 'side'. Moreover, these sub-datasets were defined each for a discharge of 30 L s^{-1} (Q30) and 100 L s^{-1} (Q100).

Table 2.7 shows the results of the statistical evaluation of the ADV velocity and resulting shear stress data using a Kolmogorov-Smirnov test. Measurements from

		Kolmogorov-Smirnov test centre versus sides		**Kolmogorov-Smirnov test traps versus flume**	
	Q	**p**	**D**	**p**	**D**
velocity	30 L s^{-1}	0.83	0.18	0.53	0.18
	100 L s^{-1}	0.95	0.15	0.23	0.43
shear stress	30 L s^{-1}	0.54	0.25	0.78	0.53
	100 L s^{-1}	0.53	0.18	0.35	0.02
		centre	**sides**	**traps**	**flume**
	n	56	112	78	90
		mean			
	Q	**centre**	**sides**	**traps**	**flume**
velocity	30 L s^{-1}	0.21	0.18	0.20	0.19
	100 L s^{-1}	0.95	0.58	0.53	0.64
shear stress	30 L s^{-1}	0.44	0.43	0.47	0.39
	100 L s^{-1}	5.34	4.93	4.43	5.91

Table 2.7: Statistical evaluation of velocity and shear stress data performed with a Kolmogorov-Smirnov test, comparing centre and side values as well as trap and overall flume values with n being the number of measurements. Additionally, the mean v and τ_0 (established using the T_z method) of the groups are listed.

the centre are compared to measurements at the side, in order to prove that patches can be defined from side to side and marginal areas do not have to be excluded. For velocity, this results in a satisfactory accordance of the two sub-datasets with p-values higher than 0.8. Concerning shear stress, side and middle values differ to a greater extent. Still, the p-values are over 0.5. If we are comparing the trap values with the overall flume values, the accordance is much weaker. For the Q30 experimental runs, the divergence is smaller than for the Q100 results. This is a clear indication that the average of the traps is not representative for the whole flume. At Q100, average velocities and shear stress for the flume are higher than for the traps. However, if we are looking at the distribution of the data, trap values are covering the same range compared to the overall flume values. Table 2.7 summarises the velocity and shear stress data at the bottom by listing the mean for all sub-datasets. Concluding, the cross-sectional variation of velocity and shear stress are not significant. Yet, traps are not representative, but are within the range of v and τ_0 of the experimental channel.

Having established the difference of v and τ_0 of the $side$, $centre$, $trap$ and $flume$ dataset, the following looks at the longitudinal distribution of flow conditions. Figure 2.8 looks at the velocity and bed shear stress distribution in Series 1. The graph is arranged as a longitudinal profile of the experimental channel. The velocity at 10 cm height is chosen as a compromise. Despite the fact that deposition might be primarily influenced by near bed velocities, the values at 5 cm distance to the bed show a high degree of fluctuation due to small scale bed patterns.

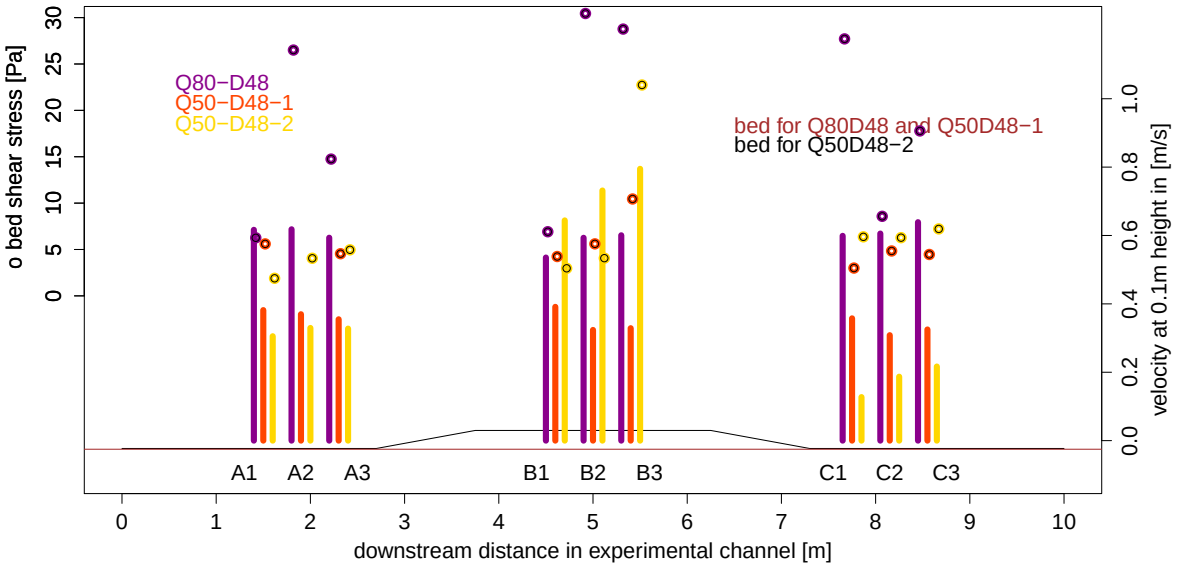

Figure 2.8: Velocity at 10 cm distance from bed (bars) and bed shear stress (circles) over trap triplets with trap names indicated at the bottom for experimental runs in Series 1 (n = 1 for S1Q50-2 and n = 3 for S1Q50-1 and S1Q80). Data from identical positions of the three experimental runs are plotted with an offset for legibility. Bed elevation is indicated with a brown line for S1Q80 and S1Q50-1 and in black for S1Q50-2.

In the case of S1Q50-2, the elevated bed caused velocities and bed shear stress to rise over its length. Remarkably, it further results in higher bed shear stress at the downstream side of the obstacle. A part of the explanation for this phenomenon is that the elevated bed forces the main flow higher up in the water column and introduces turbulences, which become effective over traps C.

The v and τ_0 distribution plots of Series 2 are grouped according to their bed of

D48 and D37. This is due to the different ADV scan routine. Figure 2.9 shows the plot for all experimental runs in Series 2 with D48.

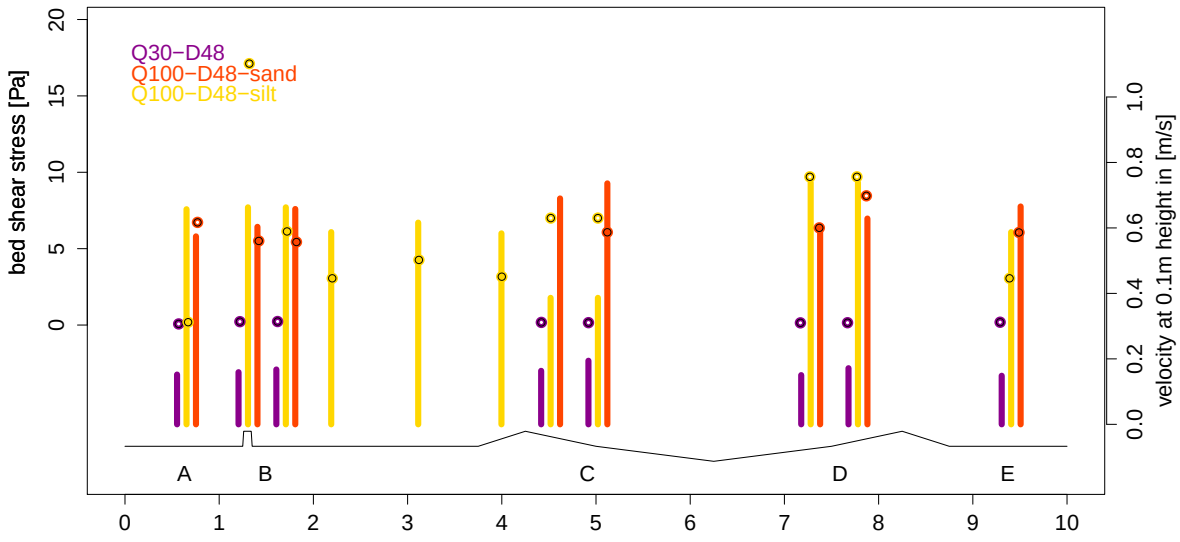

Figure 2.9: Velocity at 10 cm distance from bed (bars) and bed shear stress (circles) over traps and three extra inter trap positions for S2Q100D48-s with trap names at the bottom for experimental runs in Series 2 with a D48 bed (n=3 for all trap values and n=1 for in values between traps). Data from identical positions of the three experimental runs and trap pairs with same downstream position are plotted with an offset for legibility. Bed elevation is indicated with a black line. Where multiple readings, e.g. from beginning, middle and end of a trap, are available, values are averaged.

Again, the experimental run with low discharge shows only little variation in velocity and bed shear stress with increased values over trap pairs C and D. Velocity and bed shear stress values for higher discharge experiments are not only consistently higher, but also show more variation along the experimental channel.

Figure 2.10 shows velocity and bed shear stress for experimental runs in Series 2 with a D37 bed. Figure 2.10 does not only show values for the trap positions but also the results of a systematic scan every 62.5 cm.

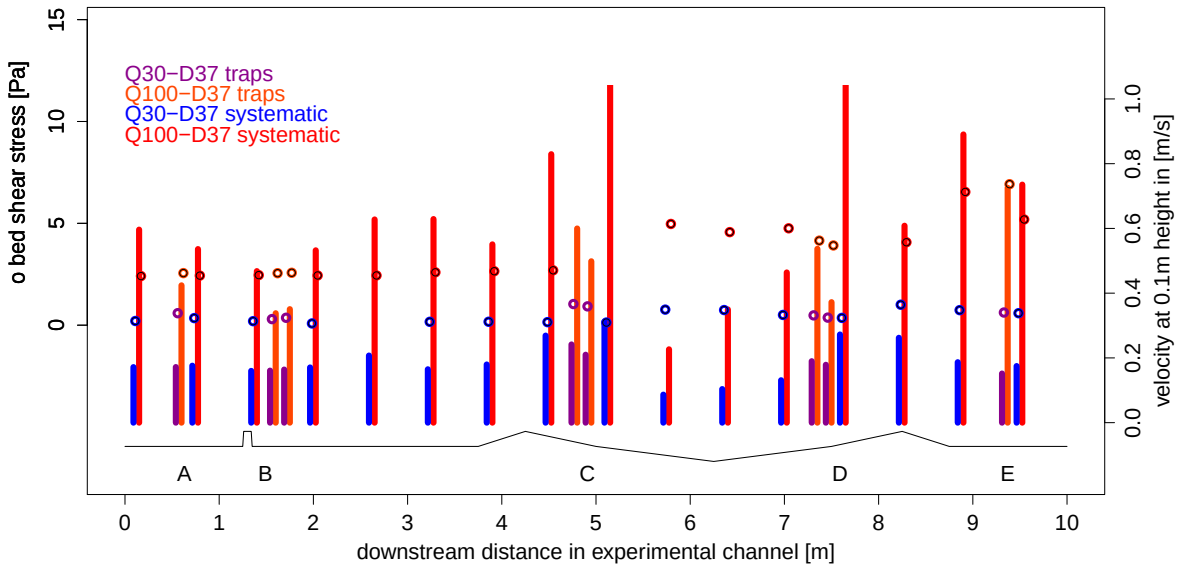

Figure 2.10: Velocity at 10 cm distance from bed (bars) and bed shear stress (circles) over traps with trap names indicated at the bottom and systematic measurements every 0.62 m for experimental runs in Series 2 with a fine D37 bed (n=3 for all positions). Data from identical positions of the three groups and trap pairs with the same downstream position are plotted with an offset for legibility. Bed elevation is indicated with a black line. Where multiple readings, e.g. from beginning, middle and end of the trap, are available, values are averaged.

The close meshed positioning of scanning points allows us to see more detailed velocity patterns for low discharge. At the upstream end of the experimental channel, velocities are stable, further into the experimental channel they increase with the rise of the bed elevation and decline again in the shallow bed area around 5 to 7 m, then rise again over the next bed elevation and recover to the same magnitude apparent at the upstream end of the experimental channel. For S2Q30D37, bed shear stress over the whole experimental channel is low. However, a moderate increase is observed over both elevations in the bed. Again, higher discharge results in higher velocity, higher bed shear stress and a higher variability of these values. The velocity distribution is very similar to the distribution for the D48 bed (as shown in Figure 2.9). Only if we are comparing the shear stress distribution, D37 exhibits considerably more equalised and lower values than D48. As seen before, the elevated bed

parts result in increased bed shear stress downstream. This shows that turbulence introduced by the elevated bed parts have further effects downstream. The effect of elevated bed areas is different for low and high discharge. At 30 L s^{-1}, the elevated bed caused only a local increase in velocity and bed shear stress. For S1Q50-2 and even more so for S2Q100 experimental runs, raised bed areas caused an acceleration of flow at the elevated point and increased local bed shear stress and additionally increased bed shear stress for positions further downstream. In summary, the velocity and bed shear stress within indentical settings shows a degree of variability which is considerable smaller than the difference between environmental settings and trap positions in Series 2.

2.3.3 Suspended fine sediment concentration

With regard to the fine sediment mass balance, the suspended sediment concentration loss from the bulk water mirrors the deposition in the interstices of the gravel bed in the experimental channel. Following Krone's formulation (Equation 2.1), the behaviour of the suspended sediment concentration loss is highly dependent on w_s, which in turn is mainly dependent on the grain size. Due to the crucial influence of grain size on settling velocity, silty and sandy experimental runs are discussed separately. This subsection first looks into the distribution of the suspended sediment in the vertical and longitudinal direction. Then, it reports on the suspended sediment concentration development during the course of all experimental runs with silty fine sediment and their absolute and effective grain size distribution. Subsequently, the concentration loss and grain size distribution of the sandy experimental runs are discussed.

Silty suspended fine sediment Figure 2.11 investigates a possible concentration profile of the suspended sediment, using data of four experimental runs.

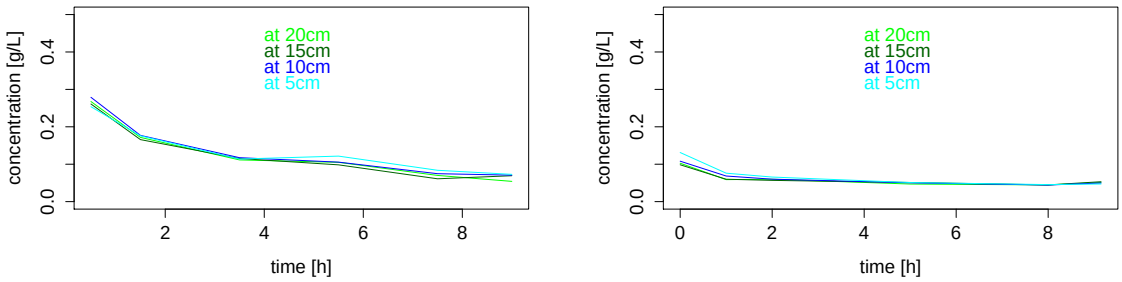

(a) S1Q50-1

(b) S1Q80

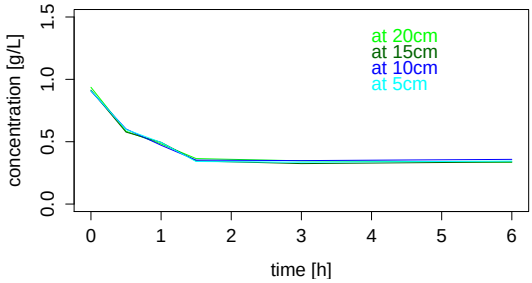

(c) S2Q30D48-1

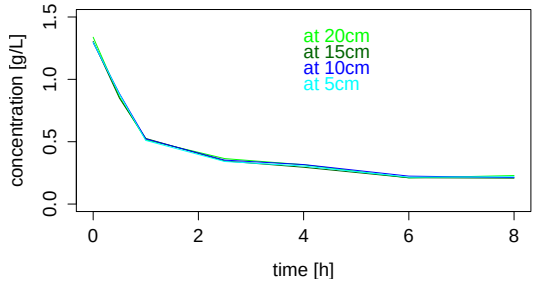

(d) S2Q100D48-1

Figure 2.11: Suspended sediment concentration layering at 5 m distance in the experimental channel for all four discharges.

For all discharges, concentration layering is not apparent after 5 m into the flume, which suggests a thorough mixing of the fine sediment. This means the flow length was too short and the water column too shallow to enable the development of a concentration profile. Also, no concentration divergence could be found between the beginning, middle and end of the flume (see Figure 2.12).

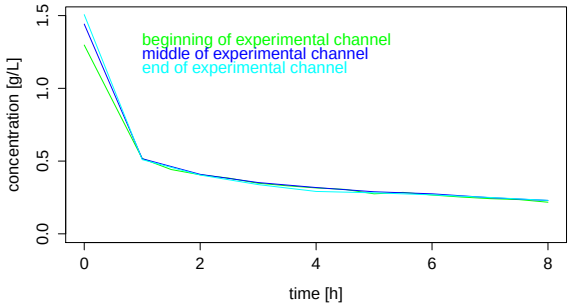

Figure 2.12: Suspended sediment concentration development at different positions in the experimental channel at minimal discharge of 30 L/s.

This allows us to generalise the concentration measured at the inlet into the experimental channel for the bulk water in the flume. Figure 2.13 shows the concentration development for experimental runs with silty fine sediment for the whole duration of each experimental run, each point being the average concentration of two bottled samples.

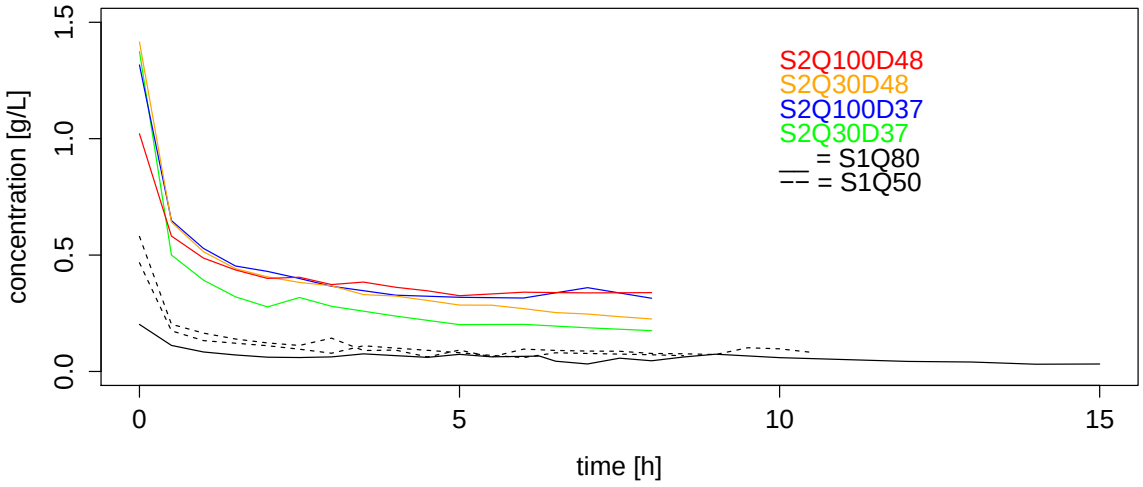

(a) Absolute Concentration Development

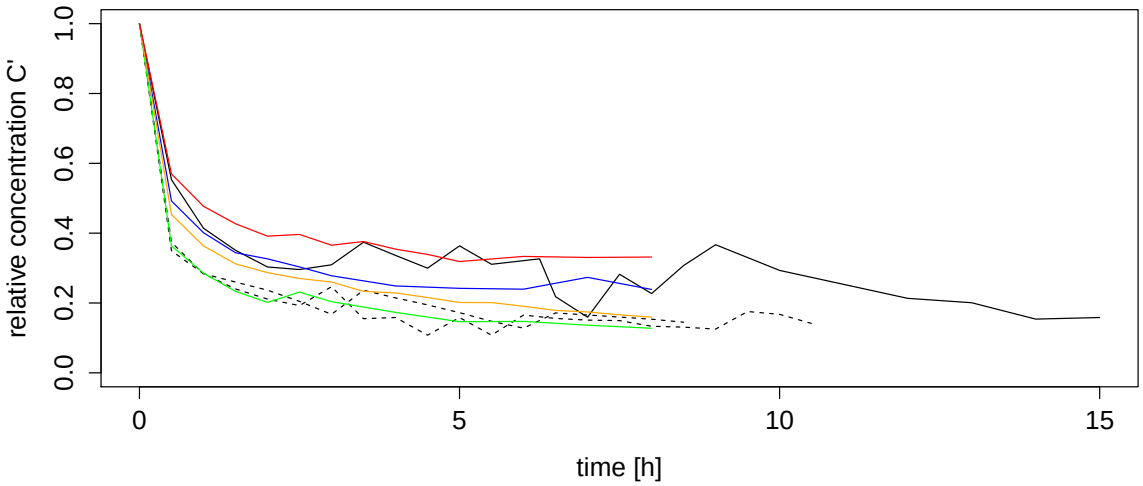

(b) Relative Concentration Development

Figure 2.13: Concentration development of experimental runs in Series 1 (in black lines) and Series 2 (with one representative of each experimental setting) represented in different colours.

Figure 2.13a gives the measured concentration [gL^{-1}] and Figure 2.13b shows the same data as dimensionless concentration C' by dividing the concentration at

time i (C_i) by the initial concentration (C_0), see Equation 2.7.

$$C' = \frac{C_i}{C_0} \tag{2.7}$$

All concentration curves experience a steep decline at the beginning of the experimental run, then level out to reach the so called equilibrium concentration. Following the theory of Krishnappan (2006), the equilibrium concentration depends on flow and grain size distribution and is a particular fraction of the initial concentration. Since all silty experimental runs use the same source of suspended sediment and consequently have the same initial suspended sediment grain size distribution, the equilibrium concentrations in Figure 2.13 are the result of the flow character. To investigate the systematic behaviour of the equilibrium concentration, the normalised concentration loss ($C'loss$) is introduced. $C'loss$ is the difference between initial concentration and final concentration divided by the initial concentration, see Equation 2.8.

$$C'loss = \frac{C_0 - C_{end}}{C_0} \tag{2.8}$$

Figure 2.14 shows a scatterplot of the normalised concentration loss compared to the mean velocity. The data shows that the concentration loss is dependent on velocity and decreases with rising mean velocities. Equilibrium concentration for D48Q100 is at 40 % of the initial concentration, whereas the equilibrium concentration for D48Q30 is at ca 20 %. The divergence for the smoother D37 bed is smaller with 30 % at Q100 and 18 % at Q30. This shows that also the two bed grain size distribution in Series 2 have an influence on equilibrium concentration. The finer D37 bed results in a higher concentration loss compared to the coarser D48 bed, both for Q30 and Q100.

Absolute and effective grain size distribution: The relation of concentration development, equilibrium concentration and discharge is only valid for the specific fine

sediment used in these experiments. Therefore, it is crucial for the further understanding of the deposition behaviour in the flume to analyse the grain size distribution of the suspended sediment.

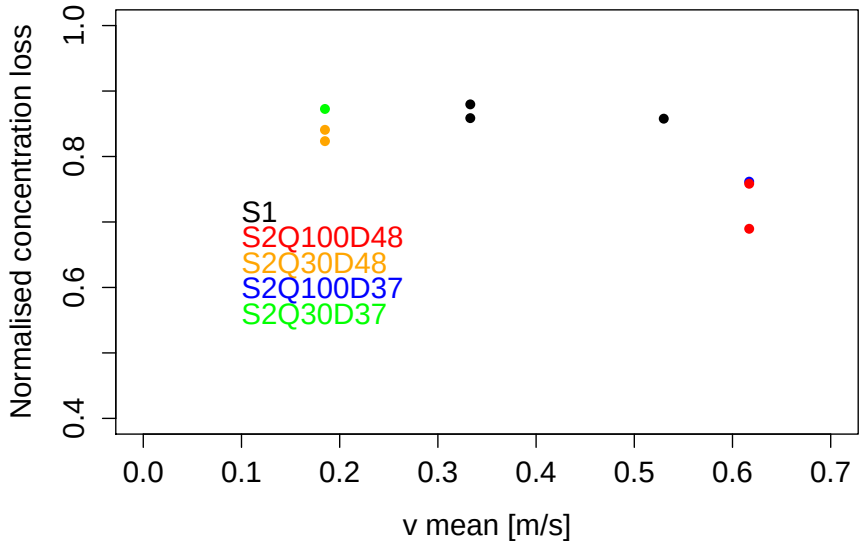

Figure 2.14: Normalised concentration loss ($C'loss$) in relationship to mean velocity for silty experimental runs.

Figure 2.15 enables us to make two comparisons, first, between the soil used as the base for the suspended fine sediment and the initial sample drawn from the bulk water, and second, between the initial sample's absolute and effective grain size distribution.

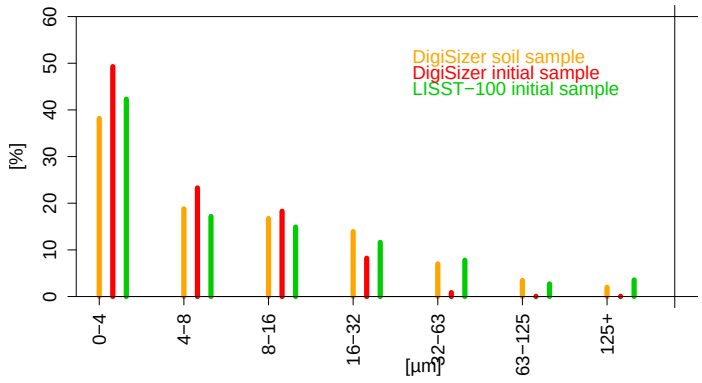

Figure 2.15: Comparison of the fine sediment grain size distributions original silty soil measured with the DigiSizer, initial suspended sediment measured with the DigiSizer and the LISST-100.

The soil grain size distribution is much coarser than the first suspended sediment sample (both measured with the DigiSizer), which is also obvious if we compare the D_{50} of 16.71 and 6.71 μm. This means particles have already left the suspended fraction in the flume and are already deposited before the first sample is taken. This problem was already noticed in the experimental setup in 2.2. Still, it also needs to be considered under the angle of the grain size distribution, when trying to compare the bulk sediment loss and the deposition measured. Moreover, the distribution of the initial suspended sediment sample is different for absolute grain size measurement (with the DigiSizer) compared to the effective grain size measurement (with the LISST-100). With a D_{50} of 17.96 μm, the effective distribution of the initial sample is slightly coarser than the absolute distribution of the soil sample. The coarser effective distribution is caused by the presence of aggregates and flocs, which are only measured with the LISST instrument but destroyed in the preparation procedure for the DigiSizer.

The next step of the grain size analysis is to understand the grain size distribution development over the term of an experimental run. Figure 2.16 shows the grain size distribution development measured for S2Q100D48-1 in 2.16a as absolute values

with the DigiSizer and in 2.16b as effective values with the LISST-100. The effective grain size distribution is the average of measurements at the beginning, middle and end of the flume with error bars indicating the total maximum and minimum. As seen before, the absolute grain size distribution is finer than the effective distribution with almost no particles coarser than 32 μm, whereas the effective grain size distribution shows ca. 30 % of the particles larger than 32 μm. Additionally, Figure 2.16a shows a fining over the term of the run with the 0-4 μm class increasing from 50 to 58 %. The fractions 8-16 μm and 16-32 μm are decreasing at the same time. The effective grain size distribution in Figure 2.16b comprises more noise, which is particularly obvious when looking at the comparatively large error bars. Nonetheless, the trends for the absolute grain size are more distinct for the effective grain size.

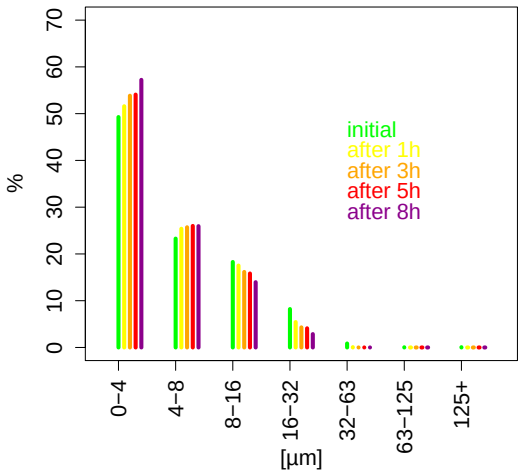

(a) Absolute Grain Size Development measured with DigiSizer during S2Q100D48-1.

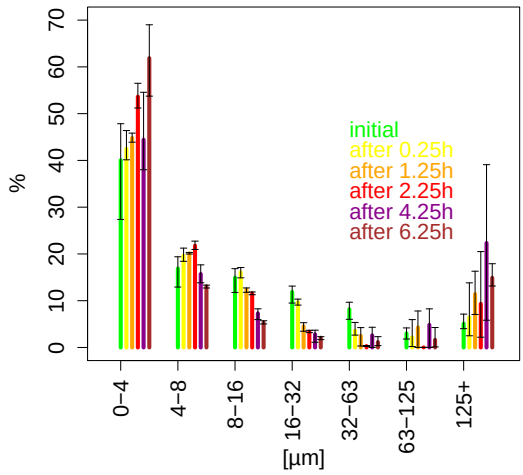

(b) Effective Grain Size Development during S2Q100D48-1, averaged from samples taken parallel from beginning, middle and end of experimental channel measured with the LISST-100. Error bars give the maximum and minimum value measured.

Figure 2.16: Grain size distribution development during S2Q100D48-1 measured as absolute and effective values from samples taken at 15 cm above the bed.

Class 0-4 μm increases relatively from 40 to 60 % and all classes between 8-125 μm experience a decline. At the same time, another process is recorded in the

overall rising fraction of particles larger than 125 μm. This increase indicates a flocculation process. Solid soil particles of 125 μm should settle out immediately. Only flocs of that size, including large proportions of water have a density low enough to stay in suspension. A similar process was recorded in Lau et al. (2001) in flume experiments with kaolinite, where floc formation was detected after ca. 150 minutes into the experimental run. Haralampides et al. (2003) as well showed floc formation in the range of 80 to 120 μm over time. Although the effective GSD shows a distinct coarser distribution than the absolute grain size distribution, it is not clear that the effective distribution is more decisive for the deposition processes. Especially after a longer period of suspended sediment transport, the effective grain size distribution can not be used with the same density as for the mineral grains to calculate values for settling velocity. Moreover, the use of absolute GSD has important practical advantages. Often it is easier to apply and it is more reproducible and applicable to dry sediment and therefore not dependent on, e.g., sample storage or suspended sediment preparation.

2.3.4 Suspended sandy fine sediment

The initial concentration for the sandy experimental runs is the sediment input divided by the total water volume. All sandy experimental runs experience an extreme steep drop in fine sediment concentration in the first minutes of the experimental run, followed by a constant very low equilibrium concentration, which can be seen in Figure 2.17a as measured C and in 2.17b in relative concentration (C').

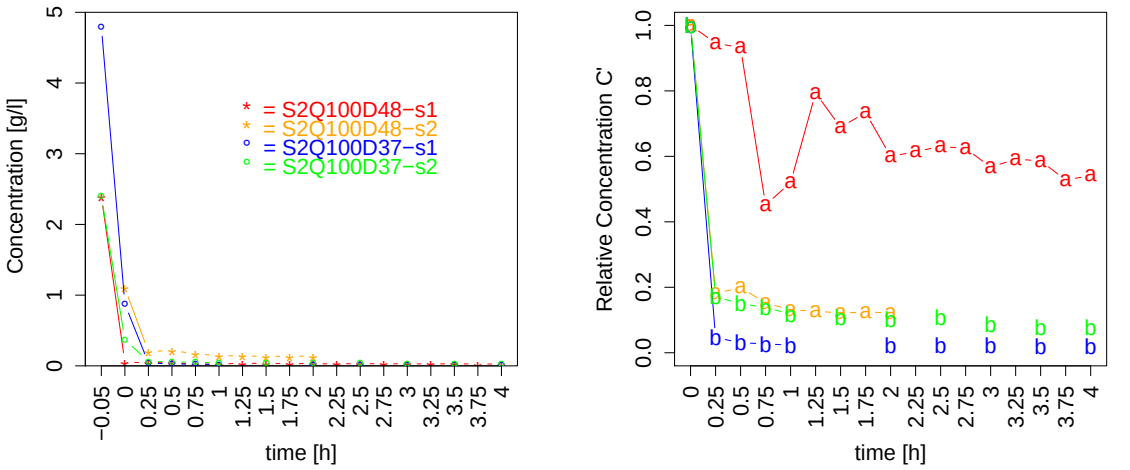

(a) Absolute Concentration Development

(b) Relative Concentration Development

Figure 2.17: Concentration development of all sandy experimental runs

All experimental runs behave very similar with a nearly complete deposition in the first 15 minutes. Only experimental run S2Q100D37-s2 with the finest sand (plotted in yellow) results in a recognisable equilibrium concentration at around 15 % of the initial input.

2.3.5 Fine sediment deposition - silt size

The final result presented in this chapter is the interstitial fine sediment deposition recorded during the different experimental runs. Fine sediment deposition is measured as the trapping ratio (TR), which is the fine sediment found in one trap given in kg m^{-2}. In the experiments, all fine sediment is derived from the suspended sediment. The single TRs are local information about fine sediment deposition. For the estimation of the overall deposition, the concept of potential deposition is used, which is based on the measured concentration loss (C_{loss}). Potential deposition ($Dpot_i$) is the measured concentration decline at point i in time applied to the area of the ex-

perimental channel, as defined in Equation 2.9.

$$Dpot_i = \frac{Closs_i * Vol}{Area} \tag{2.9}$$

with Vol being the total water volume of the flume and $Area$ the total area of the experimental channel.

Figure 2.18 shows the development of $Dpot$ and the single measured trapping ratios for silty experimental runs. The duration of the experimental run is given on the x-axis, $Dpot$ and TR are indicated on the y-axis. The TR of the single traps is plotted at the time of recovery with the trap set naming letter. For all experimental runs, TR shows a wide range of variation. Still, some general trends can be identified. In Series 1 (Figures 2.18b and 2.18a) with a flat bed and comparatively little noise and turbulence, two trends are visible in the data. (1) Especially for S1Q50-1 in Figures 2.18b, but also for S1Q80 in Figures 2.18a TR is higher for traps recovered later in the experimental run. (2) Additionally, traps A display higher trapping ratios than traps B which again are higher than TR in traps C. Trend (1), the higher TR over time is not consistent with the development of $Dpot$. $Dpot$ shows, that after an initial phase of fast deposition (approximately the first hour of the experimental run), deposition levels out to a stable value. Therefore, further deposition between the different times of recovery can only be explained with a source other than the suspended sediment, for example from the surrounding gravel bed. Another explanation for the apparent continuous deposition over time is the distance of the traps to the inlet of the experimental channel. Coarser particles can be deposited promptly after entering the experimental channel and cause enhanced deposition close to the inlet. For example, the highest TR in A1 (which is the A trap recovered last) can be explained with both theories: A1 is both the trap closest to the inlet and the trap recovered last. Trend (2) can be caused by two processes: It can either be a function of the distance to the inlet or a function of the gravel GSD, which is finest in A, medium in B and coarsest in C. A special case in S1Q80 (Figure 2.18b) is the high

TR of C at 2 h (which is trap C3). If we are looking back at Figure 2.5a, C3 has an unusually high velocity at 5 cm of approximately 0.5 ms^{-1} compared to 0.2 ms^{-1} for all other traps. This might indicate that faster velocities result in a higher deposition. This stands in contrast to the theoretical background of the Krone formulation, where higher velocities should result in less deposition. The question if this is a trend or just an outlier can not be answered at this point, but will be discussed later.

Irrespective of the trapping ratio in S1Q80 C3, the trapping data suggests that at least two of the three above described processes overlap to result in the measured trapping ratios. Although both trends (1) and (2) can in parts be explained by elevated trapping closer to the experimental channel inlet, another process needs to contribute as well, since for example trap B which has been recovered last displays a higher TR than trap A which has been recovered first. Concluding, the TR patterns in Series 1 originate most likely from a combination of the following three processes: Distance from the inlet plus either additional trapping from other sources than the suspended sediment effective over time or the effect of different gravel grain sizes in the traps. In Series 2 with the non-uniform bed, the TR displays higher variations compared to Series 1. The TR data does not show continuous higher values for recoveries later in the experimental run. Although, for some trap pairs a considerably different TR is found for the two recovery times (for example between the D traps in S2Q30D48-1 and S2Q100D48-1 in Figure 2.18c and 2.18d). In Series 2, a difference between the beginning and the end of the experimental channel is apparent. Generally, trap A has a higher TR than trap E, despite the similar bed environment and flow condition. This is a strong evidence for the existence of an increased deposition in the proximity to the inlet. Clear patterns in TR for the three trap pairs B, C and D are not obvious. Despite the high variation in TR in Series 2, there are consistent differences between the magnitude of TRs of runs with different discharge. For experimental runs with a discharge of 30 L s^{-1}, TRs range in the same magnitude as $Dpot$.

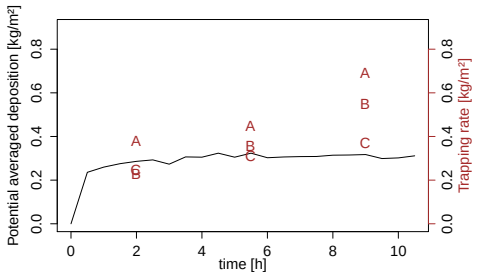

(a) S1Q50-1

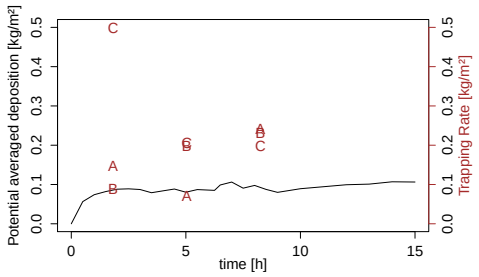

(b) S1Q80

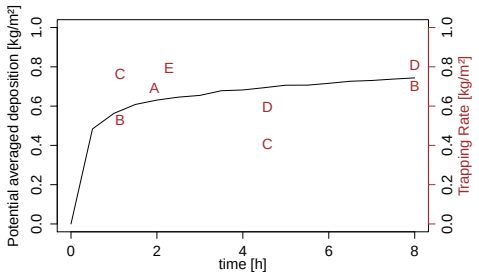

(c) S2Q30D48-1

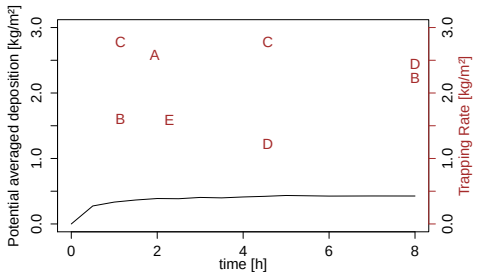

(d) S2Q100D48-1

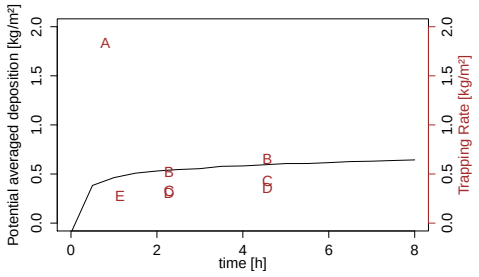

(e) S2Q30D48-2

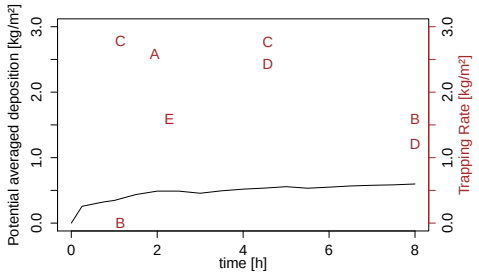

(f) S2Q100D48-2

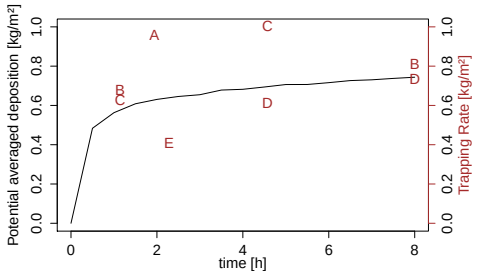

(g) S2Q30D37

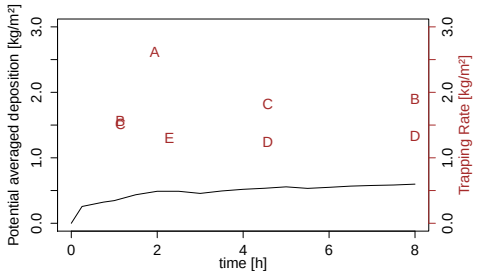

(h) S2Q100D37

Figure 2.18: Measured trapping ratio (TR), given as the trap naming capital letter plotted at time of recovery and potential deposition ($Dpot$) for experimental runs with silty fine sediment. Top panels (a and b) show Series 1 experimental runs with a complete flat bed. The six lower panels (c to h) show Series 2 Q30 runs on the left and Series 2 Q100 runs on the right, all with a non-uniform bed.

For experimental runs with Q100, the overall magnitude of TR is much higher than deposition suggested by $Dpot$. This indicates a systematic divergence in the fine sediment mass balance dependent on discharge, which will be discussed in the next paragraph.

Mass balance of silty fine sediment: In order to compare the single measured deposition ratios (TR) with the potential deposition $Dpot$, the average of the trapping ratios ($TRmean$) is used as defined in Equation 2.10.

$$TR_{mean} = \sum_{i=1}^{n} TR_i \tag{2.10}$$

Where i refers to the single traps in the experimental channel from A to F Arguably, $TRmean$ is not representative for the whole experimental channel because the flow conditions over the traps are not representative for the flow conditions in the experimental channel. Further, $TRmean$ is averaged for the different recovery times and not accounting for potential differences in deposition over time. Still, this is seen as a small error, since the main deposition from the suspended sediment is completed before the first trap is recovered and TR data does not show clear temporal trend for most experimental runs. Therefore despite its limitations, the magnitude of $TRmean$ in relationship to $Dpot$ is an indicator for the overall fine sediment mass balance. Figure 2.19 plots one data point for each silty experimental run. The x-axis is the mean velocity, which is the overall velocity deduced from the discharge and the experimental channel cross-sectional area. The y-axis shows $TRmean$ divided by $Dpot$. The data presented in Figure 2.18 suggests a disproportionate rise of $TRmean$ compared to $Dpot$ for rising discharge. Further, it suggests a higher $TRmean/Dpot$ for the rougher D48 bed.

Processes in the five minutes of the experimental run prior to the first measurement can be identified to cause this discrepancy. The fining of the grain size distribution is a first indicator for the amounts deposited. Still, the dynamics of the fine sedi-

ment in the time lag period are a black box without measurements. A further attempt to quantify the suspended concentration loss in the first five minutes was assuming an exponential decline of C. On average, this resulted in an approximately 15 % higher C_0, with only minimal higher values for Q100 compared to Q30. Therefore, this attempt alone does not deliver a coherent explanation, because it cannot explain the rise in $TRmean/Dpot$ with rising discharge. Further, the amount of sediment estimated from the concentration loss is much smaller than $TRmean$ (see Figure 2.19 with y-axis values up to 8). Even with a limited explanatory power of $TRmean$ for the whole experimental channel, this raises questions. A further indicator hinting at a fundamental problem is that the suspended load calculated from the total water volume and measured concentration is not equal to the sediment input into the flume plus the measured TR. This difference means that there is fine sediment, which is not accounted for in the measured parts of the fine sediment mass balance. The difference of the input load to the initial suspended load is higher for experimental runs with Q30 compared to Q100. Moreover, observations showed that fine sediment was deposited outside the experimental channel. After all experimental runs, a considerable accumulation of fine sediment was found at the exit of the recirculating pipe, the basin in front of the comb-like screen (see again Figure 2.2). In retrospect, deposition in this area is not surprising. High velocity and turbulence cause a high transport capacity in the recirculating pipe. When the velocity slows after the exit of the recirculating pipe into the basin in front of the comb-like screen, the transport capacity decreases and fine sediment deposits.

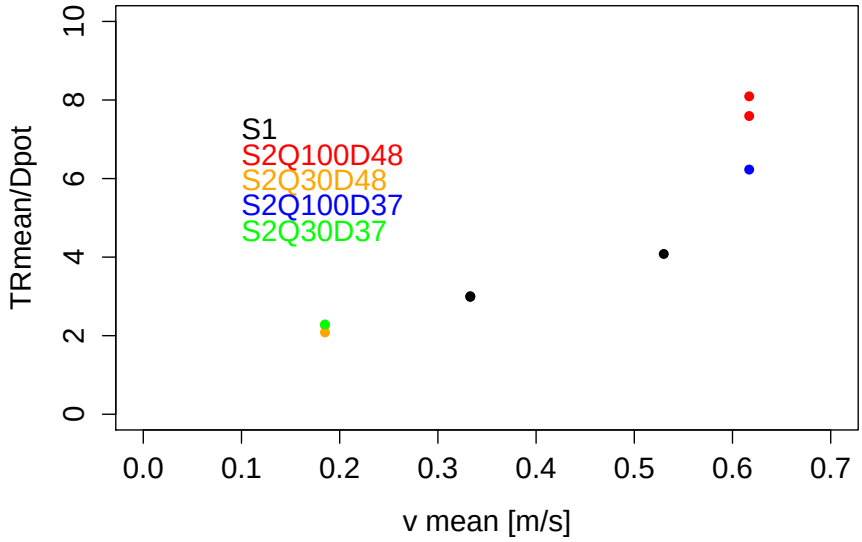

Figure 2.19: Relationship of the ration of the mean trapping ratio in relation and potential deposition to mean velocity of all experimental runs with silty fine sediment.

If the magnitude of deposition in this area is dependent on velocity and turbulence, the difference in $TRmean/Dpot$ in relationship to discharge can be explained as follows. Velocity and turbulence between the exit of the recirculating pipe and the entry into the experimental channel are lower for Q30 compared to Q100 and therefore deposition is higher. If deposition for Q100 in the unaccounted storage is lower, more coarse suspended particles enter the experimental channel and settle out in the five minutes prior to the initial concentration measurements. This theory could not be proven conclusively, despite several attempts to do so. The statistical analysis probably failed due to the high noise in the data and the comparatively low number of data points.

Grain size distribution of trapped material: The processes described above, which explain the observed TR patterns, are all connected to the fine sediment grain size. Prompt deposition of coarse grains in- and outside of the experimental channel should lead to a depletion of coarse particles in the initial sample compared to the original silty sediment. Further, the difference in the amount of deposition outside

the experimental channel between Q30 and Q100 runs should also be reflected in the grain size distribution. Higher deposition close to the inlet due to fast deposition of coarser particles should lead to the coarsest distribution of fine sediment in the traps furthest upstream. Additionally, deposition after the initial intensive suspended sediment deposition should result in a fining of trapped sediment in traps with a later recovery time.

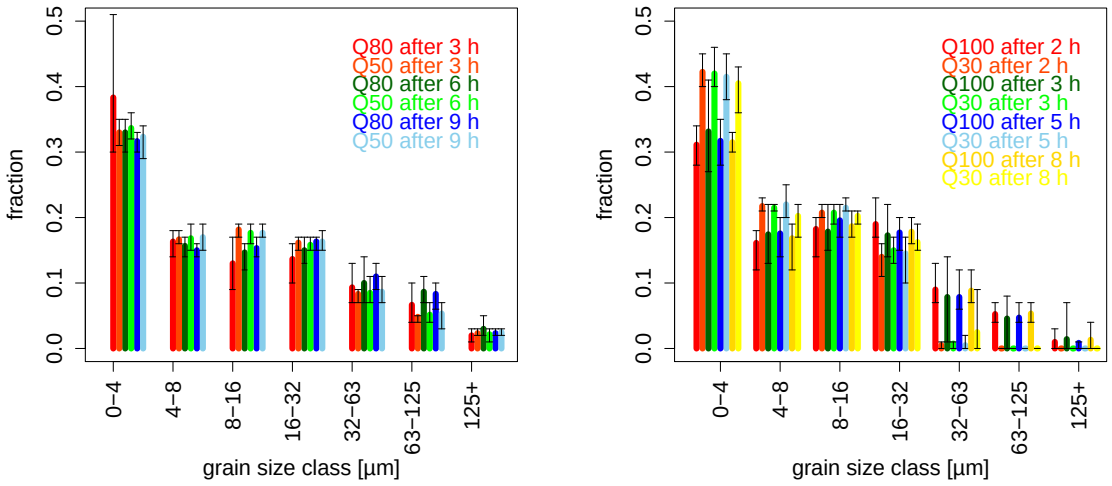

(a) Series 1 (b) Series 2

Figure 2.20: Grain size distribution of trapped material in silty experimental runs grouped in discharge and recovery time (Series 1: Q50 and Q80, 3, 6 and 9 h recovery; Series 2: Q30 and Q100, 2, 3, 5 and 8 h recovery).

Finally, the different trapping of different gravel grain sizes might be as well connected to a trapping of different grain sizes. Regarding this assumption, Figure 2.20 shows the grain size distribution of the trapped material separately for Series 1 and Series 2 with data split according to the experimental discharge and recovery time of the trap. The error bars indicate the maximum and minimum fraction measured in this group. There is no fining of the grain size distribution for the three recovery times in Series 1, respectively the four recovery times in Series 2. This means further trapping over time from sources other than the suspended sediment is not visible in the fine sediment grain size distribution of the trapped material. However, both Series 1

and Series 2 data show considerable divergences between the different discharges. In Series 1, Q50 and Q80 result in a consistent small divergence with coarser trapped material in Q80 compared to Q50. This difference is more pronounced in Series 2 between Q30 and Q100. In Q30, no material $>63\mu m$ is measured in the traps. This suggests that all coarser material is deposited outside the experimental channel. Particles $>63\mu m$ represent 12.5 % of the original silty sediment (see Table 2.2). Figure 2.21 shows the D_{50} of the trapped material for each trap and experimental runs in Series 1 (Figure 2.21a) and as averaged values for Q30 and Q100 for Series 2 (Figure 2.21b). Averaged values for the D_{50} of the trap sets in Series 1 and Series 2 are listed in Table 2.8. For silty experimental runs, the variation between the fine sediment grain size distribution of the single traps is small. The largest variation is found in Series 1, where D_{50} is coarsest for B in all three runs. Further, the finest mean D_{50} of the three runs is found for S1Q50-1 with the lowest flow velocities.

In Series 2, the average D_{50} of all traps of one discharge is remarkably similar. However, the difference in average and range between Q30 and Q100 is large. In Q30, the total variance is around 2 $\mu\mathrm{m}$, whereas in Q100 the average values of the single traps are very similar but maximum and minimum values range from 12 to 24 $\mu\mathrm{m}$. With regards to the initially stated assumption, the following conclusions can be drawn. The grain size distribution data gives clear evidence of discharge dependent loss of coarse grain sizes outside the experimental channel. The strongest effect is found for Q30 experimental runs, where all particles $>63\mu\mathrm{m}$, which is equal to 12.5 % of the silty fine sediment, are lost prior to the initial suspended sediment sample. However, this prompt loss of coarse fine sediment from the suspended load is not visible in the traps close to the inlet into the experimental channel. This means other processes than surplus trapping of coarse material close to the inlet, such as irregularities in flow, are the cause for the high trapping in A. The grain size distribution showed no evidence of fining for traps recovered later in the experimental run. This means that additional trapping from sources other than the suspended sediment are

Serie 1					
trap set	**A**	**B**	**C**		mean
S1Q80	16.3	18.0	16.9		17.1
S1Q50-1	14.0	15.78	15.7		15.2
S1Q50-2	15.3	18.8	17.2		17.1
Serie 2					
trap set	**A**	**B**	**C**	**D**	**E**
Q30 mean	10.1	9.9	10.3	11.8	10.39
Q30 min	9.1	9.2	9.3	10.2	10.0
Q30 max	11.1	10.4	11.1	14.1	10.7
Q100 mean	16.8	18.3	16.4	16.8	17.6
Q100 min	15.1	15.2	12.0	14.5	13.7
Q100 max	19.4	23.78	21.7	22.2	24.2

Table 2.8: D_{50} in μm of trapped silty material in Series 1 for all experimental runs averaged for the three trap sets and in Series 2 averaged for Q30 and Q100 for the five different trap positions.

an unlikely cause for the apparent higher trapping over times in Series 1.

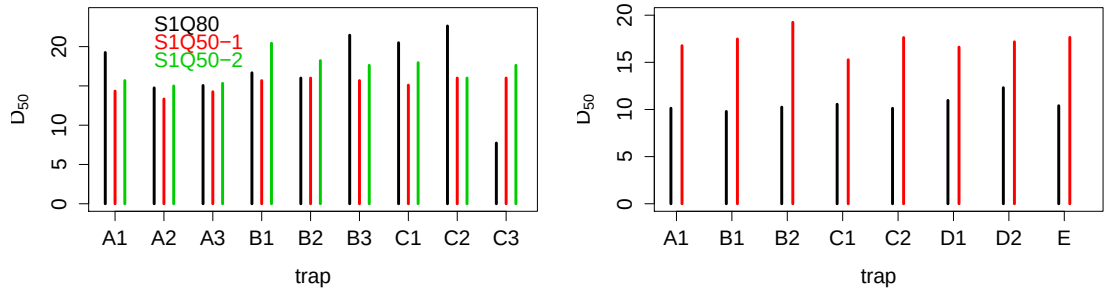

(a) Series 1 (b) Series 2

Figure 2.21: D_{50} of trapped material in silty experimental runs grouped in discharge and traps.

Analysis of trapping ratios in relation to flow: Although TR, $Dpot$ and the grain size distribution of the suspended and trapped sediment clearly show the processes causing the problems in the mass balance, no attempts of correcting the data resulted in a satisfactory and statistically defendable solution of the overall mass balance. Despite these limitations, this section investigates the relationship of the TR distribution to flow distribution.

Figure 2.22 plots observed TR versus the local flow velocities at 10 cm. The panels represent different subsets of the data for the silty experimental runs (complete dataset, Series 1 data, Series 2 data, and data for the six experimental settings) in nine different panels.

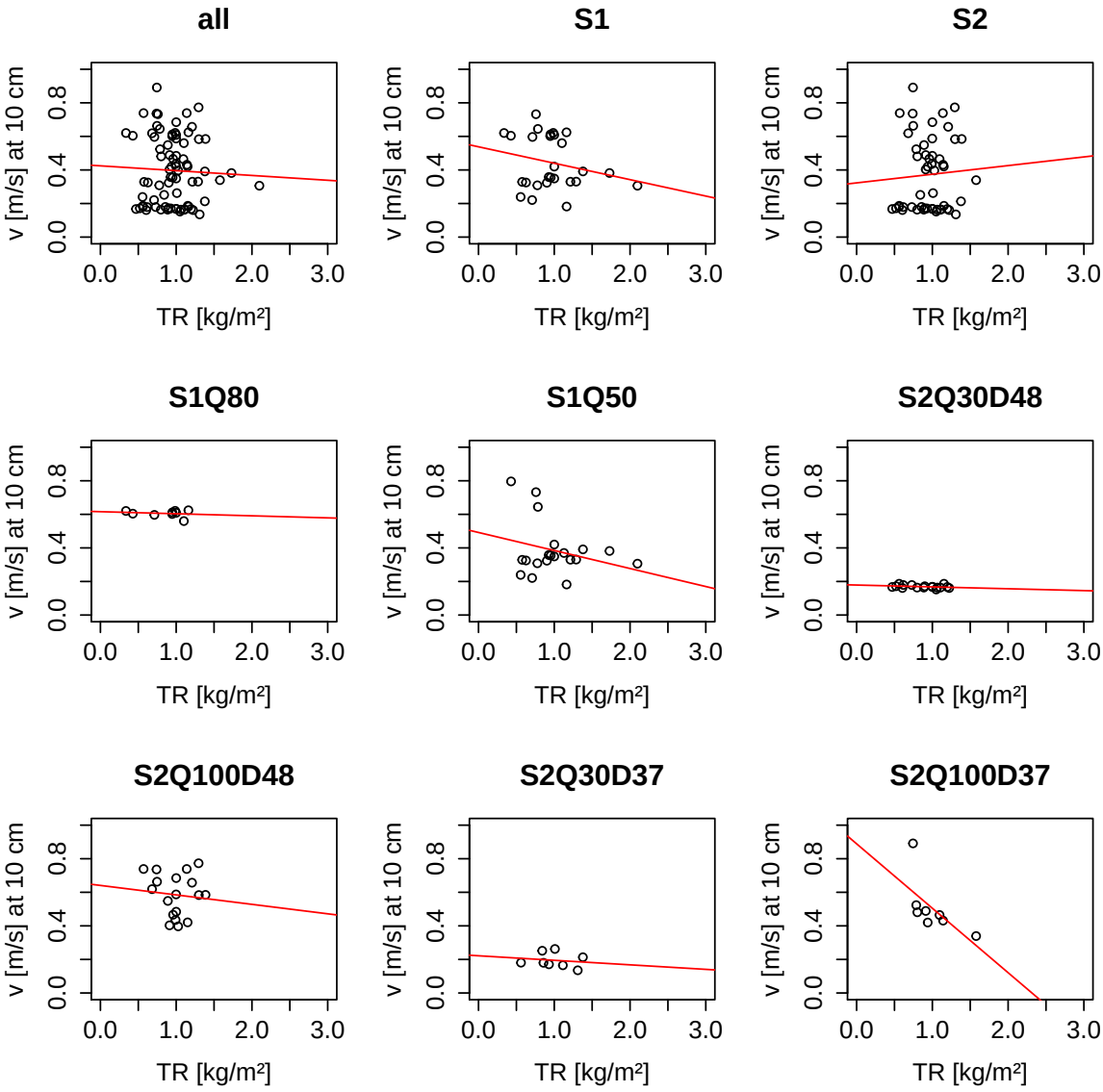

Figure 2.22: Scatterplots of TR compared to local velocity at 10 cm height above the river bed for silty experimental runs. Trend lines of least square linear regressions.

Further, the trend line of a least square linear regression was added to the plot in red. Although for some datasets trends are visible (e.g. S1 or the experimental run S2Q100D37), other datasets do not show a correlation between TR and local veloc-

ity. The lack of a consistent trend is confirmed by the results of the linear regression applied to these datasets and summarised in Table 2.9. Given the high variability of TR, data points within one experimental run are too little for a meaningful analysis of correlations. Therefore, the data of the different experimental runs need to be normalised.

dataset	r^2	**intercept**	**slope**
all	0.00	0.42	-0.03
Series1	0.05	0.54	-0.10
Series 2	0.00	0.32	0.05
S1Q80	0.03	0.62	-0.01
S1Q50	0.08	0.49	-0.11
S2Q30D48	0.09	0.17	-0.01
S2Q100D48	0.01	0.64	-0.06
S2Q30D37	0.03	0.22	-0.03
S2Q100D37	0.40	0.89	-0.34

Table 2.9: Statistical evaluation of TR compared to local velocity at 10 cm height using least square linear regressions

The normalisation of the velocities was conducted using the mean velocity calculated from discharge and channel cross-section (v_{mean}). Local shear stress was normalised using the average of all shear stress values (τ_{mean}). For the normalisation of the trapping ratios, there are two fundamentally different possibilities. On the one hand, TR can be normalised with $Dpot$ or other specifications of the measured concentration (for example load calculated from the sediment input or the final concentration). On the other hand, TR can be normalised with the average TR ($TRmean$). The latter was chosen because it is not dependent on flow per se. It shows the relationship of the single TRs towards each other in one experimental run. Figure 2.23 and 2.24 show plots of the normalised TR and normalised velocity, respectively bed shear stress for the same data set as seen in Figure 2.22. Velocity is the average velocity of the four measured heights (v-average), bed shear stress is the Tz specification.

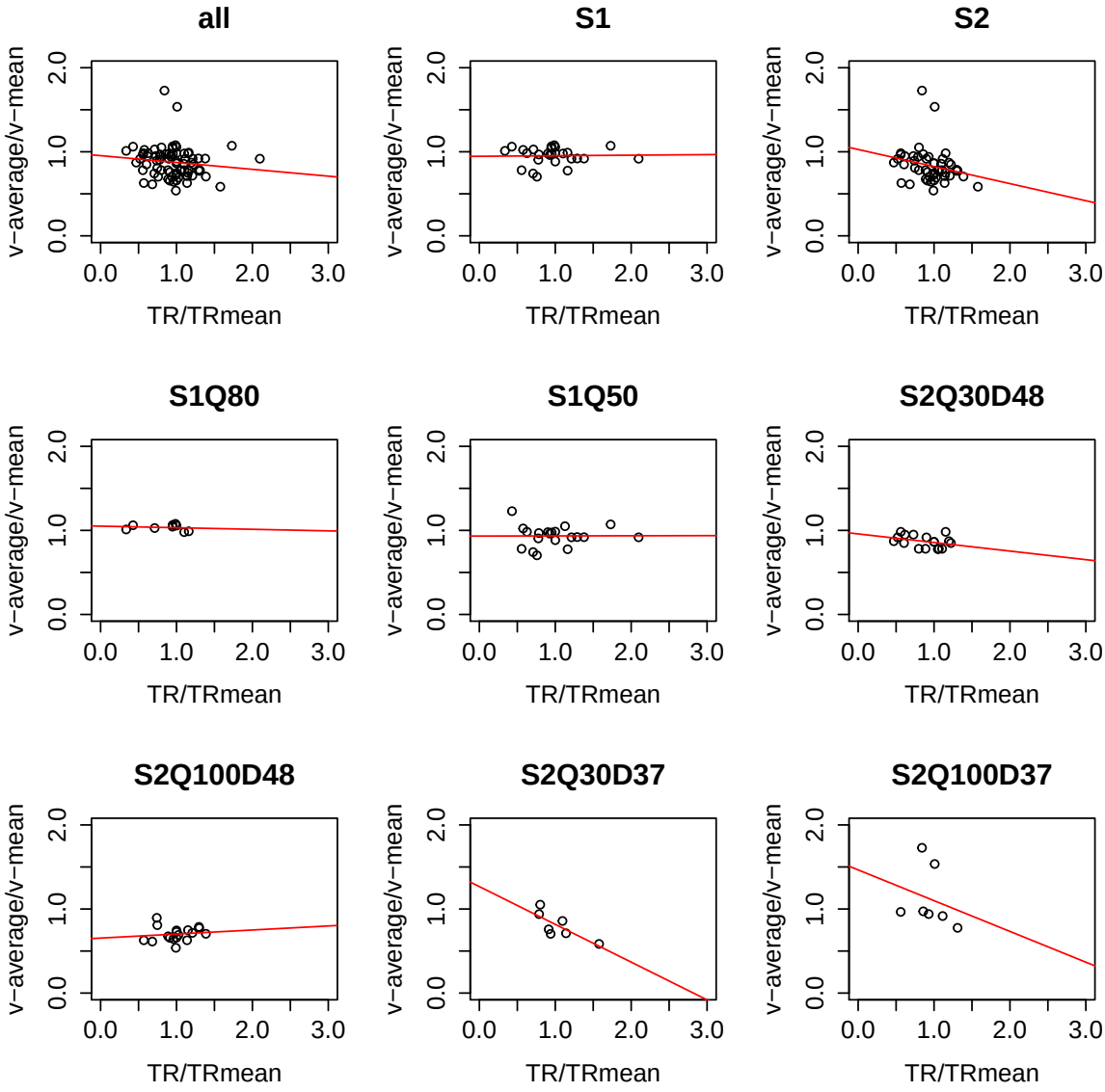

Figure 2.23: Scatterplots of TR/$TRmean$ compared to local normalised velocity for silty experimental runs. Trend lines of least square linear regressions are added in red.

The influence of velocity on TR for all experimental runs is overall weak, which also becomes obvious when looking at r^2 in Table 2.10. For Series 1 data as a whole and also for S1Q80 and S1Q50, the trend line of the linear model has a slope close to zero. This is not surprising since the experimental runs were conducted with a flat bed resulting in a lack of velocity variation. Therefore, all variation in TR can only be dependent on other factors than the variation in velocity.

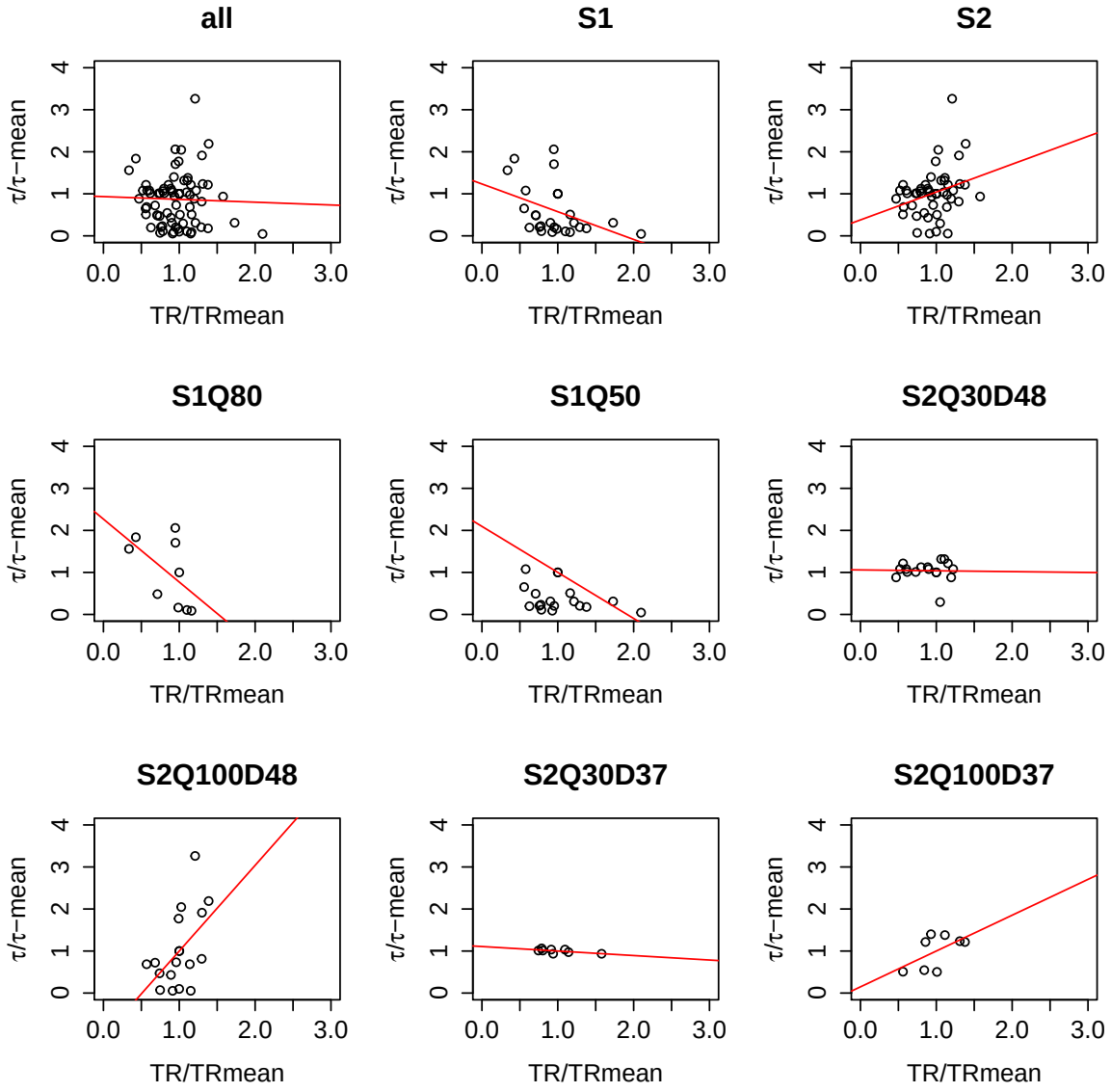

Figure 2.24: Scatterplots of TR/$TRmean$ compared to local normalised normalised bed shear stress for silty experimental runs. Trend lines of least square linear regressions are added in red.

As for Series 2, all experimental runs (apart from S2Q100D48) show a slight decline of TR/$TRmean$ with rising v-average/v-mean. This means that for a non-uniform bed the acceleration of flow over elevated bed parts reduces TR. The correlation for normalised TR and normalised τ_0 (data plotted in Figure 2.24 and statistical values listed in Table 2.10) are overall higher, but not consistent in their trend. For the flat bed setup in Series 1, TR/$TRmean$ declines with rising τ/τ-mean. Remarkably, the trend line of the linear regressions in Series 1 are very similar. In Series 2 the trend

dataset	velocity r^2	intercept	slope	bed shear r^2	stress intercept	slope
all	0.025	0.98	-0.10	0.38	1.11	-0.11
Series1	0.008	0.99	-0.03	0.17	1.23	-0.066
Series 2	0.057	1.03	-0.20	0.086	0.37	0.66
S1Q80	0.025	1.05	-0.02	0.29	2.27	-1.50
S1Q50	0.056	0.93	0	0.056	2.10	-1.10
S2Q30D48	0.130	0.96	-0.10	0	1.06	-0.02
S2Q100D48	0.017	0.65	0.05	0.26	-1.04	2.04
S2Q30D37	0.60	1.27	-0.45	0.38	1.11	-0.11
S2Q100D37	0.057	1.47	-0.37	0.31	0.15	0.85

Table 2.10: Statistical evaluation of normalised TR compared to normalised velocity and bed shear stress using least square linear regressions are added in red.

between TR/$TRmean$ and τ/τ-mean are different for low (Q30) and high discharge (Q100) experimental runs. The bed shear stress has very limited influence on the deposition behaviour for low discharge situations, whereas for Q100, higher shear stress results in higher deposition. Despite the few data points and the weak correlations, this is a remarkable finding. For a flat bed with uniform velocity, velocity has naturally no influence on the distribution of deposition. However, for a flat undisturbed bed (as used in Series 1), there is a correlation between rising bed shear stress and declining trapping ratios. In situations with altering bed elevations, the change of velocity causes a response in the deposition distribution with acceleration resulting in lower trapping ratios. This trend is stronger for the D37 bed with a lower bed roughness. With regards to shear stress, Series 2 Q30 experimental runs do not show any influence, due to uniform shear stress values for the whole experimental channel. However for higher discharge, the bed elevation changes shear stress and a clear correlation between bed shear stress and deposition can be seen. Yet, this trend is opposed to the one shown for velocity and opposed to the one described in the Krone formulation. A possible explanation for this finding is that velocity is a measure of conditions in the water column and a descriptor of the competence to transport suspended sediment. Bed shear stress, although connected to the velocity, is a measure of the roughness conditions close to the river bed. Therefore higher

bed shear stress is an indicator for turbulence and a higher probability of particle deposition. These trends regarding the interrelation of TR and flow conditions need to be treated with caution due to the small number of data points and the high noise of the trapping data.

2.3.6 Fine sediment deposition - sand size

The following section discusses the deposition during the sandy experimental runs. Here, a different fine sediment input routine was applied to ensure all sediment was deposited in the experimental channel: To avoid deposition in the area in front of the comb-like screen, sandy fine sediment was added at the upstream end of the experimental channel.

Figure 2.25 plots the trapping ratios for all four sandy experimental runs in Series 2 along the experimental channel with the flow direction from left to right. Figure 2.25a plots the data in absolute numbers, whereas Figure 2.25b normalises the TR by dividing them by $TRmean$. By far the highest trapping ratios are measured in

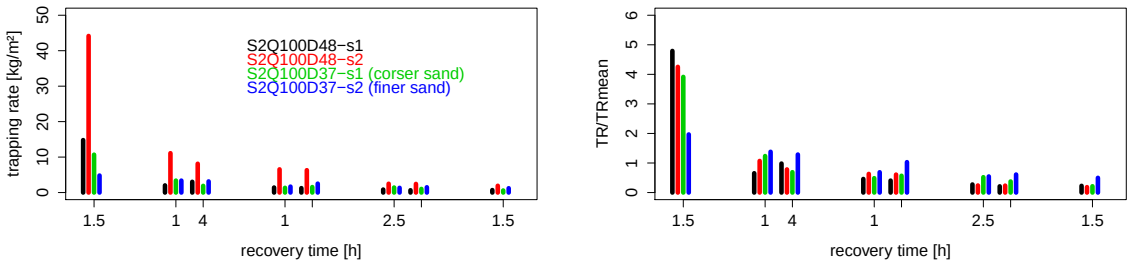

(a) TR kgm^{-2} (b) TR/$TRmean$

Figure 2.25: Trapping ratios for experimental runs with Q100 and sandy fine sediment in Series 2 ordered in downstream direction with recovery times given at bottom.

trap A at the beginning of the experimental channel. Figure 2.25 shows that the main difference in TR is dependent on the distance to the inlet. In all trap pairs, the magnitudes of TR is the same for the first and second recovery in one trap pair.

For all sandy experimental runs, TRs of B, C and D trap pairs decline in this order. TR/$TRmean$ values of trap A are very similar for all three runs with the same sandy grain size distributions. This suggests that a defined proportion of the sand gets deposited. Only for S2Q100D37-s2 with a finer sand grain size distribution, the TR for trap A is of a similar magnitude compared to the TRs of the other traps. These findings are in accordance to the experiments conducted by Grams and Wilcock (2007), where the highest sand deposition was also measured in the proximity of the flume inlet. This effect was most pronounced for experiments with coarser sand distribution, higher feeding ratios and lower discharge.

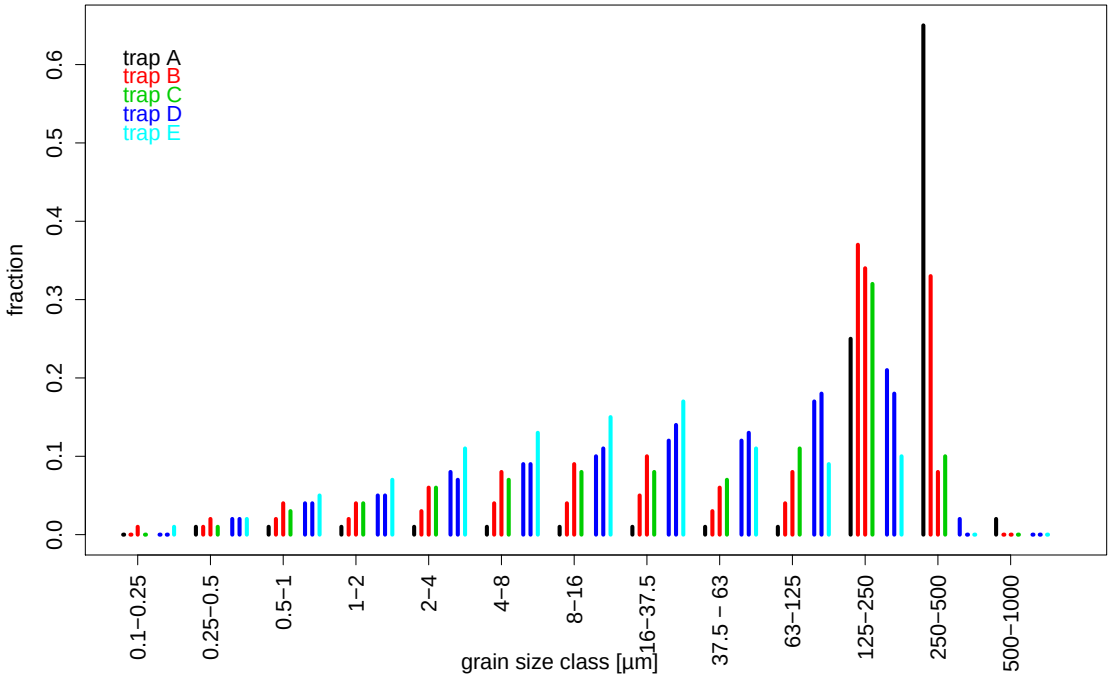

Figure 2.26: Grain size distribution of trapped fine sediment in sandy experimental runs, grouped into traps.

The high trapping ratios at the beginning and the constantly declining trapping ratios over the length of the experimental channel are closely connected to the sandy grain size distribution. Figure 2.26 shows the grain size distribution grouped into traps. The coarsest distribution is found in trap A with constant fining towards the end of the experimental channel. The flow conditions in the flume resulted in the

immediate settling of the sandy fine sediment, especially for grains coarser than 250 μ m. Therefore, trapping ratios do not reflect the difference in flow character of the trap positions but are rather the result of the travelling time of the single grains. For the coarsest sand, the time scale over which deposition occurs is shorter than the time it takes to be transported down the experimental channel.

2.4 Conclusion

Chapter 2 discussed the theoretical background, experimental setup, implementation and the results of the 14 (in two series) successful **flume based experimental runs investigating suspended fine sediment deposition**. The single experimental runs were setup identically, with the exemption of one variable to differ so the influence of this one variable on deposition behaviour could be quantified. The experimental setup recreated a **semi-natural** gravel bed. It was used to test various flow and sediment conditions. Based on the limitations of the equipment, flow and bed conditions could not exceed the maximum velocity of ca. 1 m s^{-1} and the gravel bed was restricted to grains coarser than 4 mm. The fine sediment used as the suspended load was a silty soil and quartz sand.

In terms of the implementation of the single experimental runs **a standardised bed setup** was of high priority, which resulted in minimal bed variation. Consequently, the intended variation between experimental runs and single patches was larger than the noise in the velocity and bed shear stress data.

To ensure that only the variable intended to differ indeed abbreviates from the conditions in all other experimental runs, flow and shear stress distribution was investigated in details. The flat bed in Series 1 showed **uniform flow conditions** for the middle part of the flume. However, some irregularities were observed for conditions above positions at the very beginning and very end of the experimental channel. Series 2 clearly showed the influence of bed elevation on **local flow pat-**

tern. The flow data suggests that bed structures have mainly a local influence on velocity and shear stress for low velocities (v_{mean} = 0.2 m s^{-1} or Q30). However, for higher velocities (v_{mean} = 0.67 m s^{-1} or Q100) bed structures had a clear influence on the flow character of down-stream positions, where near bed velocity declines and bed shear stress and fluctuation rises. Although flow velocity and even more so bed shear stress showed heterogeneity for seemingly identical positions and set-ups, the intended variation clearly exceeded the unintended.

With regards to the measured sediment, the fine sediment budget was measured as the **concentration development** of the suspended sediment and the **trapping ratios** of interstitial fine sediment. Simultaneous suspended sediment measurements at different levels and positions in the flume showed well mixed sediment concentrations for all positions. Therefore, the concentrations measured at the inlet into the experimental channel could be applied to the whole flume.

For all experimental runs, the **suspended sediment declined exponentially**, reaching an equilibrium concentration within the time frame of the experimental runs. An extreme fast deposition was observed for all sandy experimental runs with the deposition being completed after several minutes. For the silty fine sediment, the discharge had a crucial influence on the development of the concentration and the magnitude of the equilibrium concentration. A higher discharge results in a faster achievement of a higher equilibrium concentration, whereas for lower discharge the concentration loss is higher and continues for a longer period. The experiments could also show that the D_{50} of the bed influences the concentration development. Equilibrium concentrations for v_{mean} = 0.2 m s^{-1} (Q30) runs slightly differed with just under and just over 0.2 C_0 for a finer D37 and a coarser D48 bed respectively. This difference is more obvious for v_{mean} = 0.67 m s^{-1} (Q100) experimental runs, where for D48 the equilibrium concentration is at 0.35 C_0 compared to 0.3 C_0 for D37. Further, the concentration development is closely interlinked with the grain size distribution of the fine sediment. This is most obvious for the rapid decline of concentration during

sandy experimental runs. Therefore, finding an applicable and meaningful method to establish grain size distribution is very important. Both methods introduced here have advantages and disadvantages. **Effective grain size** measures flocs and aggregates. Unfortunately, it can only be applied to in situ suspended sediment. This means effective grain size measurements can not be carried out for source soil material or trapped sediment. **Absolute grain size** measurements show much finer grain size distribution for the same samples because aggregates and flocs are destroyed during sample preparation. Absolute measurements are easier to reproduce and can be applied to all sediments (soil, suspended and trapped material) and therefore allow comparisons. If we compare absolute measurements of soil and samples drawn at the beginning of the experimental run, a strong depletion of coarse grain sizes was found. This can be explained by the prompt deposition of coarser particles in the period between the sediment input and the initial measurement.

As a measure of overall deposition in the flume, the concept of **potential deposition** ($Dpot$) was introduced, with $Dpot$ being the measured concentration loss from the suspended load applied over the whole area of the experimental channel. The comparison of trapping ratios with $Dpot$ showed **discrepancies in the silty fine sediment mass balance**, especially for high discharge. The source of the imbalance was found to be the deposition of fast settling material outside the experimental channel in the basin between recirculating pipe and experimental channel inlet. This theory, although consistent with all data could not be confirmed conclusively with statistical methods due to the low number of data points and considerable noise in the single data points.

An investigation of the relationship between local flow conditions and trapping ratios for silty experimental runs was conducted with linear regressions. Due to the low number of data points and noise in the trapping data, the results have to be treated with care. However, the data suggests some relationships opposed to the Krone formulation. A decline of TR with rising velocity was only found for all experimental runs

with a non-uniform bed resulting in a variation of velocity. For Series 1 with uniform velocities, a clear correlation between TR and τ_0 could be shown, where TR declines with rising τ_0. In Series 2 Q30, τ_0 was uniform and therefore did not influence TR patterns. However for Q100 in Series 2, the rinsing τ_0 stands in opposition to the effects suggested by the Krone formulation. In conclusion, the following for aspect are the key results of Chapter 3:

1. The experiments confirmed that equilibrium concentrations are highly dependent on grain size. All silty experimental runs showed clear equilibrium concentrations, whereas the sandy experiment runs showed a complete deposition of all sandy grain sizes. Further, the equilibrium concentrations found in the silty experimental runs did differ between environmental settings. The highest equilibrium concentrations were found for high discharge in combination with a coarser D48 bed. The lowest equilibrium concentration could be identified for low discharge and a finer D37 bed.

2. The flume experiments showed a clear dependency of deposition patterns on the grain size distribution of the suspended sediment. Coarse sandy suspended sediment did deposit rapidly as a function of the limited transport capacity. For finer suspended sediment, the local flow patterns were most influential.

3. The comparison of the trapping ratios of all silty experimental runs with variation in local velocity and bed shear stress needs to be considered with caution, since overall variability is high. Nevertheless, the data exhibits several trends. For runs with no variation in velocity (flat bed in Series 1), τ_0 was influential for deposition with declining TR for rising τ_0. However, for the non-uniform bed and higher discharge, rising τ_0 resulted in rising TR. Due to the high variation in the data, this trend was underpinned with linear regression with low r^2.

4. As already mentioned under (1), the grain size distribution of the gravel bed

did influence the equilibrium concentration. The coarser D48 bed resulted in higher equilibrium concentrations compared to the finer D37 bed. This effect is more pronounced for the higher discharge experimental runs with higher v_{mean}.

Chapter 3

Flume scale numerical deposition model

This chapter introduces a simple numerical model for suspended fine sediment deposition based on the findings of the flume experiments discussed in Chapter 2.

The model presented here is a deposition model, calculating both the concentration loss from the water column and the deposition in the bed. Remobilisation (as a factor counterbalancing deposition) is not included as a separate process. The model is designed to explain in-bed deposition based on flow, suspended fine sediment and bed characteristics with the help of the Krone formulation (1962). The Krone formulation is both simple and comprehensive, as it includes all parameters generally believed to influence deposition. Therefore, it is often used in studies to describe fine sediment bed deposition (see amongst others Krishnappan, 2006; Liu et al., 2002; Maa et al., 2008). The model shown in this chapter assumes constant conditions for the bed structure. The model consists of a *base module* of sediment dynamics, which can be applied under different conditions. Complex environments can be modelled as a combination of numerous base modules.

Section 3.1 describes the concept of the model with reference to the Krone formulation. Section 3.2 specifies the input parameters for the model. Input data originates from two different sources: Grain size class dependent data is based on literature in-

formation. Input data defining flow and sediment conditions - for the calibration of the model - are derived from measurements during the experimental flume runs. Section 3.3 calibrates the model with regard to the model parameters and the calibration coefficient of the Krone formulation in four separate steps. The calibration data is the concentration and trapping information from the flume experiments in Chapter 2. Section 3.4 takes a closer look at the model sensitivity and performance. Finally, Section 3.5 summarises the Chapter.

3.1 Concept and execution

In addition to the theoretical framework discussed in Chapter 2, the numerical model based on the flume investigation needs to include descriptors of time and space. Equation 3.1 shows an extended Krone formulation (1962) for deposition (dep), with λ being the calibration coefficient, w_s being the settling velocity, C the suspended sediment concentration, τ_0 the bed shear stress and τ_{cr} the critical shear stress multiplied by the time span these conditions are apparent ($duration$) and the area they apply for ($area$). In the text, the formulation will only be discussed including shear stress (referred to as *shear stress deposition model*). However for the model calibration, the quotient of the local velocity divided by the critical velocity will be considered, too (see Equation 2.1, this is referred to as *velocity deposition model*).

$$Deposition = \lambda * w_s * C * (1 - (\frac{\tau}{\tau_{cr}})) * duration * area \tag{3.1}$$

Interstitial deposition is only possible up to a point, where 100 % of the available pore space is filled with fine sediment. An active deposition layer of 20 cm is assumed to be the limit of in bed deposition. Hence, maximum deposition is restricted to the pore volume of this layer. Equation 3.1 is only valid for one point with one hydraulic condition and one particle size (with according w_s, τ_{cr}) during a finite time period. To create a functional model of a continuously changing environment, en-

vironmental conditions have to be discretised. This means that points are grouped into distinct patches, particle sizes into size classes and time into time steps. The total deposition ($totDep$) is consequently the sum of deposition of all base modules executed for all different patches (patch = 1 to p), grain size classes (gsc = 1 to g) and time steps (ts = 1 to t). Equation 3.2 puts this into one formulation:

$$totDep = \sum_{gsc=1}^{g} \sum_{patch=1}^{p} \sum_{ts=1}^{t} w_{s(gsc)} * p_{(gsd)} * C_{(ts)} * (1 - (\frac{v_{(ts)}}{v_{cr(gsc)}})^2) * duration_{(ts)} * area_{(patch)} \tag{3.2}$$

With p_{gsd} being the fraction of the grain size class of the total sediment concentration. The patch sizing, the amount of grain size classes and the longevity of the time steps are primarily practical decisions. In this model on flume scale, the patches are defined by the setup of the flume experiments. Patches are identified with regard to a typical or uniform bed character and aligned along the experimental channel, each covering the whole area between the glass walls. For the calibration of the model with the experimental data, nine patches are defined.

The time step is defined as the travelling time of water through the experimental channel depending on the averaged velocity.

Nr of class	**from to** μm	D_{50} μm	ϕ
1	0-16	8	$<$6
2	16-32	24	6 to 5
3	32-63	48	5 to 4
4	63-125	94	4 to 3
5	125-250	188	3 to 2
6	250-500	375	2 to 1
7	500-1000	750	1 to 0
8	1000-2000	1500	0 to -1

Table 3.1: Grain size classes in the flume scale numerical deposition model.

The grain size classes followed the well-established ϕ-units (after Wentworth, 1928), which facilitates the use of readily available literature data for settling velocity, critical velocity and critical shear stress. Fine ϕ-classes are grouped into one grain

size class for all particles smaller 16 μm. Sediment between 16 μm and 2 mm is divided into seven further grain size classes in ϕ steps, resulting in a total of eight grain size classes, as shown in Table 3.1. For each grain size class, deposition is calculated for each patch in sequence. The amount of already deposited sediment is substracted from the suspended sediment concentration for the following patches.

3.1.1 Realisation of the model in R-code

The model is coded in *R* (R Core Team, 2012). *R* is a open source programming language as well as an environment for statistical calculations and data analysis. This software was chosen for several reasons. *R* is a frequently used software for many applications and on-line documentation is extensive and easily accessible. One of its many advantages is that it offers innumerable functions defined by other users, for example established statistical methods. Furthermore, its graphical outputs are very flexible.

The model consists of a read-in phase, followed by two nested loops. The inner loop is the execution of the base module over all patches, e.g. all hydraulic conditions. This inner loop is executed in an outer loop for all grain size classes. The deposition in each patch is zero, if the bed shear stress in the patch is higher than the critical shear stress ($\tau_0 > \tau_{cr}$). The read-in phase consists of three types of parameters referring to each one of the three sequences of summation in Equation 3.2: First, the grain size class dependent data - w_s, τ_{cr}- taken from the literature; second, patch dependent data - in the case of the calibration procedure from the experimental runs (τ, $area$, $duration$) and third, the time step specific sediment information - initially taken from the experimental runs (GSD of fine sediment in the single classes, total fine sediment) later calculated from the model. These are listed in Table 3.2. The single value sets will be described in more detail in Section 3.2.

	grain size class dependent data	**patch dependent data**	**time specific sediment information**
source	from literature	from experiments	initially from experiments, subsequently calculated by the model
dependent parameters	w_s, τ_{cr}, v_{cr}	τ, v, $duration$, $area$	p_{gsc}, C

Table 3.2: Model input parameters in dependence on the three sequences of summations of the base module, the grain size class, the patch and the time step as shown in Equation 3.2.

3.2 Input data

The input data originates from two sources. Subsection 3.2.1 introduces data from the literature concerning the grain size class dependent parameters and Subsection 3.2.2 summarises the hydrological and sedimentological data from the experimental runs for the calibration runs. A vector of input data including one value for each grain sizes or each patch is referred to as a *value set*, for example the shear stress for each patch derived from a specific method. A large number of studies deliver values for the parameter of the Krone formulation. However, their exact values vary greatly depending on the method and the specific experiments these were derived from. Since the Krone formulation is a basic a in many way simplified description of deposition and the data from the literature is derived from many specific cases, it is not possible to derive *a priori* a working combination of value sets for the model. Therfore the starting point of the calibration procedure is a wide range of value sets for each input parameter, which allows to make a general formulation useful in this specific context.

3.2.1 Input data from the literature

Settling velocity is a key parameter influencing deposition processes. Direct measurements produce the most exact values. However, all measurement methods in-

volve laborious procedures and are eventually only applicable to the one sediment mixture analysed. This stands in sharp contrast to literature data, which is often tested with several sets of data and is more likely to offer representative values. For the model of this research, four descriptions of settling velocity found in the literature were used for the calibration. These all describe settling velocity as a function of grain size, which means that settling velocity values are all based on physical principles. The data is plotted in Figure 3.1, left panel.

Model calibration runs are operated with Stokes (St), Gibbs (Gi), van Rijn (Ri) and Le Roux (Ro) value sets for settling velocity, see 1.2.2 for a detailed description.

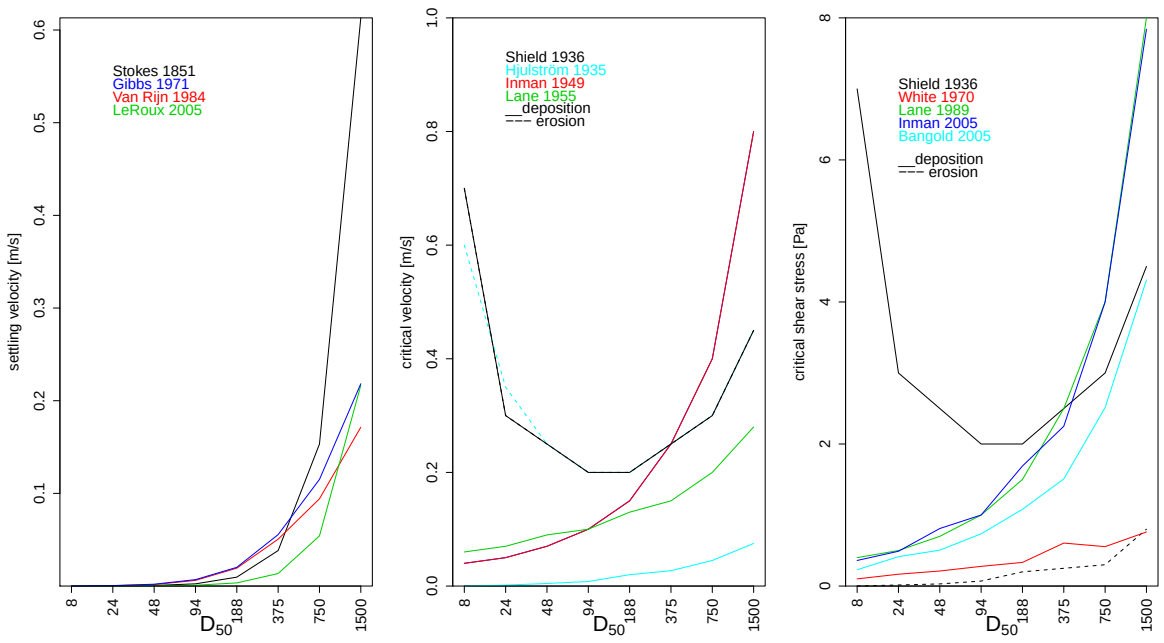

Figure 3.1: Plots of grain size dependent value sets from the literature for the eight grain size classes used in the flume scale deposition model.

Critical values for sediment transport: A critical value for sediment transport is the magnitude of force determining the thresholds for both deposition and erosion. In order to cover a large range of critical velocities, the model calibration runs are operated with Shields (Sh), Inman (In) and Lane (La) value sets for critical velocity, which are all plotted in Figure 3.1, middle panel. The critical shear stress value sets were chosen on the basis of v_{cr}. Additionally, White values (see Buffington

and Montgomery, 1997) were included, because these are comparatively low and extend the range of τ_{cr} value sets. Further, the iterative threshold curve of Bangold was added to cover the middle ranges of the τ_{cr} value sets (Bagnold, 1966). The critical values introduced here are critical velocity and shear stress for deposition. Only for Shields, both the critical values for deposition and erosion were included. Consequently, the model calibration runs were operated with Shields (Sh), White (Wh), Lane (La), Inman (In) and Bangold (Ba) value sets for critical shear stress, which are all plotted in 3.1.

3.2.2 Input data from experimental runs

For the calibration, information about environmental settings were taken from measurements during the flume experiments. Primarily, these are velocity, bed shear stress and the grain size distribution of the fine sediment but also the size of the deployed patches and the total sediment concentration. The following paragraphs will explain each of these parameters.

Velocity was directly measured with an acoustic doppler velocimeter (as described in Subsection 2.2). Values for 5, 10, 15 and 20 cm above the bed were available. Two sets of velocity information were used for the calibration: (1) The conditions in the boundary layer were believed to be crucial for fine sediment deposition. Hence, values measured at 5 cm above the bed were used in the velocity value set, named $ave5$. (2) $ave5$ values exhibit very strong fluctuations, therefore a second velocity value set was calculated using the mean velocity of all four heights and referred to as $mean$.

Bed shear stress is established following the methods described in 2.2. For the calibration, three different kinds of bed shear stress value sets were used: (1) Turbulent kinetic energy using the variation of all velocity vectors named $Txyz$, (2) turbulent

kinetic energy using only the variation of the downstream velocity vector named Tz and (3) bed shear stress derived by using the logarithmic velocity law, named log (see 1.2.1).

Grain size distribution of the fine sediment was available in three different specifications, which are all used in the calibration procedure. (1) DigiSizer data from the soil used in the experiments, named $Digisoil$, (2) averaged DigiSizer values from the initial sample drawn from the flume, named $Digiini$ and (3) averaged LISST values for the initial measurement of several experimental runs, named $LISST$. For a more detailed description of these methods see Subsection 2.2.

Other relevant values for the experimental setting were directly taken from the measurements, such as the initial sediment concentration (C_0). Table 3.3 sums up the value sets used in the calibration procedure for each of the parameters in Equation 3.2. It indicates their source and lists the the value sets by the name.

parameter for model equation	source	value sets
w_s	literature	Stokes, Gibbs, *VanRijn*, LeRoux
v_{cr}	literature	Hjulström, Shields, *Inman*, Lane
τ_{cr}	literature	Shield, *White*, Inman, Bangold
v	direct from ADV measurements	5 cm, *averaged*
τ_0	deducted from ADV measurements	$Txyz$, Tz, log
GSD	measurements	$Digisoil$, $Digiini$, $LISSTini$
C_0	measurements	
patch $area$	measurements	
time step	deduced from v_{mean} and patch length	
observed values for model calibration		
trapping rate	measurement	
concentration	measurement	

Table 3.3: Overview of value sets for model parameters and calibration data with source and specification of value sets used for calibration. Value sets emphasised in green were used in the first step of the calibration procedure, these cover the middle range of the value sets.

3.3 Calibration

The calibration of a model, using various sets of parameters, is by all means complex. The execution of all possible value set combinations as listed in Table 3.3 would result in 3456 simulation options, which each again can be calibrated with the calibration coefficients λ for each of the six environmental settings of the experimental runs. In order to reduce complexity, the calibration is carried out in four separate steps (which are listed in Table 3.4, with details about calibration data, calibration parameters, the execution and the evaluation of the single calibration steps). Step 1 aims to reduce the number of value set combinations by identifying the most suotable value sets. The step relies on graphical representation, comparing modelled (mod) and observed (obs) concentration loss.

	aim	calibration data	tested model parameters	evaluation method
Step 1	pre-selection of feasible value sets	suspended sediment concentration	all selected value sets from literature and experiments	graphical
Step 2	determine best performing value set using concentration data	suspended sediment concentration	feasible value set combinations determined in Step 1	statistical
Step 3	testing best performing value set using TR data	TRs	feasible value set combinations determined in Step 1	graphical (silty) and statistical (sandy)
Step 4	λ calibration for best performing value set combination	suspended sediment concentration	best performing value set combination from Step 2 with detailed grading of λ	statistical

Table 3.4: Overview of steps for the calibration of the flume scale deposition model, listing the aim of the four calibrations steps, the calibration data used to evaluate the performance, the parameter value sets regarded in the steps and the evaluation method (either with a graphical representation or a suite of statistical methods).

Step 1 is discussed in Subsection 3.3.2 and covers both the shear stress and velocity deposition model in the same evaluation plots. Step 2 will then execute all remaining value set combinations and compares modelled and observed concentration loss systematically with statistical methods (specified in Subsection 3.3.1). For the discussion of the calibration results, only figures for S2Q30D48 are shown in the main text, plots for all other environmental settings can be found in the Appendix. Step 2 and 3 will be discussed separately for the velocity and the shear stress deposition model. First, for all silty, then for all sandy experimental runs. Finally, the calibration is completed in Step 4 by calibrating the best performing value set brought forward with a detailed range of λ calibration coefficients .

3.3.1 Statistics used for evaluation of the calibration runs

In order to calibrate the model, a combination of widely used statistical indices was applied to compare the modelled and observed data. The 'best performance' is based on reaching optimum values in several, ideally all applied statistical indices for a value set combination. The following gives a short introduction of these indices:

The Pearson coefficient is probably the most commonly used statistical index and shown in Equation 3.3:

$$r = \frac{Cov(X,Y)}{\sigma x * \sigma y} = \frac{E((X - E(X))(Y - (E(Y))))}{\sigma x * \sigma y} \tag{3.3}$$

$$r^2 = (r)^2 \tag{3.4}$$

There is no general rule stating which r^2 is acceptable and different scientific disciplines evaluate r^2 very differently. In the calibration of the flume scale deposition model, the r^2 of the different runs are compared to each other and the best performing value set combinations are brought forward.

Linear regression model (LM): Linear regression models evaluate the quality of linear correlations between the observed and modelled values. Here a least square linear regression was applied. Conventionally, the observed data is used as the x and the modelled data as the y values. If the linear model passes through the origin, the slope shows if there is an under (slope ≥ 1) or over prediction (slope ≤ 1) of the modelled data. The value of the intercept shows a lag or offset between the two data sets. In this work, the regression lines are fitted with the modelled values treated as the independent variable and also with the flume data treated as the independent variable. Thus, two linear regressions for each model run are calculated with first the modelled data and second the observed data as the independent variable.

Mean Standard Error (MSE): Following Davies and Fearn (2006), the magnitude of errors is a very clear sign for the performance of a model. The mean standard error is the mean difference between modelled and observed values. This can be noted directly (MSE), or in a squared expression (SMSE).

$$MSE = \sum_{i=1}^{n} (x_i^{obs} - x_i^{mod}) \frac{1}{n} \tag{3.5}$$

$$SMSE = \sum_{i=1}^{n} (x_i^{obs} - x_i^{mod})^2 \frac{1}{n} \tag{3.6}$$

with x_i^{obs} as the observed value at point i and x_i^{mod} as the modelled value at point i. The MSE is only useful in cases with a consistent over- or underprediction, because positive and negative errors do cancel out. This issue is avoided by using the SMSE.

Percent Bias (PBIAS): The PBIAS is similar to the MSE. It is the expression of the error as a percentage of the observed value. A positive value suggests underestimation by the model and a negative value suggests overestimation.

$$PBIAS = \frac{\sum_{i=1}^{n} (x_i^{obs} - y_i^{mod}) * 100}{\sum_{i=1}^{n} y_i^{obs}} \tag{3.7}$$

To ensure the results of the experimental settings are comparable, all statistics are based on the same number of data points.

3.3.2 Step 1 calibration of the silty experimental runs

The aim of this step is to delimit feasible value sets by comparing modelled and observed concentration. As a starting point for the calibration runs, the value set covering the middle range of each parameter is chosen. These are highlighted green in Table 3.3. Step 1 evaluates each parameter at a time. Calibration runs were conducted for all value sets of one parameter in combination with the middle range value sets of the other parameters. The distinction between feasible and non-feasible value

set combinations bases on the comparison of observed and modelled concentration loss. For each parameter, one plot with concentration loss curves for all value sets of this parameter is shown at the end of the chapter, including the velocity and shear stress deposition model.

λ **calibration coefficient:** Figure 3.15 shows the observed concentration loss of each experimental setting (shown in panels a to f). Additionally, each panel includes the modelled concentration loss for seven different λ values with the above discussed middle values of the input parameters. λ values are reaching from 0.1 to 20. Higher λ values result in better accordance with the observed $Closs$. For λ values 3 and higher, the simulated concentration curves parallel the observed $Closs$. The difference between the shear stress and velocity deposition model gets successively larger with increasing λ. Since λ is the central calibration coefficient of the Krone formulation, all following calibration runs in Step 1 are executed with λ = 1, 5 and 7. Using these three λ values ensures that Step 1 is not excluding combination possibilities from later detailed λ calibrations in Step 4.

Grain Size Distribution: Figure 3.16 shows the results of simulations based on three different *grain size distributions*. Grain size distribution measurements from bulk water, drawn immediately after the flume experiment started ($Digiini$, $LISST$) perform less adequate than measurements from the original silty suspended sediment source ($Digisoil$). For the suspended sediment grain size distribution, effective grain size measurements ($LISST$) perform better than absolute grain size measurements ($Digiini$). Therefore, the absolute grain size distribution of the soil measured with the DigiSizer and the effective grain size distribution of the initial samples measured with the LISST-100 are used in the further calibration steps.

Settling velocity: Figure 3.17 shows the results of the different *setting velocity* value sets. The values from van Rijn and Stokes offer best fitting results, whereas LeRoux values result in lower than observed concentration loss and Gibbs values result in higher concentration loss. Therefore, the Step 2 calibration is executed with

van Rijn and Stokes value sets for settling velocity.

Critical shear stress: Figure 3.18 shows results for *critical shear stress* value sets from White, Bangold, Inman and Shield. The first three describe concentration development better than the Shields value set. Notably, Bangold and Inman results are very close. Therefore, Step 2 calibrations exclude the Bangold values and use only White and Inman critical shear stress values for further calibration.

Bed shear stress: Figure 3.19 offers plots comparing results of the three different methods to establish *bed shear stress*. $Txyz$ performs best for both fast and slow velocity experimental runs. For slow velocity experimental runs, the log method performs well, too. For the fast velocity experimental runs, the turbulent kinetic energy Tz results in better performance. To cover the two fundamental different methods, the better performing representative of the TKE method $Txyz$ and the log method are selected for further calibration.

Critical velocity: Figure 3.20 shows the results of calibration runs with three different *critical velocity* sets. The Shields value set underestimates concentration loss in all cases. Results for Inman and Lane sets are both adequate to describe the observed concentration loss and are therefore chosen for calibration Step 2 and Step 3.

Velocity: Figure 3.21 shows the concentration loss for the two *velocity* representations, the near bed velocity and the average velocity of the water column. The averaged velocity results in adequate values for the shear stress deposition model (where it is used for the calculation of one time step) as well as the velocity deposition model. The near bed velocity only delivers suitable results for the velocity deposition model. Consequently, in Step 2 and Step 3 the time step is established with the $mean$ velocity. For the velocity deposition model calibration, both $ave5$ and $mean$ are considered.

Table 3.5 lists all value sets brought forward in Step 1, in all possible value set combinations with the shear stress deposition model on the left and the velocity de-

position model on the right.

z	λ	fine GSD	w_s	τ_{cr}	τ	fine GSD	w_s	v_{cr}	v
1-3	1,5,10	$Digisoil$	Ri	Wh	$log\ (Tz)$	$Digisoil$	Ri	In	$mean$
4-6	1,5,10	$LISSTini$	Ri	Wh	$log\ (Tz)$	$LISSTini$	Ri	In	$mean$
7 -9	1,5,10	$Digisoil$	St	Wh	$log\ (Tz)$	$Digisoil$	St	In	$mean$
10-12	1,5,10	$LISSTini$	St	Wh	$log\ (Tz)$	$LISSTini$	St	In	$mean$
13-15	1,5,10	$Digisoil$	Ri	La	$log\ (Tz)$	$Digisoil$	Ri	La	$mean$
16-18	1,5,10	$LISSTini$	Ri	La	$log\ (Tz)$	$LISSTini$	Ri	La	$mean$
19-21	1,5,10	$Digisoil$	St	La	$log\ (Tz)$	$Digisoil$	St	La	$mean$
22-24	1,5,10	$LISSTini$	St	La	$log\ (Tz)$	$LISSTini$	St	La	$mean$
25-27	1,5,10	$Digisoil$	Ri	Wh	$Txyz$	$Digisoil$	Ri	In	$ave5$
28-30	1,5,10	$LISSTini$	Ri	Wh	$Txyz$	$LISSTini$	Ri	In	$ave5$
31-33	1,5,10	$Digisoil$	St	Wh	$Txyz$	$Digisoil$	St	In	$ave5$
34-36	1,5,10	$LISSTini$	St	Wh	$Txyz$	$LISSTini$	St	In	$ave5$
37-39	1,5,10	$Digisoil$	Ri	La	$Txyz$	$Digisoil$	Ri	La	$ave5$
40-42	1,5,10	$LISSTini$	Ri	La	$Txyz$	$LISSTini$	Ri	La	$ave5$
43-45	1,5,10	$Digisoil$	St	La	$Txyz$	$Digisoil$	St	La	$ave5$
46-48	1,5,10	$LISSTini$	St	La	$Txyz$	$LISSTini$	St	La	$ave5$

Table 3.5: Matrix of value sets and calibration parameters used in Step 2, with 16 value set combinations each combined with the three selected λ values. Abbreviations: z = unique number of calibration run, $LISSTini$ for LISST initial measurements, $Digisoil$ for DigiSizer soil sample, St = Stokes, Ri = van Rijn, La = Lane, Wh = White, log = logarithmic velocity law, $Txyz$ = turbulent kinetic energy using all velocity vector fluctuations, $mean$ = average velocity of all four levels, $ave5$ = averaged velocity measured at 5 cm distance to bed, $log\ (Tz)$ refers to the alteration of the value set combination from log to Tz after irregularities in the Step 3 calibration.

.

This matrix is used for systematic calibration in Step 2. The selected value sets combinations results in 16 calibration possibilities each for three λ values with z being the unique number of the combination. Each unique value set combination is run for all six experimental settings.

3.3.3 Step 2 shear stress deposition model - silty experimental runs

Figure 3.2 for S2Q30D48 (see also according Figures A.1 to A.5 in the Appendix for all other environmental settings) shows a graphical representation of the calibration statistics for Step 2 using the shear stress deposition model. The ideal value of each

statistical index is marked with a black horizontal line. Each plot consists of four subplots: each one for correlation, slope of the two linear models, intercept of the two linear models and the error in absolute and relative numbers.

For all value set combinations and each of the six experimental settings, r^2 is higher than 0.95 at least for one of the three λ values. This reveals a generally good fit of the model for concentration.

With regard to the single parameters, for the grain size distribution, the $Digsoil$ distribution results in slightly higher r^2, linear models with slopes closer to 1 and smaller intercepts as well as a in many cases a smaller error and bias. For settling velocity, overall the van Rijn value set performs better. For the critical shear stress, the Shields erosion value set is superior to the Lane value set. $Txyz$ in combination with the Shields erosion value set performs best. For λ, performance is best for different values, depending on the statistical parameter and experimental run. r^2 is highest for a low λ, but the linear model fits are better for λ = 5 and 10. Preliminary, the mid-range value of 5 is seen as an optimum for all statistical parameters and experimental runs. Additionally to the plots, all statistical values of these calibration runs are listed in Table A.1 to A.6 in the Appendix.

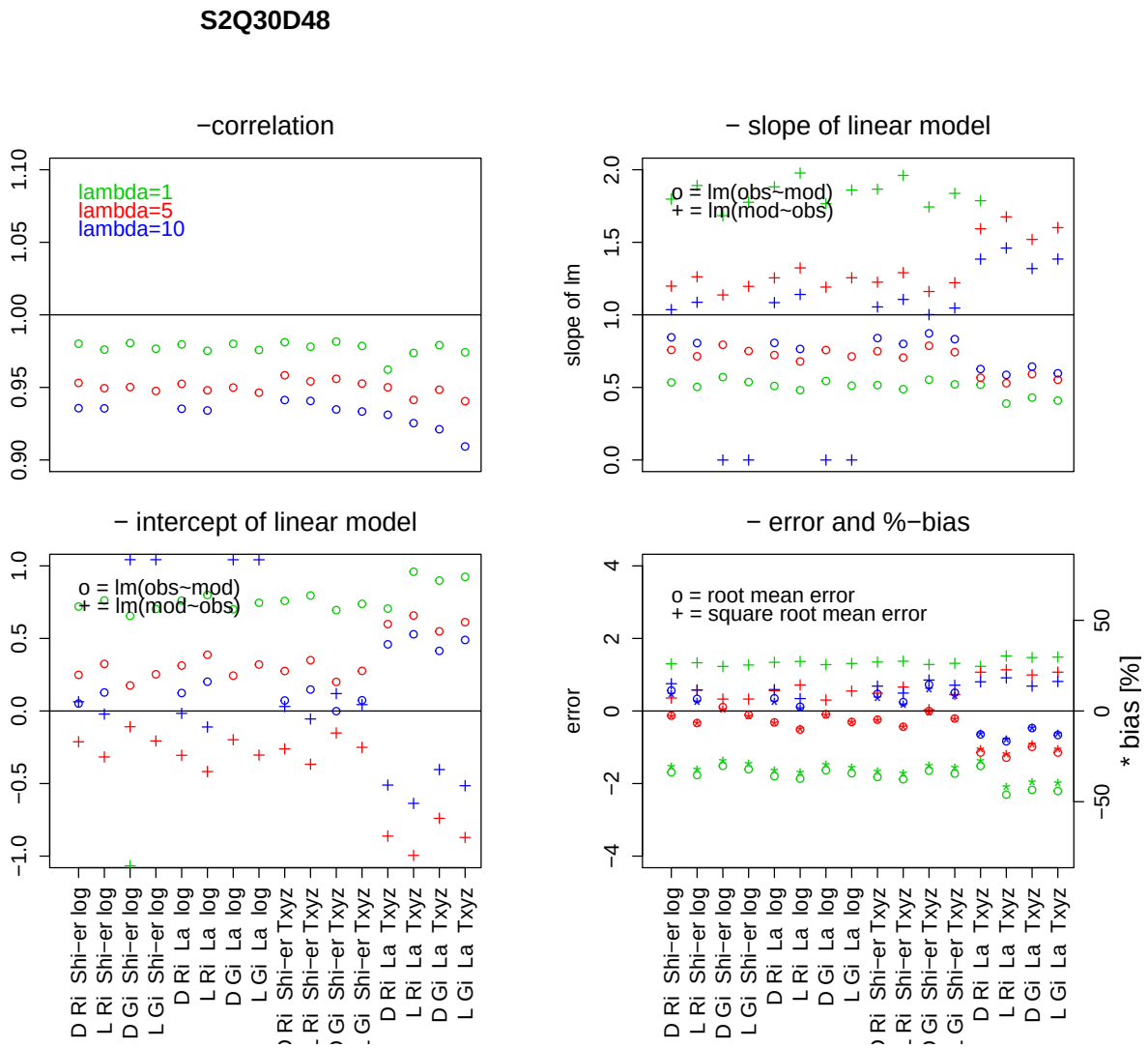

Figure 3.2: Calibration statistics for modelled and observed concentration loss in S2Q30D48, shear stress deposition model. Abbreviations as follow: L further abbrevation for $LISSTini$ = LISST-100 initial measurements, D further abbrevation for $Digisoil$ = DigiSizer soil sample, St = Stokes, Ri = van Rijn, La = Lane, Wh = White, log = logarithmic profile law, $Txyz$ = turbulent kinetic energy using all velocity vector fluctuations.

Concluding, the best performing value set for the shear stress deposition model, taking all experimental settings into account is: λ = 5, w_s = van Rijn , GSD = $Digsoil$, τ_{cr} = Shields erosion and τ = $Txyz$.

3.3.4 Step 3 shear stress deposition model - silty experimental runs

Due to the high variability and questions about the fine sediment mass balance, the trapping rate data of the experimental runs are only partially useful for the calibration. The trapping rate data showed low correlations to the flow parameters stated in the Krone formulation. However, modelled trapping rates are proportional to the same flow parameters. Consequently, the comparison of the observed and modelled trapping data for the silty experimental runs are not in line. However, a comparison of modelled and observed interstitial deposition might strengthen or weaken the validity of the value set combination determined as best performing in Step 2, in comparison to other value set combinations. Figure 3.3 for S2Q100D37 and Figure 3.4 for S2Q30D48-1 compare modelled and observed trapping rates for a selection of value set combinations. They show the different functionality of observed and modelled deposition. The top left panel shows the results of the value set combination found to perform best in Step 2. For S2Q30D48-1, given the variability within the observed data, the results are acceptable, showing higher deposition for A and B traps compared to C and D. Yet, there are strikingly higher modelled than observed TR in E for all value set combinations. Conditions over trap E are very similar to conditions over trap A, so are the modelled trapping rates. The low observed TR in E can be explained by the depletion of coarser aggregates. These have short travelling times and settle out at the upper end of the experimental channel (A and B). However, the coarser grain size distribution is not visible in the grain size distribution data in Section 2.3.5. An explanation for this is that all aggregates are destroyed during the analysis. Still, the magnitude of the predicted and observed TR is acceptable. However, Figure 3.4 shows some substantial divergences between observed and modelled trapping rates for S2Q100D37 with a higher discharge. The observed values all range in a similar magnitude, whereas the modelled values give higher TR for A, B and E and low TR for C and D.

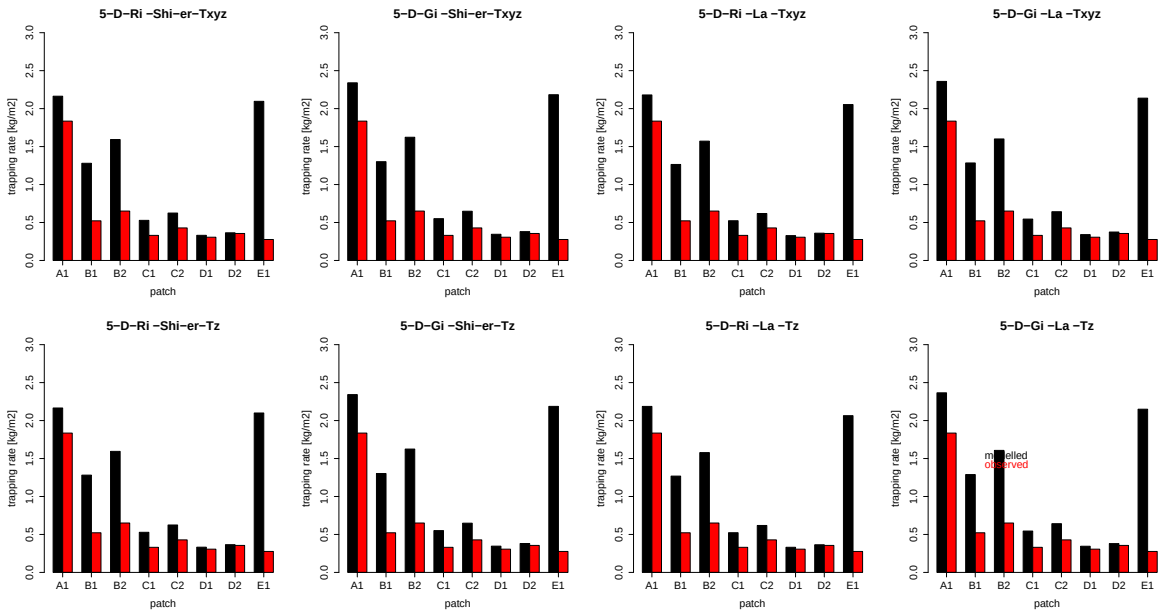

Figure 3.3: Modelled (black) and observed (red) interstitial deposition for S2Q30D48-1, shear stress deposition model. Abbreviations as follow: L further abbrevation for $LISSTini$ = LISST-100 initial measurements, D further abbrevation for $Digisoil$ = DigiSizer soil sample, St = Stokes, Ri = van Rijn, La = Lane, Wh = White, log = logarithmic profile law, $Txyz$ = turbulent kinetic energy using all velocity vector fluctuations.

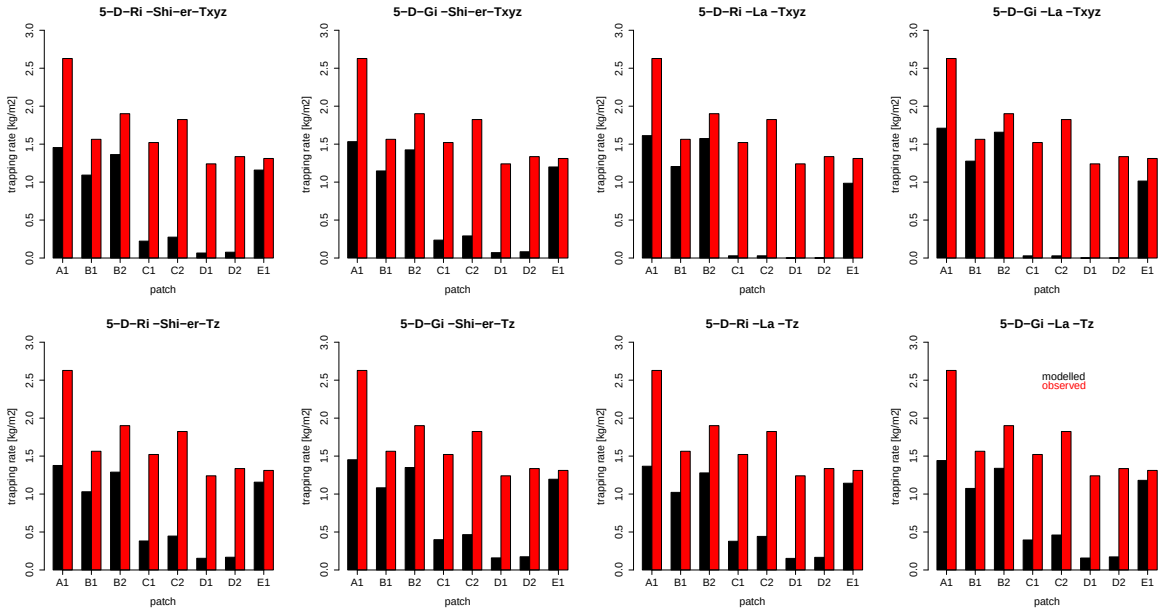

Figure 3.4: Modelled and observed interstitial deposition for S2Q100D37, shear stress deposition model. Abbreviations as follow: L further abbrevation for $LISSTini$ = LISST-100 initial measurements, D further abbrevation for $Digisoil$ = DigiSizer soil sample, St = Stokes, Ri = van Rijn, La = Lane, Wh = White, log = logarithmic profile law, $Txyz$ = turbulent kinetic energy using all velocity vector fluctuations.

Overall, these results suggest that in the experimental setting the shear stress distribution does contribute to a lesser extent to deposition patterns, as suggested by the Krone formulation. Still, the findings in both Fig. 3.3 and 3.4 do not contradict the choice of the best performing value set combination in Step 2. The alternative value set combinations (for example the ones plotted in Fig. 3.4) result in similar or worse fits for the distributions of TR.

3.3.5 Step 2 velocity deposition model - silty experimental runs

Figure 3.5 (see also according Figures A.13 to A.17 in the Appendix) shows the Step 2 calibration results for the velocity deposition model. r^2 is overall high with all values of 0.93 and higher. For the λ values, there are two trends. Low λ values result in better r^2 and higher λ values resulting in better linear model fits and smaller errors. λ = 5 is seen as a good compromise.

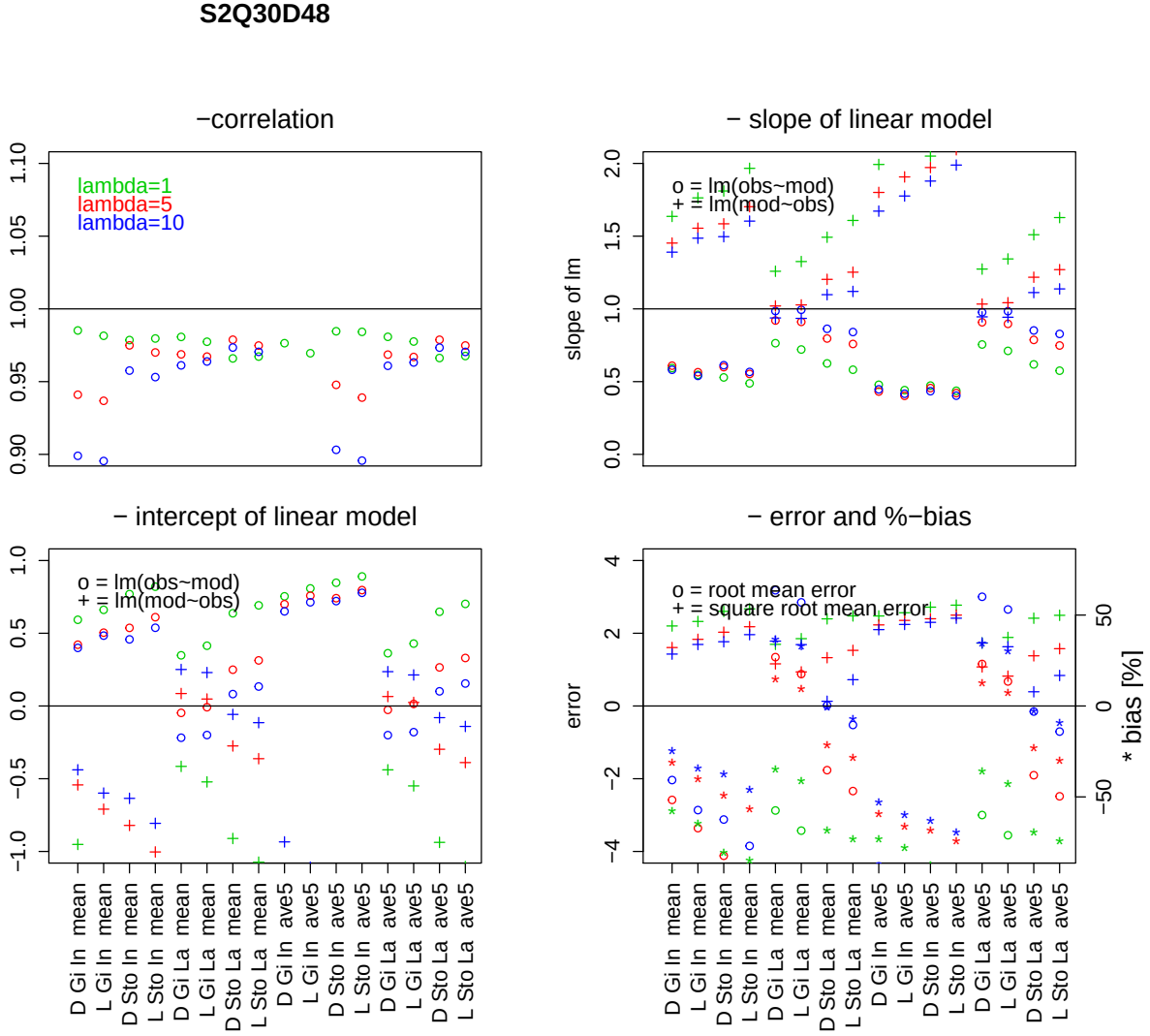

Figure 3.5: Calibration statistics for modelled and observed concentration loss in S2Q30D48, velocity deposition model. Abbreviations: L further abbrevation for $LISSTini$ = LISST-100 initial measurements, D further abbrevation for $Digisoil$ = DigiSizer soil sample, St = Stokes, Ri = van Rijn, La = Lane, Wh = White, $mean$ = mean velocity of all four levels, $ave5$ = averaged velocity measured at 5 cm distance to the bed.

In terms of the single parameters, the DigiSoil grain size distribution results in marginal better fits. For the settling velocity the picture is very clear with Gibbs values performing consistently better than Stokes values. As for the critical velocity, there is clearly a better performance of the Lane value set. For all experimental runs, the two velocity value sets achieve good results. Still, if comparing the statistical values in the table, the mean velocity performs consistently better.

Concluding, the best performing value set for the velocity deposition model, taking all experimental settings into account is: λ = 5, GSD = Digisoil, w_s= Gibbs, v_{cr}= Lane and v = $mean$.

3.3.6 Step 3 velocity deposition model - silty experimental runs

Figure 3.6 gives an example of the application of the best performing value set with regard to the modelled and observed trapping rates. The best performing value set of Step 2 is plotted as the third top panel. Again the agreement between modelled and observed TR is acceptable given the level of noise. The other plotted value set combinations perform similar (with Lane v_{cr}) or weaker (with Inman v_{cr}). As seen for the shear stress deposition model, the modelled TR in E is considerably higher than the observed TR. Figure 3.7 shows modelled and observed TR for S2Q100D37. Here the difference in the magnitude of TR between model and observation is extreme for all value set combinations. This is to be expected, since the ratio of $TRmean/Dpot$ was as high as six, showing a large discrepancy in the fine sediment mass balance (see Figure 2.19). Still, if the error in magnitude is set aside, the accordance of modelled and observed TR follows the same trends as seen before. For the traps A, B and E, modelled deposition is higher than for the elevated positions C and D. The best performing value set combination from Step 2 (third top panel) performs well compared to all other combinations. Hence, similar to the shear stress deposition model, the data presented in Figure 3.6 and 3.7 does not contradict the findings of the best performing value set combination in Step 2.

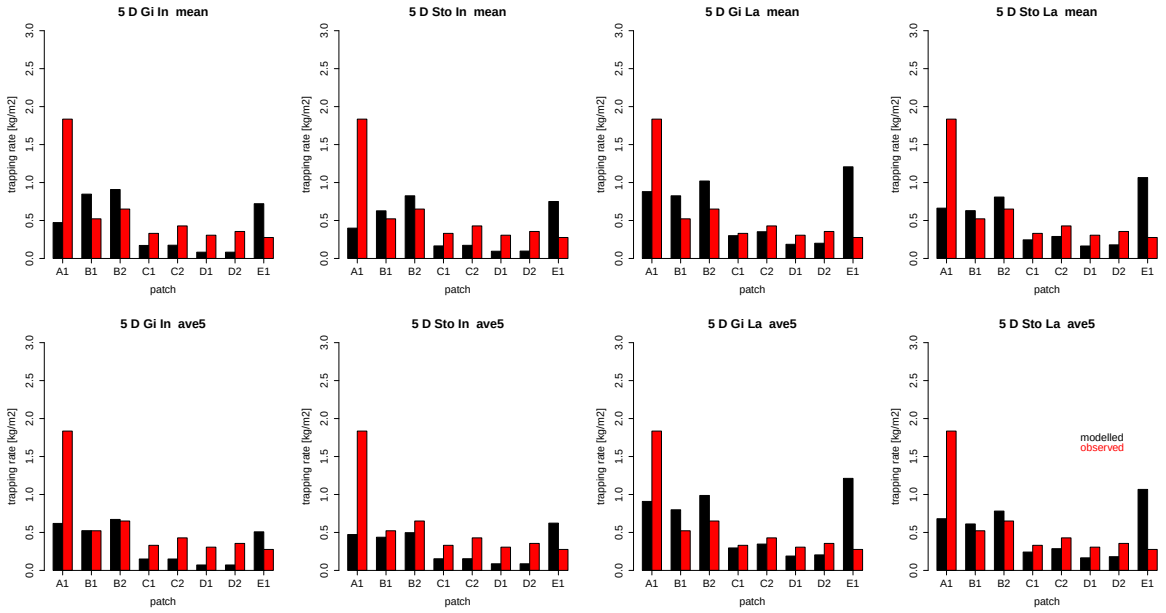

Figure 3.6: Modelled and observed interstitial deposition for S2Q30D48-1, velocity deposition model. Abbreviations: L further abbreviation for $LISSTini$ = LISST-100 initial measurements, D further abbreviation for $Digisoil$ = DigiSizer soil sample, St = Stokes, Ri = van Rijn, La = Lane, Wh = White, $mean$ = mean velocity of all four levels, $ave5$ = averaged velocity measured at 5 cm distance to the bed.

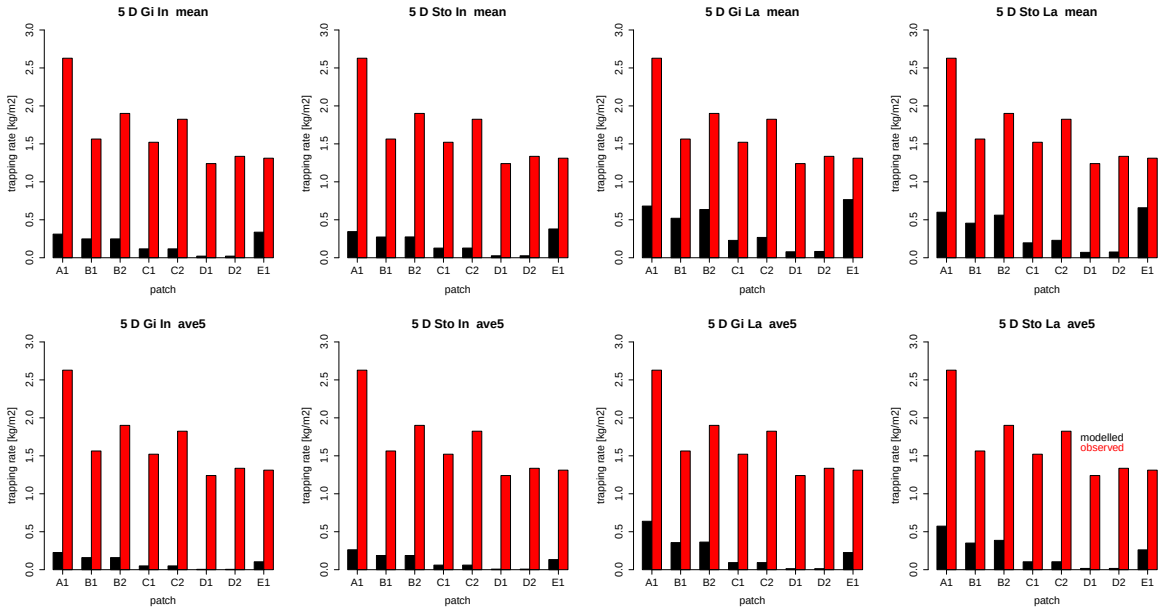

Figure 3.7: Modelled and observed interstitial deposition for S2Q100D37, velocity deposition model. Abbreviations: L further abbrevation for $LISSTini$ = LISST-100 initial measurements, D further abbrevation for $Digisoil$ = DigiSizer soil sample, St = Stokes, Ri = van Rijn, La = Lane, Wh = White, $mean$ = mean velocity of all four levels, $ave5$ = averaged velocity measured at 5 cm distance to the bed.

3.3.7 Step 1 calibration of sandy experimental

The Step 1 calibration of sandy experimental runs universally results in very good accordance of modelled and observed concentration loss. Due to the fast concentration loss, experimental data consists of one initial high concentration and all subsequent measurements close to the equilibrium concentration. The instant nature of deposition results in a lack of intermediate measurements. The calibration runs for all value set combinations result in identical good linear fits. Therefore, on grounds of Step 1, a discrimination between the single calibration runs is not possible. For Step 2, the suitable value set combinations of the silty experimental runs from Step 1 are also adopted for the sandy experimental runs. The log method to establish shear stress was replaced with the Tz method. Furthermore, calibration runs to establish the grain size distribution method are not necessary, because the sand grain size distribution was determined using square holed sieves in all cases. The results of these simulations are analysed for Step 2 and Step 3 in the following paragraphs.

3.3.8 Step 2 and 3 shear stress deposition model calibration - sandy experimental runs

Figure 3.8 shows the Step 2 calibration plot and the already discussed extreme good accordance of modelled and observed concentration loss for the shear stress deposition model. The same can be seen for the other three sandy experimental runs in Appendix A.33 to A.28 and the according Tables A.28 to A.31. For many value set combinations r^2 reaches 1. The only noticeable difference in the statistical evaluation is between runs with the $Txyz$ and Tz method. $Txyz$ shows more divergence between the different λ values and Tz results in more uniform statistical results. If a decision has to be made for the other parameters, then Gibbs settling velocity and Shields critical shear stress will perform marginally better than the van Rijn settling velocity and the Lane critical shear stress. These also performed best in the silty

experimental runs.

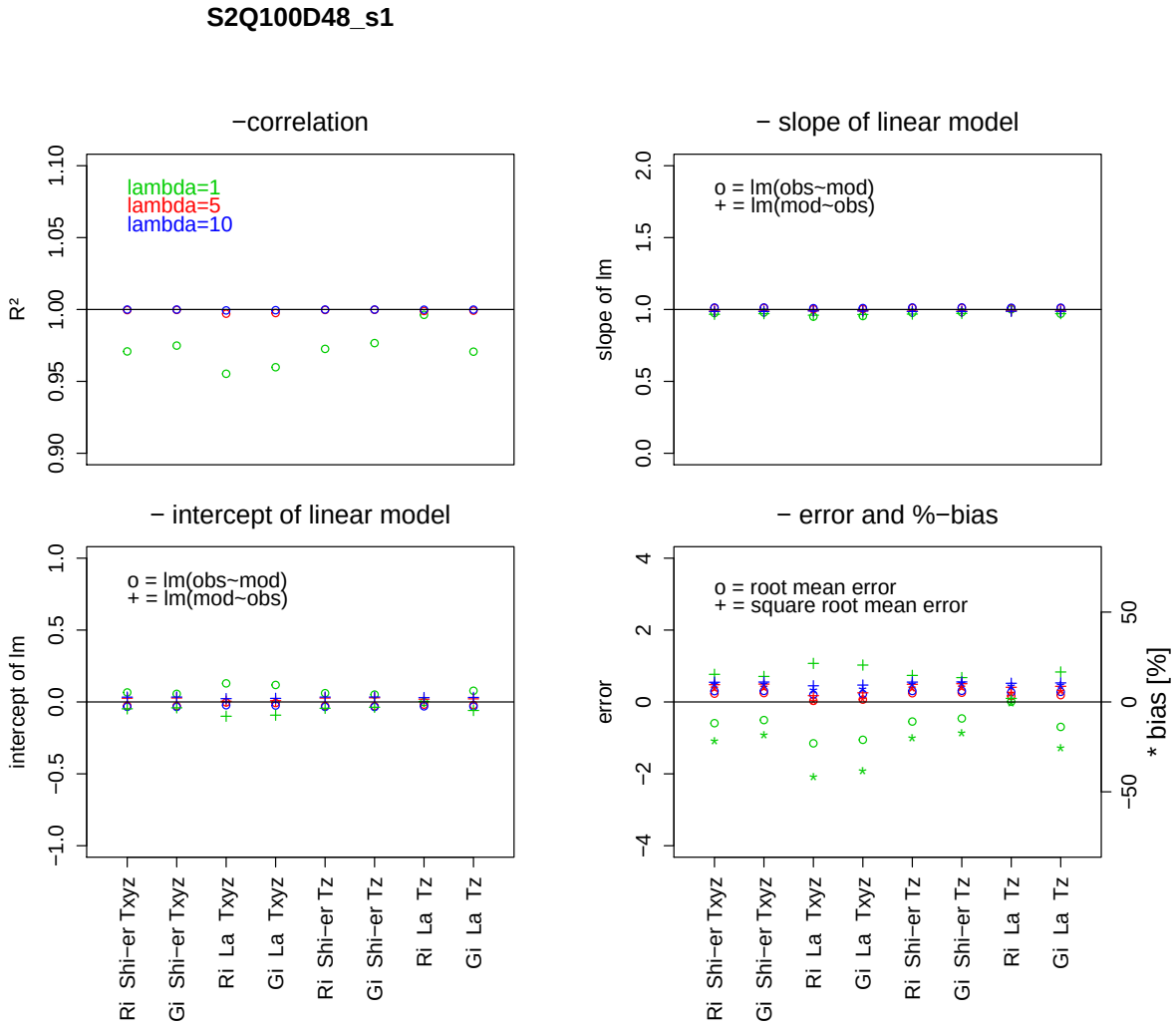

Figure 3.8: Calibration statistics for modelled and observed concentration loss in S2Q100D48-s1, shear stress deposition model. Abbreviations as follow: L further abbreviation for $LISSTini$ = LISST-100 initial measurements, D further abbreviation for $Digisoil$ = DigiSizer soil sample, St = Stokes, Ri = van Rijn, La = Lane, Wh = White, log = logarithmic profile law, $Txyz$ = turbulent kinetic energy using all velocity vector fluctuations.

Although the fit between modelled and observed concentration is very good, the modelled trapping rates of the sandy experimental runs are not in accordance with the observed trapping rates. Especially trap A and E do perform decisively different in the model compared to the experimental data, which is obvious when looking at

Figure 3.9 for S2Q100D48-s1. Calibration runs with Tz result in a complete lack of deposition for trap B to E. These discrepancies show that modelled deposition is in accordance to the v respectively τ_0 distribution, whereas the observed data suggests that the travel time of the single grains is most decisive for deposition. This means the model underestimates the particle deposition speed. To address the underestimation, one possibility is to adapt the τ_{cr} for the sandy grain size classes. Four different adaptions were applied in order to investigate if there is a systemic error in the τ_{cr} definition for sandy grain sizes.

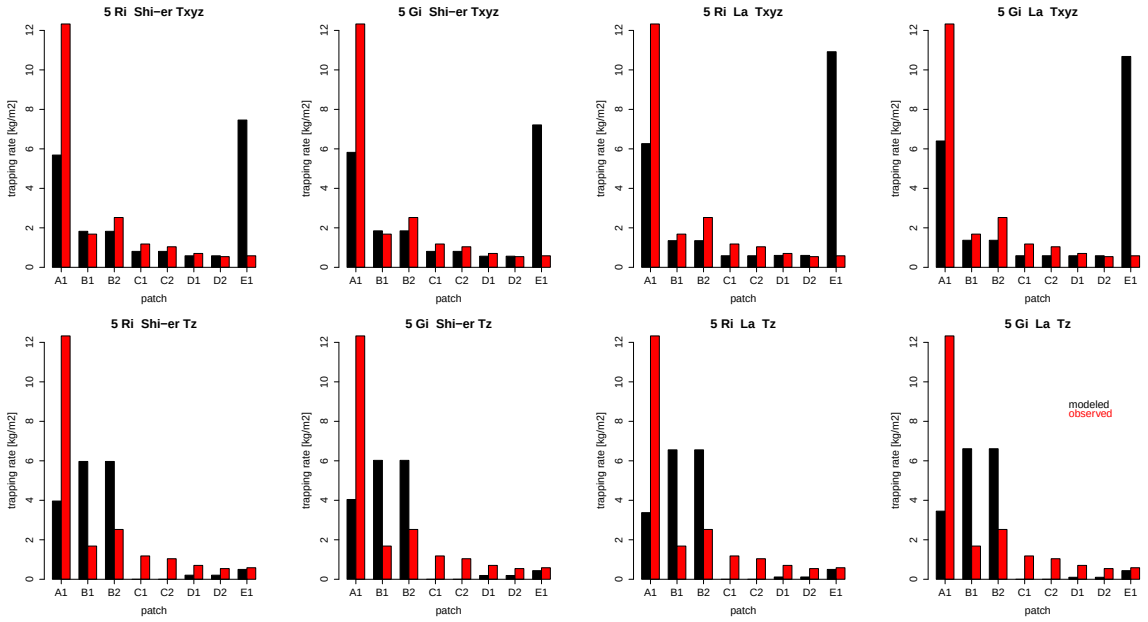

Figure 3.9: Modelled and observed interstitial deposition for selected value set combinations in S2Q100D48-s1, shear stress deposition model. Abbreviations as follow: L further abbreviation for $LISSTini$ = LISST-100 initial measurements, D further abbreviation for $Digisoil$ = DigiSizer soil sample, St = Stokes, Ri = van Rijn, La = Lane, Wh=White, log = logarithmic profile law, $Txyz$ = turbulent kinetic energy using all velocity vector fluctuations.

The adaption of the critical shear stress for grain size classes coarser than 63 μm bases on the Shields value set and is shown in Table 3.6. The adapted value sets are created by fitting exponential curves through the critical shear stress values for grain size class one to three and the critical shear stress value for the grain size class eight, of which the latter is risen from adaption to adaption. The values for grain size classes four to seven are calculated and rounded from these exponential

curves. All Step 2 calibration runs with the adapted critical shear stress value sets

grain size class	μm	Shield Pa	ad1 Pa	ad2 Pa	ad3 Pa	ad4 Pa
1	<16	7.00	7.00	7.00	7.00	7.00
2	16-32	3.00	3.00	3.00	3.00	3.00
3	32-63	2.50	2.50	2.50	2.50	2.50
4	63-125	2.00	2.50	3.00	3.50	4.00
5	125-250	2.00	3.50	5.00	6.50	8.00
6	250-500	2.50	4.50	6.50	8.50	10.50
7	500-1000	3.00	5.50	8.00	10.50	13.00
8	1000-2000	4.50	11.00	14.00	17.00	20.00

Table 3.6: Original Shields critical shear stress values set and four value sets with adapted (ad1 to ad4) critical shear stress for grain size classes four to eight.

result in very good fits with r^2 close to 1. Again, from the Step 2 calibration results no best performing value set combination can be identified. The Step 3 results for S2Q100D48-s1 are shown in Figure 3.10 with four selected value set combinations for each adaption. According plots and tables for all other sandy experimental runs can be found in the Appendix (Figures: A.37 to A.38, Tables: A.44 to A.51). The performance of the model for sandy experimental runs improves with the adaption of the critical shear stress. Modelled sedimentation covers now all positions in the experimental channel and TR for E is reduced to a similar magnitude compared to the observed value. Still, modelled TR in A is lower than the very high observed values. Remarkably, the different adaptions do not result in considerably different behaviour. This insensitivity to further increase of the τ_{cr} value shows that possibly not the τ_{cr} range, but the flow conditions measured and the marginal positions A and E are causing this discrepancy. However, the model performance would benefit from a slight increase of τ_{cr} for particles >63 μm. A possible solution is the combination of Shields values for grain size class one to four with Bangold values for grain size class five to eight.

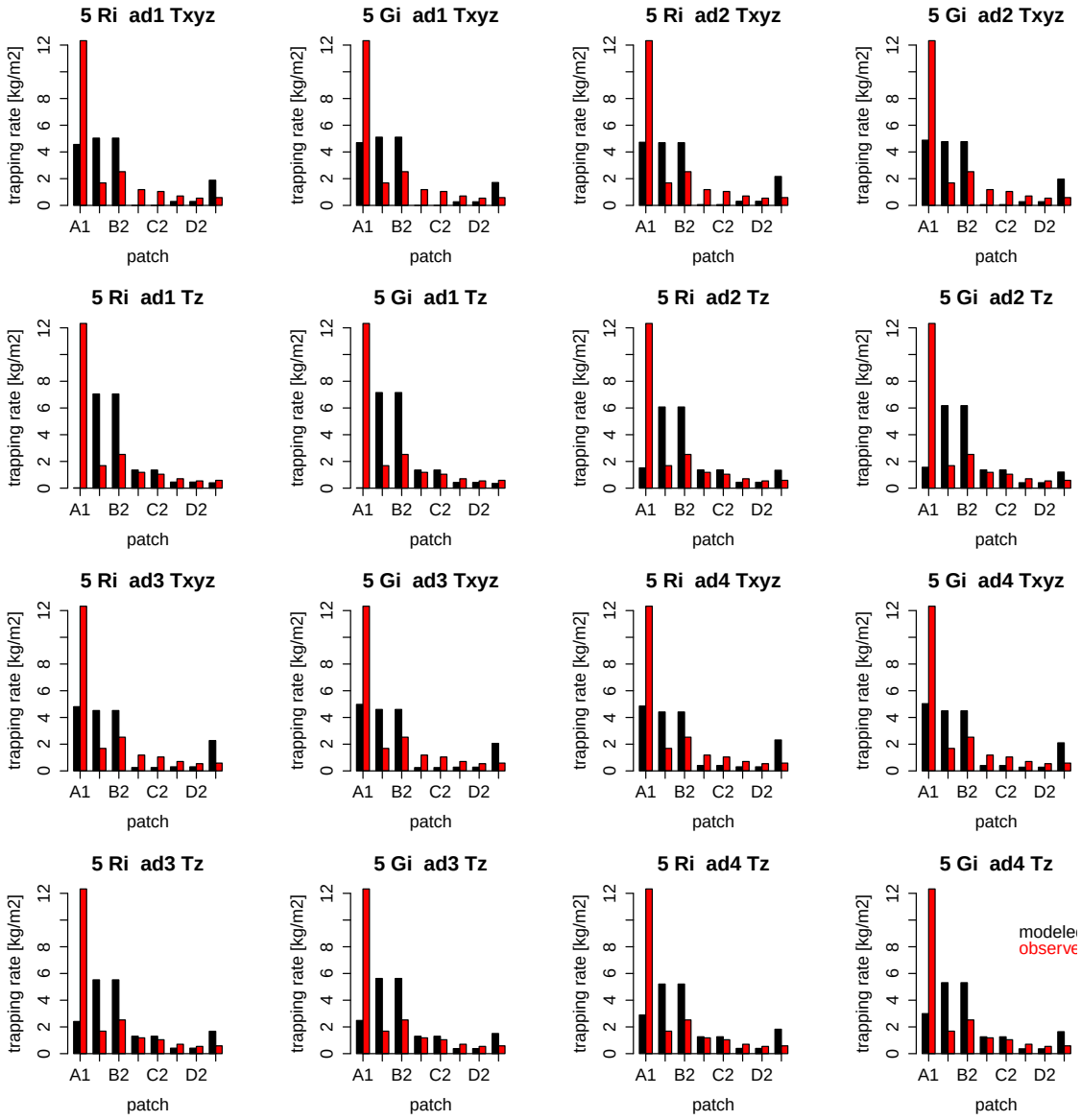

Figure 3.10: Modelled and observed interstitial deposition for selected value set combinations in S2Q100D48-s1 with adapted critical shear stress. Abbreviations as follow: L further abbreviation for $LISSTini$ = LISST-100 initial measurements, D further abbreviation for $Digisoil$ = DigiSizer soil sample, St = Stokes, Ri = van Rijn, La = Lane, Wh = White, log = logarithmic profile law, $Txyz$ = turbulent kinetic energy using all velocity vector fluctuations.

Given the consistency with the silty experimental runs, for the further application of the model, the value set combination GSD = Digisoil, λ = 5, w_s = Gibbs, critical shear stress= ad1 and shear stress= $Txyz$ is defined as the best performing value set combination.

3.3.9 Step 2 and 3 velocity deposition model calibration - sandy experimental runs

For the velocity deposition model in Step 2 of the calibration, all values set combinations perform well. Figure 3.11 plots the results of the calibration statistics for S2Q100D48-s1 for the velocity deposition model.

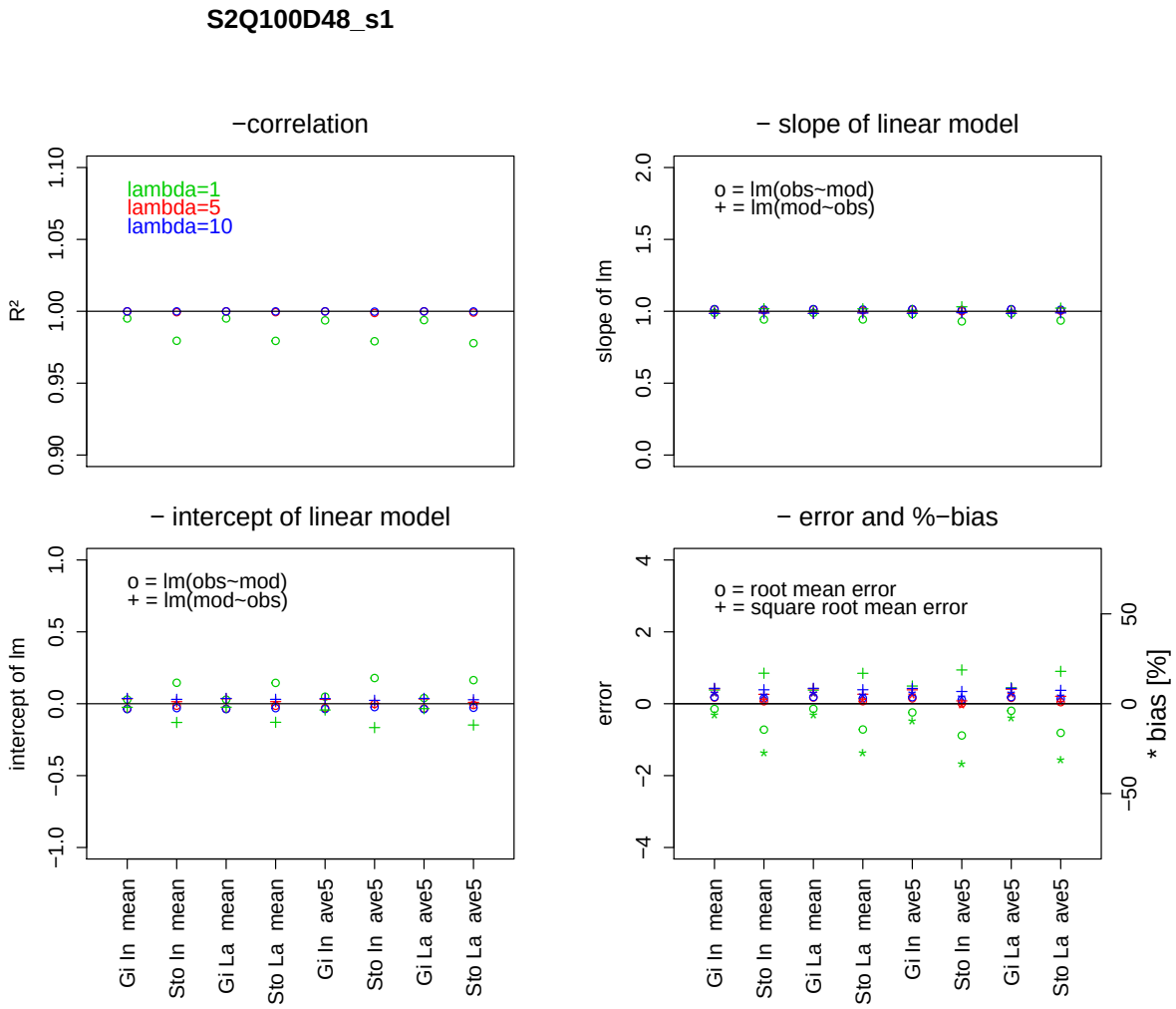

Figure 3.11: Calibration statistics for modelled and observed concentration loss in S2Q100D48-s1, velocity deposition model. Abbreviations: L further abbreviation for $LISSTini$ = LISST-100 initial measurements, D further abbreviation for $Digisoil$ = DigiSizer soil sample, St = Stokes, Ri = van Rijn, La = Lane, Wh = White, $mean$ = mean velocity of all four levels, $ave5$ = averaged velocity measured at 5 cm distance to the bed.

According plots and tables for the other sandy experimental runs can be found in the Appendix (Figure A.39 to A.41 and Table A.52 to A.55). Due to the continuously good accordance of observed and modelled concentration, the Step 2 calibration results do not include reasonable distinctions between the single value set combinations and a best performing combination can not be identified. The Step 3 calibration results of the velocity deposition model show a good accordance between modelled and observed trapping rates. Figure 3.12 plots the modelled and observed trapping rates for S2Q100D48-s1 for the velocity deposition model. According plots and tables for the other sandy experimental runs can be found in the Appendix (Figure A.42 to A.44 and Table A.56 to A.59).

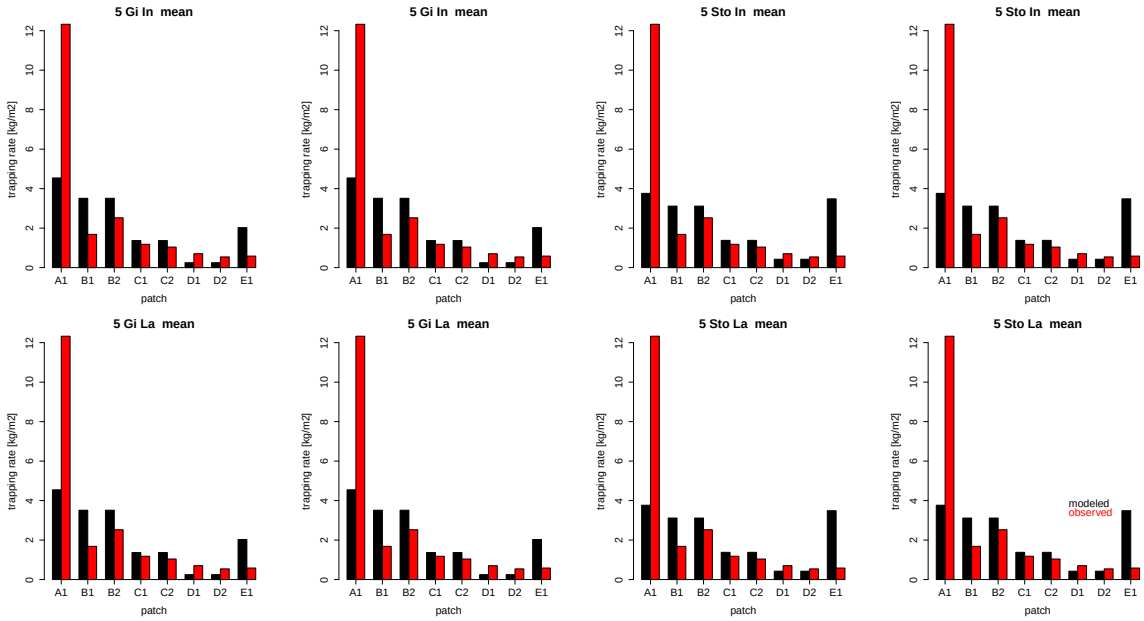

Figure 3.12: Modelled and observed interstitial deposition for selected value set combinations in S2Q100D48-s1, velocity deposition model. Abbreviations: L further abbreviation for $LISSTini$ = LISST-100 initial measurements, D further abbreviation for $Digisoil$ = DigiSizer soil sample, St = Stokes, Ri = van Rijn, La = Lane, Wh = White, $mean$ = mean velocity of all four levels, $ave5$ = averaged velocity measured at 5 cm distance to the bed.

All value set combination perform similarly well with regard to trapping rates of the sandy fine sediment fraction. However, the problem of underestimating TR in A and overestimating TR in E is also apparent, but to a lesser degree. A decision on the best performing value set combination on the grounds of the sandy experimental

runs is not possible. The only distinction is the clear superiority of λ = 5 compared to 1 and 10. With this comprehensively good performance, the choice of the best performing value set combination can only be based on the results of the calibration of the silty experimental runs. These performed best for λ = 5, GSD = Digisoil, w_s= Gibbs, v_{cr}= Lane and v= $mean$.

3.3.10 Step 4 refined λ calibration

The calibration procedure from Step 1 to Step 3 suggests the best fitting value set combinations for both deposition models.

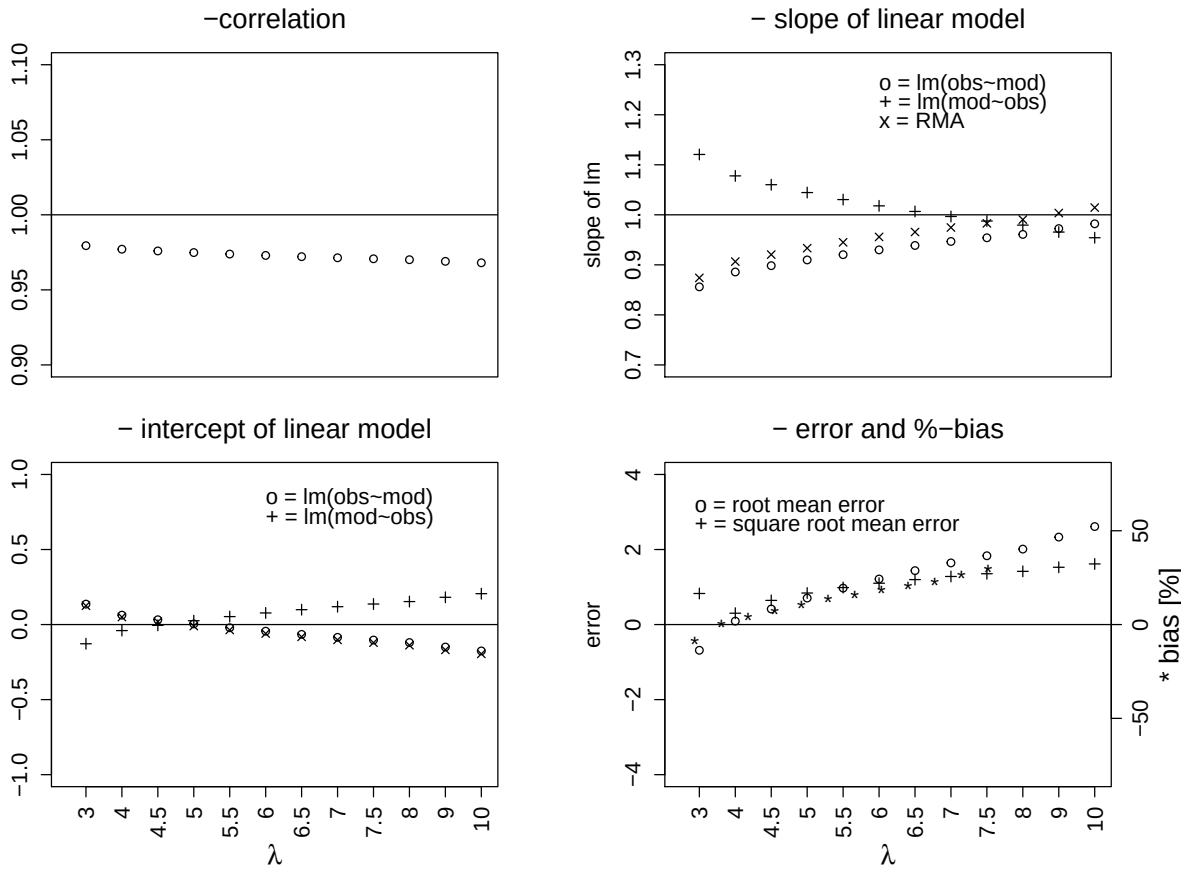

Figure 3.13: Step 4, λ calibration for modelled and observed concentration loss in S2Q30D48, shear stress deposition model.

These are both identified with λ = 5. Step 4 carries out a more detailed calibration of the λ value. Simulations of the best performing value set are executed for λ in the range between 3 and 10 in small steps (3.0, 4.0, 4.5, 5.0, 5.5, 6.0, 6.5, 7.0, 7.5, 8.0, 9.0 and 10.0). Figure 3.13 shows the result for S2Q30D48 (according plots are found in the Appendix Figure A.45 to A.49) for the shear stress deposition model. In the case of S2Q30D48, r^2 does not indicate an optimum.

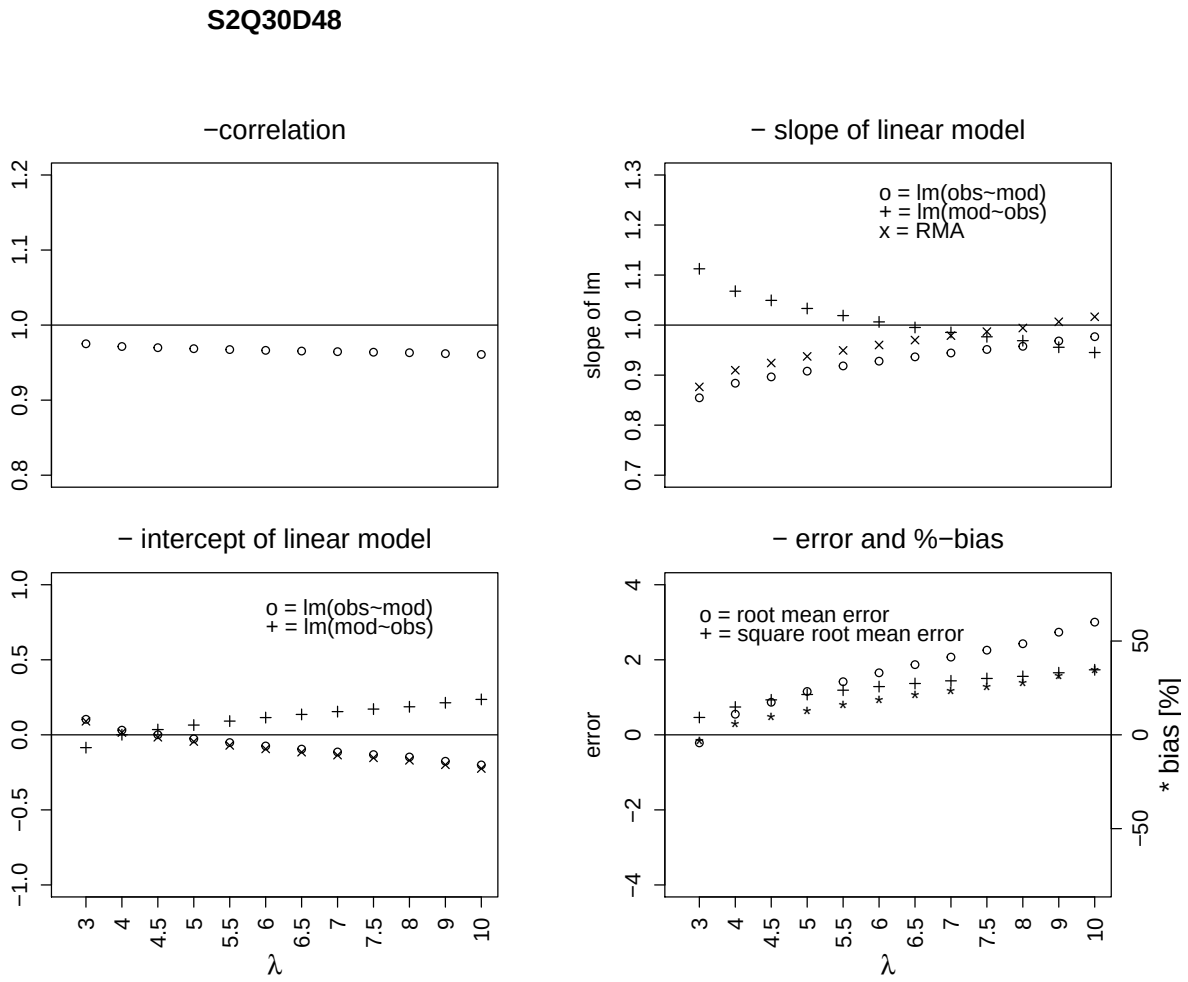

Figure 3.14: Step 4, λ calibration for modelled and observed concentration loss in S2Q30D48, velocity deposition model.

The slope of the linear model shows and optimum for 6.5, the intercept of the linear model shows an optimum for 5 and bias calculations have their optimum at 4. These diverging suggestions need to be balanced and consequently λ = 5 is

seen as a good compromise. Therefore, λ = 5 can be confirmed as the consistently best performing calibration coefficient. Figure 3.14 shows the result for S2Q30D48 (according plots are found in the Appendix A.50 to A.54) for the velocity deposition model. Again, r^2 does not result in a clear indication for a best performing λ value. The balanced result of an optimum slope at λ = 6, optimum intercept at λ = 4.5 and a smallest bias at λ =4 suggests an overall λ of 5. For all other experimental runs and all evaluated statistical parameters the optimum λ ranges between 4.5 and 6.5, which again confirms λ = 5 as the best performing calibration coefficient.

3.4 Model sensitivity and performance

This section discusses the models reaction to changes of the different input parameters and tries to exlpain the models behaviour regarding interstitial deposition in comparison to the observed data. The calibration aimed to produce a best possible fit between modelled and observed suspended concentration and interstitial deposition. With regard to the suspended concentration development, the calibration procedure could identify a well performing value set combination. Still, the existence of other value set combinations with similar good results is very likely.

In general, the concentration calibration behaves as expected. If parameters promoting deposition rise (namely these are λ, w_s, coarser GSD and the critical values), then parameters prohibiting deposition (namely v and τ) will need to be elevated as well to result in a similar deposition behaviour. For example, the log shear stress in combination with a low λ of 1 results in similar concentration loss curves as the $Txyz$ shear stress with high λ of 5 or 7 (see Figure 3.19). Furthermore, if one of the parameters promoting deposition rises and another is reduced at the same time, then again deposition curves will behave similarly. This can be seen for example in Figure 3.17, where the Gibbs w_s value set (with the highest w_s values) results in a similar concentration loss curve with λ of 1 compared to the Stokes w_s value set with

a λ of 7.

With regard to the interstitial deposition calibration, the model displays systematic discrepancies, especially for positions at the experimental channel margins. For the further discussion, the difference in the magnitude of fine sediment deposition (as discussed in 2.3.5) are set aside and only deposition of the single positions in relation to the deposition of the experimental run are discussed. For a flat bed in Series 1, modelled and observed deposition does not show systematic discrepancies, but generally a high variability. However, deposition in model runs for Series 2 display consistent patterns of discrepancy to the observed data. If set in relation of the averaged trapping of the experimental run, the modelled TR in trap A is lower than observed. Trap B is approximately in the same range, C and D are underestimated by the model and E is overestimated. An explanation for this outcome is that the modelled TR for silty experimental runs is directly dependent on the shear stresses and velocities measured above the traps, where A, B and E experience lower values than C and D. However, the observations show that the influence of velocity and shear stress are not as clear as stated by the Krone formulation (see the discussion of influence factors on TR in 2.3.5). Processes, such as deceleration (over trap A) might amplify deposition, whereas acceleration (over trap E) might lessen deposition. There is possibly a combing effect helping deposition in the elevated bed areas (at trap C and D). The model in its current state does not include any parameters accounting for the above mentioned processes. The inclusion of the above processes (or similar ones) require a new set of calibration data. This means the discrepancies between modelled and observed in-bed deposition are not a problem of the calibration, but an indicator that that the Krone formulation is not including all paramters relevant for deposition. Therefore, none of the tested value set combinations is able to deliver a better model accordance with regard to deposition patterns.

However, the modelled deposition is more consistent with the observed data for the velocity deposition model for silty and sandy experimental runs. This is in accor-

dance with the clearer correlation of velocity to TR in 2.3.5. Therefore, the velocity deposition model is seen as a good descriptor of the suspended sediment loss and a promissing starting point to improve the prediction of interstitial deposition.

Table 3.7 summarises the calibration statistics for the best performing value set combination of the silty experimental runs (Step 2). It shows a very good fit for the suspended sediment concentration. The linear regression of trapping ratios however shows again that even the best performing model runs result in a weak predition of observed deposition (Step 3).

value set	best fit	exp	$R2$	slope	intercept	SRME	%-bias
		Velocity deposition model					
		Step 2					
GSD	Digisoil	S1Q50	0.96	0.82	0.06	0.62	-13.25
w_s	Gibbs	S1Q80	0.95	0.90	-0.04	0.53	19.87
v_{cr}	Lane	S2Q30D48	0.97	0.92	-0.05	1.16	15.82
v	$mean$	S2Q30D37	0.96	0.90	0.02	0.63	5.68
λ	5	S2Q100D48	0.96	0.95	0.14	1.28	18.27
		S2Q100D37	0.97	1.11	-0.46	2.32	37.60
		Step 3					
		S1Q50	0.44	2.04	-0.12	1.23	-61.44
		S1Q80	0.32	0.18	0.07	0.79	40.15
		S2Q30D48-1	0.94	1.47	-0.02	1.20	-42.72
		S2Q30D48-2	0.54	1.01	0.19	1.25	-45.57
		S2Q30D37	0.54	0.75	0.09	0.35	3.68
		S2Q100D48-1	0.62	0.66	0.33	0.96	8.75
		S2Q100D48-2	0.68	1.20	0.20	1.69	-43.81
		S2Q100D37	0.81	0.58	0.11	1.81	33.36

Table 3.7: Calibration statistics (correlation, linear model modelled data versus observed data slope and intercept, square root mean error and percentage bias) for best performing value set combination in Step 2 and Step 3 for the velocity deposition model.

3.5 Conclusion

This chapter introduced a **numerical fine sediment deposition model** aligned to and calibrated with the results of the flume experiments described in Chapter 2. The model introduced is based on the Krone formulation (Krone, 1962) and is executed in two specifications: A shear stress dependent and a velocity dependent, referred to

as the shear stress and the velocity deposition model. The model is able to compute the concentration loss of fine sediment from the water column as well as the deposition in the bed as a function of the sediment characteristics (settling velocity, critical velocity and critical shear stress) and the competence of flow (bed shear stress and velocity). The execution of the model and all input parameters refer to fine sediment subdivided into **grain size classes** and flow conditions subdivided into **patches**. The behaviour of grains in one grain size class and the flow conditions within one patch are treated as uniform. The base module is executed for each grain size class and for each patch separately.

The model input parameters relating to the behaviour of the fine sediment are taken from the **literature**. The model input parameters relating to the flow character are taken from the **experimental data** in Chapter 2. For each model input parameter, several value sets, each consisting of different single values for each class respectively patch, were brought forward for the calibration in order to find parameters which enable the general Krone formulation to be applicable for the specific gravel-bed environment.

The **calibration successfully determined a best performing value set combination and a best performing calibration coefficient**. The calibration of the model input parameters was based on the concentration and the trapping ratio data of the two series of flume experiments covering six different environmental settings (i.e. unique combinations of bed and flow character) with two different fine sediment sources, which are described in Chapter 2. The calibration was conducted in **four consecutive calibration steps**. Step 1 used a base of mid range value sets to calibrate each model parameter on the basis of concentration curves and resulted in a **pre-selection** of feasible value sets. The feasible value sets resulted in 16 possible value set combinations, which were simulated for each three values of the calibration coefficient (λ) and all environmental settings. The resulting data was calibrated systematically in Step 2 with regard to **concentration**, applying established statistical

methods. Further, in Step 3 modelled and observed **trapping ratios** were compared. The shear stress and velocity deposition model were evaluated separately in Step 2 and 3. Further, due to their different behaviour, runs with silty and sandy fine sediment were evaluated separately.

For the **silty experimental runs**, the Step 2 calibration results for the concentration data were throughout good. However, Step 3 of the calibration could not deliver a value set combination resulting in a good agreement of modelled and observed deposition patterns. The existence of systematic disagreement of the deposition in different positions in the flume showed, that this was not a problem of the calibration procedure, but a problem of the application of the Krone formulation to the specific gravel bed environment. The author believes that only if further numerical process descriptors (for example for acceleration or combing effects) are included in the formal description of the model a better accordance of the observed and modelled deposition can be achieved. Alltogether, the performance of the velocity deposition model was more consistent for all experimental runs. The **superior performance of the velocity deposition model** is in accordance with the findings in the discussion of trapping rates in Chapter 2, where the strongest positive correlation was found for trapping rates with local velocities.

For the **sandy experimental runs**, the Step 2 calibration resulted in almost identical statistical results for all value set combinations, both for the shear stress and the velocity deposition model. These identical results are due to the very fast decline in concentration of the observed and the modelled data and the lack of measurements of intermediate concentrations. The determination of a best fitting value set combination on the ground of concentration was therefore not possible. The Step 3 of the calibration of sandy experimental runs using the shear stress deposition model showed an overestimation of the deposition speed. Consequently several **adaptions of the critical shear stress values** for the sandy grain size classes were tested. These resulted in a better accordance of modelled and observed trapping rates and

the choice of an adaption with a very good model performance. For the velocity deposition model, the Step 3 calibration of sandy experimental runs was satisfactory without the need of an adaption of the critical velocity values. In the final stage - Step 4 - of the model calibration, the best performing value set combination for both deposition models were tested with a detailed range of λ calibration coefficients. **The detailed calibration confirmed the findings** of the previous steps.

Concluding, this Chapter showed that a model based on the Krone formulation is an **adequate tool to simulate fine sediment concentration loss, but not the distribution of fine sediment deposition in the gravel bed**. In order to achieve an adequate computation of the observed interstitial deposition, new process descriptions need to be included into the numerical model. Such an extended model needs to be tested and calibrated with new experimental data quantifying these processes.

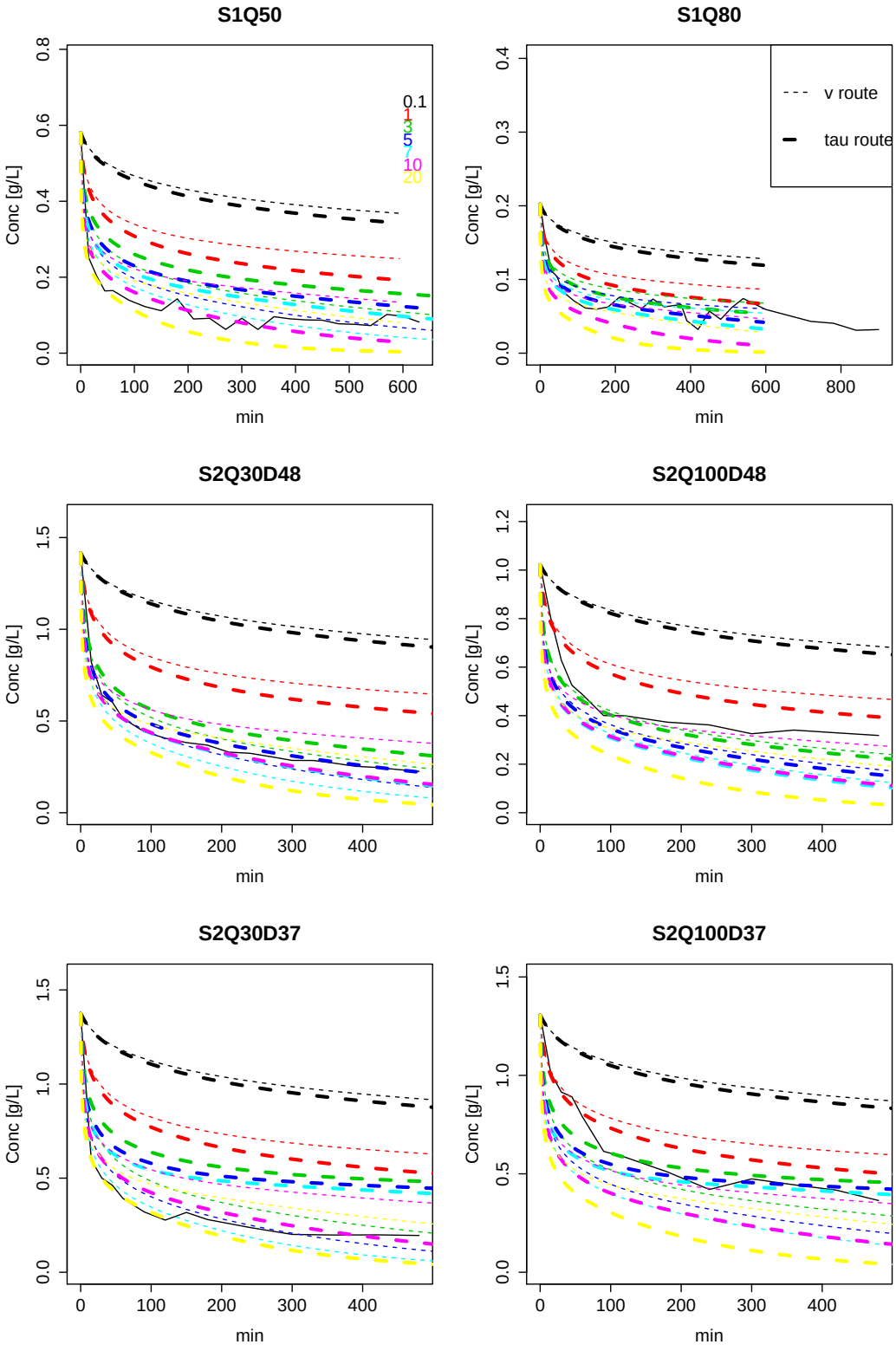

Figure 3.15: Modelled and observed concentration loss for 7 λ values in the range of 0.1 to 20.

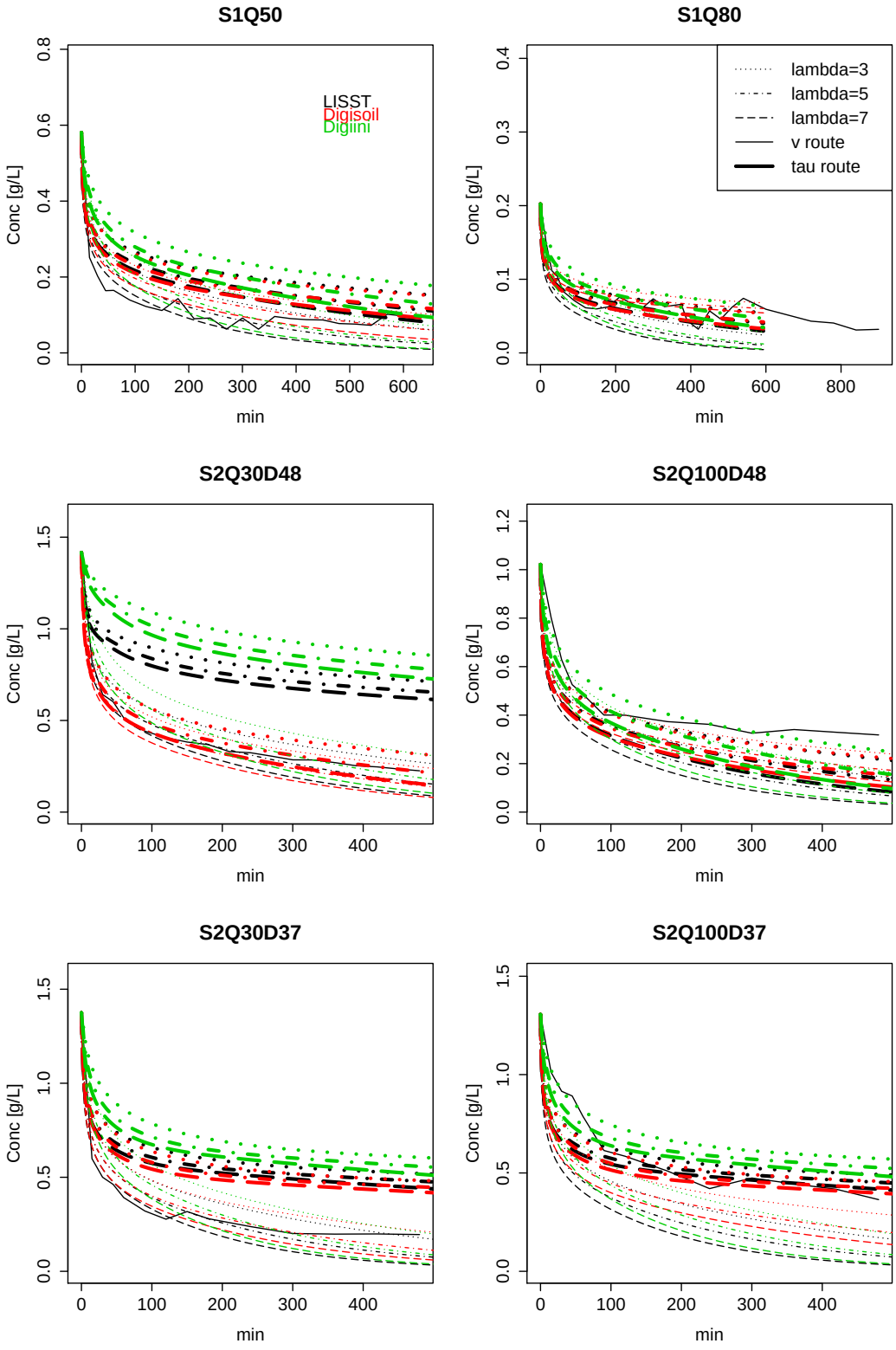

Figure 3.16: Modelled and observed concentration loss for 3 **grain size distributions**, LISST = using in situ LISST-100, DigiIni = using results of DigiSizer measurements of the initial sample, Digisoil = using DigiSizer results of the soil used in the experiments

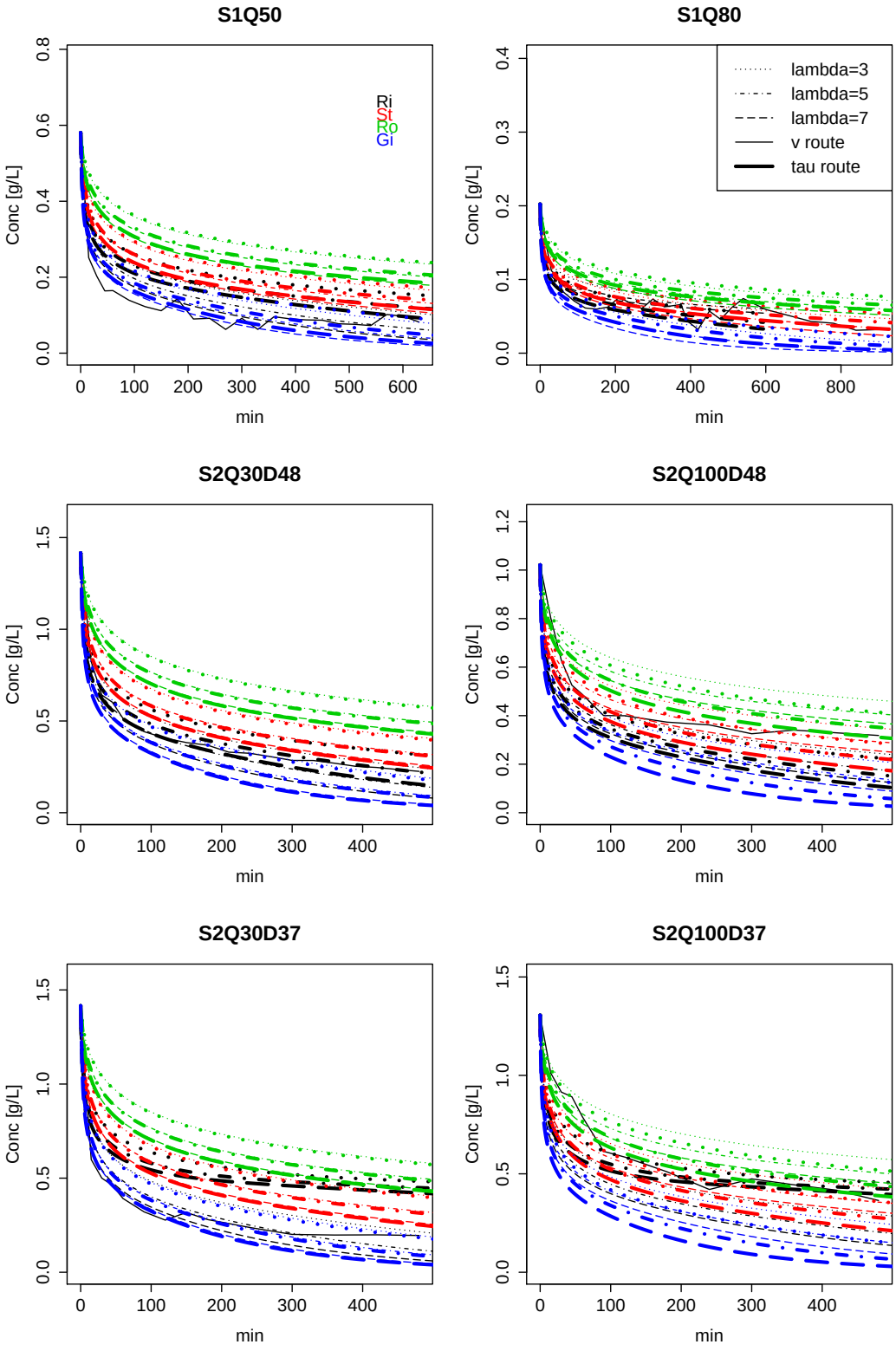

Figure 3.17: Modelled and observed concentration loss for 4 **settling velocity** value sets, Ri= vanRijn, St=Stokes, Ro= LeRoux, Gi= Gibbs.

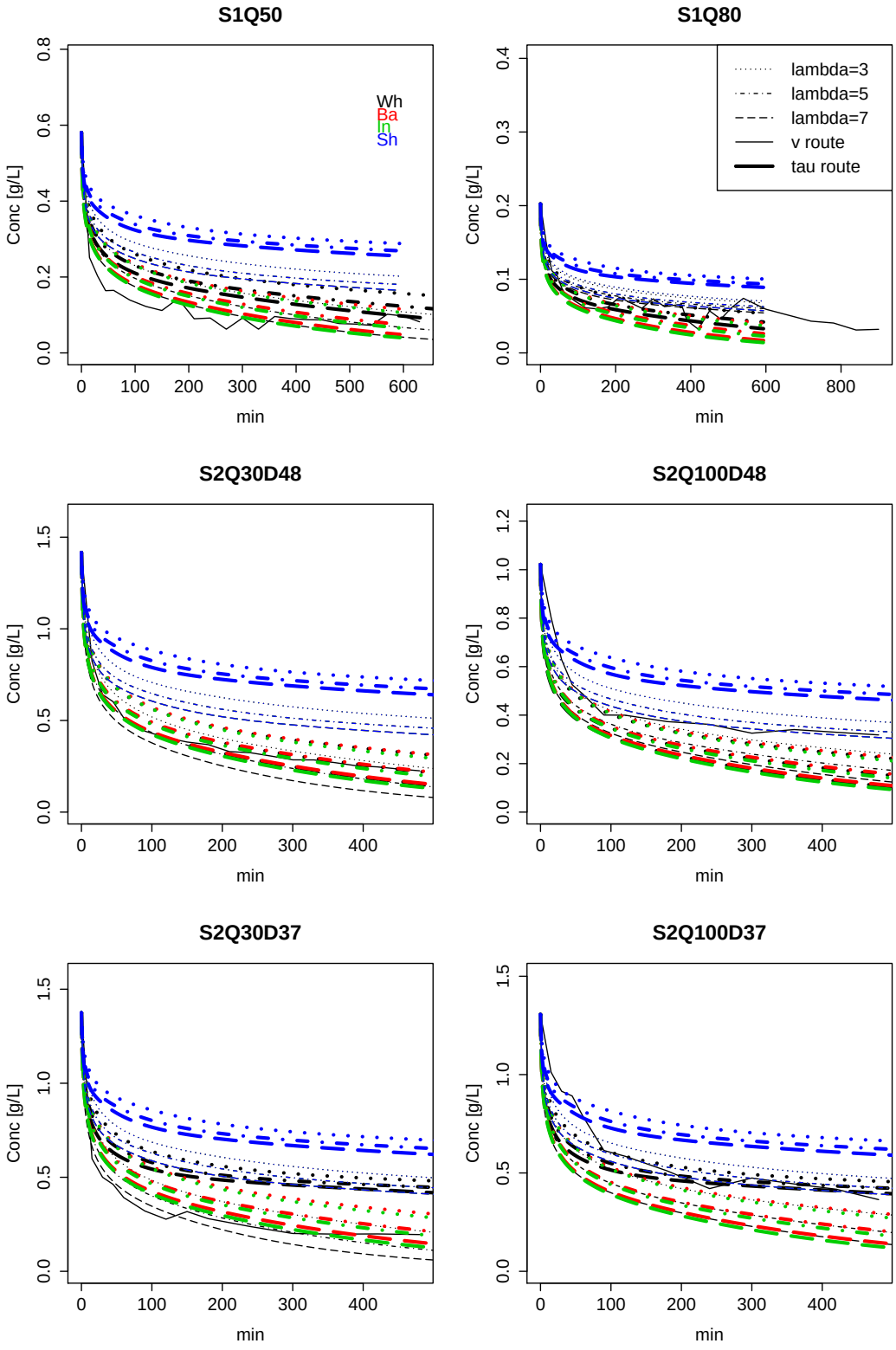

Figure 3.18: Modelled and observed concentration loss for 4 **critical shear stress** value sets, Wh=White, Ba= Bangold, In=Inman, Sh= Shields.

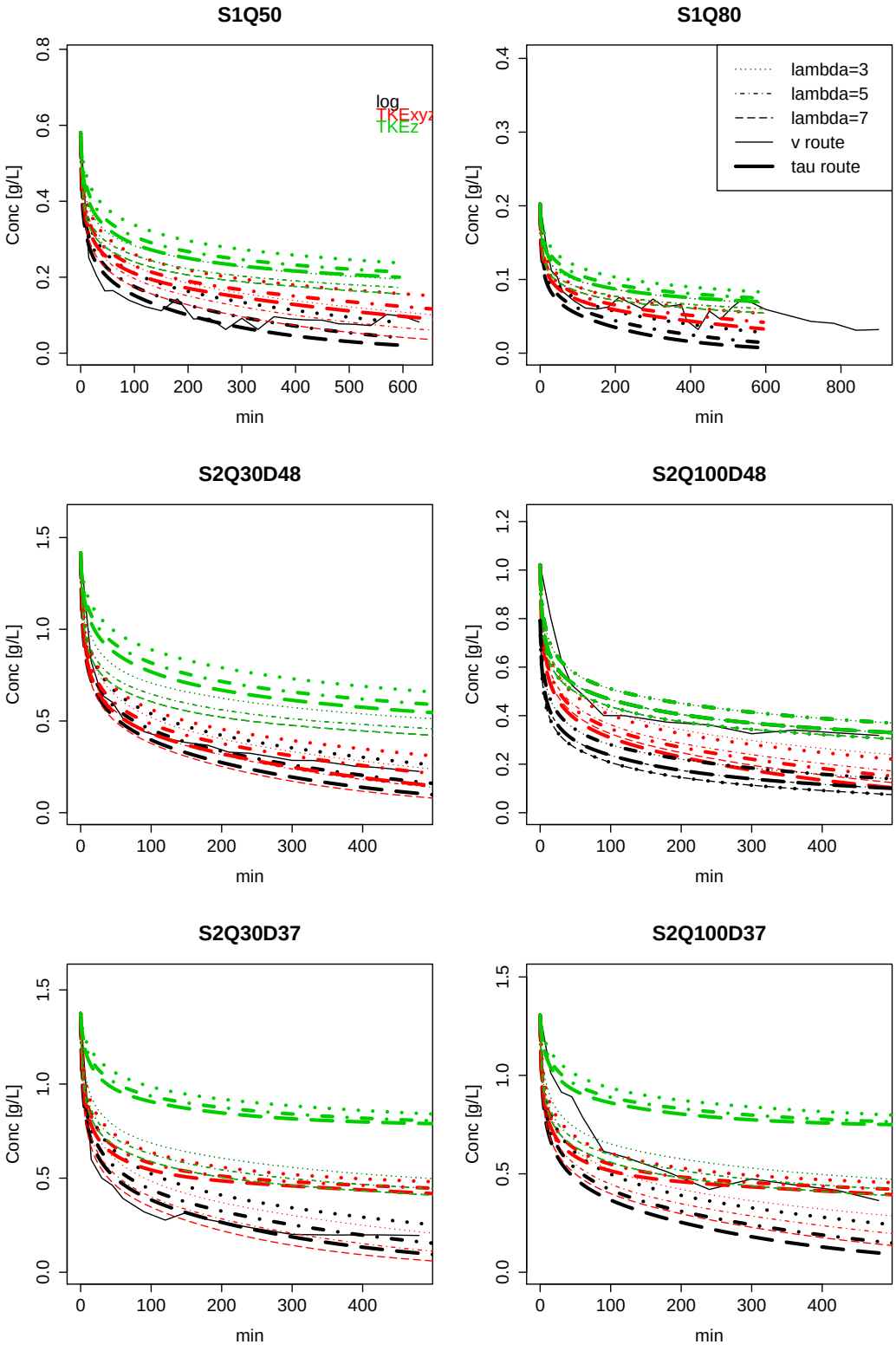

Figure 3.19: Modelled and observed concentration loss for 3 **bed shear stress** value sets, log= log law, TKExyz=turbulent kinetic energy of fluctuations of all three velocity vectors and TKEz =turbulent kinetic energy method using only fluctuations of the downstream velocity vector.

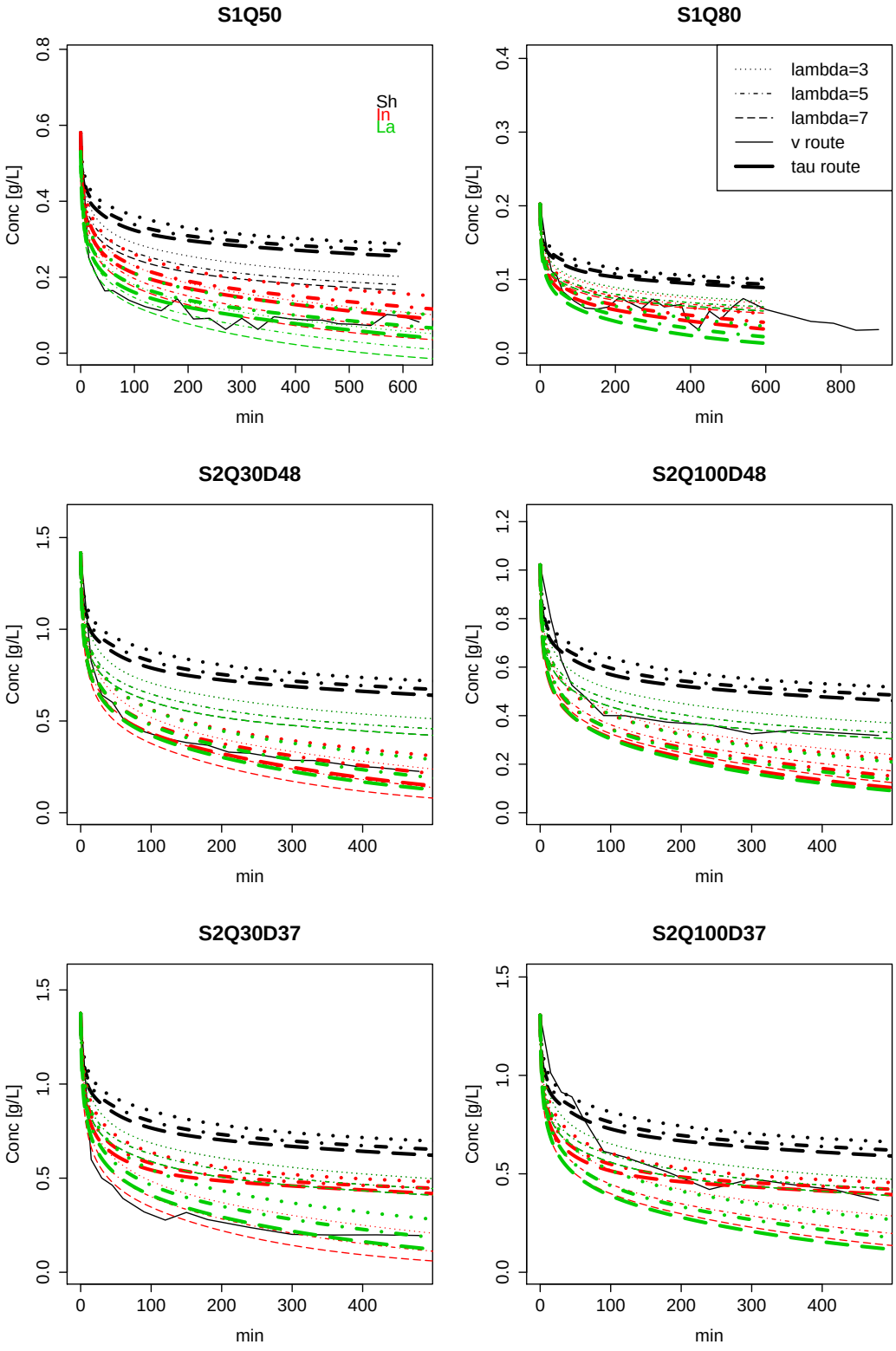

Figure 3.20: Modelled and observed concentration loss for 3 **critical velocity** value sets, Sh= Shield, In=Inman, La=Lane.

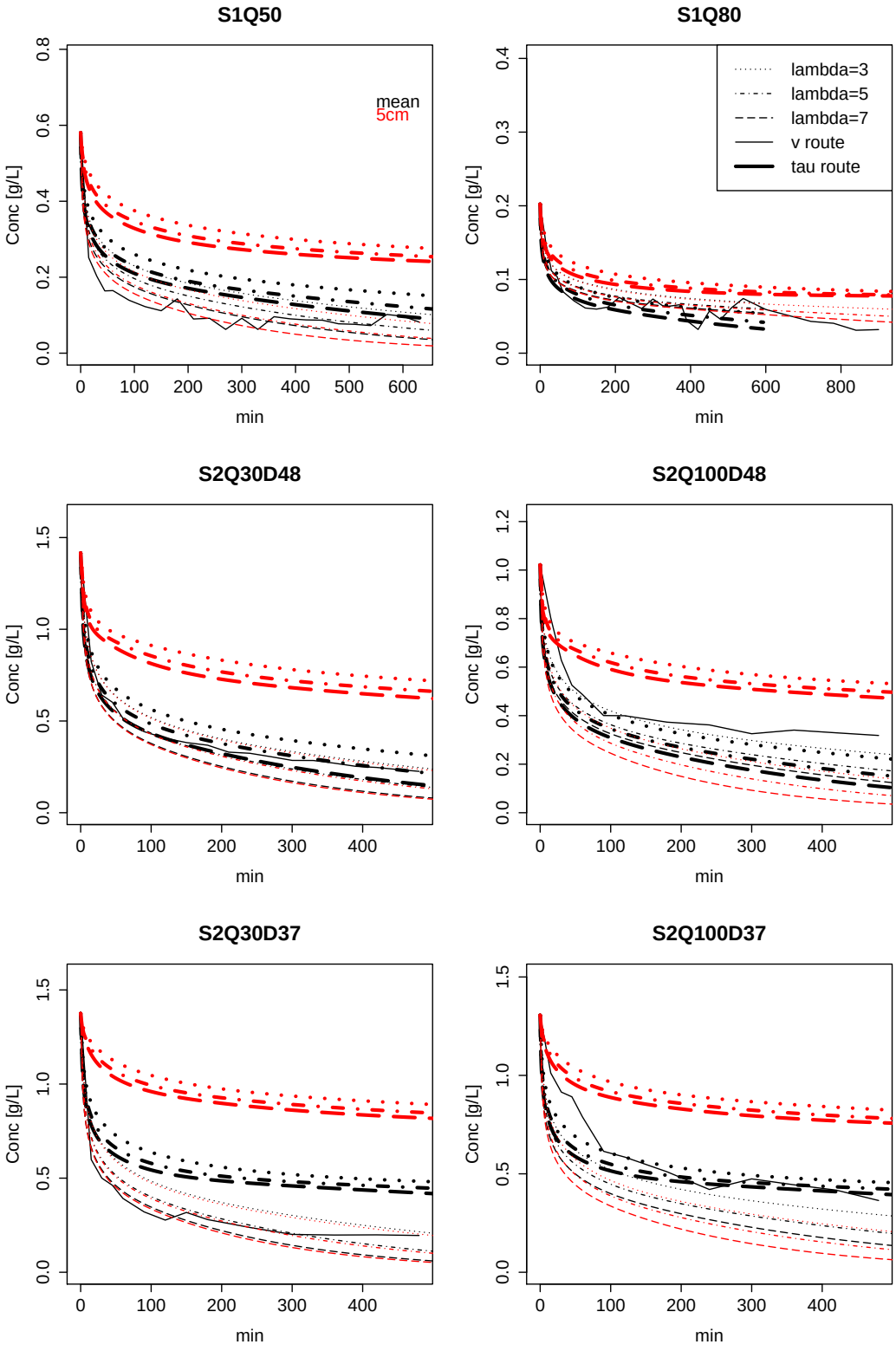

Figure 3.21: Modelled and observed concentration loss for 2 **velocity** values sets, ave5= average velocity at 5 cm above the bed and mean = mean velocity of measurements at 4 heights above the bed (5, 10, 15 and 20 cm).

Part II

Reach scale investigation

Aims of reach scale investigation

The field investigation is designed to parallel flume scale investigation. The collected field data aims to demostrate the range of different interstitial fine sediment dynamics (especially in the upper, middle and lower reaches), show the divergences in results due to the different scale and the more variable nature of the field sites and eventually verify the relations found in the flume experiments for field conditions. Also, the field data is the basis for the reach scale model calibration. As in the flume experiments, the data is collected concerning the suspended sediment, distribution of flow and magnitude and distribution of trapped sediment. Flow and sediment condition in the flume are relatively easy to measure compared to the field. Especially measurement during flow conditions with high discharge - when most fine sediment is transported - are difficult and dangerous to access. Therefore, an intermediate step to generate flow information was introduced using hydrodynamic modelling to simulate conditions during high flow. This leads to three chapters in the reach scale investigation: Chapter 4 reports on all fieldwork carried out to produce a hydrodynamic model, establish key discharge and sediment dynamics and to measure fine sediment deposition. Chapter 5 picks up on the data collected for the hydrodynamic models. It specifies the generation of coherent elevation models for the study reaches, shows the setup of hydrodynamic models in the software package Delft3D and calibrates these models with the collected field data. Finally, Chapter 6 details the adaption of the flume scale fine sediment deposition model to be applied at the reach scale. For the model calibration, the results of hydrodynamic simulations for conditions during calibration periods are connected with the measured suspended sediment and deposition data from the field itself. Finally, in order to test its applicability, the reach scale model is used to simulate scenarios of sediment transport and deposition.

Chapter 4

Fieldwork

This chapter is divided into four main sections. Section 4.1 describes the River Culm catchment and gives an introduction into the characteristics of the three study reaches where the field investigations took place. The data collection included information for direct calibration data, like the turbidity record and trapping rates during calibration periods. Additionally, field data is collected for the setup of an auxiliary hydrodynamic model, which is used to sample indirectly the velocity and shear stress conditions during the calibration periods. Section 4.2 describes the methods used to collect the data to setup a hydrodynamic model for the study reaches. Section 4.3 covers the gravel bed sampling. It describes the methods applied to retrieve samples and the evaluation of their grain size distributions. This section also describes the systematic patterns and divergences in and between the three study reaches. Section 4.4 discusses the methods used to measure fine sediment in suspension and in the river bed. This includes the turbidity and stage record and their transformation into concentration, discharge and suspended sediment loads. Further, the section introduces two methods of fine-grained bed sediment sampling. Finally, Section 4.5 concludes on the principal findings of the chapter and sign posts the potential for further use of the field data.

4.1 Description of field reaches

Figure 4.1 shows an elevation map of the River Culm catchment with arrows pointing to the three field study reaches and their corresponding gauging stations (Smithincott with the gauging station on the site of the study reach, Stonyford with the gauging station about 1 km downstream at Woodmill and Rewe with the gauging station 500 m downstream in Rewe village).

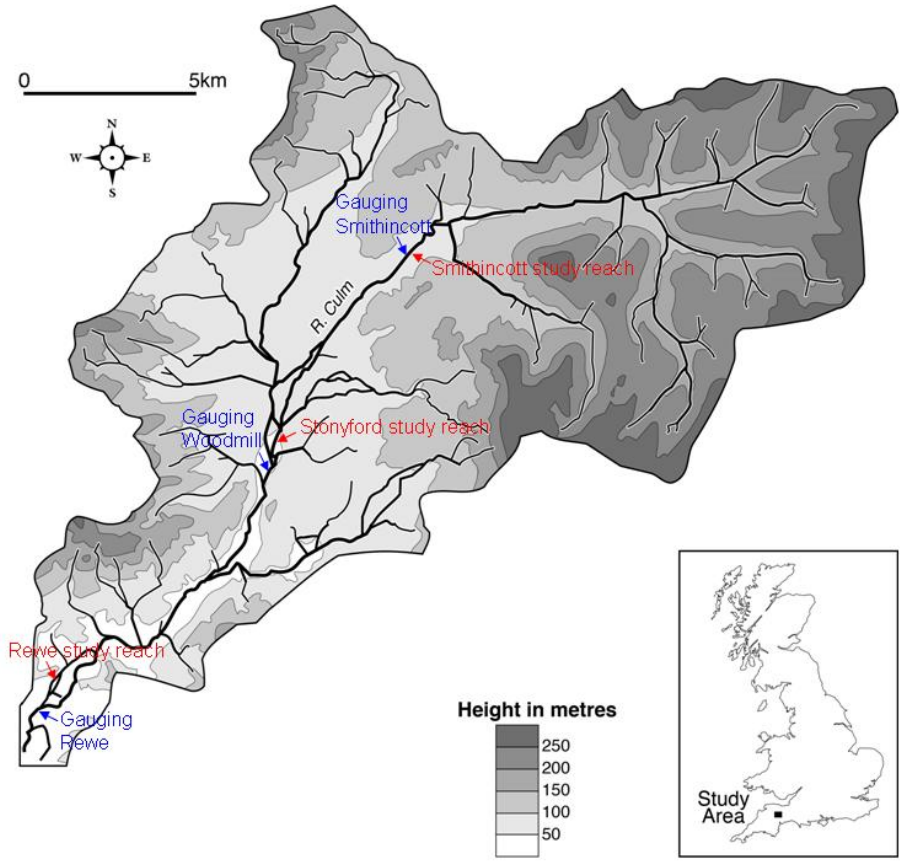

Figure 4.1: Map of the River Culm catchment with field study reaches (indicated with red arrows) and associated gauging stations (indicated with blue arrows), base map generated by and published with the kind permission of the University of Exeter Geography Department, Map Office.

The River Culm is a main tributary of the River Exe in Devon. It rises close to the former RAF airfield Culmhead in the Blackdown Hills at 267 m.a.s.l. and stretches from there approximately 50 km to join the River Exe 5 km north of Exeter at 17 m.a.s.l.. A major tributary to the River Culm is the Spratford Stream, in

Collumpton just upstream of the second study reach (Stonyford). The Culm covers a drainage area of 276 km^2. The River Culm is a gravel bed river with the present fluvial environment reworking relict pointbars and other channel deposits dating from the Pleistocene (Hardy et al., 2000).

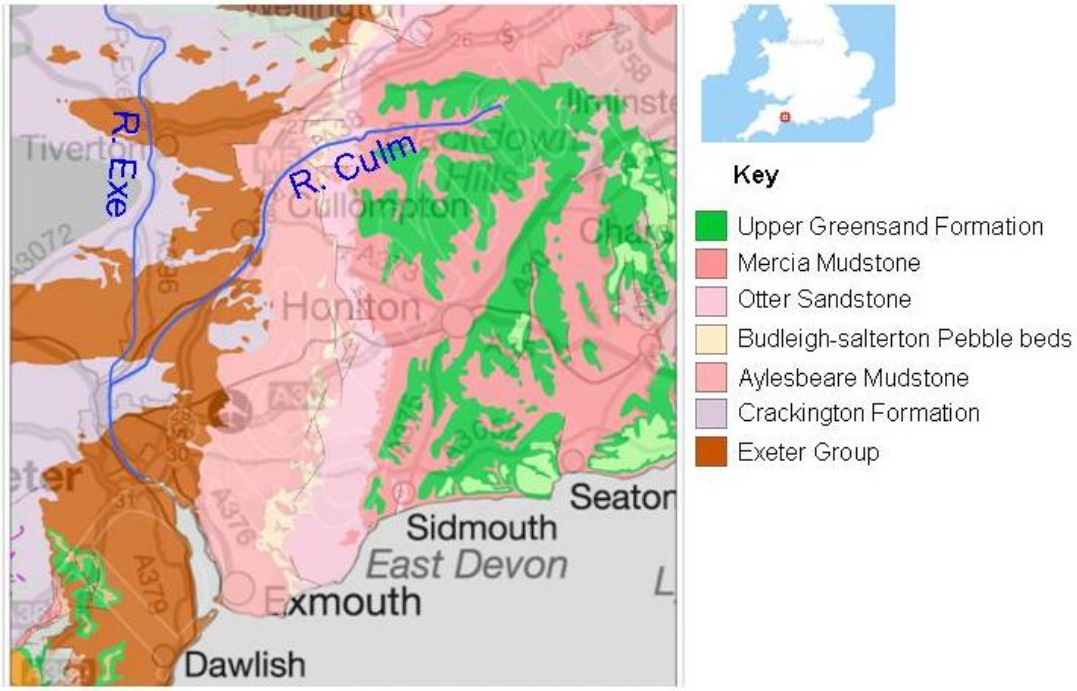

Figure 4.2: Geological map of the River Culm catchment, showing main bedrock types, source: Digimap Geology (Digimap, 2012)

Figure 4.2 shows the bedrock for the River Culm catchment and parts of the River Exe catchment. The area is completely underlain by sedimentary rocks. All valleys are formed by fluvial erosion since no glaciation occurred during the last ice age. The area is dominated by agricultural land use with mainly villages and a few small towns. Pastures for grazing and fodder crops (e.g. maize) make up most of the agricultural land. Patchy bush vegetation extends in varying degrees of thickness along the river banks. After Hardy et al. (2000), the Culm bankful discharge is exceeded on average five to eight times per year. Maximum suspended sediment concentrations in the Culm are around 1000 mgL^{-1} (Walling and Moorhead, 1987). A monitoring program over 731 days by Ashbridge (1990) suggested that 7 % of the total suspended sediment was transported in one day and only 4 % of the total

sediment load is associated with non storm events. The three study reaches are located at 20 km, 26 km and 40 km (measured based on Open Street Map data) from the source and are representative of different hydraulic regimes. On the one hand, the study reaches were choosen to cover a preferably large range of typical gravel bed river conditions. On the other hand, the best possible infrastructure was decicive. In the case of Rewe and Stonyford, the availability of A gauging stations and previous research were pivotal. THe reach at Smithincott was identified as a suitable compliment with ustream characteristics, a predominant natural flow path, still acceptable access and a welcoming permission of the farmer. All study reaches are at least ten times the average channel widths long, as suggested in Bunte and Abt (2001) to include all morphological variability. Furthermore, the reaches are chosen to have little interference from large fixed structures like large woody debris or human made steps and weirs. With regards to the classification of the reaches, the Smithincott reach is still a part of the headwaters, whereas the Stonyford reach and Rewe reach are parts of the middle and lower reaches, respectively. All fields surrounding the study reaches are used for grazing and the production of silage grass.

Before discussing the nature of the individual reaches, this paragraph gives a short overview of the structures present in gravel bed rivers. A meandering gravel bed river, such as the River Culm, typically has a riffle-pool-bar structure (Rosgen, 1994). During low flow conditions, pools are deep areas with slower flow, riffles are more shallow and fast flowing areas and bars are generally exposed during low flow conditions. Pools are found in the outside area of a channel bend and bars in the inside, whereas riffles occur in the straight stretch connecting two bends. Flow typically occurs in two helices, where one main helix is in the middle and inside of a bend and a smaller one at the outside. Over the riffles, the two helices reach equal dimensions. After the riffle, the former smaller helix develops into the larger helix and the former larger helix into the smaller outside helix. The small double helix in

the pool causes scour, whereas the larger helix inside the bend supports sediment deposition. The equal helices over riffles encourage a bar to build up in the middle of the riffle. This was first shown in flume experiments by Einstein and Shen (1964) and confirmed with more sophisticated measurements and models by Ferguson (2003b), who created a model of meander development. Furthermore, bars can be divided into head (upstream end) and tail (downstream end) and pools into head, middle and tail. Riffles inherit a more even structure and are therefore not subdivided. Different reach types can, however, show different kind of riffles. This work differentiates rapids and runs. Rapids support supercritical flow with Froude numbers larger than one (Fr$>$1) even during low flow conditions, whereas runs are defined as a more shallow and straight stretches of a river with sub-critical flow during low flow. This classification is based on the work of Bunte and Abt (2001).

4.1.1 Smithincott, Uffculm

Figure 4.3: Satellite image of river channel and floodplain at Smithincott outlining the original study reach in blue, final study reach in green and a gravel bar which formed in December 2009 in white. The latter was not yet formed when satellite image was taken. The date (01/01/2010) watermarked on the Google image is not correct because, first, the gravel bar in the upper part of the reach is not visible, despite low water levels with exposed gravel and, second, trees are foliated. It seems plausible that the picture was taken in summer 2009. Additionally, new features appeared between 2010 and 2011 in red, these features being a gravel bar blocking inflow in the lower meander bow and a new cut through connecting the upper part of the reach directly to its outlet.

Figure 4.3 shows a satellite picture of the study reach at Smithincott. The blue outline shows the original study reach with measurements from spring 2009 (240 m straight length and 270 m including meander). The red outline shows the study reach eventually used in the model, which was sampled in summer 2011 (130 m straight length and 163 m with meander), with a water level drop at low flow from 73.4 to 72.5 m.a.s.l. and an average channel width of 20 m. This study reach is situated 500 m downstream of the small Southwest Water works house at the bridge

between Uffculm and Smithincott. With 20 km distance to the source and a channel slope of 0.6 %, it is the reach with the highest sediment transport capacity, the least regulated and most dynamic flow, resulting in considerable gravel movement each winter. The main features formed in the 4 years of this study are the appearance of a new gravel bar in the upper north flowing part of the study reach (winter 2009/2010) and the cut through in combination with channel blockage in the lower part of the study reach at the end of the west flowing channel. The gravel bar succession can be seen between Images 4.4a, 4.4b and 4.4c. These three pictures all show the upper part of the study reach at low flow with the straight channel flowing south to north, where a gravel bar is indicated in white outlines in Figure 4.3. Figure 4.4a, which was taken from the east river bank facing west, shows no gravel in the middle of the channel. Figure 4.4b, which was taken from a similar position facing more upstream in a southern direction, shows the first occurrence of the gravel bar in December 2009, which then further grew as shown in Figure 4.4c, which was taken from the west river bank facing downstream in a northerly direction and showing the maximum extent of the gravel bar. The new channel is shown in Figure 4.4d. It cuts through the highly vegetated area inside the meander bow with extreme steep banks and high rates of bank erosion (several large blocks of bank material were found in the channel). In the same period, a gravel bar built up at the entrance into the meander bow channel. The combination of limited accessibility and high fine sediment input from bank erosion, rather than suspended sediment deposition and a change of flow regime led to the decision to exclude this part of the channel from the study reach.

(a) Riffle at Smithincott reach September 2009 with wooded area in a meander bow in the background and trap survey equipment in the foreground.

(b) New build up of gravel bar on riffle at Smithincott, December 2009.

(c) Maximum extension of new gravel bar at Smithincott January 2010.

(d) Densely vegetated new cut channel at Smithincott, July 2011, with fast flow causing strong bank erosion.

Figure 4.4: Photographs showing different views of the channel at Smithincott between September 2009 and July 2011.

Therefore, the final study reach includes only two riffles and three pools and is ca. ten times the river width. The most upstream pool is deep with an overgrown bar at the inside bend. The upstream riffle displays a typical two part structure with a large gravel bar in the middle, starting with the run character at the top. It develops into a rapid before reaching the mid-reach pool. The mid-reach pool is accompanied by a large, comparatively fresh gravel bar at the inside of the bend. This leads into the second riffle with run character all the way through until reaching the pool at the downstream end of the reach. This pool descends into a slack water area at the outside of the bend and a smaller gravel bar at the inside. Additionally, the pool

is blocked by a fallen tree stretching from the bar into approximately the middle of the wetted channel at low flow. The river channel around Smithincott is fairly unmanaged. The study reach displayed comparatively little obstruction and only one occurrence of large woody debris, which was less than in all adjacent stretches of the river.

4.1.2 Stonyford, Collumpton

Figure 4.6 shows the study reach at Stonyford. It is located 1 km downstream of the Cullompton M5 exit and ca. 26 km from its source. A 0.55 m (47.55-46.9 m.a.s.l.) water level drop over this 285 m reach results in a slope of 0.2 %. It signifies a typical middle reach section. The channel is mainly straight with a width between 15 and 25 m. Therefore, the reach is in accordance with the criteria to cover the full variability of the reach, with the lengths of the reach being about 15 times the channel width (Bunte and Abt, 2001). The banks are covered in very little bush and tree vegetation. Some bank erosion caused by grazing cows caused a minimal change to the channel banks. Over the last four years, no substantial gravel movement was observed.

Figure 4.5: Gravel sampling equipment at the Stonyford reach, spring 2010, with small grassy island in the background.

Figure 4.6: Satellite image of channel and floodplain at Stonyford, with the study reach outlined in red.

Concerning the riffle-pool-bar structures, the reach incorporates one pool tail (upstream end of reach), two full pools and three riffles. Furthermore, two grassy islands with steep rims are present in the study reach (one can be seen in Figure 4.5). The upstream riffle is slightly disturbed since it is a ford used by cattle. The ford like riffle part is followed by a short stretch of rapids, reaching into the first and only pronounced pool of the reach, which is not accompanied by a gravel bar. The pool ends in a run like riffle, which includes the smaller of the two grassy islands. This run does not develop into a full pool. Therefore, the second pool can be seen as a mixture of a run like riffle and a pool. An overgrown gravel bar is situated at the inside of this bend. This is again leading into a riffle with clear rapid character accompanied by a grassy island.

4.1.3 Rewe

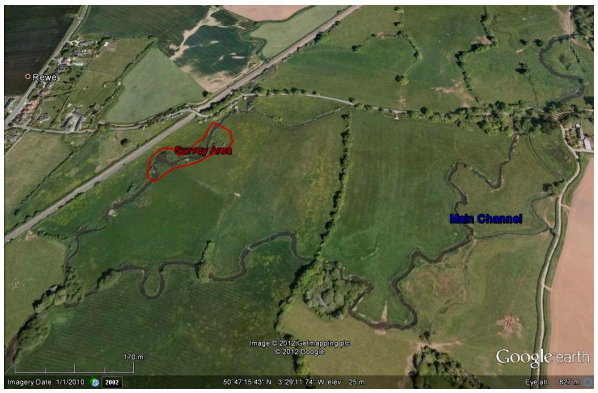

(a) Satellite overview of the Rewe area with two split channels between Columbjohn and Rewe - main channel to the right and smaller side channel with red outlined survey area to the left, close to railway line.

(b) Image of the upstream riffle in the Rewe study reach in Summer 2010.

Figure 4.7: The Rewe study reach.

The study reach at Rewe is located just downstream of the railway bridge between Rewe and Columbjohn. The reach is located 40 km from the source and close to the inflow of the River Culm into the River Exe. It is typical for the lower reaches of the study river. Figure 4.7a shows a satellite image of the area surrounding the

study reach at Rewe. The channel is split into two sub channels, with approximately the same size. The relative size of the two channels was calculated from four width measurements on site and 20 equidistant satellite image measurements of both side channels. The non-investigated split channel is on average 4 % wider. This means the investigated channel represents approximately 50 % of the discharge of the River Culm at this site. The whole floodplain is ca. 450 m wide. The side channel shown at the top of the satellite image was chosen due to its accessibility, in particular regarding the surveying of the river bed. The selected sub-channel is shown in Figure 4.8. The inflow into the two side channels is not controlled by a weir and therefore they have the same flood dynamics. The survey reach is 237 m long and the water level drops from 25.45 to 25.20 m.a.s.l. which results in a slope of 0.1 % - a typical inclination of a lower reach channel. With an average width of 12 m the length is more than 20 times the channel widths. The upstream pool is deep without a gravel bar and carries on into a riffle with a run character. The river has an extensive floodplain accommodating slow waning floods and long water logged periods every year. Following Walling et al. (1986) the floodplain between Rewe and Stoke Cannon is inundated with floodwater five times in the winter months with a typical inundation depth of 40 cm for the mean annual flood and 70 cm for the fifty year flood. The reach is lined by very little bank vegetation. Grazing takes place right up to the river edge. In the four years of this study, no evidence of gravel movement or bank erosion was observed. Three pools, one pool head (at the outflow of the reach) and three riffles are present in the study reach. The second pool is deeper and accompanied by an overgrown gravel bar at the inside bend of the pool and ends into a sparse vegetated gravel bar. This bar runs parallel to the second riffle, which shows a rapid character with very shallow and fast flow during low flow. The third pool is accompanied by a slack water area at the outside of the bend and the inside gravel bar is small and overgrown. The riffle leaving this pool, again displays a rapid character and ends in a run like pool head at the outflow of the study reach.

Figure 4.8: Satellite image of the split channel and floodplain at Rewe, with the study reach outlined in red.

In conclusion, these three study reaches cover the main fluvial structures of the River Culm with head water, middle and lower reaches. Their accompanying gauging stations were in one case set up for the purpose on site (Smithincott) and in the remaining two other cases by the University of Exeter and the Environmental Agency (Woodmill for Stonyford reach and Rewe village for the Rewe study reach). All fieldwork was planned to cover all three study reaches with the same methods and intensity. These methods are described in the following Sections.

4.2 Data for hydrodynamic model

The investigation of flow conditions in the field is restricted, especially during periods relevant for fine sediment deposition, i.e. during floods. Direct depth and velocity measurements during high stage and sediment concentration are difficult and in

many cases dangerous. Therefore, the aim is to predict flow conditions indirectly using the simulation results of hydrodynamic models of the study reaches. To setup these models, specified data had to be collected: a) GPS measured elevation points (in transects at half a river width, including parts of the floodplain) to create a digital elevation model (DEM); b) control GPS measurements of the river bed in a longitudinal profile to test the quality of the DEM; c) water surface, depth and velocity data for boundary condition definition and calibration. Subsection 4.2.1 shows the equipment and general approach to the GPS elevation survey, which includes also the positions of all other sampling. Subsection 4.2.2 explains how additional data for the calibration of the hydrodynamic model was collected. Detailed information on the application of this data can be found in Chapter 5.

4.2.1 Elevation survey

Figure 4.9 shows photos of the differential GPS used for the elevation survey and the localisation of all sampling points. It is a Leica GPS System 500/1200 Full RTK Base Station and Rover Kit. This system consists of a stationary reference station (GPS 500) shown in 4.9a recording one position over longer period of time (at least 2 h). This setup allows users to measure positions with errors smaller than 3 cm and an average accuracy of 1 cm in the x,y and z direction. Accuracy only proved to be challenging in the direct proximity to trees, where additional points were measured by hand and digitised in a supplementary step. At each field site, three reference points were measured on each single survey day. The largest error recorded between two measurements of the same reference point was 2.97 cm. This high accuracy is possible because raw GPS base station data was post processed with data from RINEX (Receiver Independent Exchange Format) local reference stations. Post processing was carried out with the instrument specific Leica GeoOffice software. The elevation surveys were carried out over several days.

(a) Leica 500 base station

(b) Leica 1200 rover

Figure 4.9: Differential GPS used for the elevation survey with a base station for exact reference and mobile rover for detailed mapping of river bed, bank and floodplain

Elevation sampling at Smithincott was completed in July 2011, elevation sampling at Stonyford in May 2010 and elevation sampling at Rewe in June 2009. Plots of sampling point distribution and further processing can all be found in Chapter 5.

4.2.2 Calibration measurements

For the setup of the hydrodynamic model, depth and velocity field data are necessary for calibrating the roughness. For this purpose, during a period with low discharge and good accessibility, ten cross-sections each with ten sampling points were used in each study reach to collect data on bed elevation, water depth and velocity in the down- and cross-stream directions. Due to fundamental changes in parts of the channel at Smithincott, a reduction of the length was necessary, resulting in a limitation to seven study cross-sections. The bed and water surface points for these

cross-sections and a longitudinal profile of the bed elevation and water surface was GPS surveyed at the same period. These measurements were carried out during one day each and are refereed to as calibration conditions. The position of the cross-section was defined by a rope across the channel in orthogonal direction to the main flow and ten roughly equidistant positions across channel were marked with pegs. A picture of such a cross-section at Rewe is shown in Figure 4.10a. Velocity was measured at 40 % of hand measured water depth, which experiments have shown is the average velocity of the vertical profile (see Herschy, 1995). The comparison of the distance of GPS measured bed elevation and water surface with hand measured depth showed a mean error of 2.7 % with a maximum of 7.2 %.

(a) Calibration flow cross-section

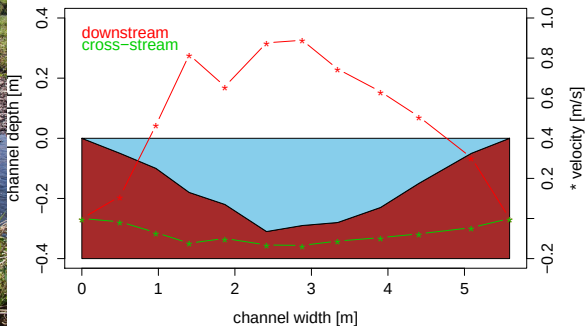

(b) Typical profile for Smithincott

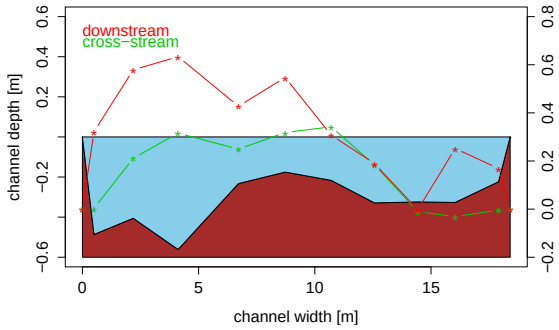

(c) Typical profile for Stonyford

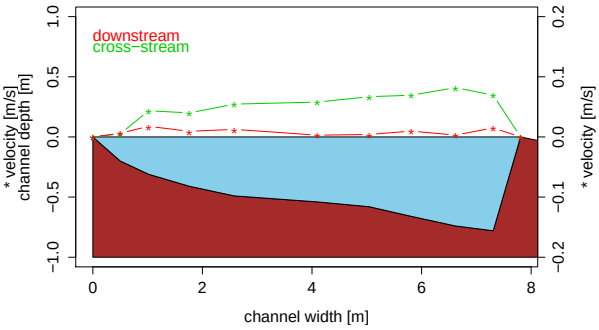

(d) Typical profile for Rewe

Figure 4.10: Image of one study cross-section with positions marked with pegs and the selection of one typical cross-section of the calibration measurement for each study reach. Showing bed elevation in relation to water surface using hand measured depth (y-axis on the left) as well as the velocity in down-stream (red) and cross-stream direction (green) with positive values for flow to the left and negative values for flow to the right (y-axis on the right).

Figure 4.10b to 4.10d shows a profile of one cross-section for each study reach as an example with bed and water surface as well as velocity in the down and cross stream direction. The Smithincott cross-section is positioned in the shallower part of the reach in the middle of a riffle. For the Stonyford study reach with the widest profile overall, a divided cross-section is shown with a main flow area and a side area with considerable horizontal flow. This cross-section is positioned just upstream of the larger grassy island. The study reach at Rewe exhibits medium channel widths with a deep profile and slow velocities. Notably, this is just half of the River Culm due to the split channel at this position. The cross-section in Figure 4.10d is a typical example.

The discharge for calibration conditions was calculated by segmenting the cross-section. Total discharge is the sum of the product of width (w_i), depth (D_i) and downstream velocity (v_i) of each segment as shown in Equation 4.1.

$$Q = \sum_{i=1}^{10} w_i * d_i * v_i \tag{4.1}$$

4.3 Gravel bed grain size distribution

This section reports the character of the gravel bed in the three study reaches. Gravel characteristics, although not a variable in the Krone formulation, play a central role for fine sediment deposition and resuspension. The gravel grain size distribution as the foremost factor in gravel bed characteristics determines the pore volume available for sediment deposition. It affects the bed roughness and is key to the re-suspension of fine sediment, which is believed to occur when the gravel framework starts to move. Subsection 4.3.1 shows the methods used to sample bed gravel grain size distribution and the statistics applied. Subsection 4.3.2 displays the distributions and corresponding indices for the three survey reaches.

4.3.1 Bed grain size sampling and summary statistics

The aim of the bed grain size distribution sampling is to understand the range of grain sizes present in one reach and to understand the variability in distribution between sub-environments and over cross-sections. Moreover, the data should enable comparisons between the study reaches to show spatial trends and variations in the catchment of the River Culm.

The spatial variability of bed material is influenced by several factors. There are some general rules to which the sampled bed grain size distributions can be compared. At larger scales, the grain size distribution of bed material becomes finer with the decline of the slope in a downstream direction. Various factors can cause a deviation from this rule, the most important being tributaries delivering inputs with contrasting grain size distributions, human management and changes in the overall landscape. Local variation in a reach is determined by the main flow line (the thalweg) and the riffle-pool-bar sequences. The coarsest material is found in the thalweg with the highest transport capacities. Bars exhibit all transportable grain sizes with coarsest material at the head and fining towards the tail. Riffle sections support the coarser distributions and the finest distributions are expected in pool areas, as shown in many studies e.g. Keller (1971); Diplas (1994). Still, there are studies describing a reverse distribution pattern for riffles and pools. This can be explained by the velocity and shear stress distribution during high and recessing floods and the associated transport capacity (Thompson et al., 1999; Sawyer et al., 2010; Bunte and Abt, 2001). During low flow conditions riffles exhibit higher flow velocities than pools. At bankful discharge, a reversal of velocity and shear stress occurs. Coarse particles scour from the deep pool with only particles coarser than the transport capacity remaining. The mobilised particles deposit on the riffles, which feature lower shear stresses. This process leads to a coarser distribution in the pool compared to the riffle. This finding was first described by Keller (1971) and was confirmed and refined later for example by Thompson et al. (1999). However in many cases during

recessing stages, pools move towards lower shear stresses, whereas riffles are still exposed to comparatively higher shear stresses. This causes finer material to be removed from riffles and deposited in the pool. Reflecting the higher variability in shear stresses in pools, both coarser and finer particles should be found in pools compared to riffles with a smaller grain size range as argued by Lisle (1979) and Campbell and Sidle (1985). The results of the gravel grain size distribution investigation is discussed in the context of the above theories.

Regarding grain size distribution sampling, all methods are laborious. Therefore, the amount of sampling was limited. Within this research project, four samples a day were a realistic work load. To harvest the maximum information with a minimum of sampling points, two strategies were employed. The first strategy was to sample cross-sections with four to five samples across reach typical features. The second strategy, which was only applied at Smithincott, consisted of the intensified random sampling of a riffle run, which is an area of potential fish spawning. The downstream riffle at Smithincott was equipped with a grid of 30x60 m with 1 m grid cells. 60 grid cells were chosen with the R function sample (R Core Team, 2012). Selected cells located outside the river channel were excluded. Additionally to these two strategies, traps (discussed in Section 4.4.2) were included in the gravel grain size distribution data set. All in all, a total of 22 gravel samples for the Rewe study reach, 20 for the Stonyford study reach and 46 samples for the Smithincott study reach were analysed. After Bunte and Abt (2001), the error of a sampled grain size distribution depends on the mass of the maximal grain size found in the sampling area and is therefore equivalent to the percentage of the total sample accounted for by the coarsest particles. If, for example, the largest particles are allowed to cause an error of 5 %, the total mass will need to be 20 times that of the coarsest particle. A 5 % error is seen as adequate by the author. The coarsest particle found in a preliminary gravel count had a mass of 1.94 kg. Therefore, samples were chosen to be larger than 40 kg. Since the weighing of a sample in the middle of a stream is

(a) 40 L grab sample with square mouthed shovel in background

(b) Wet sieving of gravel sample at river bank

Figure 4.11: Gravel grain size distribution sampling

not feasible, weight was converted into volume. Particles coarser than 8 mm were defined to be part of the bed framework. The weighing of several volumes of gravel proved that a sample of 40 L would guarantee a bed framework content larger than 40 kg with an average mass of bed material of 53 kg.

On the above basis, the sampling technique applied was volumetric grab sampling. A square mouthed shovel was used to fill a 40 L bucket. Amour layer and subsurface substrate were not differentiated since the fine sediment gravel traps applied for fine sediment measurements are also not designed to make this differentiation. The dug hole had an approximate depth of 0.2 m (aiming to replicate depth of the gravel traps) and was 0.5 m in diameter. A complete dug sample with submerged shovel and hole in the bed in the background is shown in Figure 4.11a. Following Grost et al. (1991), this method applied to shallow streams produces similar results compared to more elaborate gravel sampling methods like excavator-cores or freeze coring. At the same time, it is superior in its ease of application with minimal equipment requirements and fast application. After the digging, the sample was directly analysed on the river bank. The application of the sieving procedure on the bank with buckets for each grain size class and sieves can be seen in Figure 4.11b. In a first

step, particles coarser than 45 mm were sorted through templates and the remaining sample was sieved in five to ten portions through consecutively smaller sieves. To flush off smaller particles attached to the coarser grains, all steps included rinsing with clear river water. The rinsing water was not collected and therefore the analysis of the silty sediment was not possible. The sorted samples were weighed with an electric spring scale with an accuracy of 20 g in a drained but still damp condition. Afterwards the material was refilled into the river bed hole. All grain size distribution statistics were computed using the open access software GRADISTAT (Blott and Pye, 2001). GRADISTAT is a Microsoft Excel based computer program calculating numerous statistics from distribution data using different recognised methods using ϕ-based as well as metric based calculations. Although GRADISTAT computes 43 different statistical values for each sample, only a selection of the distribution statistics were analysed: the D_{50}, the geometric mean, the range between high and low percentiles (here D_{90} - D_{10}), the degree of sorting, the skewness towards fine or coarse distributions and the kurtosis. A similar selection is for example used in Milne (1982) or discussed by Kondolf and Wolman (1993) with regard to ideal spawning gravel for salmon and trout. The following lists the evaluated indices in more detail:

Percentiles are grain sizes for which a defined amount of sediment in the distribution is finer than the given size. For example, the D_{25} is the grain size where 25 % of the sample is finer and 75 % of the sample is coarser than the given grain size. GRADISTAT uses arithmetic calculations to determine different percentiles, as shown in Equation 4.2 and 4.3:

$$\frac{log_2 S - log_2(S^-)}{P - P^-} = \frac{log_2(S^+) - log_2(S^-)}{P^+ - P^-} \tag{4.2}$$

$$S = 2^{(log_2 S - log_2(S^-)) * \frac{log_2(S^+) - log_2(S^-)}{P^+ - P^-}} \tag{4.3}$$

With S as the mean grain size of the class, S^- as the lower limit and S^+ as the upper limit of the grain size class, with corresponding P as the fraction within the grain size, P^- the fraction finer and P^+ the fraction coarser than the given grain size class. The most prominent percentile used to compare sediment samples is the D_{50}, where 50 % of material is coarser and 50 % is finer. Percentiles for gravel are given in mm.

Mean is the average value of a grain size distribution. GRADISTAT calculates 6 different mean values, which all vary from D_{50}, but offer similar comparison between samples. The following means are used in the analysis, both after the method of moments: arithmetic $\bar{x}_{am}$ and geometric $\bar{x}_{gm}$ mean, as shown in Equation 4.4 and 4.5:

$$\bar{x}_{am} = \frac{\sum f * m}{100} \tag{4.4}$$

$$\bar{x}_{gm} = exp^{\frac{\sum f * ln(m)}{100}} \tag{4.5}$$

The mean after the Folk and Ward method (Folk and Ward, 1957), as shown in Equation 4.6:

$$\bar{x}_g = exp^{\frac{lnD_{16}+lnD_{50}+lnD84}{3}} \tag{4.6}$$

The following indices are only calculated and used for the geometric method of moments:

Sorting is a descriptive value proportional to the amount of sediment between D_{16} and D_{84}, respectively 68.26 % of the sediment centred around the D_{50} and is therefore another measure for the standard deviation. The calculation of the sorting index in the geometric method of moments (σ_g) is shown in Equation 4.7 with m_m as the midpoint of each grain size class:

$$\sigma_g = exp\sqrt{\frac{\sum (lnm_m - ln\bar{x}_g)^2}{100}} \tag{4.7}$$

Sorting index	σ_g	**Skewness index**	Sk_g	**Kurtosis index**	K_g
well sorted	$\leq$ 1.4	fine skewed	$\leq$-0.43	platykurtic	$\leq$ 2.55
moderate sorted	1.4to 2	not skewed	-0.43 to 0.43	mesokurtic	2.55 to 3.7
poorly sorted	$\geq$ 2	coarse skewed	$\geq$ 0.43	leptokurtic	$\geq$ 3.7

Table 4.1: Sorting, skewness and kurtosis index, calculated with the geometric method of moments and their interpretation in three categories.

Skewness is a measure of the deviation from a normal distribution, in other words how symmetric the distribution is arranged around the mean. Negative values describe a bias towards the finer, positive values a bias towards the coarser side of the mean. The skewness index (Sk_g) is given in Equation 4.8:

$$Sk_g = \frac{\sum f(lnm_m - ln\bar{x}_g)^3}{100ln\bar{x}_g^3} \tag{4.8}$$

Kurtosis describes the peakedness or flatness of a distribution. Platykurtic distribution means a wide range with a low peak, leptokurtic a small range with a steep peak and mesokurtic samples cover intermediate ranges and peaks. The calculation for the kurtosis index (K_g) is shown in Equation 4.9:

$$K_g = \frac{\sum f(lnm_m - ln\bar{x}_g)^4}{100ln\bar{x}_g^4} \tag{4.9}$$

Concluding, Table 4.1 lists the three indices and their interpretation.

4.3.2 Evaluation of the gravel grain size distribution

The discussion in this subsection evaluates the GSD of the study reaches and incorporates local flow conditions, represented by velocity magnitude and water depth. Velocity and depth data originates from calibration flow measurements. This evaluation aims to measure naturally occuring variability in gravel grain sizes and make a statement on the possibility to distinguish patches on the basis of indexes such as the mean gravel grain size. Velocity magnitude was chosen because it is independent of the main flow direction of the cross-section. The velocity and depth survey

over the GSD sampling points was carried out over several days. The stage varied up to 3 cm either side of the stage at calibration conditions. The depth during calibration flow conditions is relevant because riffles, pools and bars are defined in relation to water depth at low water. The velocity magnitude might be of little relevance to the bed grain size distribution, since bed forming conditions can alter or even reverse velocity distributions. Still, velocity magnitude at the calibration flow highlights the distinction of riverine sub-environments. Figure 4.12 shows an overview of the grain size distribution of all gravel samples and traps in the Smithincott study reach with additional information on flow conditions during calibration stage. All data is sorted according to the rising D_{50}. It shows a continuous and wide range of D_{50} with fewer samples at the coarse end. The divergence between the D_{50} and geometric mean is minimal. The D_{10} has an even monotonically rising distribution when sorted by D_{50}, whilst the D_{90} shows fluctuations. Distributions are found with small and large differences between the D_{10} and the D_{90}. The combination of velocity and depth are not following a clear trend. Still, a very small D_{50} is associated with the shallow to middle water depth and slow velocities, whereas a large D_{50} is associated with deep water and slow velocities. To investigate the differentiation of flow sub-environments, Figure 4.13 shows three plots to characterise the gravel samples. All samples exhibit a moderate to well sorted distribution with a slight trend towards better sorting for larger ranges, as seen in the top plot. The middle plot shows a trend, that coarser D_{50} is associated with deeper parts of the channel. This is in accordance with the theory of Keller (1971) and Thompson et al. (1999). Also, the pool samples (trap set 1) exhibit the poorest sorting (whilst still moderately sorted). Overall, the statistical indices of the sampling sub-environment form clusters. The random samples taken on the riffle run exhibit comparatively low D_{50} and small ranges of D_{90} - D_{10}. This is clearly different to the coarser D_{50} of the second cross-section and trap set 2, which are both situated on the further upstream riffle with a rapid character. The first cross-section reaches from riffle environment (sample 1) into a pool environment (sample

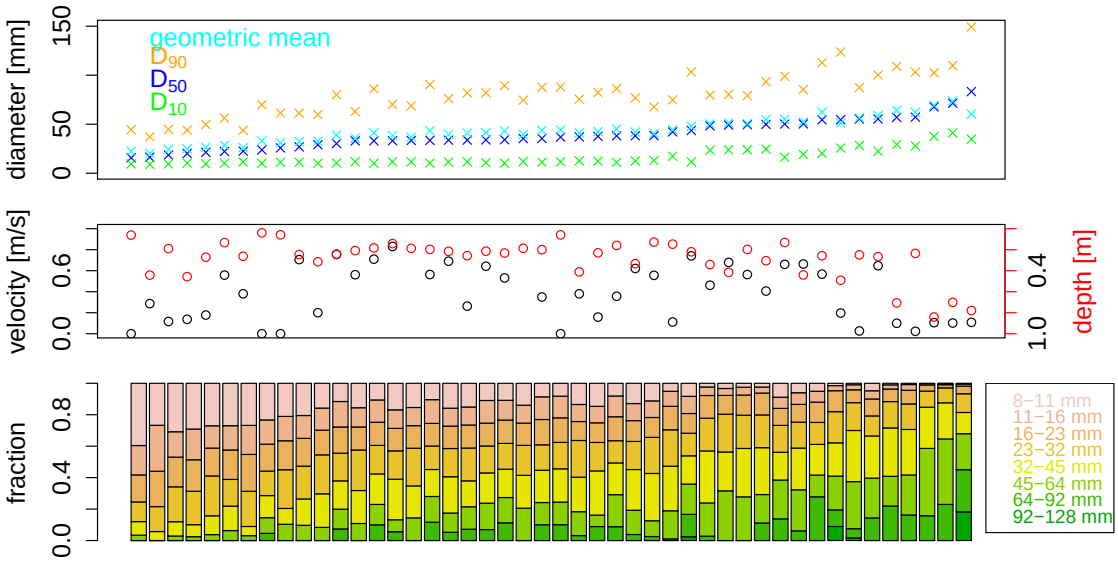

Figure 4.12: Smithincott survey reach gravel grain size distribution and indices ordered by increasing D_{50} for all 46 samples. Top plot showing D_{10}, D_{50}, D_{90} and geometric mean after the method of moments. Middle plot showing flow conditions represented by velocity magnitude and water depth during calibration flow conditions and bottom barplot showing grain size distribution of particles coarser than 8 mm.

2) and shows a fining in the same direction. This fining is the opposite trend found when comparing trap set 1 in the upstream pool (light green) with the riffle data. The riffle data shows finer material at the head of a pool compared to the tail of the pool, which contradicts the finding in Sear (1996), who reported the fining of bed sediment over the course of a gravel-bed river pool. A possible explanation might be that the pool area sampled with trap set 1 is rather the head of the extensive gravel bar and sample 5 of the first cross-section reaches into a calm zone at the side of the pool and is therefore not a typical pool head sample. Generally in this reach, coarsest material is found in the pool, medium grain size distribution over the riffle rapid and the finest in the riffle run. Accordingly, the range between D_{90} and D_{10} is largest for the pool samples (trap set 1) and still comparatively large for samples associated with the riffle rapid and smallest for the samples taken from the riffle run. Based on these findings, riffles are a more uniform environment compared to the gradients

found between pool samples. Still, the difference in D_{50} between two riffle samples can be larger than between pool and riffle samples.

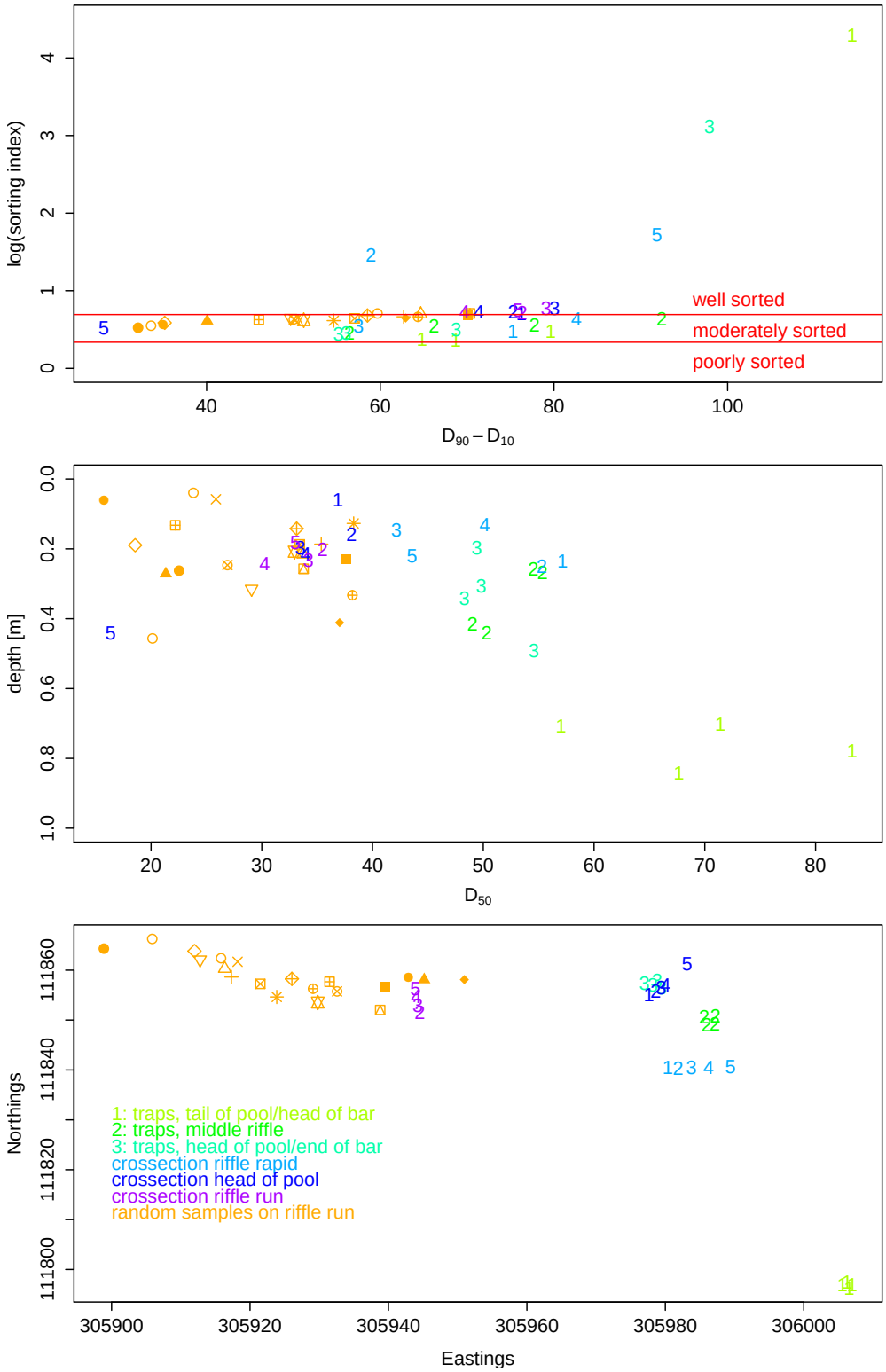

tliers.pdf: 720x720 pixel, 72dpi, 25.40x25.40 cm, bb=0 0 720 720

Figure 4.13: Scatterplots of of D_{90} - D_{10} versus logarithmic sorting index (top), D_{50} versus water depth (middle) and bottom plot for reference with the location of gravel samples taken in the Smithincott study reach. Trap sets are represented by colour and one number, cross-sections by colour and numbered consecutively, random samples are plotted with distinctive shapes for recognition in all three plots of the gravel GSD in the Smithincott reach.

This means the D_{50} on its own is no clear indicator to distinguish pool and riffle environments. Figure 4.14 shows an overview of the grain size distribution of all gravel samples and traps in the Stonyford study reach with additional information on flow conditions during calibration stage sorted according to the D_{50} diameter. It shows a continuous range of D_{50} with little divergences to the geometric mean. The D_{10} sorted according to rising D_{50} does not rise but fluctuates around values between 10 and 25 mm. The D_{90} shows a rising trend with rising D_{50} but also inherits some variation. Compared to the Smithincott reach, D_{50} and geometric mean are higher. Velocity magnitude and depth are more steady. A clear trend of fast velocities with shallow water depth and vice versa can be observed.

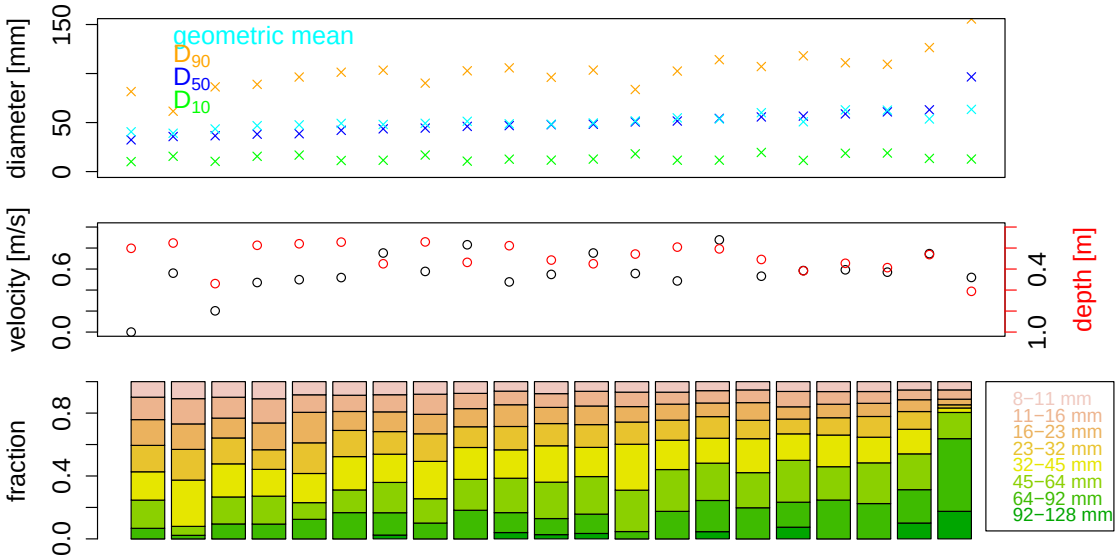

Figure 4.14: Stonyford survey reach gravel grain size distribution and indices arranged by increasing D_{50} for all 21 samples. Top plot showing D_{10}, D_{50}, D_{90} and geometric mean after the method of moments. Middle plot showing flow conditions represented by velocity magnitude and water depth during calibration flow condition and bottom barplot showing grain size distribution of particles coarser than 8 mm

The sub-environments investigated by gravel sampling in the Stonyford study reach are shown in Figure 4.15, right plot, with flow direction in a fairly straight channel from top left to bottom right end of the plot. Samples include three trap sets, the

first positioned in a riffle rapid, the second on the side of a riffle run and the third in the main flow area of the same riffle run. Furthermore, three cross-sections were sampled, the first at the tail of a pool, the second crossing trap set 2 and 3 at the beginning of the riffle run and the third in the middle of the same riffle run. The smaller variety of positions is due to a smaller variance in the overall study reach.

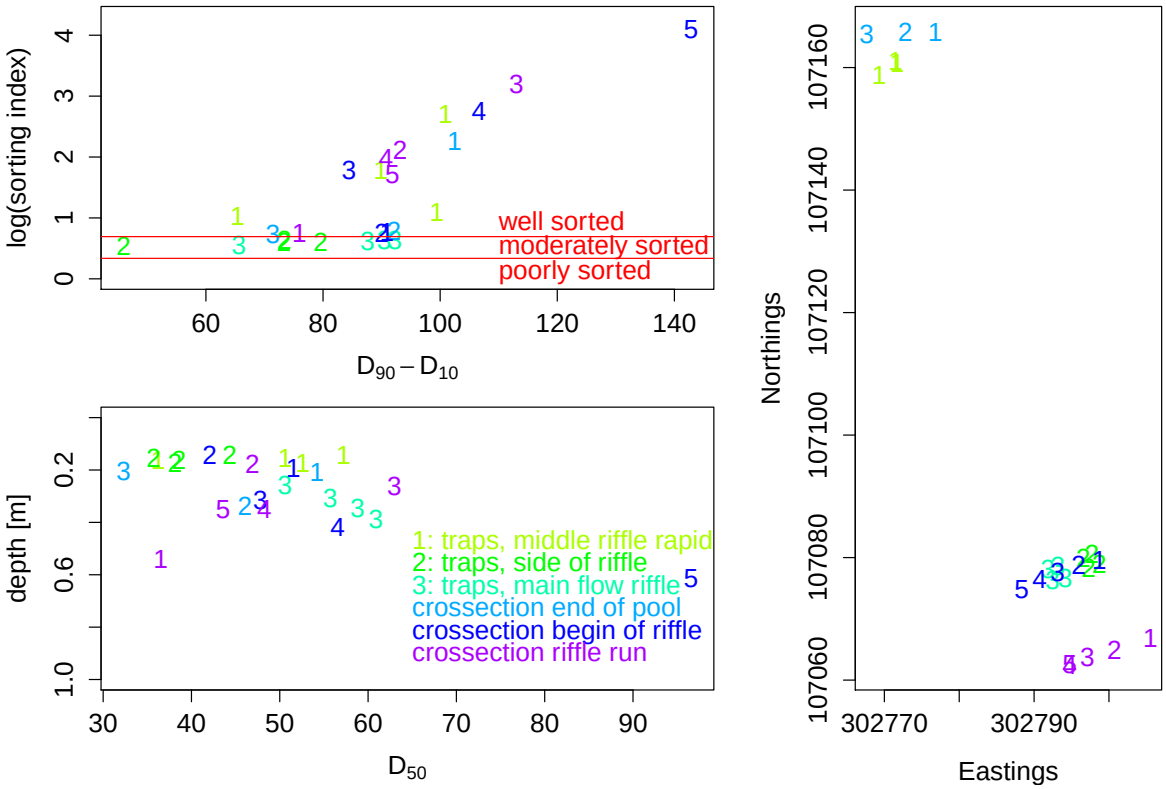

Figure 4.15: Scatterplots of D_{90} - D_{10} versus logarithmic sorting index (top left), D_{50} versus water depth (bottom left) and reference with the location of gravel samples taken in the Stonyford study reach (right). Trap sets are represented by colour and one number, cross-sections by colour and numbered consecutively.

The depth variation is comparatively small between 0.15 to 0.5 m and reflects the smaller variation in the reach. Remarkably, there is a clear distinction between trap set 2 and 3 with the overlaying second cross-section in dark blue showing a clear deepening from trap 1 to 5. The third, mid riffle cross-section has a deeper and more uniform depth. Looking at the D_{50}, trap set 1 and 3, both in the thalweg, are similar, whereas trap set 2 has a lower D_{50}. Samples from the tail of the pool show smaller D_{50} compared to the samples from riffle rapids and riffle runs with the

main flow. The D_{50} does not enable a clear distinction between the sampled sub-environments. The same applies for the distribution of the range between D_{90} and D_{10} in the top plot. The smallest D_{90} - D_{10} is associated with the smallest D_{50} in trap set 2. D_{90} - D_{10} is larger for the riffle samples with main flow, this includes trap set 1 and the higher numbered traps of cross-section 2 and 3. Even more than at Smithincott, the D_{90}-D_{10} in the Stonyford reach correlates positively with the sorting index. Most samples in the Stonyford reach are well sorted, only some samples from trap set 2 show moderate sorting. Overall, the samples in the Stonyford reach are more homogeneous in their D_{50} but distribute over a larger range regarding D_{90}-D_{10} and sorting than the Smithincott samples.

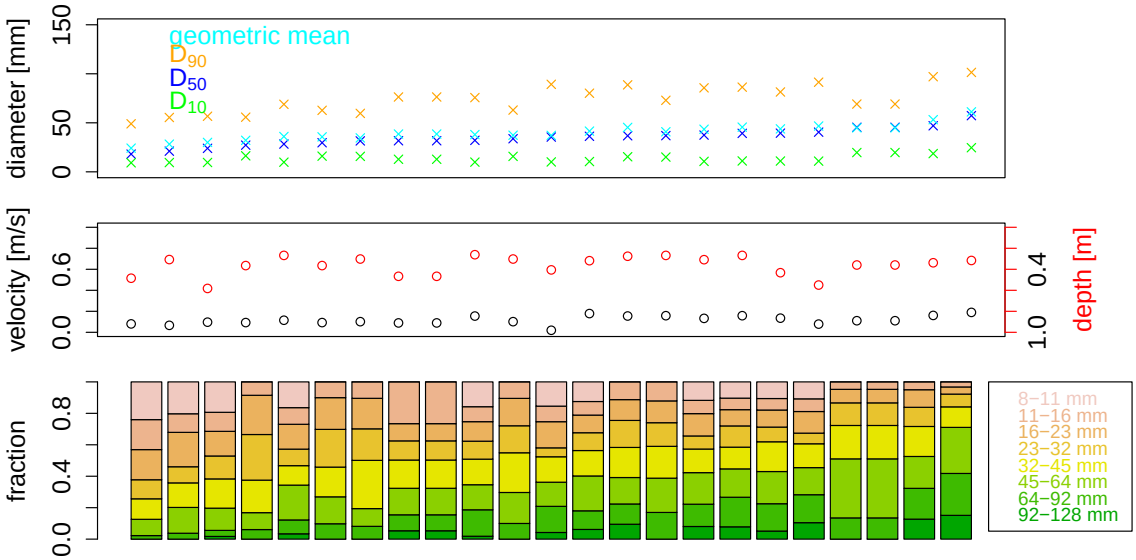

Figure 4.16: Rewe survey reach gravel grain size distribution and indices ordered by increasing D_{50} for all 23 samples. Top plot showing D_{10}, D_{50}, D_{90} and geometric mean after the method of moments. Middle plot showing flow conditions represented by velocity magnitude and water depth during low flow conditions and bottom barplot showing grain size distribution of particles coarser than 8 mm.

Figure 4.16 shows an overview of the grain size distribution of all gravel samples and traps in the Rewe study reach with additional information on flow conditions during calibration stage, sorted according to the D_{50} diameter.

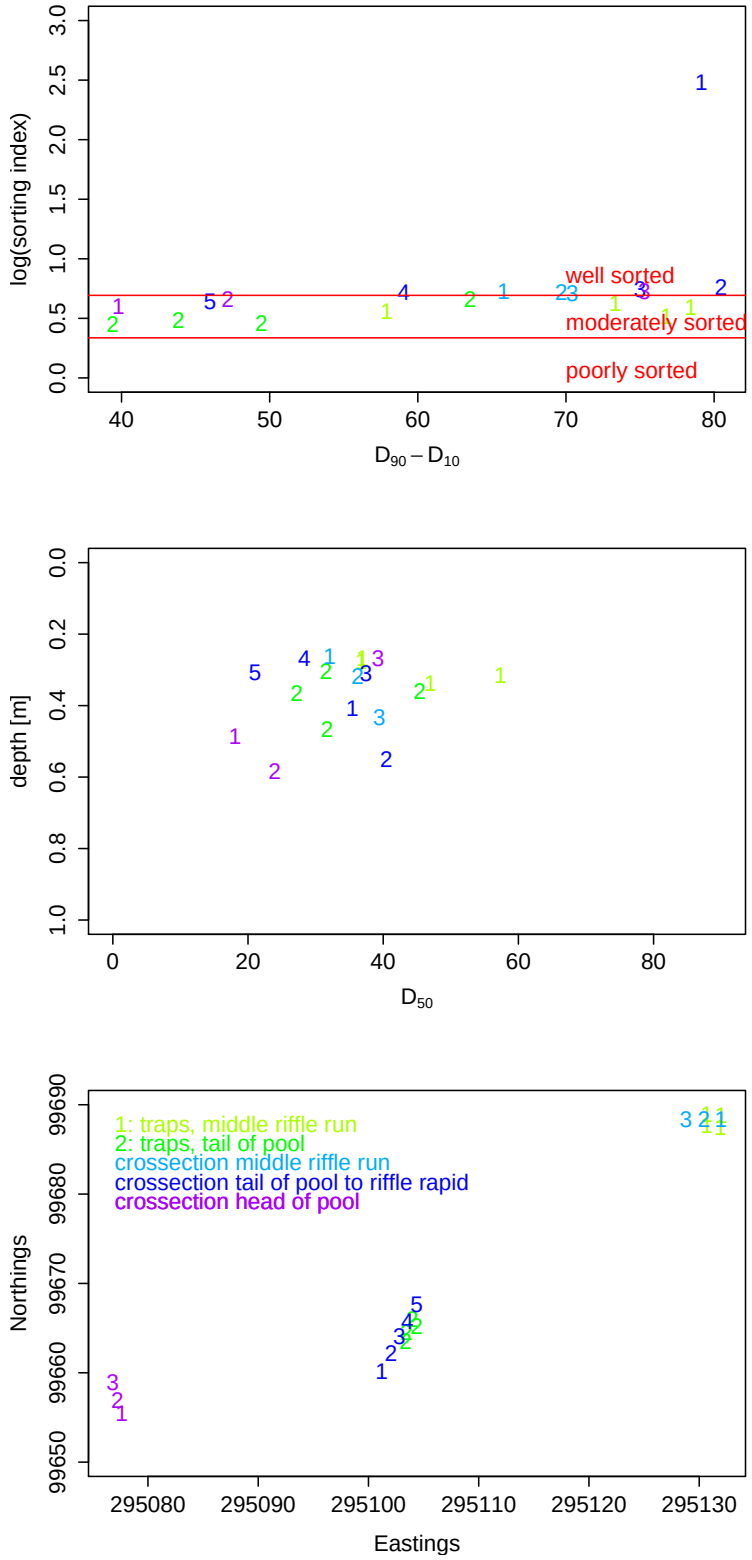

Figure 4.17: Scatterplots of of D_{90} - D_{10} versus logarithmic sorting index (top), D_{50} versus water depth (middle) and reference with the location of gravel samples taken in the Rewe study reach (bottom). Trap sets are represented by colour and one number, cross-sections by colour and numbered consecutively.

It shows a continuous range of D_{50} with little divergences to the geometric mean. D_{10} rises continuously with sorted D_{50} and D_{90} shows some fluctuations with a clear over all rising trend. Throughout the sample positions, velocity is slow and the water is comparatively deep. In general, faster velocities are associated with shallower parts of the channel. D_{50} and geometric cover smaller ranges and are overall lower than in the two other study reaches.

The bottom plot in Figure 4.17 shows the positions of the sub-environments sampled in the Rewe study reach with the flow from top right to the bottom left. The gravel samples in the Rewe study reach include two trap sets, one in a riffle run and one at the tail of a pool and three sets of traps aligned in cross-sections. Of the three cross-section, two cover areas with trap and show the cross channel gradient. A third cross-section is located on the head of a pool following a very short riffle rapid. This means in the Rewe study reach only three distinguished sub-environments are sampled. Nevertheless, the three environments represent a large proportion of the variation in the reach. The D_{50} of all samples covers a smaller and finer range than the other two study reaches. This is to be expected for the lower reaches of a river. Still, there is clear differentiation of the sampled sub-environments: The coarsest particles were found on the riffle, middle sizes at the tail of the pool/beginning of the riffle and the finest gravel on the pool head. The distribution of the water depth above the samples is also more uniform (between 0.2 and 0.6 m) compared to the other two study reaches. The range of D_{90} to D_{10} is similar to Stonyford. The difference shows more variation than the D_{50}, but does not show a clear distinction between the sampled sub-environments. The sorting index is moderate for riffle samples and moderate to good for all samples associated with pool positions. This stands in contrast to the results in Smithincott and the theory of larger ranges and weaker sorting in pools. An explanation might be the lack of a velocity reverse in this more uniform flow environment. The more uniform nature of this reach compared to the other is connected with its position in the catchment with shallow slopes and smaller differ-

	Smithincott		Stonyford		Rewe	
D_{50} [mm]	15-83	(39,36)	32-97	(50,48)	18-57	(35,35)
D_{10} [mm]	9-41	(16,12)	10-19	(14,13)	9-24	(14,13)
D_{90} [mm]	37-149	(80,80)	62-156	(102,103)	49-101	(74,76)
mean [mm]	20-73	(44,42)	39-63	(51,49)	24-61	(40,39)
velocity [m s^{-1}]	0.01-1.35	(0.42,0.39)	0.2-0.87	(0.56,0.56)	0.02-0.19	(0.12,0.11)
depth [m]	0.04-0.84	(0.28,0.23)	0.14-0.61	(0.28,0.26)	0.26-0.58	(0.36,0.33)
sorting	1.4-73.8	(4.0,1.9)	1.7-60.4	(7.8,2.1)	1.6-12.0	(2.3,1.9)
skewness	-6.6-0.7	(-0.5,-0.3)	-4.7-0.0	(-1.6,-0.7)	-3.3-0.4	(-0.3,-0.2)
kurtosis	1.8-2.8	(4.0,2.1)	1.8-28.5	(7.9,2.3)	1.8-13.2	(2.6,2.0)
D_{90}/D_{10}	2.7-6.67	(5.5,5.5)	4.0-12.2	(7.7,8.2)	3.4-8.9	(5.8,5.9)
D_{90}-D_{10}[mm]	28-114	(64,65)	45-142	(88,90)	39-80	(60,64)

Table 4.2: Comparison of gravel grain size distribution parameter and indices for all three reaches with range and their mean and median in brackets, mean of distribution, sorting, skewness and kurtosis index are calculated with the geometric method of moments.

ences between riffles and pool in this reach.

Comparison of reaches Table 4.2 lists the range of summary statistic values, flow velocity and water with their mean and median in brackets. In all reaches, the deep pools could not be sampled but samples covered all other sub-environments (namely head and tail of pools and riffles). A lack of pool samples is apparent in all reaches and the sorted D_{50} values do not show gaps or plateaus but a continuous rise in all cases. This means, with some caution, that not only are the ranges of values found in the three study reaches comparable, but also their means and medians.

The most obvious observation, when looking at Table 4.2 is that the percentiles in the Smithincott study reach cover a larger range than in the other two reaches. This is not surprising since it is the steepest and most natural reach. We can expect to find a fining of bed material over the course of a river as well as narrowing of the range of bed grain size distribution characteristics (Bunte and Abt, 2001). This is not the case in this study. Coarsest distributions are found in the Stonyford study reach. This is due to the managed nature of this study reach, which causes rapid discharge equally over the reach with a scour of fine sediment and the lack of quiet or slack water zones. This is also obvious in the velocity distribution over the samples during low flow, which exhibit a smaller range, but a higher mean and similar mean depth

compared to the same measurements in the Smithincott study reach. The input of coarser material through the Stratford stream can be an additional cause. The study reach at Rewe shows results in accordance with published theory. Rewe has the finest D_{50}, mean, D_{90}, D_{10} and also covers in each case a smaller range for all parameters. Figure 4.18 shows scatterplots of six parameters, where each reach is presented in a different colour to investigate overall trends. The x-axis is always the D_{50}, which, as discussed before, shows Smithincott covering a wide range, Stonyford values being centred in the middle and top of this range and Rewe values in the lower part of the Smithincott range. A similar distribution can be described for the velocities above gravel samples, shown in the left plot in the top row. Rewe samples cover only a very small and slow range of velocities. This pattern of Smithincott samples covering the whole range and Rewe samples at one end, Stonyford at the other end of this range can also be found for the depth distribution (see middle plot, top row) with Rewe towards deeper and Stonyford samples towards the shallower end of the range. Looking at depth and D_{50} data from all reaches, a clear trend of coarsening towards deeper water can be seen at Smithincott, whereas at Stonyford or Rewe, the data plots do not demonstrate a clear trend. Nevertheless, if we are comparing Rewe with Smithincott data, the finer D_{50} at Rewe correlates with a deeper flow compared to the coarser D_{50} from Stonyford. Looking at the top right plot in Figure 4.18, the ratio of coarse to fine grain sizes represented by D_{90}/D_{10} is largest for the reach with the coarsest grain size distribution and the smallest for those with fine grain size distribution, as seen in the data from Stonyford and Rewe. However, data from Smithincott shows low ratios for very high D_{50} and a peak of the same ratio for middle D_{50} values. This means that coarse samples at Smithincott are deprived of fine and middle grain sizes, compared to samples with comparatively coarse grains at Stonyford.

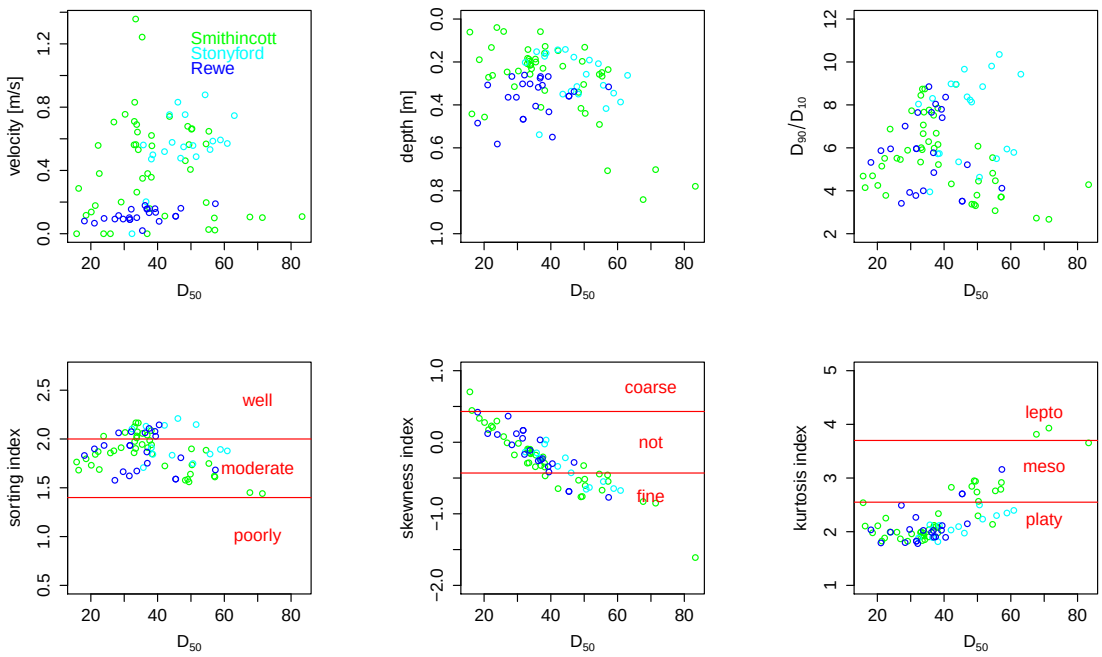

Figure 4.18: Comparative scatterplots of D_{50} in all study reaches with flow character (velocity magnitude and depth at low flow).

Looking at the bottom left graph in the same figure, sorting overall seems to be not connected to D_{50} and is similar in all three reaches with moderate to well sorted values. In the case of skewness, a clear correlation to D_{50} can be observed. Fine D_{50} correlates with no skewness and coarse D_{50} correlates with fine skewness. This means Rewe values are not skewed, whereas Stonyford data displays samples with a trend towards fine skewness. Moreover, another separation between the three reaches is apparent, best visible if we are comparing Smithincott data to Rewe data. Smithincott data covers lower skewness indices compared to Rewe data for the same D_{50} values. Finally, the kurtosis index in the bottom right plot of Figure 4.18 rises with rising D_{50}. Comparing the reaches, the increase of the kurtosis index seems to be clearer for data from Smithincott, compared to samples with the same D_{50} from Stonyford.

Concluding the discussion of gravel grain size distribution, it can be remarked that a large range of distributions is covered in the bed sampling of the three field study reaches. In each reach but also for all samples as a whole, the differentiation of

sub-environments with regard to their bed grain size distributions is possible. For example the deepest sampling areas are associated with the coarsest D_{50}. This differentiation is more pronounced in the headwater reach at Smithincott than for the middle reaches represented by Stonyford and weakest for the representative of the lower reaches, i.e. the Rewe study reach. Further a clear distinction regarding gravel grain size can bee seen between the three study reaches. In brief, the data from Smithincott covers the largest range, with Rewe data on one end and Stonyford data at the other end of this spectrum. Despite these opposed grain size distribution ranges, Rewe and Stonyford have more in common with regard to the correlation of D_{50} to the other statistics, like ratio of D_{90}/D_{10} or skewness, than each of them with data from Smithincott. As a oveall result, the data gathered here can show trends of relationships, however it is not sufficient to subdivide the natural reaches into distinct patches for the purpose of generalisation in the model.

4.4 Fine sediment dynamics

This section covers the investigation of fine sediment as suspended load and as interstitial fines in the gravel bed. The suspended load is recorded as turbidity. The interstitial sediment within the gravel bed is measured with a re-suspension method and with retrievable basket traps. Subsection 4.4.1 shows the typical suspended sediment dynamics for the three study reaches. It includes the calibration of the field turbidity record with bottled samples to provide a conversion into suspended sediment concentration and the investigation into the fine sediment grain size distribution. After this, Subsection 4.4.2 reports on channel bed fine sediment storage and deposition showing the results of a cylinder re-suspension method and the application of sediment basket traps.

4.4.1 Suspended fine-grained sediment

All suspended fine sediment records are based on the data collected by optical turbidity probes with an embedded self-cleaning wiper set at 10 minute record intervals. The probes were Analite NEP9504GU 195/4/30-G Turbidity Probes (by McVan Instruments, Australia) with a 4000 NTU (Nephelometric Turbidity Unit) point at 1V and a 30 m depth rating. The turbidity probes were used in conjunction with 21X data loggers from Campbell Scientific. The initial setup calibration was done using 1000 ppm formazin solution (equivalent to 1000 mg L^{-1}) and the zero point in clear water (as suggested in the manual McVan Instruments, 2007). The turbidity probes were deployed in conjunction with PDCR1830 pressure stage sensors from Campbell Scientific, located at the gauging stations shown in the map in Figure 4.1. The maintenance included a two weekly readout of the data and the cleaning of the sensor heads and joist as well as an approximately monthly change of batteries.

The literature reports on several challenges when calibrating optical data with mass sediment concentrations. For example Clifford et al. (1995) finds s-shaped relation curves between the mass concentration and the optical response curves as well as different curves for different grain size distributions of the fine sediment. Nevertheless, data in the range of 0-0.5 gL^{-1} resides in the linear section of this relationship curve. This is consistent with the findings of Kineke and Sternberg (1992), who state that a linear relationship is prevalent for concentrations smaller than 10 gL^{-1}. This was confirmed by the research of Guilln et al. (2008) and Minella et al. (2008) with low concentrations in marine environments with explicit linear relations. With maximum concentrations in the River Culm at storm runoff of 1000 mgL^{-1} (Walling and Moorehead, 1987; Lambert and Walling, 1987) and available calibration data only up to 280 mgL^{-1}, the available turbidity data was calibrated with the mass concentration measurements using linear regression. For calibration purposes bottled samples were drawn during days of fieldwork with low stages. Additionally to derive data for higher concentration ranges, samples were drawn during three days with high dis-

charge (3.11.2009, 14.11.2009 and 23.11.2009). Storm periods are of special interest because the principal periods of sediment runoff are connected with flood events and these can potentially result in interstitial storage of fine sediment. One 0.5 L sample for mass concentration measurements and additionally a ca. 10 L sample for grain size distribution measurements. Figure 4.19 shows the scatterplots and the linear model fit for the three study reaches. In all three cases, the linear regressions result in intercepts close to zero, slopes slightly lower than 1 and correlations higher than 0.97. With these strong ratings, further adjustment of the turbidity record was not considered necessary. The grain size distribution of the samples drawn parallel

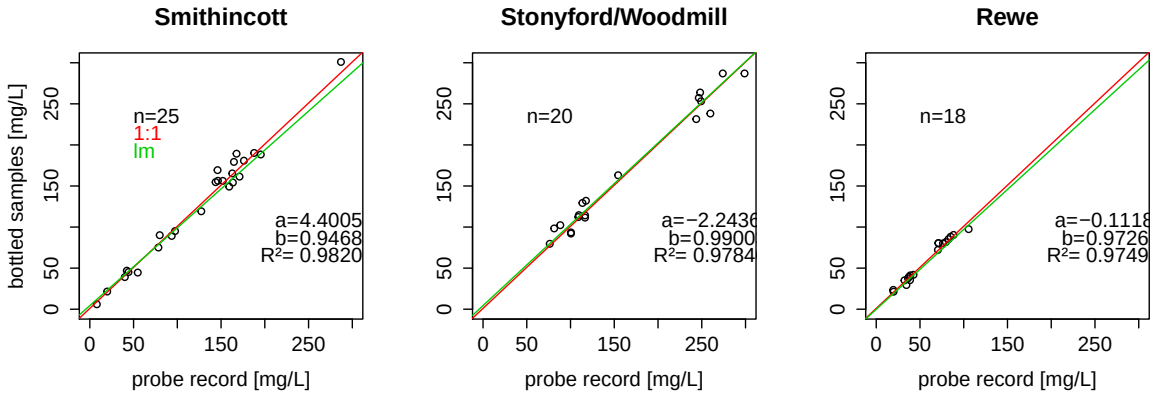

Figure 4.19: Turbidity probe calibration for all three study reaches, with 1:1 line giving ideal correlation and linear model fit lm. Additionally key values of the linear regression with a the intercept, b the slope and r the coefficient of correlation.

to the mass concentration samples are shown as averaged results in Figure 4.20. Some of the samples with concentrations lower than 100 mg L^{-1} could not be analysed in the DigiSizer, due to the lack of material. Therefore, the sample number n is lower than for the concentration calibration. The D_{50} of the samples declined from 9.35 at Smithincott, over 8.98 at Stonyford to 7.36 μm at Rewe. This is in the same order of magnitude as the D_{50} averaged for Rewe and Woodmill reported by Phillips and Walling (1999) of 8 and 11 μm for winter and summer. The grain size distribution data provides limited insight into grain size dynamics. Overall, the samples exhibit very high variability, like Walling and Moorehead (1989) found in the River Exe. A much higher number of samples would be necessary to establish clear distribution

trends for distinct discharge situations, such as rising, peaking and receding floods.

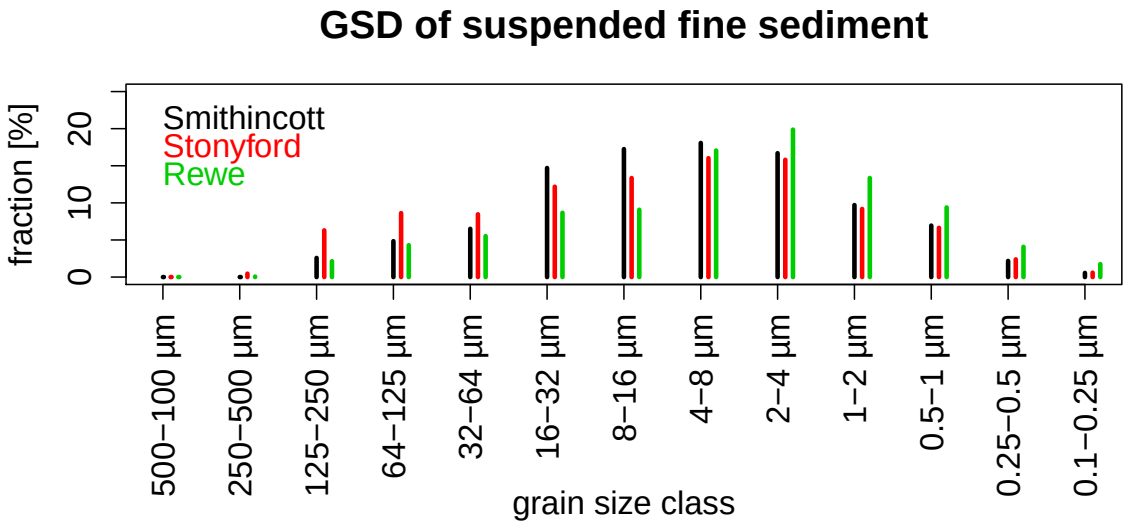

Figure 4.20: Averaged grain size distribution for the concentration calibration samples (Smithincott n=16, Stonyford n=15 and Rewe n=4).

The turbidity records allow for an estimation of the suspended sediment load in the single study reaches. Therefore, records from the 27.10.09 to the 04.12.09 were chosen as a period of intermediate frequent winter floods to show the suspended sediment and stage dynamics of the three study reaches. In a second step, a stage discharge relationship for all reaches is developed and used for the suspended sediment load calculations.

Figure 4.21 compares the stage record of the three gauging stations. This data shows a clear time lag of peak stage between the three sites. Moreover, these hydrographs show the typical behaviour for the three parts of the river (upper, middle and lower reach). At Smithincott, the stage record displays a very reactive curve with numerous small events, steep rising peaks and slightly slower recessing floods. The Woodmill stage record shows a very similar pattern, but with less fluctuations. Finally, the stage records from Rewe show truncated, wider, more symmetric peaks and no small fluctuations in the curve. The time lag between Smithincott and Woodmill is ca. 4 h, with a further 8 h to Rewe. This means for a peak to travel from Smithincott to Rewe it takes about 12 h. Which again means it travels at ca 1.5 km h^{-1} between

Smithincott and Woodmill and ca. 1.75 km h^{-1} between Woodmill and Rewe. Applying the velocities to the distance between the gauging stations and the reaches, this means the peak travels through the Stonyford reach ca 40 min before it is recorded in Woodmill. At Rewe, the peak travels though the study reach ca 17 min before it is recorded on the Rewe village gauging station. This divergence is acceptable since it is much shorter than the investigated periods of flood and bed sediment deposition.

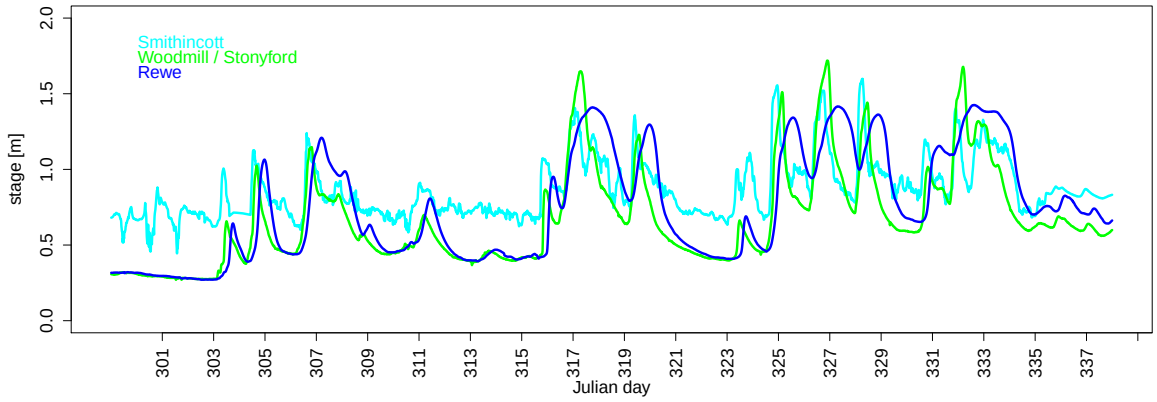

Figure 4.21: Stage record of the three gauging stations for the period from 27.10.09 to 04.12.09.

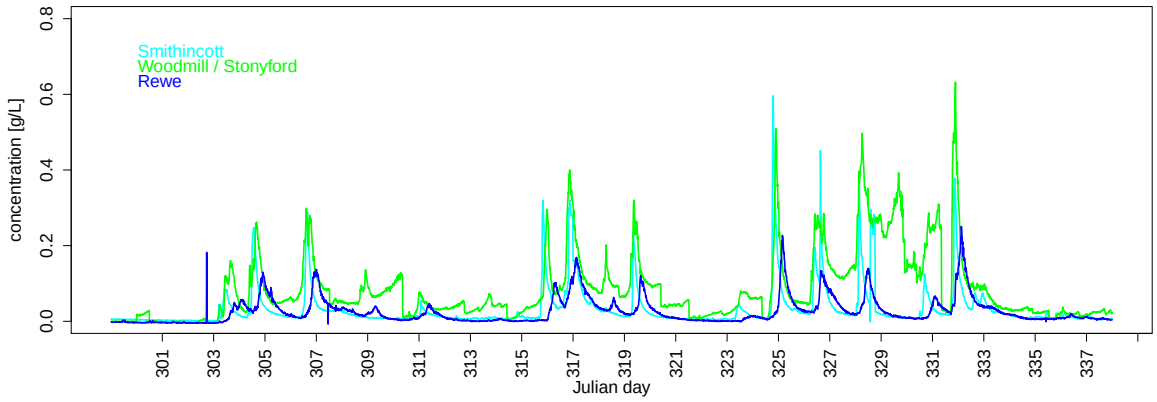

Figure 4.22: Suspended sediment concentration of the three gauging stations for the period from 27.10.09 to 04.12.09.

The associated turbidity records are shown in Figure 4.22. The records include several turbidity peaks. The highest peaks are found at Smithincott and Woodmill,

in two cases reaching 600 mg L^{-1} . The turbidity peaks in Smithincott wane faster compared to Woodmill. Furthermore, the record at Woodmill shows additional peaks compared to Smithincott (e.g. at day 309).This pattern most likely reflects the influence of the major tributary - the Stradford Stream- just upstream of the Stonyford study reach. Turbidity at Rewe rises to lower maxima, ca. 50 % or less of the peak concentrations at Smithincott and Woodmill. In order to calculate suspended loads from this data, stage records have to be converted into discharges (Q) and multiplied by the suspended sediment concentration. Equation 4.1 already shows how Q was calculated for calibration conditions. A stage discharge relationship was developed in order to calculate Q for stages that were not recorded. The calculation of Q for various stages is based on data from the cross-sections, slope and water level data from calibration measurements and the Gaukler-Manning formula for open channels with a Strickler roughness coefficient with k_s = 20 (as used in Harnischmacher, 2007). Equation 4.10 was applied to ten segments for each three cross-sections in each study reach and averaged.

$$Q = A * k_s * R_{hyd}^{2/3} * S_{hyd}^{1/2} \tag{4.10}$$

With A as the area crossed by the water, k_s the Strickler roughness coefficient, R_{hyd} the hydraulic radius and S_{hyd} the slope of the hydraulic gradient. This resulted in the following relationships:

for Smithincott:

$$Q = 0.1230 * e^{(2.3982 * stage)} \tag{4.11}$$

for Stonyford:

$$Q = 0.612 * e^{(1.791 * stage)} \tag{4.12}$$

and for Rewe:

$$Q = 0.184 * e^{(1.082 * stage)} \tag{4.13}$$

Figure 4.23 summarises the discharge and suspended sediment load for all three reaches. Discharge in the Smithincott reach is over all the smallest and the highest discharge is found at Stonyford. Data from the study reach at Rewe was doubled to account for the whole River Culm. Discharge and suspended sediment loads behave parallel to the stage and turbidity records discussed above, with steepest peaks at Smithincott, intermediate and more rounded peaks at Woodmill and truncated discharge and slower rising and recessing suspended sediment loads at Rewe.

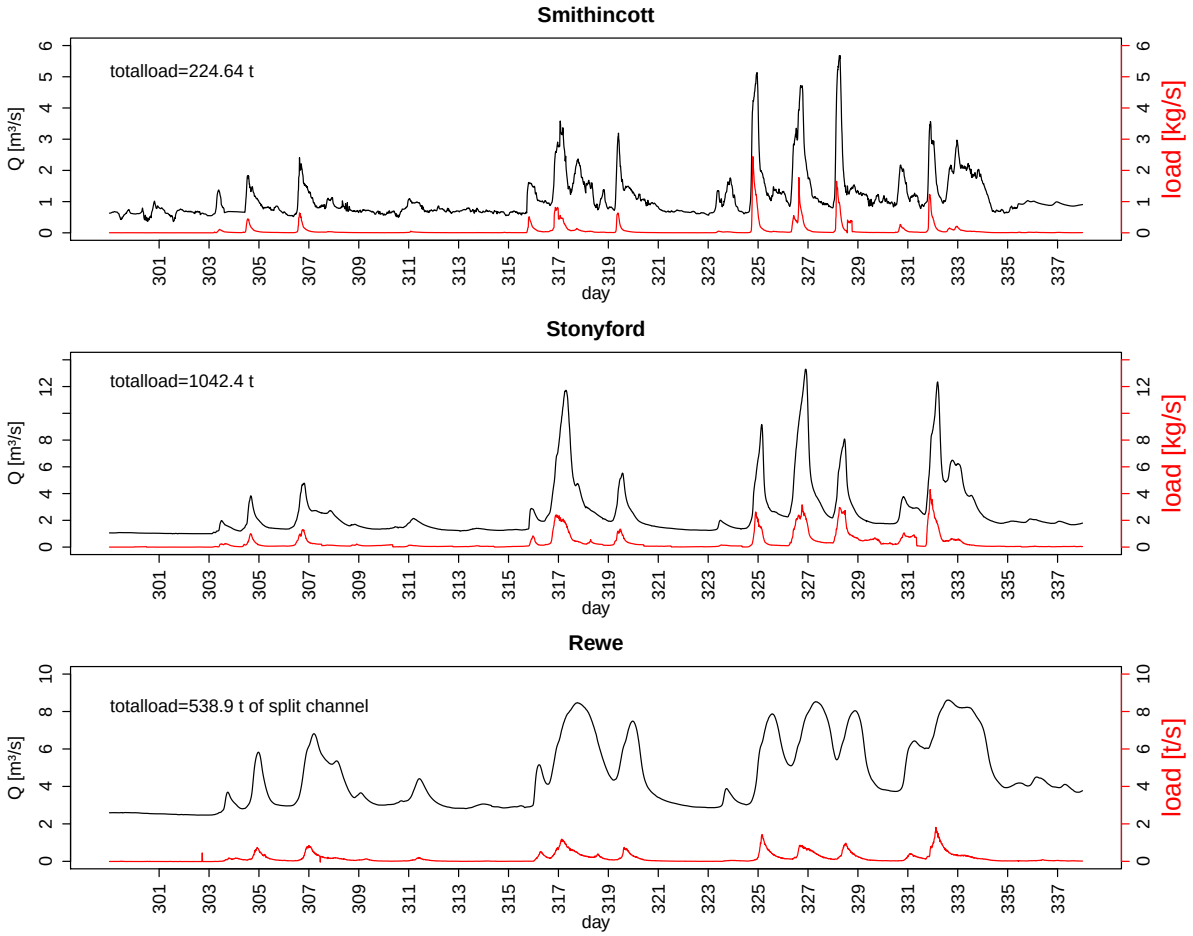

Figure 4.23: Discharge and suspended sediment load of the three study reaches for a period in autumn/winter 2009 from 27.10.09 to 04.12.09.

Calculated with the above equations, the load at Smithincott is 224.64 t, which is approximately 2.5 % of the annual suspended sediment load of the River Exe basin (according to Lambert and Walling, 1987). The total load at Woodmill is four times as high with 1042.4 t, which corresponds to 11 % of the total suspended sediment load

of the River Exe basin. It is of a similar magnitude to the load passing through the combined channels at Rewe with 2x538.9 = 1077.8 t, which is equivalent to 12 % of the River Exe basin suspended sediment load. This sums up to a total discharge at Smithincott of 3.7 million m^3, 8.3 million m^3 at Woodmill and 15.1 million m^3 at Rewe in the investigated period.

4.4.2 Interstitial sediment

Two methods were applied to measure interstitial fine sediment, a re-suspension method, which measures interstitial sediment storage and, a basket trap method, which measures the interstitial deposition during a known period, referred to as the trapping period.

Cylinder re-suspension technique to measure fine sediment storage: Figure 4.24 shows the field sampling setup for the re-suspension method. This method was applied in several other studies in medium size gravel-bed Rivers, e.g. in the studies of Lambert and Walling (1988); Collins and Walling (2006); Owens et al. (1999); Collins and Walling (2007b) and Walling et al. (1998). Its advantage is the easy and instantaneous applicability and low material costs. A metal cylinder seals off a specified bed area and the overlaying water column from the surrounding river. The cylinder used in this study had a diameter of 0.45 m, enclosing an area of 0.61 m^2. It was lowered onto the river bed and submerged into the gravel bed as deep as possible. The water depth in the cylinder was noted. After this, the gravel in the cylinder was agitated with a rod in order to mobilise fine sediment stored in the gravel bed. For standardisation purposes, this was done with 30 vigorous stirs penetrating the bed as deep as possible. Immediately after the last stir, a bottled sample of 0.5 L was collected. Three more bottled samples were collected each after another ten vigorous stirs. Later these samples were filtered in the laboratory and the concentration was determined with the same method as used for flume experiment concentration

measurements. The sediment concentration was then multiplied by the total water enclosed in the cylinder (area of the cylinder (A) times water depth (H).

(a) Sampling fine channel bed sediment using the re-suspension technique at Rewe, spring 2009

(b) Filter residues of bottled suspended sediment samples from re-suspension method

Figure 4.24: Photographs applying the cylinder fine sediment re-suspension technique

The resulting suspended sediment mass was divided by the enclosed area. This provides an measure of channel bed fine sediment storage in kg m^{-2} as shown in Equation 4.4.2.

$$storage = \frac{H * A * C}{A} \tag{4.14}$$

This procedure was applied to four positions in each of the three study reaches from February 2009 to September 2009 on seven occasions. The naming of the sampling positions was based on the reach defining letter (S=Smithincott, F=StonyFord and R=Rewe), plus C for cylinder in the re-suspension method and numbers (1 to 4) for each position. The concentration of the replica bottled samples was highly variable with no apparent chronological pattern to the four samples. A complete re-suspension of fine sediment using this method is difficult to achieve. This means bottles with lower concentration are caused by a partial re-suspension. Following

this logic, the highest filtered concentration can be assumed to be most representative of the actual fine sediment storage in situ. Consequently, for the evaluation, only the bottled sample with the highest fine sediment concentration is considered in the bed sediment storage results. Intrusion in the bed with the rod was strenuous and limited to the upper layer of the bed. The depth of intrusion was measured comparing markers on the rod with the cylinder rim. The average agitation depth was 5 cm. This means the storage measured is approximately the storage in the amour layer of a gravel-bed river.

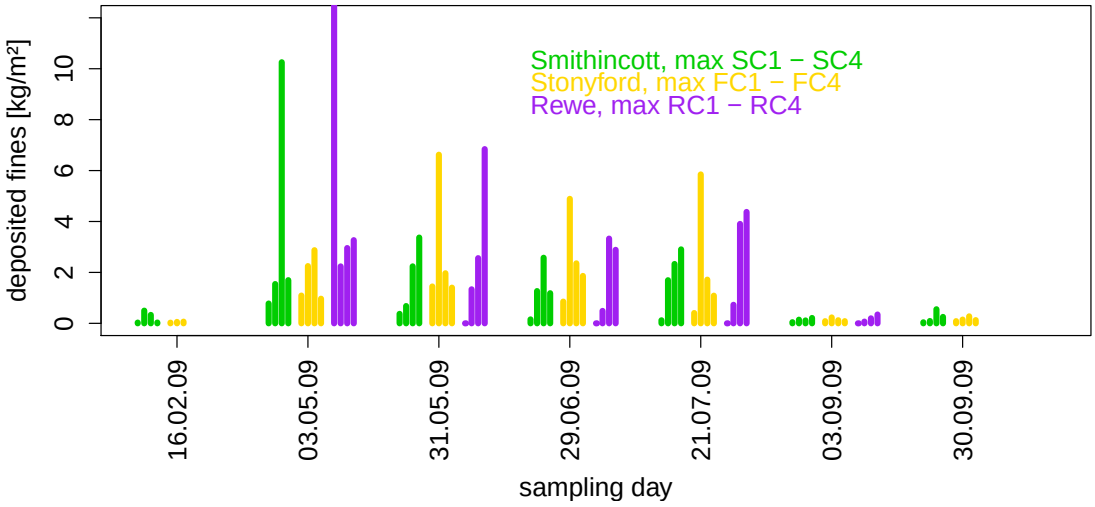

Figure 4.25: Fine-grained sediment storage measured with the cylinder re-suspension method over nine months in 2009 for four positions in each study reach.

	Smithincott	**Stonyford**	**Rewe**
sample point C1	beginning of riffle rapid	mid stream riffle	riffle tail
sample point C2	mid riffle rapid	near bank riffle end	pool end
sample point C3	side pool	near island	riffle run
sample point C4	end of riffle rapid	mid channel riffle run	pool beginging

Table 4.3: Re-suspension method sampling point characteristics.

Figure 4.25 shows the maximum measured storage at the four positions in each of the three field reaches for all seven sampling days. The characteristics of the single sampling points can be seen in Table 4.3. These points were chosen to cover as

much variability within the individual reaches as possible, although with the restriction of water depth of a maximum at 0.8 m (based on the dimensions of the sampling cylinder). This variability is evident in the results. The different sampling positions show consistent storage patterns for all seven measurements. An exception is RC1 with extraordinary high storage measured on the 03.05.09, but consistently low storage for all other dates. The highest storage is consistently apparent in side positions like SC3, FC2 and RC4. Lowest storage is measured on riffles. The difference between summer and autumn/winter measurements is particularly evident, with highest storage during periods with little or no flood events. This means, although there is variation in the amount of storage over the year, the relative storage, if comparing positions in one channel, is similar with positions of high and low storage. Furthermore, the data suggest highest storage rates during periods of lasting low discharge. Published work about seasonal patterns of within-channel fine sediment storage are rare and mostly reflect data of one year or season. An example of a study reporting on temporal storage over 18 months is Collins and Walling (2007b). They sampled 29 positions in the River Frome and Piddle catchments, without detecting a clear seasonal pattern. Both high storage in summer compared to winter and high storage in winter compared to summer was observed. Other studies like Walling et al. (2003) and Wilson et al. (2005) also report the lack of consistent seasonal patterns for in-channel fine sediment storage. This suggests that either there is no general seasonal trend in in-channel fine sediment storage or storage is highly variable throughout. The collection of representative data to provide confirmation of the existence of true seasonal patterns in bed sediment storage would need a long-term (several years) and more detailed sampling programme (e.g. after every runoff event responsible for fine sediment transport).

Gravel filled retrievable basket trap method: In contrast to the cylinder re-suspension method, which measures the fine sediment storage on, and in, the bed at the time of sampling, the gravel filled traps are designed to measure deposition during the

(a) Gravel fine sediment trap F3-A just after installation for trapping Period 1

(b) Gravel fine sediment trapS1-B just before recovery in trapping Period 1

Figure 4.26: Gravel filled fine sediment traps installed in the river bed

period between their installation and recovery, a so-called trapping period. The traps are identical to the ones used in the Flume experiments.The installation, recovery and assessment of the traps in the field was labour intensive and had to be timed carefully during relatively low stage. Similar to the gravel grain size sampling, pits of approximately 25 cm depth and a diameter of 0.5 m were excavated and bed material was stored in several 40 L buckets. The content of one representative, bed material filled bucket was then sieved through square hole sieves and assessed regarding the gravel grain size distribution as described in Section 4.3. Material finer than 8 mm was discarded. The pore volume of the gravel was established measuring the displacement of water through gravel addition in a bucket. The water volume was converted into potential deposition in kg, assuming a density of trapped material of 2.6 kg m^{-2}. The empty traps with rolled down sleeves (as shown in the photograph in Figure 2.3a) and additional strings for sleeve pull up were positioned in the holes, filled with the analysed trap gravel and carefully surrounded by the untreated excavated material. For the installation of these basket traps, a diversion of flow (generated using several upstream buckets and boards) was necessary to avoid immediate fine sediment flush into the excavated pit or trap during installation.

The most sensitive part during trap recovery was the pulling up of the permeable sleeves. Bed alignment during the trapping periods caused smaller gravel to pene-

trate through the metal grid and jam the sleeves. With upstream flow diversion and careful digging by hand the sleeves were loosened, pulled up and folded over the top of the basket trap. Only then, the whole trap was extracted out of the bed and into a bucket. The separation of sediment trap framework ($>$8 mm) and trapped interstitial material was performed in the field using square holed sieves and rinsing with clear river water. The rinsing water with trapped material $<$8 mm (approximately 30 L per trap) was then returned to the laboratory. Grain size distribution was determined in two separate grain size ranges and with two different methods. Initially, the sample was left to settle for four days and clear water was decanted. The remaining sample was dried at 105 °C. After this, the whole sample was ground carefully. Particles coarser than 0.5 mm were separated into classes by dry sieving through square holed sieves. Material finer than 0.5 mm was weighed and thoroughly mixed to take two 5 g sub-samples for DigiSizer analysis (as described in 2.2.2). The results of the coarser grain size distribution are displayed in heat colours from red to yellow and referred to as the coarser range. The yellow bar represents the fraction used for further DigiSizer analysis. These DigiSizer results for material smaller than 0.5 mm are shown in rainbow colours from orange to purple and are referred to as the finer range (see Fig. 4.29, 4.31,4.34,4.36, 4.39 and 4.41).

		Smithincott	**Stonyford**	**Rewe**
Period 1	install	16.08.09 (228)	22.09.09 (265)	28.09.09 (271)
	recover	29.10.09 (302)	07.10.09 (280)	30.10.09 (304)
	days	74	15	33
	days with C $>$ 100 mgL^{-1}	4	0	6
Period 2	install	29.10.09 (302)	28.10.09 (301)	30.10.09 (304)
	recover	05.12.09 (339)	05.12.09 (339)	5/6.12.09 (339/340)
	days	40	38	35/36
	days with C $>$ 100 mgL^{-1}	13	13	15

Table 4.4: Installation and recovery dates (Julian Days in brackets) of retrievable basket traps, total duration and days with suspended sediment concentration above 100 mgL^{-1} during the trapping Period 1 and Period 2 (C= suspended sediment concentration).

Each study reach, named with the reach defining letter (S=Smithincott, F=Stonyford

and R=Rewe) was equipped with three sets of basket traps, named with numbers (1, 2, and 3). To identify the individual traps in the sets, letters (from A to D) were used as labels. Table 4.4 summarises the duration and the occurrence of flood events during the six successful trapping periods. Unfortunately another recovery of the traps was not possible. On Julian Day 350 (16.12.09) a high winter flood eroded the gravel traps at Smithincott and Stonyford. In February 2010, only destroyed trap parts could be recovered. The assembly and installation of new traps was not feasible within the budget and time frame of this research project.

In the following discussion, separately for each study reach, the position of the traps, their gravel grain size distribution and water depth as well as velocity during calibration conditions is discussed. A graph showing the stage and turbidity record for the trapping period is shown with the same ranges on the axis for all reaches. This is followed by a detailed analysis of the trapping rates and the grain size distribution of the trapped material. For the majority of the retrievable basket traps, the amounts of trapped interstitial material did not get close to the available pore space. Even with the assumption of a much lower density for the ingress of interstitial material, the pore space is not restrictive to sediment deposition.

Trapping periods at Smithincott: Traps in the Smithincott study reach were positioned in three sets as distinct clusters. The upstream set S1 was positioned at the end of a pool, S2 at the side of the channel in the middle of a riffle and S3 more centrally at the end of the same riffle close to the middle bar. Figure 4.27 gives an overview of the grain size distribution of the framework in the bottom graph. Water depth and velocity during calibration conditions are plotted in the top graph. Additionally to the gravel, the pore space is indicated as x. This is given in kg as potential material solidly filling the gaps (with a density of 2500 kgm^{-3}). This high pore volume of around 50 % in the traps is due to the lack of any alignment and the restriction of the walls of the gravel traps. The gravel grain size distribution is finest in S1 at the end of the pool.

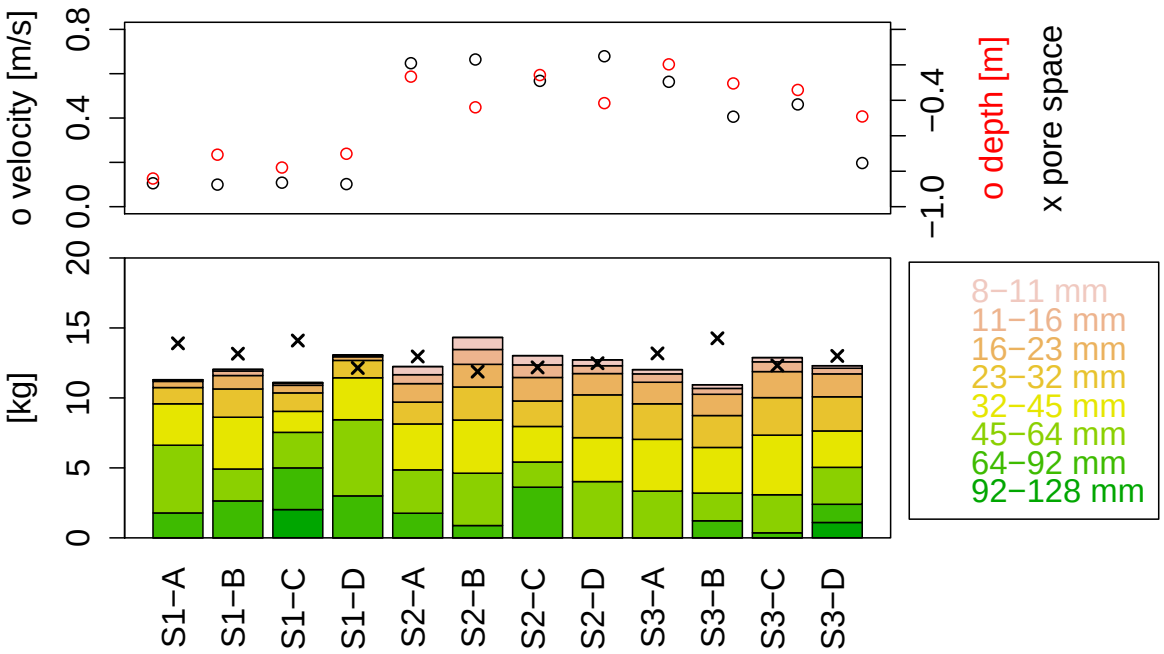

Figure 4.27: Gravel grain size distribution of the framework material in the retrievable basket traps in the Smithincott study reach.

S2 and S3 have very similar distributions with larger variation between the individual traps than between the three sets.

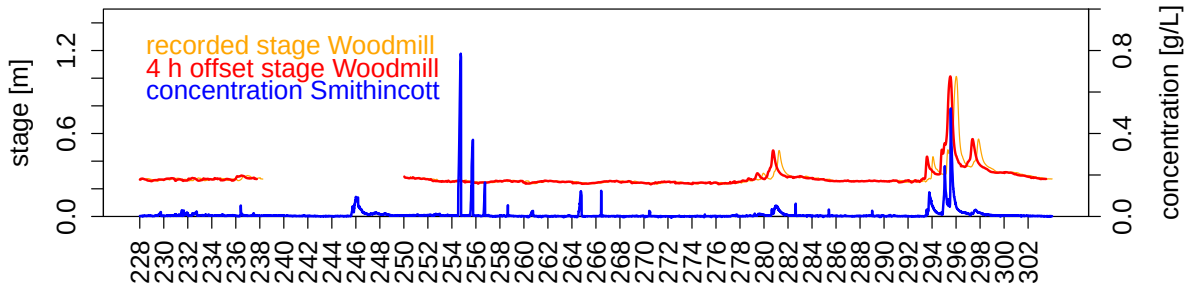

Figure 4.28: Stage record and suspended sediment concnetration for the first trapping period at Smithincott, Julian Days 228 to 302 (from 15.08.09 to 29.10.09), with auxiliary stage record from Woodmill to replace faulty records from the Smithincott gauging station.

Figure 4.28 shows the Stage record and suspended sediment concnetration for the first trapping period in the Smithincott study reach. Unfortunately, for this period the pressure tube of the stage probe was clogged by insects and temperature dependent fluctuations were recorded. Therefore, the stage record from Woodmill was

introduced as a reference. The flood peak time lag between Smithincott and Woodmill is approximately 4 h (see Figure 4.21). To observe the synchronism of stage and suspended sediment concentration, the Rewe stage was plotted with this 4 h offset. The Woodmill stage record shows no major change in stage from Julian Day 228 to 278. The suspended sediment concentration for this period shows some short and very high peaks, which are likely due to short-lived obstructions and disturbances (e.g. leaves or other debris, crossing cows) and which are therefore not relevant for the suspended sediment budget. More relevant for fine sediment deposition are events which were recorded as longer sediment peaks and correspond with the rises in the stage record at Woodmill. These are mainly the events around Julian Days 294 to 298.

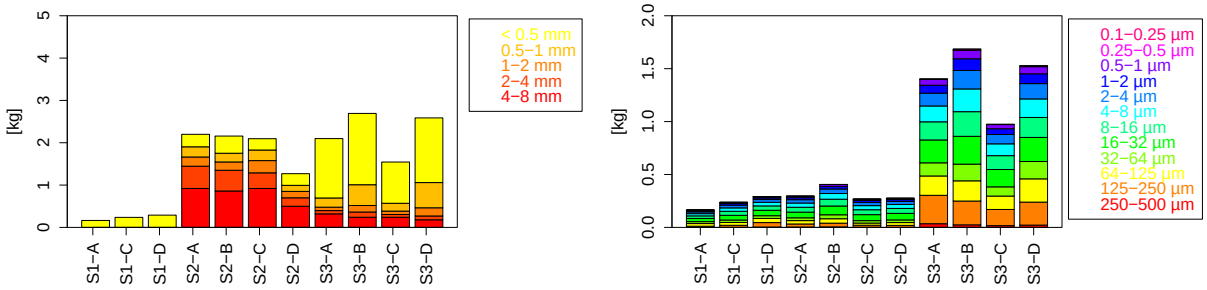

(a) Total trapped material, sieved grain size classes

(b) Trapped material finer 500 μm, grain size classes measured with DigiSizer

Figure 4.29: Grain size distribution of trapped material in Period 1 in the Smithincott study reach.

Figure 4.29 shows the total trapped material and its grain size distribution. The recovery of trap S1-B was not successful. Trap S1-B was therefore excluded from the evaluation. The amounts and GSD of the trapped material show a clear distinction between the individual trap sets. Trap set S1 experienced very little trapping (less than 0.5 kg for all traps) and the ingressed material was all finer than 0.5 mm. In S2, sediment trapping was higher, with most material coarser than 0.5 mm. S3 exhibits similar high trapping rates to S2, with about 50 % of the ingressed material smaller than 0.5 mm. The variation in trap set S3 is higher compared to the other two sets. Notably in Figure 4.29b, the grain size distribution of material $<$0.5 mm measured

with the DigiSizer, exhibits a very similar distribution in all traps, despite the different amounts of ingressed material involved. The low trapping in S1 is probably due to the acceleration of flow at that position. S3 on the contrary is a position experiencing deceleration and therefore higher sediment deposition.

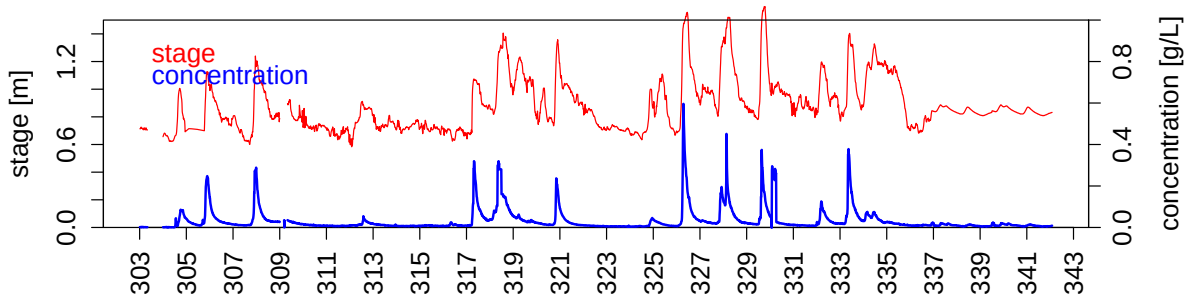

Figure 4.30: Stage record and suspended sediment concentration of the second trapping period in the Smithincott study reach, Julian Day 303 to 343 (from 29.10.09 to 03.12.09).

A cleaning of the pressure equalizing tube and the application of insecticides solved the problem with the stage record at Smithincott. The second trapping period at Smithincott has an uninterrupted stage and suspended sediment concentration record with approximately 13 middle range flood events as shown in Figure 4.30. In these data records, suspended sediment concentration and stage coincide well with suspended sediment concentration peaks in the rising phase of the flood. The period 2 at Smithincott was characterised by regular rainfall. The recovery of the retrievable basket traps took place after four days without precipitation.

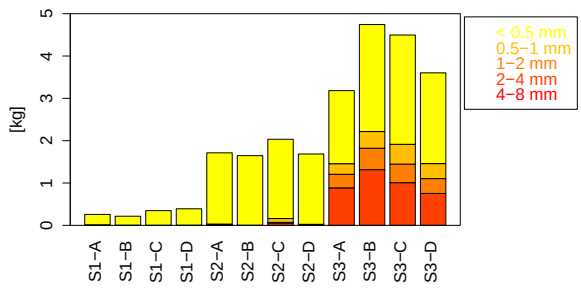

(a) Total trapped material, sieved grain size classes

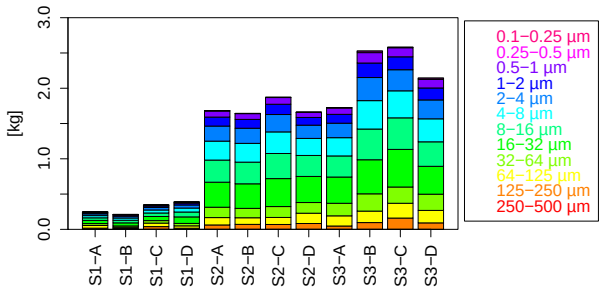

(b) Trapped material finer 500 μm, grain size classes measured with DigiSizer

Figure 4.31: Grain size distribution of trapped material in Period 2 in the Smithincott study reach.

The average sediment trapping in Period 2 is higher than in Period 1, as shown in Figure 4.31. Furthermore, traps within one set show a very similar behaviour, whereas the distinction between trap sets is even clearer than during Period 1. The trapping for S1 is only slightly higher than in Period 1 and again predominantly in finer grain size range. This similarity to Period 1 is remarkable, since much more sediment was flushed through the study reach. Traps S2 did not trap considerably more material but experienced a strong shift from coarser to mainly material finer than 0.5 mm. Traps S3 also experienced a strong increase in fine material with a 100 % increase in trapping mainly due to the ingress of finer sediment. The shift of coarse trapping from S2 to S3 and the general strong increase of trapped material finer than 0.5 mm in all traps is a pronounced difference between Period 1 with one event and Period 2 with 13 events. This means in the one main event in Period 1, coarse material was only transported to the middle of the riffle. During the 13 events in Period 2, coarse material was transported over the whole riffle and did only settle out at the end of the riffle in S3. Fine material, still transported during lower stage, settled out evenly at the riffle middle (S2) and end positions (S3). S1 trapped disproportionately little material, all finer than 0.5 mm. A reason for this can be seen in the acceleration of flow at S1 during all stages. Again, the measurements with the DigiSizer showed a very similar distribution of the fine fractions in all of the retrievable basket traps.

Trapping periods in Stonyford Figure 4.32 shows the gravel grain size distributions for the retrievable basket traps in the Stonyford study reach. F1 is positioned at the beginning of a riffle in a shallow and relatively fast flowing part of the reach, just downstream of a ford-like stretch. Unfortunately, this trap set could only be recovered in Period 1, because during the second trapping period cow trampling destroyed the traps. F2 and F3 were positioned roughly at the same cross-section of the river. F2 traps were positioned in the side channel, upstream of a reach typical grassy island. F3 traps were positioned as far into the main flow as feasible. The gravel grain size

distribution of the three trap sets are not distinctly different.

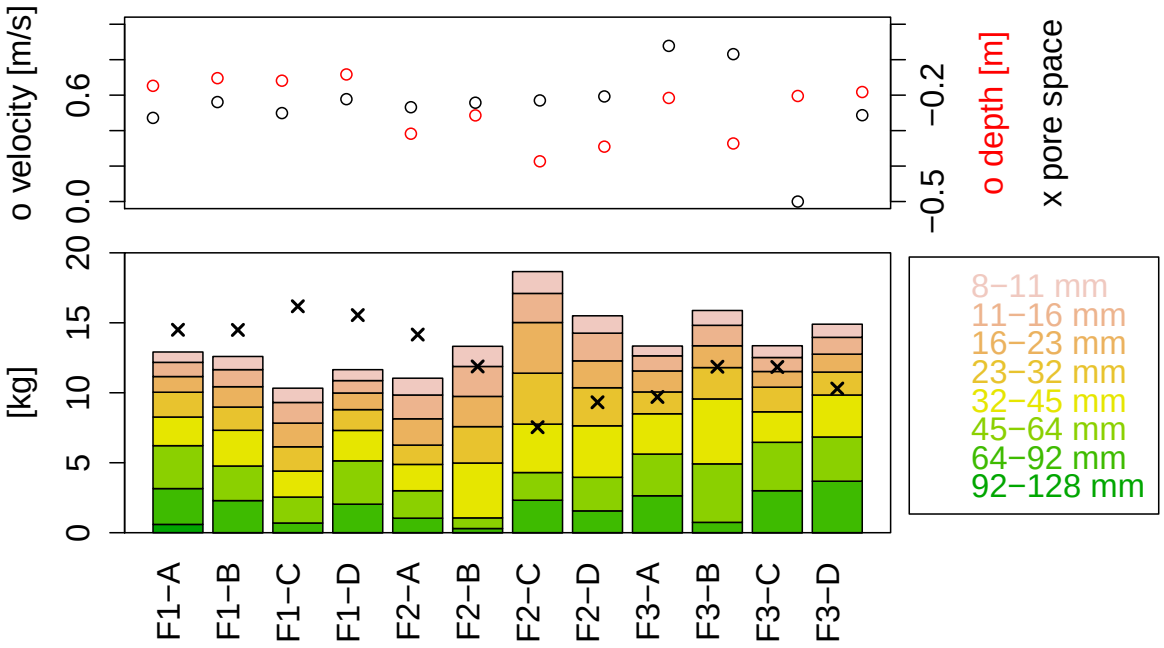

Figure 4.32: Gravel grain size distribution of famework material in the retrievable basket traps in the Stonyford study reach

The variation between two traps within one set is larger than between the individual sets. F1 and F3 are slightly coarser than F2. The four traps comprising set F1 exhibit uniform depth and velocity conditions - shallow and fast flowing. F2 traps are positioned deeper with similar velocities during calibration conditions. F3 traps show the largest variation in depth and velocity but overall intermediate depth and high velocities.

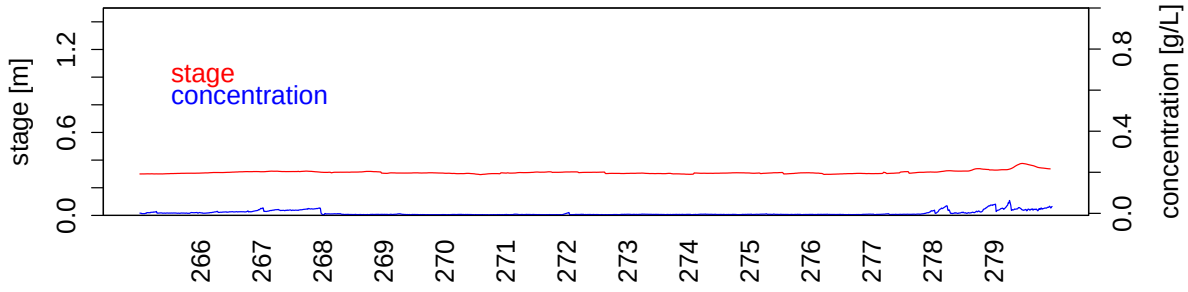

Figure 4.33: Stage record and suspended sediment concnetration of Period 1 at Stonyford, Julian Day 265 to 280 (from 22.09.09 to 07.10.09).

Figure 4.33 shows the Stage record and suspended sediment concnetration at Woodmill for Period 1 in the Stonyford study reach. In the whole period, only one small event on Julian Day 279 was noted in the stage record. The suspended sediment concentration shows several small increases, at Julian Day 268, 278 and 279. These might be due to fouling of the optical sensor. However, even if these are actual concentration rises, all increases are lower than 0.1 g L^{-1}, and therefore seen as irrelevant in the context of fine sediment deposition. Overall, suspended sediment concentrations are very low. Therefore, trapped material in Period 1 at Stonyford can be assumed to originate from the bed in the proximity of the basket trap.

Figure 4.34 shows the amounts and the GSD of the trapped material for Period 1 in the Stonyford reach. Trapping is low and remarkably similar with ca 0.4 kg for all traps. The GSD of the material is distinctly different for each trap set.

The difference in GSD is an indicator for a different GSD in the surrounding bed and shows that the trap sets are chosen in different sub-environments of the Stonyford channel study reach. The coarsest material is found in set F1, suggesting a lack of fines in the surrounding bed. F2 traps captured a mix of fine and coarse material. Trap set F3 experienced the lowest sediment trapping with mainly fine-grained material.

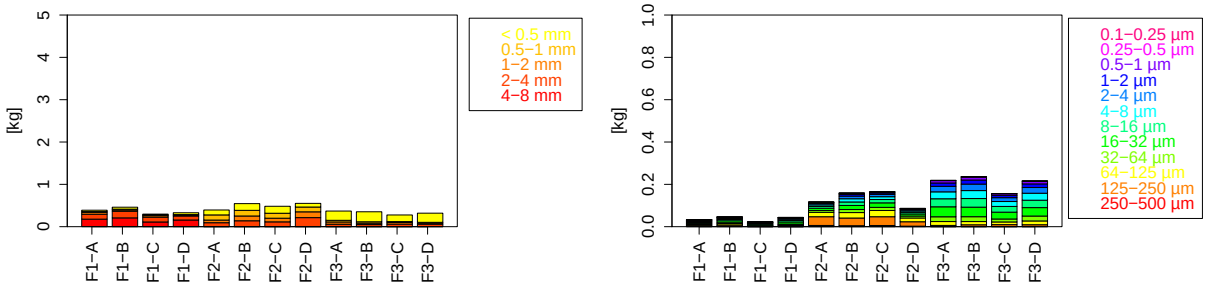

(a) Total trapped material, sieved grain size classes

(b) Trapped material finer 500 μm, grain size classes measured with DigiSizer

Figure 4.34: Grain size distribution of trapped material in Period 1 in the Stonyford study reach.

The stage record in Figure 4.35 for Period 2 at Stonyford shows 13 events. The suspended sediment concentration and stage records show good agreement with

concentration peaks at the beginning of each flood event.

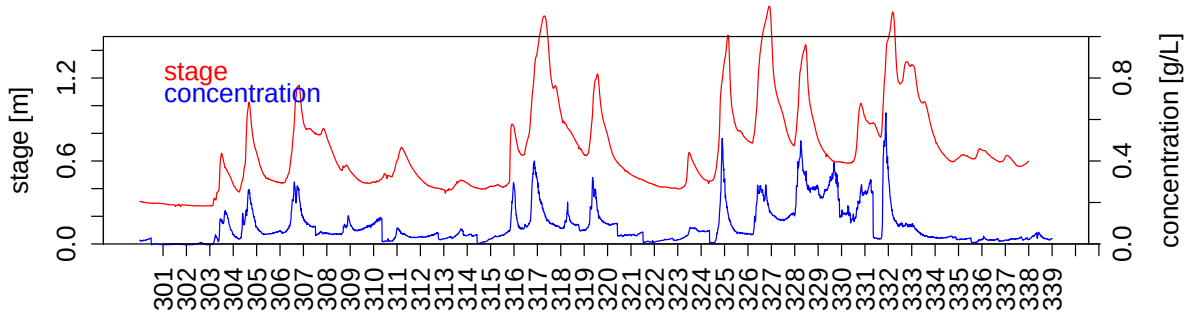

Figure 4.35: Stage record and suspended sediment concentration of Period 2 at Stonyford, Julian Day 339 (from 28.10.09 to 05.12.09).

As mentioned above, F1 traps were disturbed and destroyed by cows. Additionally, there were problems during the recovery of trap F2-A, hence no data for these traps is available for Period 2. Figure 4.36 shows the sediment trapping by the remaining seven traps. The two sets demonstrate distinctly different data. Sediment trapping by set F3 was much higher than set F2, which was mainly due to the ingress of fine sediment. This is remarkable because in theory the main channel experiences higher velocities and therefore less sedimentation. A reason for higher trapping might be the higher supply of fine sediment compared to the side with less discharge.

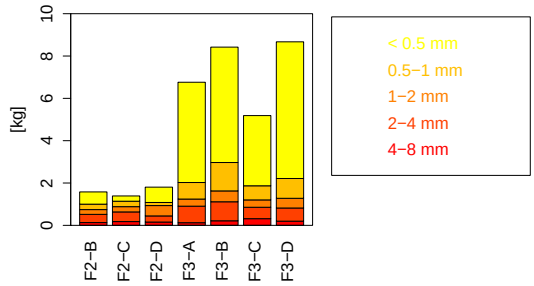

(a) Total trapped material, sieved grain size classes

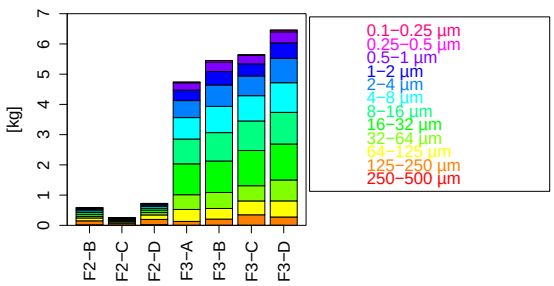

(b) Trapped material smaller 500 μm, grain size classes measured with DigiSizer

Figure 4.36: Grain size distribution of trapped material in Period 2 in the Stonyford study reach.

Trapping periods at Rewe: Only 2 trap sets were installed in the Rewe study reach of which trap R1-A got destroyed during the first trapping period. Therefore, Figure 4.37 only shows the summary data for the remaining seven traps. R1 traps were positioned on a riffle in a cluster, R2 traps were installed at the end of a pool beginning of a riffle and aligned in a cross-section. This means the traps are positioned continuously deeper from R2-A to R2-D.

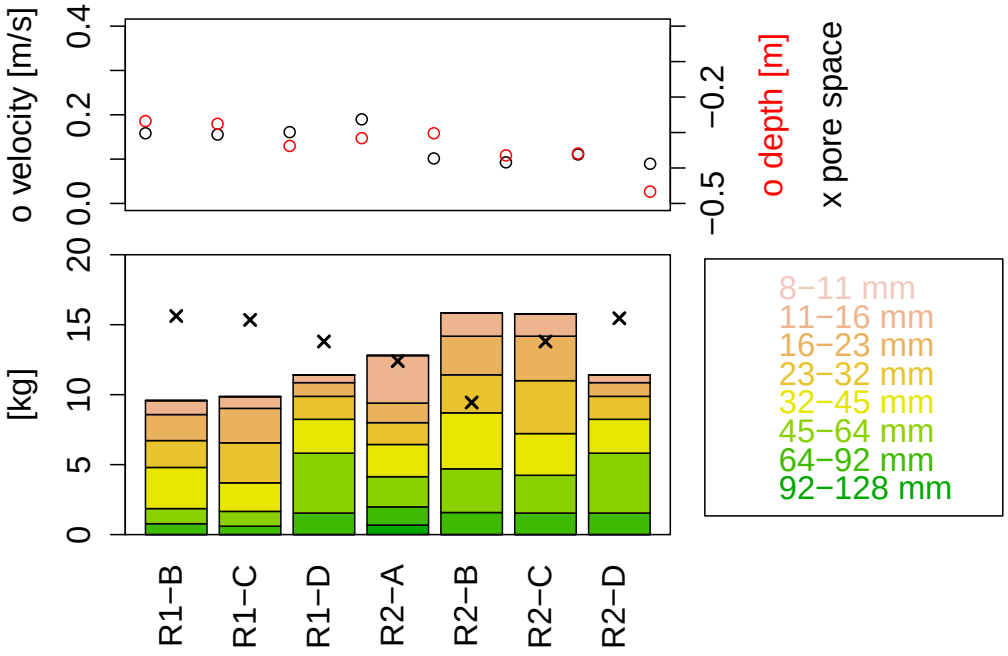

Figure 4.37: Gravel grain size distribution of framework material in the retrievable basket traps in the Rewe study reach

Depth and velocity differ over a much smaller range than in the other two study reaches due to the more uniform nature of this particular reach. R1 traps are shallower with faster flow, whereas R2 traps are positioned deeper and experience slower velocities.

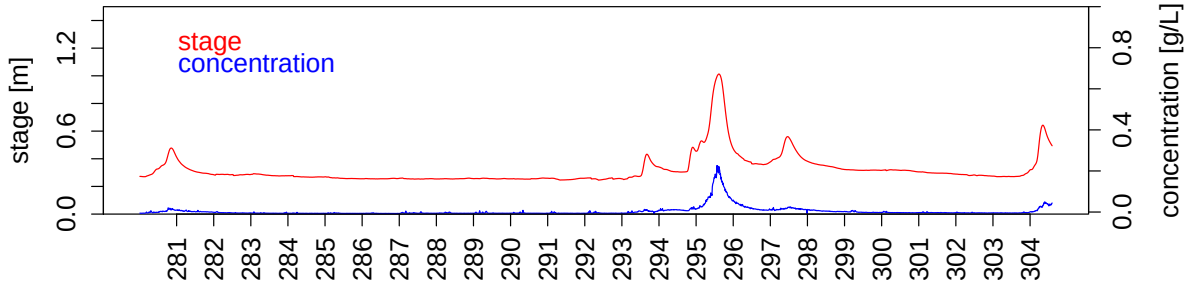

Figure 4.38: Stage record and suspended sediment concentration of Period 1 at Rewe, Julian Day 281 to 304 (from 28.09.09 to 30.10.09).

The first trapping period at Rewe shows only one major event in the stage record, see Figure 4.38. The stage record of the major event is noticeably symmetric, showing clearly the more inert hydrological responses of the reach. It is likely that the trapped material represents the result of flow and sediment characteristics associated with this event.

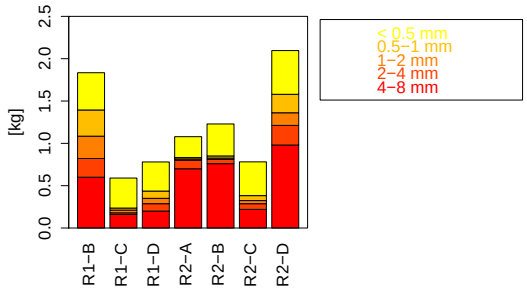

(a) Total trapped material, sieved grain size classes

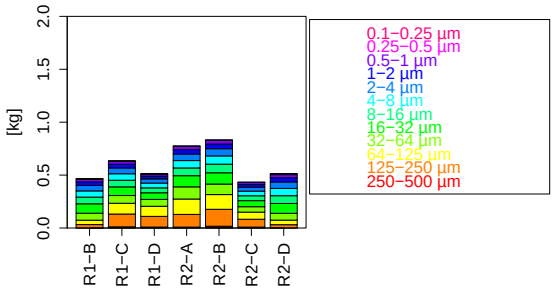

(b) Trapped material smaller 500 μm, grain size classes mesure with DigiSizer

Figure 4.39: Grain size distribution of trapped material in Period 1 in the Rewe study reach.

Figure 4.39 does not show a clear difference in trapping between basket trap sets R1 and R2. There is a high variation of trapping within the individual sets, which is much higher than for the sets at Smithincott and Stonyford. As an average, set R2 exhibits higher trapping rates than R1. A larger proportion of the material is coarser than 4 mm. This means during high velocities, when coarse particles are moved, the traps experienced diverse conditions but during periods of slower velocities with high suspended sediment load, conditions over the traps are similar, resulting in

similar amounts of fine sediment deposition. Again, the amount of trapped material of the fine size range varies but the distribution of the fine fraction measured with the DigiSizer is remarkably similar for all seven traps.

Trapping Period 2 at Rewe includes ten major events shown in Figure 4.40. The stage record shows a symmetrical rise and recession for each flood event. The suspended sediment concentration coincides with the stage records. The suspended sediment concentration rises at the beginning of the rising stage and declines fast after the peak. The peak suspended sediment concentration at Rewe is much lower compared to the other gauging stations.

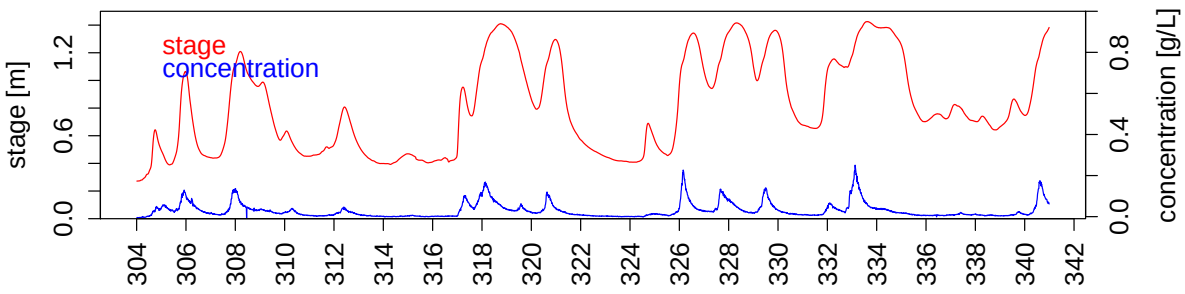

Figure 4.40: Stage record and suspended sediment concentration for the Period 2 at Rewe, Julian Day 304 to 342 (from 30.10.09 to 05.12.09).

The sediment trapping in Period 2 is not higher but more equally distributed over all traps compared to Period 1. Moreover, the fraction represented by coarse material is greater for Period 2. The lack of a clear difference is remarkable. Period 2 experienced ten days of high stage and suspended sediment concentration compared to only three days in Period 1 (see Figure 4.41).

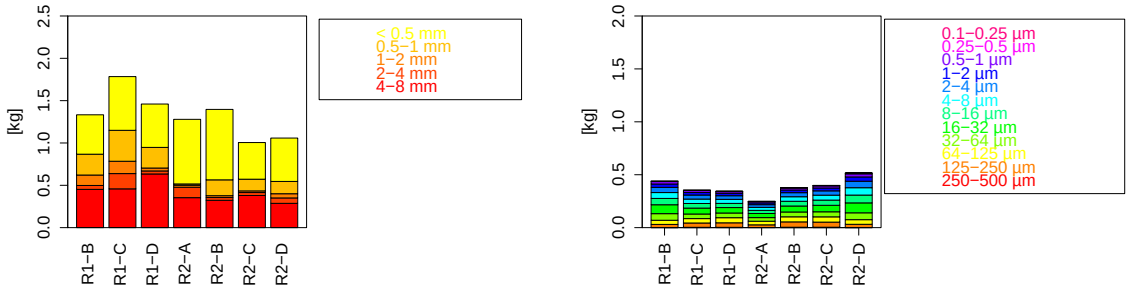

(a) Total trapped material, sieved grain size classes

(b) Trapped material smaller 500 μm, grain size classes measured with DigiSizer

Figure 4.41: Grain size distribution of trapped material in Period 2 in the Rewe study reach

This suggests that fine sediment did not ingress the traps during every flood event. The distinction between the sediment trapping rates of trap sets R1 and R2 is minimal, with slightly higher trapping for R1 compared to R2 in Period 2. The comparison of Periods 1 and 2 at Rewe suggests that one event or many events of a comparable magnitude can result in very similar amounts of fine-grained sediment deposition. One event is likely to cause higher variation in sediment trapping between the individual traps comprising any set, whereas in contrast, if the same channel position experiences several events, sediment deposition is likely to be more spatially uniform.

There is little information in the literature about the relationship between suspended sediment load in the trapping period and measured deposition. However, there is some information in Zimmermann and Lapointe (2005) who compared sediment deposition with the total sediment dose experienced by the trap. The study includes results of interstitial deposition measured with basket traps at four streams. In two of the streams, a clear positive correlation between sediment dose and trapping is apparent but the other two show a very weak correlation. This suggests there is no stringent correlation between suspended sediment load and interstitial sediment trapping rates. Still, the data collected by this study cannot be compared directly to the results of the published study, because in Zimmermann and Lapointe (2005) only one trapping period was evaluated. Frostick et al. (1984a) did use compart-

ment traps with different recovery times for each compartment. However, the data is not presented in a way to get insights into the difference between their weekly and monthly sampling. The fact that it is not mentioned suggests that monthly measurements are similar to the sum of the weekly amounts in this period.

When appreciating the field data of this study, the re-suspension of interstitial fine sediment needs to be discussed. Some authors believe re-suspension of the interstitial fine-grained material is only possible when the gravel framework is mobilised, see Kirchner et al. (1990). Still, processes with flow conditions below the threshold for mobilisation of the gravel bed can also have effects on the bed structure, like the 'jiggeling' of grains described in Beschta and Jackson (1979). The process of loosening of the gravel framework by high velocities allowing higher interstitial flows to flush fines without actually changing the gravel bed structure could be a possible explanation for the lack of additional sediment trapping during longer trapping periods. This behaviour would not require actual bed framework mobilisation.

4.5 Field data resume

The choice of the River Culm in the Exe basin as the study area and the three study reaches Smithincott in the upper, Stonyford in the middle and Rewe in the lower reaches showed the **clear difference in the character of the river channel and its bed**. Each study reach was representative by including all major features of the river (namely riffles, bars, pools). The **acquisition of data for the hydrodynamic model** was comprehensive. An extensive GPS elevation point survey resulted in data with little gaps for all reaches. Data for areas with insufficient data points were collected using manual measurements. For the calibration conditions, water depth and velocity were recorded at up to ten cross-sections per reach.

94 samples for gravel grain size distribution were collected in the three study reaches. This is a large data set for gravel count data. However, the data is not

sufficient to generate a gravel grain size distribution covering the whole study reach channel. The sample points are biased towards more shallow areas. Since this bias is apparent in all three study reaches, comparison between the data of the study reaches is acceptable. The results for the single reaches show a clear delimitation of grain size ranges and indexes for the three study reaches. The most upstream and most natural study reach at Smithincott covered the widest range of different grain size distributions and indices. The gravel bed at Stonyford was found to support a coarser grain size distribution and the indices reside around one end of the range of values found at Smithincott. Gravel grain size distribution at Rewe was finer, with indices covering the opposite end of the range compared to Stonyford.

The turbidity and stage records for the three reaches show **distinct and typical behaviour** for the three parts of the river course. At Smithincott, stage and turbidity are very reactive and show marked fluctuations. At Stonyford, the stage and turbidity record is less responsive. At Rewe, the stage record shows almost symmetrical peaks with the turbidity record peaking in the early part of the stage peak. Turbidity peaks are much smaller at Rewe, compared to the other two study reaches.

Calculating the **suspended sediment loads** from discharge curves using the Gaukler-Manning equation, the sediment loads for the same winter period double from Smithincott to Stonyford and again from Stonyford to Rewe. Moreover, the suspended sediment load of this study period with many flood events contributes a significant proportion (12 %) of the total suspended sediment load of the River Exe basin.

This high suspended sediment runoff is accompanied by **large amounts of fine sediment ingress into the channel bed**. Interstitial fine sediment was measured using two methods: A re-suspension method measuring storage and a retrievable basket trap method measuring deposition during two periods of autumn/winter floods in each of the study reaches. The re-suspension method showed a consistent fine sediment storage pattern for the four positions measured in each study reach. The

results suggest **higher storage during the low discharge summer months** compared to the spring and autumn months.

The retrievable basket trap based method measures deposition in the period between installation and recovery. Retrievable basket traps were positioned in sets of four in distinct different sub-environments of the river channel (namely: pool tail, riffle and pool head). The deposition measurements showed consistently similar interstitial sediment trapping within one trap set and a **clear difference in deposition between these sub-environments**. The retrievable basket trap data showed that even during periods with a lack of suspended sediment transport in the water column (period 1 in Stonyford), fine sediment from the surrounding bed moved into the sediment traps, suggestiong two pathways of fine sediment; horizontal from the water column into the bed and vertical transport through the gravel framework. Furthermore, the data showed that periods with many flood events do not result in a higher deposition compared to periods with fewer events, suggesting that traps experienced not only deposition, but also re-suspension prior to bed entrainment and/or the cease of fine sediment deposition due to sealing of the upper layers.

Overall, the deposition information gained is of high relevance, which becomes particularly clear, when we are comparing the field measured interstitial storage and deposition rates with data from the literature. The magnitude of interstitial sediment deposition and storage found in the River Culm is considerably higher than data published in recent literature, both for the River Culm and comparable rivers. This core result is supported by both methods used in the field, i.e. the re-suspension method, which establishes the instantaneous fine-grained sediment content in the upper layer and the basket trap method, which investigate ingress over the deployment periods (see also Chapter 1, Table 1.1). Further, this observation is still valid, if substracting finse sediment amounts which have potentially moved in from the surrounding bed such as found in the first trapping period in Stonyford). Since both fundamentally different methods lead to the same result, a methodical error is unlikely. In addition,

the re-suspension method as well as the retrievable basket trap design conforms to those used in the other studies cited in Table 1.1. Nonetheless, the question why these diverging results between the recent literature and this research came about, is highly relevant. Reasons, such as temporal or spatial variation in the sampling procedure, can of course not be excluded. Hence, a more detailed investigation of this divergence is necessary to fully understand the cause of this finding.

Still, the complexity of the flow and sediment environment in the study reaches made it **difficult to interpret variability in interstitial sediment trapping** in the different periods. We can expect that with the consideration of velocity and shear stress and localised discharge information from the hydrodynamic model a more coherent interpretation of the localisation of the sediment trapping data is possible. This is realised in the reach scale numerical deposition model in Chapter 6.

Chapter 5

Hydrodynamic models

This Chapter sets out to develop a hydrodynamic model for each of the three field study reaches. The hydrodynamic models will be used as the source of the flow information for the reach scale fine sediment deposition model (introduced in Chapter 6). Hydrodynamic models of the field reaches are an effective tool to estimate detailed flow data for the complete range of discharge situations, without laborious and potentially dangerous direct measurements during high discharge. Figure 5.1 guides through this chapter by following the steps necessary to setup hydrodynamic models for the study reaches. The process includes four stages (represented in the four levels in Figure 5.1):

- the field data of the study reaches (see Chapter 4),
- the processing of the field data into a format suitable for the hydrodynamic model input,
- the hydrodynamic simulations (which in this chapter are calibration runs) and
- the calibration of the hydrodynamic models.

Every hydrodynamic model is based on elevation information for the river channel and its flood plain. Section 5.1 shows how the GPS point elevation information from the field surveys is converted into detailed elevation models for the study reaches

(for details see Subsection 4.2.1 in the preceding chapter). The point elevation data was transformed into a coherent Digital Elevation Model (DEM) employing the triangulation method of the software *ArcGIS*.

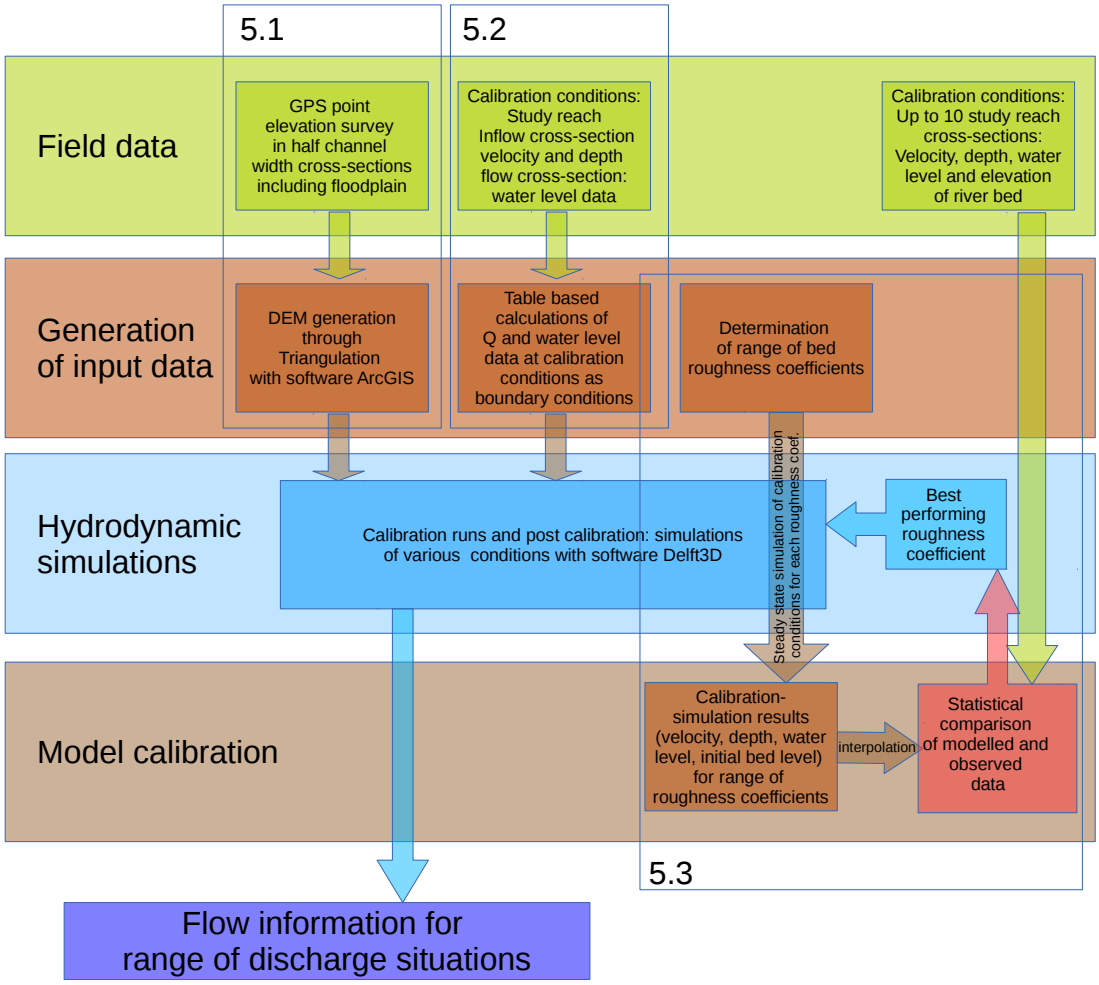

Figure 5.1: Flowchart of the setup and calibration of the hydrodynamic models including four levels: field data, data processing, hydrodynamic simulations and model calibration. Elements combined in blue rimmed boxes have reference number indicating the chapter section where these aspects are discussed.

Section 5.2 describes the input parameters necessary for the setup of a hydrodynamic model with the software Delft3D. Foremost, these are the boundary conditions at the inlet and outlet of the model reach. For the hydrodynamic simulation at hand, these are the discharge and water level during the calibration conditions. Section 5.3 describes the model calibration, which aims to identify a suitable bed roughness

coefficient for each of the reaches. The section also shows the determination of a range of roughness coefficient values used in the model calibration. Further, the section elaborates how the best fitting bed roughness coefficient is chosen. The selection of the optimum bed roughness coefficient is based on the comparison of modelled and observed water depth, water level and velocity data using graphical and statistical methods. The calibrated model is deployed for simulations for a range of discharge situations. The output of these simulations is already indicated in the flowchart in Figure 5.1 and their use will be described in the subsequent Chapter 6.

5.1 DEM setup

The original elevation field data consists of points aligned along transects that are orthogonal to the channel downstream direction, including river-bed and river-bank. The distance between transects is approximately half the channel width. The points are measured with a differential GPS with very high accuracy (see 4.2.1). In very deep, highly vegetated or generally inaccessible areas the data exhibit some gaps. To fill these gaps, where possible, depths were measured using a survey pole and a tape measure. The following shows the transformation of the point elevation data into a DEM for each of the study reaches.

5.1.1 Triangulation method

Triangulation is the transformation of point data into a representation of a surface. The surface consists of a network of non-overlapping triangles, which is a Triangulated Irregular Network (TIN). The triangulation method applied here is based on the Delaunay triangulation, which does not allow points in the plane of a triangle and defines criteria about the angles of the triangles. The Delauny triangulation does not result in a unique TIN, which means different triangles can be a solution for the same point data. The triangulation of the elevation points was conducted with the

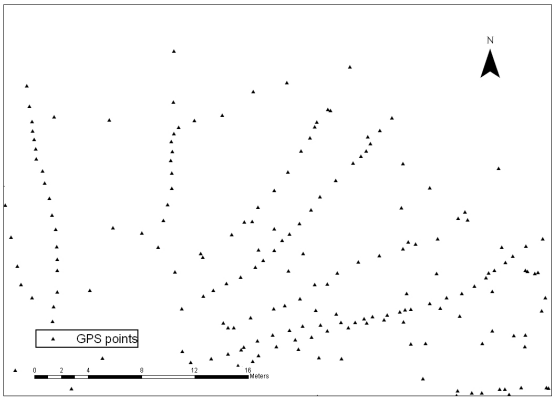

(a) GPS point elevation data

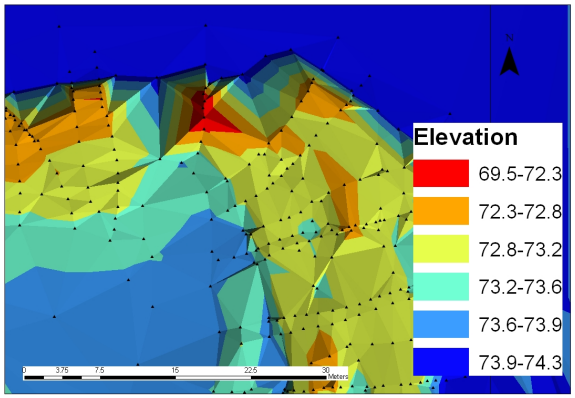

(b) Initial TIN from GPS points

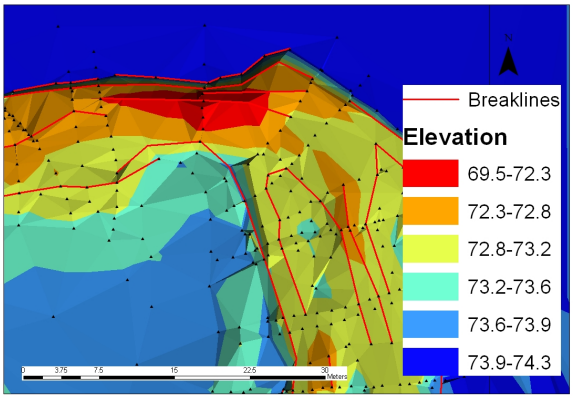

(c) Refined DEM with breaklines

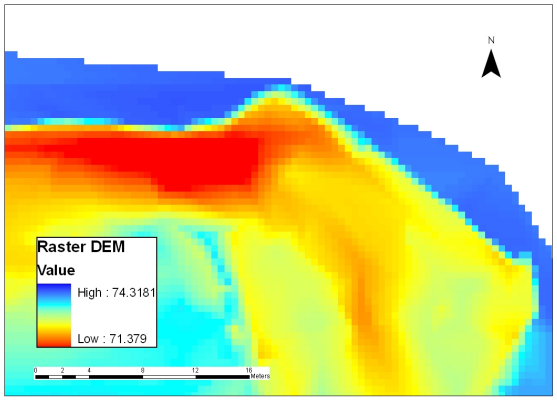

(d) Final raster DEM

Figure 5.2: Example of the process of converting point elevation data into a TIN and the refining of the TIN to generate a smooth raster DEM.

3DAnalyst tool of the *ArcGIS* software package. Inconsistencies in the surface representation were smoothed by adding breaklines into the TIN. Breaklines prevent triangle edges between two points separated by the breakline. Triangles of the TIN are prevented from crossing the breaklines.

Figure 5.2 shows the process of converting the original GPS points (5.2a) into a smooth raster DEM (5.2d) exemplified with a cutout of the Smithincott study reach. The *ArcGIS* tool *'points to TIN'* initially produces a patchy and sometimes unrealistic surface from the original elevation points (Figure 5.2b), as the triangulation is operated isotropic when choosing neighbouring points. Yet, the elevation in a river channel has a strong anisotropic character with a systematic difference in elevation between channel and bank points. The triangulation across anisotropic divides

causes unrealistic elevations in such a triangle. Breaklines which are *3Dpolylines* (shown in 5.2c) can ensure that the long edges of the TIN triangles are aligned along the divide in an elevation. For a river channel, this mainly means the long edges of the triangles are aligned in downstream direction. Typically, those breaklines were chosen to run on top of the cut bank, along the thalweg and along features in areas with limited measurement points. The refinement of the TIN was done by repeating the following steps:

- identify areas with irregularities
- generate breaklines for this area
- add breaklines to the TIN
- if repetition of the three steps above leads to a satisfactory TIN, then convert final TIN into a regular raster grid

The resulting raster DEM shows an even surface representing the reach in 0.5 m squares as shown in Figure 5.2d.

5.1.2 DEM generation for the three study reaches

Smithincott DEM: Figure 5.3 shows the final raster DEM superimposed by the original GPS measurement points of the study reach at Smithincott. The highlighted squares show areas with insufficient point elevation data. Data gaps are defined as areas where GPS measurement point transects are more than half a channel width apart or areas where features are smaller than half a channel width. The green boxed area is a slack water area with a deep mud accumulation. In this area, it is both hard to define at which point the bed starts and it is impossible to wade without running the risk of getting stuck. Luckily, hydraulic information for this area is not critical, since almost no flow occurs. Still, additional visual observations of the bed height in the slack water area are included in the TIN.

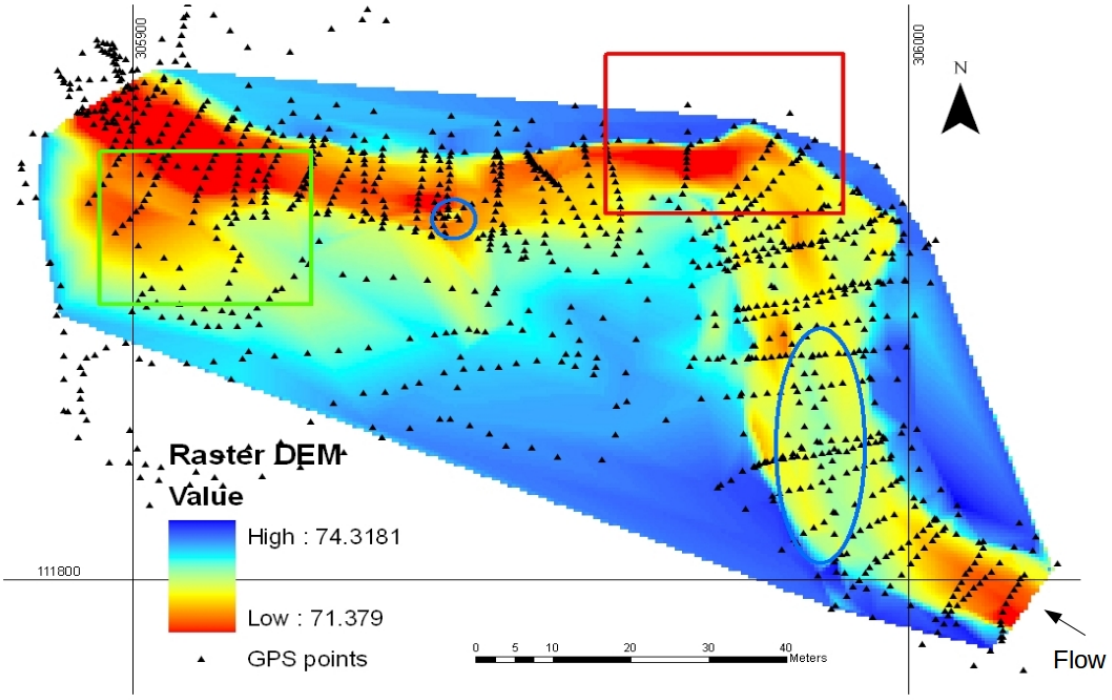

Figure 5.3: Final raster DEM for the Smithincott study reach overlain by measured GPS elevation points.

In contrast, the red boxed area contributes strongly to the discharge. It is an area of fast flow in a deep pool. In the field, the depth was measured with a pole and the distance to a GPS point with a measuring tape. Hand measured data was later digitised and included in the TIN. Another challenge is the handling of smaller features such as the little island indicated by the blue circle or the longitudinal island further upstream indicated by the blue oval. The contour of the island was protected by breaklines. The same procedure was applied for the little bay forming south of the blue circled island. A breakline was inserted along the top of the gravel bar to avoid edges between two points from opposite sides of the bar.

Stonyford DEM: Figure 5.4 shows the raster DEM for the study reach at Stonyford superimposed by the original GPS measurement points. Again, boxed and circled areas indicate areas with data gaps. The red boxed area is covered by thick, over-

hanging vegetation, which made it impossible to obtain a GPS signal of the required quality. Also, the area is too deep and it is impossible to wade with equipment. Hence, points were measured using a pole whilst partly swimming. Since the flow is very slow, pole depth measurements can be considered.

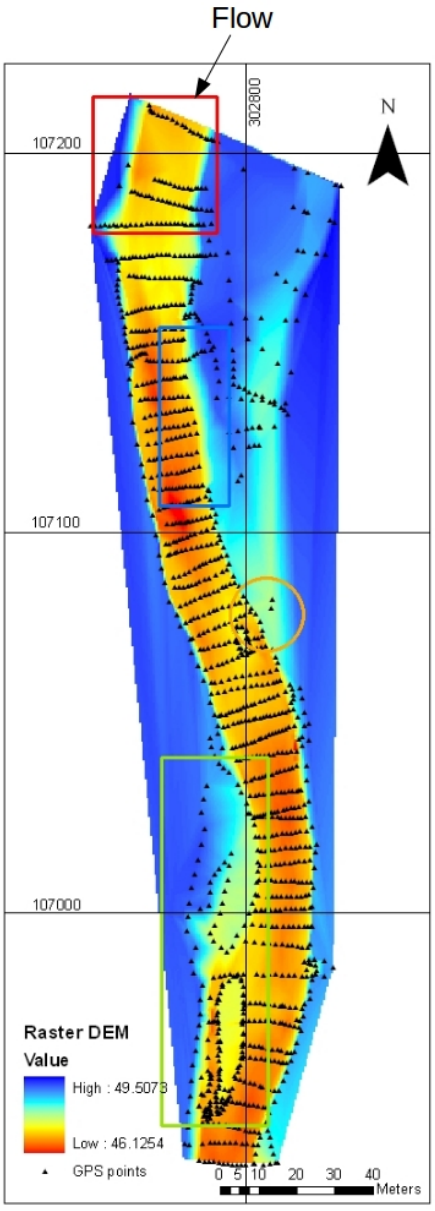

Figure 5.4: Final raster DEM for the Stonyford study reach.

Measuring the horizontal distance to GPS measurement points was more challenging. The errors for the horizontal position of the hand measured points are esti-

mated to be in the order of $\pm$25 cm.

The river bank in the blue boxed area is covered in thick bramble vegetation, hence no direct access was possible. Height estimates could be obtained from points measured outside the bramble covered area directly up- and downstream. This procedure resulted in a good representation of the bank morphology, because the elevation variation in downstream direction is minimal in this area. The green box encloses an area of complex channel morphology due to an island with steep edges. This area was populated with a high number of points around the channel island. Finally, the orange circle indicates an old channel outlet, which is only roughly included in the DEM. The side channel is not inundated before the bankful discharge of the main channel is exceeded and therefore not critical for the discharge. Areas containing data gaps are highlighted.

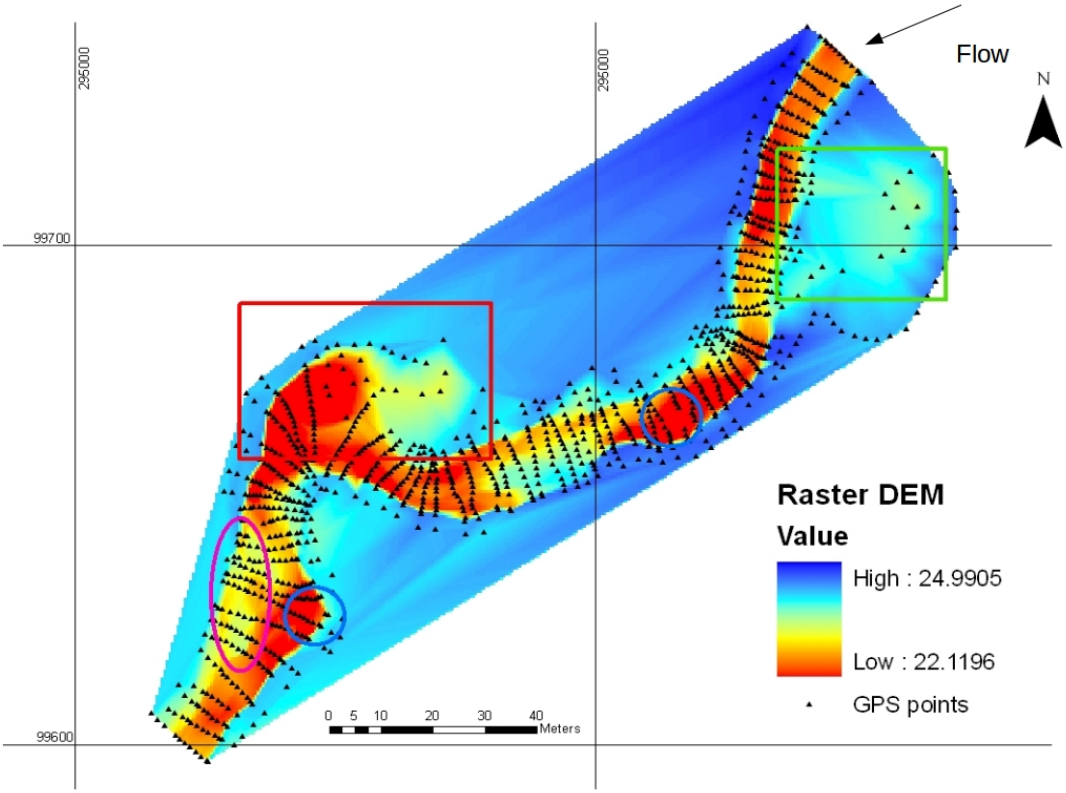

Figure 5.5: Final raster DEM for the Rewe study reach.

Rewe DEM: Figure 5.5 shows the final raster DEM for the reach at Rewe overlain by the originally measured GPS points. The red boxed area is a deep and muddy slack water area. Some points were measured with the GPS. Additional points were estimated using the bed elevation at the downstream end of the slack water area. The green box encloses an old channel, which is active during small floods. The muddy and highly vegetated area made crossing a challenge, therefore additional points were added estimating the depth by eye. An area with structures smaller than the survey distance is marked by the purple oval. The morphology of the island and the back channel was strengthened with breaklines.

5.1.3 Evauation of the DEM accuracy

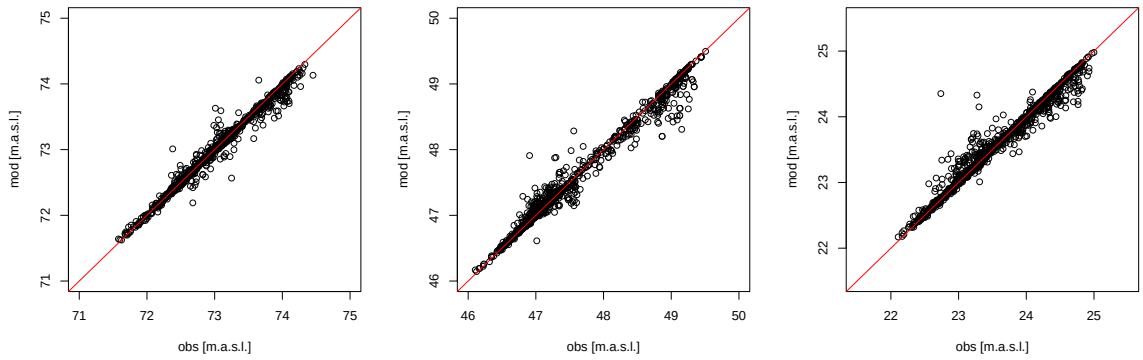

(a) Smithincott (b) Stonyford (c) Rewe

Figure 5.6: Comparison plot of model DEM (mod) and observed field GPS points (obs) used for TIN and DEM creation, with red 1:1 line.

In this subsection, the accuracy of the DEMs is tested with a two stage quality check. Figure 5.6 shows the comparison of the DEM data with the original point elevation data used for the DEM construction and Figure 5.7 shows the comparison with an independent control point elevation dataset. Each figure shows one scatterplot for each reach with the observed data on the x-axis (obs) and DEM data on the y-axis (mod). The optimum fit 1:1 line is added in red. As an indicator of agreement, the coefficient of determination (r^2) and the squared mean standard error (SMSE) are

used (both are described in Chapter 3). Regarding the model evaluation in Figure 5.6, the Smithincott reach has a very good model fit, with r^2 = 0.98 and a squared standard error of less than 1 cm. For the Stonyford reach, the correlation is similar, with r^2 = 0.98 and a standard squared error of 1.4 cm. The reach at Rewe diverges slightly more from the original data with r^2 = 0.97 and a squared standard error of 1.6 cm. Generally, lower elevations within a reach result in a better fit. The lower elevation points are channel points. Elevation data points in the channel area are more frequent compared to the floodplain area and therefore the DEM is of a higher accuracy in the channel. This good fit is further supported by the results shown in

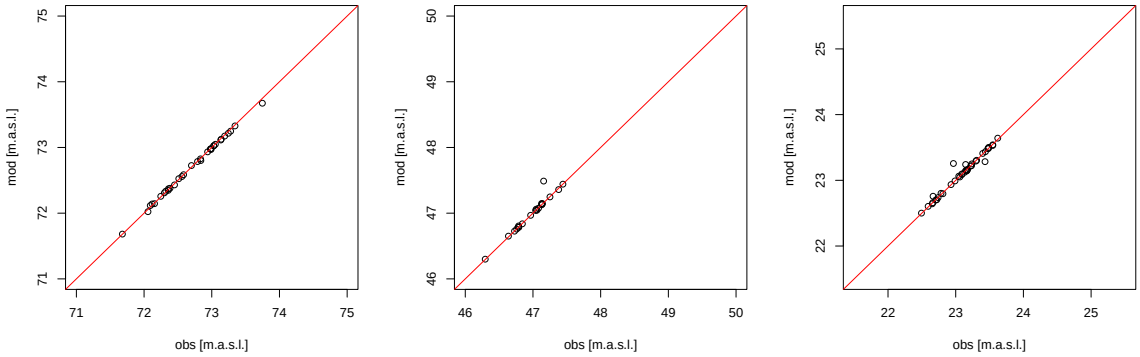

(a) Smithincott (b) Stonyford (c) Rewe

Figure 5.7: Comparison of model DEM (mod) and extra control field GPS points (obs), which did not contribute to TIN and DEM creation, with red 1:1 line.

Figure 5.7. Here the observed data are control point measurements, which are not used in the DEM generation. The DEM shows a better accordance with the control data than with the original data points used to generate the DEM. The coefficients of determination are similar or slightly weaker (because fewer data points exist) with r^2 = 0.99 for Smithincott, 0.94 for Stonyford and 0.96 for Rewe. Squared standard errors are smaller with $<$1 mm, 12 mm and 3 mm, respectively. The better fit compared to the original data is the result of the fact that the control points are all positioned in the channel with the higher accuracy compared to the floodplain. Table 5.1 lists r, r^2 and SMSE for all three reaches, each for the original and control GPS point

	original data			**control data**		
	Smithincott	Stonyford	Rewe	Smithincott	Stonyford	Rewe
r	0.988	0.990	0.983	0.999	0.967	0.981
r^2	0.975	0.981	0.966	0.999	0.935	0.964
SMSE m	0.009	0.014	0.016	0.000	0.012	0.003
slope	1.0	1.03	0.91	0.97	1.03	0.97
intercept	0.04	-2.26	4.03	2.35	-1.38	0.80

Table 5.1: Correlation and squared standard error of DEM data compared to original point elevation data used for DEM generation (original) and DEM data compared to point elevation of a control data set (control).

measurements.

5.2 Input data

Delft3D is a commonly used hydrodynamic modelling software developed by a Dutch company called “Deltares Systems”. Delft3D is a suite of software tools with several modules to simulate hydrodynamic behaviour. It can simulate 3D or 2D flow with a hydrostatic pressure assumption, which is described in the manual as “non steady flow in relatively shallow waters” (Deltares, 2010). This means the vertical lengths of the modelled water body is much smaller than the horizontal length and the shallow water equation can be applied. Moreover, it can include external factors and secondary processes (such as air pressure, salinity profiles, pollution sources, etc.). All explanations in this section refer to the setup of calibration runs with a constant water level and discharge over the whole period of the simulation run. The aim of each single run is to achieve a steady condition for all hydrodynamic parameters. For the hydrodynamic models in this study, the following modules of Delft3D were used:

- the Delft3D *grid* module to produce a grid and an associated bathymetry file based on the raster DEM,
- the Delft3D *flow* module to generate input definition files and to execute the actual simulations and

- the Delft3D utility *QUICKVIEW* which is used to view and export results of the model calibration runs.

Grid and bathimetry

The *grid* module is suitable to built a model grid (with the utility *RGFGRID*) and to produce a bathymetry file (with the utility *QUICKIN*). *RGFGRID* is a graphical instrument, which is able to create a curvilinear or rectilinear grid. The possibility of loading sample files of the field location into the visual workspace can give valuable information on how to lay out the grid. *QUICKIN* provides the tools to build a bathymetry file from sample files. For all three study reaches, a curvilinear grid is chosen with parallel running outer borders following the streamline including between 5 to 10 m of the floodplain on each side of the channel. A curvilinear grid alows to adapt to the river channel morphology and to recreate a complex river channel with a relative low number of grid cells (Gailani et al., 1996). The morphologic grid of the Smithincott reach with the bathymetry information in the background is shown in Figure 5.8 with an inverse depth scale as required by Delft3D. The equivalent images for the Stonyford and Rewe reaches can be seen in Appendix A.56 and A.57. The grids are a result of drawing stream line parallel splines by hand following the bank line. Spline lines orthogonal to the stream line are defined to follow the survey cross-sections and additional orthogonal spline lines are added between these. With those splines as a backdrop, *RGFGRID* produces a first grid with M cells in the downstream direction and N cells in cross stream direction. In further steps, the grid was refined and orthogonalised. Using grid refinement, grid cells with a resolution smaller than 0.5 m in edge length in any direction are generated. The grid cells in n direction are finer in the channel than on the floodplain to provide more detailed information while allowing a reasonable simulation time. The grid uses a Cartesian coordinate system in alignment with the British National Grid. All hydrodynamic parameters are modelled for each grid cell but not all at the centre point of the grid cell. Delft3D uses

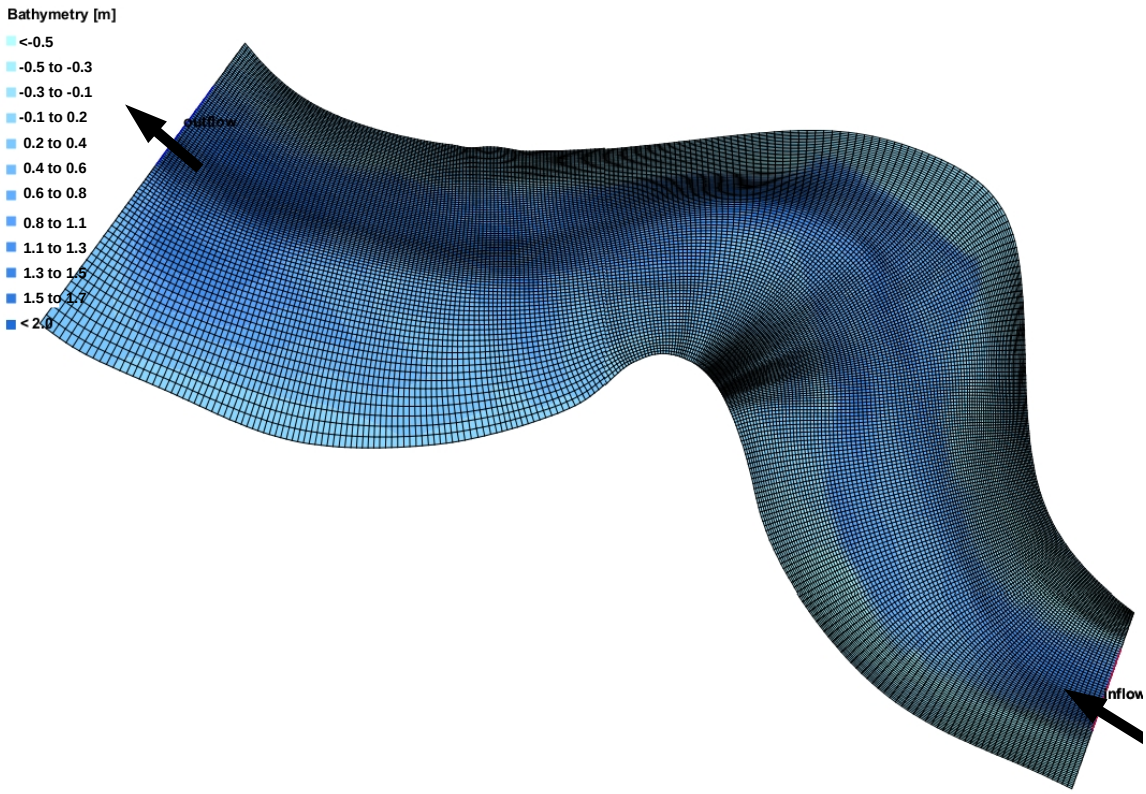

Figure 5.8: Morphologic grid of Smithincott study reach underlain by bathymetry information given in depth relating to model zero as used in Delft3D.

a so called staggered grid. This means that different parameters are calculated at different positions in the morphologic grid. Figure 5.9 shows the staggered grid as printed in the Delft3D Flow user manual (Deltares, 2010, p.5-9). This is relevant for the further extraction and interpolation of results in order to compare modelled parameters with field observations. The source of the bathymetry used in Delft3D is the DEM raster file obtained by post processing the field data in ArcGis as described in Section 5.1.1. Before reading the exported xyz files into Delft3D, a conversion from elevation to depth was applied. This was done by subtracting the maximum elevation value from all elevations and multiplying the term by (-1). The resulting file had to be split so that each file contained less than 5000 points in order to be read into *QUICKIN*. Again, triangulation was used (this time with *QUICKIN*) to read depth data into the grid file. Some areas on the floodplain were not represented in the raster

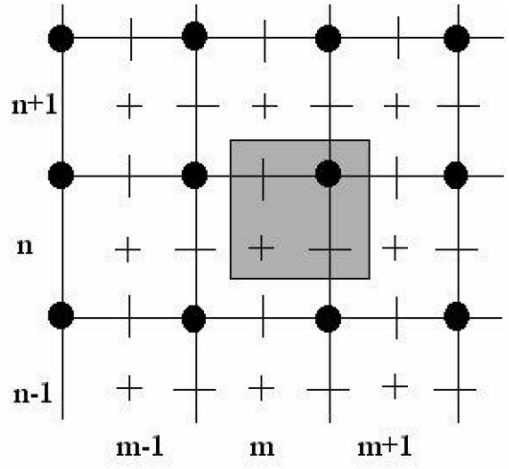

Figure 5.9: Staggered grid as shown in Delft3D Flow manual.

• Water depth

+ Water Level

grey area area with same grid reference

— velocity in m direction (downstream)

| velocity in n direction (cross stream)

DEM. For these areas, grid cell values were established by internal diffusion, which expands adjacent grid cell information into areas without data points. This procedure results in a flat floodplain.

	calibration condition WL drop	**calibration condition mean Q**	**No of study cross-sections for calibration**	**95% confidence interval of mean Q**
	m	m^3		
Smithincott	0.99	0.76	7	$\pm$0.19 m^3s^{-1}
Stonyford	0.59	2.7	10	$\pm$0.26 m^3s^{-1}
Rewe	0.24	0.25	9	$\pm$0.11 m^3s^{-1}

Table 5.2: Water level drop and mean discharge during calibration conditions for the three study reaches with number of study cross-section for Q calculation and the 95 % confidence interval of the mean Q. The data is used for the boundary conditions definition in Delft3D hydrodynamic calibration runs.

5.2.1 Input parameters for the simulation

The Delft3D *flow* module hosts the actual simulation. The input parameters for a simulation are set and saved in a *mdf* file. Input parameters can be grouped into physical, numerical and output related parameters. The following parameters were

defined in the *mdf*-file, when setting up a steady state simulation (as it was the case for all calibration runs).

(1) Physical parameters

- The location, the length and the conditions at the upper and lower boundary of the model reach: The conditions of the upstream boundary or inlet are defined as discharge. The conditions at the downstream boundary or outlet are defined with a water level. Both boundaries were aligned to the cross-section furthest upstream, respectively furthest downstream. The discharge is calculated using depth and velocity measurement during calibration conditions (see 4.3). Table 5.2 shows the discharge used for the model input, which is the average of all discharges (Q) at the study cross-sections. The table also lists the number of cross-sections and the 95 % confidence interval of all three study reaches. Water level information derives from directly measured GPS elevation points of the survey cross-section furthest downstream. The length of the inlet and outlet was chosen to be long enough to cover the wetted area during bankful discharge.

- The geometry of the model reach: This is given as the grid and bathimetry file as discussed above.

- The initial water depth: This was chosen to cover the whole reach with 0.5 m of water at the beginning of the simulation.

- The bed roughness coefficient: Two different specifications of the roughness coefficient were applied in the calibration procedure: A uniform value for the whole reach and a value calculated for each grid cell depending on the local water depth.

- Additional parameters: These were set to zero or default settings. For example, secondary flow was not activated and the water density and kinematic viscosity

were left on default with 1000 gL^{-1} and 1 m^2s^{-1}, which are typical values for fresh water at 20 ° C.

(2) Numerical and output related parameters

- The time frame and time step of the simulation: The model time step is set at 0.002 minutes for each run. Experience showed that for a steady discharge and water level, after 30 minutes simulation time, stable conditions were reached for all model parameters in the three study reaches. To ensure that these stable conditions were achieved, the runtime of each simulation was set to 2 h.

- Output file frequency: A full record of all modelled hydrodynamic conditions was saved for every two minutes of the simulation.

5.2.2 Records and simulation output

In Delft3D, there are many different options for data export. The utility *QUICKVIEW* in the *flow* module is a platform, which allows to view model results as graphs and to export them as tables in different formats. The results are examined using graphical representation of morphological and hydrodynamic conditions as contour maps, vector plots and row output values, which are listing positions and values of hydrodynamic variables in a simple xyz file. In the case of the calibration runs, the development of hydrodynamic conditions in the study reach of the two simulation hours are examined. Only after these reached stable values, the sampling of the hydrodynamic conditions is performed once, typically at the end of the simulation period.

5.3 Calibration

The aim of the model calibration was to establish a well performing uniform bed roughness coefficient for each study reach of the hydrodynamic model. This calibration is conducted by evaluating the correlation of observed and modelled hydro-

dynamic parameters for simulations with different bed roughness coefficient values. Therefore, 10 to 20 simulation runs per reach were conducted using identical input parameters for calibration conditions, apart from the bed roughness coefficients. Subsection 5.3.1 discusses the possibilities of roughness coefficient inclusion in Delft3D hydrodynamic simulations. Subsection 5.3.2 defines the range of roughness coefficient used in the calibration runs. The hydrodynamic records of the different calibration runs are compared with the actual field data using a suite of calibration statistics. Explanations of these statistics are found in Subsection 5.3.3.

In order to gain information from the simulation records for the same parameters and positions measured in the field, an interpolation is necessary. This is described in Subsection 5.3.4. The subsection 5.3.5 then analysis the calibration results for the single study reaches.

5.3.1 Delft3D's roughness coefficients

Delft3D offers three different input possibilities for roughness coefficients (c): The Manning coefficient (n_{Ma}), the Chezy coefficient (c_{Chezy}) and the White-Colebrook roughness length (k_s) with its corresponding roughness coefficient ($c_{White-Colebrook}$). The main difference in these approaches is the relationship between the roughness coefficient (n_{Ma} or c) and the flow depth (d) of the flow equation. The Manning equation for velocity includes depth to the power of $\frac{2}{3}$, whilst the Chezy equation uses depth to the power of $\frac{1}{2}$. Slope (S_{hyd}) is included in the same way in both equations. The Manning (5.1) and Chezy (5.2) equation are given below.

$$v_{mean} = \frac{1}{n_{Ma}} d^{2/3} S^{1/2} \tag{5.1}$$

$$v_{mean} = c d^{1/2} S^{1/2} \tag{5.2}$$

In the simulations for this work, the Chezy equation (5.2) was used with two different roughness coefficients c: On the one hand, the depth independent c_{Chezy} and on

the other hand the White-Colebrook roughness coefficient ($c_{White-Colebrook}$), which is calculated from k_s and the local depth for each grid cell of the hydrodynamic model. The White-Colebrook roughness coefficient is traditionally described as the reciprocal value of the dimensionless Darcy-Weisbach roughness coefficient (f_D) (see Brkic, 2011; Barr and White, 1975). k_s is connected to the roughness coefficient in Equation 5.2 by Equation 5.3. For each location in the model domain, $c_{White-Colebrook}$ is calculated using the local depth (Equation 5.3).

$$c_{White-Colebrook-Delft} = 18 * log_{10} \frac{12 * d}{k_s} \tag{5.3}$$

5.3.2 Estimation of initial roughness coefficients

Although it is not used directly in the calibration runs, estimates of Mannings n provide a valid starting point for the c_{Chezy} and k_s determination. Estimates of n_{Ma} are derived from river reach characteristics using methods outlined in many handbooks (e.g. Arcement et al., 1984) after the method of Cowan (1956). In this instruction, n_{Ma} is the sum of four sub-roughness-coefficients and a meander correction factor as shown in Equation 5.4 (where n_1 refers to surface roughness, n_2 to the cross-section variation, n_3 to the density of obstructions, n_4 to the vegetation grow and m the meander correction).

$$n_{Ma} = (n_1 + n_2 + n_3 + n_4) * m \tag{5.4}$$

The Chezy roughness coefficient can be estimated from n_{Ma} as defined in Equation 5.5:

$$c_{Chezy} = \frac{d_{mean}^{1/6}}{n_{Ma}} \tag{5.5}$$

This results in the Chezy roughnesses coefficient for an average water depth at the calibration flow conditions for the different reaches as follows: Smithincott average depth of 0.32 m: $c_{Chezy} = \frac{0.32^{1/6}}{0.063} = 13.13$, Stonyford with an average depth of 0.38 m:

$c_{Chezy} = \frac{0.38^{1/6})}{0.052} = 16.37$ and Rewe with an average depth of 0.61 m: $c_{Chezy} = \frac{0.61^{1/6}}{0.0759} = 12.15$.

	Smithincott	**Stonyford**	**Rewe**
n_{Ma}	0.063	0.052	0.076
c_{Chezy}	13.13	16.37	11.74
k_s after McGahey	0.30	0.24	0.24
k_s after Bettes	1.86	1.56	1.14

Table 5.3: Estimated roughness coefficients for all three field reaches

These coefficients are also listed in Table 5.3. Regarding the roughness length, there are several suggestions in the literature on how to estimate k_s directly either from n_{Ma} or from the bed grain size distribution. McGahey and Samuels (2004) suggest an estimate of k_s using the first component of the n_{Ma} estimate as shown in Equation 5.6.

$$k_s = (\frac{n_1}{0.038})^6 \tag{5.6}$$

The bed grain size based estimations are all based on Charltons estimation, which is shown in Equation 5.7, see Bettess (1999).

$$k_s = 3 * D_{84} \tag{5.7}$$

Estimates for k_s from Equation 5.6 and 5.7 are shown in Table 5.3. The roughness length cannot be larger than the river depth. For the calibration, a range of values were chosen around the estimates in Table 5.3. Table 5.4 lists the c_{Chezy} and k_s values used in the different calibration runs. The simulation runs with these roughness coefficients are later referred to for Chezy roughnes coefficients as c1 to c200 and for k_s as w for White-Colebrook roughness coefficients with k_s in cm, namely w200 to w1.

	Smithincott	**Stonyford**	**Rewe**	**run is referred to as**
c_{Chezy}	1, 2.4, 5, 10, 14, 20 ,40, 80, 200	5, 10, 12, 15, 20, 30, 40, 80, 100	5, 10, 15, 20 , 30, 40, 100	c1 to c200
k_s in cm for White-Colebrook	200, 150, 100, 30, 10, 5, 1	150, 100, 30, 10, 5, 1	100, 30, 10, 5, 1	w200 to w1

Table 5.4: Bed range of roughness coefficient values chosen for the calibration runs of the Delft3D hydrodynamic models for one set of calibration runs with C_{Chezy} and one set with k_s for each of the study reaches.

5.3.3 Calibration statistics

There are no standardised procedures to calibrate a hydrodynamic model. Many studies use single indices like the Nash-Sutcliffe Index (e.g. Montanari et al., 2009). Other studies use multi-step methods like the GLUE method (General Likelihood Uncertainty Estimation) including indices like the Nash-Sutcliffe index in their more elaborate likelihood estimation (e.g. Hostache et al., 2009). The GLUE method is especially useful when evaluating the optimum of several calibration parameters using weighted likelihood estimates (which are described and applied e.g. in Beven and Binley, 1992; Ratto et al., 2001). Some methods are even more complex, like the computation of sensitivity indices shown in Saltelli (2002). For the roughness calibration of the hydrodynamic models with one calibration parameter - the bed roughness - a less complex approach is favoured. Moriasi et al. (2007) suggest in their paper on calibration of watershed models the use of a combination of graphical and statistical model evaluations. They even define some thresholds for the single indices but generally conclude that best performance is achieved when most indices approach their optimum. Davies and Fearn (2006) also suggest the use of simple methods and focus on relative error and bias computation, since these are easy to understand and are less sensitive to datum points and the magnitude of values. Accordingly, the calibration will be based on simple statistical methods. The best

model performance is defined as the point where ideally all statistical indices reach their optimum (or at least are close to their optimum). The following list outlines the statistical methods used in the hydrodynamic model calibration. The statistical methods are used to compare the model output data from simulations with different bed roughness coefficients values to the observed field data. Some of the statistical methods were already introduced in Chapter 3, these methods will only be listed and are not further elaborated here.

The Pearson coefficient the linear regression model (LM) were already introduced as a means to compare the quality of accordance between observed and simulated parameters.

Reduced Major Axis (RMA): In addition to the linear regression, the RMA is identified. This is a method frequently used, when variables on the x ad y axis are both prone to error and are expected to form a symmetric relationship Carling (2009). It is an especially recommended method if the parameter of the relationship are of interest Leduc (1987). The RMA is located between the two linear regression lines. The slope of the RMA is determined by the standard deviation of the values on the y-axis divided by the standard deviation of the values on the x-axis as shown in Equations 5.8 and 5.9 with σ_x being the standard deviation of the values on the x-axis, n the number of samples, x values plotted on the x-axis with $\bar{x}$ as their predictand (according y are values on the y-axis and can be used to calculate σ_y). a is the slope of the RMA (Equation 5.9) and b the intercept (Equation 5.10).

$$\sigma_x = \sqrt{\frac{1}{n} * \sum_{i=1}^{n} (x_i - \bar{x})} \tag{5.8}$$

$$a = \frac{\sigma_y}{\sigma_x} \tag{5.9}$$

$$b = \bar{y} - a * \bar{x} \tag{5.10}$$

RMA plots: As a visual representation of the linear models and the RMA, a plot of the observed versus the modelled data is fitted with three regression lines: First, the linear regression line of the modelled versus the observed data, then the inverted linear regression line of the observed versus the modelled data, and third, the regression line of the RMA.

Mean Standard Error (MSE) and Squared Mean Standard Error (SMSE) were as well already introduced in Section 3.3.1 and are repeated in the following Equations:

$$MSE = \sum_{i=1}^{n} (x_i^{obs} - x_i^{mod}) \frac{1}{n} \tag{5.11}$$

$$SMSE = \sum_{i=1}^{n} (x_i^{obs} - x_i^{mod})^2 \frac{1}{n} \tag{5.12}$$

Percent Bias (PBIAS): is a similar statistic index to the standard error but set in relation to the order of magnitude of the parameter. It is the expression of the error as a percentage of the observed value. A positive value suggests underestimation by the model and a negative value suggests overestimation in percent.

$$PBIAS = \frac{\sum_{i=1}^{n} (x_i^{obs} - y_i^{mod}) * 100}{\sum_{i=1}^{n} y_i^{obs}} \tag{5.13}$$

The Nash-Sutcliffe index (NS) is a measure for model efficiency and compares the correlation of modelled and observed data with the 1:1-line. It is discussed in detail for hydrological models by McCuen et al. (2006) and Jain and Sudheer (2008). It is a normalised statistic and stating the magnitude of noise in the data. Values range from 1 to $-\infty$. The calculation of NS is shown in Equation 5.14.

$$NS = 1 - \frac{\sum_{i=1}^{t} (obs_i - mod_i)^2}{\sum_{i=1}^{t} (obs_i - \bar{obs})^2} \tag{5.14}$$

A value of 1 suggests a perfect fit. Continuously more negative values suggests a continuously poorer agreement between the model and the observation. Jain and

Sudheer (2008) believe that the Nash-Sutcliffe index is not an adequate tool to test the performance of a model (at least not on its own). McCuen et al. (2006) conclude that it is a valuable index but that under certain circumstances (e.g. in the presence of extreme outliers or a systematic offset) it does not produce sensible guidelines. Nevertheless it is a widely used index for example by Montanari et al. (2009). In this work, the Nash-Sutcliffe index is only discussed as an addition to the statistical indices outlined above.

5.3.4 Interpolation of the model output

Only modelled parameters matching the collected field data are relevant for the calibration, which are in this case: water level information, water depth and velocity (vectors and magnitude). Data from the simulations can be exported for all grid cells at one point in time resulting in up to 80,000 data points. In comparison, on average 100 field measurements of depth and velocity were gathered in each study reach. Furthermore, model grid points with hydrodynamic information are not identical to positions of measurements in the field. To compare these two datasets, model records have to be interpolated for the positions with available field data. The method used here is a weighted nearest neighbour interpolation. This is carried out using the R function '*pick.from.points*', which is shown in Equation 5.15, see also (Brenning, 2011).

$$dis = \sum_{i=1}^{n} dis_i * \frac{\frac{1}{\triangle_i}}{\sum_{j=1}^{n} \frac{1}{\triangle_i}} \tag{5.15}$$

Where dis is the interpolated model value at the measurement point location, dis_i is the model output location i, which is separated from the measurement location by the distance $\triangle_i$ and n the number of points for interpolation included in a given radius. With a pick radius of 0.5 m a minimum of four points are included in the interpolation. For all scalar data (water level, water depths, velocity magnitude) this interpolation is sufficient. For vector data (down- and cross-stream velocity), a further adaption is necessary. All velocity field measurements were collected along a straight transect,

being orthogonal to the main flow direction, where the u-axis is in transect direction (from the left to the right bank) and the v-axis is the downstream main flow direction (referred to as u- and v-velocity). Each transect lies at a different angle to the geographic east (here x-axis) and north (here y-axis), which are used as the coordinate system in the Delft3D records. For the comparison of the downstream and cross-stream velocity components, the Delft3D results need to be rotated to fit the u- and v-velocities measured in the field. All Delft3D velocity vector data was rotated separately for each transect from the x- and y-velocity vectors to u- and v-velocity vectors system.

5.3.5 Calibration results

Tables including a multitude of calibration runs and calibration statistics are confusing and hard to interpret. Therefore, the following discussion is based on a graphical representation of the calibration statistics. Graphs were developed combining plots for different calibration statistics for each of the calibration parameters for all runs of roughness coefficient values. This was done separately for c_{Chezy} and k_s. The graphs plot statistical indices in the y-axis for all calibration runs with different bed roughness coefficient values along the x-axis. Statistical indices referring to the left y-axis are plotted in such a way that their ideal value plots are in the centre of the graph. Statistical indices referring to the right y-axis are plotted with their ideal value at the top of the graph. The Nash-Sutcliffe index and the SMSE are used as accessory statistics only mentioned in the discussion. In order to highlight possible systematic deviations over the course of the reach, further parameters are investigated. These are the water level as a longitudinal profile and the water depth split into cross-sections. These are plotted for best fitting roughness parameter as well as extreme rough and extreme smooth runs with c_{Chezy} and k_s coefficients in one plot for each reach. Finally, for a detailed analysis of the results of the best fitting roughness coefficients, RMA plots for water depth and downstream velocity are presented.

Calibration of the Smithincott study reach: Figure 5.10 shows the graphical representation of the statistical evaluation of the calibration runs for the Smithincott study reach with c_{Chezy} values. It consists of five sub-plots, each showing the statistical indices for one calibration parameter. Different calibration runs line up along the x-axis from runs with a high bed roughness at the left to runs with a smooth bed roughness at the right.

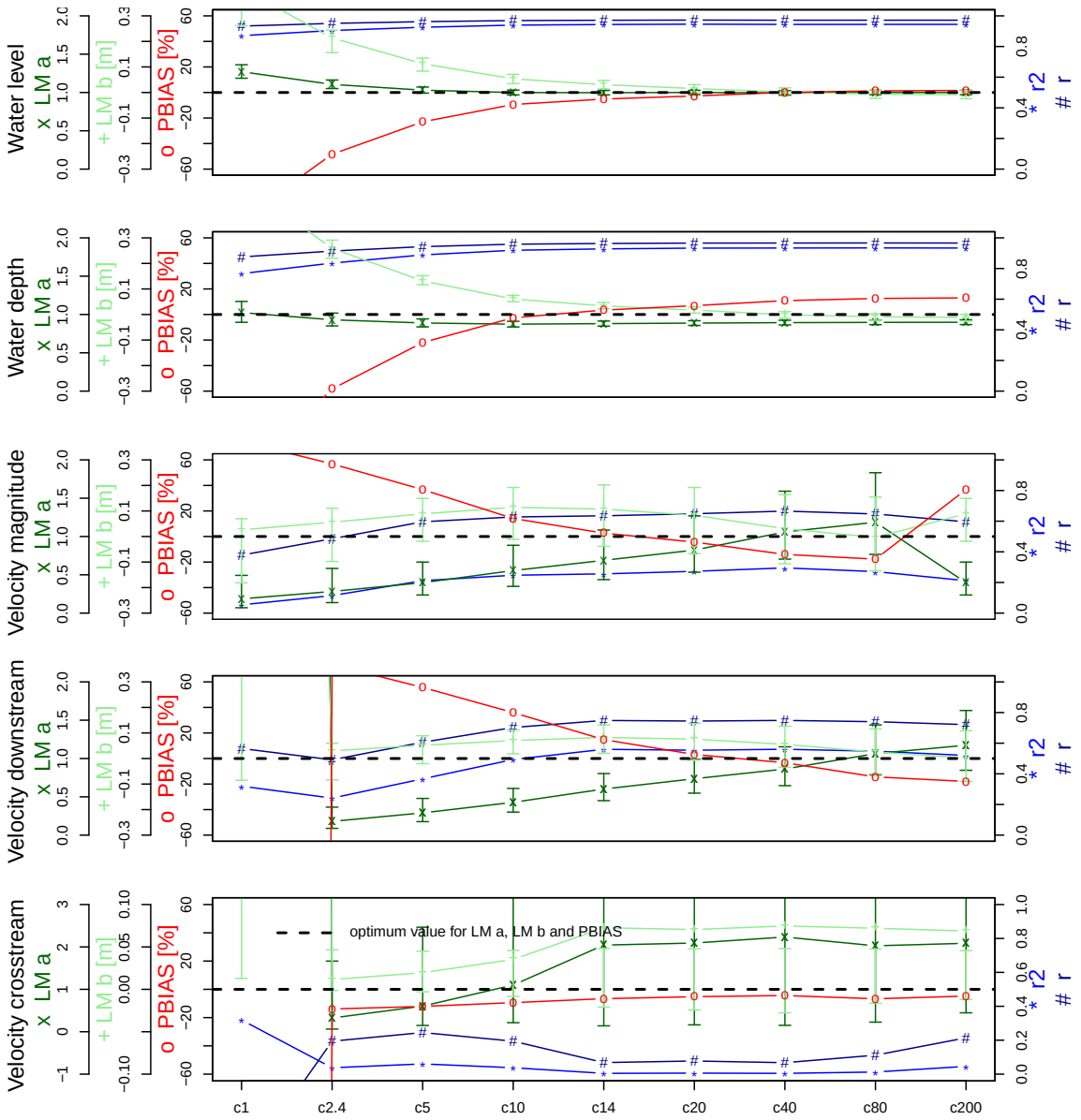

Figure 5.10: Smithincott study reach, statistical evaluation of a set of calibration runs with Chezy roughness coefficient , LMa = the slope of the RMA, LMb = intercept of the RMA, PBIAS = percentage bias, r = Pearson correlation coefficient and r^2 = coefficient of determination. For example, c1: calibration run with c_{Chezy} = 1, c200: calibration run with c_{Chezy} = 200. The datum of the water level is the water level at the downstream end of the reach.

The line-up of the statistical indices for the different calibrations runs forms a curve. The two sub-plots at the top - water level and water depth - give a very clear indication that calibration runs with smoother roughness coefficients generate a better fit with the observed data. The curves for all indices for water level and water depth levels off close to the ideal value towards smoother calibration runs. For runs

with smoother values than c10, there is no significant change. This suggests that for a smooth c_{Chezy}, the roughness is controlled mainly by grid roughness and not bed roughness, which is associated with the DEM. For the three velocity calibrations, the curves of the indices are not that clear. For all velocity calibrations, the r and r^2 values suggest a best fit between c20 and c40. This finding is supported by the bias calculation, which reaches zero for approximately the same calibration run. For the velocity magnitude and the downstream velocity calibrations, optimum LMa and LMb and smallest PBIAS are achieved for c40. The cross-stream velocity is associated with uncertainties. The statistical indices for this parameter generally suggest a poor fit. Regarding the Nash-Sutcliffe index for water depth, it reaches its highest value of 0.86 at c20 and 0.85 for c40. The highest Nash-Sutcliffe coefficients for a downstream velocity is 0.54 at c40. SMRE for the water depth is small with less than 2 cm for c40. The smallest error for downstream velocity calibration with -0.01 ms^{-1} was found at c20 and also c40. Concluding, a c_{Chezy} of c40 appears to be the calibration run with the optimum output.

The statistical evaluation of the White-Colebrook runs are shown in Figure 5.11. r and r^2 show that water level and water depth are insensitive to the bed roughness coefficient value. The slope and intercept of the RMA and PBIAS show a flattening of the index curves close to the optimum for runs with a bed roughness coefficient smoother than w10. The calibration of the velocity magnitude and the downstream velocity show a similar trend with optimum results for w15 and w10. For velocity magnitude and downstream velocity, RMA, LMa and LMb suggest w10 as the optimum but PBIAS reaches zero for rougher calibration runs around w30. The cross-stream velocity results are again difficult to interpret. On the one hand, the overall error is generally less than 10 %, which is good. On the other hand, r, r^2, LMa and LMb suggest a better agreement between model and field measurements for both very rough and very smooth run.

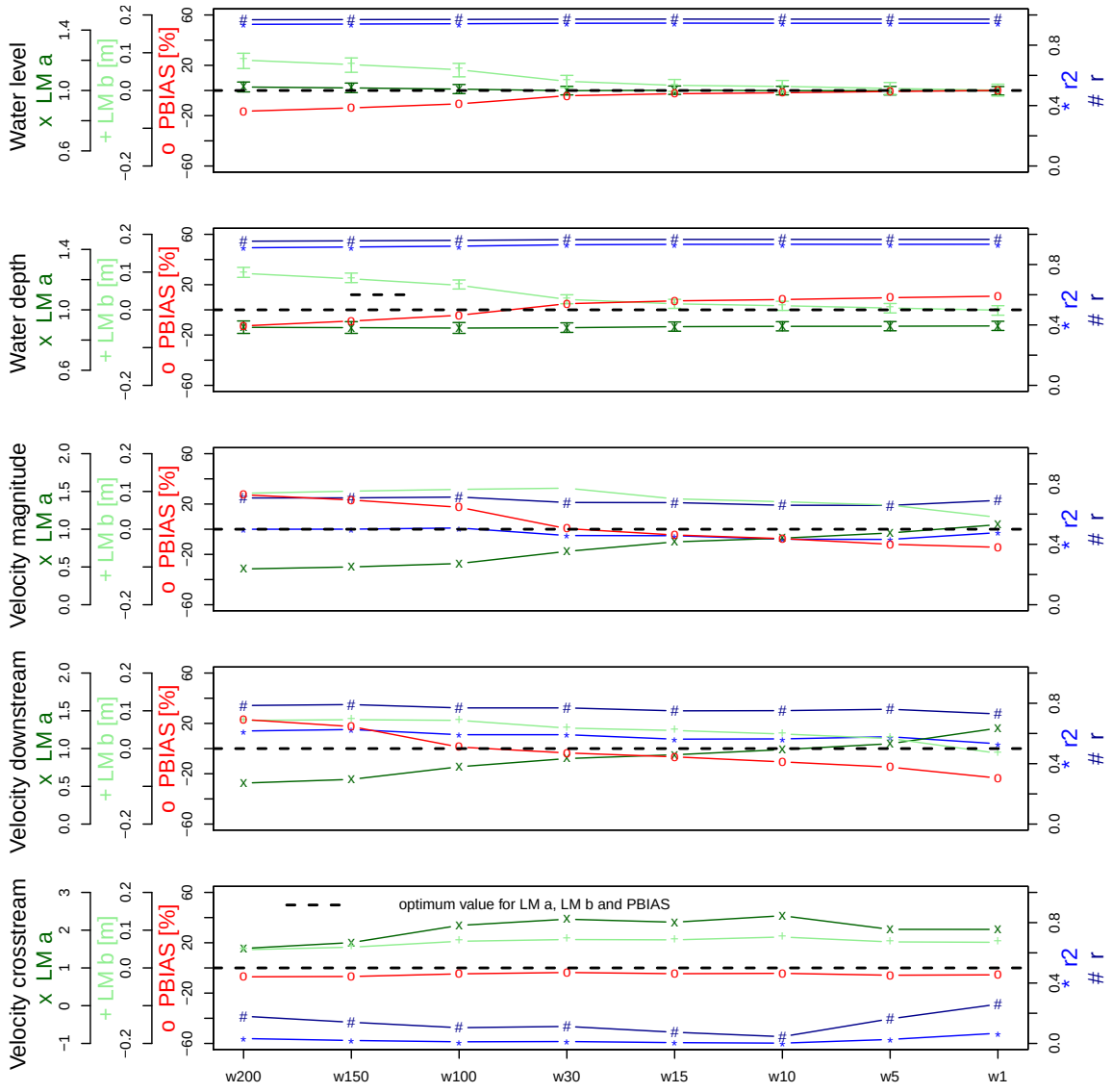

Figure 5.11: Smithincott study reach, statistical evaluation of a set of calibration runs with White-Colebrook roughness coefficient , LMa = the slope of the RMA, LMb = intercept of the RMA, PBIAS = percentage bias, r = Pearson correlation coefficient and r^2 = coefficient of determination. For example, w1: calibration run with k_s = 1 cm, w10: calibration run with k_s = 10 cm. The datum of the water level is the water level at the downstream end of the reach.

The Nash-Sutcliffe index reaches its maximum of 0.86 at w15 for water depth and with 0.53 at w10 for downstream velocity. Errors for w15 are small with the SMSE for water depth being 0.02 m and for downstream velocity 0.02 ms^{-2}. Concluding the above discussion, a value of w15 is seen as the optimum fitting roughness. In order to pick up on any longitudial systematic bias, Figure 5.12a at the end of the chap-

ter compares six selected modelled and the observed water level and water depth. The selected model runs are the two runs with the best performing bed roughness coefficients (c40 and w15) and each the roughest and the smoothest run for both specifications of the bed roughness coefficient (c2.4, c40 and c200 and w200, w15 and w1). Longitudial water level data for Smithincott were not available. Therefore, Figure 5.12a shows the observed and modelled water level for each of the survey cross-sections. The cross-section two is split into two channels around an island and therefore it is represented by two water levels. Overall, no obvious downstream bias can be detected. The water level for optimum roughness values (c40 and w15) show maximum errors of less than 2 cm. For cross-section five, the modelled data is underestimating and for cross-section two b, the modelled data is overestimating the water level. In Figure 5.12b, a similar result can be noted for water depth. Only at cross-section one modelled depth for c40 and w15 are systematically lower and for cross-section five higher than the observed values. The maximum bias is small with less than 5 cm. To complete the calibration discussion for the reach in Smithincott, Figure 5.13 shows scatterplots for water depth and downstream velocity with modelled versus observed linear regression lines in green and the reciprocal linear regression line of observed versus modelled data in blue. The RMA is plotted in red and the 1:1 line in black. The fit for water depth data is very good. The downstream velocity shows considerable noise, which was not as obvious in plot 5.10 and 5.11. This suggests that although the overall trend in predicting velocity magnitude is acceptable, the prediction quality of the singel locations is weak. Comparing graph 5.13a with 5.13b and 5.13c with 5.13d shows that the differences in fit between runs with c_{Chezy} and $c_{White-Colebrook}$ optimum bed roughness coefficients are small.

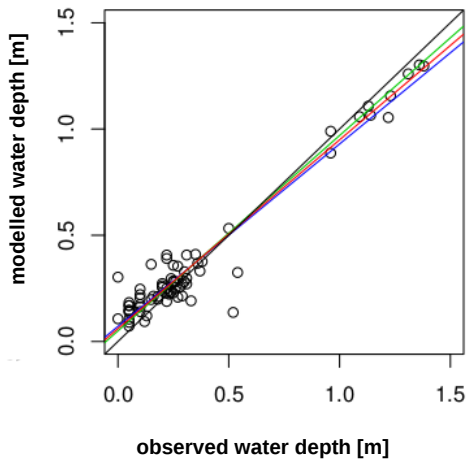

(a) c40

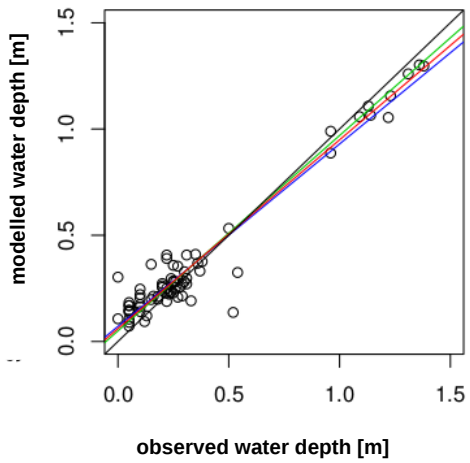

(b) w15

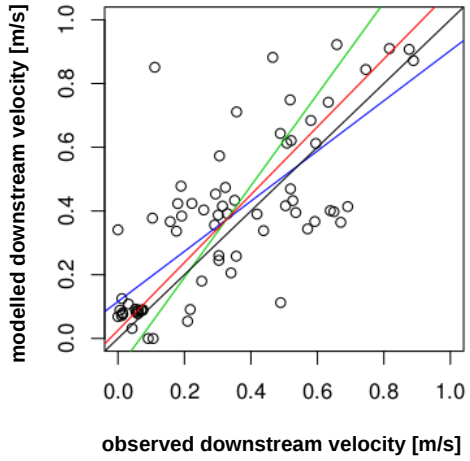

(c) c40

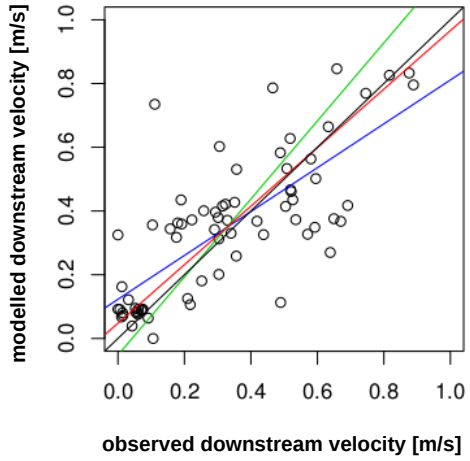

(d) w15

Figure 5.13: Smithincott study reach, RMA plots for water depth and downstream velocity for both best fitting roughness coefficients c40 and w15, green line = lm modelled versus observed, blue line = lm observed versus modelled , red line = RMA and black line = 1:1 line.

Calibration of the Stonyford study reach: Figure 5.14 shows the graphical representation of the statistical indices for the calibration runs with c_{Chezy} for the Stonyford study reach. For water level and water depth, r and r^2 are generally high and insensitive to variations of the roughness coefficient. Similar behaviour, but for lower values for r and r^2 can be seen for the three velocity specifications.

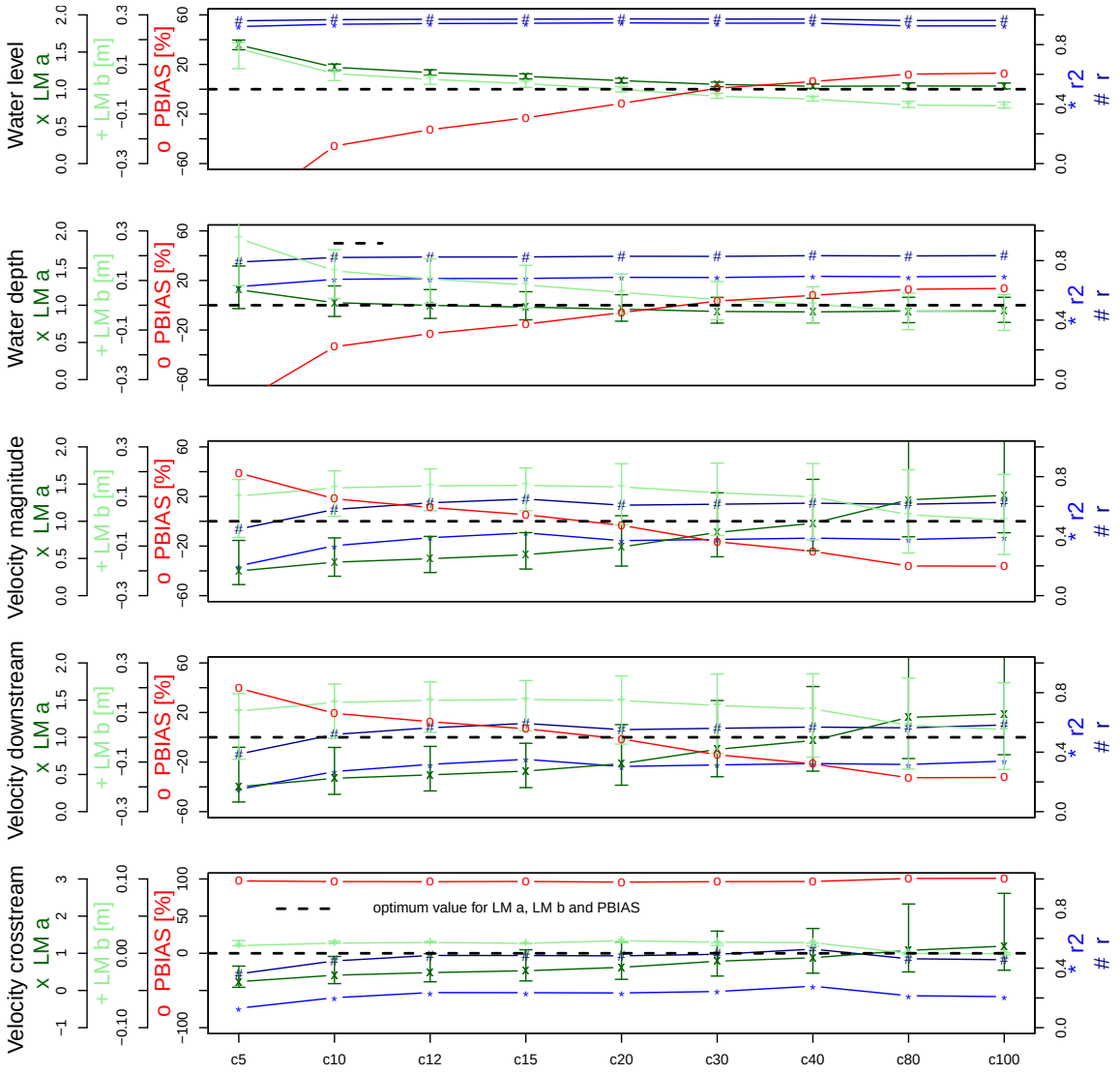

Figure 5.14: Stonyford study reach, statistical evaluation of a set of calibration runs with Chezy roughness coefficient , LMa = the slope of the RMA, LMb = intercept of the RMA, PBIAS = percentage bias, r = Pearson correlation coefficient and r^2 = coefficient of determination. For example c1: calibration run with c_{Chezy} = 1, c200 = calibration run with c_{Chezy} = 200. The datum of the water level is the water level at the downstream end of the reach.

LMa and LMb curves for the water level and water depth reach the best results for smooth coefficients, similar to the Smithincott study reach. LMa and LMb cross their ideal value between c30 and c40 for all calibration parameters (apart from cross-stream velocity), suggesting this as the optimum value. PBIAS reaches zero for rougher calibration runs of c20. In order to make a descision, the additional indices are consulted. The Nash-Sutcliffe index shows an optimum for water depth calibra-

tion of 0.54 for c30 and c40 with a decline for both smoother and rougher coefficients. The SMSE for water depth is smallest at c30 with a value of 0.012 m^2. Therefore, c30 is assumed as the optimum Chezy bed roughness coefficient calibration run for Stonyford.

Figure 5.15 shows the graphical representation of the statistical indices for the White-Colebrook simulations at the Stonyford reach. Again, r and r^2 values are not sensitive to changes in the roughness coefficient for all parameters.

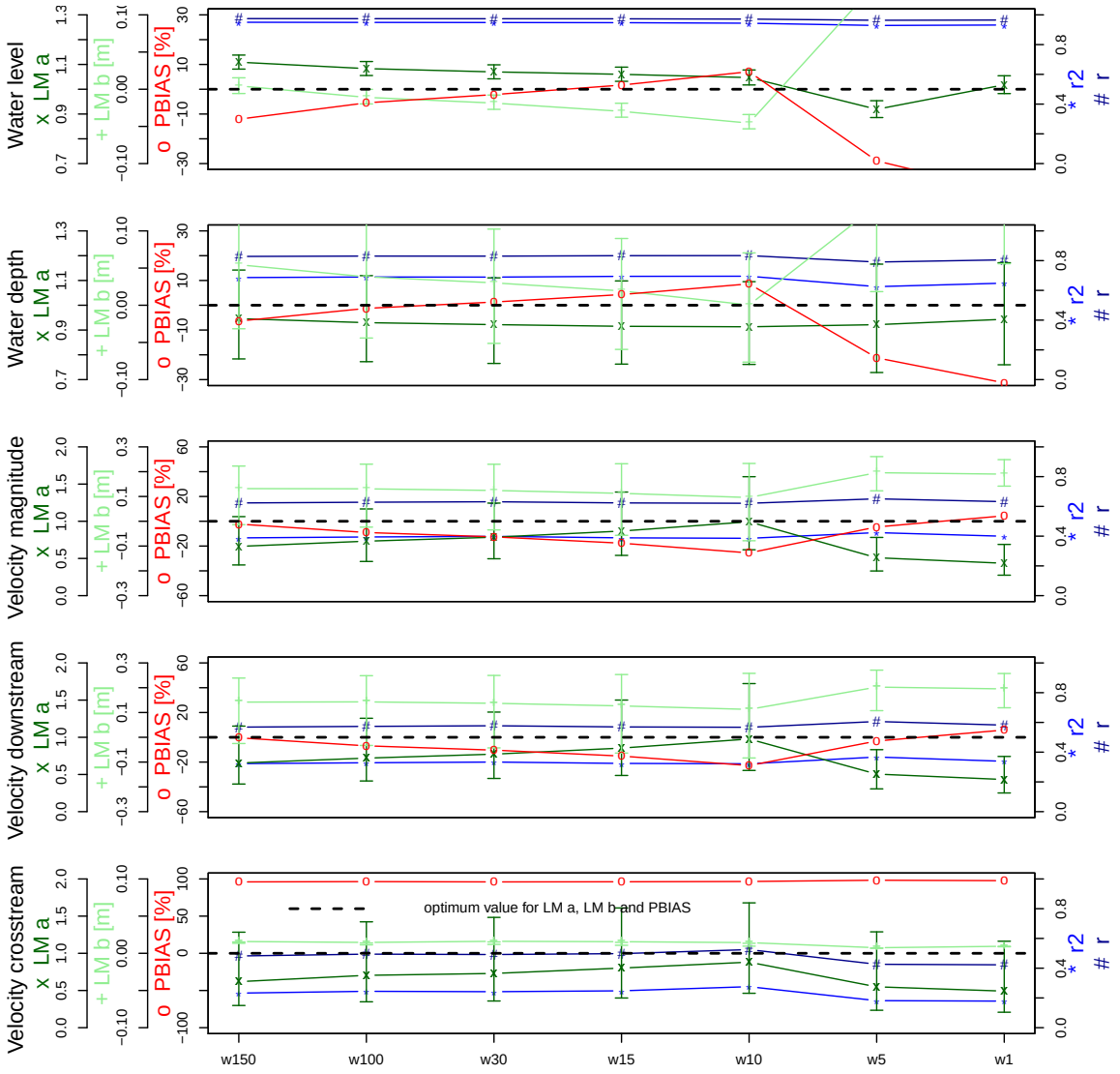

Figure 5.15: Stonyford study reach, statistical evaluation of a set of calibration runs with White-Colebrook roughness coefficient , LMa = the slope of the RMA, LMb = intercept of the RMA, PBIAS = percentage bias, r = Pearson correlation coefficient and r^2 = coefficient of determination. For example, w1: calibration run with k_s = 1 cm, w10: calibration run with k_s = 10 cm. The datum of the water level is the water level at the downstream end of the reach.

Other statistical indices for runs smoother than w10 are indicating a very poor accordance of modelled and observed parameters. LMa, LMb and PBIAS curves for water level, water depth and all three velocities calibrations show a sharp change in trend at w10. This is in contrast to Smithincott, where smoother runs performed consistently well. Additional calibration parameters also suggest an optimum for w10 or w5, with the best Nash-Sutcliffe results for a water depth of 0.55 m at w5 and

0.54 m at w10. The smallest SMSE is 0.08 m^2 at w10 and w15. Therefore, w10 is brought forward as the best performing calibration run. Figure 5.16 at the end of the chapter shows observed parameters and parameters resulting from runs with the optimum as well as extreme bed roughness coefficients (c10, c30, c100 and w100, w10, w5). Figure 5.16a shows the longitudinal profile for the Stonyford study reach with an approximately 2 m distance between points for observed and modelled water levels. The observed data comprises some clear outliers (point ID 36 and 44). If these are ignored, the general fit for c30 and w10 is very good. Figure 5.16b shows the observed and modelled depth for all study cross-sections in the reach. The observed and modelled data differ for some positions in cross-section 1, 4 and 9, but there is no evidence for a systematic bias. In general, the modelled depth in c30 and w10 accords well with the observed data. Regarding the run with the smallest k_s (w1), the longitudinal water level data shows an overestimation of the water level at the upstream end. Finally, for calibration results in the Stonyford reach, Figure 5.17 shows scatterplots superimposed by the regression lines for both linear models, the RMA and the 1:1 line for c30 and w10. The plot for water depth shows very good results. However, similar to te results in Smithincott, the downstream velocity plot shows considerable noise for all data points. Still, the RMA for downstream velocity is both for c30 and w10 very close to the 1:1 line. Again this suggests that mean velocity in the reach is predicted correctly, but local velocities are connected with considerately high errors.

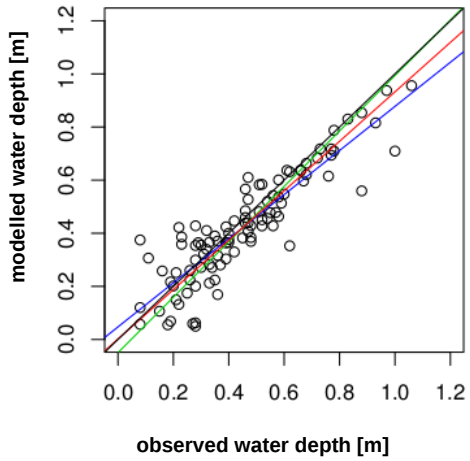

(a) c30

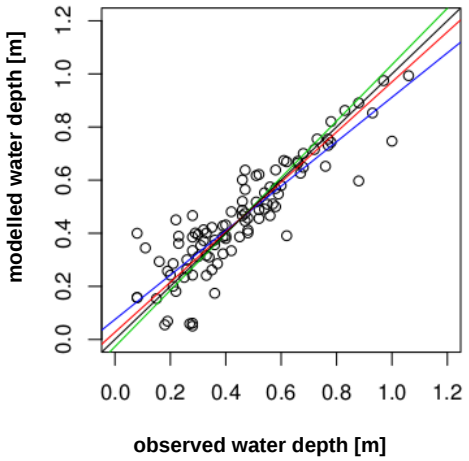

(b) w10

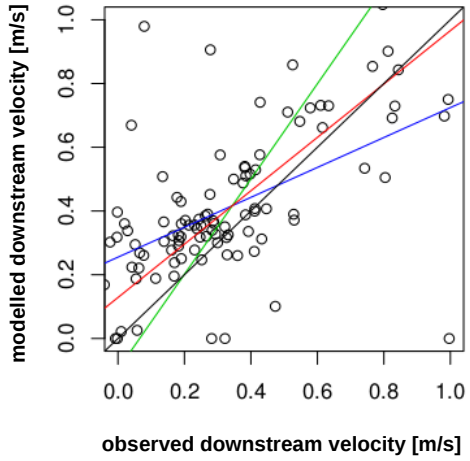

(c) c30

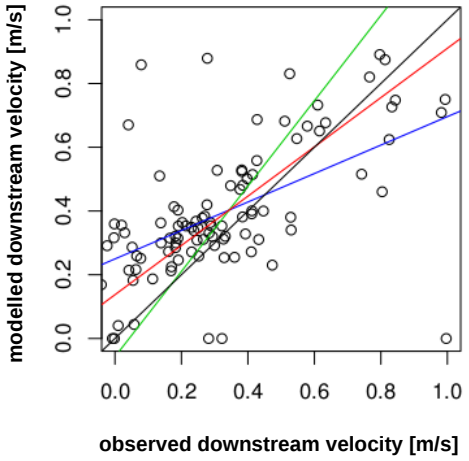

(d) w10

Figure 5.17: Stonyford study reach, RMA plots for water depth and downstream velocity for both best fitting roughness coefficients c30 and w10, green line = lm modelled versus observed, blue line = lm observed versus modelled , red line = RMA and black line = 1:1 line.

Calibration of the Rewe study reach: Figure 5.18 shows a graphical representation of statistical indices for calibration runs with the c_{Chezy} roughness for water level, water depth and the three velocities for the study reach at Rewe. For water level and depth, all calibration indices are insensitive to changes in the bed roughness. Inferior values are recorded only for the very rough c5 . For velocity magnitude and downstream velocity, the statistical indices - if regarded as a curve - approach the

optimum around c15 and runs with a higher bed roughness. Despite the lack of a clear optimum in the statistical indices' curves, the magnitude of the indices are similar to the optimum performance of the other two study reaches.

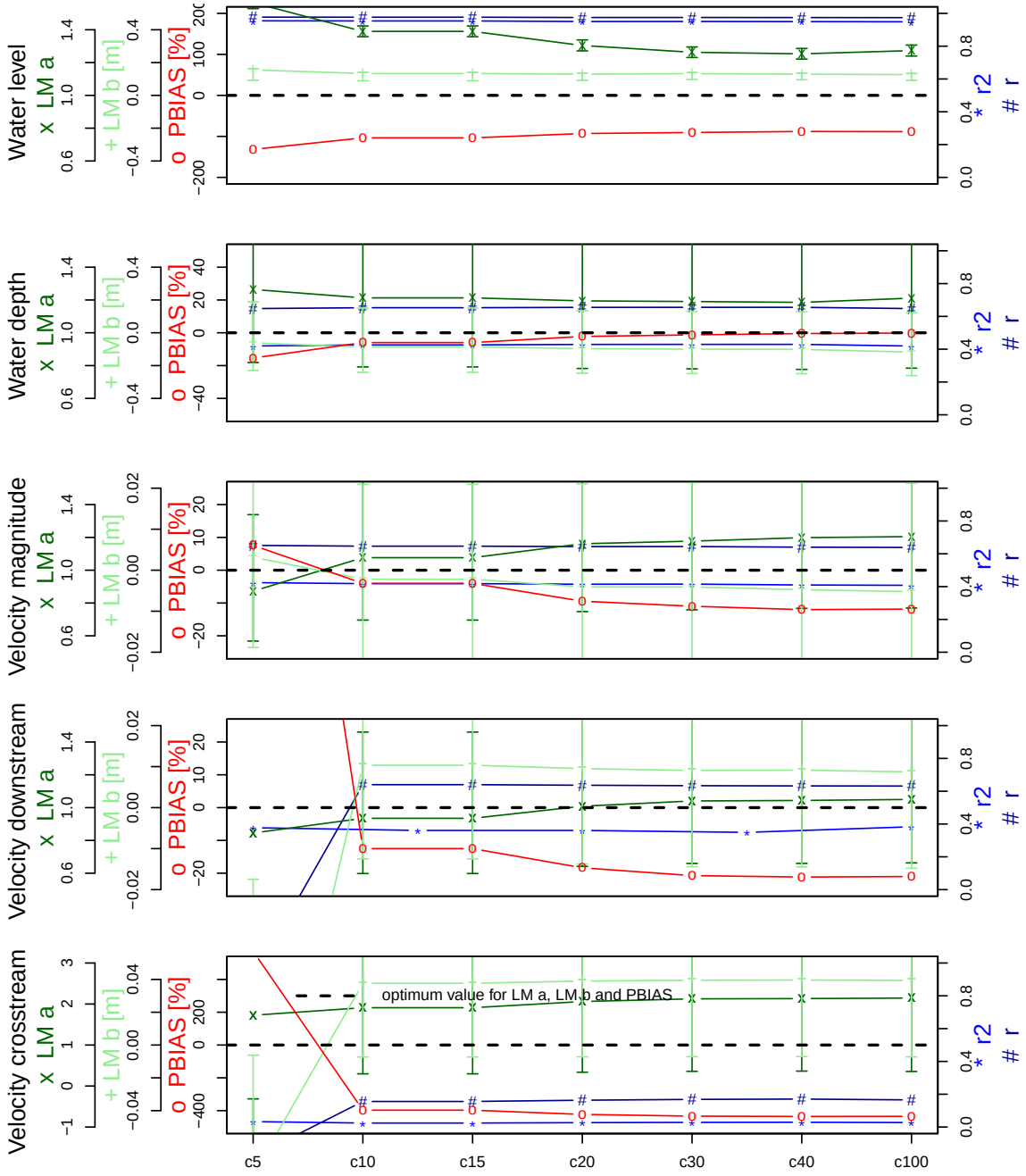

Figure 5.18: Rewe study reach, statistical evaluation of a set of calibration runs with Chezy roughness coefficient , LMa = the slope of the RMA, LMb = intercept of the RMA, PBIAS = percentage bias, r = Pearson correlation coefficient and r^2 = coefficient of determination. For example, c1: calibration run with c_{Chezy} = 1, c200: calibration run with c_{Chezy} = 200. The datum of the water level is the water level at the downstream end of the reach.

For example, r and r^2 for water level are close to 1 and PBIAS for water depth is approximately zero for all calibration runs. The only indication for an optimum is the change in trend at c10. Overall, this suggests a limited influence of the bed roughness compared to the other study reaches.

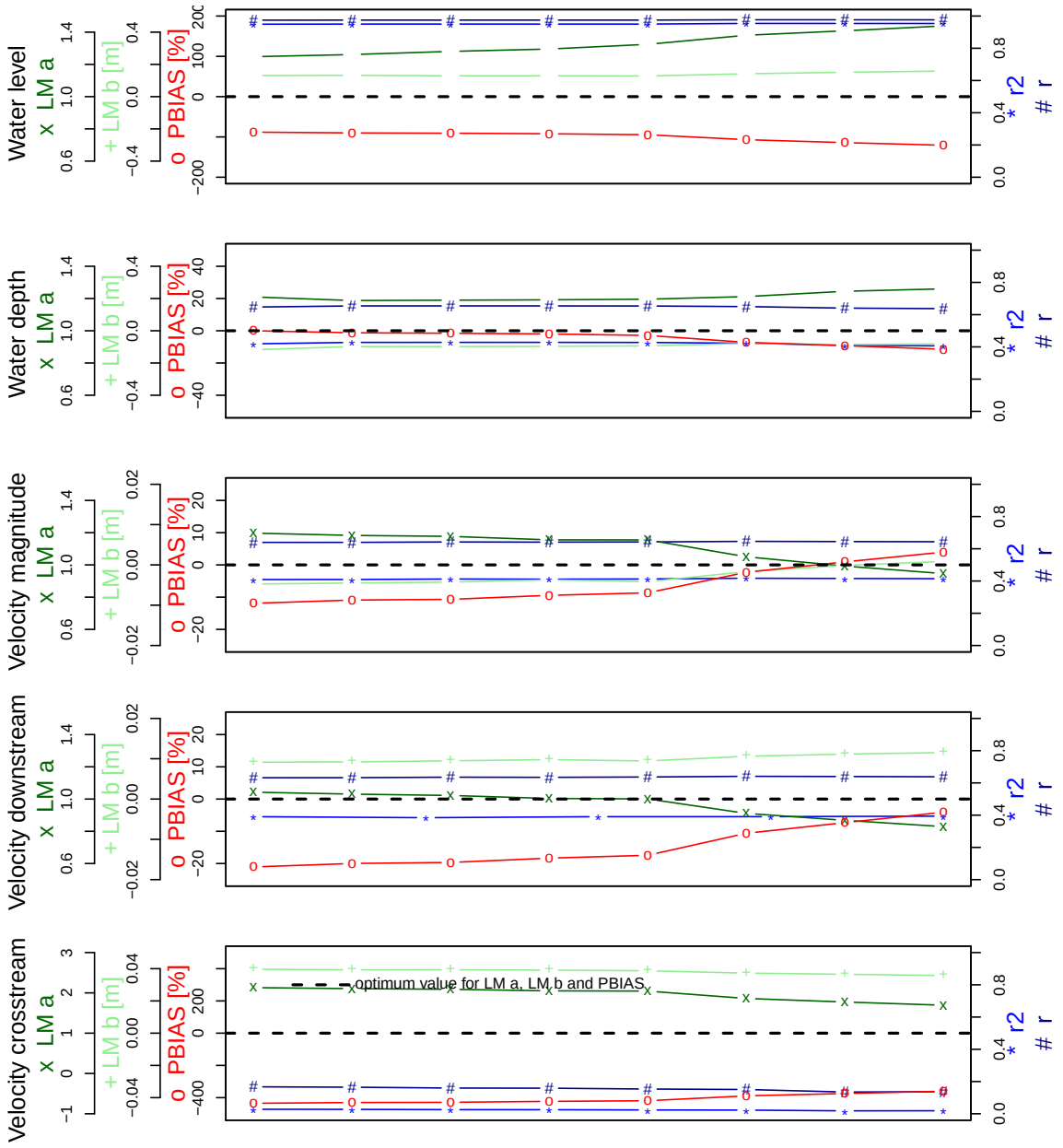

Figure 5.19: Rewe study reach, statistical evaluation of a set of calibration runs with White-Colebrook roughness coefficient , LMa = the slope of the RMA, LMb = intercept of the RMA, PBIAS = percentage bias, r = Pearson correlation coefficient and r^2 = coefficient of determination. For example, w1: calibration run with k_s = 1 cm, w10: calibration run with k_s = 10 cm. The datum of the water level is the water level at the downstream end of the reach.

The cause for this is probably the comparatively slow and deep flow. For the White-Colebrook coefficient, the statistical indices are also insensitive to changes in the bed roughness coefficient for water level and water depth, see Figure 5.19. In the case of the velocity calibration, indices approach an optimum for w10 and runs with smoother values. Therefore, w10 is defined as the best performing calibration run.

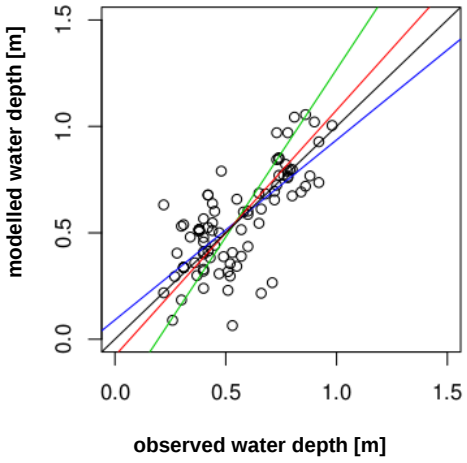

(a) c40

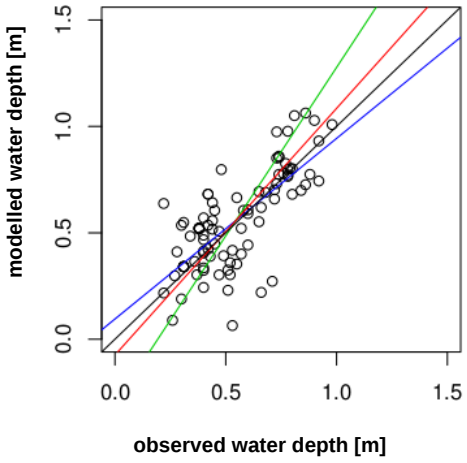

(b) w10

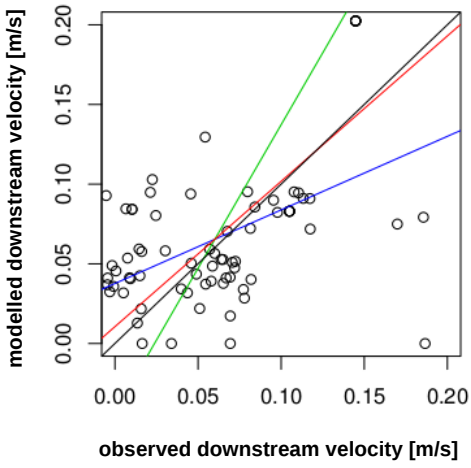

(c) c40

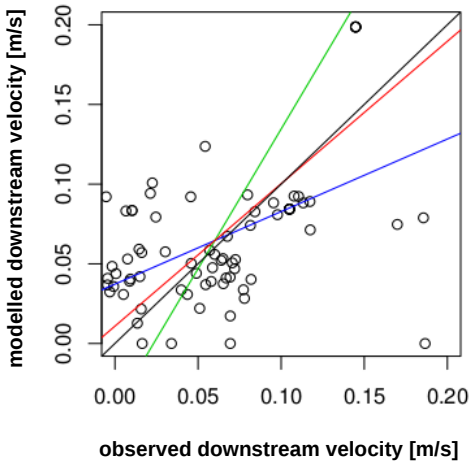

(d) w10

Figure 5.21: Rewe study reach, RMA plots for water depth and downstream velocity for both best fitting roughness coefficients c40 and w15, green line = lm modeled versus observed, blue line = lm observed versus modeled , red line = RMA and black line = 1:1 line.

	c_{Chezy}	k_s (White-Colebrook)
Smithincott	40	15
Stonyford	30	10
Rewe	40	10

Table 5.5: Optimum C_{Chezy} and k_s for White-Colebrook roughness coefficient for the three study reaches as resulting from the above bed roughness coefficient calibrations.

Figure 5.21 offers scatterplots of water depth and downstream velocity for runs with c40 and w10 and confirms their similar performance to the other two study reaches. Although data is scattered broadly on both sides of the 1:1 line, also for water depth, the regression lines of the linear models and especially the RMA plots close to the 1:1 line. One reason for the weaker performance of the hydrodynamic model in the Rewe reach compared to the other two study reaches is the smaller range of all calibration parameters. The Rewe study reach experiences the smallest water level drop of only 25 cm (compared to 99 and 59 cm in Smithincott and Stonyford) and the smallest discharge for the calibration conditions of 0.25 m^3 (see Table 5.2). In a smaller range of parameter values, errors of the same magnitude have a stronger influence on calibration statistics. Further, in a study reach with a low slope, bed roughness is of minor importance and consequently changes of bed roughness coefficient values are not resulting in different hydrodynamic behaviour.

5.4 Conclusion

This chapter showed in detail the **generation of high accuracy DEMs** for the three study field reaches. It explains the conversion of field point elevation data into a complete surface representation. The conversion was achieved with the triangulation method of the ArcMap 3D analyst component of the geo-spatial software ArcGIS. This procedure included the use of additional breaklines. These breaklines are an effective tool to deal with areas of weak data cover, especially for the application on

linear structures, like the flow channel edges of the streams.

The resulting DEMs were applied as the source for the geometry and bathimetry information in the hydrodynamic simulations. The **hydrodynamic models were simulated with the software Delft3D**, more exactly its FLOW module. The physical, numerical and output related parameters necessary for a model definition file were discussed. Simulations were set up to recreate the conditions during the calibration measurements. In the hydrodynamic model, these were specified as the conditions at the upper (inlet) and lower (outlet) boundary, i.e. the discharge at the inlet and water level at the outlet of the model reach during calibration conditions.

The hydrodynamic models were calibrated to establish **the best performing roughness coefficient**. For this purpose, two different specifications of the bed roughness coefficient were chosen: c_{Chezy} with a constant coefficient for the whole reach and $c_{White-Colebrook}$ with a separate calculation of the bed roughness coefficient from k_s for each grid cell depending on local water depth. For the three study reaches and for both specifications of the bed roughness coefficient, up to nine calibration runs with a wide range of the values were executed.

The run with the best performing roughness coefficient for each reach and each roughness specification was determined with a suite of well-established statistical methods. These statistical indices all test the accordance of modelled and observed calibration parameters. The calibration parameters are as follows: water level, water depth, velocity magnitude, cross- and downstream velocity. The parameters were all measured in the field during the calibration conditions. Using a **suite of simple statistical indices was seen as superior to a complex sensitivity analysis** or the dependence on a typical performance index (for example the Nash-Sutcliff index) on its own. This made the evaluation easy to comprehend and avoided the proneness to errors of a single method. In order to avoid long tables for each of the indices, graphs were developed condensing the information of the different statistical indices. Each graph consisted of five sub-plots, one for each of the calibration parameters.

In each sub-plot, the statistical indices were values in the y-axis with each run as a point along the x-axis. The y-axis range was chosen is such a way, that the ideal value for the correlation coefficients (which is 1 for r and r^2) was plotted on the top and for all other indices the ideal value was located in the middle of the plot. Best performance was defined as the point where ideally all indices reach their optimum.

With this method, for all study reaches and both bed roughness coefficient specification, a best performing calibration run could be identified. For the Smithincott and Rewe study reach, smooth bed roughness coefficients performed consistently well and the roughest of these coefficients was chosen. The constant good performance of smooth bed roughness coefficient shows that for calibration conditions the overall roughness is dominated by the channel roughness. In the Stonyford study reach, the calibration indices showed both a deterioration for the very rough as well as the very smooth calibration runs. This means in Stonyford, with the coarsest bed grain size and the straightest channel, the bed roughness is more influential for the overall roughness compared to the other two reaches. From the calibration at hand, it is not possible to decide upon the superior functionality of c_{Chezy} and the depth dependent $c_{White-Colebrook}$. This can be accounted to the fact, that for the modelled study reaches, the channel roughness is more decisive than the bed roughness. This is visible in the uniform performance of a wide range of bed roughness coefficients.

The **hydrodynamic models developed here show a good fit for the water level of the study reaches**. However, the prediction of local velocity, the main parameter of interest for further sediment modelling, is connected to considerable variation around the 1:1 line. There are two areas of explanation for this. On the one hand, the model can only be a simplified representation of the real world. For example field velocity data is inevitable more variable than the grid cell averaged velocity given by the model and the DEMs, although based on high accuracy differential GPS data are set up with data points of half a river width distance in downstream direction, which is much more than the local bed structures influencing flow. On the other

hand Delft3D was executed with a 2D representation of flow. This is a comparatively simple representation of flow and might not be sufficient to calculate the complex processes influencing local flow distribution. Although the package Delft3D is not specifically evaluated, the benchmark EA paper Villanueva et al. (2008) reports similar problems with the prediction of velocity for a suite of 14 hydrodynamic model packages. These suggest, that an highly accurate flow velocity prediction, needs a) a complex process representation (3D) and ideally calibration information from more than just one discharge situation. Still, restricted to the available time frame and resources, a simulation of flood runoff with the above calibrated hydrodynamic models is seen as the best approach to estimate local velocities for a wide range of discharge conditions and the fact, that the scatter plot of modelled and observed local velocity is distributed evenly around the 1:1 line suggests a random, not systematic divergence. Therefore the results of simulations for high discharge will be used in the subsequent chapter as the flow information in the reach scale numerical model for suspended sediment deposition.

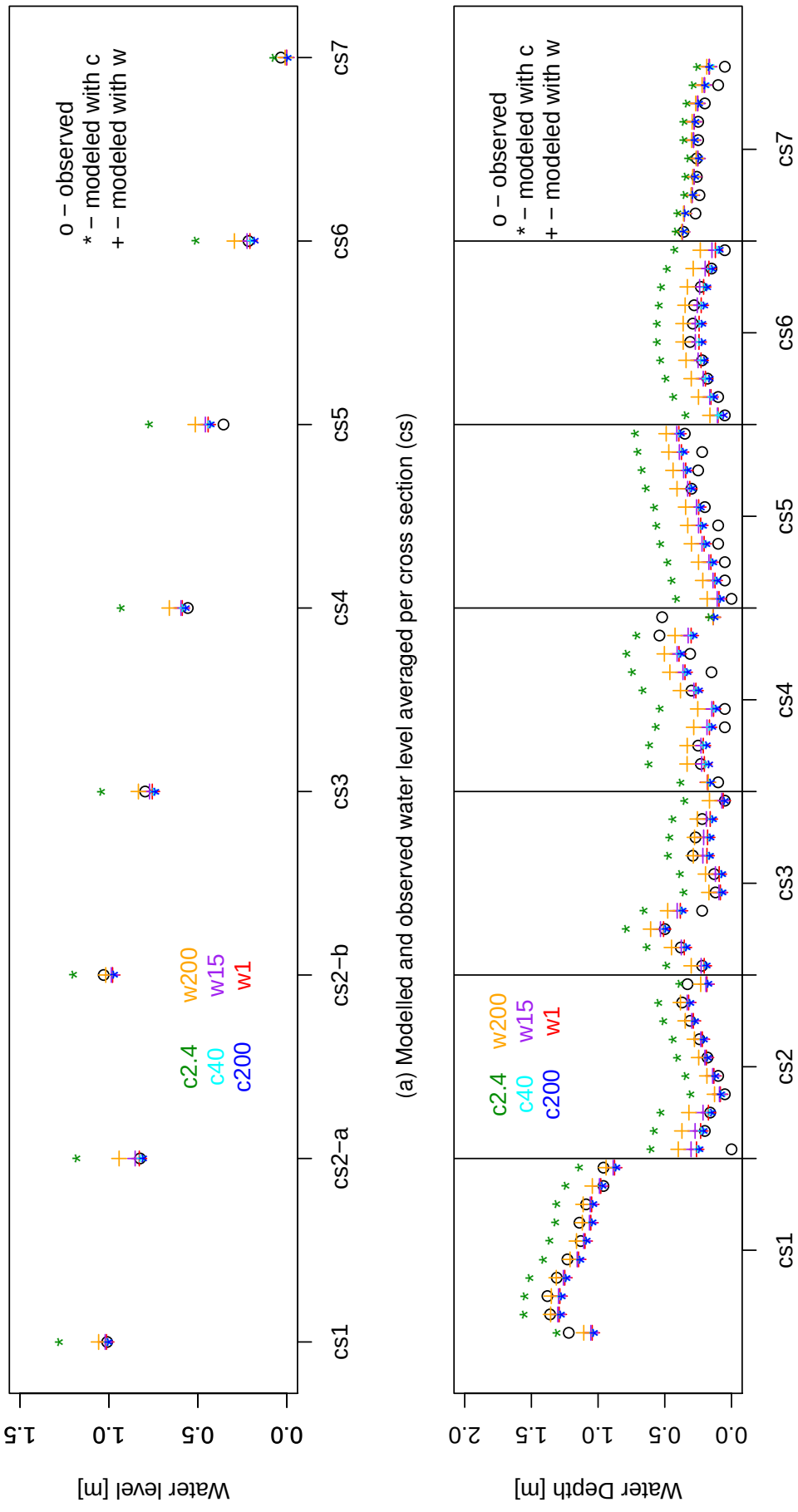

Figure 5.12: Smithincott study reach detailed view of modelled and observed water level and depth data.

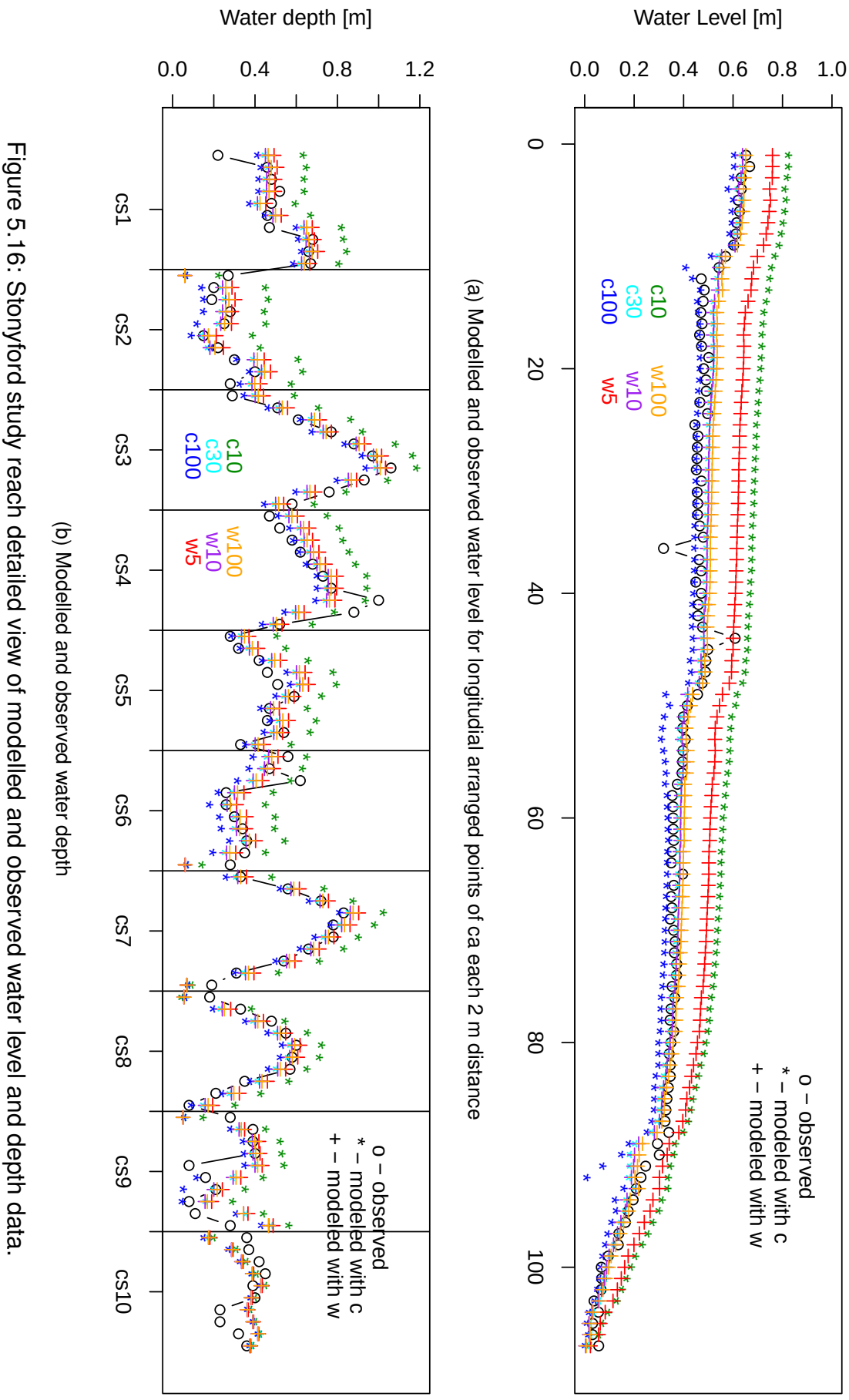

(a) Modelled and observed water level for longitudial arranged points of ca each 2 m distance

(b) Modelled and observed water depth

Figure 5.16: Stonyford study reach detailed view of modelled and observed water level and depth data.

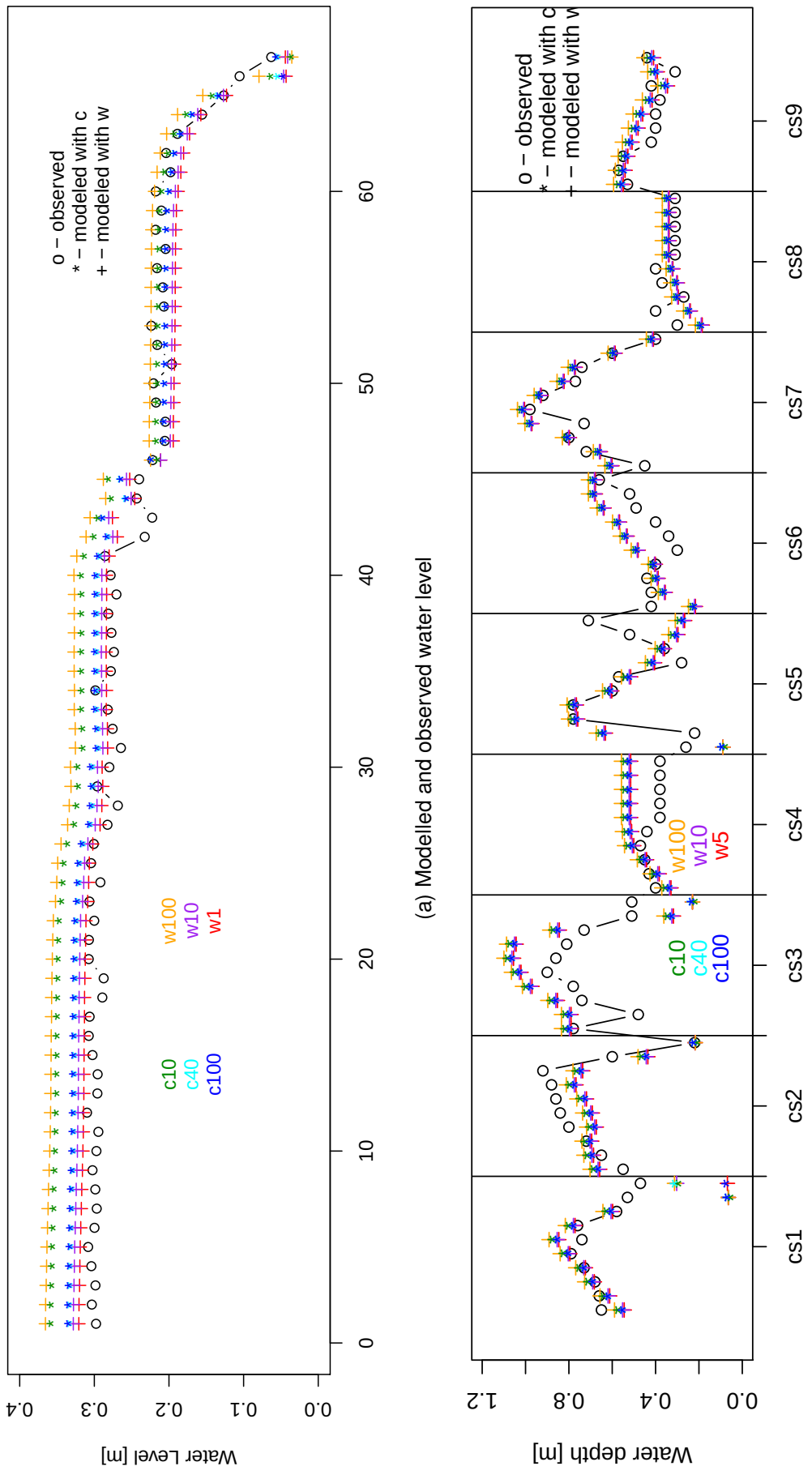

Figure 5.20: Rewe study reach detailed view of modelled and observed water level and depth data.

Chapter 6

Reach scale numerical deposition model

This chapter introduces a suspended sediment deposition model applicable to river reaches. A river reach is defined as a stretch of river, which experiences uniform cross-sectional discharge and suspended sediment concentration, typically a reach of several hundred meters in length. The model is based on the flume scale suspended sediment deposition model (discussed in Chapter 3) and the geometry of the field study reaches. It is be set up with a combination of field data (Chapter 4) and simulation data from the hydrodynamic models of the study reaches (Chapter 5). In order to accommodate the larger scale of the reach compared to the flume model and the changing flow conditions over time, several adaptions are introduced. The adaptions regard the calculation of the suspended sediment concentration, the execution of longer time periods with changing discharge and suspended sediment concentration and the introduction of thresholds for net re-suspension of the interstitial sediment.

Section 6.1 demonstrates the adaptation of the model structure from flume to reach scale. Section 6.2 focuses on the source and format of the input data for the reach scale model. Input data for the calibration of the model originates from three sources. These are the best performing model parameters from the flume scale

suspended sediment deposition model, field measured suspended sediment records and according trapping rates for the calibration period, which are the trapping periods in the field, and flow information from the hydrodynamic models from simulations recreating the discharge conditions during the trapping periods.

Section 6.3 reports on the model calibration. The calibration determines the best performing bed shear stress threshold for the re-suspension of the interstitial fine sediment. In Section 6.4, the model is executed for a winter flood period for the three study reaches. Finally, Section 6.5 concludes the chapter.

6.1 Model structure

The model introduced here focuses on the interstitial deposition of suspended sediment in single reaches of a catchment. The reach scale deposition model is based on the flume scale model in Chapter 3. Deposition is described as a function of sediment and velocity using the Krone formulation. Analogous to the flume scale model, the reach scale model consists of a base module for deposition, which is executed separately for all grain size classes and all patches. A patch is an area, which can be treated as uniform with regard to its flow and sediment conditions. Deposition for each patch is the sum of the deposition of the single grain size classes in this patch. Also, according to the flume scale model, deposition is inhibited, if the local velocity exceeds the critical value of the suspended sediment.

Nevertheless, four major adaptations were undertaken in order to upscale the model to the field situations: (1) A simplification of the suspended sediment calculation is introduced. Instead of calculating the concentration loss from one patch into a consecutive patch, the sediment concentration in the water column for one reach is driven by its turbidity record. This is based on the assumption that for a reach the upstream input of suspended sediment exceeds the concentration loss in the reach by orders of magnitude. Consequently, the location of the grid cells within the

reach and their coherence is not relevant during the model execution. (2) The model is only applied to grain sizes finer than 500 μm, because, first, all sediment measured in the field bottled samples was finer than 500 μm and consequently coarser sediment was not recorded in the turbidity probe record. Second, the behaviour of sediment $>$500 μm was not tested fully, due to the restrictions of the flume available at Exeter University. This resulted in a lack of valid calibration data for these grain sizes. (3) The model was adapted to changing discharge and sediment conditions for the model period. (4) The re-suspension of the interstitial fine sediment is included. Kirchner et al. (1990) showed that fine sediment trapped in gravel pockets is not re-suspended until the bed structure moves. Consequently, only if the bed framework is mobilised then the fine sediment stored within the channel will be re-suspended. However, the findings of this work propose a further mechanism of flushing. Traps did not consistently accumulate fine sediment over longer trapping periods, although the gravel structure did not move in the trapping period and traps were not all filled to their maximum available pore space. This suggests a flushing mechanism effective during flow conditions, which only loosens the gravel framework without actually moving the single gravel grains further downstream. In the model, re-suspension is represented by a complete flushing of the gravel bed above a velocity threshold, which sets interstitial storage of fine sediment to zero. The functionality of this threshold is tested in the calibration procedure.

Due to the better performance of the velocity deposition model compared to the shear stress deposition model, the reach scale model is executed with the velocity specification of the suspended sediment deposition model.

6.2 Input data

The model uses three groups of input data, see Table 6.1. Calibration results from the flume scale model, which define the parameters in the Krone formulation (w_s, v_{cr},

Source of input data	data type	specification
Flume scale model	parameters of Krone equation	best performing value set combination determined in the flume scale numerical deposition model calibration
Field measurements	standard gauging station information	
	a) stage record	defined as steps of a defined stage range
	b) suspended sediment record	averaged C for each stage step
Hydrodynamic models	step wise steady state simulations	
	a) geometry	size of patches identical to hydrodynamic grid cells
	b) velocity distribution	output data from hydrodynamic simulations for all stage steps

Table 6.1: Input data for the reach scale suspended sediment deposition model grouped in three sources

λ), direct field data, which is data readily available from standard gauging stations, namely stage and suspended sediment record and information about patch size and location and the velocity distribution in the single patches, which is taken from the hydrodynamic models of the single field reaches. The following sections discuss each data source in more detail.

6.2.1 Data from flume scale numerical deposition model

The speed of deposition of the suspended sediment from the water column into the bed and the critical velocities for the single grain size classes are quantified using the parameters calibrated in the flume scale model. These are the settling velocity of the single grain size classes, the critical velocity and the calibration coefficient λ. The best performing value set determined in the flume experiments uses Gibb's w_s, Lane's v_{cr} and λ = 5 (see Section 3.3.6).

6.2.2 Data from direct field measurements

The most common parameters measured at gauging stations are the stage record and the turbidity. For these two parameters, continuous records for all three study reaches with measurements every 15 minutes are available. The transformation of turbidity records into suspended sediment concentrations is demonstrated in Section 4.4.1. Stage and suspended sediment concentration are the main signifiers for short term changes in the hydraulic and sedimentological characteristics of a stream. For example, stage and suspended sediment records allow estimates of the discharge and sediment load of a flood (see Section 4.4.1). Periods of flood with changing sediment and stage record are the main interest of the model simulation. For the calibration of the model, the data of interest are the records between the time of trap installation and trap recovery, i.e. the trapping or calibration periods. For the model this data is discretised in time steps with a defined stage range, so called stage steps. The range discretised in one stage step is a 5 cm change in the stage record. Furthermore, the time series table lists the average suspended sediment concentration, starting time, end time and duration. Additionally, the suspended sediment grain size distribution needs to be defined. Here, bottled samples from a range of discharge and turbidity situations were measured regarding their absolute grain size distribution (see 4.4). The grain size distribution measured does not show a correlation between discharge and grain size distribution and only a slight variation between the three study reaches. Therefore, the same suspended sediment grain size distribution is applied to all time steps. Nevertheless, the variation between the study reaches is included in the model. The grain size distribution measured in the field is similar to the grain size distribution of the silty fine sediment used as the source of suspended sediment in the flume experiments. This means that the application of the best performing values set combination from the flume scale model to define the speed of suspended sediment deposition is an admissible measure.

6.2.3 Data from hydrodynamic models

For each of the three study reaches a hydrodynamic model was setup using the software Delft3D. Chapter 5 offers a detailed description. The models are the source of two types of input data. The model grid serves as the source for the patch position and size. These patches are the quadrangles of the curvilinear grid used for the hydrodynamic model. The quadrangles (grid cells) within the river channel are smaller than the ones on the floodplain. Patches are typically smaller than 0.5 m in edge length, with an average size of 0.15 m^2 in the Smithincott study reach, 0.17 m^2 in the Stonyford study reach and 0.17 m^2 in the Rewe study reach. For more detail, see Section 5.2. Alongside the patch definition, the hydrodynamic models are the source of all flow information. The flow information is the depth averaged velocity and the bed shear stress in each patch for the different stage steps. Additionally, information about water level and water depth are valuable sources for the evaluation of the hydrodynamic simulation quality. For each stage step, a simulation with a stable stage and discharge is run with Delft3D. The Delft3D hydrodynamic simulation for each stage step is run until all output parameters have stabilised. The experience from the calibration runs in Chapter 5 shows that at the latest after 30 minutes of simulation time with a fixed stage and discharge no significant variation is apparent in the output parameters. In order to show that after this time period, no further changes are to be expected, simulations for each stage step were run for one hour simulation time. The hydrodynamic simulations of the single stage steps were compiled in one simulation run per reach to avoid setting up a large number of different model runs. Stage and discharge are set to change synchronously from one stage step to the next every simulation hour. One possible output format in Delft3D is a time series for an observation point for any kind of output parameter. Figure 6.1 shows a graphical representation of the water level of the Stonyford study reach at seven observation points. The observation points are positioned midstream and distributed over the whole length of the study reach. The water level shows a very steep drop

at the being of the simulation run (due to an initial water cover of 0.5 m for the whole study reach). Thereafter, for the first stage step and all subsequent stage steps the water level remains steady for the simulation time with a stable stage and discharge definition.

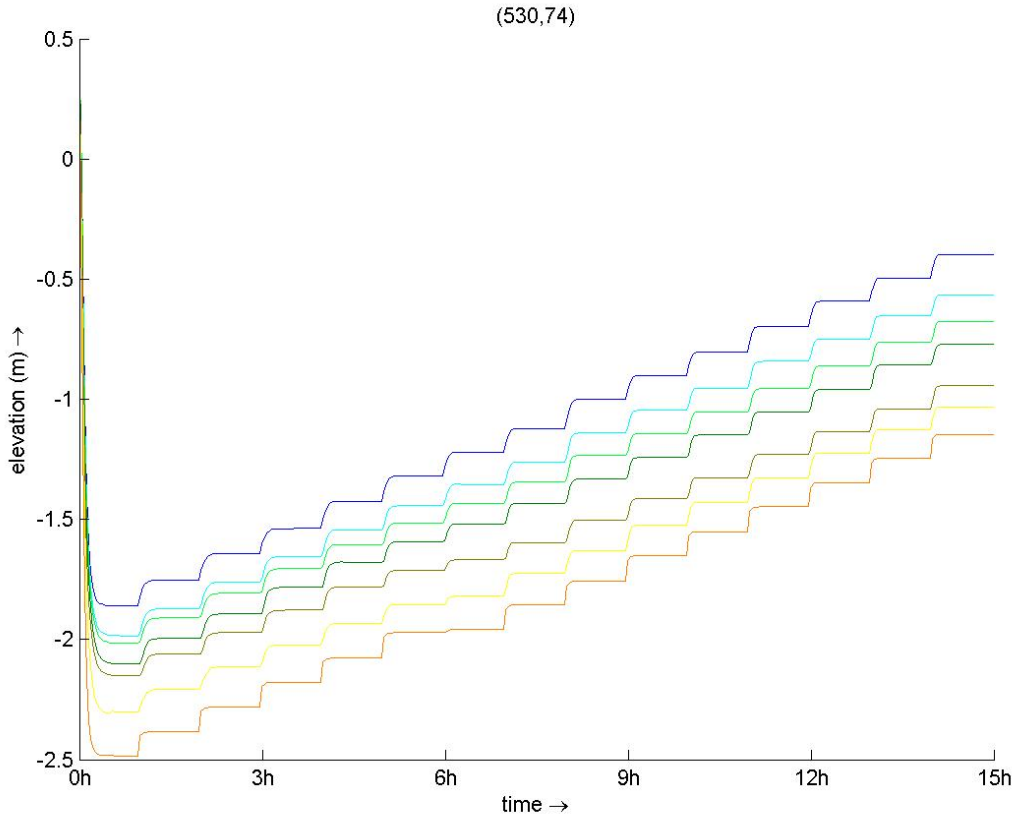

Figure 6.1: Delft3D hydrodynamic model water level as an example for the output parameter development at seven midstream observation points in the Stonyford study reach showing the quality of the single simulation steps.

The equivalent plots for the other reaches and for the development of bed shear stress and velocity at the same observation points can be found in the Appendix A.58 to A.63.

6.3 Calibration

6.3.1 Calibration procedure

The behaviour of the suspended sediment in the reach was initiated after the calibration results of the flume scale numerical suspended sediment deposition model. The parameters controlling the suspended sediment deposition are based entirely on the flume scale model calibration. The calibration conducted here aims to establish conditions for interstitial sediment re-suspension.

The calibration of the reach scale deposition model is based on six periods with field trapping information in the winter of 2009/2010, which are defined as the calibration periods. The stage and turbidity record and the trapping rates of these periods are already discussed in detail in 4.4.2. Table 6.2 summarises the main characteristics for the calibration periods and states the key dimension of the model runs, the number of patches, the number of stage steps and the range of the suspended concentration and the range of the stage level.

	Period	duration days	days with high C	No patches	patch size mean m^2	No stage steps	C from mg L^{-1}	range to	stage from m	range to
Smithincott	1	74	4	30000	0.15	37	1	326	0.60	1.33
	2	40	13			381	1	455	0.58	1.59
Stonyford	1	15	0	82500	0.17	6	0	24	0.24	0.31
	2	38	13			370	1	619	0.28	1.72
Rewe	1	33	6	32500	0.17	37	0	229	0.26	1.03
	2	35/36	15			307	2	289	0.28	1.42

Table 6.2: Characteristic parameters for the six calibration periods, No being the number of patches respectively stage steps in a calibration run, C being the average suspended sediment concentration of the stage step.

The calibration is based on the comparison of measured trapping rates and the modelled interstitial deposition in the equivalent patches. Depending on the calibration period, these are eight to twelve traps, grouped in two or three trap sets (see Section 4.4.2 for more detail). This small number of calibration points makes it difficult to calibrate nuances of the fine sediment deposition process. However, the accordance of measured interstitial trapping and modelled interstitial deposition is a

very clear indicator of the successful upscaling of the suspended sediment deposition model and its general performance.

Within-channel fine sediment is not constantly accumulating but is re-suspended into the water column at threshold conditions. As a starting point for the calibration, the threshold for re-suspension of the interstitial sediment in the model is set at the excess of the critical bed shear stress (τ_{cr}) with the power to mobilise the D_{90} of the gravel bed. Mobilisation of the bed D_{90} was also used in Petit (1994) as the criteria for complete bed movement. The critical value for bed framework mobilisation, is based on the review paper of Buffington and Montgomery (1997). In particular, the dimensionless shear stress (τ^*) from Diplas and Parker (1992) was chosen as a reference. It is based on the D_{50} of the subsurface bed grain size (D_{50ss}) and was tested with data from riffle-pool rivers similar to the River Culm. Furthermore, other authors like Dinehart (2012), Wilcock (1988) and Wathen et al. (1997) report similar mobilisation thresholds for riffle-pool gravel bed rivers. Diplas definition of τ^* is given in Equation 6.1 with D_i being the grain size in question (here the D_{90}).

$$\tau^*_{cri} = 0.087 \frac{D_i}{D_{50ss}}^{-0.94} \tag{6.1}$$

Dimensionless critical shear stress is transferred into critical shear stress using Equation 6.2 with $\rho_s - \rho_f$ being the difference between solid and fluid density and g being the gravitational acceleration.

$$\tau_{cr-bed} = \tau^*_{cr_i} * (\rho_s - \rho_f) * g * D_i \tag{6.2}$$

The critical shear stress for the mobilisation of the gravel bed was calculated using results from the gravel count in the reaches (see Chapter 4). The critical shear stress to move the D_{90} in the single reaches was 59 Pa at Smithincott, 71 Pa at Stonyford and 57 Pa at Rewe. Based on these values defined for each reach, nine adaptations of the thresholds were calculated (with 0.1, 0.2, 0.3, 0.4, 0.5, 0.6, 0.7, 0.8 and 0.9

threshold		f1	f2	f3	f4	f5	f6	f7	f8	f9	f10
Smithincott	Pa	5.9	11.8	17.7	23.6	29.5	35.4	41.3	47.2	53.1	59
Stony	Pa	7.1	14.2	21.3	28.4	35.5	42.6	49.7	56.8	63.9	71
Rewe	Pa	5.7	11.4	18.1	23.8	29.5	35.2	40.9	46.6	52.3	57

Table 6.3: Thresholds of interstitial re-suspension as fractions of the critical bed shear stress for the movement of the D_{90} of the gravel bed, after Diplas and Parker (1992).

times the critical value, see Table 6.3) resulting in ten flushing thresholds. For each threshold, a model run was executed. The deposition results for each threshold are compared to the observed interstitial trapping and the best performing threshold is brought forward for the execution of the scenario runs.

6.3.2 Interstitial deposition in the calibration periods

Figure 6.2 to 6.7 show distribution plots of modelled interstitial deposition in the reaches at the end of the calibration periods. For each reach, one calibration period was taken as an example and plotted for selected re-suspension thresholds. Deposition is displayed in discrete classes and observed trap positions are indicated with red dots. The plots show a wide range of modelled deposition from 0 up to the maximum of 240 kg m^{-2}. The deposition distribution is typical, with highest deposition found at the sides of the channel and in pools and lowest deposition at bars and riffle runs (as also suggested by Walling et al., 2003).

Noticeably, the distribution of deposition in Smithincott (Figure 6.2 to 6.3b) consists of a small celled mosaic of different levels of deposition, whereas both Stonyford and Rewe deposition are more uniform over the reach. The mosaic nature of deposition at Smithincott is most distinct for low re-suspension thresholds. For higher thresholds deposition reaches uniform maximum values (compare Figure 6.2 with the lowest re-suspension threshold of f1 =5.9 Pa to Figure 6.3b for a threshold of f5 = 29.5 Pa).

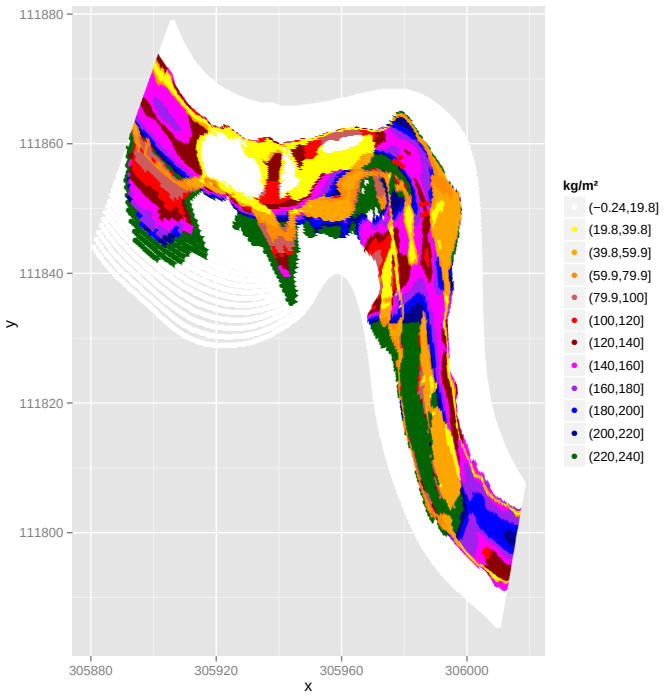

Figure 6.2: Distribution of interstitial deposition for calibration Period 1 at Smithincott with threshold f1 = 5.9 Pa. Deposition is displayed in discrete classes from 0 to 240 kg m^{-2}, x as easting, y as northing. The positions of the traps are indicated as red dots.

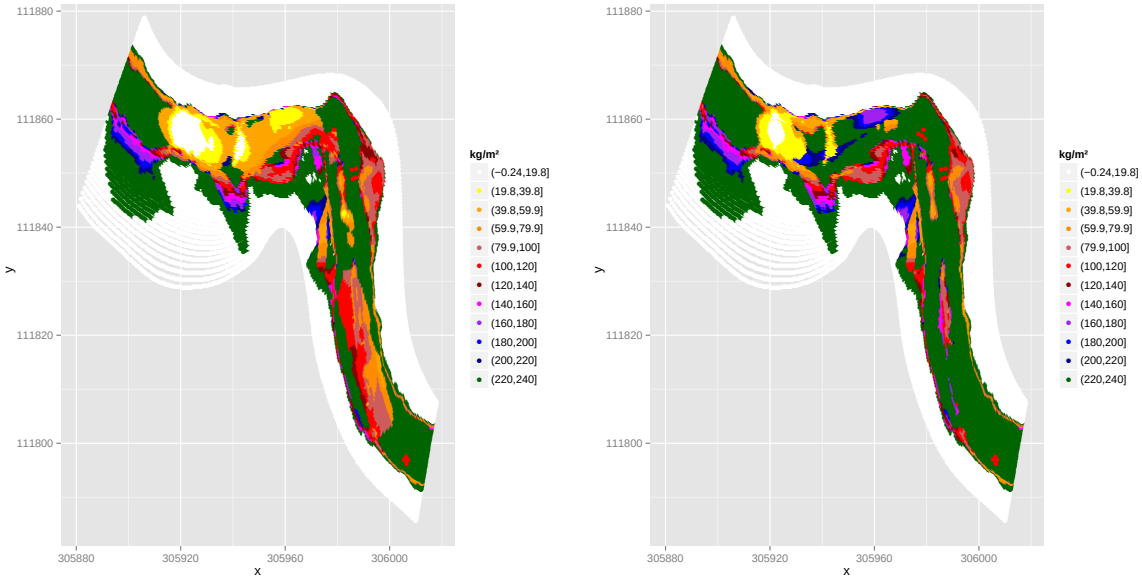

(a) Threshold f3 = 17.7 Pa

(b) Threshold f5 = 29.5 Pa

Figure 6.3: Distribution of interstitial deposition for calibration Period 1 at Smithincott with threshold f3 = 17.7 Pa and f5 = 29.5 Pa. Deposition is displayed in discrete classes from 0 to 240 kg $^{-2}$, x as easting, y as northing. The positions of the traps are indicated as red dots.

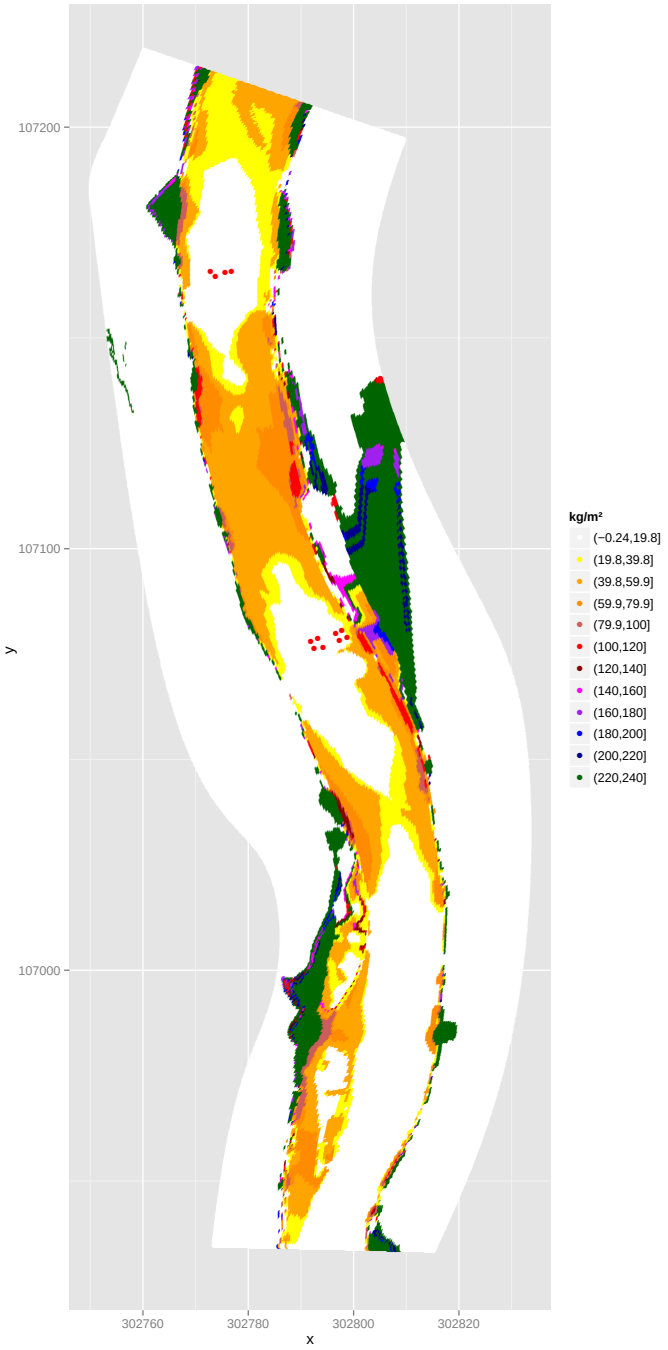

Figure 6.4: Distribution of interstitial deposition for calibration Period 2 at Stonyford with threshold f1 = 7.1 Pa. Deposition is displayed in discrete classes from 0 to 240 kg m^{-2}, x as easting, y as northing. The positions of the traps are indicated as red dots.

For all re-suspension thresholds, the modelled deposition at Stonyford is distributed more uniformly across the reach for a low threshold (f1 = 7.1 Pa, shown in Figure 6.4). River stretches with riffles experience low deposition for most of the area

between the two banks. Only a very narrow side ribbon at the channel edges experiences higher deposition. Pool areas experience medium deposition, again covering the whole area from bank to bank. With rising thresholds, the ribbon of high deposition along the river edges grows wider (see Figure 6.5a) and eventually fills up the reach uniformly with maximum deposition (here at threshold f5 = 35.5 Pa).

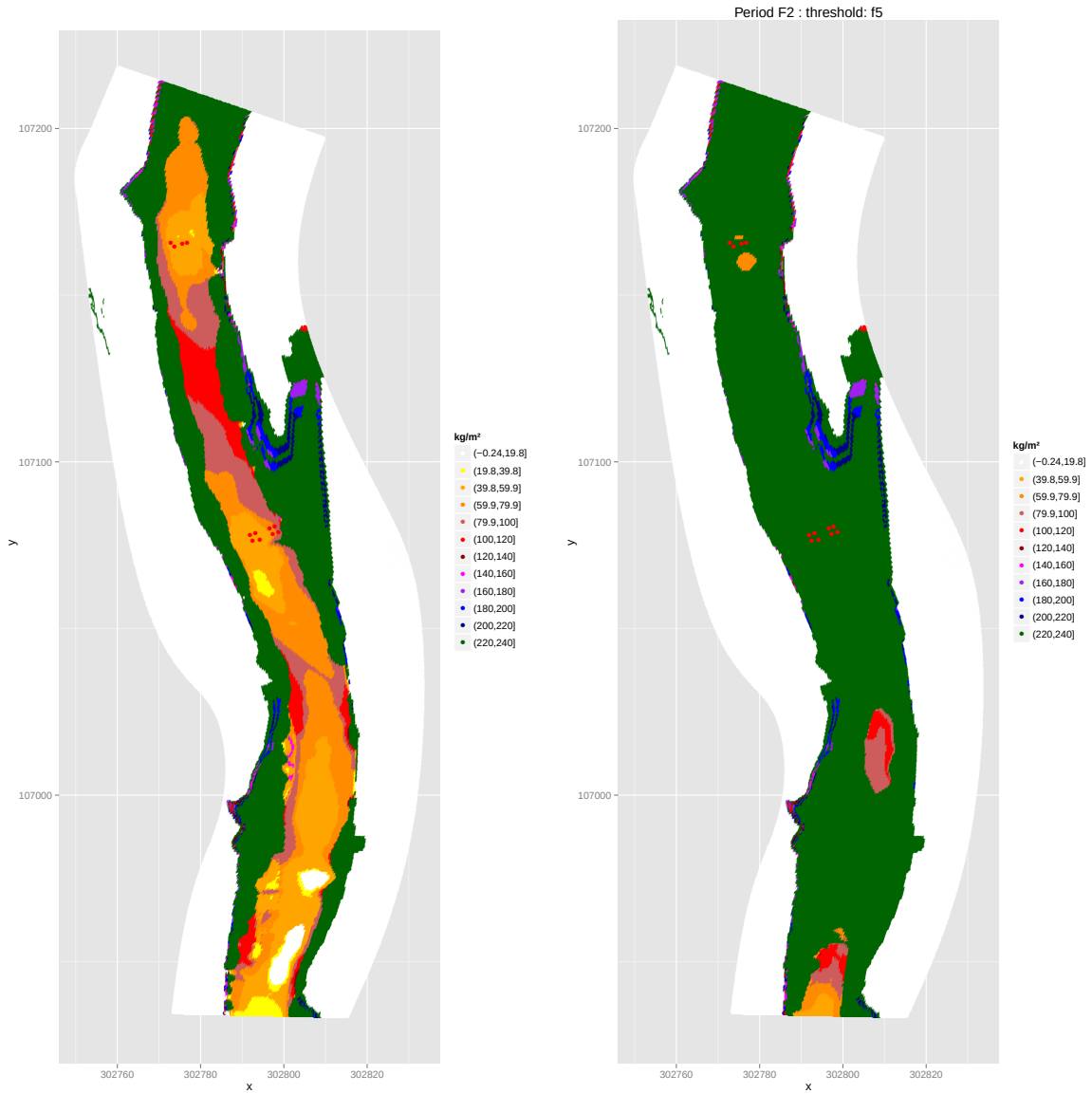

(a) Threshold f3

(b) Threshold f5

Figure 6.5: Distribution of interstitial deposition for calibration Period 2 at Stonyford with threshold f3 = 21.3 Pa und f5 = 35.5 Pa. Deposition is displayed in discrete classes from 0 to 240 kg m^{-2}, x as easting, y as northing. The positions of the traps are indicated as red dots.

Figure 6.6 compares the modelled interstitial deposition for threshold f1 = 5.7 Pa for calibration Period 1 and Period 2 at Rewe. Deposition in Period 1 (with lower discharge and lower maximum suspended sediment concentration, see Table 6.2) results in a higher deposition throughout. The mean deposition in Period 1 is 44.6 kg m^{-2} compared to 28.2 kg m^{-2} in the more dynamic Period 2 period (see Table 6.4). For any other threshold than f1 in Period 1, modelled interstitial deposition is identical to the one plotted in Figure 6.6a. The reason for this is that the flow conditions in the calibration period do not exceed this threshold. Therefore, the deposition in Figure 6.6a is the complete suspended sediment deposition without loss due to re-suspension. This means deposition results from Period 1 are not significant for the definition of the re-suspension threshold. In Period 2, flow conditions do exceed f1 and f2 flushing thresholds. However, the flow conditions are very uniform, resulting in larger stretches of uniform deposition over larger parts of the reach.

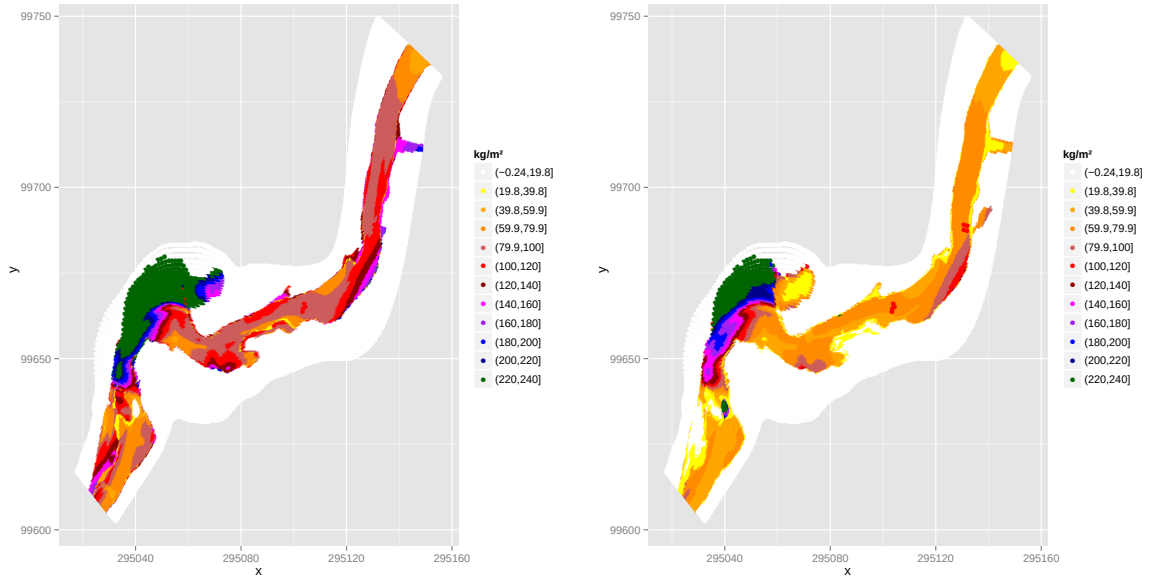

(a) Period 1 f1

(b) Period 2 f1

Figure 6.6: Distribution of interstitial deposition for calibration Period 1 and 2 at Rewe with threshold f1 = 5.7 Pa. Deposition is displayed in discrete classes from 0 to 240 kg m^{-2}, x as easting, y as northing. The positions of the traps are indicated as red dots.

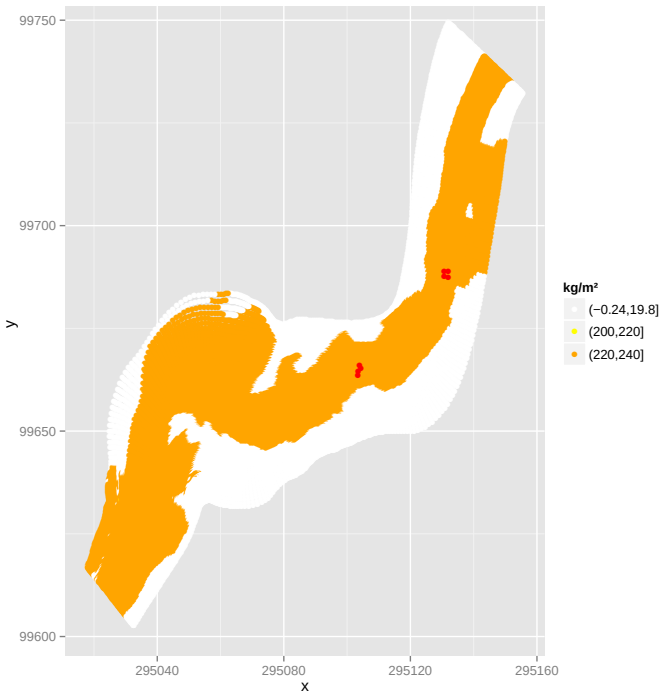

Figure 6.7: Distribution of interstitial deposition for calibration Period 2 at Rewe with threshold f3 = 17.1 Pa. Deposition is displayed in discrete classes from 0 to 240 kg m^{-2}, x as easting, y as northing. The positions of the traps are indicated as red dots.

Further, for the calibration run with threshold f3 = 17.1 Pa, the maximum deposition is reached in the whole reach, see Figure 6.7. The lack of threshold conditions in the Rewe study reach is in accordance with the typical behaviour of a lower reach. During flood runoff, the whole floodplain is inundated and contributes to overall discharge causing the flow in the main river channel to rise to less extreme peaks (see description of discharge and suspended load dynamics of the reaches in Subsection 4.4.1). Table 6.4 summarises the mean deposition in the wetted area of the reaches for selected re-suspension thresholds. This overview demonstrates the sensitivity of the model to the re-suspension threshold with rising mean deposition in the reach for rising thresholds. Further, it demonstrates that longer trapping periods, with higher stages and higher suspended sediment concentration (here Period 2) do not result in higher interstitial deposition. Both for the reach at Smithincott and the reach at Rewe, the modelled interstitial deposition in Period 1 is consistently higher than in Period 2. For the reach at Stonyford, this is not true because calibration Period 1 at Stony-

ford reach experienced very limited suspended sediment concetrations, resulting in a maximum deposition of only 5 kg m^{-2}.

	Threshold	**f1**	**f2**	**f3**	**f5**	**f7**	**f10**
	Deposition in	kg m^{-2}	kg m^{-2}	kg m^{-2}	kg m^{-2}	kg m^{-2}	kg m^{-2}
Smithincott	Period 1	44	80	97	102		104
Smithincott	Period 2	23	24		50	90	125
Stonyford	Period 1	4			5		
Stonyford	Period 2	29		67	100	103	103
Rewe	Period 1	45	95	102			
Rewe	Period 2	285		152			

Table 6.4: Mean deposition [kg m^{-2}] in the wetted areas of the study reaches for the different calibration periods and selected flushing thresholds.

6.3.3 Statistical evaluation of modelled and observed interstitial deposition

Although, the above plots show a consistent behaviour of the model, they also display several problem for the model re-suspension threshold calibration. Re-suspension threshold calibration is based on a small number of traps, each giving only one value for the whole trapping period. The traps are generally located in areas of deposition of similar magnitude. Most diverse, but still dominantly mid-stream trap positions are found at Smithincott. In comparison, the trap positions at Stonyford are all located mid riffle, only at different distances from the river bank. The study reach in Rewe experiences relatively little diversification over the whole reach and differences in observed positions are very small. Further, the calibration of the flume scale deposition model already showed the difficulties of the model to predict deposition correctly. The evaluation of the model performance suggested influence by factors other than the local flow on local deposition. Nevertheless, the observed trapping data is valuable to investigate the applicability and potential good performance of the model on reach scale. The accordance of the magnitude of measured and modelled interstitial deposition is a criterion for the quality of the model setup and upscaling to reach

scale. Due to these limitations, this evaluation refrains from the more complex statistical examination employed for the calibration of the flume scale deposition model (Chapter 2) and the hydrodynamic models (Chapter 5). However, least square linear regressions of modelled and observed interstitial deposition for the trap positions deliver a general picture of the performance of the model. The regression applied is forced through the origin. The evaluation of r^2 delivers a scale for the accordance of the modelled and observed interstitial deposition of the single positions. The slope of the linear model shows the accordance of modelled and observed interstitial deposition magnitude. In order to illustrate the results, plots with observed versus modelled interstitial deposition are shown. These include all thresholds, which differ regarding the modelled deposition of the trap positions. Further the linear regression lines are superimposed.

Figure 6.8 plots the data for Period S1 at Smithincott. The left panel shows that there is more variability in the modelled compared to the observed data. Most re-suspension thresholds over predict deposition. The right panel shows that there is a weak accordance between modelled and predicted deposition especially for trap set S1. S1 is located at the exit of a pool and experiences flow acceleration. This is possibly one position with similar problems as the ones found for traps C and D in the flume scale deposition model. The statistical evaluation does give a clear indication towards the best accordance in magnitude but not regarding the correlation of the different trap positions (see Table 6.5). A threshold of f1 = 0.59 Pa results in the best performance for this period. The results of Period S2 at Smithincott are shown in Figure 6.9. Here, the model fit is better than for Period 1. The best performing re-suspension threshold resides between f1 and f2, see Table 6.6.

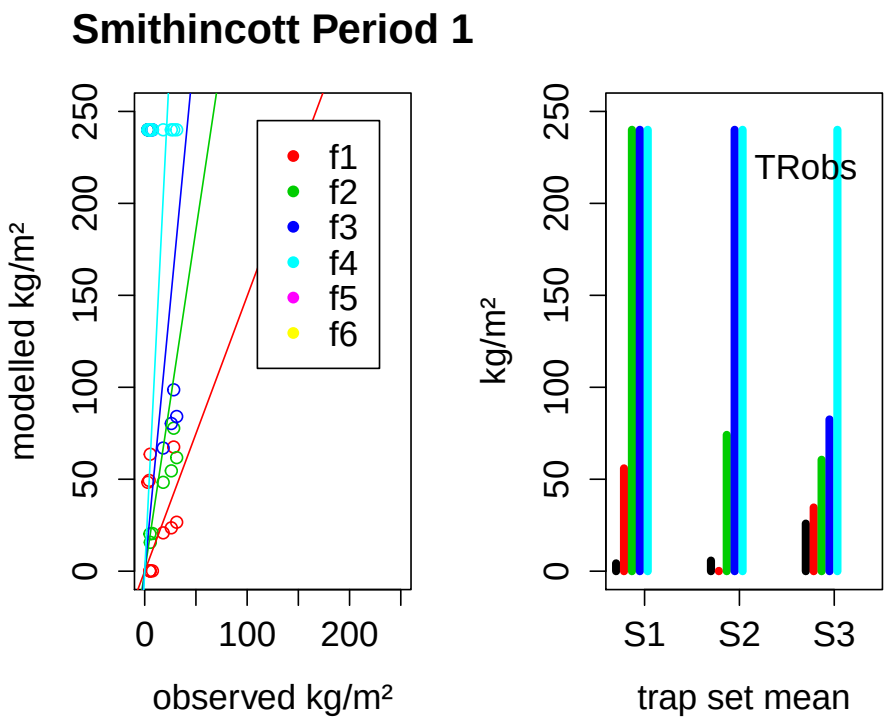

Figure 6.8: Modelled and observed interstitial deposition for different re-suspension threshold for Period 1 at Smithincott. The left shows scatter plots of observed and modelled data with superimposed linear regression lines. The right panel shows the mean deposition of the trap sets for the observed data and the calibration runs with different re-suspension thresholds with observed values in black.

threshold	**f1**	**f2**	**f3**	**f4**
r^2	0.05	0.20	0.87	
slope	1.49	3.71	5.83	11.27

Table 6.5: Results of linear regression of observed and modelled interstitial deposition in calibration Period 1 at Smithincott.

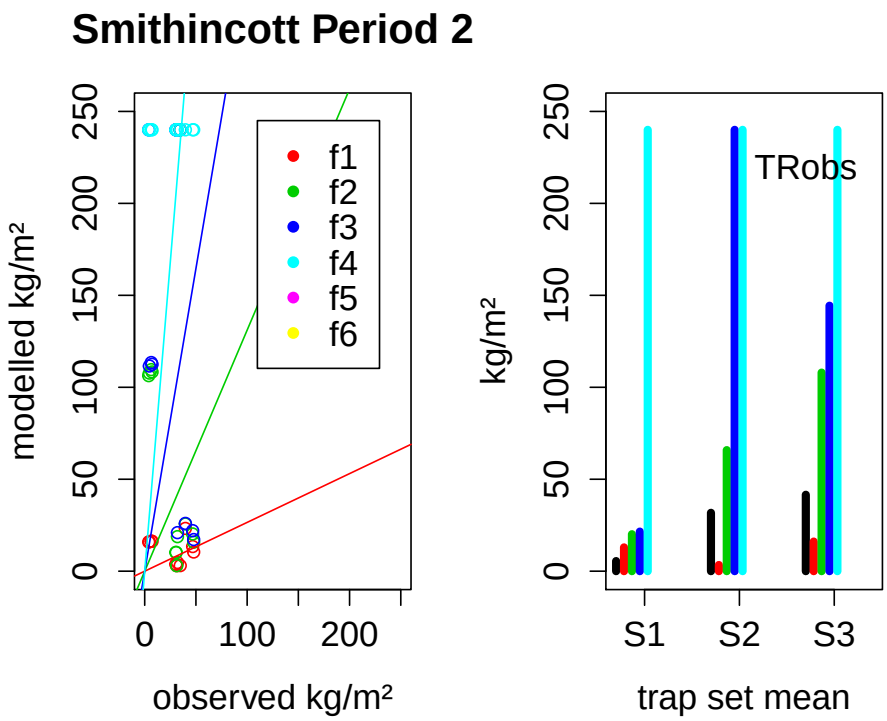

Figure 6.9: Modelled and observed interstitial deposition for different re-suspension threshold for Period 2 at Smithincott. The left shows scatter plots of observed and modelled data with superimposed linear regression lines. The right panel shows the mean deposition of the trap sets for the observed data and the calibration runs with different re-suspension thresholds with observed values in black.

threshold	**f1**	**f2**	**f3**	**f4**
r^2	0.12	0.19	0.10	
slope	0.56	1.64	3.11	11.27

Table 6.6: Results of linear regression of observed and modelled interstitial deposition in calibration Period 2 at Smithincott.

The results of Period 1 at Stonyford are shown in Figure 6.10. Period 1 at Stonyford experiences only small amounts of suspended sediment and flow conditions does not exceed re-suspension threshold f2 = 14.2 Pa. Although the results without re-suspension result in similar magnitudes to the observed deposition, threshold f1 performs better. The observed and modelled interstitial deposition correlates with an r^2 of 0.52 and the linear regression results in a slope of 1.05 (see Table 6.7).

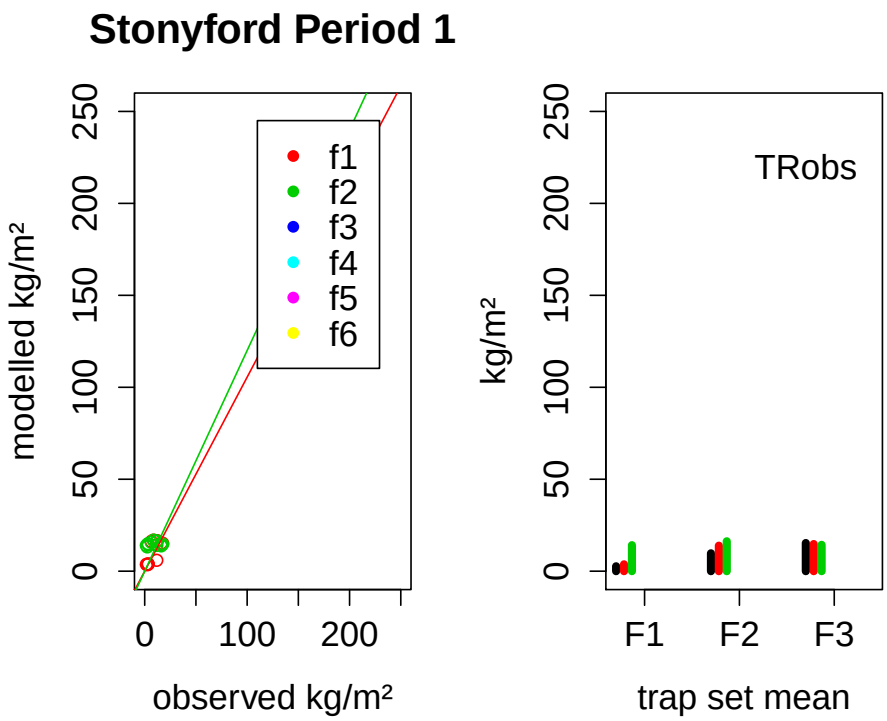

Figure 6.10: Modelled and observed interstitial deposition for different re-suspension threshold for Period 1 at Stonyford. The left shows scatter plots of observed and modelled data with superimposed linear regression lines. The right panel shows the mean deposition of the trap sets for the observed data and the calibration runs with different re-suspension thresholds with observed values in black.

threshold	**f1**	**f2**
r^2	0.52	0.03
slope	1.05	1.20

Table 6.7: Results of linear regression of observed and modelled interstitial deposition in calibration Period 1 at Stonyford.

The results of Period 2 at Stonyford are shown in Figure 6.11. Here, the deposition for the trap positions rises from threshold f1 = 7.1 Pa to f5 = 35.5 Pa continuously. However, the modelled deposition shows very little variability within one calibration run (see left panel), although the observed deposition is in F2 is only approximately 15 % of the deposition in F3. Only at threshold f4 = 28.4 Pa, this difference is also modelled but with an approximately 2.5 fold over prediction. The statistical evaluation in Table 6.8 suggests a best performing threshold around f3.

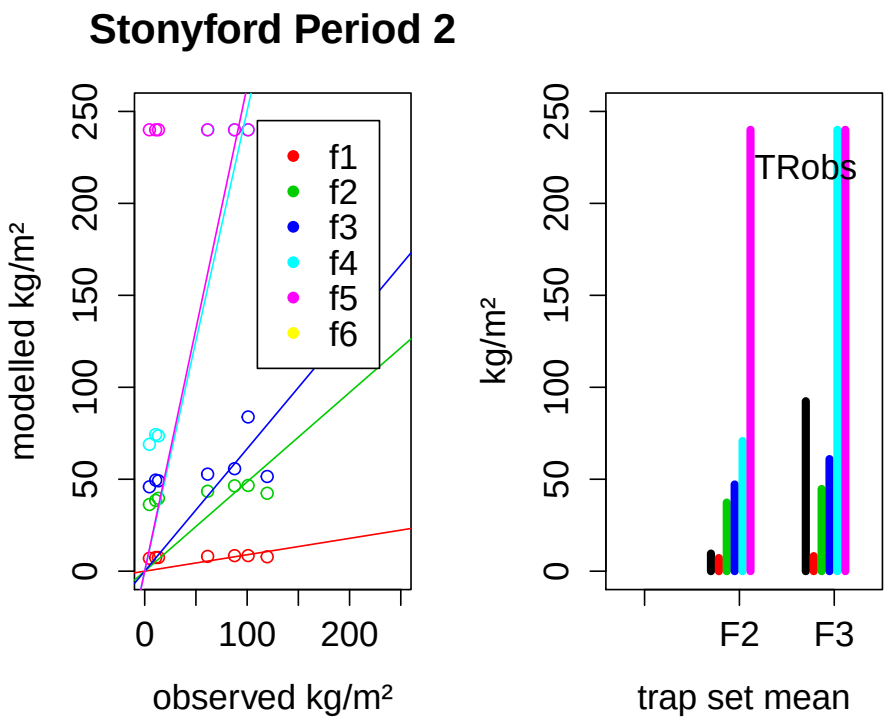

Figure 6.11: Modelled and observed interstitial deposition for different re-suspension threshold for Period 2 at Stonyford. The left shows scatter plots of observed and modelled data with superimposed linear regression lines. The right panel shows the mean deposition of the trap sets for the observed data and the calibration runs with different re-suspension thresholds with observed values in black.

threshold	**f1**	**f2**	**f3**	**f4**	**f5**
r^2	0.65	0.68	0.31	0.87	
slope	0.09	0.49	0.67	2.50	2.64

Table 6.8: Results of linear regression of observed and modelled interstitial deposition in calibration Period 2 at Stonyford.

Period 1 at Rewe is not documented here because the flow during this period did not exceed threshold f1 = 0.57 Pa. However, the magnitude of modelled and observed data are in good accordance. The results of Period 2 at Rewe are shown in Figure 6.12. The reach in Rewe in this period exhibits almost no variability between the modelled interstitial deposition of the single trap positions. Therefore, only the magnitude of the modelled interstitial deposition can be used as an indicator for best performing threshold. Consequently f1 = 5.7 Pa, which results in a slope of 1.15 can

be seen as the best performing threshold for the Rewe study reach.

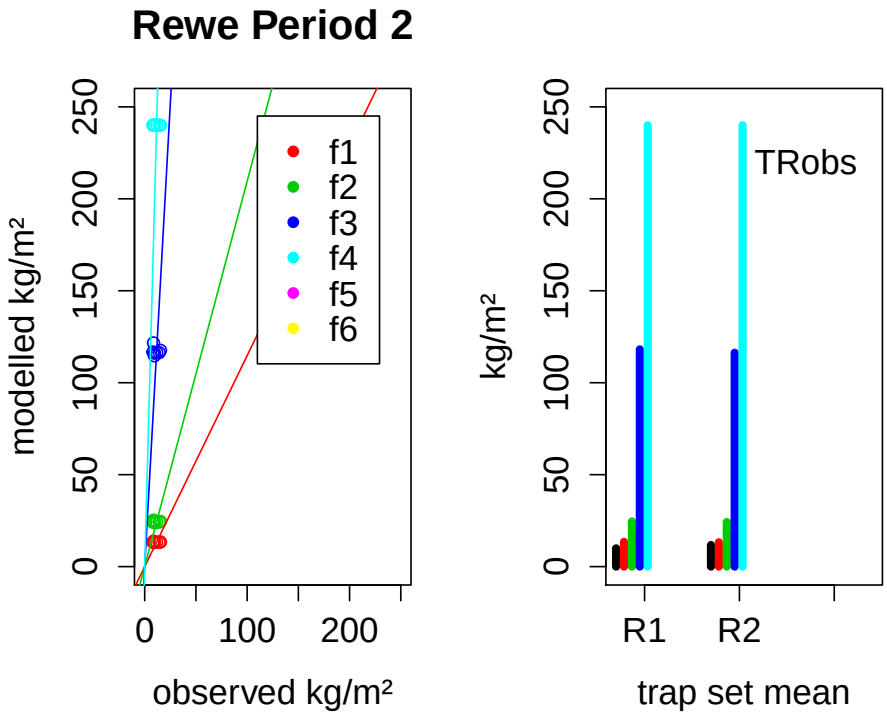

Figure 6.12: Modelled and observed interstitial deposition for different re-suspension threshold for Period 1 at Rewe. The left shows scatter plots of observed and modelled data with superimposed linear regression lines. The right panel shows the mean deposition of the trap sets for the observed data and the calibration runs with different re-suspension thresholds with observed values in black.

threshold	**f1**	**f2**	**f3**	**f4**
r^2	0.00	0.00	0.00	
slope	1.15	2.10	10.06	20.65

Table 6.9: Results of linear regression of observed and modelled interstitial deposition in calibration Period 2 at Rewe.

Overall, the re-suspension threshold calibration suggests low re-suspension threshold of 10 to 20 % of the initially established threshold. This is unexpectedly low, especially considering that interstitial sediment can only be re-suspended during gravel mobilisation. There are three possible explanations for these findings. First, there are processes causing re-suspension prior to the full mobilisation of the gravel bed; second, the suspended grain size distribution is defined too coarse and consequently

the accordant critical velocity for deposition (τ_{cr}) is too low and settling velocity (w_s) too high; or third, the suspended sediment downward flux (λ ,$C^{\star}w_s$) is defined too high. The latter suggests that for a fully satisfactory model performance the suspended sediment downward flux needs to be reduced. Two findings strengthen this theory. First, in Period 1 at Smithincott calibration runs with all threshold did over estimate deposition. This means, at least for the application in Smithincott, the modelled deposition is too high. Second in Period 2 at Stonyford, the best accordance between observed and modelled deposition pattern was found for the f4 threshold, however with a 2.5 fold too high deposition estimate. Supposedly modelled downward flux was only 20 % of the current value, a threshold of f4 in Stonyford would be in very good accordance with the observed data.

Nevertheless, the data available at this point in time is not sufficient to explain the cause of a potentially lower downward flux in the field compared to the flume. This means, a reduction of the downward flux would be purely justified with its counterbalancing effect on the re-suspension threshold. A similar argument is true for a potential adaption of the suspended sediment grain size distribution and the according the critical velocity.

Nevertheless, in order to demonstrate a principal field application, the following section discusses scenarios modelled with an unaltered downward flux and unaltered suspended sediment grain size distribution in combination with the re-suspension thresholds of 10 and 20 % of the maximum value.

6.4 Deposition scenarios

The scenarios modelled for this subsections are the winter flood period already introduced in Section 4.4.1. For all study reaches, several events with high stages and high suspended sediment concentrations were measured (see Figure 4.21 and 4.22). The simulation of interstitial deposition for this period aims to show the appli-

cability of the model and to aid the undertanding of the different dynamics of upper, middle and lower reaches. Due to the lack of a exact definition of a re-suspension threshold, the distribution of interstitial deposition for all reaches is modelled with both thresholds f1 and f2. Furthermore, the distribution of modelled interstitial sediment over the course of the scenario period is investigated.

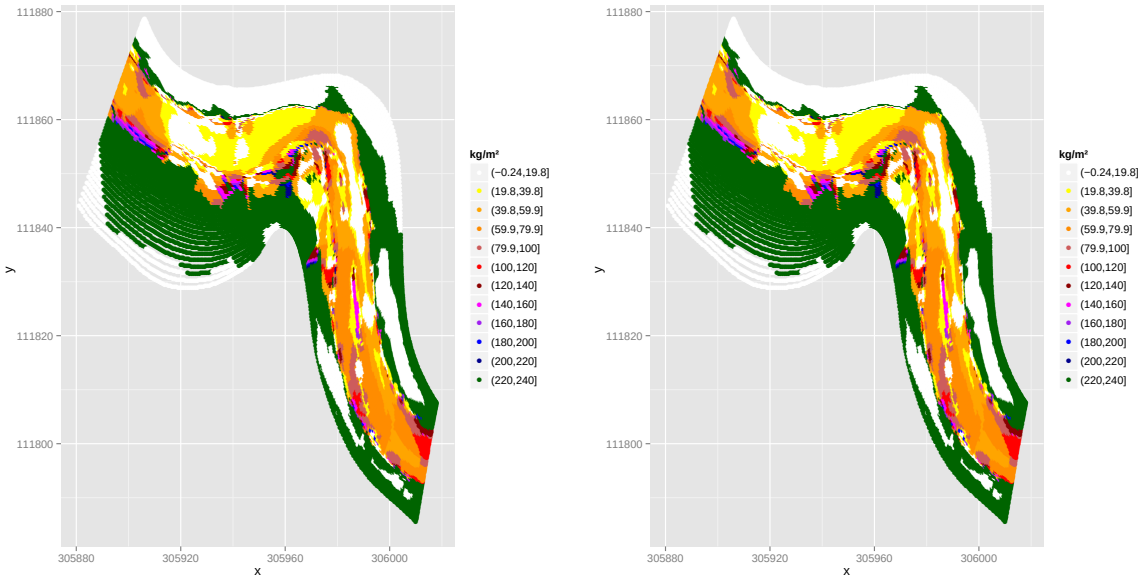

(a) Threshold f1 = 5.9 Pa

(b) Threshold f2 = 11.8 Pa

Figure 6.13: Distribution of deposition at end of the scenario period at Smithincott with threshold f1 = 5.9 Pa and f2 = 11.8 Pa. Deposition is displayed in discrete classes from 0 to 240 kg m^{-2}, x as easting, y as northing.

Smithincott Figures 6.13a and 6.13b compare the interstitial deposition at the end of the scenario period at Smithincott for f1 and f2. The differences in interstitial deposition for these two threshold are marginal with a mean deposition of 136 kg m^{-2} for f1 compared to 138 kg m^{-2} for f2.

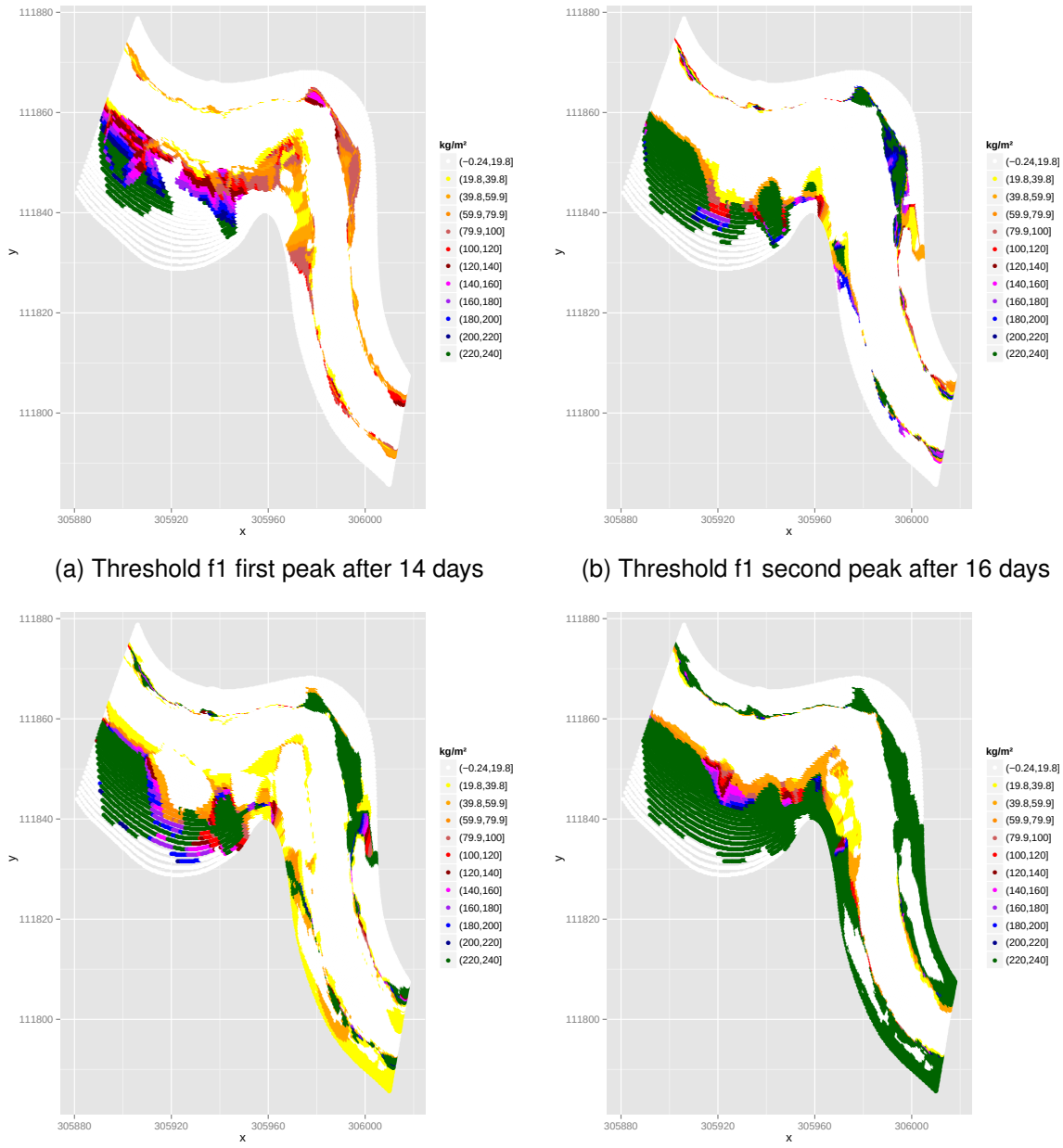

(a) Threshold f1 first peak after 14 days

(b) Threshold f1 second peak after 16 days

(c) Smith f1 peak 5 after 38 days

(d) Smith f1 peak 6 after 44 days

Figure 6.14: Distribution of interstitial deposition for scenario peak 1, 2, 5 and 6 at Smithincott with threshold f1 = 5.9 Pa. Deposition is displayed in discrete classes from 0 to 240 kg m^{-2}, x as easting, y as northing.

However for a threshold of f3, the complete deposition for the whole reach is at the maximum of 240kg m^{-2}. Again, the small scale mosaic of deposition for this reach is clearly visible. The plots in Figure 6.14 show the modelled interstitial deposition for four discharge peaks in the scenario period at Smithincott with the f1 threshold. They clearly show that each discharge peak clears the main channel from interstitial

deposition. However, slack water and side areas constantly accumulate interstitial deposits. In the days after a peak with a complete re-suspension, rapid interstitial deposition takes place. This is shown in Figure 6.15 for a threshold of f1. Here, directly after a peak with a maximum stage of 1.5 m and a maximum suspended sediment concentration of 234 mg L^{-1} (causing the re-suspension of interstitial deposition in the main channel), deposition is limited to side and slack water areas (Figure 6.15a). However, only four days and eight hours after the last re-suspension, the channel is filled in with interstitial deposits covering main parts of the main channel.

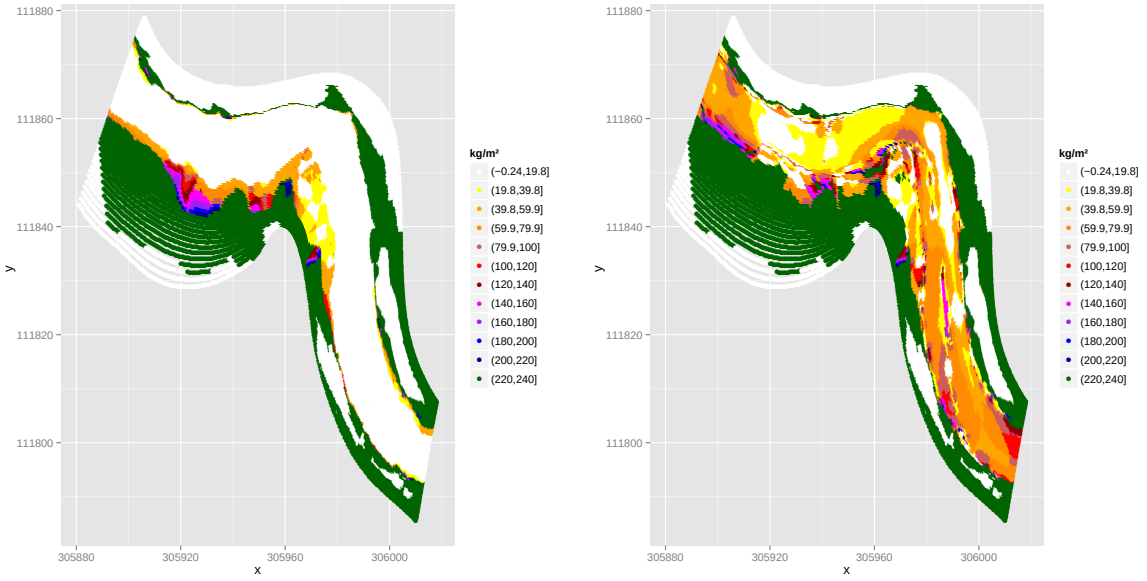

(a) Threshold f1 re-suspension peak at end of scenario period

(b) Threshold f1 4 days 8 hour after last re-suspension

Figure 6.15: Distribution of deposition for scenario at Smithincott with threshold f1 = 5.9 Pa during and 4 days after a stage speak with re-suspension of interstitial sediment in the main channel. Deposition is displayed in discrete classes from 0 to 240 kg m^{-2}, x as easting, y as northing.

The period after the re-suspension had a mean stage of 0.74 m and a mean suspended sediment concentration of 27 mg L^{-1}. This period shows the fast dynamic of modelled interstitial deposits and the relevance of high discharge for the flushing of the gravel pores.

Stonyford Figure 6.16a and 6.16b compare the interstitial deposition at the end of the scenario period at Stonyford. The differences in interstitial deposition for these two threshold are distinct with a mean deposition of 103 kg m^{-2} for f1 compared to 129 kg m^{-2} for f2.

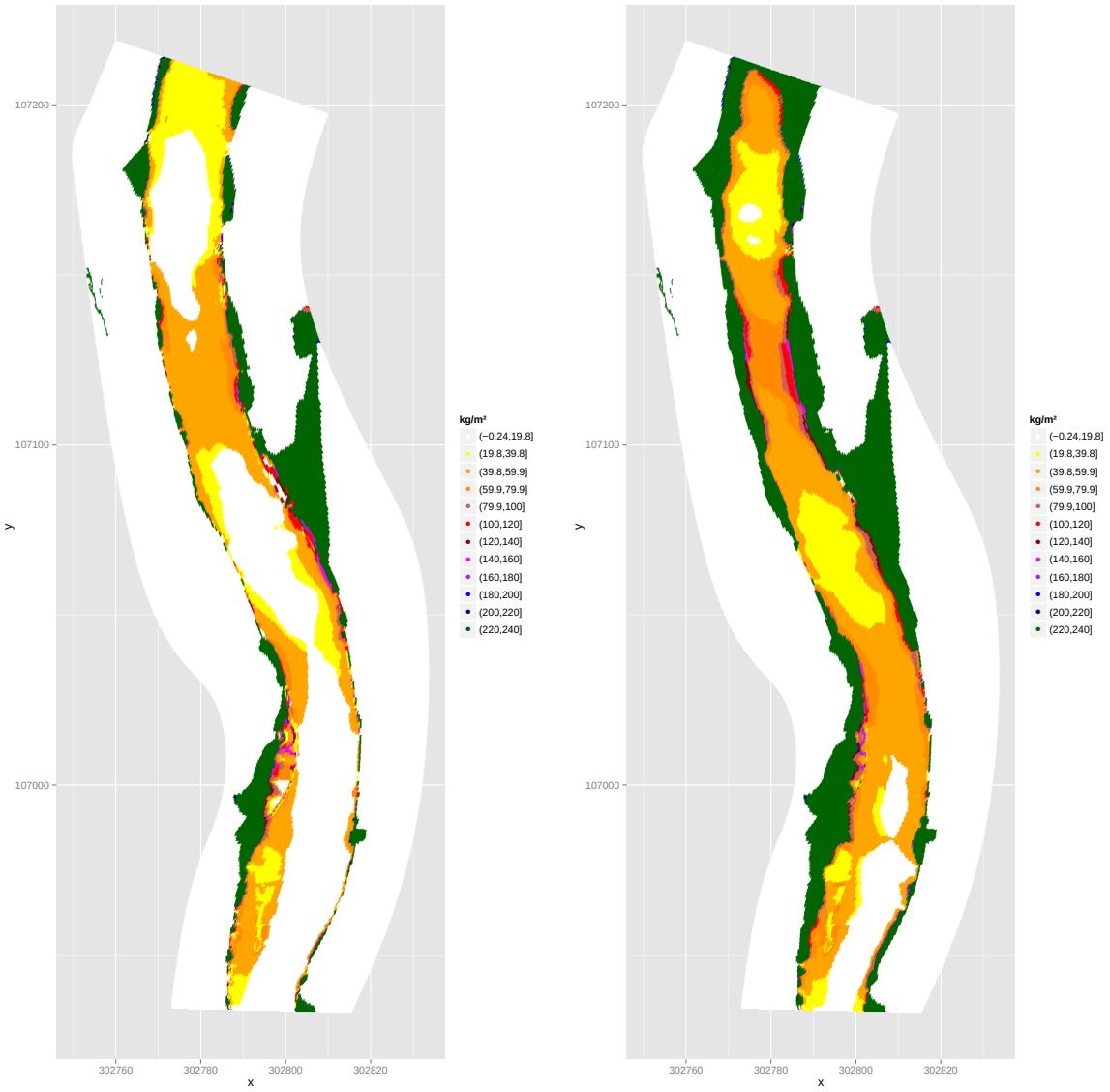

(a) Threshold f1=7.1 Pa (b) Threshold f2=14.2 Pa

Figure 6.16: Distribution of interstitial deposition for end of the scenario Period at Stonyford with threshold f1 = 7.1 Pa and f2 = 14.2 Pa. Deposition is displayed in discrete classes from 0 to 240 kg m^{-2}, x as easting, y as northing.

For higher re-suspension threshold the distribution of interstitial deposition is similar to f2. Figure 6.17 shows interstitial deposition at Stonyford for the same stage

peaks as the Smithincott peak 1 and peak 5. In contrary to Smithincott, the re-suspension is only complete for the riffle areas of the main channel. Pool areas experience further suspended sediment deposition. The interstitial deposits increase from peak to peak.

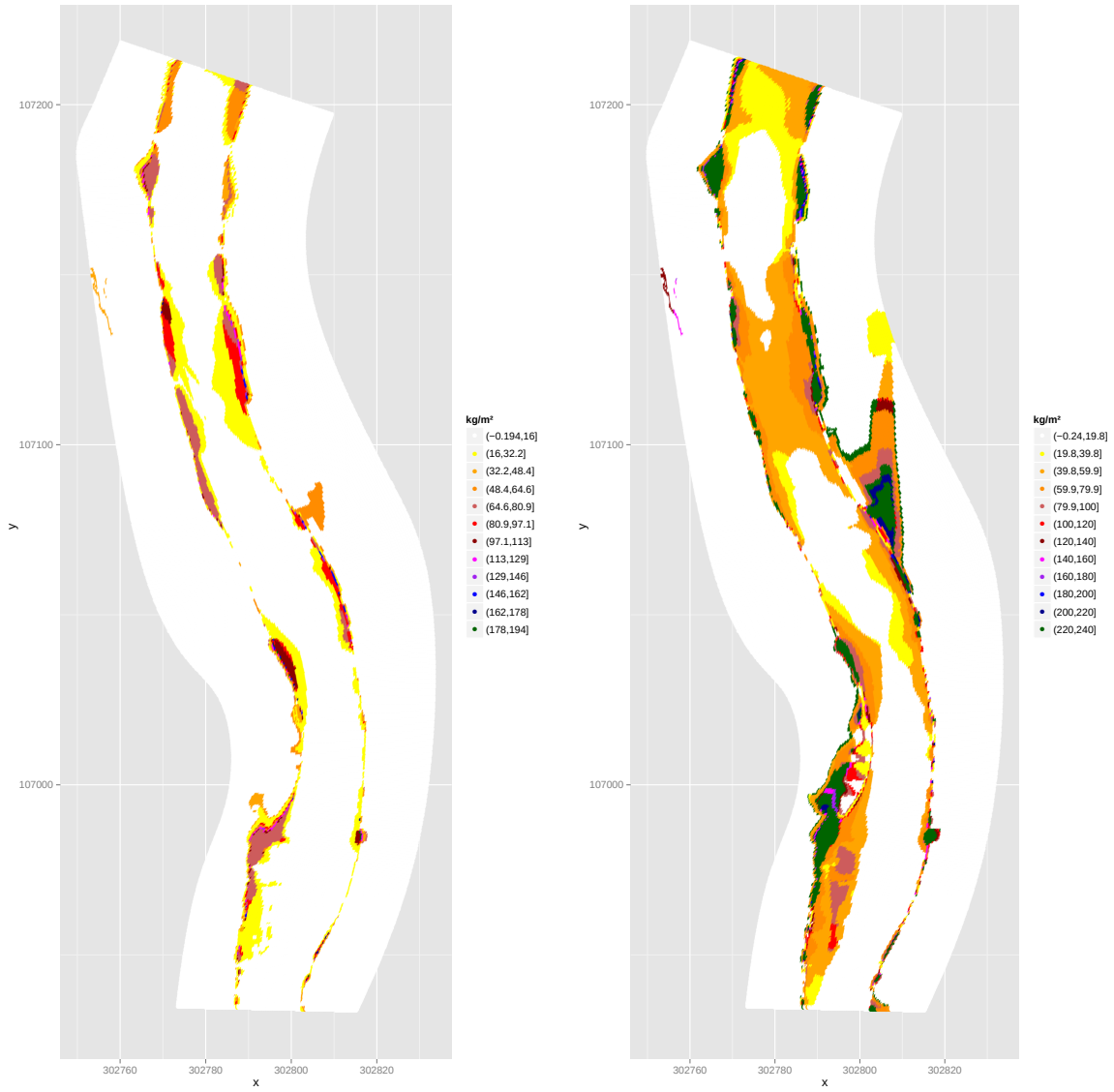

(a) Threshold f1 peak 1 at Julian day 307 (b) Threshold f1 peak 4 at Julian day 333

Figure 6.17: Distribution of interstitial deposition of the scenario at Smithincott with threshold f1 = 5.9 Pa for two selected stage peaks. Deposition is displayed in discrete classes from 0 to 240 kg m^{-2}, x as easting, y as northing.

During peak 1, average deposition in the wetted channel is 18 kg m^{-2} (displayed in Figure 6.17a, with a stage of 1.25 m), increasing to 48 kg m^{-2} for peak 2 at Julian

day 327 and cummulating with 183 kg m^{-2} for peak 4 (displayed in Figure 6.17b, with a stage of 1.3 m).

Rewe For the Rewe reach, bed shear stresses are also not in excess of the threshold f2 = 11.4 Pa for the scenario period. Especially for the distribution of interstitial deposition at the end of the scenario period, the two threshold do not differ, as Figure 6.18a and 6.18a show an almost identical uniform deposition of 240 kg m^{-2} in the area of the wetted channel.

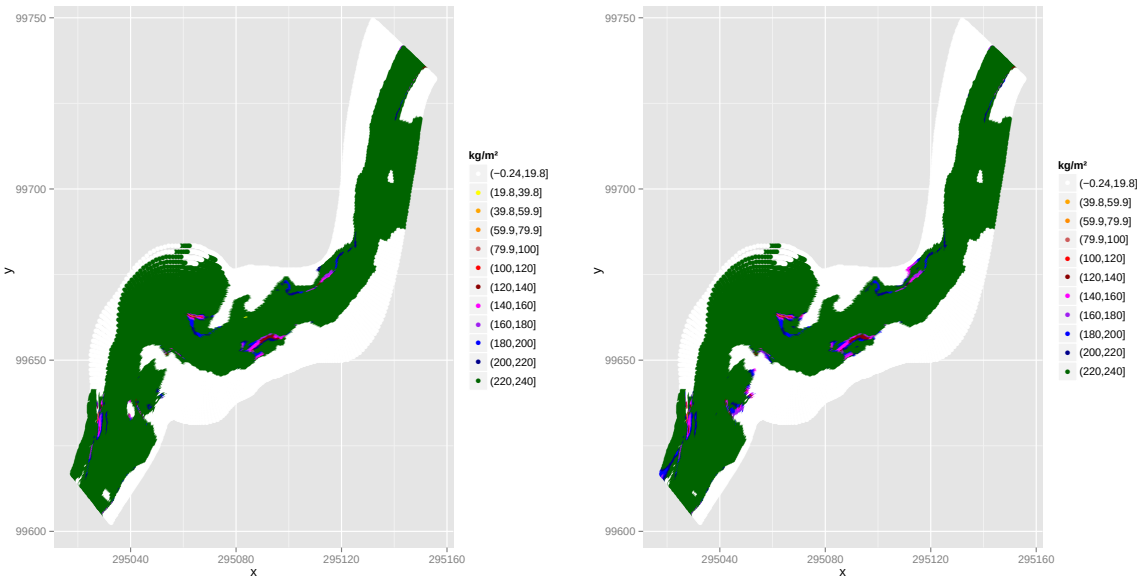

(a) Threshold f1 = 5.7 Pa (b) Threshold f2 = 11.4 Pa

Figure 6.18: Distribution of deposition for scenario at Rewe with threshold f1 = 5.7 Pa and f2 = 11.4 Pa. Deposition displayed in discrete classes from 0 to 240 kg m^{-2}, x as easting, y as northing.

This means, under the given conditions, Rewe's modelled interstitial deposition accumulates until the maximum deposition is reached.

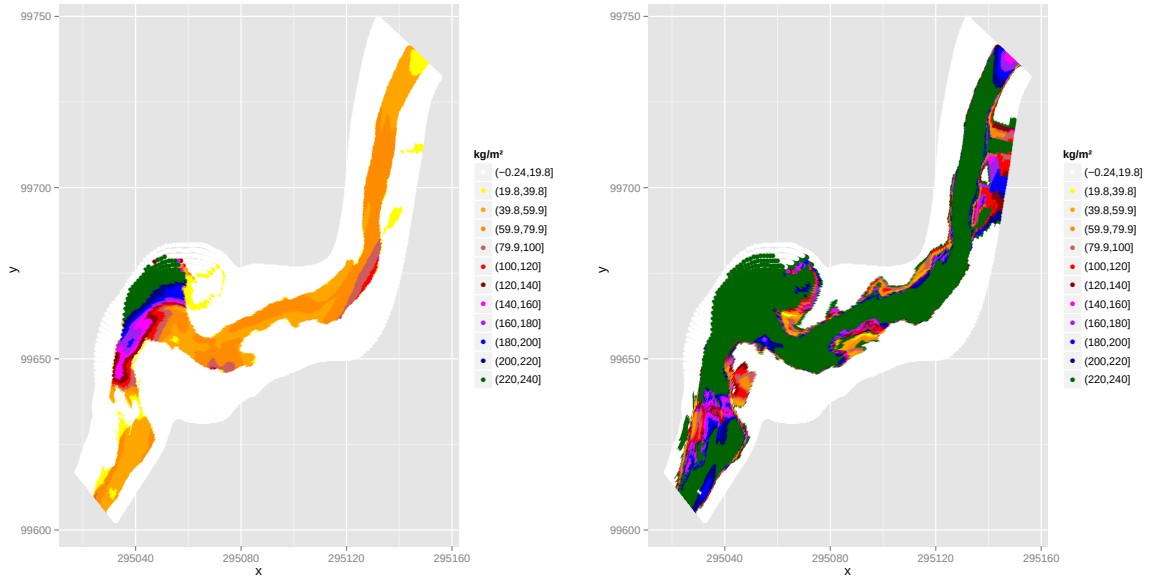

(a) Rewe f1 peak 1, genau gleich wie f2

(b) Rewe f1 peak 3

Figure 6.19: Distribution of deposition for Scenario at Rewe with threshold f1 = 5.7 Pa for two selected peaks. Deposition displayed in discrete classes from 0 to 240 kg m^{-2}, x as easting, y as northing.

Figure 6.19a and 6.19b show the deposition at Rewe after the stage peak of 1.3 m at Julian day 307 and the stage peak of 1.4 m at Julian day 333, the same peaks as shown for the Stonyford reach. For Rewe, the wetted channel experienced almost uniform deposition over this period. Only the small riffle stretch at the downstream end of the reach experiences re-suspension.

Overall, the model in its current stage simulates high variations over time in interstitial fine-grained sediment. For the six weeks of simulated winter run off, the model predicts rapid change of phases of high interstitial deposition and flushing of the gravel bed. This dynamic is most pronounced for the reach at Smithincott, where the whole wetted channel is cleaned from interstitial fine during stage peaks. In Stonyford, this dynamic change is only true for riffle stretches and in Rewe it is restricted to riffle runs.

6.5 Conclusion

This chapter consolidated **all parts of the research project in the setup of a reach scale numerical suspended sediment deposition model**. The model is an advancement of the flume scale model presented in Chapter 3. It can calculate local interstitial deposition and re-suspension in patches of a reach in dependence on the stage and suspended sediment concentration, which are easily available field records (see Chapter 4).

Further the model includes the simulation results of the hydrodynamic models in Chapter 5. The patches in the deposition model were defined according to the grid cells in the hydrodynamic models. Also, the **velocity distribution for the deposition model was extracted from hydrodynamic model simulations** for a wide range of stage levels.

The model structure, in its basic parts, was resumed from the flume scale model, which means, the model is also based on the Krone formulation. Moreover, the **best performing value set for the parameters in the Krone formulation were also adopted from the flume scale model**.

However, some adaptions were applied. The major adaptions for model upscaling were the simplification of the concentration definition and the inclusion of a threshold for net re-suspension. In the calibration procedure of the reach scale model, different **thresholds of interstitial sediment re-suspension were tested**, which originally based on the critical bed shear stress of mobilisation of the D_{90} of the gravel bed.

Calibration of this threshold (at this stage) was limited to the examination of the general applicability of the model to reach scale. Above the uncertainty already connected to the flume scale fine sediment deposition model (3) and the estimation of local velocity (Chapter 5), the major short coming of the reach scale model calibration was the **small number of observation points of interstitial deposition**, their relatively similar positions within the main river channel and their coarse temporal resolution (weeks). Moreover, the field investigations did not answer any questions

about the mechanism of re-suspension and the implementation of the re-suspension threshold purely depends on literature findings. Nevertheless, the calibration could show that for low re-suspension thresholds (10-20 % of the critical bed shear stress for the mobilisation of the D_{90} of the gravel bed) the **magnitudes of modelled interstitial deposition range in the same order of magnitude as the measured trapping ratios for all reaches**. The good performance of the same re-suspension threshold in all three reaches suggests that the model can recreate suspended sediment deposition processes for a wide range of conditions. The modelled deposition patterns, although only tested for dominantly mid stream positions, show deposition pattern consistent with the literature. For example, deposition is the highest in deeper pools and on the river margins, as for example stated by Walling et al. (2003). However, the accuracy of the prediction of the processes within the calibration period could not be verified due to the lack of any data on re-suspension and sealing processes.

The scenario simulations showed that from a numerical aspect the model is applicable to reach scale. Further, even given the high level of uncertainty, it can show that **the three reaches experience distinct different patterns of re-suspension**. For the Smithincott reach, the flood event of the scenario period led to complete re-suspension of the interstitial deposits within the main channel area and deposition amounts were dependent on the time distance from the last re-suspension threshold. In Stonyford, the re-suspension was only true for the riffle stretches of the main channel. Pool areas experienced continuous further deposition. In Rewe, re-suspension thresholds were exceeded only locally and interstitial fine-grained sediment was accumulated over the whole scenario period in the complete water covered area until maximum deposition was reached.

At this stage, the reach scale fine sediment deposition model can be seen as a potential scaffolding for further development. The short comings of this work and also the options for further development will be discussed in detail in the Chapter 7.

Chapter 7

Conclusion and outlook

The core aim of this research is to investigate and predict interstitial fine sediment deposition and how it relates to the local characteristics of the gravel bed and the flow. The focus lies on the intrusion of silt and clay size particles into the coarse gravel framework, because these particles hold the highest potential of ecological degradation (Walling et al., 2003; Sear et al., 2014). This stands in contrast to most experimental studies investigating interstitial fine with a focus on sand intrusion in gravels such as Einstein and Krone (1962); Beschta and Jackson (1979); Carling (1984b); Sambrook Smith and Ferguson (1996); Rathburn and Wohl (2003); Curran (2007). What further sets this work apart from the majority of research in this area is the comprehensive approach to the examination of interstitial sediment deposition. This work applies the same methods to both the relatively small-scale and carefully controlled experimental flume work, and the larger scale work conducted in the field study reaches. In order to gain a clearer understanding of the processes involved in interstitial fine sediment deposition, this work uses a numerical model to formally analyse the laboratory data and to enable the prediction of interstitial deposition at small temporal and spatial scales. In this sense, the thesis employs two fundamental elements of research in the physical sciences: 1) Upscaling from the small experimental to the large natural field scale; and 2) The methodological step from descriptive data collection to analytical numerical modelling.

The process delivered a large data set: For example this research developed a large field data set on interstitial fine sediment - with 60 basket trap and more than 80 re-suspension samples distributed over reaches. Therefore, the data outlines exceptionally well the range of interstitial fine sediment deposition with regards to seasonal and spatial variation. Overall, the amount of fine sediment found is much higher, than averages recorded in the literature for both the River Culm and comparable rivers and therefore stresses the relevance of interstitial fine sediment as part of the fine sediment budget. Of special interest is the high interstitial storage found during the summer months with a stable river bed, which was not recorded before to that extent. Further, the basket traps delineated different deposition behaviour of river reaches with different flow regime. The upper reaches are characterised by rapid changes in the interstitial fine sediment storage, whereas the lower reaches are more prone to continuous fine interstitial deposition and are possible flushed only a few times a year. Further, the results of the large number of flume experiments with a systematic approach to parameter testing delivered a data set which shed light into expected and unexpected processes influencing interstitial fine sediment deposition. For example the flume data stressed the importance of a separate evaluation of coarser non-cohesive (sand) and finer cohesive (silt and clay) sediment. The local distribution of sandy fine sediment is governed by gravity and therefore dependent on the flow conditions in the water column, whereas the local distribution of deposition of finer cohesive sediment appears to be influenced by several other processes such as the combing effect of the gravel frame work and local turbulences in introduced by the structures of the river bed. On top of this comprehensive data acquisition (for more detail see Chapter 2 and 4), the research project succeeded in developing a fully functioning numerical model for interstitial fine sediment deposition applicable for both the flume and field scale based on the Krone (1962) formulation using the statistical software R. This model includes the main parameters believed to influence deposition and still remains fairly moderate with regards to input data requirements.

However, despite a carefully designed and implemented research approach resulting in the above achievements, every step in this research project was characterised by challenges and problems, cumulating in the inability of the numerical model to predict the observed rates of fine sediment deposition both in the flume and even less satisfactory in the field scale fine sediment deposition model. This concluding chapter discusses the study results in the light of the work of other researchers, to assess the setbacks of this research in the context of current debates in the field of environmental modelling, and to identify improvements that could be made future research.

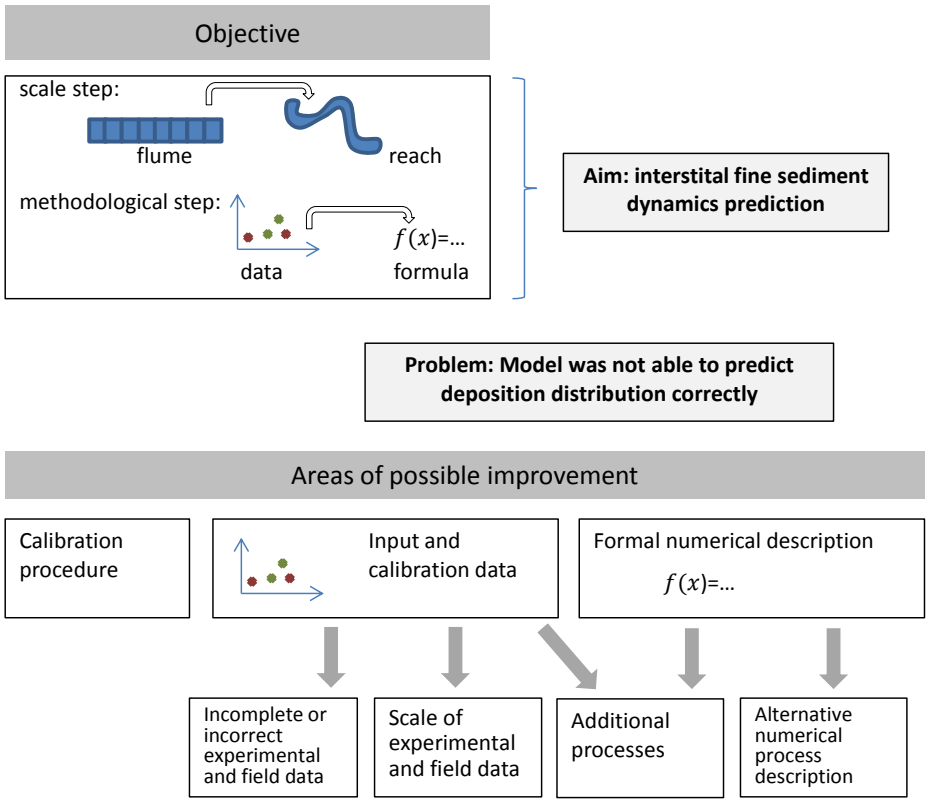

Figure 7.1: Possible areas of model improvement

The effort to systematically analyse the causes of discrepancies between the modelled and the observed data is what Beven (2007, 2010) describes as ‘a model as a part of a learning process‘. Such a critical examination allows the model to

evolve and ideally, to get closer to ‘a description of the real system‘ (Beven, 2010). In particular, because this work failed to achieve its declared objective to predict interstitial sediment dynamics, clarification of where the work towards the model and where the model itself went wrong is crucial for any further investigation. Given the multi-scale and multi-technique approach implemented in this study, possible areas of improvement range from the data acquisition, to the formal description of the underling science in the model, to the processes of model calibration The outline of the following discussion is shown in Figure 7.1. It starts with the area, which might be improved most readily - the calibration of the model and continues to discuss the the more complex and inevitably interlinked areas of data acquisition and formal model representation.

7.1 The calibration process

There are several reasons why a model may not reproduce the real world. A failure of the calibration procedure is relatively easy to address and this is therefore discussed first. In this work, all three calibration procedures (for the flume scale sediment deposition model, the hydrodynamic model applied to the field reaches, and the reach scale sediment deposition model) used a suite of robust, yet simple statistical approaches (as used by many other studies, see Legates and McCabe, 1999; Boyle et al., 2000; Davies and Fearn, 2006; Moriasi et al., 2007; Montanari et al., 2009) to compare observed and modelled data with the aim of optimising the agreement between the model results and the observed data.

The calibration procedure applied to the flume scale sediment deposition model (Chapter 3.3) concentrated primarily on the ability of the model to represent the loss of suspended sediment from the water column. This was carried out using observations of suspended sediment concentration to calculate the bulk sediment load transported in the flume. The calibration process used a wide range of calibration

parameters and resulted in good agreement between the modelled and observed concentration loss for all fine sediment grain sizes and experimental settings. This good accordance was evident for several different combinations of the calibration parameters. The fact that the best performance of the model was not associated with a unique combination of model parameters, but rather with numerous alternative parameter sets is a phenomena referred to as equifinality (Beven and Freer, 2001; Kirchner, 2006) or *swiss cheese* problem (Abbaspour et al., 2007). The concept of equifinality states that in complex systems (originally biological systems) several different process descriptions can result in the same outcome. More precisely in this case, it occurs when the statistical fit between model results and empirical data is similar for multiple model setups. For the case at hand, the occurrence of similar model predictions when using different combinations of calibration parameters is not surprising, because the different calibration parameters counterbalance each other. For example, if the model is executed with a set of higher settling velocities (e.g. derived using the formula of Gibbs after Loch, 2001) in combination with higher threshold deposition velocities (e.g. derived using the formula of Inman, 1952), this combination results in a similar concentration loss, as if the process is described by lower settling velocities (e.g. Le Roux, 1991) and lower threshold velocities for deposition (Lane, as used in Miller et al., 1977, see for all Figure 3.5). Since the model is intended primarily to quantify the rate of sediment deposition under given environmental conditions, both solutions can be seen as correct process descriptions.

The second step of the model calibration process used data collected during the flume experiments. It involved the comparison of modelled and observed rates of interstitial fine sediment deposition. We observed that the model could be calibrated to reproduce the observed data for sand sized particles, where the limited competence of flow in the flume channel caused rapid deposition, mainly in the upper part of the experimental channel. Similar deposition patterns in flume experiments were also observed by Carling (1984b); Rathburn and Wohl (2003); Curran (2007) and

Wooster et al. (2008) suggesting that the deposition of sand is dominantly driven by particle settling. The calibration of the model with respect to the deposition of silt and clay sized particles did not result in a similar (good) fit to the flume data. In particular, all of the sets of calibration parameters that were examined resulted in a discrepancy between modelled and observed deposition at the positions close to the beginning and end of the experimental channel. This strongly suggests that in areas of changing flow pattern (e.g. where flow enters and exits the flume, out of and into the recirculation pipes) more complex flow structures influence the deposition process, which are not represented by the model or successfully characterized by the velocity measurements and shear stress estimates used to implement the model. A multi-parameter calibration (Cheng et al., 2002; Efstratiadis and Koutsoyiannis, 2010) using, in this case, both sediment concentration loss data and deposition rate data, did not improve the model performance. The reason, why the calibration procedure cannot improve the fit of the local deposition distribution lies within the representation of the parameters controlling local deposition in the model. The calibration procedure does not include the option to change the controls of local deposition for single locations, but only for the whole set (which are experimentally defined values for all locations). This means although we can find an optimum in the statistical calibration procedure, this optimum calibration parameter set does not enable the model to predict the location of sediment deposition correctly, which suggests that either the flow information is not adequate to describe controls on deposition or a crucial process is missed in the numerical process description.

In the case of the calibration of the hydrodynamic models which were applied to the field study reaches, the calibration procedure was based on the same statistical indices as those used in the flume experiment plus the hydrological model specific Nash-Sutcliffe index (Chapter 5.3). Here, only one calibration parameter (the bed roughness coefficient) was adjusted to optimize the agreement between the model and field observations of a set of calibration data (water level, water depth and water

velocity). The calibration procedure identified an optimum bed roughness coefficient for each of the three field reaches. However, the optimum was not fully satisfactory in terms of model performance. In some cases, the model predictions were not sensitive to changes in the calibration parameter, thus a range of different bed roughness coefficients resulted in very small changes in the model output (especially for the study reach at Rewe). In addition, while the calibrated hydrodynamic model yielded adequate predictions of water level and water depth, predictions of flow velocity were less accurate. The scatter plot of observed and modelled velocity values displayed a large cloud of data points (see Figures in Chapter 5.3.5). The close fit between the 1:1 line and the reduced major axis (Davies and Fearn, 2006) for the line of best fit between modelled and observed velocity suggests that these discrepancies are local and randomly distributed, and are not associated with systematic errors, which could have been reduced by the calibration procedure. This may mean that the hydrodynamic model is not able to represent the heterogeneity of the natural system. Alternatively, it may reflect noise in the field dataset. Both of these issues reflect the fact that the model is relatively simple in many respects. For example, it is based on depth-averaged, two-dimensional hydrodynamic equations that neglect three-dimensional flow structures and turbulent processes. In contrast, the field measurements of velocity are a product of more complex phenomena operating (and measured) at much finer spatial and temporal scales.

The application of the fine sediment deposition model at the field scale (Chapter 6.3) aimed to calibrate the model by defining a suitable resuspension threshold (the critical flow velocity required to mobilise the gravel framework and therefore cause complete fine sediment flushing from the bed). The calibration data comprised the observed fine sediment deposition for a data set of 60 basket traps collected during six calibration periods. The model calibration succeeded in defining a threshold that enabled the model to reproduce the magnitude of the observed deposition over the study reaches a whole. However, no agreement was found between observed and

predicted values for the intra-reach deposition. This may be connected to the same causes as the problems of local deposition prediction in the flume scale model. Beyond, a field specific problem is the long time periods over which the sediment traps were deployed. Alternatively, it may reflect the failure of the hydrodynamic model to predict local variations in velocity within the study reaches, as described above.

All three model calibration procedures were implemented carefully and yet the approaches adopted here do not enable the model to reproduce the real system adequately. This suggests that the cause of the weak model performance in all three cases lies within the other two possible areas (see Figure 7.1). Consequently, the second area to look for improvement is the acquisition of input and calibration data.

7.2 Data acquisition

The flume experiments (Chapter 2) were intended to provide the initial basis for understanding the relationships between fine sediment deposition, bed characteristics and flow conditions. Consequently, this component of the research is evaluated first with regard to the acquisition of the model input and calibration data. One strength of the experimental setup was its ability to recreate some aspects of the variability of natural gravel-bed rivers (e.g. by using a wide range of gravel grain sizes and a bed characterised by alternating topographic highs and lows in experimental Series 2). This introduced a high degree of complexity in the flow conditions compared to a flat bed (see Series 1 and many other experimental studies, such as Beschta and Jackson, 1979; Schlchli, 1992; Grams and Wilcock, 2007; Wooster et al., 2008).

Flow velocity was measured using ADVs at four positions above the river bed and for several positions along the river bed in down and cross stream direction, including several positions above each trap and three lateral positions for each location along the experimental channel. Despite this attempt to characterise the variability of flow within the flume, the measured velocity data and the derived bed shear stress values

displayed very weak correlations to measured local deposition rates for silt and clay sized particles, see for example the velocity at 10 cm height in Figure 2.22. One implication of this observation is that deposition of silt and clay size particles might be independent of local flow conditions. However, this goes against the general perception of fine sediment transport processes (Chapter 1.2.2). Based on these observations, one could conclude that the flow measurements do not characterise the hydrodynamic mechanisms that control fine sediment deposition adequately, either because they are lacking in detail or were implemented at the wrong locations.

With respect to the latter possibility, it has been observed that conditions measured outside the boundary layer may be of only limited value as predictors of fine sediment deposition (Carling, 1984b), because processes that control deposition occur very close to the gravel bed (and closer than lowest velocity measurements made here, which were located 0.05 m above the bed). A further affirmation that the lack of correlation between flow hydrodynamics and sedimentation rates is likely a result of issues linked to the flow data acquisition, is provided by the existence of comparable studies which identified clear relationships between flow conditions and the depositional behaviour of silt and clay size particles. These studies characterised the complexity of the flow with measurements made at higher spatial resolutions also closer to, or within, the bed (such as Brasington et al., 2000; Lawless and Robert, 2001; Strom, 2004; Hosseini et al., 2006; Tonina, 2005). From these results it can be deduced that for silt and clay sized particles gravitational forces (e.g. characterised by particle settling alone) counteracted by the mean transport capacity of the flow (when not measured close to the bed) are not sufficient to explain local rates and patterns of sediment deposition. For these grain sizes, turbulent processes occurring close to or even within the gravel bed (Kirchner et al., 1990; Beven, 2010) are likely the dominant influence on sediment deposition.

One approach to improve the potential for testing the simple modelling framework is to simplify the experimental setup (e.g., by using a narrower range of sedi-

ment sizes and minimizing topographic variability with the flume channel). However, these conditions within the flume are already less complex than conditions of natural gravel-bed rivers. Consequently, a move towards a more simplistic experimental setup is not seen as the solution to the problems identified above. Instead, improved flow measurements are required in order to characterise the hydrodynamic heterogeneity within the flume at finer spatial and temporal scales, and close the gravel bed. A first step towards an improved measurement of flow heterogeneity is a more detailed velocity sampling in horizontal direction and vertical positions. However, with the ADV-set used in this research, measurements closer to the bed is not feasible and alternative approaches need to be considered to investigate the conditions in the boundary layer. For example, the influence of single gravel bed structures on flow could be measured isolated from the deposition experiments with a bed setup featuring just one of the three main bed alterations (obstacle, rising and falling bed) with the aim to evaluate the overlapping flow structures separately (such as Papanicolaou et al., 2010; Moustakidis et al., 2012). A different and possibly enlightening approach to detect flow structures near and in the experimental gravel bed are dye experiments (Salehin et al., 2004; Tsakiris and Papanicolaou, 2008; Reidenbach and Koehl, 2011). For example, Tsakiris and Papanicolaou (2008) visualised turbulent flow structures around artificial boulders with injected dye. Such visual records of flowpaths help to identify areas of turbulences, diverging and converging flow. A further possibility to measure the strength of flow conditions within the gravel framework is the use of pressure tubes within the gravel bed (such as used in Tonina, 2005).

In addition to the collection of improved hydrodynamic datasets, the ability of the model to predict fine sediment deposition might be improved by the collection of data that better characterises the gravel framework structure of the bed. The influence of gravel grain sizes on flow and deposition is recognised by several researchers (Lisle and Madej, 1992; Wooster et al., 2008; Cui et al., 2008). In this study, Series 1

experimental runs were intended to measure the influence of gravel grain size on deposition. However, this aim was not met due to the very small differences in observed deposition between the traps with different gravel grain size distributions. The minimal differences are more prone to noise in the sedimentation rate data, which may conceal a relationship between the gravel bed sediment size and local deposition. At a larger scale, the Series 2 experimental runs could show that a finer gravel framework enhances fine sediment deposition. The fact that only two different gravel grain sizes distributions were used in the flume experiments made it difficult to include an index of gravel grain size in the model. Despite this, other researchers, such as Wooster et al. (2008) succeeded in measuring the influence of framework grain size on fine sediment deposition. They divided an experimental flume into segments with different gravel grain sizes. The deposition differences between segments were also clearer in the latter study due to the use of a much higher fine sediment input (introduced at a constant feeding rate, which in some experiments led to total saturation of the gravel-bed). This approach reduced relative errors in the measurement of fine sediment deposition compared to experiments characterised by lower sediment supply and hence deposition, as in this study. The implication is that the ability to derive data able to discriminate between different model setups might be improved by conducting experiments using higher fine sediment loads, and indeed perhaps a much wider range of fine sediment concentrations than those considered here.

A further difference worth noting is the much smaller gravel grain size used in the Wooster et al. (2008) experiments compared to the experiments conducted here. The relation between the grain size of the suspended sediment and the pore size is highly relevant for deposition (Cui et al., 2008). It is possible that the unnaturally large pore space in the experiments (due to the restriction to larger gravel sizes and the fact that the bed was not water-worked, which results in unnatural bed structure) of this research in combination with the very fine material in suspension, contributed to the difficulties experienced when attempting to identify clear relationships between

sediment deposition and bed material size in the Series 1 experiments. In order to overcome this lack of finer gravel in the bed framework, at least for the bed sediment traps, a mesh fabric could be used to enclose the gravel traps. Alternatively, the gravel framework could be fixed in the traps with glue. The use of a fixed gravel framework, for the traps or possibly for the topmost gravel bed layer, could also improve standardisation between the single experimental runs (i.e. if the same traps were used in all experiments).

The question of how far the fine sediment travels vertically into the trap and how far this sediment travels horizontally through the trap may be crucial for determining how much sediment remains in the trap, rather than passing through it or being remobilised from the bed surface. This is indicated to some extent by the differences in observed deposition between traps located in areas of rising and falling bed height. In order to better understand the importance of these processes it is possible to carry out a set of experiments using traps with open and closed side walls synchronously, or experiments in which deposition at different levels within the bed is quantified by burying traps deeper in the substrate.

A further area of data uncertainty is the characterisation of the suspended sediment grain size and settling characteristics. The combined use of LISST and Digi-Sizer measurements in this study provides a means of quantifying both the effective and absolute grain sizes of fine sediment. However, both methods have clear limitations when relating the grain size to settling behaviour (because neither approach provides information on particle density or shape). A much more detailed investigation of the relationship between fine sediment grain size and deposition rates is required, particularly in the light of the very different performances of the model for sand sized compared to silt and clay sized particles. The development of flocs and the associated alteration of depositional behaviour over time has been recognised by Kranck (1975); Mehta and Partheniades (1975); Stone and Droppo (1994); Droppo and Ongley (1998); Fettweis (2008). Such a mechanism was also visible in the ex-

perimental data acquired in this study, although it could not be incorporated into the numerical model of sediment deposition due to a lack of data needed to parameterise and evaluate the representation of such processes. One possible solution to this is the use of high resolution camera technology to observe the motion of single particles, as used by Brasington et al. (2000) and Haralampides et al. (2003). In both studies, a Malvern particle size analyser was used to show the settling and the formation of flocs during the experiments.

The data measured in the field for evaluating the hydrodynamic model is also a sources of potential error that may lead to poor model performance. For example, one reason for the weak performance of the hydrodynamic model could also lie with the field measurements of flow velocity used to calibrate the model. One explanation for the poor hydrodynamic model performance is the high spatial and temporal heterogeneity of the natural flow velocity (Kirchner et al., 1990). Thus, the flow velocity measured at one point in the field is not necessarily representative of a whole model grid cell. Similarly, the small number of velocity measurements made at each cross-section makes it difficult to obtain a reliable estimate of the discharge through the section, as is evident in the high variability in the discharge estimates at the different cross-sections in each reach (see Table 5.2). Linked to this problem of flow heterogeneity, the weak agreement between observed and simulated local velocity can also be caused by the quality of the bathimetric information used for constructing the model grid. Although the elevation survey for the DEM was performed with a differential GPS, the survey points were arranged in cross-sections separated by a distance of approximately half a river width distance. This means that small near-bed structures, known to be influential on local velocity (Lawless and Robert, 2001; Strom, 2004; Papanicolaou et al., 2010) are not included in the bed topography of the model. Furthermore, one could argue that for the application of a hydrodynamic model that aims to predict conditions over a range of flow discharges, the calibration data is required over a similar range of flow conditions. In contrast, model calibration

in the current study has been carried out using only low flow data. The availability of flow depth and velocity data for a wider range of discharges is particularly important because the influence of bed topography is highly dependent on the depth of the water column (Hendriks et al., 2006). Moreover, it is likely that the parametrisation of bed roughness should be depth dependent, and that roughness coefficients should vary as a function of discharge.

The main shortcoming of the calibration process implemented for the sediment deposition model at the field scale is that it relies purely on the basket trap deposition data. Moreover, application of the sediment trap technique in the field faces major problems. For example, due to the inaccessibility of the river during the winter flood season, traps were installed within the river for long periods of several weeks. Large amounts of sediment were trapped during these periods, however, there was limited information on the processes leading to this deposition. For example, the traps did not record how often fine sediment moved in and out of the trap. Similarly, it was not possible to determine if the interstitial fine sediment was affected by processes such as the sealing of the top layer of the bed due to clogging by fine sediment (as in the experiments of Beschta and Jackson, 1979; Wooster et al., 2008). In addition, the temporal resolution of the field data (weeks) and the numerical model (hours or finer) are fundamentally different. If the reach scale model aims to deliver predictions on a sub-flood time scale, shorter trap application time intervals are crucial for a better model evaluation. Given the difficulty of sampling from the river bed during high flow conditions it is not obvious what the solution to this problem is. In addition, any solution would inevitably require a higher sampling frequency and hence higher equipment and labour costs (compared to this study). Sediment traps with solid side walls (for example used by Mahoney and Erman, 1984; Phillips and Walling, 1999; Zimmermann and Lapointe, 2005) may be an option that would enable faster and easier recovery, possibly even from the river bank, because these do not require sleeves to be pulled by to ensure sediment remains trapped, and because they do

not suffer from the interlocking of bed sediment outside the trap with the trap itself. Also compartmented traps such as used by Frostick et al. (1984a) with different sealing times for the compartments could help towards a higher temporal resolution of trap data. Nevertheless, trap installation would still depend on the accessibility of the bed. With sufficient man power, deposition samples can be drawn at high discharge with plate sediment traps (similar to those used by Kozerski, 2002) several times during a storm event with high sediment loads.

However, a common weakness of all sediment traps is the lack of any record of the re-mobilsation of the interstitial fine sediment. Data quantifying this process is crucial for addressing a major source of uncertainty in the model as it stands. Therefore, a reliable description of interstitial fine sediment re-suspension is necessary. Although several authors believe that the re-mobilisation of fine sediment deposited in the gravel framework is only possible if the whole bed moves (Ashworth and Ferguson, 1989; Diplas and Parker, 1992; Klingeman, 1998; Lauck et al., 1993), there are other studies suggesting re-suspension prior to such a threshold. Allan and Frostick (1999) were the first to describe a dilation effect of the bed just before the threshold of entrainment of the river bed was exceeded. Whether such lifting of the gravel framework does allow fines to intrude and be deposited rapidly (Allan and Frostick, 1999; Brasington et al., 2000) or whether it enables sediment flushing from the bed (Marquis and Roy, 2012) is not yet fully understood. One possible approach for investigating re-suspension under field conditions is to increase flow velocities artificially. This could be achieved by the installation of boards located to concentrate flow on one area of the river channel with synchronous sediment concentration and flow velocity measurements, combined with the observation of gravel movement.

7.3 Model process representation

The need for a more detailed investigation of the processes controlling fine sediment deposition in gravel-bed rivers, as demonstrated in the previous section, attests to the existence of a considerable gap in the conceptual understanding of these processes. To address this situation requires the collection of flow and sediment transport and deposition data at higher spatial and temporal resolutions compared to this study. However, several aspects of the comparison between model results and flume and field data in this study show that the deposition equation used in the numerical model (Krone, 1962) is not an adequate and sufficient description of the processes controlling fine sediment deposition (especially silt and clay sized sediment) in a gravel bed. At this point, it is difficult to be certain which additional processes are effectively influencing the fine sediment deposition and need to be included in the formal model description. However, it is clear that the model outcome can benefit greatly from the inclusion of other conceptual elements in the numerical description (see also discussion in Rathburn and Wohl, 2003, on conceptual components and scales in fine sediment transport models).

It seems likely that is be necessary to include a more complex description of flow conditions within such a revised numerical model. As a starting point, the effect of micro-scale bedforms (e.g. pebble clusters) and mean and turbulent near-bed flow structures need to be considered (Hassan and Reid, 1990; Strom, 2004). Given its relevance in many fine sediment studies, the model needs to specifically consider the conditions in the boundary layer as the most active region of bulk water and gravel bed interaction (Carling, 1984b; Van Rijn, 1984b; Krishnappan, 1994). This is closely connected to the occurrence of hyporheic flow (Tonina, 2005) and therefore the possibility of horizontal fine sediment movement through the gravel framework. A differentiation of vertical and horizontal fine sediment movement is an approach that should be considered, too. An example of such a model, concentrating on the conditions in the boundary layer, was developed by Van Rijn (1984b) where explicitly

the concentration in the so called active layer close to the bed is the object of his deposition equation. However, while the use of three-dimensional models to simulate flow structures and fine sediment transport through the water column is relatively common (e.g. Lawless and Robert, 2001; Shams et al., 2002; Ji et al., 2002; Bouma et al., 2007; Ali et al., 2011) , definition of model boundary conditions representing sediment erosion and deposition at the bed is less certain, and likely requires the development and testing of new theory. Such boundary conditions are also influenced by the properties of the gravel framework. Some indications of the influence of the bed gravel grain size were evident in the experimental data collected in this study (e.g. higher deposition in the finer gravel bed with a D_{50} of 37 mm compared to a D_{50} of 48 mm). However, the relationship between substrate grain size and fine sediment deposition is complex, involving feedbacks between gravel size, porosity, roughness, near-bed flow and flow/sediment exchanges between the water column and substrate. Additionally, the representation of these processes in numerical models requires further attention.

In the current model, fine sediment is characterised by its absolute grain size, which is much smaller than the effective grain size. The inclusion of grain sizes (and possible grain shapes and densities) more representative of fluvial fine sediment is likely necessary for a more accurate prediction of sedimentation. In addition, it may also be necessary to include flocculation processes within the numerical model as implemented in the model developed by Krishnappan (1994), who successfully simulated conditions during deposition experiments in an annular flume. Given the significance of accurate and detailed flow information for prediction improvement, the model requires a suitable numerical representation of the flow structures caused by micro-forms and in the boundary layer. To achieve this for the model on reach scale, flow needs to be represented using a three-dimensional approach based on Computational Fluid Dynamics approaches, rather than the two-dimensional representation used for this research which is not able to represent many controls on local velocity

variability (Lawless and Robert, 2001; Shams et al., 2002; Tsakiris and Papanicolaou, 2008).

In addition, processes such as parallel turbulent re-suspension during the deposition (described in Carling, 1984b) need to be locally differentiated, possibly in relation to the above mentioned micro-forms of the gravel bed. Furthermore, as discussed with regards to the acquisition of the field data, processes connected to the (potentially) complete re-suspension of interstitial fine sediment and associated with the movement of the gravel framework need to be investigated further and incorporated with the model. It is clear, that in order to enable the representation of such a multitude of parallel processes, a single deposition equation is not likely to be sufficient to describe the movement of fine sediment from suspended load through the entry in the gravel framework to the deposition in the pore space and possible re-suspension. A model giving consideration to such different processes needs an extended conceptual structure, possibly with different modules representing the single processes. The numerical description of a larger number of processes within one model is potentially easier with a detachment from physically based descriptors and the use of a more empirical approach. Lauck et al. (1993) for example, used stochastic process descriptions to describe random raining of sediment particles dropping into a predefined pore space of a heterogeneous gravel framework consisting of several layers. The stochastic descriptions determined the process of a single particle moving from one layer into the next deeper layer. The end of the sedimentation process was reached, when the predefined pore space of one layer (foremost the top layer) was completely saturated with fine sediment. Wooster et al. (2008) and Cui et al. (2008) used this approach in each of their models, where for example Cui et al. (2008) described the intrusion of fine sediment into a stable gravel framework using a continuity equation including a pore space dependent trapping coefficient. Sakthivadivel and Einstein (1970) also developed a stochastic description of fine sediment deposition from intra-gravel flow. They described the critical ratio

between the pore size of the framework and the size of the sediment, with a threshold of the fine sediment being 50% of pore space. This causes clogging and inhibits smaller particles to infiltrate deeper. Another stochastic approach was pursued by Kleinhans and van Rijn (2002) with experimentally determined relations between deposition and bed shear stress, fine sediment particle size and turbulence. Further, their model includes a hindrance effect and a representation of the concept of Ferguson (2003a), where non uniform flow results in higher transport rates than a uniform flow of the same average strength. There is considerable scope for improving the physical basis of the flow and sediment transport equations used in this study. However, even having done this, and having coupled such advances with suitable field or experimental datasets, a further problem with the process description remains to be overcome, in the form of the need to upscale model results from the fine spatial and temporal scales at which processes operate to the larger scales at which information on bed siltation is required.

This study attempted to address the need for upscaling using a combined laboratory and field-based approach. However, significant differences exist between the laboratory and the natural environment that are problematic and make direct extrapolation of flume data to the field very challenging (Rathburn and Wohl, 2003). These include differences in the magnitude and degree of variability in flow conditions between these environments (depths and velocities in the flume being typically smaller and less variable than in nature) and differences in both sediment grain size characteristics. For example, although, the intra trap gravel grain size distributions in the flume experiments and in the field were broadly comparable, the natural gravel surrounding the traps had a much finer size distribution. Since horizontal water and sediment movements within the bed might be crucial, and the gravel framework strongly influences the infiltration process (Lisle and Madej, 1992), such phenomena can change the depositional behaviour of the traps fundamentally. Moreover, the traps in the flume were used with a much lower fine sediment concentration and a much finer

suspended sediment grain size distribution. In contrast to the flume, the occurrence of pore clogging through higher and coarser fractions of interstitial fine sediment is very likely and a completely different process than the one measured in the flume experiments of this study.

To conclude, the general demand for more data and a better process representation in the model is the main result of this final discussion. At the end of such a labour intensive study aiming to understand and model the dynamics of interstitial fine sediment, it becomes very clear that the research started from a conceptual viewpoint which was too simplistic to explain the observed interstitial deposition. The experimental, field and the modelling work showed that the comprehensive approach applied could show the general framework in which deposition takes place but fell short in investigating several processes relevant for interstitial fine sediment dynamics. Particularly the investigation of processes operating at fine spatial scales were not investigated in a sufficient depth to be able to use the data for process description and quantification. However, this does not mean that the data acquisition and the modelling work was not valuable as such. In an area where it generally proves challenging to measure process heterogeneity at the temporal and spatial scales sufficient to enable model prediction at the resolution relevant to ecological processes (e.g. fish spawning), the data acquired and the modelling conducted here reflect an effort not met by many other studies. Furthermore, in the sense of a learning process, this last Chapter, has outlined a long list of additional promising methods to further enhance the process understanding and to deliver a more detailed investigation of the heterogeneity controlling fine sediment deposition in gravel beds. It is worth noting though that the adoption of these more sophisticated methods comes with a significant increase in time and costs.

As a general recommendation, further work, restricted to the time limits of a few years, should decide if its aim is to conduct a broad investigation of the many processes that influence fine sediment deposition on and in the river bed, or to examine

a single process in depth. If approaching the subject from a modelling perspective, this study has shown that simplified equations applied at large spatial scales are unlikely to yield accurate predictions, principally due to the complexity of the processes controlling interstitial deposition. Therefore, enhanced modelling in this area should be executed with the focus on a detailed process description, applied at fine temporal and spatial resolutions, and supported by empirical datasets acquired at commensurate scales.

Appendix A

Modeling Fine Sediment Behavior in Gravel-Bed Rivers

A.1 Flume scale deposition model

A.1.1 Step 2, shear stress deposition model, silty experimetnal runs

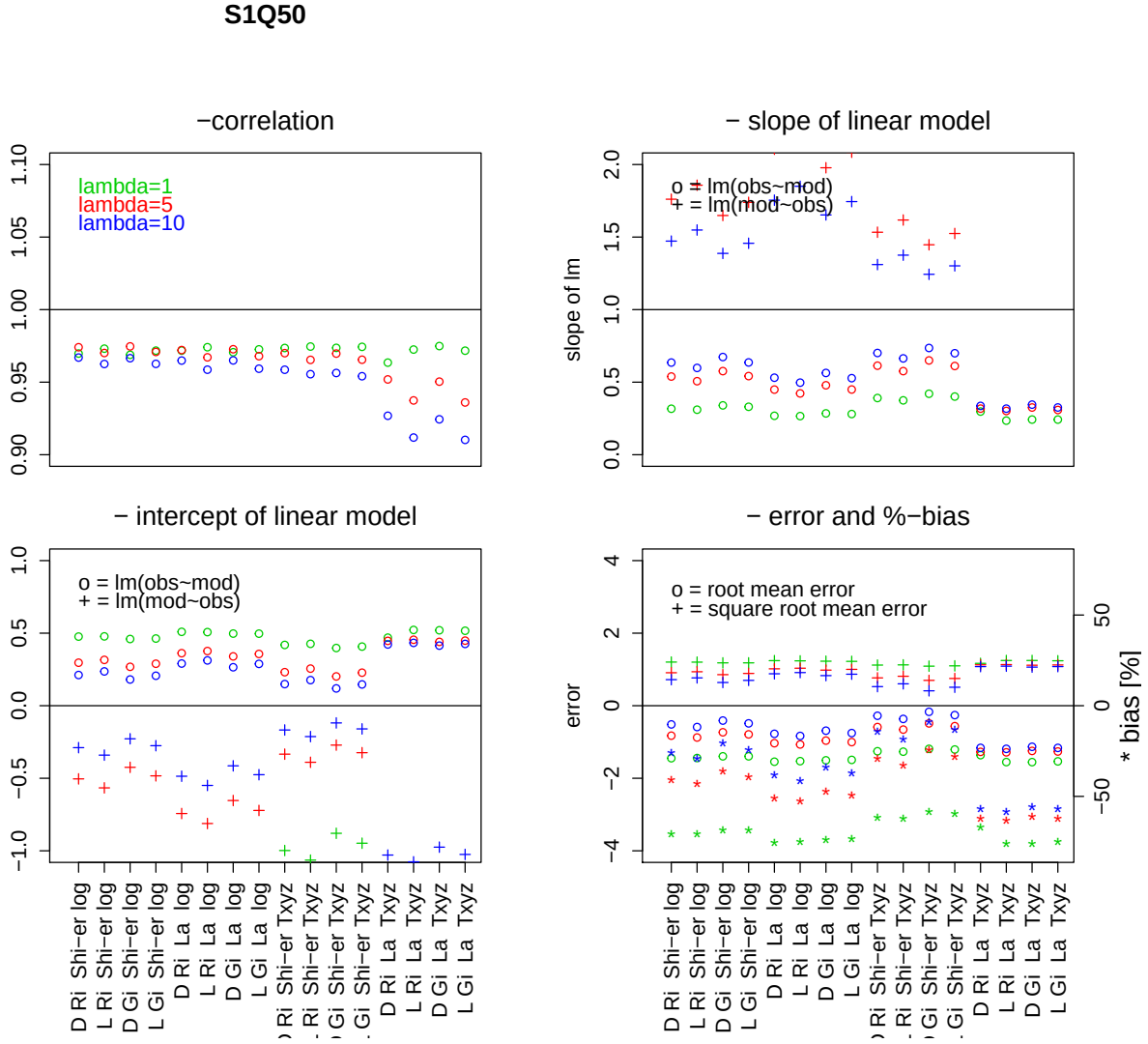

Figure A.1: Graphical representaiton of statisitcal evaluation of modeled and observed suspended sediment concentration loss in S1Q50, shear stress deposition model

	r^2	LM_{mo}		LM_{om}		RMA		Error		
		a	b	a	b	a	b	MSE	SMSE	PBIAS
1DRi Shi-erlog	0.97	0.32	0.48	2.97	-1.39	0.33	0.47	-1.45	1.20	-70.14
5DRi Shi-erlog	0.97	0.54	0.30	1.76	-0.50	0.55	0.29	-0.83	0.91	-40.02
10DRi Shi-erlog	0.97	0.64	0.21	1.47	-0.29	0.66	0.20	-0.52	0.72	-25.00
1LRi Shi-erlog	0.97	0.31	0.48	3.05	-1.44	0.32	0.47	-1.44	1.20	-69.88
5LRi Shi-erlog	0.97	0.51	0.32	1.86	-0.57	0.52	0.31	-0.88	0.94	-42.46
10LRi Shi-erlog	0.96	0.60	0.24	1.55	-0.34	0.62	0.23	-0.59	0.77	-28.50
1DGi Shi-erlog	0.97	0.34	0.46	2.76	-1.25	0.35	0.46	-1.40	1.18	-67.61
5DGi Shi-erlog	0.97	0.58	0.27	1.65	-0.42	0.59	0.26	-0.73	0.86	-35.52
10DGi Shi-erlog	0.97	0.67	0.18	1.39	-0.23	0.70	0.17	-0.41	0.64	-19.85
1LGi Shi-erlog	0.97	0.33	0.46	2.86	-1.30	0.34	0.46	-1.40	1.18	-67.58
5LGi Shi-erlog	0.97	0.54	0.29	1.74	-0.48	0.56	0.28	-0.79	0.89	-38.29
10LGi Shi-erlog	0.96	0.64	0.21	1.46	-0.28	0.66	0.20	-0.49	0.70	-23.60
1DRi La log	0.97	0.27	0.51	3.52	-1.77	0.28	0.51	-1.54	1.24	-74.81
5DRi La log	0.97	0.45	0.36	2.11	-0.74	0.46	0.36	-1.03	1.02	-50.07
10DRi La log	0.96	0.53	0.29	1.75	-0.49	0.55	0.28	-0.77	0.88	-37.54
1LRi La log	0.97	0.27	0.51	3.56	-1.79	0.27	0.50	-1.53	1.24	-74.06
5LRi La log	0.97	0.42	0.38	2.21	-0.81	0.44	0.37	-1.07	1.03	-51.76
10LRi La log	0.96	0.50	0.31	1.85	-0.55	0.52	0.30	-0.83	0.91	-40.39
1DGi La log	0.97	0.28	0.50	3.31	-1.62	0.29	0.49	-1.51	1.23	-72.96
5DGi La log	0.97	0.48	0.34	1.98	-0.65	0.49	0.34	-0.96	0.98	-46.60
10DGi La log	0.97	0.56	0.26	1.65	-0.41	0.58	0.26	-0.69	0.83	-33.36
1LGi La log	0.97	0.28	0.50	3.37	-1.66	0.29	0.49	-1.49	1.22	-72.38
5LGi La log	0.97	0.45	0.36	2.08	-0.72	0.46	0.35	-1.00	1.00	-48.63
10LGi La log	0.96	0.53	0.29	1.74	-0.48	0.55	0.28	-0.75	0.87	-36.55
1DRi Shi-erTxyz	0.97	0.39	0.42	2.43	-1.00	0.40	0.42	-1.26	1.12	-60.83
5DRi Shi-erTxyz	0.97	0.61	0.23	1.53	-0.33	0.63	0.22	-0.59	0.77	-28.51
10DRi Shi-erTxyz	0.96	0.70	0.15	1.31	-0.17	0.73	0.14	-0.28	0.53	-13.43
1LRi Shi-erTxyz	0.97	0.37	0.43	2.54	-1.06	0.38	0.42	-1.27	1.13	-61.42
5LRi Shi-erTxyz	0.97	0.58	0.26	1.62	-0.39	0.60	0.25	-0.66	0.81	-31.89
10LRi Shi-erTxyz	0.96	0.66	0.18	1.38	-0.21	0.69	0.17	-0.36	0.60	-17.66
1DGi Shi-erTxyz	0.97	0.42	0.40	2.26	-0.88	0.43	0.39	-1.19	1.09	-57.61
5DGi Shi-erTxyz	0.97	0.65	0.20	1.45	-0.27	0.67	0.19	-0.49	0.70	-23.64
10DGi Shi-erTxyz	0.96	0.74	0.12	1.24	-0.12	0.77	0.11	-0.17	0.41	-8.17
1LGi Shi-erTxyz	0.97	0.40	0.41	2.37	-0.95	0.41	0.40	-1.21	1.10	-58.51
5LGi Shi-erTxyz	0.97	0.61	0.23	1.52	-0.32	0.63	0.22	-0.56	0.75	-27.31
10LGi Shi-erTxyz	0.95	0.70	0.15	1.30	-0.16	0.73	0.14	-0.26	0.51	-12.54
1DRi La Txyz	0.96	0.30	0.47	3.12	-1.44	0.31	0.47	-1.36	1.17	-66.05
5DRi La Txyz	0.95	0.32	0.45	2.85	-1.24	0.33	0.44	-1.27	1.13	-61.64
10DRi La Txyz	0.93	0.34	0.42	2.55	-1.03	0.36	0.41	-1.16	1.08	-56.31
1LRi La Txyz	0.97	0.24	0.52	4.02	-2.08	0.24	0.52	-1.55	1.25	-75.29
5LRi La Txyz	0.94	0.30	0.45	2.91	-1.28	0.32	0.45	-1.29	1.13	-62.27
10LRi La Txyz	0.91	0.32	0.43	2.62	-1.08	0.35	0.42	-1.19	1.09	-57.61
1DGi La Txyz	0.97	0.24	0.52	3.92	-2.02	0.25	0.52	-1.56	1.25	-75.35
5DGi La Txyz	0.95	0.33	0.44	2.78	-1.19	0.34	0.43	-1.25	1.12	-60.39
10DGi La Txyz	0.92	0.35	0.41	2.48	-0.97	0.37	0.40	-1.13	1.06	-54.86
1LGi La Txyz	0.97	0.24	0.52	3.90	-1.99	0.25	0.51	-1.53	1.24	-74.35
5LGi La Txyz	0.94	0.31	0.45	2.84	-1.23	0.33	0.44	-1.26	1.12	-61.18
10LGi La Txyz	0.91	0.33	0.43	2.55	-1.02	0.36	0.41	-1.16	1.08	-56.34

Table A.1: Calibration statistics for modeled and observed suspended sediment concentration loss in S1Q50, shear stress deposition model

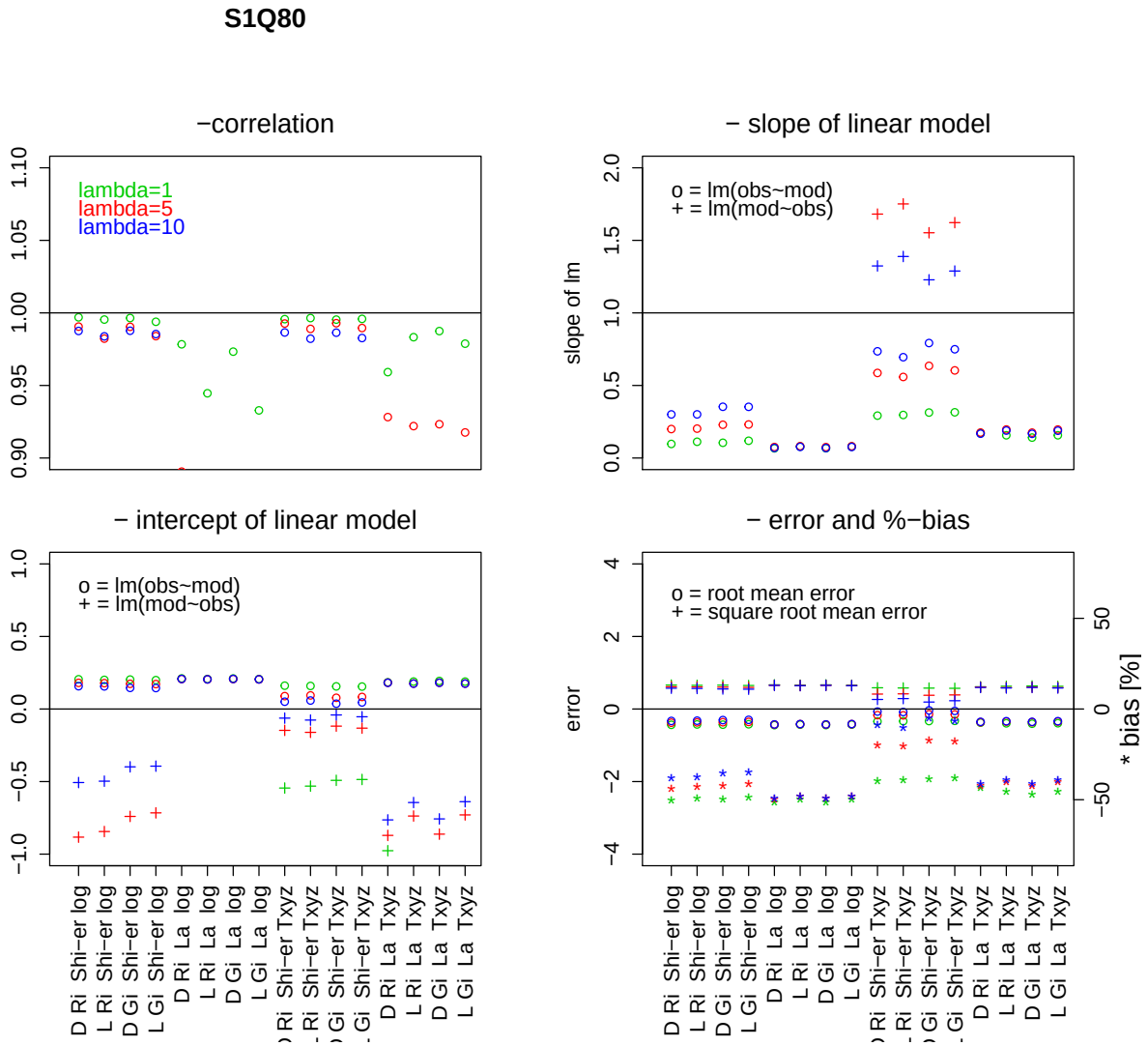

Figure A.2: Graphical representaiton of statisitcal evaluation of modeled and observed suspended sediment concentration loss in S1Q80, shear stress deposition model

	r^2	LM_{mo}		LM_{om}		RMA		Error		
		a	b	a	b	a	b	MSE	SMSE	PBIAS
1DRi Shi-erlog	1.00	0.10	0.20	10.26	-2.10	0.10	0.20	-0.44	0.66	-49.66
5DRi Shi-erlog	0.99	0.20	0.18	4.92	-0.88	0.20	0.18	-0.38	0.61	-43.01
10DRi Shi-erlog	0.99	0.30	0.16	3.25	-0.51	0.30	0.16	-0.33	0.57	-37.41
1LRi Shi-erlog	1.00	0.11	0.20	8.84	-1.78	0.11	0.20	-0.43	0.65	-48.44
5LRi Shi-erlog	0.98	0.20	0.18	4.77	-0.84	0.21	0.18	-0.37	0.61	-42.01
10LRi Shi-erlog	0.98	0.30	0.16	3.22	-0.50	0.31	0.16	-0.32	0.57	-36.61
1DGi Shi-erlog	1.00	0.10	0.20	9.46	-1.92	0.11	0.20	-0.43	0.66	-49.14
5DGi Shi-erlog	0.99	0.23	0.17	4.28	-0.74	0.23	0.17	-0.36	0.60	-41.47
10DGi Shi-erlog	0.99	0.35	0.15	2.76	-0.40	0.36	0.14	-0.31	0.55	-34.74
1LGi Shi-erlog	0.99	0.12	0.20	8.31	-1.65	0.12	0.20	-0.42	0.65	-47.91
5LGi Shi-erlog	0.98	0.23	0.17	4.19	-0.72	0.23	0.17	-0.36	0.60	-40.50
10LGi Shi-erlog	0.99	0.35	0.14	2.75	-0.39	0.36	0.14	-0.30	0.55	-34.00
1DRi La log	0.98	0.07	0.21	14.35	-3.02	0.07	0.21	-0.44	0.67	-50.61
5DRi La log	0.89	0.08	0.21	10.48	-2.14	0.08	0.21	-0.43	0.65	-48.74
10DRi La log	0.81	0.07	0.21	9.52	-1.92	0.09	0.20	-0.43	0.65	-48.39
1LRi La log	0.94	0.08	0.21	11.26	-2.31	0.08	0.21	-0.43	0.66	-49.15
5LRi La log	0.84	0.08	0.20	8.61	-1.71	0.10	0.20	-0.42	0.65	-47.52
10LRi La log	0.78	0.08	0.20	7.87	-1.55	0.10	0.20	-0.41	0.64	-47.25
1DGi La log	0.97	0.07	0.21	14.03	-2.94	0.07	0.21	-0.44	0.67	-50.45
5DGi La log	0.88	0.08	0.21	10.35	-2.11	0.09	0.21	-0.43	0.65	-48.68
10DGi La log	0.80	0.07	0.21	9.38	-1.89	0.09	0.20	-0.42	0.65	-48.35
1LGi La log	0.93	0.08	0.21	11.04	-2.26	0.08	0.21	-0.43	0.66	-48.99
5LGi La log	0.83	0.08	0.20	8.50	-1.69	0.10	0.20	-0.42	0.65	-47.47
10LGi La log	0.77	0.08	0.20	7.78	-1.53	0.10	0.20	-0.41	0.64	-47.22
1DRi Shi-erTxyz	1.00	0.29	0.16	3.39	-0.54	0.29	0.16	-0.34	0.59	-39.05
5DRi Shi-erTxyz	0.99	0.59	0.09	1.68	-0.15	0.59	0.09	-0.17	0.41	-19.28
10DRi Shi-erTxyz	0.99	0.74	0.05	1.32	-0.06	0.75	0.05	-0.07	0.26	-7.91
1LRi Shi-erTxyz	1.00	0.30	0.16	3.35	-0.53	0.30	0.16	-0.34	0.58	-38.28
5LRi Shi-erTxyz	0.99	0.56	0.09	1.75	-0.16	0.56	0.09	-0.17	0.42	-19.86
10LRi Shi-erTxyz	0.98	0.69	0.06	1.39	-0.08	0.71	0.06	-0.08	0.29	-9.42
1DGi Shi-erTxyz	1.00	0.31	0.16	3.16	-0.49	0.31	0.16	-0.33	0.58	-37.80
5DGi Shi-erTxyz	0.99	0.64	0.08	1.55	-0.12	0.64	0.08	-0.14	0.38	-16.36
10DGi Shi-erTxyz	0.99	0.79	0.04	1.23	-0.04	0.80	0.03	-0.04	0.19	-4.21
1LGi Shi-erTxyz	1.00	0.31	0.15	3.15	-0.49	0.32	0.15	-0.33	0.57	-37.10
5LGi Shi-erTxyz	0.99	0.60	0.08	1.62	-0.13	0.61	0.08	-0.15	0.39	-17.19
10LGi Shi-erTxyz	0.98	0.75	0.05	1.29	-0.05	0.76	0.04	-0.05	0.23	-5.95
1DRi La Txyz	0.96	0.17	0.18	5.37	-0.98	0.18	0.18	-0.38	0.61	-42.79
5DRi La Txyz	0.93	0.18	0.18	4.91	-0.87	0.19	0.18	-0.36	0.60	-41.45
10DRi La Txyz	0.86	0.17	0.18	4.43	-0.76	0.19	0.18	-0.35	0.59	-40.26
1LRi La Txyz	0.98	0.16	0.19	6.18	-1.16	0.16	0.19	-0.39	0.63	-44.88
5LRi La Txyz	0.92	0.20	0.18	4.33	-0.74	0.21	0.17	-0.35	0.59	-39.56
10LRi La Txyz	0.86	0.19	0.17	3.91	-0.64	0.22	0.17	-0.34	0.58	-38.28
1DGi La Txyz	0.99	0.14	0.19	6.93	-1.34	0.14	0.19	-0.41	0.64	-46.12
5DGi La Txyz	0.92	0.17	0.18	4.88	-0.86	0.19	0.18	-0.36	0.60	-41.33
10DGi La Txyz	0.86	0.17	0.18	4.40	-0.76	0.19	0.18	-0.35	0.59	-40.20
1LGi La Txyz	0.98	0.16	0.19	6.12	-1.15	0.16	0.19	-0.39	0.63	-44.63
5LGi La Txyz	0.92	0.20	0.18	4.29	-0.73	0.21	0.17	-0.35	0.59	-39.44
10LGi La Txyz	0.85	0.19	0.17	3.88	-0.64	0.22	0.17	-0.34	0.58	-38.21

Table A.2: Calibration statistics for modeled and observed suspended sediment concentration loss in S1Q80, shear stress deposition model

	r^2	LM_{mo}		LM_{om}		RMA		Error		
		a	b	a	b	a	b	MSE	SMSE	PBIAS
1 D Ri Shi-er log	0.96	0.70	0.52	1.32	-0.64	0.73	0.50	-4.72	2.17	-55.57
5 D Ri Shi-er log	0.97	0.86	0.12	1.09	-0.10	0.89	0.11	-0.56	0.75	-6.60
10 D Ri Shi-er log	0.96	0.94	-0.06	0.99	0.10	0.97	-0.08	1.32	1.15	15.59
1 L Ri Shi-er log	0.96	0.65	0.58	1.40	-0.76	0.68	0.56	-5.17	2.27	-60.95
5 L Ri Shi-er log	0.96	0.84	0.18	1.11	-0.15	0.87	0.16	-1.10	1.05	-12.93
10 L Ri Shi-er log	0.96	0.93	-0.02	0.99	0.07	0.97	-0.04	0.87	0.93	10.23
1 D Gi Shi-er log	0.96	0.73	0.46	1.26	-0.53	0.76	0.44	-4.14	2.04	-48.80
5 D Gi Shi-er log	0.97	0.89	0.06	1.05	-0.02	0.92	0.04	0.11	0.33	1.31
1 L Gi Shi-er log	0.96	0.69	0.52	1.34	-0.65	0.72	0.50	-4.63	2.15	-54.51
5 L Gi Shi-er log	0.96	0.87	0.10	1.06	-0.07	0.91	0.08	-0.40	0.63	-4.71
1 D Ri La log	0.96	0.67	0.57	1.38	-0.74	0.69	0.55	-5.16	2.27	-60.79
5 D Ri La log	0.97	0.82	0.19	1.14	-0.18	0.85	0.18	-1.20	1.10	-14.18
10 D Ri La log	0.96	0.89	0.02	1.04	0.02	0.93	0.00	0.60	0.78	7.11
1 L Ri La log	0.96	0.62	0.63	1.48	-0.88	0.65	0.61	-5.60	2.37	-65.97
5 L Ri La log	0.96	0.79	0.25	1.17	-0.25	0.82	0.23	-1.77	1.33	-20.85
10 L Ri La log	0.96	0.88	0.07	1.04	-0.02	0.92	0.04	0.10	0.31	1.14
1 D Gi La log	0.96	0.70	0.51	1.33	-0.63	0.73	0.50	-4.62	2.15	-54.41
5 D Gi La log	0.97	0.85	0.13	1.10	-0.11	0.88	0.11	-0.57	0.75	-6.71
1 L Gi La log	0.96	0.65	0.57	1.41	-0.77	0.68	0.56	-5.09	2.26	-59.97
5 L Gi La log	0.96	0.83	0.19	1.12	-0.16	0.86	0.17	-1.12	1.06	-13.18
1 D Ri Shi-er Txyz	0.95	0.69	0.54	1.32	-0.66	0.72	0.52	-5.01	2.24	-58.99
5 D Ri Shi-er Txyz	0.97	0.87	0.14	1.09	-0.11	0.89	0.12	-0.77	0.88	-9.04
10 D Ri Shi-er Txyz	0.96	0.94	-0.04	0.99	0.09	0.97	-0.07	1.15	1.07	13.51
1 L Ri Shi-er Txyz	0.95	0.65	0.60	1.41	-0.80	0.68	0.58	-5.44	2.33	-64.07
5 L Ri Shi-er Txyz	0.96	0.84	0.19	1.11	-0.17	0.87	0.17	-1.30	1.14	-15.30
10 L Ri Shi-er Txyz	0.96	0.93	-0.01	0.99	0.05	0.97	-0.03	0.69	0.83	8.13
1 D Gi Shi-er Txyz	0.96	0.73	0.48	1.26	-0.56	0.76	0.46	-4.43	2.10	-52.18
5 D Gi Shi-er Txyz	0.97	0.90	0.07	1.05	-0.04	0.93	0.05	-0.09	0.30	-1.04
10 D Gi Shi-er Txyz	0.96	0.96	-0.11	0.96	0.15	1.00	-0.13	1.84	1.36	21.71
1 L Gi Shi-er Txyz	0.96	0.68	0.54	1.34	-0.68	0.71	0.52	-4.89	2.21	-57.61
5 L Gi Shi-er Txyz	0.96	0.87	0.12	1.06	-0.08	0.91	0.10	-0.60	0.77	-7.02
10 L Gi Shi-er Txyz	0.96	0.96	-0.08	0.96	0.12	1.00	-0.10	1.43	1.20	16.89
1 D Ri La Txyz	0.97	0.60	0.61	1.58	-0.92	0.62	0.60	-5.11	2.26	-60.19
5 D Ri La Txyz	0.97	0.64	0.52	1.47	-0.72	0.66	0.50	-4.13	2.03	-48.67
10 D Ri La Txyz	0.96	0.69	0.38	1.33	-0.46	0.72	0.37	-2.74	1.65	-32.26
1 L Ri La Txyz	0.96	0.48	0.84	1.93	-1.59	0.50	0.83	-7.44	2.73	-87.64
5 L Ri La Txyz	0.96	0.59	0.58	1.56	-0.86	0.62	0.57	-4.68	2.16	-55.15
10 L Ri La Txyz	0.96	0.65	0.45	1.40	-0.57	0.68	0.43	-3.35	1.83	-39.46
1 D Gi La Txyz	0.96	0.55	0.76	1.71	-1.25	0.57	0.75	-6.76	2.60	-79.59
5 D Gi La Txyz	0.97	0.66	0.47	1.42	-0.62	0.68	0.45	-3.66	1.91	-43.13
10 D Gi La Txyz	0.96	0.71	0.33	1.28	-0.37	0.74	0.31	-2.22	1.49	-26.14
1 L Gi La Txyz	0.97	0.51	0.81	1.85	-1.45	0.52	0.80	-7.10	2.66	-83.63
5 L Gi La Txyz	0.96	0.62	0.53	1.50	-0.75	0.64	0.52	-4.23	2.06	-49.88
10 L Gi La Txyz	0.95	0.67	0.40	1.34	-0.48	0.71	0.38	-2.83	1.68	-33.31

Table A.3: Calibration statistics for modeled and observed suspended sediment concentration loss in S2Q30D48, shear stress deposition model

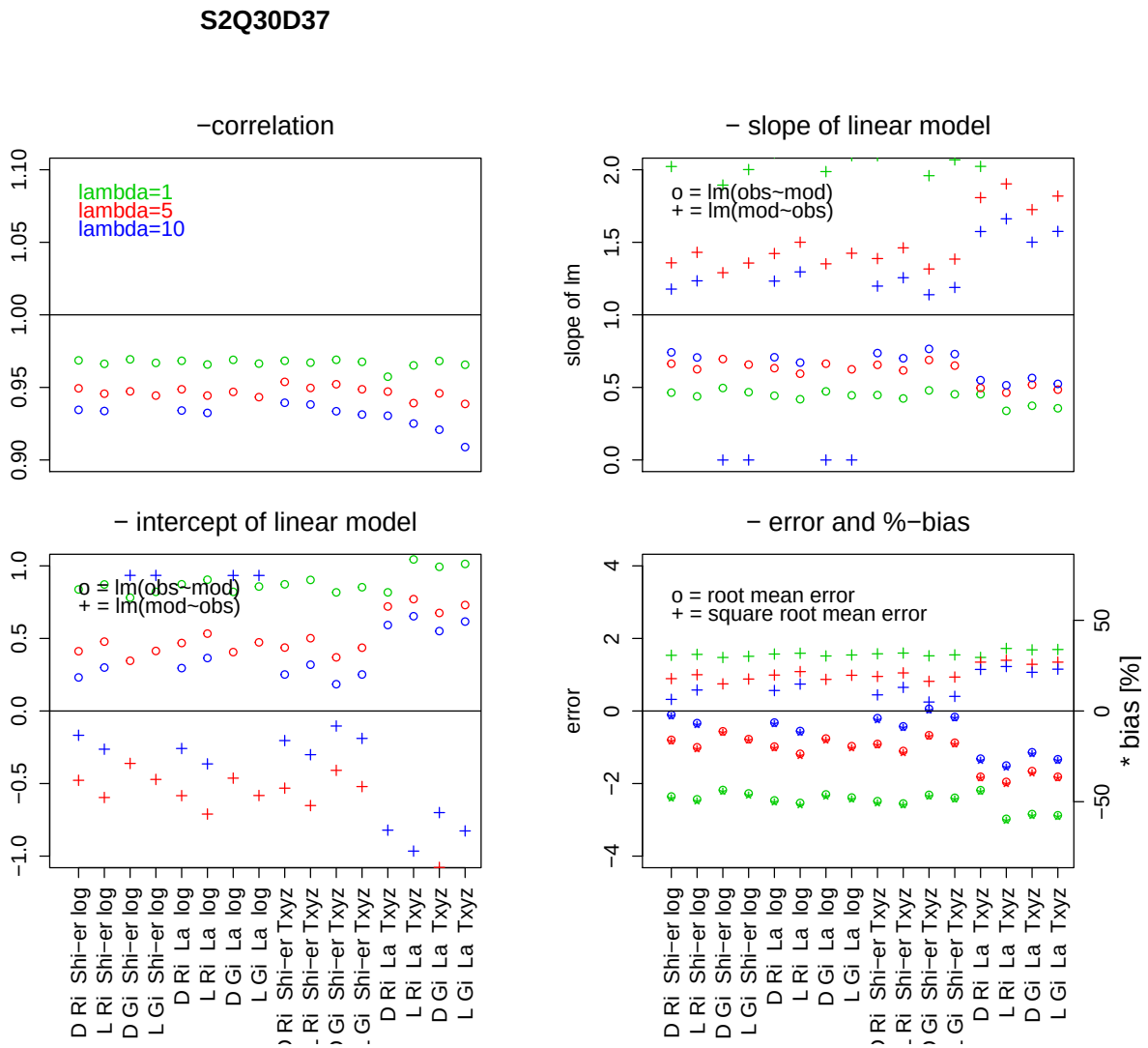

Figure A.3: Graphical representaiton of statisitcal evaluation of modeled and observed suspended sediment concentration loss in S2Q30D37, shear stress deposition model

	r^2	LM_{mo}		LM_{om}		RMA		Error		
		a	b	a	b	a	b	MSE	SMSE	PBIAS
1DRi Shi-erlog	0.97	0.46	0.84	2.02	-1.64	0.48	0.83	-2.36	1.53	-47.31
5DRi Shi-erlog	0.95	0.66	0.41	1.36	-0.48	0.70	0.38	-0.80	0.89	-15.97
10DRi Shi-erlog	0.93	0.74	0.23	1.18	-0.17	0.79	0.19	-0.10	0.32	-2.05
1LRi Shi-erlog	0.97	0.44	0.87	2.13	-1.80	0.45	0.86	-2.43	1.56	-48.88
5LRi Shi-erlog	0.95	0.63	0.48	1.43	-0.60	0.66	0.45	-1.00	1.00	-20.09
10LRi Shi-erlog	0.93	0.71	0.30	1.23	-0.26	0.76	0.26	-0.33	0.58	-6.71
1DGi Shi-erlog	0.97	0.50	0.78	1.89	-1.43	0.51	0.77	-2.18	1.48	-43.73
5DGi Shi-erlog	0.95	0.70	0.35	1.29	-0.36	0.73	0.31	-0.56	0.75	-11.23
1LGi Shi-erlog	0.97	0.47	0.82	2.00	-1.59	0.48	0.81	-2.27	1.51	-45.63
5LGi Shi-erlog	0.94	0.66	0.41	1.36	-0.47	0.70	0.38	-0.78	0.88	-15.57
1DRi La log	0.97	0.44	0.87	2.12	-1.80	0.46	0.86	-2.46	1.57	-49.49
5DRi La log	0.95	0.63	0.47	1.42	-0.58	0.67	0.44	-0.98	0.99	-19.70
10DRi La log	0.93	0.71	0.30	1.23	-0.26	0.76	0.25	-0.32	0.56	-6.40
1LRi La log	0.97	0.42	0.90	2.23	-1.96	0.43	0.89	-2.53	1.59	-50.87
5LRi La log	0.94	0.59	0.53	1.50	-0.71	0.63	0.50	-1.18	1.09	-23.68
10LRi La log	0.93	0.67	0.36	1.30	-0.36	0.72	0.32	-0.55	0.74	-11.06
1DGi La log	0.97	0.47	0.82	1.99	-1.58	0.49	0.81	-2.30	1.52	-46.17
5DGi La log	0.95	0.66	0.41	1.35	-0.46	0.70	0.37	-0.76	0.87	-15.23
1LGi La log	0.97	0.45	0.86	2.10	-1.74	0.46	0.84	-2.38	1.54	-47.88
5LGi La log	0.94	0.62	0.47	1.42	-0.58	0.66	0.44	-0.97	0.98	-19.46
1DRi Shi-erTxyz	0.97	0.45	0.87	2.10	-1.78	0.46	0.86	-2.49	1.58	-49.91
5DRi Shi-erTxyz	0.95	0.66	0.44	1.39	-0.53	0.69	0.41	-0.91	0.95	-18.21
10DRi Shi-erTxyz	0.94	0.74	0.25	1.20	-0.20	0.78	0.21	-0.20	0.44	-3.96
1LRi Shi-erTxyz	0.97	0.42	0.90	2.21	-1.94	0.44	0.89	-2.55	1.60	-51.20
5LRi Shi-erTxyz	0.95	0.62	0.50	1.46	-0.65	0.65	0.47	-1.10	1.05	-22.13
10LRi Shi-erTxyz	0.94	0.70	0.32	1.26	-0.30	0.75	0.28	-0.42	0.65	-8.51
1DGi Shi-erTxyz	0.97	0.48	0.82	1.96	-1.55	0.49	0.80	-2.31	1.52	-46.41
5DGi Shi-erTxyz	0.95	0.69	0.37	1.32	-0.41	0.72	0.34	-0.67	0.82	-13.42
10DGi Shi-erTxyz	0.93	0.77	0.18	1.14	-0.10	0.82	0.14	0.06	0.25	1.23
1LGi Shi-erTxyz	0.97	0.45	0.85	2.07	-1.71	0.47	0.84	-2.39	1.55	-48.04
5LGi Shi-erTxyz	0.95	0.65	0.44	1.38	-0.52	0.69	0.41	-0.88	0.94	-17.57
10LGi Shi-erTxyz	0.93	0.73	0.25	1.19	-0.19	0.78	0.21	-0.16	0.40	-3.26
1DRi La Txyz	0.96	0.45	0.82	2.02	-1.58	0.47	0.80	-2.18	1.48	-43.81
5DRi La Txyz	0.95	0.50	0.72	1.81	-1.22	0.52	0.70	-1.81	1.35	-36.39
10DRi La Txyz	0.93	0.55	0.59	1.57	-0.82	0.59	0.56	-1.31	1.15	-26.38
1LRi La Txyz	0.97	0.34	1.04	2.75	-2.82	0.35	1.03	-2.97	1.72	-59.69
5LRi La Txyz	0.94	0.46	0.77	1.90	-1.37	0.49	0.75	-1.95	1.40	-39.25
10LRi La Txyz	0.93	0.52	0.65	1.66	-0.97	0.56	0.62	-1.50	1.23	-30.18
1DGi La Txyz	0.97	0.37	0.99	2.51	-2.44	0.39	0.98	-2.84	1.69	-57.05
5DGi La Txyz	0.95	0.52	0.68	1.73	-1.08	0.55	0.65	-1.66	1.29	-33.25
10DGi La Txyz	0.92	0.57	0.55	1.50	-0.70	0.61	0.51	-1.14	1.07	-22.85
1LGi La Txyz	0.97	0.36	1.01	2.62	-2.60	0.37	1.00	-2.87	1.70	-57.72
5LGi La Txyz	0.94	0.48	0.73	1.82	-1.23	0.52	0.70	-1.81	1.35	-36.40
10LGi La Txyz	0.91	0.52	0.62	1.58	-0.83	0.58	0.57	-1.33	1.15	-26.71

Table A.4: Calibration statistics for modeled and observed suspended sediment concentration loss in S2Q30D37, shear stress deposition model

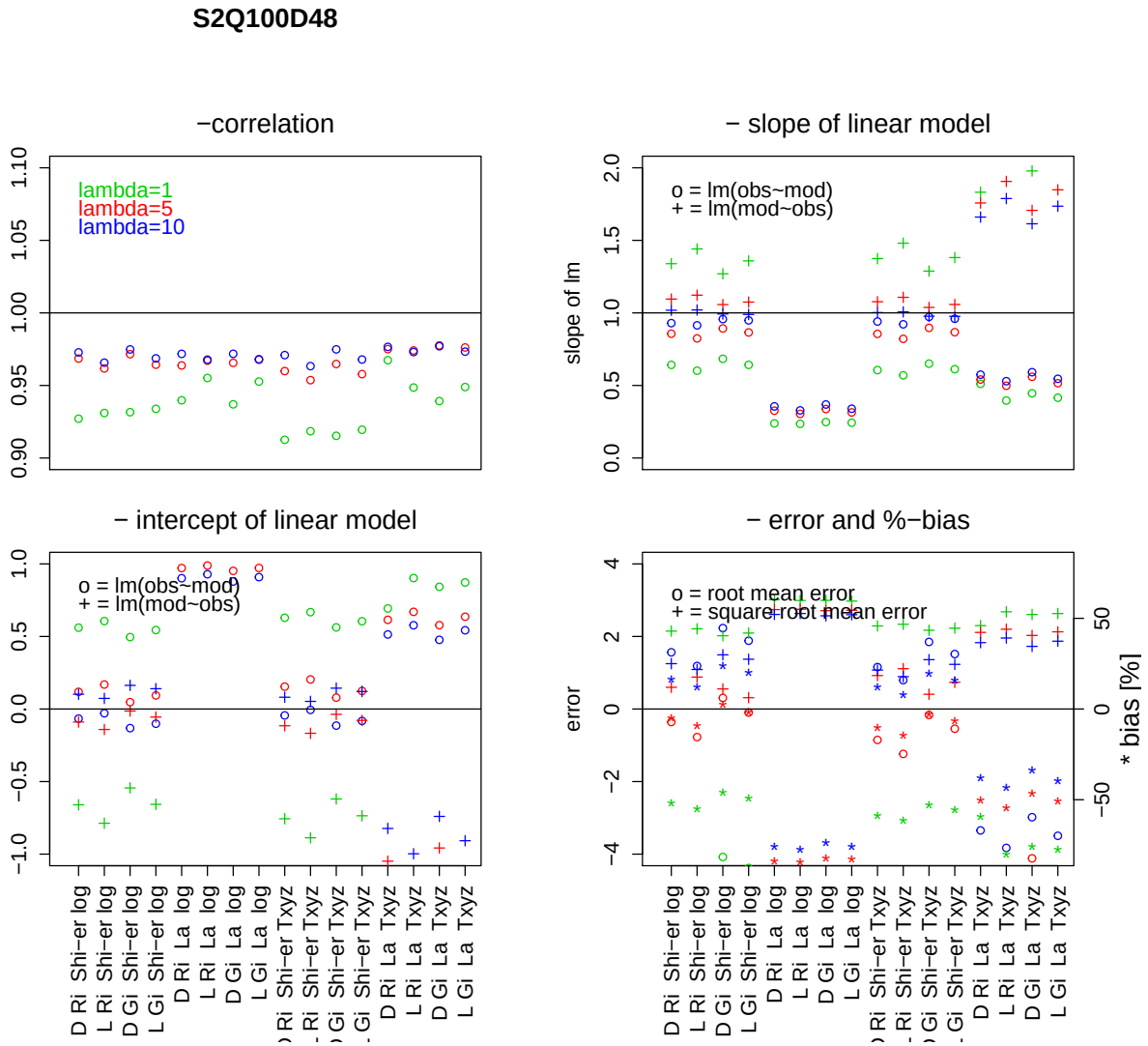

Figure A.4: Graphical representaiton of statisitcal evaluation of modeled and observed suspended sediment concentration loss in S2Q100D48, shear stress deposition model

	r^2	LM_{mo}		LM_{om}		RMA		Error		
		a	b	a	b	a	b	MSE	SMSE	PBIAS
1 D Ri Shi-er log	0.97	0.71	0.49	1.33	-0.61	0.73	0.47	-4.18	2.04	-46.23
5 D Ri Shi-er log	0.97	0.86	0.09	1.09	-0.06	0.89	0.07	-0.02	0.14	-0.21
10 D Ri Shi-er log	0.96	0.93	-0.09	0.99	0.14	0.97	-0.11	1.87	1.37	20.66
1 L Ri Shi-er log	0.97	0.66	0.55	1.42	-0.74	0.68	0.54	-4.63	2.15	-51.29
5 L Ri Shi-er log	0.97	0.84	0.14	1.11	-0.12	0.87	0.12	-0.56	0.75	-6.15
10 L Ri Shi-er log	0.96	0.93	-0.05	0.99	0.10	0.97	-0.08	1.41	1.19	15.61
1 D Gi Shi-er log	0.97	0.74	0.42	1.28	-0.51	0.76	0.41	-3.60	1.90	-39.87
5 D Gi Shi-er log	0.97	0.89	0.02	1.05	0.02	0.92	0.00	0.65	0.81	7.23
1 L Gi Shi-er log	0.97	0.69	0.49	1.36	-0.63	0.72	0.48	-4.09	2.02	-45.24
5 L Gi Shi-er log	0.96	0.88	0.07	1.06	-0.03	0.91	0.05	0.14	0.38	1.57
1 D Ri La log	0.97	0.67	0.54	1.40	-0.72	0.69	0.53	-4.62	2.15	-51.14
5 D Ri La log	0.97	0.82	0.16	1.14	-0.15	0.85	0.15	-0.66	0.81	-7.33
10 D Ri La log	0.96	0.89	-0.01	1.04	0.06	0.93	-0.04	1.15	1.07	12.68
1 L Ri La log	0.97	0.63	0.60	1.50	-0.86	0.65	0.59	-5.06	2.25	-56.01
5 L Ri La log	0.97	0.79	0.22	1.18	-0.22	0.82	0.20	-1.23	1.11	-13.59
10 L Ri La log	0.96	0.88	0.03	1.05	0.02	0.92	0.01	0.64	0.80	7.07
1 D Gi La log	0.97	0.71	0.48	1.34	-0.61	0.73	0.47	-4.08	2.02	-45.15
5 D Gi La log	0.97	0.85	0.10	1.10	-0.07	0.88	0.08	-0.03	0.17	-0.31
1 L Gi La log	0.97	0.66	0.54	1.43	-0.74	0.68	0.53	-4.55	2.13	-50.37
5 L Gi La log	0.96	0.83	0.15	1.12	-0.13	0.86	0.13	-0.58	0.76	-6.39
1 D Ri Shi-er Txyz	0.97	0.70	0.51	1.34	-0.65	0.72	0.50	-4.47	2.11	-49.45
5 D Ri Shi-er Txyz	0.97	0.87	0.10	1.09	-0.08	0.89	0.09	-0.23	0.48	-2.50
10 D Ri Shi-er Txyz	0.96	0.94	-0.08	0.99	0.12	0.97	-0.10	1.69	1.30	18.70
1 L Ri Shi-er Txyz	0.97	0.65	0.57	1.43	-0.78	0.68	0.56	-4.90	2.21	-54.23
5 L Ri Shi-er Txyz	0.97	0.84	0.16	1.11	-0.13	0.87	0.14	-0.76	0.87	-8.38
10 L Ri Shi-er Txyz	0.96	0.93	-0.04	1.00	0.09	0.97	-0.07	1.23	1.11	13.64
1 D Gi Shi-er Txyz	0.97	0.74	0.45	1.28	-0.54	0.76	0.43	-3.89	1.97	-43.05
5 D Gi Shi-er Txyz	0.97	0.90	0.03	1.05	0.00	0.92	0.02	0.45	0.67	5.02
10 D Gi Shi-er Txyz	0.96	0.96	-0.15	0.96	0.19	1.00	-0.17	2.39	1.54	26.41
1 L Gi Shi-er Txyz	0.97	0.69	0.51	1.36	-0.66	0.71	0.50	-4.35	2.09	-48.16
5 L Gi Shi-er Txyz	0.97	0.88	0.08	1.06	-0.05	0.91	0.06	-0.05	0.23	-0.60
10 L Gi Shi-er Txyz	0.96	0.96	-0.11	0.96	0.16	1.00	-0.14	1.98	1.41	21.88
1 D Ri La Txyz	0.97	0.60	0.58	1.58	-0.89	0.62	0.57	-4.57	2.14	-50.58
5 D Ri La Txyz	0.97	0.64	0.49	1.47	-0.68	0.66	0.48	-3.59	1.89	-39.75
10 D Ri La Txyz	0.96	0.69	0.36	1.33	-0.42	0.72	0.34	-2.20	1.48	-24.32
1 L Ri La Txyz	0.97	0.49	0.82	1.95	-1.57	0.50	0.82	-6.90	2.63	-76.38
5 L Ri La Txyz	0.96	0.59	0.56	1.56	-0.83	0.62	0.54	-4.14	2.03	-45.84
10 L Ri La Txyz	0.95	0.65	0.43	1.39	-0.53	0.68	0.40	-2.81	1.68	-31.09
1 D Gi La Txyz	0.98	0.55	0.73	1.73	-1.24	0.56	0.72	-6.22	2.49	-68.82
5 D Gi La Txyz	0.97	0.66	0.44	1.42	-0.58	0.68	0.43	-3.12	1.77	-34.54
10 D Gi La Txyz	0.95	0.71	0.31	1.28	-0.33	0.74	0.28	-1.68	1.30	-18.57
1 L Gi La Txyz	0.97	0.51	0.79	1.87	-1.43	0.52	0.78	-6.56	2.56	-72.61
5 L Gi La Txyz	0.96	0.62	0.51	1.50	-0.72	0.64	0.49	-3.69	1.92	-40.88
10 L Gi La Txyz	0.95	0.67	0.38	1.34	-0.44	0.71	0.35	-2.29	1.51	-25.32

Table A.5: Calibration statistics for modeled and observed suspended sediment concentration loss in S2Q100D48, shear stress deposition model

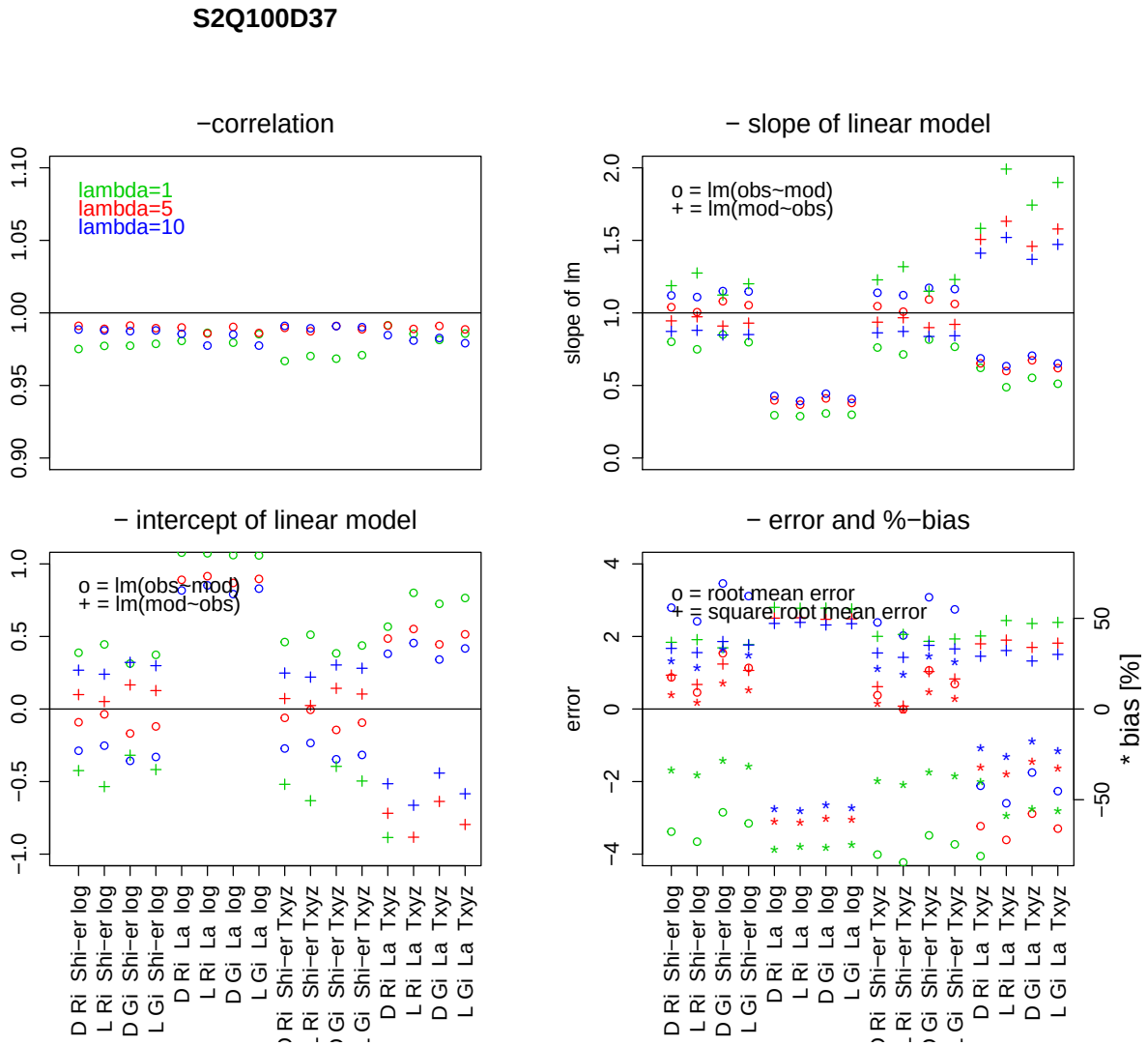

Figure A.5: Graphical representaiton of statisitcal evaluation of modeled and observed suspended sediment concentration loss in S2Q100D37, shear stress deposition model

	r^2	LM_{mo}		LM_{om}		RMA		Error		
		a	b	a	b	a	b	MSE	SMSE	PBIAS
1 D Ri Shi-er log	0.98	0.80	0.39	1.19	-0.42	0.82	0.37	-3.38	1.84	-32.95
5 D Ri Shi-er log	0.99	1.04	-0.09	0.94	0.10	1.05	-0.10	0.87	0.93	8.50
10 D Ri Shi-er log	0.99	1.12	-0.29	0.87	0.27	1.13	-0.30	2.79	1.67	27.22
1 L Ri Shi-er log	0.98	0.75	0.45	1.27	-0.53	0.77	0.43	-3.66	1.91	-35.63
5 L Ri Shi-er log	0.99	1.01	-0.04	0.97	0.05	1.02	-0.04	0.46	0.68	4.45
10 L Ri Shi-er log	0.99	1.11	-0.25	0.88	0.24	1.12	-0.26	2.42	1.55	23.55
1 D Gi Shi-er log	0.98	0.85	0.31	1.12	-0.32	0.87	0.30	-2.85	1.69	-27.75
5 D Gi Shi-er log	0.99	1.08	-0.17	0.91	0.17	1.09	-0.18	1.54	1.24	14.97
10 D Gi Shi-er log	0.99	1.15	-0.36	0.85	0.32	1.16	-0.37	3.46	1.86	33.73
1 L Gi Shi-er log	0.98	0.80	0.37	1.20	-0.42	0.82	0.36	-3.15	1.78	-30.72
5 L Gi Shi-er log	0.99	1.05	-0.12	0.93	0.13	1.06	-0.13	1.13	1.06	11.04
10 L Gi Shi-er log	0.99	1.15	-0.33	0.85	0.30	1.16	-0.34	3.11	1.76	30.34
1 D Ri La log	0.98	0.30	1.08	3.26	-3.49	0.30	1.07	-7.85	2.80	-76.51
5 D Ri La log	0.99	0.40	0.89	2.47	-2.18	0.40	0.89	-6.28	2.51	-61.17
10 D Ri La log	0.99	0.43	0.82	2.27	-1.83	0.43	0.81	-5.57	2.36	-54.23
1 L Ri La log	0.99	0.29	1.07	3.37	-3.60	0.29	1.07	-7.72	2.78	-75.20
5 L Ri La log	0.99	0.37	0.92	2.64	-2.40	0.37	0.91	-6.33	2.52	-61.63
10 L Ri La log	0.98	0.39	0.85	2.43	-2.04	0.40	0.85	-5.70	2.39	-55.54
1 D Gi La log	0.98	0.31	1.06	3.12	-3.28	0.31	1.06	-7.74	2.78	-75.40
5 D Gi La log	0.99	0.41	0.87	2.39	-2.06	0.41	0.87	-6.11	2.47	-59.58
10 D Gi La log	0.99	0.44	0.79	2.19	-1.71	0.45	0.79	-5.37	2.32	-52.33
1 L Gi La log	0.99	0.30	1.06	3.26	-3.42	0.30	1.06	-7.62	2.76	-74.22
5 L Gi La log	0.99	0.38	0.90	2.56	-2.28	0.38	0.89	-6.18	2.49	-60.24
10 L Gi La log	0.98	0.41	0.83	2.35	-1.92	0.42	0.82	-5.53	2.35	-53.86
1 D Ri Shi-er Txyz	0.97	0.76	0.46	1.23	-0.52	0.79	0.44	-4.01	2.00	-39.09
5 D Ri Shi-er Txyz	0.99	1.05	-0.06	0.94	0.07	1.06	-0.07	0.38	0.62	3.69
10 D Ri Shi-er Txyz	0.99	1.14	-0.27	0.86	0.25	1.15	-0.28	2.39	1.54	23.25
1 L Ri Shi-er Txyz	0.97	0.71	0.51	1.32	-0.63	0.74	0.50	-4.23	2.06	-41.21
5 L Ri Shi-er Txyz	0.99	1.01	-0.01	0.97	0.02	1.02	-0.02	-0.01	0.08	-0.06
10 L Ri Shi-er Txyz	0.99	1.12	-0.23	0.87	0.22	1.13	-0.24	2.03	1.42	19.75
1 D Gi Shi-er Txyz	0.97	0.82	0.38	1.15	-0.40	0.84	0.36	-3.48	1.87	-33.94
5 D Gi Shi-er Txyz	0.99	1.09	-0.14	0.90	0.14	1.10	-0.15	1.07	1.03	10.38
10 D Gi Shi-er Txyz	0.99	1.17	-0.35	0.84	0.30	1.18	-0.35	3.08	1.76	30.02
1 L Gi Shi-er Txyz	0.97	0.77	0.44	1.23	-0.50	0.79	0.42	-3.73	1.93	-36.35
5 L Gi Shi-er Txyz	0.99	1.06	-0.09	0.92	0.10	1.07	-0.10	0.69	0.83	6.70
10 L Gi Shi-er Txyz	0.99	1.16	-0.32	0.84	0.28	1.18	-0.32	2.75	1.66	26.76
1 D Ri La Txyz	0.99	0.62	0.57	1.58	-0.89	0.63	0.56	-4.05	2.01	-39.50
5 D Ri La Txyz	0.99	0.65	0.49	1.51	-0.72	0.66	0.48	-3.23	1.80	-31.46
10 D Ri La Txyz	0.98	0.69	0.38	1.41	-0.51	0.70	0.37	-2.12	1.45	-20.62
1 L Ri La Txyz	0.99	0.49	0.80	1.99	-1.57	0.49	0.80	-5.95	2.44	-57.97
5 L Ri La Txyz	0.99	0.60	0.55	1.63	-0.88	0.61	0.55	-3.61	1.90	-35.16
10 L Ri La Txyz	0.98	0.63	0.45	1.52	-0.66	0.65	0.45	-2.60	1.61	-25.32
1 D Gi La Txyz	0.98	0.55	0.72	1.74	-1.24	0.56	0.72	-5.56	2.36	-54.13
5 D Gi La Txyz	0.99	0.67	0.45	1.46	-0.64	0.68	0.44	-2.89	1.70	-28.12
10 D Gi La Txyz	0.98	0.71	0.34	1.37	-0.44	0.72	0.33	-1.75	1.32	-17.07
1 L Gi La Txyz	0.99	0.51	0.77	1.90	-1.43	0.52	0.76	-5.70	2.39	-55.53
5 L Gi La Txyz	0.99	0.62	0.51	1.58	-0.80	0.63	0.51	-3.30	1.82	-32.13
10 L Gi La Txyz	0.98	0.65	0.42	1.47	-0.58	0.67	0.41	-2.26	1.50	-22.06

Table A.6: Calibration statistics for modeled and observed suspended sediment concentration loss in S2Q100D37, shear stress deposition model

A.1.2 Step 3, shear stress deposition model, silty experimetnal runs

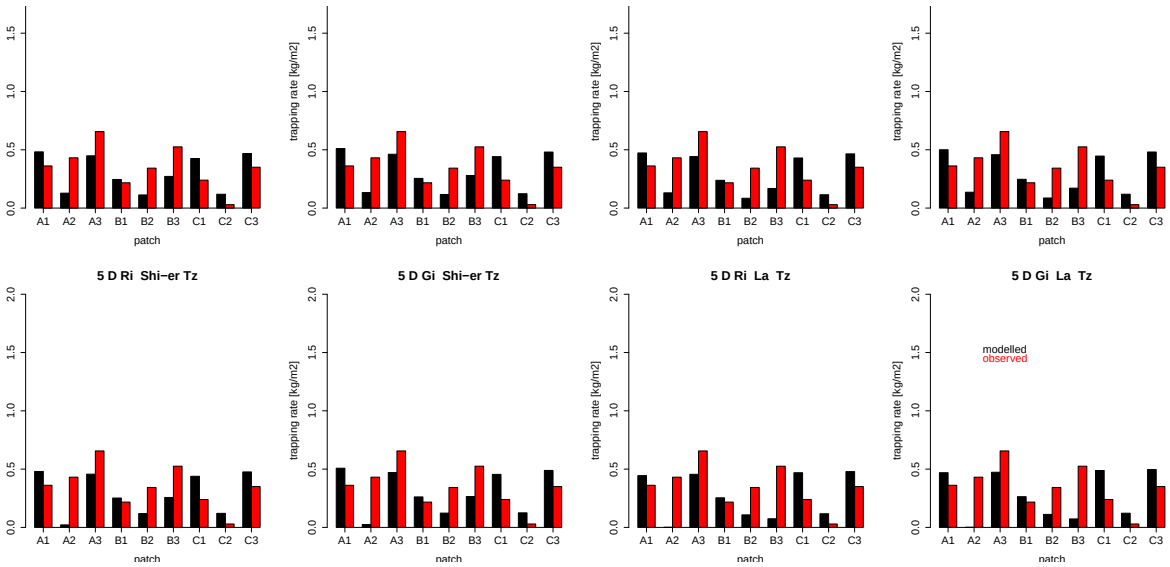

Figure A.6: Modelled and observed interstitial deposition in S1Q50, shear stress deposition model for eight selected value set combinations

	TR		r^2	LM_{mo}		LM_{om}		RMA		Error		
	obs	mod		a	b	a	b	a	b	MSE	SMSE	PBIAS
1 D Ri Shi-er Txyz	0.35	0.23	0.35	0.23	0.15	0.53	0.23	0.66	-0.00	1.10	1.05	34.79
5 D Ri Shi-er Txyz	0.35	0.30	0.35	0.31	0.19	0.41	0.23	0.87	-0.01	0.45	0.67	14.37
10 D Ri Shi-er Txyz	0.35	0.33	0.31	0.31	0.22	0.31	0.25	1.00	-0.02	0.21	0.46	6.66
1 L Ri Shi-er Txyz	0.35	0.22	0.36	0.22	0.14	0.57	0.23	0.63	-0.00	1.19	1.09	37.84
5 L Ri Shi-er Txyz	0.35	0.29	0.37	0.32	0.18	0.43	0.22	0.86	-0.01	0.51	0.71	16.17
10 L Ri Shi-er Txyz	0.35	0.32	0.30	0.31	0.22	0.30	0.25	1.01	-0.03	0.24	0.49	7.74
1 D Gi Shi-er Txyz	0.35	0.24	0.34	0.24	0.16	0.50	0.23	0.69	-0.00	1.00	1.00	31.69
5 D Gi Shi-er Txyz	0.35	0.31	0.35	0.32	0.20	0.38	0.23	0.91	-0.01	0.35	0.59	11.17
10 D Gi Shi-er Txyz	0.35	0.33	0.28	0.29	0.23	0.26	0.26	1.04	-0.03	0.14	0.37	4.41
1 L Gi Shi-er Txyz	0.35	0.23	0.35	0.23	0.15	0.54	0.23	0.66	-0.00	1.09	1.05	34.68
5 L Gi Shi-er Txyz	0.35	0.31	0.36	0.33	0.19	0.40	0.23	0.90	-0.01	0.40	0.63	12.66
10 L Gi Shi-er Txyz	0.35	0.33	0.25	0.27	0.24	0.23	0.27	1.07	-0.04	0.17	0.41	5.27
1 D Ri La Txyz	0.35	0.22	0.27	0.18	0.15	0.41	0.26	0.67	-0.02	1.21	1.10	38.26
5 D Ri La Txyz	0.35	0.28	0.26	0.24	0.20	0.29	0.27	0.92	-0.04	0.61	0.78	19.29
10 D Ri La Txyz	0.35	0.31	0.23	0.25	0.22	0.22	0.28	1.06	-0.06	0.36	0.60	11.30
1 L Ri La Txyz	0.35	0.21	0.28	0.18	0.14	0.44	0.26	0.64	-0.02	1.30	1.14	41.34
5 L Ri La Txyz	0.35	0.28	0.28	0.25	0.19	0.31	0.27	0.90	-0.04	0.68	0.82	21.46
10 L Ri La Txyz	0.35	0.31	0.22	0.24	0.22	0.21	0.29	1.07	-0.07	0.40	0.63	12.75
1 D Gi La Txyz	0.35	0.23	0.27	0.19	0.16	0.38	0.26	0.71	-0.02	1.12	1.06	35.39
5 D Gi La Txyz	0.35	0.29	0.26	0.25	0.21	0.27	0.27	0.96	-0.04	0.51	0.71	16.12
10 D Gi La Txyz	0.35	0.32	0.20	0.22	0.24	0.18	0.29	1.11	-0.07	0.27	0.52	8.66
1 L Gi La Txyz	0.35	0.22	0.28	0.19	0.15	0.41	0.26	0.67	-0.02	1.21	1.10	38.46
5 L Gi La Txyz	0.35	0.29	0.27	0.26	0.20	0.28	0.27	0.95	-0.05	0.57	0.75	18.00
10 L Gi La Txyz	0.35	0.32	0.18	0.20	0.25	0.16	0.30	1.14	-0.08	0.31	0.56	9.85
1 D Ri Shi-er Tz	0.35	0.22	0.25	0.19	0.15	0.34	0.28	0.75	-0.04	1.17	1.08	37.03
5 D Ri Shi-er Tz	0.35	0.29	0.27	0.26	0.20	0.28	0.27	0.98	-0.05	0.53	0.73	16.88
10 D Ri Shi-er Tz	0.35	0.32	0.25	0.27	0.22	0.22	0.28	1.10	-0.07	0.29	0.54	9.16
1 L Ri Shi-er Tz	0.35	0.21	0.26	0.19	0.15	0.36	0.27	0.71	-0.04	1.26	1.12	39.97
5 L Ri Shi-er Tz	0.35	0.29	0.29	0.28	0.19	0.30	0.26	0.96	-0.05	0.59	0.77	18.60
10 L Ri Shi-er Tz	0.35	0.31	0.24	0.27	0.22	0.22	0.28	1.10	-0.07	0.32	0.56	10.09
1 D Gi Shi-er Tz	0.35	0.23	0.25	0.20	0.16	0.32	0.28	0.78	-0.04	1.07	1.03	33.98
5 D Gi Shi-er Tz	0.35	0.30	0.27	0.27	0.21	0.26	0.27	1.02	-0.05	0.43	0.66	13.71
10 D Gi Shi-er Tz	0.35	0.33	0.21	0.25	0.24	0.19	0.29	1.14	-0.07	0.21	0.46	6.80
1 L Gi Shi-er Tz	0.35	0.22	0.26	0.20	0.15	0.35	0.27	0.75	-0.04	1.16	1.08	36.85
5 L Gi Shi-er Tz	0.35	0.30	0.28	0.28	0.20	0.28	0.27	1.00	-0.05	0.48	0.69	15.12
10 L Gi Shi-er Tz	0.35	0.32	0.20	0.23	0.24	0.17	0.29	1.15	-0.08	0.23	0.48	7.43
1 D Ri La Tz	0.35	0.25	0.11	0.11	0.21	0.12	0.32	0.98	-0.10	0.94	0.97	29.77
5 D Ri La Tz	0.35	0.27	0.12	0.13	0.22	0.11	0.32	1.08	-0.11	0.75	0.87	23.84
10 D Ri La Tz	0.35	0.29	0.10	0.12	0.25	0.08	0.33	1.23	-0.14	0.50	0.71	16.01
1 L Ri La Tz	0.35	0.19	0.14	0.10	0.16	0.18	0.32	0.75	-0.07	1.41	1.19	44.84
5 L Ri La Tz	0.35	0.26	0.13	0.14	0.21	0.12	0.32	1.06	-0.11	0.82	0.91	26.07
10 L Ri La Tz	0.35	0.29	0.10	0.12	0.25	0.08	0.33	1.23	-0.14	0.55	0.74	17.49
1 D Gi La Tz	0.35	0.21	0.12	0.10	0.18	0.15	0.32	0.84	-0.08	1.23	1.11	39.17
5 D Gi La Tz	0.35	0.28	0.11	0.13	0.23	0.10	0.32	1.13	-0.12	0.66	0.81	20.79
10 D Gi La Tz	0.35	0.30	0.07	0.10	0.27	0.06	0.33	1.28	-0.14	0.42	0.65	13.23
1 L Gi La Tz	0.35	0.20	0.13	0.10	0.17	0.17	0.32	0.79	-0.08	1.33	1.15	42.11
5 L Gi La Tz	0.35	0.27	0.12	0.14	0.22	0.11	0.32	1.11	-0.12	0.72	0.85	22.75
10 L Gi La Tz	0.35	0.30	0.06	0.08	0.27	0.05	0.34	1.29	-0.15	0.45	0.67	14.38

Table A.7: Calibration statistics for modelled and observed interstitial deposition in S1Q50, shear stress deposition model

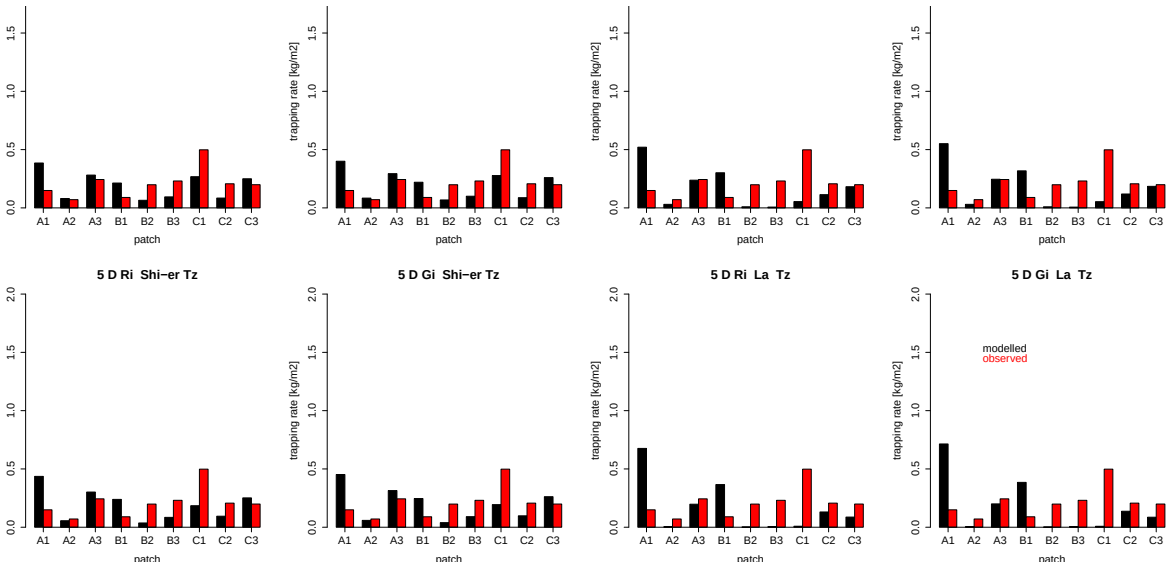

Figure A.7: Modelled and observed interstitial deposition in S1Q80, shear stress deposition model for eight selected value set combinations

	TR		r^2	LM_{mo}		LM_{om}		RMA		Error		
	obs	mod		a	b	a	b	a	b	MSE	SMSE	PBIAS
1 D Ri Shi-er Txyz	0.21	0.14	0.05	0.15	0.11	0.30	0.17	0.70	-0.00	0.59	0.77	31.31
5 D Ri Shi-er Txyz	0.21	0.19	0.05	0.21	0.15	0.24	0.16	0.92	-0.00	0.17	0.41	8.76
10 D Ri Shi-er Txyz	0.21	0.21	0.04	0.21	0.17	0.20	0.17	1.03	-0.00	-0.01	0.08	-0.36
1 L Ri Shi-er Txyz	0.21	0.14	0.05	0.14	0.11	0.32	0.17	0.67	-0.00	0.65	0.81	34.57
5 L Ri Shi-er Txyz	0.21	0.19	0.05	0.20	0.14	0.25	0.16	0.91	-0.00	0.20	0.45	10.70
10 L Ri Shi-er Txyz	0.21	0.21	0.04	0.21	0.16	0.20	0.17	1.03	-0.01	0.01	0.11	0.67
1 D Gi Shi-er Txyz	0.21	0.15	0.05	0.16	0.12	0.30	0.16	0.73	-0.00	0.53	0.73	27.89
5 D Gi Shi-er Txyz	0.21	0.20	0.05	0.21	0.15	0.23	0.16	0.96	-0.00	0.10	0.31	5.09
10 D Gi Shi-er Txyz	0.21	0.22	0.04	0.21	0.17	0.19	0.17	1.05	-0.01	-0.06	0.24	-3.02
1 L Gi Shi-er Txyz	0.21	0.14	0.05	0.15	0.11	0.31	0.16	0.70	-0.00	0.59	0.77	31.10
5 L Gi Shi-er Txyz	0.21	0.20	0.05	0.21	0.15	0.23	0.16	0.95	-0.00	0.13	0.35	6.67
10 L Gi Shi-er Txyz	0.21	0.21	0.04	0.21	0.17	0.18	0.17	1.06	-0.01	-0.04	0.21	-2.25
1 D Ri La Txyz	0.21	0.12	0.07	-0.25	0.17	-0.28	0.24	0.94	-0.08	0.80	0.89	42.31
5 D Ri La Txyz	0.21	0.16	0.09	-0.41	0.25	-0.22	0.24	1.38	-0.13	0.43	0.66	22.85
10 D Ri La Txyz	0.21	0.18	0.10	-0.51	0.29	-0.19	0.24	1.64	-0.16	0.26	0.51	13.59
1 L Ri La Txyz	0.21	0.11	0.06	-0.22	0.16	-0.29	0.24	0.88	-0.07	0.86	0.93	45.39
5 L Ri La Txyz	0.21	0.16	0.09	-0.40	0.24	-0.22	0.24	1.33	-0.12	0.49	0.70	25.93
10 L Ri La Txyz	0.21	0.18	0.10	-0.51	0.28	-0.19	0.24	1.63	-0.17	0.30	0.55	15.95
1 D Gi La Txyz	0.21	0.13	0.07	-0.27	0.18	-0.27	0.24	1.00	-0.08	0.74	0.86	39.33
5 D Gi La Txyz	0.21	0.17	0.09	-0.44	0.26	-0.21	0.24	1.46	-0.14	0.37	0.61	19.55
10 D Gi La Txyz	0.21	0.19	0.10	-0.55	0.31	-0.18	0.24	1.75	-0.18	0.19	0.43	9.81
1 L Gi La Txyz	0.21	0.12	0.07	-0.24	0.17	-0.28	0.24	0.94	-0.08	0.80	0.90	42.55
5 L Gi La Txyz	0.21	0.16	0.09	-0.43	0.25	-0.21	0.24	1.42	-0.14	0.42	0.65	22.40
10 L Gi La Txyz	0.21	0.18	0.10	-0.56	0.30	-0.18	0.24	1.76	-0.18	0.22	0.47	11.82
1 D Ri Shi-er Tz	0.21	0.14	0.00	-0.05	0.15	-0.07	0.22	0.84	-0.04	0.63	0.80	33.65
5 D Ri Shi-er Tz	0.21	0.19	0.00	-0.01	0.19	-0.01	0.21	1.07	-0.04	0.20	0.45	10.71
10 D Ri Shi-er Tz	0.21	0.21	0.00	0.00	0.21	0.00	0.21	1.18	-0.04	0.03	0.17	1.47
1 L Ri Shi-er Tz	0.21	0.13	0.00	-0.04	0.14	-0.06	0.22	0.79	-0.03	0.69	0.83	36.77
5 L Ri Shi-er Tz	0.21	0.18	0.00	0.00	0.18	0.00	0.21	1.05	-0.04	0.24	0.49	12.65
10 L Ri Shi-er Tz	0.21	0.20	0.00	0.01	0.20	0.01	0.21	1.17	-0.04	0.05	0.22	2.49
1 D Gi Shi-er Tz	0.21	0.15	0.00	-0.04	0.16	-0.05	0.22	0.87	-0.04	0.57	0.75	30.14
5 D Gi Shi-er Tz	0.21	0.19	0.00	0.00	0.19	0.00	0.21	1.11	-0.04	0.13	0.36	7.01
10 D Gi Shi-er Tz	0.21	0.21	0.00	0.00	0.21	0.00	0.21	1.21	-0.04	-0.02	0.16	-1.28
1 L Gi Shi-er Tz	0.21	0.14	0.00	-0.03	0.15	-0.05	0.22	0.83	-0.03	0.63	0.79	33.25
5 L Gi Shi-er Tz	0.21	0.19	0.00	0.01	0.19	0.01	0.21	1.09	-0.04	0.16	0.40	8.59
10 L Gi Shi-er Tz	0.21	0.21	0.00	0.01	0.21	0.01	0.21	1.21	-0.04	-0.01	0.10	-0.52
1 D Ri La Tz	0.21	0.15	0.12	-0.56	0.27	-0.21	0.24	1.63	-0.19	0.53	0.73	28.22
5 D Ri La Tz	0.21	0.16	0.12	-0.63	0.30	-0.19	0.24	1.83	-0.22	0.41	0.64	21.65
10 D Ri La Tz	0.21	0.18	0.12	-0.75	0.34	-0.16	0.24	2.16	-0.27	0.23	0.48	12.22
1 L Ri La Tz	0.21	0.11	0.11	-0.38	0.19	-0.29	0.24	1.15	-0.13	0.86	0.93	45.56
5 L Ri La Tz	0.21	0.16	0.12	-0.60	0.28	-0.19	0.24	1.76	-0.21	0.47	0.68	24.86
10 L Ri La Tz	0.21	0.18	0.12	-0.73	0.33	-0.16	0.24	2.13	-0.27	0.28	0.53	14.65
1 D Gi La Tz	0.21	0.13	0.11	-0.45	0.22	-0.26	0.24	1.32	-0.15	0.74	0.86	39.32
5 D Gi La Tz	0.21	0.17	0.12	-0.67	0.31	-0.18	0.24	1.94	-0.24	0.34	0.59	18.27
10 D Gi La Tz	0.21	0.19	0.12	-0.79	0.36	-0.15	0.24	2.30	-0.29	0.16	0.40	8.29
1 L Gi La Tz	0.21	0.12	0.11	-0.41	0.21	-0.27	0.24	1.23	-0.14	0.80	0.90	42.57
5 L Gi La Tz	0.21	0.17	0.12	-0.64	0.30	-0.18	0.24	1.88	-0.23	0.40	0.63	21.24
10 L Gi La Tz	0.21	0.19	0.12	-0.79	0.35	-0.15	0.24	2.29	-0.29	0.19	0.44	10.33

Table A.8: Calibration statistics for modelled and observed interstitial deposition in S1Q80, shear stress deposition model

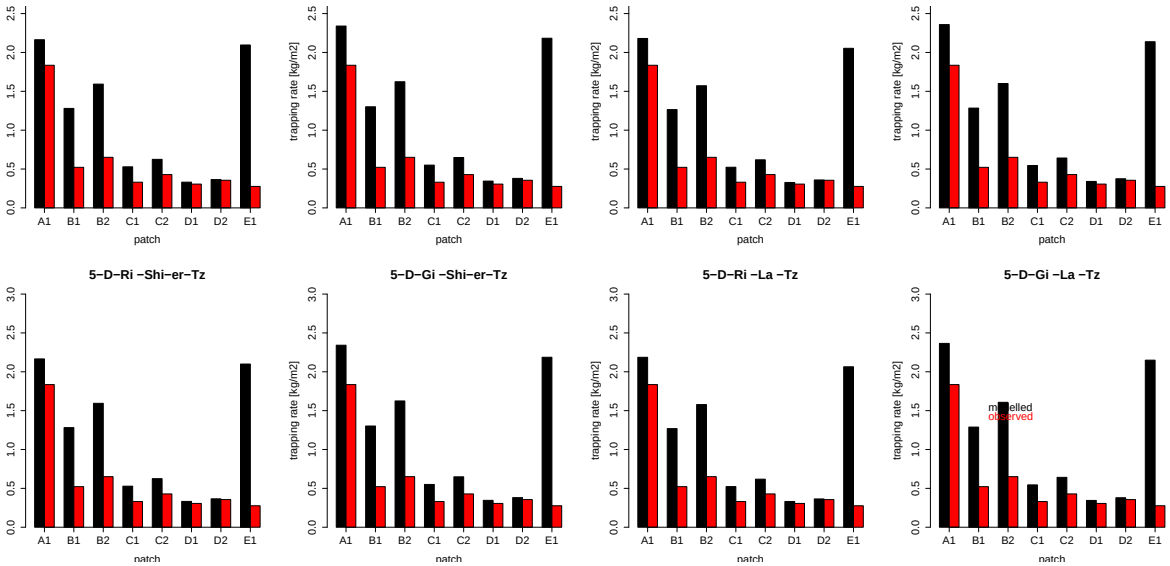

Figure A.8: Modelled and observed interstitial deposition in S2Q30D48-2, shear stress deposition model for eight selected value set combinations

	TR		r^2	LM_{mo}		LM_{om}		RMA		Error		
	obs	mod		a	b	a	b	a	b	MSE	SMSE	PBIAS
1 D Ri Shi-er Txyz	0.59	0.80	0.35	0.35	0.60	0.34	0.32	1.02	0.20	-1.72	1.31	-36.57
5 D Ri Shi-er Txyz	0.59	1.12	0.59	0.87	0.61	0.40	0.14	1.47	0.26	-4.28	2.07	-90.87
10 D Ri Shi-er Txyz	0.59	1.24	0.77	1.46	0.38	0.40	0.09	1.90	0.12	-5.18	2.27	-109.99
1 L Ri Shi-er Txyz	0.59	0.76	0.37	0.35	0.55	0.38	0.30	0.96	0.20	-1.38	1.18	-29.36
5 L Ri Shi-er Txyz	0.59	1.09	0.66	0.96	0.52	0.45	0.10	1.46	0.22	-3.98	2.00	-84.66
10 L Ri Shi-er Txyz	0.59	1.17	0.80	1.64	0.21	0.39	0.13	2.04	-0.03	-4.69	2.17	-99.77
1 D Gi Shi-er Txyz	0.59	0.85	0.35	0.38	0.62	0.33	0.31	1.08	0.21	-2.09	1.45	-44.44
5 D Gi Shi-er Txyz	0.59	1.17	0.62	0.97	0.60	0.40	0.12	1.56	0.26	-4.67	2.16	-99.15
10 D Gi Shi-er Txyz	0.59	1.28	0.74	1.52	0.39	0.36	0.13	2.05	0.07	-5.53	2.35	-117.57
1 L Gi Shi-er Txyz	0.59	0.80	0.38	0.39	0.58	0.37	0.29	1.02	0.21	-1.73	1.32	-36.87
5 L Gi Shi-er Txyz	0.59	1.14	0.69	1.08	0.50	0.44	0.09	1.57	0.21	-4.38	2.09	-93.09
10 L Gi Shi-er Txyz	0.59	1.22	0.73	1.66	0.24	0.32	0.20	2.29	-0.12	-5.07	2.25	-107.65
1 D Ri La Txyz	0.59	0.80	0.36	0.36	0.58	0.36	0.30	1.01	0.20	-1.66	1.29	-35.26
5 D Ri La Txyz	0.59	1.11	0.61	0.89	0.59	0.42	0.12	1.46	0.25	-4.19	2.05	-89.11
10 D Ri La Txyz	0.59	1.22	0.78	1.48	0.35	0.41	0.09	1.90	0.10	-5.08	2.25	-108.03
1 L Ri La Txyz	0.59	0.75	0.38	0.36	0.54	0.40	0.28	0.95	0.19	-1.32	1.15	-28.09
5 L Ri La Txyz	0.59	1.07	0.67	0.98	0.50	0.46	0.09	1.46	0.22	-3.89	1.97	-82.78
10 L Ri La Txyz	0.59	1.16	0.81	1.67	0.18	0.40	0.13	2.05	-0.04	-4.59	2.14	-97.59
1 D Gi La Txyz	0.59	0.84	0.37	0.39	0.61	0.34	0.30	1.07	0.21	-2.03	1.42	-43.04
5 D Gi La Txyz	0.59	1.16	0.64	0.99	0.58	0.41	0.11	1.55	0.25	-4.58	2.14	-97.30
10 D Gi La Txyz	0.59	1.27	0.75	1.54	0.36	0.37	0.12	2.05	0.06	-5.44	2.33	-115.63
1 L Gi La Txyz	0.59	0.80	0.40	0.40	0.56	0.39	0.27	1.00	0.21	-1.67	1.29	-35.50
5 L Gi La Txyz	0.59	1.12	0.70	1.10	0.47	0.45	0.08	1.57	0.20	-4.29	2.07	-91.08
10 L Gi La Txyz	0.59	1.21	0.74	1.68	0.22	0.32	0.20	2.29	-0.14	-4.97	2.23	-105.52
1 D Ri Shi-er Tz	0.59	0.80	0.35	0.35	0.60	0.34	0.32	1.02	0.20	-1.73	1.31	-36.74
5 D Ri Shi-er Tz	0.59	1.12	0.59	0.87	0.61	0.40	0.14	1.47	0.26	-4.29	2.07	-91.11
10 D Ri Shi-er Tz	0.59	1.24	0.77	1.46	0.38	0.40	0.09	1.90	0.12	-5.19	2.28	-110.24
1 L Ri Shi-er Tz	0.59	0.76	0.37	0.35	0.55	0.38	0.30	0.96	0.20	-1.39	1.18	-29.52
5 L Ri Shi-er Tz	0.59	1.09	0.66	0.96	0.52	0.45	0.10	1.47	0.22	-3.99	2.00	-84.87
10 L Ri Shi-er Tz	0.59	1.18	0.80	1.64	0.21	0.39	0.13	2.05	-0.03	-4.71	2.17	-100.00
1 D Gi Shi-er Tz	0.59	0.85	0.35	0.38	0.63	0.33	0.31	1.08	0.21	-2.10	1.45	-44.62
5 D Gi Shi-er Tz	0.59	1.17	0.62	0.97	0.60	0.40	0.12	1.56	0.26	-4.68	2.16	-99.39
10 D Gi Shi-er Tz	0.59	1.28	0.74	1.52	0.39	0.36	0.13	2.05	0.07	-5.54	2.35	-117.80
1 L Gi Shi-er Tz	0.59	0.81	0.38	0.39	0.58	0.37	0.29	1.02	0.21	-1.74	1.32	-37.04
5 L Gi Shi-er Tz	0.59	1.14	0.69	1.08	0.50	0.44	0.09	1.58	0.21	-4.39	2.10	-93.31
10 L Gi Shi-er Tz	0.59	1.22	0.73	1.66	0.24	0.32	0.20	2.29	-0.12	-5.07	2.25	-107.84
1 D Ri La Tz	0.59	1.01	0.50	0.64	0.63	0.39	0.19	1.28	0.26	-3.37	1.84	-71.58
5 D Ri La Tz	0.59	1.12	0.61	0.89	0.59	0.42	0.12	1.47	0.25	-4.23	2.06	-89.87
10 D Ri La Tz	0.59	1.23	0.78	1.49	0.36	0.41	0.09	1.91	0.11	-5.13	2.26	-108.97
1 L Ri La Tz	0.59	0.76	0.38	0.36	0.54	0.40	0.29	0.95	0.20	-1.34	1.16	-28.45
5 L Ri La Tz	0.59	1.08	0.67	0.98	0.50	0.46	0.09	1.46	0.22	-3.93	1.98	-83.48
10 L Ri La Tz	0.59	1.17	0.81	1.67	0.19	0.40	0.13	2.05	-0.04	-4.63	2.15	-98.48
1 D Gi La Tz	0.59	0.84	0.37	0.39	0.61	0.34	0.30	1.07	0.21	-2.05	1.43	-43.48
5 D Gi La Tz	0.59	1.17	0.64	0.99	0.58	0.41	0.11	1.56	0.25	-4.62	2.15	-98.12
10 D Gi La Tz	0.59	1.27	0.75	1.54	0.37	0.36	0.12	2.06	0.06	-5.49	2.34	-116.63
1 L Gi La Tz	0.59	0.80	0.40	0.40	0.57	0.39	0.27	1.01	0.21	-1.69	1.30	-35.91
5 L Gi La Tz	0.59	1.13	0.70	1.10	0.48	0.45	0.09	1.57	0.20	-4.32	2.08	-91.84
10 L Gi La Tz	0.59	1.21	0.73	1.69	0.22	0.32	0.20	2.30	-0.14	-5.01	2.24	-106.46

Table A.9: Calibration statistics for modelled and observed interstitial deposition in S2Q30D48-2, shear stress deposition model

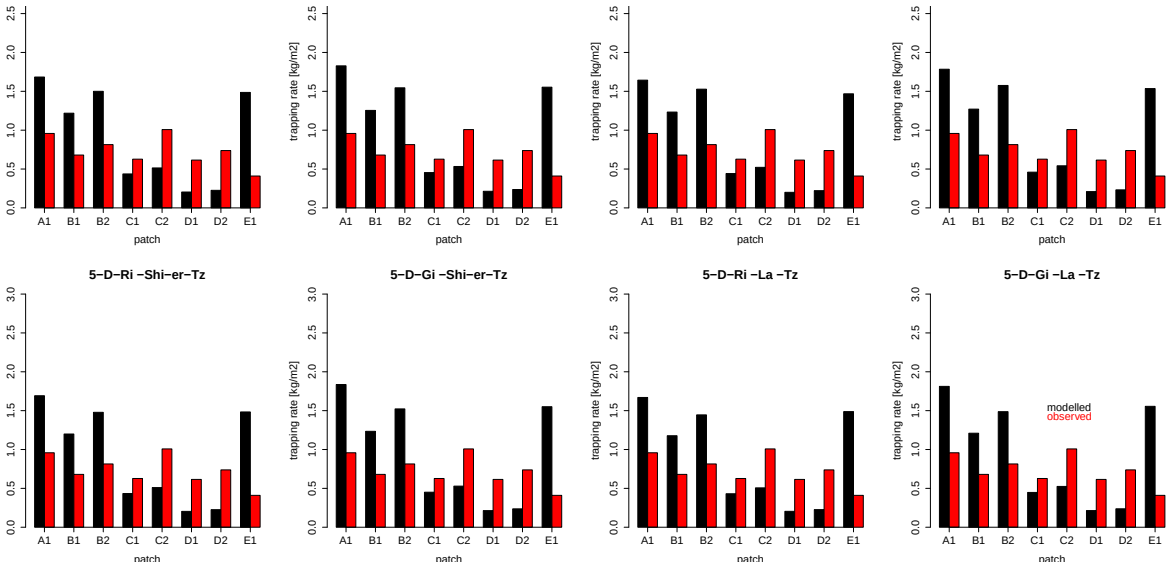

Figure A.9: Modelled and observed interstitial deposition in S2Q30D37, shear stress deposition model for eight selected value set combinations

	TR		r^2	LM_{mo}		LM_{om}		RMA		Error		
	obs	mod		a	b	a	b	a	b	MSE	SMSE	PBIAS
1 D Ri Shi-er Txyz	0.73	0.65	0.17	-0.38	0.93	-0.08	0.78	2.22	-0.97	0.65	0.81	11.16
5 D Ri Shi-er Txyz	0.73	0.91	0.05	0.15	0.80	0.02	0.72	3.21	-1.44	-1.42	1.19	-24.26
10 D Ri Shi-er Txyz	0.73	1.02	0.18	0.75	0.47	0.05	0.68	4.08	-1.96	-2.33	1.53	-39.86
1 L Ri Shi-er Txyz	0.73	0.61	0.15	-0.31	0.84	-0.07	0.77	2.09	-0.91	0.93	0.96	15.90
5 L Ri Shi-er Txyz	0.73	0.89	0.11	0.34	0.64	0.03	0.70	3.22	-1.47	-1.24	1.11	-21.24
10 L Ri Shi-er Txyz	0.73	0.99	0.23	0.97	0.28	0.05	0.68	4.31	-2.16	-2.05	1.43	-35.11
1 D Gi Shi-er Txyz	0.73	0.69	0.17	-0.39	0.97	-0.07	0.78	2.34	-1.02	0.36	0.60	6.15
5 D Gi Shi-er Txyz	0.73	0.95	0.06	0.21	0.80	0.02	0.71	3.39	-1.53	-1.77	1.33	-30.21
10 D Gi Shi-er Txyz	0.73	1.07	0.12	0.50	0.70	0.03	0.70	4.35	-2.11	-2.70	1.64	-46.20
1 L Gi Shi-er Txyz	0.73	0.65	0.14	-0.30	0.87	-0.06	0.77	2.20	-0.96	0.65	0.81	11.10
5 L Gi Shi-er Txyz	0.73	0.93	0.12	0.41	0.64	0.03	0.70	3.46	-1.59	-1.63	1.27	-27.78
10 L Gi Shi-er Txyz	0.73	1.04	0.10	0.45	0.71	0.02	0.71	4.77	-2.45	-2.48	1.58	-42.44
1 D Ri La Txyz	0.73	0.65	0.17	-0.37	0.92	-0.08	0.78	2.20	-0.96	0.68	0.83	11.65
5 D Ri La Txyz	0.73	0.91	0.05	0.16	0.79	0.02	0.72	3.18	-1.42	-1.41	1.19	-24.06
10 D Ri La Txyz	0.73	1.02	0.19	0.75	0.48	0.05	0.68	4.02	-1.92	-2.33	1.53	-39.86
1 L Ri La Txyz	0.73	0.61	0.14	-0.30	0.83	-0.07	0.77	2.07	-0.90	0.96	0.98	16.42
5 L Ri La Txyz	0.73	0.88	0.11	0.35	0.63	0.03	0.70	3.20	-1.45	-1.22	1.10	-20.85
10 L Ri La Txyz	0.73	0.99	0.23	0.97	0.28	0.05	0.68	4.23	-2.11	-2.04	1.43	-34.84
1 D Gi La Txyz	0.73	0.68	0.16	-0.38	0.96	-0.07	0.78	2.32	-1.01	0.39	0.62	6.63
5 D Gi La Txyz	0.73	0.95	0.06	0.21	0.80	0.02	0.71	3.37	-1.51	-1.76	1.33	-30.06
10 D Gi La Txyz	0.73	1.07	0.12	0.49	0.71	0.03	0.70	4.27	-2.05	-2.72	1.65	-46.41
1 L Gi La Txyz	0.73	0.65	0.13	-0.29	0.86	-0.06	0.77	2.18	-0.95	0.68	0.82	11.63
5 L Gi La Txyz	0.73	0.93	0.12	0.41	0.63	0.04	0.70	3.42	-1.57	-1.60	1.27	-27.42
10 L Gi La Txyz	0.73	1.04	0.09	0.44	0.72	0.02	0.71	4.67	-2.37	-2.48	1.58	-42.43
1 D Ri Shi-er Tz	0.73	0.65	0.17	-0.39	0.93	-0.08	0.78	2.21	-0.97	0.68	0.82	11.59
5 D Ri Shi-er Tz	0.73	0.90	0.05	0.16	0.79	0.02	0.72	3.19	-1.43	-1.38	1.17	-23.53
10 D Ri Shi-er Tz	0.73	1.02	0.19	0.77	0.46	0.05	0.68	4.08	-1.97	-2.28	1.51	-38.95
1 L Ri Shi-er Tz	0.73	0.61	0.15	-0.31	0.84	-0.07	0.78	2.08	-0.91	0.95	0.98	16.32
5 L Ri Shi-er Tz	0.73	0.88	0.11	0.35	0.63	0.03	0.70	3.21	-1.47	-1.20	1.10	-20.55
10 L Ri Shi-er Tz	0.73	0.98	0.23	0.99	0.26	0.05	0.68	4.33	-2.19	-2.00	1.41	-34.20
1 D Gi Shi-er Tz	0.73	0.68	0.17	-0.40	0.97	-0.07	0.78	2.33	-1.02	0.39	0.62	6.61
5 D Gi Shi-er Tz	0.73	0.95	0.06	0.22	0.79	0.02	0.71	3.38	-1.53	-1.72	1.31	-29.45
10 D Gi Shi-er Tz	0.73	1.06	0.12	0.52	0.68	0.03	0.70	4.36	-2.12	-2.65	1.63	-45.29
1 L Gi Shi-er Tz	0.73	0.65	0.14	-0.31	0.87	-0.06	0.77	2.20	-0.96	0.68	0.82	11.55
5 L Gi Shi-er Tz	0.73	0.93	0.12	0.41	0.63	0.03	0.70	3.45	-1.59	-1.58	1.26	-27.05
10 L Gi Shi-er Tz	0.73	1.04	0.10	0.47	0.69	0.02	0.71	4.80	-2.48	-2.43	1.56	-41.56
1 D Ri La Tz	0.73	0.80	0.06	-0.16	0.92	-0.02	0.75	2.74	-1.20	-0.57	0.76	-9.80
5 D Ri La Tz	0.73	0.89	0.04	0.13	0.80	0.01	0.72	3.15	-1.41	-1.30	1.14	-22.18
10 D Ri La Tz	0.73	1.00	0.18	0.72	0.48	0.04	0.69	4.03	-1.94	-2.18	1.48	-37.32
1 L Ri La Tz	0.73	0.61	0.16	-0.33	0.84	-0.08	0.78	2.06	-0.90	1.00	1.00	17.17
5 L Ri La Tz	0.73	0.87	0.10	0.32	0.64	0.03	0.70	3.17	-1.44	-1.12	1.06	-19.16
10 L Ri La Tz	0.73	0.97	0.22	0.94	0.28	0.05	0.68	4.28	-2.16	-1.90	1.38	-32.47
1 D Gi La Tz	0.73	0.68	0.18	-0.41	0.98	-0.08	0.78	2.31	-1.01	0.44	0.67	7.57
5 D Gi La Tz	0.73	0.94	0.05	0.18	0.80	0.02	0.72	3.34	-1.50	-1.64	1.28	-28.00
10 D Gi La Tz	0.73	1.05	0.11	0.46	0.71	0.02	0.70	4.31	-2.10	-2.55	1.60	-43.66
1 L Gi La Tz	0.73	0.64	0.15	-0.32	0.88	-0.07	0.78	2.17	-0.95	0.73	0.85	12.47
5 L Gi La Tz	0.73	0.92	0.11	0.38	0.64	0.03	0.70	3.40	-1.57	-1.49	1.22	-25.54
10 L Gi La Tz	0.73	1.02	0.09	0.41	0.72	0.02	0.71	4.77	-2.47	-2.33	1.53	-39.86

Table A.10: Calibration statistics for modelled and observed interstitial deposition in S2Q30D37, shear stress deposition model

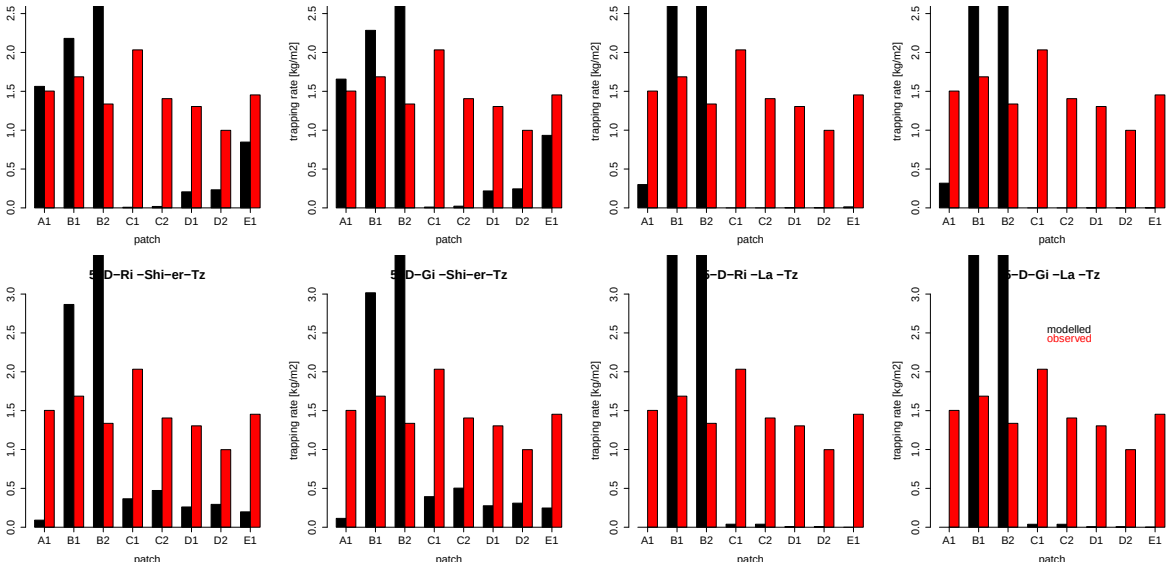

Figure A.10: Modelled and observed interstitial deposition in S2Q100D48-1, shear stress deposition model for eight selected value set combinations

	TR		r^2	LM_{mo}		LM_{om}		RMA		Error		
	obs	mod		a	b	a	b	a	b	MSE	SMSE	PBIAS
1 D Ri Shi-er Txyz	1.47	0.57	0.27	-0.36	1.10	-0.20	1.58	1.35	-1.41	7.18	2.68	61.24
5 D Ri Shi-er Txyz	1.47	0.89	0.22	-0.48	1.59	-0.11	1.56	2.13	-2.24	4.64	2.15	39.58
10 D Ri Shi-er Txyz	1.47	1.05	0.19	-0.50	1.78	-0.07	1.54	2.60	-2.76	3.34	1.83	28.47
1 L Ri Shi-er Txyz	1.47	0.54	0.27	-0.35	1.06	-0.21	1.58	1.29	-1.35	7.36	2.71	62.81
5 L Ri Shi-er Txyz	1.47	0.86	0.23	-0.47	1.55	-0.11	1.56	2.07	-2.17	4.85	2.20	41.34
10 L Ri Shi-er Txyz	1.47	1.04	0.19	-0.49	1.76	-0.07	1.54	2.58	-2.74	3.42	1.85	29.15
1 D Gi Shi-er Txyz	1.47	0.61	0.27	-0.39	1.18	-0.19	1.58	1.45	-1.51	6.82	2.61	58.20
5 D Gi Shi-er Txyz	1.47	0.94	0.22	-0.50	1.67	-0.10	1.56	2.28	-2.40	4.18	2.05	35.69
10 D Gi Shi-er Txyz	1.47	1.12	0.18	-0.51	1.87	-0.06	1.54	2.81	-3.00	2.79	1.67	23.83
1 L Gi Shi-er Txyz	1.47	0.59	0.27	-0.37	1.13	-0.19	1.58	1.39	-1.44	7.02	2.65	59.89
5 L Gi Shi-er Txyz	1.47	0.92	0.22	-0.49	1.64	-0.10	1.56	2.23	-2.34	4.36	2.09	37.22
10 L Gi Shi-er Txyz	1.47	1.12	0.18	-0.51	1.87	-0.06	1.54	2.83	-3.03	2.78	1.67	23.68
1 D Ri La Txyz	1.47	0.35	0.01	-0.02	0.39	-0.01	1.47	1.78	-2.26	8.89	2.98	75.87
5 D Ri La Txyz	1.47	0.56	0.02	0.06	0.47	0.01	1.46	3.21	-4.15	7.22	2.69	61.64
10 D Ri La Txyz	1.47	0.70	0.03	0.12	0.53	0.01	1.46	4.09	-5.29	6.14	2.48	52.37
1 L Ri La Txyz	1.47	0.34	0.02	-0.03	0.38	-0.01	1.47	1.63	-2.04	8.96	2.99	76.48
5 L Ri La Txyz	1.47	0.53	0.02	0.06	0.44	0.01	1.46	3.00	-3.86	7.46	2.73	63.69
10 L Ri La Txyz	1.47	0.67	0.03	0.12	0.49	0.01	1.46	3.86	-4.99	6.38	2.52	54.39
1 D Gi La Txyz	1.47	0.38	0.01	-0.02	0.41	-0.01	1.47	1.95	-2.47	8.69	2.95	74.18
5 D Gi La Txyz	1.47	0.60	0.02	0.07	0.50	0.01	1.46	3.50	-4.53	6.88	2.62	58.72
10 D Gi La Txyz	1.47	0.76	0.03	0.13	0.57	0.01	1.46	4.39	-5.67	5.66	2.38	48.27
1 L Gi La Txyz	1.47	0.37	0.01	-0.03	0.40	-0.01	1.47	1.78	-2.24	8.79	2.96	74.98
5 L Gi La Txyz	1.47	0.57	0.02	0.08	0.46	0.01	1.46	3.29	-4.24	7.14	2.67	60.93
10 L Gi La Txyz	1.47	0.73	0.03	0.12	0.56	0.01	1.46	4.15	-5.34	5.84	2.42	49.86
1 D Ri Shi-er Tz	1.47	0.62	0.03	-0.04	0.69	-0.02	1.48	1.44	-1.49	6.73	2.59	57.39
5 D Ri Shi-er Tz	1.47	0.98	0.07	0.14	0.78	0.04	1.43	1.87	-1.76	3.84	1.96	32.79
10 D Ri Shi-er Tz	1.47	1.17	0.13	0.26	0.80	0.06	1.39	2.00	-1.76	2.33	1.53	19.90
1 L Ri Shi-er Tz	1.47	0.60	0.02	-0.03	0.64	-0.01	1.47	1.36	-1.40	6.93	2.63	59.08
5 L Ri Shi-er Tz	1.47	0.96	0.07	0.12	0.78	0.04	1.43	1.77	-1.63	4.06	2.01	34.63
10 L Ri Shi-er Tz	1.47	1.16	0.12	0.23	0.82	0.06	1.39	1.93	-1.66	2.43	1.56	20.77
1 D Gi Shi-er Tz	1.47	0.67	0.02	-0.03	0.72	-0.01	1.47	1.52	-1.55	6.34	2.52	54.12
5 D Gi Shi-er Tz	1.47	1.05	0.09	0.17	0.80	0.05	1.42	1.91	-1.74	3.31	1.82	28.27
10 D Gi Shi-er Tz	1.47	1.25	0.14	0.29	0.83	0.07	1.38	2.04	-1.74	1.71	1.31	14.56
1 L Gi Shi-er Tz	1.47	0.65	0.01	-0.02	0.68	-0.01	1.47	1.43	-1.45	6.56	2.56	55.94
5 L Gi Shi-er Tz	1.47	1.03	0.08	0.15	0.81	0.05	1.42	1.81	-1.62	3.50	1.87	29.86
10 L Gi Shi-er Tz	1.47	1.25	0.13	0.25	0.88	0.06	1.38	1.98	-1.66	1.73	1.32	14.76
1 D Ri La Tz	1.47	0.70	0.02	0.10	0.55	0.01	1.46	4.09	-5.30	6.16	2.48	52.52
5 D Ri La Tz	1.47	0.81	0.03	0.17	0.56	0.01	1.46	4.82	-6.26	5.25	2.29	44.81
10 D Ri La Tz	1.47	0.97	0.05	0.29	0.55	0.01	1.46	5.92	-7.70	3.95	1.99	33.66
1 L Ri La Tz	1.47	0.45	0.01	0.03	0.41	0.00	1.46	2.43	-3.11	8.13	2.85	69.32
5 L Ri La Tz	1.47	0.75	0.04	0.18	0.49	0.01	1.46	4.42	-5.73	5.71	2.39	48.69
10 L Ri La Tz	1.47	0.91	0.05	0.30	0.47	0.01	1.46	5.52	-7.19	4.47	2.11	38.09
1 D Gi La Tz	1.47	0.51	0.00	0.00	0.51	0.00	1.46	2.92	-3.78	7.64	2.76	65.22
5 D Gi La Tz	1.47	0.86	0.04	0.20	0.57	0.01	1.46	5.17	-6.71	4.82	2.20	41.14
10 D Gi La Tz	1.47	1.04	0.05	0.32	0.57	0.01	1.46	6.33	-8.24	3.44	1.85	29.33
1 L Gi La Tz	1.47	0.48	0.01	0.03	0.44	0.00	1.46	2.65	-3.41	7.86	2.80	67.04
5 L Gi La Tz	1.47	0.80	0.04	0.21	0.49	0.01	1.46	4.76	-6.18	5.30	2.30	45.26
10 L Gi La Tz	1.47	0.97	0.05	0.31	0.52	0.01	1.46	5.97	-7.77	3.94	1.99	33.64

Table A.11: Calibration statistics for modelled and observed interstitial deposition in S2Q100D48-1, shear stress deposition model

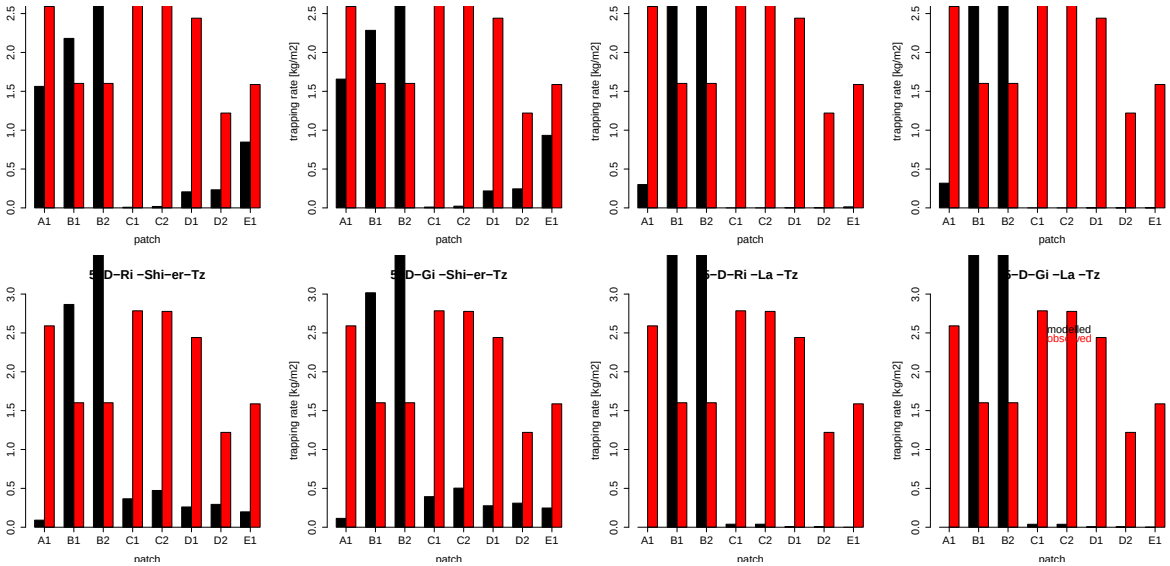

Figure A.11: Modelled and observed interstitial deposition in S2Q100D48-2, shear stress deposition model for eight selected value set combinations

	TR		r^2	LM_{mo}		LM_{om}		RMA		Error		
	obs	mod		a	b	a	b	a	b	MSE	SMSE	PBIAS
1 D Ri Shi-er Txyz	2.08	0.57	0.54	-0.34	1.28	-0.83	2.55	0.64	-0.77	12.06	3.47	72.64
5 D Ri Shi-er Txyz	2.08	0.89	0.52	-0.53	1.98	-0.51	2.53	1.01	-1.22	9.52	3.09	57.35
10 D Ri Shi-er Txyz	2.08	1.05	0.48	-0.60	2.29	-0.39	2.48	1.24	-1.52	8.22	2.87	49.51
1 L Ri Shi-er Txyz	2.08	0.54	0.54	-0.33	1.23	-0.88	2.55	0.61	-0.73	12.25	3.50	73.75
5 L Ri Shi-er Txyz	2.08	0.86	0.52	-0.51	1.91	-0.52	2.53	0.98	-1.18	9.73	3.12	58.59
10 L Ri Shi-er Txyz	2.08	1.04	0.47	-0.57	2.23	-0.38	2.47	1.23	-1.51	8.30	2.88	49.99
1 D Gi Shi-er Txyz	2.08	0.61	0.54	-0.37	1.39	-0.78	2.56	0.69	-0.82	11.70	3.42	70.49
5 D Gi Shi-er Txyz	2.08	0.94	0.52	-0.56	2.10	-0.47	2.52	1.09	-1.31	9.07	3.01	54.60
10 D Gi Shi-er Txyz	2.08	1.12	0.47	-0.63	2.41	-0.35	2.47	1.34	-1.66	7.68	2.77	46.23
1 L Gi Shi-er Txyz	2.08	0.59	0.54	-0.36	1.33	-0.82	2.56	0.66	-0.78	11.90	3.45	71.69
5 L Gi Shi-er Txyz	2.08	0.92	0.51	-0.54	2.04	-0.48	2.52	1.06	-1.28	9.25	3.04	55.68
10 L Gi Shi-er Txyz	2.08	1.12	0.45	-0.60	2.37	-0.33	2.45	1.35	-1.68	7.66	2.77	46.13
1 D Ri La Txyz	2.08	0.35	0.46	-0.39	1.16	-0.54	2.27	0.85	-1.41	13.78	3.71	82.97
5 D Ri La Txyz	2.08	0.56	0.43	-0.65	1.91	-0.28	2.23	1.53	-2.61	12.11	3.48	72.92
10 D Ri La Txyz	2.08	0.70	0.41	-0.79	2.34	-0.21	2.22	1.94	-3.34	11.02	3.32	66.38
1 L Ri La Txyz	2.08	0.34	0.47	-0.36	1.09	-0.60	2.28	0.78	-1.27	13.85	3.72	83.40
5 L Ri La Txyz	2.08	0.53	0.41	-0.59	1.75	-0.29	2.23	1.43	-2.43	12.35	3.51	74.37
10 L Ri La Txyz	2.08	0.67	0.39	-0.71	2.15	-0.21	2.22	1.84	-3.14	11.26	3.36	67.81
1 D Gi La Txyz	2.08	0.38	0.45	-0.42	1.25	-0.49	2.26	0.93	-1.54	13.58	3.68	81.78
5 D Gi La Txyz	2.08	0.60	0.42	-0.70	2.06	-0.25	2.23	1.67	-2.86	11.77	3.43	70.86
10 D Gi La Txyz	2.08	0.76	0.41	-0.85	2.53	-0.20	2.22	2.09	-3.58	10.54	3.25	63.49
1 L Gi La Txyz	2.08	0.37	0.46	-0.39	1.18	-0.54	2.27	0.85	-1.39	13.67	3.70	82.34
5 L Gi La Txyz	2.08	0.57	0.41	-0.63	1.89	-0.26	2.22	1.56	-2.67	12.02	3.47	72.42
10 L Gi La Txyz	2.08	0.73	0.39	-0.77	2.33	-0.20	2.22	1.97	-3.36	10.73	3.28	64.61
1 D Ri Shi-er Tz	2.08	0.62	0.19	-0.13	0.89	-0.27	2.25	0.69	-0.80	11.61	3.41	69.92
5 D Ri Shi-er Tz	2.08	0.98	0.15	-0.13	1.25	-0.16	2.24	0.89	-0.86	8.73	2.95	52.56
10 D Ri Shi-er Tz	2.08	1.17	0.16	-0.15	1.49	-0.17	2.27	0.95	-0.81	7.22	2.69	43.46
1 L Ri Shi-er Tz	2.08	0.60	0.18	-0.12	0.85	-0.28	2.24	0.65	-0.75	11.81	3.44	71.12
5 L Ri Shi-er Tz	2.08	0.96	0.15	-0.13	1.23	-0.18	2.25	0.84	-0.79	8.94	2.99	53.86
10 L Ri Shi-er Tz	2.08	1.16	0.18	-0.17	1.51	-0.20	2.31	0.92	-0.74	7.32	2.71	44.07
1 D Gi Shi-er Tz	2.08	0.67	0.18	-0.13	0.94	-0.25	2.24	0.72	-0.82	11.23	3.35	67.61
5 D Gi Shi-er Tz	2.08	1.05	0.14	-0.13	1.32	-0.16	2.24	0.91	-0.83	8.20	2.86	49.37
10 D Gi Shi-er Tz	2.08	1.25	0.18	-0.17	1.61	-0.18	2.30	0.97	-0.76	6.59	2.57	39.69
1 L Gi Shi-er Tz	2.08	0.65	0.18	-0.12	0.89	-0.26	2.24	0.68	-0.76	11.44	3.38	68.90
5 L Gi Shi-er Tz	2.08	1.03	0.16	-0.13	1.30	-0.18	2.26	0.86	-0.76	8.38	2.90	50.49
10 L Gi Shi-er Tz	2.08	1.25	0.21	-0.20	1.66	-0.22	2.35	0.94	-0.71	6.61	2.57	39.83
1 D Ri La Tz	2.08	0.70	0.43	-0.83	2.42	-0.22	2.23	1.95	-3.34	11.04	3.32	66.49
5 D Ri La Tz	2.08	0.81	0.43	-0.99	2.86	-0.19	2.23	2.29	-3.95	10.14	3.18	61.04
10 D Ri La Tz	2.08	0.97	0.44	-1.23	3.52	-0.15	2.23	2.82	-4.88	8.83	2.97	53.17
1 L Ri La Tz	2.08	0.45	0.40	-0.47	1.42	-0.35	2.23	1.16	-1.95	13.01	3.61	78.34
5 L Ri La Tz	2.08	0.75	0.42	-0.89	2.60	-0.20	2.23	2.10	-3.62	10.59	3.25	63.78
10 L Ri La Tz	2.08	0.91	0.43	-1.13	3.25	-0.16	2.22	2.63	-4.55	9.35	3.06	56.30
1 D Gi La Tz	2.08	0.51	0.41	-0.57	1.70	-0.30	2.23	1.39	-2.38	12.53	3.54	75.45
5 D Gi La Tz	2.08	0.86	0.43	-1.06	3.07	-0.18	2.23	2.46	-4.25	9.71	3.12	58.45
10 D Gi La Tz	2.08	1.04	0.44	-1.33	3.79	-0.15	2.23	3.01	-5.22	8.32	2.88	50.12
1 L Gi La Tz	2.08	0.48	0.41	-0.51	1.55	-0.32	2.23	1.26	-2.14	12.74	3.57	76.74
5 L Gi La Tz	2.08	0.80	0.42	-0.96	2.80	-0.19	2.23	2.27	-3.90	10.19	3.19	61.36
10 L Gi La Tz	2.08	0.97	0.44	-1.24	3.55	-0.15	2.23	2.84	-4.92	8.83	2.97	53.16

Table A.12: Calibration statistics for modelled and observed interstitial deposition in S2Q100D48-2, shear stress deposition model

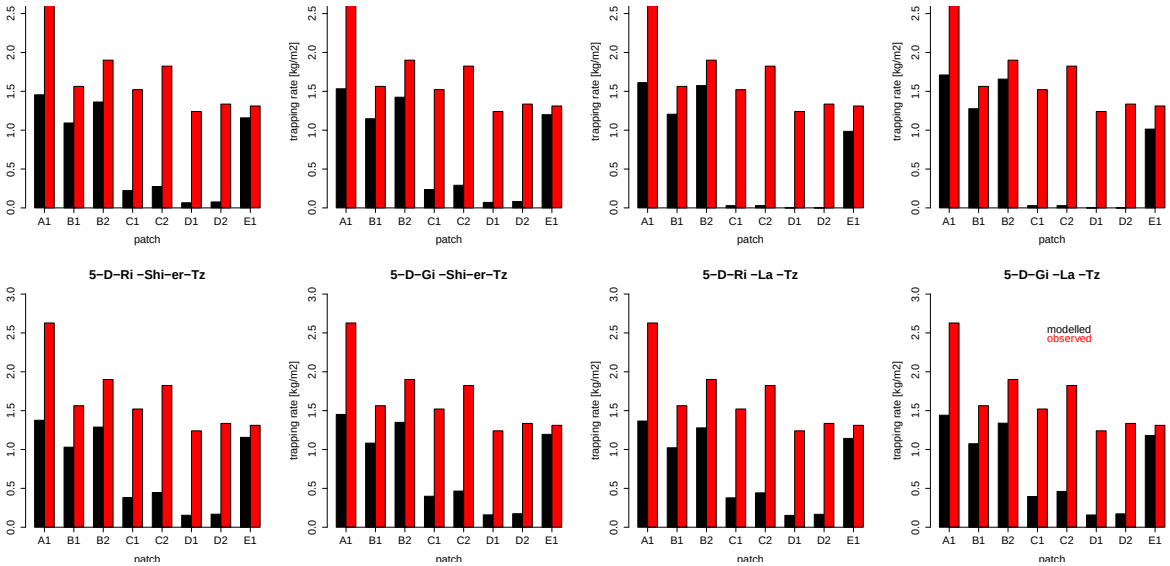

Figure A.12: Modelled and observed interstitial deposition in S2Q100D37, shear stress deposition model for eight selected value set combinations

	TR		r^2	LM_{mo}		LM_{om}		RMA		Error		
	obs	mod		a	b	a	b	a	b	MSE	SMSE	PBIAS
1 D Gi In mean	1.67	0.41	0.43	0.28	-0.05	0.67	1.39	0.64	-0.65	10.02	3.16	75.16
5 D Gi In mean	1.67	0.36	0.50	0.27	-0.10	0.91	1.34	0.55	-0.56	10.48	3.24	78.68
10 D Gi In mean	1.67	0.35	0.64	0.36	-0.24	1.14	1.26	0.56	-0.58	10.49	3.24	78.72
1 L Gi In mean	1.67	0.39	0.46	0.28	-0.07	0.75	1.37	0.60	-0.61	10.18	3.19	76.42
5 L Gi In mean	1.67	0.32	0.51	0.26	-0.10	1.03	1.33	0.50	-0.51	10.73	3.27	80.49
10 L Gi In mean	1.67	0.32	0.66	0.34	-0.25	1.27	1.25	0.52	-0.54	10.73	3.28	80.51
1 D Sto In mean	1.67	0.38	0.45	0.26	-0.05	0.76	1.37	0.59	-0.60	10.25	3.20	76.91
5 D Sto In mean	1.67	0.39	0.49	0.30	-0.10	0.80	1.35	0.61	-0.62	10.17	3.19	76.34
10 D Sto In mean	1.67	0.36	0.47	0.26	-0.08	0.86	1.36	0.55	-0.56	10.48	3.24	78.64
1 L Sto In mean	1.67	0.37	0.48	0.27	-0.08	0.86	1.35	0.56	-0.57	10.39	3.22	77.98
5 L Sto In mean	1.67	0.36	0.49	0.27	-0.09	0.89	1.35	0.55	-0.56	10.48	3.24	78.64
10 L Sto In mean	1.67	0.33	0.49	0.25	-0.09	0.98	1.35	0.50	-0.51	10.72	3.27	80.46
1 D Gi La mean	1.67	0.68	0.47	0.48	-0.11	0.46	1.35	1.01	-1.00	7.85	2.80	58.91
5 D Gi La mean	1.67	0.81	0.49	0.59	-0.17	0.40	1.34	1.21	-1.20	6.81	2.61	51.09
10 D Gi La mean	1.67	0.89	0.54	0.73	-0.31	0.40	1.31	1.34	-1.34	6.17	2.48	46.29
1 L Gi La mean	1.67	0.65	0.48	0.46	-0.12	0.50	1.34	0.96	-0.95	8.11	2.85	60.90
5 L Gi La mean	1.67	0.79	0.49	0.57	-0.17	0.42	1.34	1.17	-1.16	7.04	2.65	52.83
10 L Gi La mean	1.67	0.87	0.54	0.71	-0.31	0.41	1.31	1.32	-1.32	6.33	2.52	47.49
1 D Sto La mean	1.67	0.55	0.48	0.39	-0.10	0.60	1.34	0.80	-0.79	8.95	2.99	67.17
5 D Sto La mean	1.67	0.71	0.50	0.53	-0.16	0.47	1.33	1.05	-1.04	7.63	2.76	57.28
10 D Sto La mean	1.67	0.75	0.48	0.54	-0.14	0.43	1.34	1.12	-1.11	7.29	2.70	54.70
1 L Sto La mean	1.67	0.52	0.50	0.38	-0.12	0.66	1.32	0.76	-0.75	9.18	3.03	68.92
5 L Sto La mean	1.67	0.66	0.50	0.49	-0.15	0.51	1.33	0.98	-0.97	8.03	2.83	60.23
10 L Sto La mean	1.67	0.72	0.49	0.52	-0.15	0.46	1.34	1.07	-1.06	7.57	2.75	56.81
1 D Gi In ave5	1.67	0.25	0.69	0.29	-0.24	1.65	1.26	0.42	-0.45	11.34	3.37	85.14
5 D Gi In ave5	1.67	0.19	0.77	0.27	-0.27	2.17	1.25	0.36	-0.40	11.81	3.44	88.63
10 D Gi In ave5	1.67	0.19	0.83	0.34	-0.37	2.04	1.27	0.41	-0.49	11.79	3.43	88.50
1 L Gi In ave5	1.67	0.25	0.69	0.29	-0.23	1.67	1.25	0.41	-0.44	11.36	3.37	85.22
5 L Gi In ave5	1.67	0.18	0.77	0.26	-0.25	2.32	1.25	0.33	-0.37	11.89	3.45	89.26
10 L Gi In ave5	1.67	0.18	0.83	0.32	-0.35	2.16	1.27	0.39	-0.46	11.88	3.45	89.13
1 D Sto In ave5	1.67	0.25	0.69	0.29	-0.23	1.64	1.26	0.42	-0.45	11.35	3.37	85.18
5 D Sto In ave5	1.67	0.23	0.75	0.31	-0.29	1.83	1.25	0.41	-0.46	11.51	3.39	86.41
10 D Sto In ave5	1.67	0.19	0.76	0.27	-0.26	2.17	1.25	0.35	-0.40	11.81	3.44	88.65
1 L Sto In ave5	1.67	0.25	0.69	0.29	-0.23	1.67	1.25	0.41	-0.44	11.36	3.37	85.25
5 L Sto In ave5	1.67	0.21	0.74	0.28	-0.25	2.01	1.25	0.37	-0.41	11.66	3.41	87.52
10 L Sto In ave5	1.67	0.18	0.76	0.25	-0.24	2.32	1.25	0.33	-0.37	11.90	3.45	89.28
1 D Gi La ave5	1.67	0.46	0.75	0.62	-0.58	0.89	1.26	0.84	-0.94	9.66	3.11	72.46
5 D Gi La ave5	1.67	0.45	0.83	0.79	-0.87	0.87	1.28	0.95	-1.14	9.73	3.12	73.02
10 D Gi La ave5	1.67	0.47	0.86	0.93	-1.09	0.80	1.29	1.08	-1.34	9.60	3.10	72.05
1 L Gi La ave5	1.67	0.43	0.75	0.59	-0.55	0.95	1.25	0.79	-0.88	9.85	3.14	73.91
5 L Gi La ave5	1.67	0.41	0.83	0.74	-0.82	0.94	1.28	0.89	-1.06	10.01	3.16	75.15
10 L Gi La ave5	1.67	0.43	0.87	0.89	-1.05	0.85	1.30	1.02	-1.27	9.87	3.14	74.11
1 D Sto La ave5	1.67	0.40	0.70	0.48	-0.41	1.02	1.26	0.69	-0.75	10.13	3.18	75.99
5 D Sto La ave5	1.67	0.45	0.79	0.69	-0.70	0.90	1.26	0.88	-1.01	9.70	3.11	72.78
10 D Sto La ave5	1.67	0.44	0.81	0.73	-0.78	0.90	1.27	0.90	-1.06	9.83	3.13	73.75
1 L Sto La ave5	1.67	0.38	0.71	0.47	-0.40	1.08	1.25	0.66	-0.71	10.28	3.21	77.12
5 L Sto La ave5	1.67	0.41	0.79	0.63	-0.64	0.99	1.26	0.80	-0.92	10.04	3.17	75.33
10 L Sto La ave5	1.67	0.40	0.82	0.68	-0.73	0.98	1.27	0.83	-0.98	10.11	3.18	75.87

Table A.13: Calibration statistics for modelled and observed interstitial deposition in S2Q100D37, shear stress deposition model

A.1.3 Step 2, velocity deposition model, silty experimetnal runs

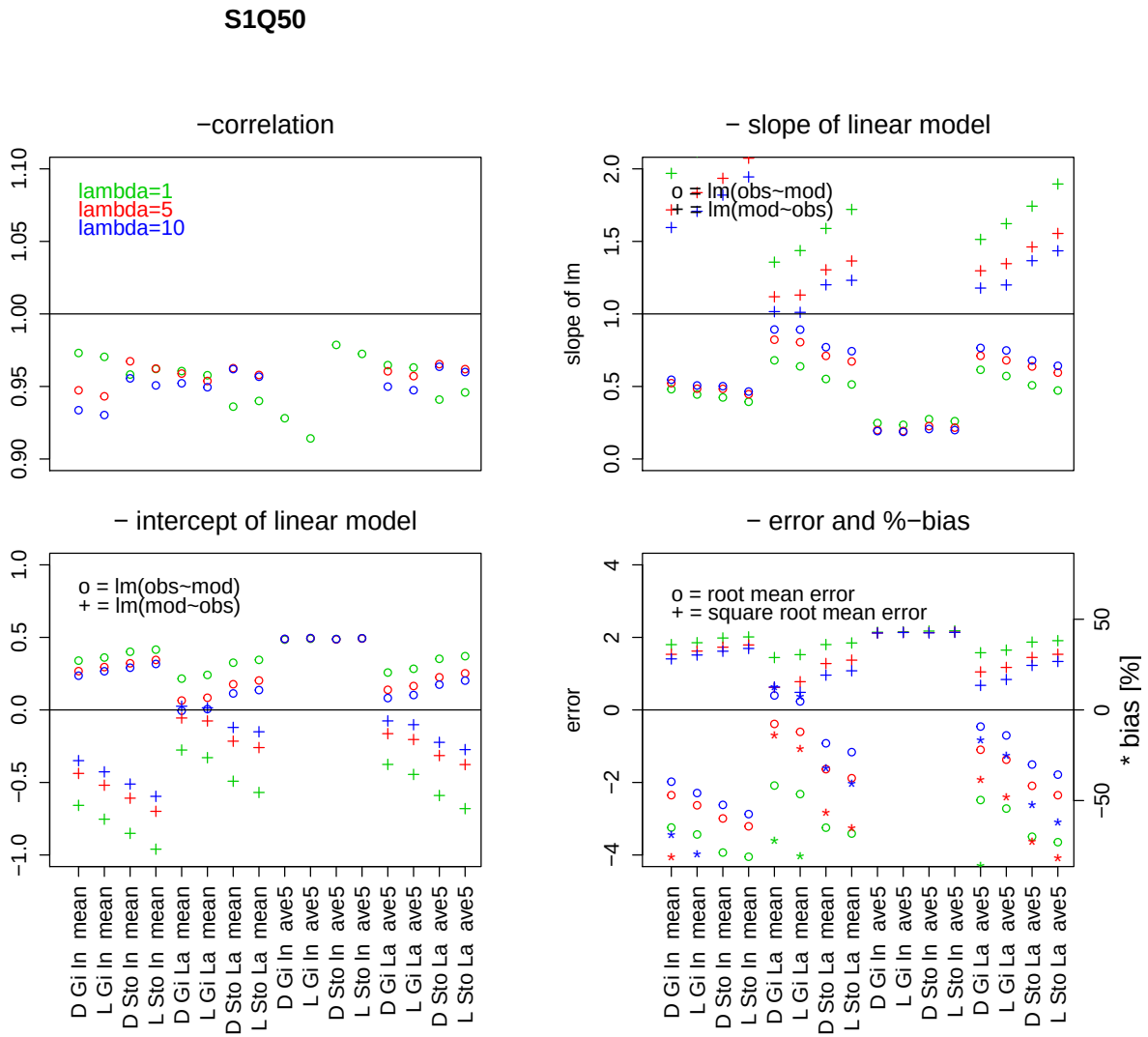

Figure A.13: Graphical representaiton of statisitcal evaluation of modeled and observed suspended sediment concentration loss in S1Q50, velocity deposition model

	r^2	LM_{mo}		LM_{om}		RMA		Error		
		a	b	a	b	a	b	MSE	SMSE	PBIAS
1 D Gi In mean	0.97	0.48	0.34	1.97	-0.66	0.49	0.34	-3.24	1.80	-111.15
5 D Gi In mean	0.95	0.52	0.27	1.72	-0.44	0.55	0.26	-2.35	1.53	-80.58
10 D Gi In mean	0.93	0.55	0.24	1.60	-0.35	0.59	0.23	-1.98	1.41	-67.84
1 L Gi In mean	0.97	0.44	0.36	2.12	-0.75	0.46	0.36	-3.43	1.85	-117.72
5 L Gi In mean	0.94	0.48	0.30	1.84	-0.52	0.51	0.29	-2.63	1.62	-90.16
10 L Gi In mean	0.93	0.51	0.27	1.71	-0.43	0.54	0.26	-2.29	1.51	-78.58
1 D Sto In mean	0.96	0.42	0.40	2.16	-0.85	0.44	0.40	-3.93	1.98	-134.83
5 D Sto In mean	0.97	0.48	0.32	1.93	-0.61	0.50	0.32	-2.99	1.73	-102.58
10 D Sto In mean	0.96	0.50	0.29	1.82	-0.51	0.53	0.29	-2.62	1.62	-89.77
1 L Sto In mean	0.96	0.39	0.42	2.35	-0.96	0.41	0.41	-4.05	2.01	-138.82
5 L Sto In mean	0.96	0.45	0.34	2.07	-0.70	0.46	0.34	-3.21	1.79	-110.02
10 L Sto In mean	0.95	0.46	0.32	1.94	-0.60	0.49	0.31	-2.87	1.69	-98.48
1 D Gi La mean	0.96	0.68	0.22	1.36	-0.28	0.71	0.21	-2.09	1.44	-71.48
5 D Gi La mean	0.96	0.82	0.06	1.12	-0.06	0.86	0.06	-0.39	0.62	-13.25
10 D Gi La mean	0.95	0.89	-0.01	1.02	0.03	0.94	-0.02	0.40	0.63	13.66
1 L Gi La mean	0.96	0.64	0.24	1.44	-0.33	0.67	0.24	-2.32	1.52	-79.57
5 L Gi La mean	0.95	0.80	0.08	1.13	-0.08	0.84	0.08	-0.60	0.78	-20.74
10 L Gi La mean	0.95	0.89	0.01	1.01	0.01	0.94	-0.00	0.23	0.48	8.02
1 D Sto La mean	0.94	0.55	0.33	1.59	-0.49	0.59	0.32	-3.25	1.80	-111.30
5 D Sto La mean	0.96	0.71	0.18	1.30	-0.22	0.74	0.17	-1.63	1.28	-56.01
10 D Sto La mean	0.96	0.77	0.11	1.20	-0.12	0.80	0.11	-0.92	0.96	-31.55
1 L Sto La mean	0.94	0.51	0.34	1.72	-0.57	0.55	0.34	-3.41	1.85	-116.87
5 L Sto La mean	0.96	0.67	0.20	1.36	-0.26	0.70	0.20	-1.88	1.37	-64.56
10 L Sto La mean	0.96	0.74	0.14	1.23	-0.15	0.78	0.13	-1.16	1.08	-39.90
1 D Gi In ave5	0.93	0.25	0.48	3.48	-1.65	0.27	0.48	-4.59	2.14	-157.27
5 D Gi In ave5	0.77	0.20	0.49	3.00	-1.38	0.26	0.48	-4.51	2.12	-154.47
10 D Gi In ave5	0.74	0.19	0.49	2.88	-1.32	0.26	0.48	-4.50	2.12	-154.18
1 L Gi In ave5	0.91	0.24	0.49	3.55	-1.71	0.26	0.49	-4.64	2.15	-158.94
5 L Gi In ave5	0.77	0.19	0.49	3.06	-1.43	0.25	0.48	-4.57	2.14	-156.52
10 L Gi In ave5	0.74	0.19	0.50	2.96	-1.37	0.25	0.48	-4.56	2.14	-156.28
1 D Sto In ave5	0.98	0.27	0.49	3.49	-1.70	0.28	0.49	-4.73	2.17	-162.06
5 D Sto In ave5	0.87	0.23	0.49	3.34	-1.57	0.26	0.48	-4.55	2.13	-155.82
10 D Sto In ave5	0.80	0.21	0.49	3.12	-1.45	0.26	0.48	-4.52	2.13	-154.81
1 L Sto In ave5	0.97	0.26	0.49	3.63	-1.78	0.27	0.49	-4.76	2.18	-163.08
5 L Sto In ave5	0.86	0.22	0.49	3.39	-1.61	0.25	0.48	-4.60	2.14	-157.66
10 L Sto In ave5	0.79	0.20	0.49	3.17	-1.49	0.25	0.48	-4.57	2.14	-156.81
1 D Gi La ave5	0.96	0.61	0.26	1.51	-0.38	0.64	0.25	-2.49	1.58	-85.19
5 D Gi La ave5	0.96	0.71	0.14	1.30	-0.16	0.74	0.13	-1.10	1.05	-37.64
10 D Gi La ave5	0.95	0.77	0.08	1.18	-0.08	0.81	0.07	-0.46	0.68	-15.73
1 L Gi La ave5	0.96	0.57	0.28	1.62	-0.44	0.59	0.28	-2.72	1.65	-93.22
5 L Gi La ave5	0.96	0.68	0.16	1.35	-0.20	0.71	0.16	-1.37	1.17	-47.05
10 L Gi La ave5	0.95	0.75	0.10	1.20	-0.10	0.79	0.09	-0.70	0.84	-24.11
1 D Sto La ave5	0.94	0.51	0.35	1.74	-0.59	0.54	0.35	-3.50	1.87	-119.86
5 D Sto La ave5	0.97	0.64	0.23	1.46	-0.31	0.66	0.22	-2.09	1.45	-71.74
10 D Sto La ave5	0.96	0.68	0.17	1.37	-0.22	0.70	0.17	-1.51	1.23	-51.64
1 L Sto La ave5	0.95	0.47	0.37	1.90	-0.68	0.50	0.36	-3.65	1.91	-125.00
5 L Sto La ave5	0.96	0.60	0.25	1.55	-0.38	0.62	0.25	-2.35	1.53	-80.60
10 L Sto La ave5	0.96	0.64	0.20	1.43	-0.27	0.67	0.20	-1.78	1.34	-61.18

Table A.14: Calibration statistics for modeled and observed suspended sediment concentration loss in S1Q80, shear stress deposition model

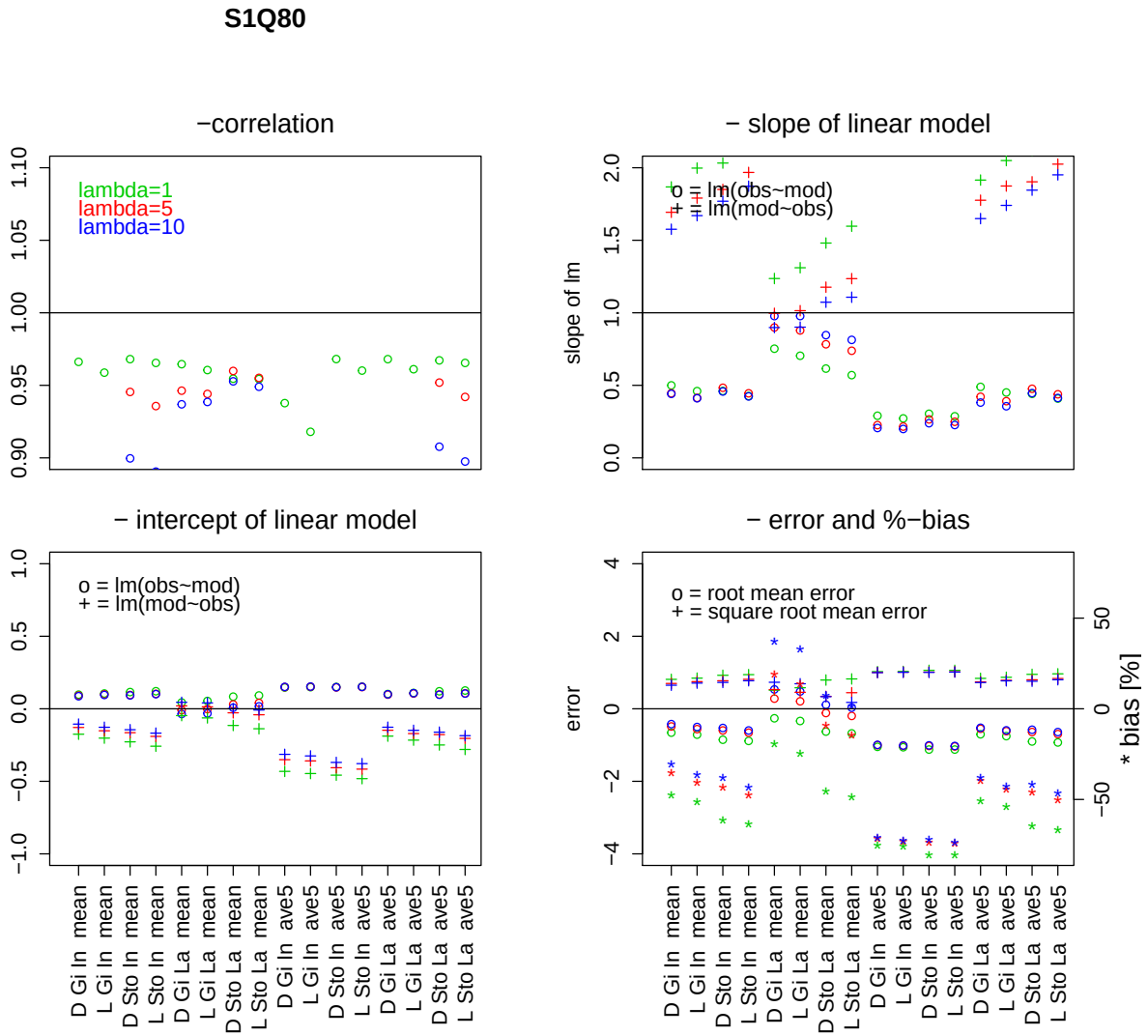

Figure A.14: Graphical representaiton of statisitcal evaluation of modeled and observed suspended sediment concentration loss in S1Q80, velocity deposition model

	r^2	LM_{mo}		LM_{om}		RMA		Error		
		a	b	a	b	a	b	MSE	SMSE	PBIAS
1 D Gi In mean	0.97	0.50	0.10	1.87	-0.18	0.52	0.10	-0.66	0.81	-46.67
5 D Gi In mean	0.87	0.45	0.09	1.69	-0.13	0.51	0.08	-0.49	0.70	-34.57
10 D Gi In mean	0.83	0.44	0.09	1.58	-0.11	0.53	0.08	-0.42	0.65	-29.95
1 L Gi In mean	0.96	0.46	0.11	2.00	-0.20	0.48	0.10	-0.71	0.84	-50.58
5 L Gi In mean	0.86	0.41	0.10	1.79	-0.15	0.48	0.09	-0.56	0.75	-39.78
10 L Gi In mean	0.83	0.41	0.10	1.67	-0.13	0.50	0.09	-0.50	0.71	-35.61
1 D Sto In mean	0.97	0.46	0.12	2.03	-0.23	0.48	0.11	-0.85	0.92	-60.49
5 D Sto In mean	0.95	0.48	0.09	1.85	-0.16	0.51	0.09	-0.60	0.77	-42.38
10 D Sto In mean	0.90	0.46	0.09	1.77	-0.14	0.51	0.09	-0.53	0.73	-37.49
1 L Sto In mean	0.97	0.43	0.12	2.19	-0.26	0.44	0.12	-0.89	0.94	-62.82
5 L Sto In mean	0.94	0.44	0.10	1.97	-0.19	0.48	0.10	-0.66	0.81	-46.75
10 L Sto In mean	0.89	0.42	0.10	1.87	-0.17	0.48	0.10	-0.60	0.77	-42.40
1 D Gi La mean	0.96	0.75	0.04	1.24	-0.05	0.78	0.04	-0.26	0.51	-18.59
5 D Gi La mean	0.95	0.90	-0.01	1.00	0.02	0.95	-0.01	0.28	0.53	19.87
10 D Gi La mean	0.94	0.98	-0.04	0.90	0.04	1.04	-0.04	0.53	0.73	37.88
1 L Gi La mean	0.96	0.70	0.05	1.31	-0.06	0.73	0.05	-0.34	0.58	-23.85
5 L Gi La mean	0.94	0.88	-0.00	1.01	0.01	0.93	-0.01	0.21	0.45	14.63
10 L Gi La mean	0.94	0.98	-0.03	0.90	0.04	1.04	-0.04	0.48	0.69	33.78
1 D Sto La mean	0.95	0.62	0.08	1.48	-0.11	0.64	0.08	-0.63	0.79	-44.58
5 D Sto La mean	0.96	0.78	0.03	1.18	-0.03	0.82	0.03	-0.12	0.34	-8.29
10 D Sto La mean	0.95	0.85	0.01	1.07	0.00	0.89	0.00	0.11	0.33	7.89
1 L Sto La mean	0.95	0.57	0.09	1.60	-0.14	0.60	0.09	-0.68	0.82	-48.08
5 L Sto La mean	0.96	0.74	0.04	1.24	-0.04	0.77	0.04	-0.20	0.44	-13.95
10 L Sto La mean	0.95	0.81	0.02	1.11	-0.01	0.86	0.01	0.03	0.18	2.20
1 D Gi In ave5	0.94	0.29	0.15	3.03	-0.43	0.31	0.14	-1.05	1.02	-74.39
5 D Gi In ave5	0.77	0.23	0.15	2.62	-0.35	0.29	0.14	-1.00	1.00	-71.07
10 D Gi In ave5	0.71	0.21	0.15	2.41	-0.31	0.29	0.14	-0.99	1.00	-70.50
1 L Gi In ave5	0.92	0.27	0.15	3.10	-0.45	0.30	0.15	-1.06	1.03	-75.17
5 L Gi In ave5	0.76	0.22	0.15	2.65	-0.36	0.29	0.14	-1.02	1.01	-72.34
10 L Gi In ave5	0.70	0.20	0.15	2.46	-0.32	0.28	0.14	-1.01	1.01	-71.87
1 D Sto In ave5	0.97	0.30	0.15	3.08	-0.46	0.31	0.15	-1.12	1.06	-79.73
5 D Sto In ave5	0.88	0.27	0.15	2.91	-0.41	0.30	0.14	-1.03	1.01	-72.67
10 D Sto In ave5	0.81	0.24	0.15	2.72	-0.37	0.30	0.14	-1.01	1.00	-71.48
1 L Sto In ave5	0.96	0.29	0.15	3.22	-0.48	0.30	0.15	-1.12	1.06	-79.72
5 L Sto In ave5	0.86	0.25	0.15	2.95	-0.42	0.29	0.15	-1.04	1.02	-73.68
10 L Sto In ave5	0.79	0.23	0.15	2.75	-0.38	0.29	0.15	-1.03	1.01	-72.68
1 D Gi La ave5	0.97	0.49	0.10	1.91	-0.19	0.51	0.10	-0.70	0.84	-49.88
5 D Gi La ave5	0.86	0.42	0.10	1.78	-0.15	0.49	0.09	-0.55	0.74	-39.01
10 D Gi La ave5	0.79	0.38	0.10	1.65	-0.13	0.48	0.09	-0.52	0.72	-37.11
1 L Gi La ave5	0.96	0.45	0.11	2.05	-0.22	0.47	0.11	-0.75	0.87	-53.44
5 L Gi La ave5	0.86	0.39	0.11	1.87	-0.17	0.46	0.10	-0.62	0.79	-43.80
10 L Gi La ave5	0.79	0.36	0.11	1.74	-0.15	0.45	0.10	-0.59	0.77	-42.13
1 D Sto La ave5	0.97	0.44	0.12	2.12	-0.25	0.46	0.12	-0.90	0.95	-63.91
5 D Sto La ave5	0.95	0.48	0.10	1.90	-0.18	0.50	0.10	-0.64	0.80	-45.37
10 D Sto La ave5	0.91	0.45	0.10	1.85	-0.16	0.49	0.09	-0.58	0.76	-40.94
1 L Sto La ave5	0.97	0.41	0.13	2.28	-0.28	0.42	0.12	-0.93	0.96	-65.84
5 L Sto La ave5	0.94	0.44	0.11	2.02	-0.20	0.47	0.10	-0.70	0.83	-49.42
10 L Sto La ave5	0.90	0.41	0.11	1.95	-0.19	0.46	0.10	-0.64	0.80	-45.51

Table A.15: Calibration statistics for modeled and observed suspended sediment concentration loss in S1Q80, shear stress deposition model

	r^2	LM_{mo}		LM_{om}		RMA		Error		
		a	b	a	b	a	b	MSE	SMSE	PBIAS
1 D Gi In mean	0.99	0.59	0.59	1.64	-0.95	0.60	0.59	-4.84	2.20	-57.04
5 D Gi In mean	0.94	0.61	0.42	1.45	-0.54	0.65	0.40	-2.58	1.61	-30.42
10 D Gi In mean	0.90	0.58	0.40	1.39	-0.44	0.65	0.36	-2.04	1.43	-23.99
1 L Gi In mean	0.98	0.55	0.66	1.76	-1.14	0.56	0.65	-5.40	2.32	-63.64
5 L Gi In mean	0.94	0.56	0.50	1.55	-0.71	0.60	0.48	-3.36	1.83	-39.56
10 L Gi In mean	0.90	0.54	0.48	1.49	-0.60	0.60	0.45	-2.86	1.69	-33.72
1 D Sto In mean	0.98	0.53	0.77	1.81	-1.37	0.54	0.76	-6.77	2.60	-79.75
5 D Sto In mean	0.97	0.60	0.54	1.58	-0.82	0.62	0.53	-4.12	2.03	-48.52
10 D Sto In mean	0.96	0.61	0.46	1.50	-0.63	0.64	0.44	-3.12	1.77	-36.77
1 L Sto In mean	0.98	0.49	0.82	1.97	-1.59	0.50	0.81	-7.13	2.67	-84.01
5 L Sto In mean	0.97	0.55	0.61	1.70	-1.00	0.57	0.60	-4.75	2.18	-55.94
10 L Sto In mean	0.95	0.57	0.54	1.60	-0.81	0.59	0.52	-3.85	1.96	-45.32
1 D Gi La mean	0.98	0.76	0.35	1.26	-0.42	0.78	0.34	-2.87	1.70	-33.84
5 D Gi La mean	0.97	0.92	-0.05	1.02	0.09	0.95	-0.07	1.34	1.16	15.82
10 D Gi La mean	0.96	0.99	-0.22	0.94	0.25	1.02	-0.24	3.18	1.78	37.48
1 L Gi La mean	0.98	0.72	0.41	1.33	-0.52	0.74	0.40	-3.43	1.85	-40.37
5 L Gi La mean	0.97	0.91	-0.01	1.03	0.05	0.94	-0.03	0.88	0.94	10.34
10 L Gi La mean	0.96	0.99	-0.20	0.93	0.23	1.03	-0.22	2.85	1.69	33.56
1 D Sto La mean	0.97	0.63	0.64	1.49	-0.91	0.65	0.62	-5.74	2.40	-67.61
5 D Sto La mean	0.98	0.80	0.25	1.20	-0.27	0.81	0.24	-1.76	1.33	-20.78
10 D Sto La mean	0.97	0.86	0.08	1.10	-0.06	0.89	0.07	0.02	0.13	0.20
1 L Sto La mean	0.97	0.58	0.69	1.61	-1.07	0.60	0.68	-6.14	2.48	-72.28
5 L Sto La mean	0.97	0.76	0.31	1.25	-0.36	0.78	0.30	-2.34	1.53	-27.55
10 L Sto La mean	0.97	0.84	0.13	1.12	-0.11	0.87	0.12	-0.52	0.72	-6.15
1 D Gi In ave5	0.98	0.48	0.75	1.99	-1.47	0.49	0.75	-6.13	2.48	-72.15
5 D Gi In ave5	0.88	0.43	0.70	1.80	-1.13	0.49	0.66	-4.97	2.23	-58.56
10 D Gi In ave5	0.86	0.45	0.65	1.67	-0.93	0.52	0.61	-4.41	2.10	-51.95
1 L Gi In ave5	0.97	0.44	0.81	2.13	-1.68	0.46	0.80	-6.57	2.56	-77.41
5 L Gi In ave5	0.88	0.40	0.76	1.91	-1.30	0.46	0.72	-5.54	2.35	-65.24
10 L Gi In ave5	0.86	0.42	0.71	1.78	-1.11	0.48	0.67	-5.03	2.24	-59.24
1 D Sto In ave5	0.98	0.47	0.85	2.05	-1.72	0.48	0.84	-7.39	2.72	-86.98
5 D Sto In ave5	0.95	0.46	0.74	1.97	-1.40	0.48	0.73	-5.75	2.40	-67.76
10 D Sto In ave5	0.90	0.43	0.72	1.88	-1.24	0.48	0.69	-5.29	2.30	-62.30
1 L Sto In ave5	0.98	0.44	0.89	2.22	-1.95	0.44	0.89	-7.69	2.77	-90.56
5 L Sto In ave5	0.94	0.42	0.80	2.09	-1.60	0.45	0.78	-6.24	2.50	-73.48
10 L Sto In ave5	0.90	0.40	0.78	1.99	-1.43	0.45	0.75	-5.83	2.41	-68.61
1 D Gi La ave5	0.98	0.76	0.36	1.27	-0.44	0.77	0.35	-3.00	1.73	-35.32
5 D Gi La ave5	0.97	0.91	-0.03	1.03	0.07	0.94	-0.04	1.16	1.07	13.61
10 D Gi La ave5	0.96	0.98	-0.20	0.95	0.24	1.02	-0.22	3.00	1.73	35.38
1 L Gi La ave5	0.98	0.71	0.43	1.34	-0.55	0.73	0.42	-3.55	1.89	-41.86
5 L Gi La ave5	0.97	0.90	0.01	1.04	0.02	0.93	-0.00	0.67	0.82	7.94
10 L Gi La ave5	0.96	0.98	-0.18	0.94	0.21	1.02	-0.20	2.65	1.63	31.26
1 D Sto La ave5	0.97	0.62	0.65	1.51	-0.94	0.64	0.63	-5.83	2.41	-68.62
5 D Sto La ave5	0.98	0.79	0.27	1.22	-0.30	0.80	0.25	-1.90	1.38	-22.42
10 D Sto La ave5	0.97	0.85	0.10	1.11	-0.08	0.88	0.09	-0.15	0.39	-1.80
1 L Sto La ave5	0.97	0.58	0.70	1.63	-1.10	0.59	0.69	-6.22	2.49	-73.24
5 L Sto La ave5	0.97	0.75	0.33	1.27	-0.39	0.77	0.32	-2.48	1.58	-29.25
10 L Sto La ave5	0.97	0.83	0.15	1.14	-0.14	0.85	0.14	-0.70	0.84	-8.28

Table A.16: Calibration statistics for modeled and observed suspended sediment concentration loss in S2Q30D48, shear stress deposition model

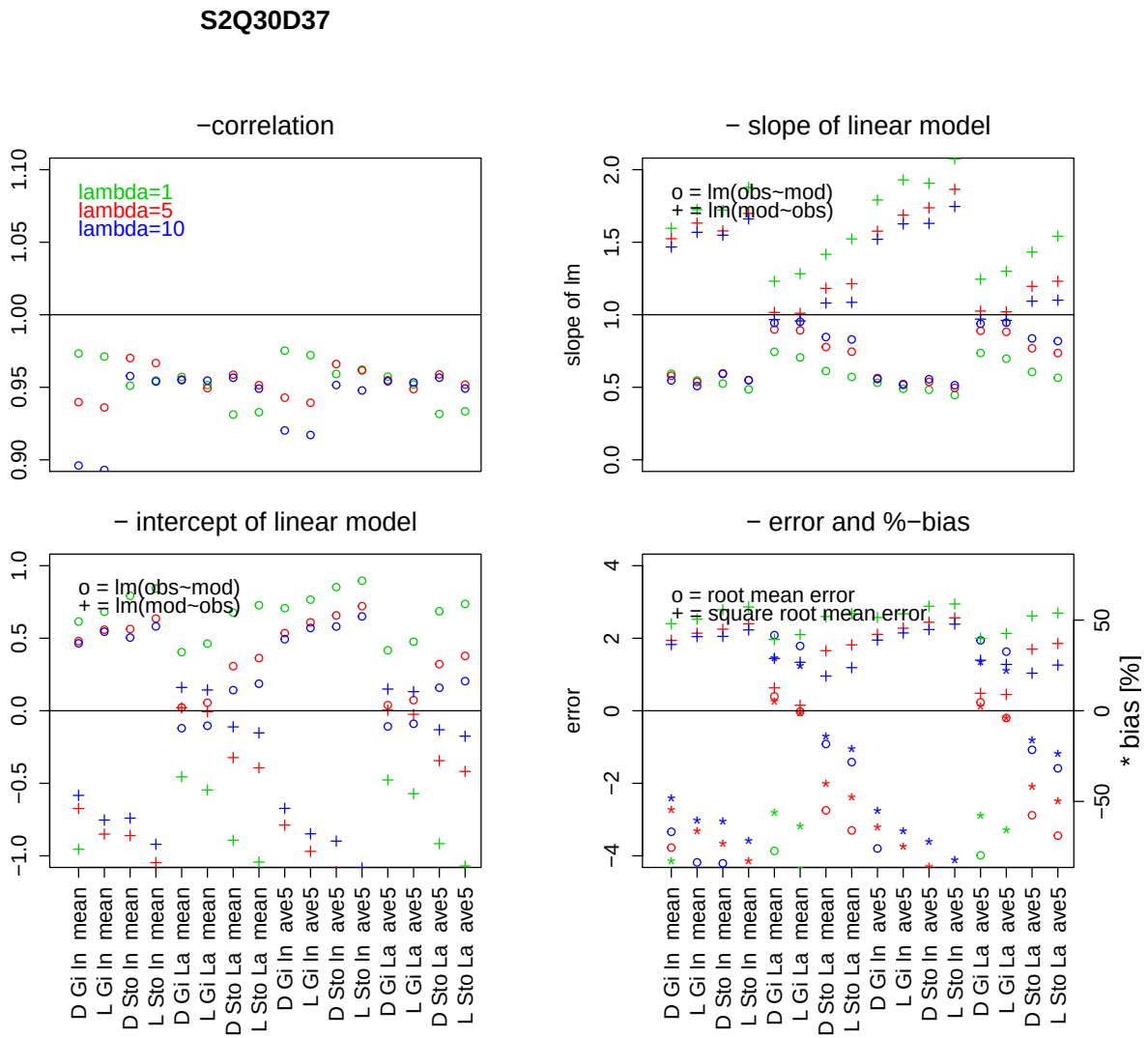

Figure A.15: Graphical representaiton of statisitcal evaluation of modeled and observed suspended sediment concentration loss in S2Q30D37, velocity deposition model

	r^2	LM_{mo}		LM_{om}		RMA		Error		
		a	b	a	b	a	b	MSE	SMSE	PBIAS
1 D Gi In mean	0.97	0.59	0.61	1.60	-0.95	0.61	0.61	-5.76	2.40	-82.12
5 D Gi In mean	0.94	0.58	0.48	1.52	-0.67	0.62	0.46	-3.77	1.94	-53.83
10 D Gi In mean	0.90	0.55	0.47	1.47	-0.58	0.61	0.43	-3.34	1.83	-47.60
1 L Gi In mean	0.97	0.55	0.68	1.72	-1.15	0.56	0.67	-6.37	2.52	-90.88
5 L Gi In mean	0.94	0.54	0.56	1.63	-0.85	0.57	0.54	-4.58	2.14	-65.30
10 L Gi In mean	0.89	0.51	0.54	1.57	-0.75	0.57	0.51	-4.18	2.04	-59.64
1 D Sto In mean	0.95	0.53	0.79	1.72	-1.32	0.55	0.78	-7.77	2.79	-110.85
5 D Sto In mean	0.97	0.60	0.56	1.58	-0.86	0.61	0.55	-5.06	2.25	-72.22
10 D Sto In mean	0.96	0.59	0.50	1.55	-0.74	0.62	0.49	-4.21	2.05	-60.00
1 L Sto In mean	0.95	0.49	0.84	1.88	-1.54	0.51	0.83	-8.18	2.86	-116.71
5 L Sto In mean	0.97	0.55	0.64	1.70	-1.05	0.57	0.63	-5.74	2.40	-81.93
10 L Sto In mean	0.95	0.55	0.58	1.66	-0.92	0.57	0.57	-4.97	2.23	-70.89
1 D Gi La mean	0.96	0.74	0.40	1.23	-0.46	0.78	0.39	-3.87	1.97	-55.13
5 D Gi La mean	0.96	0.90	0.02	1.02	0.02	0.94	0.00	0.40	0.63	5.68
10 D Gi La mean	0.95	0.94	-0.12	0.97	0.16	0.99	-0.14	2.08	1.44	29.73
1 L Gi La mean	0.95	0.71	0.46	1.28	-0.55	0.74	0.44	-4.42	2.10	-62.98
5 L Gi La mean	0.95	0.89	0.06	1.01	-0.01	0.94	0.03	-0.02	0.15	-0.33
10 L Gi La mean	0.95	0.95	-0.10	0.96	0.14	1.00	-0.13	1.79	1.34	25.47
1 D Sto La mean	0.93	0.61	0.68	1.42	-0.89	0.66	0.65	-6.76	2.60	-96.35
5 D Sto La mean	0.96	0.78	0.31	1.18	-0.32	0.81	0.29	-2.75	1.66	-39.16
10 D Sto La mean	0.96	0.85	0.14	1.08	-0.11	0.89	0.12	-0.92	0.96	-13.07
1 L Sto La mean	0.93	0.57	0.73	1.52	-1.04	0.61	0.71	-7.18	2.68	-102.42
5 L Sto La mean	0.95	0.75	0.36	1.21	-0.39	0.78	0.34	-3.30	1.82	-47.09
10 L Sto La mean	0.95	0.83	0.19	1.09	-0.15	0.87	0.16	-1.42	1.19	-20.18
1 D Gi In ave5	0.98	0.53	0.71	1.79	-1.24	0.54	0.70	-6.61	2.57	-94.29
5 D Gi In ave5	0.94	0.56	0.54	1.58	-0.79	0.60	0.52	-4.44	2.11	-63.34
10 D Gi In ave5	0.92	0.56	0.49	1.52	-0.67	0.61	0.47	-3.80	1.95	-54.17
1 L Gi In ave5	0.97	0.49	0.77	1.93	-1.45	0.50	0.76	-7.15	2.67	-101.96
5 L Gi In ave5	0.94	0.52	0.61	1.69	-0.97	0.56	0.59	-5.19	2.28	-73.97
10 L Gi In ave5	0.92	0.52	0.57	1.63	-0.85	0.56	0.55	-4.60	2.15	-65.64
1 D Sto In ave5	0.96	0.48	0.85	1.91	-1.58	0.50	0.84	-8.30	2.88	-118.45
5 D Sto In ave5	0.97	0.54	0.66	1.74	-1.11	0.56	0.65	-5.96	2.44	-84.99
10 D Sto In ave5	0.95	0.56	0.58	1.63	-0.90	0.58	0.57	-5.01	2.24	-71.46
1 L Sto In ave5	0.96	0.45	0.90	2.07	-1.82	0.46	0.89	-8.67	2.94	-123.60
5 L Sto In ave5	0.96	0.50	0.72	1.86	-1.31	0.52	0.71	-6.56	2.56	-93.57
10 L Sto In ave5	0.95	0.51	0.65	1.75	-1.08	0.54	0.64	-5.70	2.39	-81.34
1 D Gi La ave5	0.96	0.74	0.42	1.24	-0.48	0.77	0.40	-3.99	2.00	-56.85
5 D Gi La ave5	0.95	0.89	0.04	1.03	0.00	0.93	0.02	0.23	0.48	3.33
10 D Gi La ave5	0.95	0.94	-0.11	0.97	0.15	0.98	-0.13	1.94	1.39	27.70
1 L Gi La ave5	0.95	0.70	0.48	1.30	-0.57	0.73	0.46	-4.54	2.13	-64.74
5 L Gi La ave5	0.95	0.88	0.07	1.02	-0.02	0.93	0.05	-0.20	0.45	-2.88
10 L Gi La ave5	0.95	0.95	-0.09	0.96	0.13	0.99	-0.11	1.63	1.28	23.25
1 D Sto La ave5	0.93	0.61	0.69	1.43	-0.92	0.65	0.66	-6.84	2.62	-97.55
5 D Sto La ave5	0.96	0.77	0.32	1.20	-0.34	0.80	0.31	-2.88	1.70	-41.09
10 D Sto La ave5	0.96	0.84	0.16	1.09	-0.13	0.87	0.14	-1.08	1.04	-15.34
1 L Sto La ave5	0.93	0.57	0.74	1.54	-1.07	0.61	0.72	-7.26	2.69	-103.57
5 L Sto La ave5	0.95	0.74	0.38	1.23	-0.42	0.77	0.36	-3.44	1.86	-49.11
10 L Sto La ave5	0.95	0.82	0.20	1.10	-0.18	0.86	0.18	-1.59	1.26	-22.63

Table A.17: Calibration statistics for modeled and observed suspended sediment concentration loss in S2Q30D37, shear stress deposition model

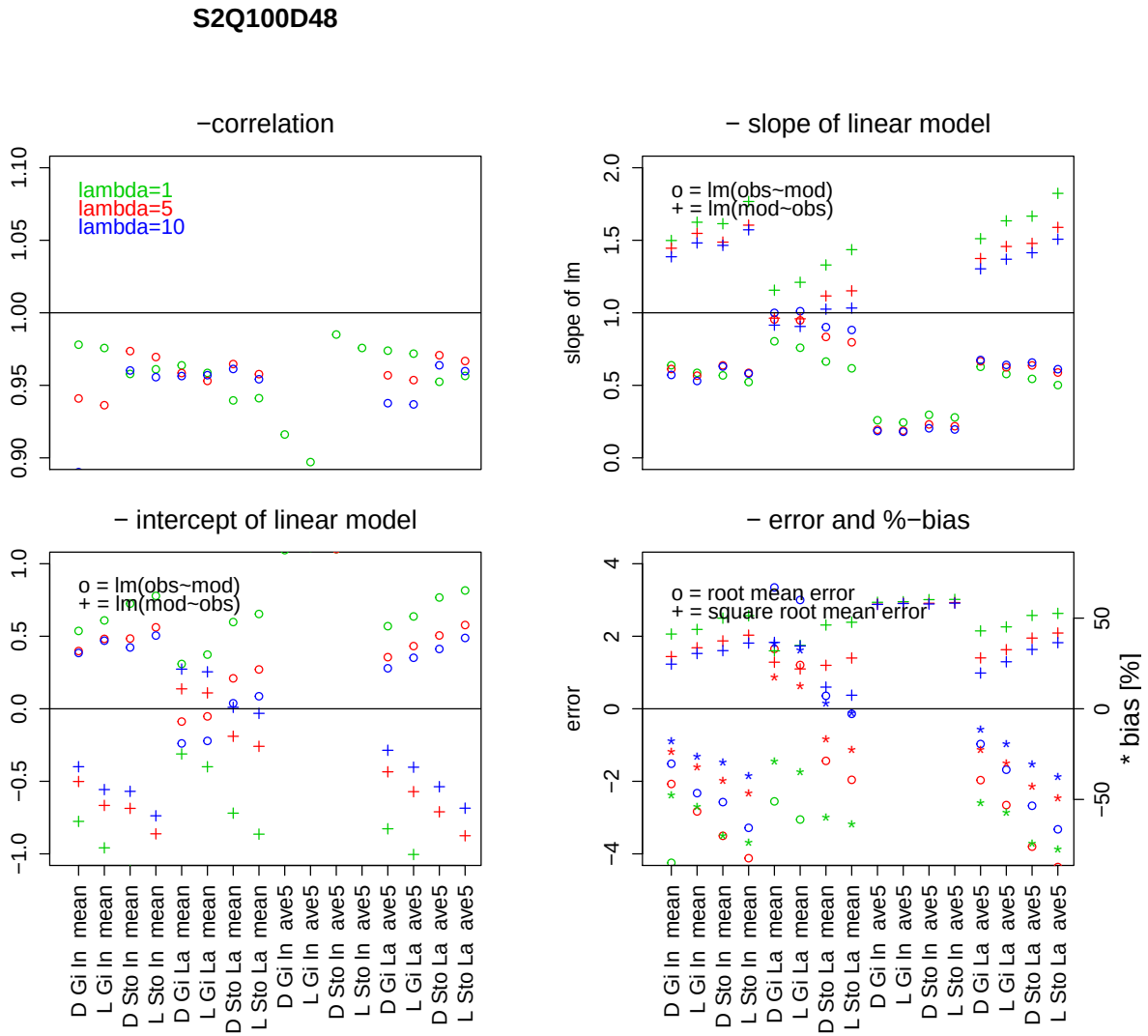

Figure A.16: Graphical representaiton of statisitcal evaluation of modeled and observed suspended sediment concentration loss in S2Q100D48, velocity deposition model

	r^2	LM_{mo}		LM_{om}		RMA		Error		
		a	b	a	b	a	b	MSE	SMSE	PBIAS
1 D Gi In mean	0.98	0.64	0.54	1.50	-0.78	0.65	0.53	-4.25	2.06	-47.02
5 D Gi In mean	0.94	0.61	0.40	1.45	-0.50	0.65	0.37	-2.07	1.44	-22.95
10 D Gi In mean	0.89	0.57	0.38	1.39	-0.40	0.64	0.34	-1.52	1.23	-16.78
1 L Gi In mean	0.98	0.59	0.61	1.62	-0.96	0.60	0.60	-4.79	2.19	-53.03
5 L Gi In mean	0.94	0.57	0.48	1.55	-0.67	0.61	0.46	-2.83	1.68	-31.34
10 L Gi In mean	0.89	0.53	0.47	1.48	-0.56	0.60	0.43	-2.33	1.53	-25.75
1 D Sto In mean	0.96	0.57	0.72	1.61	-1.12	0.59	0.71	-6.25	2.50	-69.16
5 D Sto In mean	0.97	0.64	0.48	1.49	-0.69	0.65	0.47	-3.50	1.87	-38.79
10 D Sto In mean	0.96	0.63	0.42	1.46	-0.57	0.66	0.41	-2.57	1.60	-28.49
1 L Sto In mean	0.96	0.52	0.78	1.77	-1.33	0.54	0.76	-6.58	2.57	-72.89
5 L Sto In mean	0.97	0.59	0.56	1.60	-0.86	0.60	0.55	-4.12	2.03	-45.62
10 L Sto In mean	0.96	0.58	0.50	1.57	-0.74	0.61	0.49	-3.28	1.81	-36.35
1 D Gi La mean	0.96	0.80	0.31	1.16	-0.31	0.83	0.29	-2.55	1.60	-28.27
5 D Gi La mean	0.96	0.95	-0.09	0.96	0.14	1.00	-0.11	1.65	1.28	18.27
10 D Gi La mean	0.96	1.00	-0.24	0.91	0.27	1.05	-0.27	3.35	1.83	37.05
1 L Gi La mean	0.96	0.76	0.37	1.21	-0.40	0.79	0.35	-3.05	1.75	-33.81
5 L Gi La mean	0.95	0.95	-0.05	0.96	0.11	0.99	-0.08	1.21	1.10	13.37
10 L Gi La mean	0.96	1.01	-0.22	0.91	0.25	1.06	-0.25	3.00	1.73	33.21
1 D Sto La mean	0.94	0.66	0.60	1.33	-0.72	0.71	0.57	-5.34	2.31	-59.08
5 D Sto La mean	0.96	0.83	0.21	1.12	-0.19	0.86	0.19	-1.44	1.20	-15.90
10 D Sto La mean	0.96	0.90	0.04	1.03	0.01	0.94	0.01	0.36	0.60	3.96
1 L Sto La mean	0.94	0.62	0.65	1.44	-0.86	0.66	0.63	-5.69	2.39	-63.02
5 L Sto La mean	0.96	0.80	0.27	1.15	-0.26	0.83	0.25	-1.96	1.40	-21.69
10 L Sto La mean	0.95	0.88	0.09	1.03	-0.03	0.92	0.06	-0.14	0.37	-1.55
1 D Gi In ave5	0.92	0.26	1.09	3.24	-3.44	0.28	1.08	-8.62	2.94	-95.45
5 D Gi In ave5	0.71	0.19	1.11	2.63	-2.62	0.27	1.06	-8.31	2.88	-92.06
10 D Gi In ave5	0.68	0.18	1.12	2.50	-2.44	0.27	1.06	-8.29	2.88	-91.73
1 L Gi In ave5	0.90	0.24	1.11	3.30	-3.54	0.27	1.09	-8.71	2.95	-96.49
5 L Gi In ave5	0.71	0.19	1.13	2.68	-2.70	0.26	1.08	-8.45	2.91	-93.59
10 L Gi In ave5	0.68	0.18	1.13	2.56	-2.55	0.27	1.08	-8.43	2.90	-93.32
1 D Sto In ave5	0.99	0.30	1.10	3.27	-3.58	0.30	1.10	-9.06	3.01	-100.30
5 D Sto In ave5	0.84	0.23	1.10	3.06	-3.18	0.27	1.07	-8.47	2.91	-93.73
10 D Sto In ave5	0.75	0.20	1.11	2.77	-2.80	0.27	1.07	-8.35	2.89	-92.45
1 L Sto In ave5	0.98	0.28	1.11	3.41	-3.77	0.29	1.11	-9.10	3.02	-100.70
5 L Sto In ave5	0.82	0.22	1.12	3.09	-3.24	0.27	1.09	-8.58	2.93	-94.99
10 L Sto In ave5	0.74	0.20	1.12	2.81	-2.87	0.26	1.08	-8.48	2.91	-93.92
1 D Gi La ave5	0.97	0.63	0.57	1.51	-0.83	0.64	0.56	-4.61	2.15	-51.05
5 D Gi La ave5	0.96	0.67	0.36	1.37	-0.43	0.70	0.34	-1.97	1.40	-21.79
10 D Gi La ave5	0.94	0.67	0.28	1.30	-0.29	0.72	0.25	-0.97	0.99	-10.76
1 L Gi La ave5	0.97	0.58	0.64	1.63	-1.00	0.59	0.63	-5.10	2.26	-56.47
5 L Gi La ave5	0.95	0.62	0.43	1.46	-0.57	0.65	0.41	-2.66	1.63	-29.40
10 L Gi La ave5	0.94	0.64	0.35	1.37	-0.40	0.68	0.32	-1.68	1.30	-18.60
1 D Sto La ave5	0.95	0.54	0.77	1.67	-1.22	0.57	0.75	-6.63	2.57	-73.35
5 D Sto La ave5	0.97	0.64	0.51	1.48	-0.71	0.66	0.49	-3.80	1.95	-42.09
10 D Sto La ave5	0.96	0.66	0.41	1.41	-0.54	0.68	0.40	-2.67	1.64	-29.61
1 L Sto La ave5	0.96	0.50	0.82	1.82	-1.43	0.52	0.80	-6.92	2.63	-76.58
5 L Sto La ave5	0.97	0.59	0.58	1.59	-0.88	0.61	0.56	-4.36	2.09	-48.31
10 L Sto La ave5	0.96	0.61	0.49	1.51	-0.69	0.64	0.47	-3.32	1.82	-36.80

Table A.18: Calibration statistics for modeled and observed suspended sediment concentration loss in S2Q100D48, shear stress deposition model

Figure A.17: Graphical representaiton of statisitcal evaluation of modeled and observed suspended sediment concentration loss in S2Q100D37, velocity deposition model

./pics_flumoCal/CalStep2v_S2Q100D37_all16.pdf

	r^2	LM_{mo}		LM_{om}		RMA		Error		
		a	b	a	b	a	b	MSE	SMSE	PBIAS
1 D Gi In mean	0.94	0.50	0.60	1.76	-0.98	0.53	0.58	-3.33	1.83	-32.47
5 D Gi In mean	0.81	0.42	0.60	1.56	-0.68	0.52	0.52	-2.38	1.54	-23.23
10 D Gi In mean	0.80	0.43	0.56	1.49	-0.57	0.54	0.48	-1.99	1.41	-19.43
1 L Gi In mean	0.93	0.46	0.66	1.88	-1.14	0.49	0.64	-3.73	1.93	-36.34
5 L Gi In mean	0.80	0.39	0.65	1.65	-0.82	0.49	0.58	-2.88	1.70	-28.10
10 L Gi In mean	0.79	0.40	0.62	1.58	-0.71	0.50	0.54	-2.53	1.59	-24.66
1 D Sto In mean	0.99	0.54	0.65	1.82	-1.16	0.55	0.64	-4.35	2.09	-42.38
5 D Sto In mean	0.89	0.46	0.61	1.72	-0.90	0.52	0.57	-3.01	1.73	-29.29
10 D Sto In mean	0.83	0.43	0.61	1.62	-0.76	0.51	0.54	-2.62	1.62	-25.54
1 L Sto In mean	0.99	0.50	0.70	1.96	-1.35	0.50	0.70	-4.63	2.15	-45.12
5 L Sto In mean	0.88	0.43	0.66	1.83	-1.05	0.48	0.62	-3.44	1.85	-33.51
10 L Sto In mean	0.83	0.40	0.66	1.71	-0.90	0.48	0.60	-3.10	1.76	-30.17
1 D Gi La mean	0.99	0.91	0.07	1.08	-0.06	0.92	0.06	0.01	0.11	0.11
5 D Gi La mean	0.97	1.07	-0.33	0.88	0.33	1.10	-0.35	3.86	1.96	37.60
10 D Gi La mean	0.96	1.11	-0.46	0.83	0.44	1.16	-0.50	5.38	2.32	52.43
1 L Gi La mean	0.99	0.86	0.13	1.13	-0.13	0.87	0.13	-0.48	0.69	-4.69
5 L Gi La mean	0.98	1.08	-0.30	0.88	0.30	1.10	-0.32	3.46	1.86	33.74
10 L Gi La mean	0.97	1.13	-0.46	0.83	0.43	1.17	-0.49	5.08	2.25	49.53
1 D Sto La mean	0.99	0.78	0.35	1.26	-0.42	0.79	0.34	-2.55	1.60	-24.86
5 D Sto La mean	0.98	0.94	-0.03	1.03	0.05	0.95	-0.04	1.02	1.01	9.92
10 D Sto La mean	0.98	1.01	-0.20	0.94	0.22	1.04	-0.22	2.67	1.63	25.99
1 L Sto La mean	0.99	0.72	0.41	1.35	-0.54	0.73	0.41	-2.93	1.71	-28.54
5 L Sto La mean	0.98	0.91	0.03	1.07	-0.01	0.92	0.02	0.52	0.72	5.03
10 L Sto La mean	0.98	1.00	-0.16	0.95	0.18	1.03	-0.18	2.21	1.49	21.53
1 D Gi In ave5	0.82	0.25	0.98	2.65	-2.35	0.31	0.94	-6.04	2.46	-58.81
5 D Gi In ave5	0.66	0.20	1.01	2.20	-1.80	0.30	0.93	-5.83	2.42	-56.84
10 D Gi In ave5	0.64	0.19	1.01	2.12	-1.71	0.30	0.93	-5.81	2.41	-56.66
1 L Gi In ave5	0.80	0.24	1.00	2.70	-2.42	0.30	0.95	-6.14	2.48	-59.80
5 L Gi In ave5	0.66	0.19	1.02	2.25	-1.88	0.29	0.95	-5.96	2.44	-58.11
10 L Gi In ave5	0.64	0.19	1.02	2.18	-1.79	0.29	0.94	-5.95	2.44	-57.96
1 D Sto In ave5	0.93	0.31	0.96	2.86	-2.67	0.33	0.95	-6.36	2.52	-62.00
5 D Sto In ave5	0.75	0.23	0.99	2.49	-2.15	0.30	0.94	-5.93	2.44	-57.79
10 D Sto In ave5	0.69	0.20	1.00	2.29	-1.91	0.30	0.93	-5.86	2.42	-57.06
1 L Sto In ave5	0.92	0.29	0.98	2.95	-2.78	0.31	0.96	-6.42	2.53	-62.55
5 L Sto In ave5	0.74	0.22	1.01	2.52	-2.21	0.29	0.95	-6.05	2.46	-58.90
10 L Sto In ave5	0.68	0.20	1.02	2.33	-1.97	0.29	0.95	-5.98	2.45	-58.30
1 D Gi La ave5	0.99	0.76	0.28	1.28	-0.34	0.77	0.27	-1.48	1.21	-14.38
5 D Gi La ave5	0.96	0.85	0.00	1.08	0.05	0.89	-0.02	1.45	1.20	14.11
10 D Gi La ave5	0.95	0.92	-0.15	0.98	0.21	0.97	-0.18	2.85	1.69	27.78
1 L Gi La ave5	0.99	0.71	0.35	1.37	-0.46	0.72	0.35	-1.98	1.41	-19.25
5 L Gi La ave5	0.96	0.83	0.07	1.13	-0.02	0.86	0.04	0.87	0.93	8.51
10 L Gi La ave5	0.96	0.92	-0.11	1.00	0.17	0.96	-0.14	2.33	1.53	22.74
1 D Sto La ave5	0.99	0.67	0.50	1.47	-0.72	0.67	0.49	-3.55	1.88	-34.61
5 D Sto La ave5	0.98	0.78	0.21	1.23	-0.23	0.80	0.20	-0.66	0.81	-6.43
10 D Sto La ave5	0.97	0.82	0.09	1.15	-0.06	0.84	0.08	0.56	0.75	5.48
1 L Sto La ave5	0.99	0.61	0.56	1.60	-0.88	0.62	0.56	-3.88	1.97	-37.84
5 L Sto La ave5	0.98	0.73	0.28	1.31	-0.34	0.75	0.27	-1.21	1.10	-11.78
10 L Sto La ave5	0.97	0.78	0.16	1.21	-0.15	0.80	0.15	-0.02	0.15	-0.22

Table A.19: Calibration statistics for modeled and observed concentration loss in S2Q100D37, velocity route

A.1.4 Step 3, velocity deposition model, silty experimetnal runs

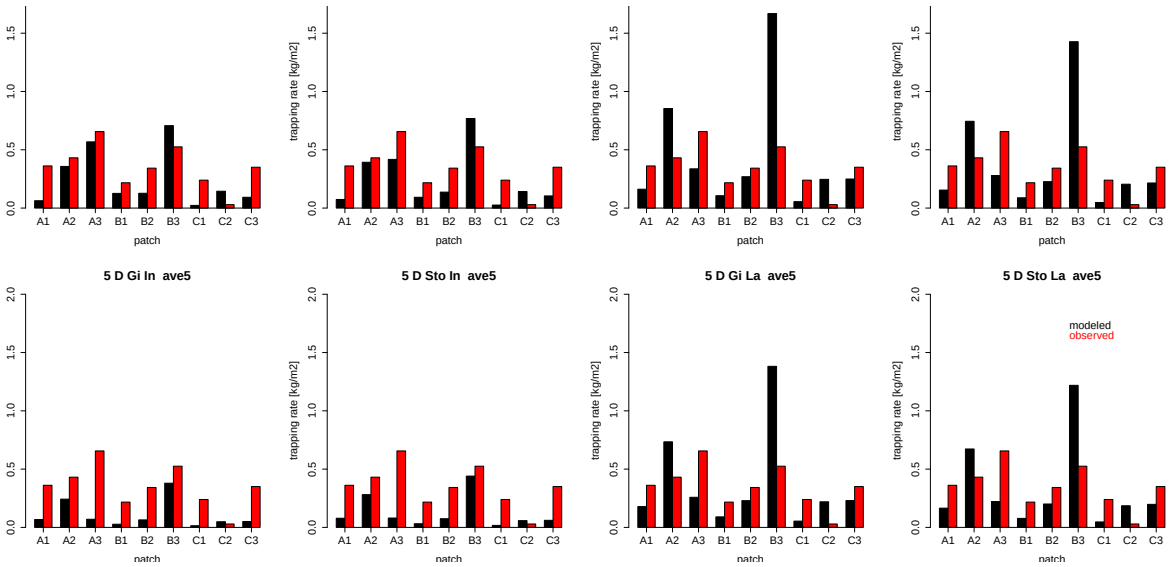

Figure A.18: Modelled and observed interstitial deposition in S1Q50, velocity deposition model for eight selected value set combinations

	TR		r^2	LM_{mo}		LM_{om}		RMA		Error		
	obs	mod		a	b	a	b	a	b	MSE	SMSE	PBIAS
1 D Gi In mean	0.35	0.24	0.61	0.84	-0.05	0.45	0.24	1.37	-0.24	0.99	0.99	31.36
5 D Gi In mean	0.35	0.25	0.74	0.99	-0.10	0.55	0.22	1.34	-0.22	0.94	0.97	29.96
10 D Gi In mean	0.35	0.25	0.75	1.03	-0.11	0.55	0.21	1.37	-0.23	0.87	0.93	27.73
1 L Gi In mean	0.35	0.23	0.61	0.79	-0.05	0.48	0.24	1.29	-0.22	1.12	1.06	35.46
5 L Gi In mean	0.35	0.22	0.74	0.90	-0.09	0.60	0.22	1.22	-0.20	1.14	1.07	36.10
10 L Gi In mean	0.35	0.23	0.76	0.95	-0.10	0.60	0.21	1.25	-0.21	1.07	1.04	34.03
1 D Sto In mean	0.35	0.22	0.54	0.72	-0.03	0.41	0.26	1.33	-0.25	1.19	1.09	37.78
5 D Sto In mean	0.35	0.24	0.66	0.88	-0.07	0.50	0.23	1.33	-0.23	1.00	1.00	31.67
10 D Sto In mean	0.35	0.24	0.72	0.93	-0.09	0.55	0.22	1.30	-0.22	1.02	1.01	32.48
1 L Sto In mean	0.35	0.21	0.54	0.68	-0.03	0.43	0.26	1.25	-0.23	1.30	1.14	41.25
5 L Sto In mean	0.35	0.22	0.66	0.80	-0.06	0.55	0.23	1.20	-0.20	1.21	1.10	38.34
10 L Sto In mean	0.35	0.22	0.72	0.85	-0.08	0.61	0.22	1.18	-0.20	1.21	1.10	38.39
1 D Gi La mean	0.35	0.36	0.48	1.12	-0.03	0.21	0.28	2.34	-0.46	-0.09	0.31	-3.00
5 D Gi La mean	0.35	0.44	0.49	1.38	-0.04	0.17	0.28	2.84	-0.56	-0.79	0.89	-25.17
10 D Gi La mean	0.35	0.47	0.49	1.48	-0.05	0.16	0.27	3.01	-0.58	-1.09	1.05	-34.73
1 L Gi La mean	0.35	0.35	0.48	1.09	-0.03	0.21	0.28	2.25	-0.44	0.04	0.20	1.21
5 L Gi La mean	0.35	0.43	0.49	1.36	-0.05	0.17	0.28	2.80	-0.55	-0.71	0.84	-22.61
10 L Gi La mean	0.35	0.47	0.49	1.47	-0.05	0.16	0.27	2.99	-0.58	-1.04	1.02	-33.15
1 D Sto La mean	0.35	0.29	0.48	0.92	-0.03	0.25	0.28	1.91	-0.38	0.52	0.72	16.48
5 D Sto La mean	0.35	0.38	0.49	1.18	-0.04	0.20	0.28	2.44	-0.48	-0.24	0.49	-7.47
10 D Sto La mean	0.35	0.41	0.49	1.28	-0.04	0.18	0.28	2.63	-0.52	-0.49	0.70	-15.63
1 L Sto La mean	0.35	0.28	0.48	0.88	-0.03	0.27	0.28	1.81	-0.36	0.66	0.81	20.86
5 L Sto La mean	0.35	0.36	0.49	1.13	-0.04	0.21	0.28	2.31	-0.46	-0.05	0.21	-1.44
10 L Sto La mean	0.35	0.39	0.49	1.25	-0.05	0.19	0.28	2.57	-0.51	-0.38	0.62	-12.06
1 D Gi In ave5	0.35	0.13	0.48	0.40	-0.00	0.57	0.27	0.83	-0.16	1.94	1.39	61.66
5 D Gi In ave5	0.35	0.11	0.49	0.33	-0.01	0.73	0.27	0.67	-0.13	2.19	1.48	69.40
10 D Gi In ave5	0.35	0.11	0.51	0.35	-0.02	0.74	0.27	0.69	-0.13	2.18	1.48	69.10
1 L Gi In ave5	0.35	0.13	0.48	0.39	-0.01	0.59	0.27	0.82	-0.15	1.97	1.40	62.60
5 L Gi In ave5	0.35	0.10	0.49	0.31	-0.01	0.79	0.27	0.63	-0.12	2.26	1.50	71.57
10 L Gi In ave5	0.35	0.10	0.52	0.33	-0.02	0.80	0.27	0.64	-0.13	2.25	1.50	71.27
1 D Sto In ave5	0.35	0.13	0.47	0.39	-0.00	0.57	0.27	0.83	-0.16	1.95	1.39	61.70
5 D Sto In ave5	0.35	0.12	0.49	0.38	-0.01	0.63	0.27	0.78	-0.15	2.03	1.42	64.40
10 D Sto In ave5	0.35	0.11	0.49	0.32	-0.01	0.73	0.27	0.67	-0.13	2.19	1.48	69.45
1 L Sto In ave5	0.35	0.13	0.48	0.39	-0.01	0.59	0.27	0.81	-0.15	1.97	1.40	62.62
5 L Sto In ave5	0.35	0.11	0.49	0.34	-0.01	0.69	0.27	0.71	-0.13	2.13	1.46	67.69
10 L Sto In ave5	0.35	0.10	0.49	0.30	-0.01	0.79	0.27	0.62	-0.12	2.26	1.50	71.61
1 D Gi La ave5	0.35	0.32	0.47	0.96	-0.01	0.23	0.28	2.04	-0.39	0.25	0.50	7.89
5 D Gi La ave5	0.35	0.38	0.47	1.11	-0.01	0.20	0.27	2.34	-0.44	-0.22	0.47	-7.10
10 D Gi La ave5	0.35	0.42	0.48	1.25	-0.02	0.18	0.27	2.62	-0.50	-0.65	0.81	-20.59
1 L Gi La ave5	0.35	0.31	0.47	0.91	-0.01	0.24	0.28	1.93	-0.37	0.40	0.63	12.79
5 L Gi La ave5	0.35	0.36	0.47	1.06	-0.01	0.21	0.27	2.25	-0.43	-0.08	0.29	-2.63
10 L Gi La ave5	0.35	0.41	0.48	1.22	-0.02	0.19	0.27	2.56	-0.48	-0.55	0.74	-17.53
1 D Sto La ave5	0.35	0.27	0.47	0.81	-0.02	0.28	0.28	1.71	-0.33	0.75	0.87	23.92
5 D Sto La ave5	0.35	0.33	0.47	0.99	-0.01	0.23	0.27	2.08	-0.40	0.17	0.41	5.24
10 D Sto La ave5	0.35	0.35	0.47	1.02	-0.01	0.22	0.27	2.16	-0.41	0.03	0.18	1.08
1 L Sto La ave5	0.35	0.25	0.48	0.77	-0.02	0.30	0.28	1.61	-0.31	0.89	0.94	28.23
5 L Sto La ave5	0.35	0.31	0.47	0.92	-0.01	0.25	0.27	1.93	-0.37	0.39	0.62	12.38
10 L Sto La ave5	0.35	0.33	0.47	0.97	-0.01	0.23	0.27	2.05	-0.39	0.20	0.45	6.38

Table A.20: Calibration statistics for modelled and observed interstitial deposition in S1Q50, velocity deposition model

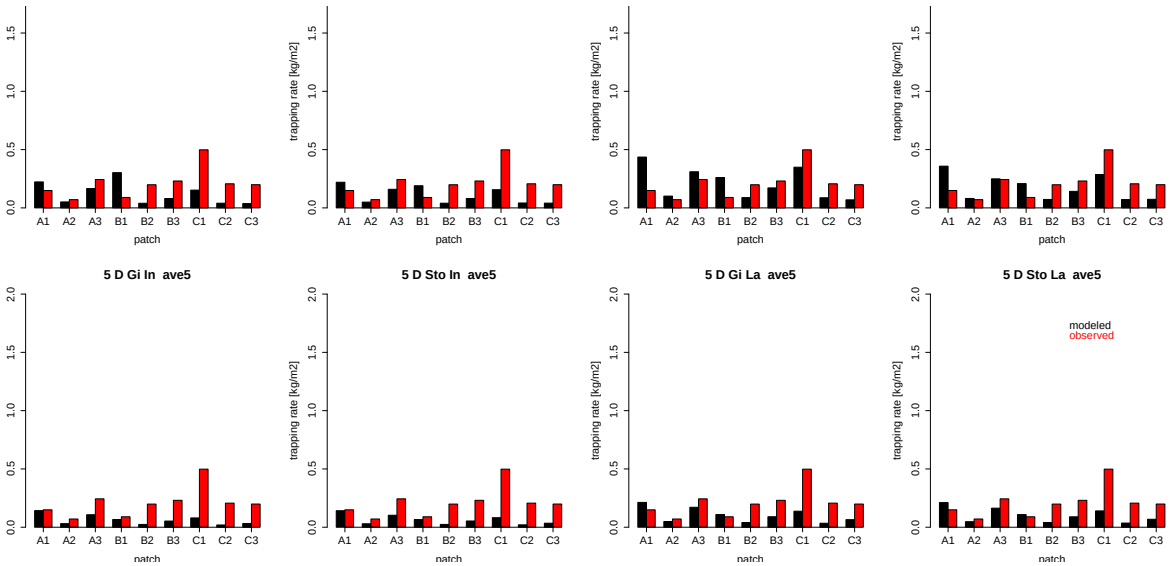

Figure A.19: Modelled and observed interstitial deposition in S1Q80, velocity deposition model for eight selected value set combinations

	TR		r^2	LM_{mo}		LM_{om}		RMA		Error		
	obs	mod		a	b	a	b	a	b	MSE	SMSE	PBIAS
1 D Gi In mean	0.21	0.11	0.22	0.11	0.08	0.42	0.16	0.52	-0.00	0.93	0.96	49.06
5 D Gi In mean	0.21	0.12	0.07	-0.05	0.13	-0.09	0.22	0.77	-0.04	0.79	0.89	42.13
10 D Gi In mean	0.21	0.13	0.19	-0.19	0.17	-0.18	0.23	1.02	-0.08	0.72	0.85	38.35
1 L Gi In mean	0.21	0.10	0.22	0.11	0.08	0.46	0.16	0.48	-0.00	0.98	0.99	52.15
5 L Gi In mean	0.21	0.11	0.08	-0.06	0.13	-0.11	0.22	0.72	-0.04	0.87	0.93	46.00
10 L Gi In mean	0.21	0.12	0.19	-0.18	0.15	-0.20	0.23	0.93	-0.08	0.84	0.91	44.29
1 D Sto In mean	0.21	0.10	0.29	0.14	0.07	0.61	0.15	0.47	-0.00	1.01	1.01	53.66
5 D Sto In mean	0.21	0.11	0.11	0.07	0.09	0.20	0.19	0.58	-0.01	0.91	0.95	48.11
10 D Sto In mean	0.21	0.11	0.02	0.01	0.11	0.03	0.21	0.64	-0.02	0.89	0.94	47.29
1 L Sto In mean	0.21	0.09	0.28	0.13	0.07	0.64	0.15	0.44	-0.00	1.06	1.03	56.28
5 L Sto In mean	0.21	0.10	0.08	0.05	0.09	0.15	0.19	0.57	-0.02	0.97	0.99	51.54
10 L Sto In mean	0.21	0.10	0.02	0.01	0.10	0.03	0.21	0.58	-0.02	0.99	0.99	52.46
1 D Gi La mean	0.21	0.16	0.38	0.29	0.10	0.49	0.13	0.77	-0.00	0.44	0.67	23.50
5 D Gi La mean	0.21	0.21	0.31	0.34	0.14	0.28	0.15	1.09	-0.02	0.01	0.12	0.71
10 D Gi La mean	0.21	0.22	0.29	0.34	0.15	0.24	0.16	1.18	-0.03	-0.10	0.32	-5.54
1 L Gi La mean	0.21	0.15	0.37	0.27	0.10	0.50	0.13	0.74	-0.00	0.51	0.71	26.98
5 L Gi La mean	0.21	0.20	0.29	0.32	0.14	0.26	0.16	1.10	-0.03	0.05	0.21	2.41
10 L Gi La mean	0.21	0.22	0.29	0.34	0.15	0.25	0.16	1.16	-0.03	-0.06	0.25	-3.23
1 D Sto La mean	0.21	0.13	0.39	0.23	0.08	0.64	0.13	0.60	0.00	0.74	0.86	39.06
5 D Sto La mean	0.21	0.17	0.32	0.28	0.11	0.37	0.15	0.88	-0.01	0.34	0.59	18.23
10 D Sto La mean	0.21	0.19	0.33	0.32	0.12	0.34	0.15	0.97	-0.02	0.19	0.44	10.25
1 L Sto La mean	0.21	0.12	0.38	0.22	0.08	0.66	0.13	0.57	0.00	0.80	0.89	42.37
5 L Sto La mean	0.21	0.16	0.29	0.25	0.11	0.33	0.16	0.88	-0.02	0.41	0.64	21.65
10 L Sto La mean	0.21	0.18	0.33	0.31	0.12	0.35	0.15	0.94	-0.02	0.27	0.52	14.30
1 D Gi In ave5	0.21	0.06	0.30	0.08	0.04	1.04	0.14	0.28	0.00	1.33	1.15	70.28
5 D Gi In ave5	0.21	0.06	0.15	0.05	0.05	0.45	0.18	0.34	-0.01	1.33	1.15	70.65
10 D Gi In ave5	0.21	0.06	0.10	0.03	0.05	0.29	0.19	0.34	-0.02	1.38	1.17	72.99
1 L Gi In ave5	0.21	0.06	0.30	0.08	0.04	1.09	0.14	0.27	0.00	1.34	1.16	71.11
5 L Gi In ave5	0.21	0.06	0.12	0.04	0.05	0.34	0.19	0.35	-0.01	1.35	1.16	71.60
10 L Gi In ave5	0.21	0.05	0.10	0.03	0.04	0.34	0.19	0.31	-0.01	1.42	1.19	75.50
1 D Sto In ave5	0.21	0.06	0.30	0.08	0.04	1.08	0.14	0.28	0.00	1.33	1.16	70.72
5 D Sto In ave5	0.21	0.06	0.17	0.06	0.05	0.52	0.18	0.33	-0.01	1.33	1.15	70.64
10 D Sto In ave5	0.21	0.06	0.19	0.06	0.05	0.62	0.17	0.30	-0.01	1.37	1.17	72.71
1 L Sto In ave5	0.21	0.06	0.30	0.08	0.04	1.10	0.14	0.27	0.00	1.35	1.16	71.48
5 L Sto In ave5	0.21	0.06	0.12	0.04	0.05	0.34	0.19	0.35	-0.01	1.35	1.16	71.68
10 L Sto In ave5	0.21	0.05	0.20	0.05	0.04	0.73	0.17	0.27	-0.00	1.42	1.19	75.25
1 D Gi La ave5	0.21	0.10	0.32	0.14	0.07	0.72	0.14	0.44	0.01	0.99	0.99	52.31
5 D Gi La ave5	0.21	0.10	0.22	0.11	0.08	0.43	0.17	0.50	-0.00	0.98	0.99	51.82
10 D Gi La ave5	0.21	0.10	0.18	0.09	0.08	0.35	0.18	0.51	-0.01	1.02	1.01	54.17
1 L Gi La ave5	0.21	0.09	0.32	0.13	0.07	0.76	0.14	0.42	0.01	1.04	1.02	55.08
5 L Gi La ave5	0.21	0.09	0.19	0.09	0.08	0.38	0.17	0.49	-0.01	1.03	1.02	54.81
10 L Gi La ave5	0.21	0.09	0.18	0.08	0.07	0.40	0.18	0.46	-0.01	1.11	1.05	58.71
1 D Sto La ave5	0.21	0.09	0.32	0.13	0.06	0.80	0.14	0.41	0.00	1.07	1.04	56.95
5 D Sto La ave5	0.21	0.10	0.24	0.12	0.08	0.48	0.16	0.49	-0.00	0.98	0.99	52.05
10 D Sto La ave5	0.21	0.10	0.25	0.12	0.07	0.53	0.16	0.47	-0.00	1.02	1.01	53.88
1 L Sto La ave5	0.21	0.09	0.32	0.12	0.06	0.83	0.14	0.39	0.00	1.12	1.06	59.22
5 L Sto La ave5	0.21	0.09	0.19	0.09	0.07	0.39	0.17	0.49	-0.01	1.04	1.02	55.11
10 L Sto La ave5	0.21	0.09	0.25	0.10	0.07	0.60	0.16	0.42	-0.00	1.10	1.05	58.45

Table A.21: Calibration statistics for modelled and observed interstitial deposition in S1Q80, velocity deposition model

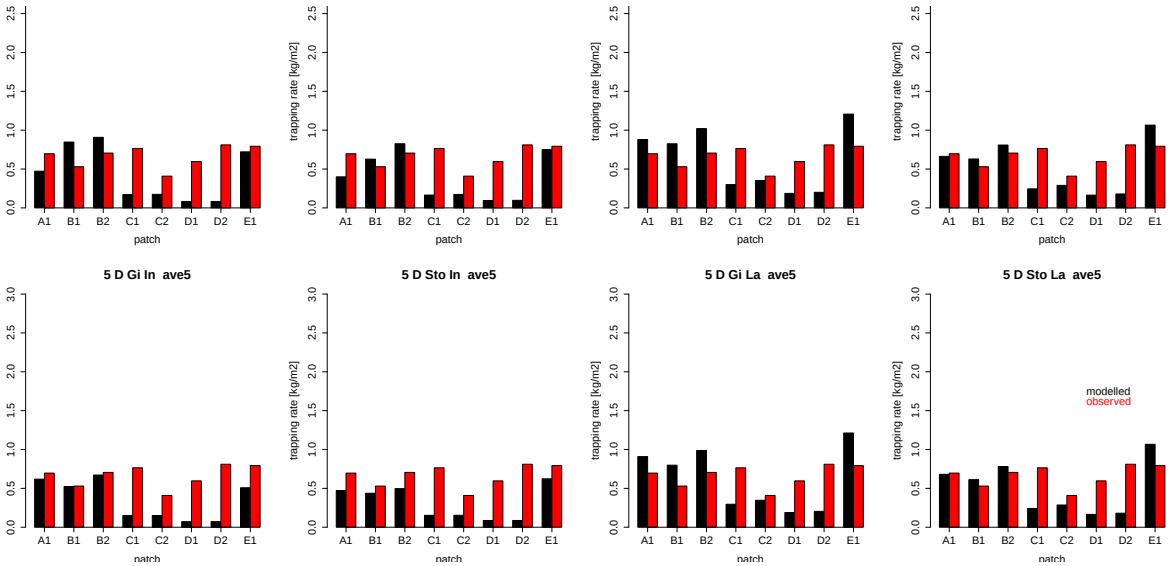

Figure A.20: Modelled and observed interstitial deposition in S2Q30D48-1, velocity deposition model for eight selected value set combinations

	TR		r^2	LM_{mo}		LM_{om}		RMA		Error		
	obs	mod		a	b	a	b	a	b	MSE	SMSE	PBIAS
1 D Gi In mean	0.66	0.41	0.16	0.35	0.18	0.07	0.63	2.19	-1.04	1.99	1.41	37.55
5 D Gi In mean	0.66	0.43	0.04	0.10	0.36	0.02	0.66	2.49	-1.22	1.84	1.36	34.77
10 D Gi In mean	0.66	0.39	0.00	0.00	0.38	0.00	0.66	2.36	-1.18	2.21	1.49	41.73
1 L Gi In mean	0.66	0.39	0.15	0.30	0.19	0.07	0.63	2.04	-0.96	2.20	1.48	41.46
5 L Gi In mean	0.66	0.39	0.04	0.08	0.34	0.02	0.66	2.28	-1.12	2.15	1.47	40.48
10 L Gi In mean	0.66	0.34	0.00	0.00	0.34	0.00	0.66	2.10	-1.05	2.57	1.60	48.53
1 D Sto In mean	0.66	0.33	0.22	0.37	0.09	0.13	0.62	1.68	-0.78	2.65	1.63	50.01
5 D Sto In mean	0.66	0.39	0.14	0.31	0.19	0.07	0.64	2.16	-1.04	2.17	1.47	40.94
10 D Sto In mean	0.66	0.42	0.08	0.18	0.30	0.03	0.65	2.37	-1.15	1.95	1.40	36.74
1 L Sto In mean	0.66	0.30	0.22	0.33	0.08	0.15	0.62	1.51	-0.70	2.91	1.71	54.87
5 L Sto In mean	0.66	0.36	0.14	0.27	0.18	0.07	0.64	1.96	-0.94	2.45	1.56	46.16
10 L Sto In mean	0.66	0.38	0.07	0.15	0.28	0.03	0.65	2.17	-1.06	2.24	1.50	42.29
1 D Gi La mean	0.66	0.51	0.23	0.55	0.15	0.10	0.61	2.38	-1.07	1.23	1.11	23.24
5 D Gi La mean	0.66	0.62	0.19	0.56	0.25	0.07	0.62	2.88	-1.29	0.33	0.58	6.28
10 D Gi La mean	0.66	0.63	0.19	0.56	0.26	0.06	0.62	2.94	-1.32	0.27	0.52	5.18
1 L Gi La mean	0.66	0.49	0.22	0.50	0.16	0.10	0.62	2.26	-1.01	1.42	1.19	26.74
5 L Gi La mean	0.66	0.60	0.19	0.54	0.24	0.07	0.62	2.79	-1.25	0.48	0.69	9.09
10 L Gi La mean	0.66	0.61	0.20	0.57	0.23	0.07	0.62	2.86	-1.29	0.42	0.65	7.94
1 D Sto La mean	0.66	0.38	0.26	0.47	0.08	0.14	0.61	1.82	-0.82	2.23	1.49	42.07
5 D Sto La mean	0.66	0.51	0.23	0.56	0.14	0.10	0.61	2.37	-1.07	1.26	1.12	23.76
10 D Sto La mean	0.66	0.57	0.21	0.55	0.21	0.08	0.62	2.66	-1.19	0.72	0.85	13.62
1 L Sto La mean	0.66	0.35	0.26	0.43	0.07	0.16	0.61	1.66	-0.75	2.50	1.58	47.08
5 L Sto La mean	0.66	0.48	0.23	0.52	0.13	0.10	0.61	2.23	-1.00	1.49	1.22	28.10
10 L Sto La mean	0.66	0.55	0.20	0.52	0.21	0.08	0.62	2.54	-1.14	0.91	0.95	17.19
1 D Gi In ave5	0.66	0.35	0.20	0.34	0.12	0.12	0.62	1.69	-0.77	2.51	1.58	47.34
5 D Gi In ave5	0.66	0.35	0.11	0.20	0.21	0.06	0.64	1.83	-0.87	2.54	1.59	47.87
10 D Gi In ave5	0.66	0.32	0.08	0.15	0.22	0.04	0.65	1.91	-0.94	2.72	1.65	51.21
1 L Gi In ave5	0.66	0.33	0.18	0.29	0.13	0.12	0.62	1.59	-0.72	2.67	1.64	50.42
5 L Gi In ave5	0.66	0.32	0.10	0.17	0.20	0.06	0.64	1.69	-0.80	2.78	1.67	52.46
10 L Gi In ave5	0.66	0.28	0.08	0.14	0.19	0.05	0.65	1.68	-0.83	3.03	1.74	57.20
1 D Sto In ave5	0.66	0.30	0.25	0.36	0.06	0.17	0.61	1.45	-0.66	2.91	1.71	54.94
5 D Sto In ave5	0.66	0.31	0.20	0.31	0.11	0.13	0.62	1.53	-0.70	2.79	1.67	52.68
10 D Sto In ave5	0.66	0.33	0.14	0.23	0.18	0.08	0.64	1.66	-0.77	2.67	1.63	50.31
1 L Sto In ave5	0.66	0.27	0.25	0.33	0.05	0.19	0.61	1.30	-0.59	3.15	1.77	59.36
5 L Sto In ave5	0.66	0.29	0.20	0.27	0.11	0.14	0.62	1.39	-0.63	3.02	1.74	56.90
10 L Sto In ave5	0.66	0.30	0.13	0.19	0.17	0.08	0.64	1.53	-0.71	2.90	1.70	54.69
1 D Gi La ave5	0.66	0.51	0.24	0.56	0.13	0.10	0.61	2.36	-1.06	1.26	1.12	23.77
5 D Gi La ave5	0.66	0.62	0.21	0.59	0.22	0.07	0.62	2.86	-1.28	0.36	0.60	6.82
10 D Gi La ave5	0.66	0.63	0.21	0.61	0.23	0.07	0.62	2.94	-1.32	0.28	0.53	5.33
1 L Gi La ave5	0.66	0.48	0.23	0.51	0.14	0.10	0.61	2.24	-1.00	1.45	1.20	27.32
5 L Gi La ave5	0.66	0.60	0.21	0.58	0.22	0.08	0.62	2.77	-1.24	0.52	0.72	9.74
10 L Gi La ave5	0.66	0.61	0.22	0.62	0.20	0.08	0.62	2.86	-1.29	0.43	0.66	8.16
1 D Sto La ave5	0.66	0.38	0.26	0.47	0.07	0.15	0.61	1.80	-0.81	2.25	1.50	42.51
5 D Sto La ave5	0.66	0.50	0.25	0.58	0.12	0.10	0.61	2.36	-1.06	1.29	1.14	24.32
10 D Sto La ave5	0.66	0.57	0.22	0.57	0.19	0.08	0.62	2.64	-1.18	0.75	0.87	14.22
1 L Sto La ave5	0.66	0.35	0.26	0.43	0.06	0.16	0.61	1.65	-0.74	2.52	1.59	47.51
5 L Sto La ave5	0.66	0.47	0.24	0.54	0.11	0.11	0.61	2.21	-0.99	1.52	1.23	28.74
10 L Sto La ave5	0.66	0.54	0.22	0.54	0.18	0.09	0.62	2.52	-1.13	0.95	0.97	17.91

Table A.22: Calibration statistics for modelled and observed interstitial deposition in S2Q30D48-1, velocity deposition model

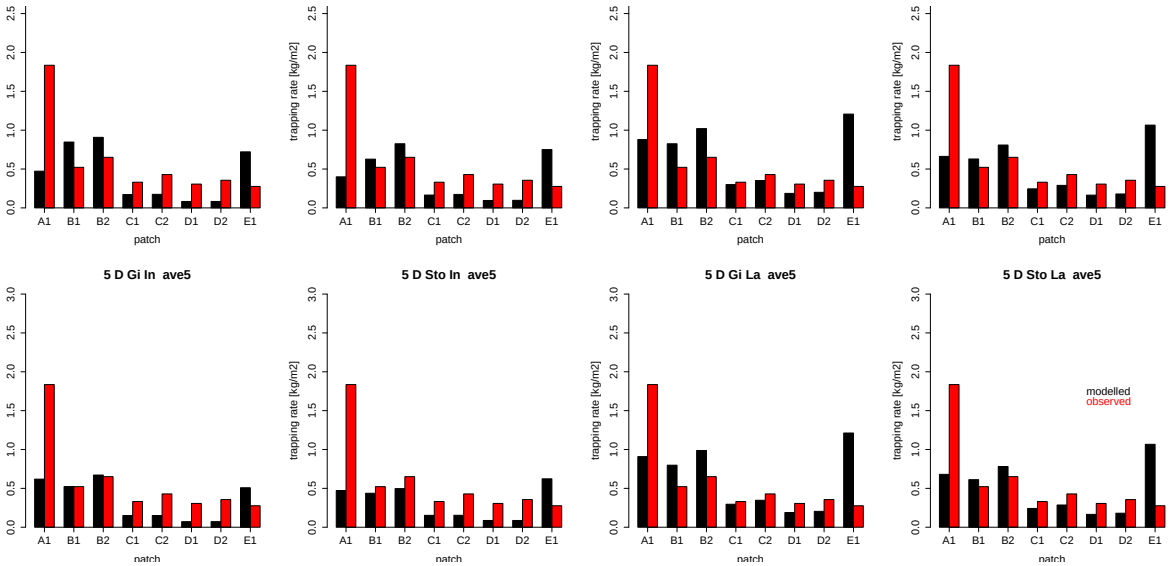

Figure A.21: Modelled and observed interstitial deposition in S2Q30D48-2, velocity deposition model for eight selected value set combinations

	TR		r^2	LM_{mo}		LM_{om}		RMA		Error		
	obs	mod		a	b	a	b	a	b	MSE	SMSE	PBIAS
1 D Gi In mean	0.59	0.41	0.19	0.12	0.35	0.33	0.45	0.59	0.07	1.39	1.18	29.59
5 D Gi In mean	0.59	0.43	0.20	0.13	0.35	0.29	0.46	0.68	0.03	1.24	1.12	26.46
10 D Gi In mean	0.59	0.39	0.16	0.10	0.33	0.25	0.49	0.64	0.01	1.61	1.27	34.31
1 L Gi In mean	0.59	0.39	0.23	0.13	0.31	0.42	0.43	0.55	0.06	1.60	1.26	34.01
5 L Gi In mean	0.59	0.39	0.21	0.13	0.32	0.34	0.45	0.62	0.03	1.55	1.24	32.90
10 L Gi In mean	0.59	0.34	0.15	0.08	0.29	0.26	0.50	0.57	0.01	1.98	1.41	41.98
1 D Sto In mean	0.59	0.33	0.17	0.08	0.28	0.38	0.46	0.45	0.06	2.05	1.43	43.64
5 D Sto In mean	0.59	0.39	0.14	0.08	0.34	0.24	0.49	0.58	0.05	1.57	1.25	33.42
10 D Sto In mean	0.59	0.42	0.19	0.12	0.35	0.29	0.47	0.64	0.04	1.35	1.16	28.69
1 L Sto In mean	0.59	0.30	0.17	0.07	0.26	0.42	0.46	0.41	0.06	2.31	1.52	49.12
5 L Sto In mean	0.59	0.36	0.15	0.08	0.31	0.28	0.49	0.53	0.04	1.85	1.36	39.31
10 L Sto In mean	0.59	0.38	0.20	0.12	0.31	0.35	0.46	0.59	0.04	1.64	1.28	34.95
1 D Gi La mean	0.59	0.51	0.28	0.18	0.40	0.43	0.37	0.65	0.13	0.63	0.80	13.47
5 D Gi La mean	0.59	0.62	0.34	0.26	0.47	0.43	0.32	0.78	0.16	-0.27	0.52	-5.65
10 D Gi La mean	0.59	0.63	0.33	0.26	0.47	0.41	0.33	0.80	0.16	-0.32	0.57	-6.89
1 L Gi La mean	0.59	0.49	0.30	0.19	0.38	0.50	0.35	0.61	0.13	0.82	0.90	17.41
5 L Gi La mean	0.59	0.60	0.34	0.26	0.45	0.45	0.32	0.76	0.16	-0.12	0.34	-2.48
10 L Gi La mean	0.59	0.61	0.31	0.24	0.47	0.40	0.34	0.78	0.15	-0.18	0.42	-3.79
1 D Sto La mean	0.59	0.38	0.22	0.11	0.32	0.45	0.42	0.49	0.09	1.63	1.28	34.70
5 D Sto La mean	0.59	0.51	0.25	0.16	0.41	0.39	0.39	0.64	0.13	0.66	0.81	14.05
10 D Sto La mean	0.59	0.57	0.32	0.23	0.44	0.44	0.33	0.72	0.15	0.12	0.35	2.62
1 L Sto La mean	0.59	0.35	0.22	0.10	0.29	0.48	0.42	0.45	0.09	1.90	1.38	40.34
5 L Sto La mean	0.59	0.48	0.26	0.16	0.39	0.42	0.39	0.61	0.12	0.89	0.94	18.94
10 L Sto La mean	0.59	0.55	0.33	0.23	0.42	0.47	0.33	0.69	0.14	0.31	0.56	6.64
1 D Gi In ave5	0.59	0.35	0.37	0.17	0.25	0.81	0.31	0.46	0.08	1.91	1.38	40.64
5 D Gi In ave5	0.59	0.35	0.56	0.28	0.18	1.12	0.20	0.50	0.05	1.94	1.39	41.24
10 D Gi In ave5	0.59	0.32	0.60	0.31	0.14	1.16	0.21	0.52	0.02	2.12	1.46	45.00
1 L Gi In ave5	0.59	0.33	0.41	0.18	0.22	0.95	0.27	0.43	0.08	2.08	1.44	44.10
5 L Gi In ave5	0.59	0.32	0.57	0.26	0.16	1.25	0.19	0.46	0.05	2.18	1.48	46.40
10 L Gi In ave5	0.59	0.28	0.60	0.27	0.12	1.31	0.22	0.46	0.02	2.43	1.56	51.75
1 D Sto In ave5	0.59	0.30	0.26	0.10	0.24	0.68	0.39	0.39	0.07	2.31	1.52	49.20
5 D Sto In ave5	0.59	0.31	0.37	0.15	0.22	0.89	0.31	0.41	0.07	2.20	1.48	46.66
10 D Sto In ave5	0.59	0.33	0.51	0.23	0.20	1.12	0.22	0.45	0.06	2.07	1.44	43.98
1 L Sto In ave5	0.59	0.27	0.26	0.09	0.21	0.75	0.39	0.35	0.06	2.55	1.60	54.19
5 L Sto In ave5	0.59	0.29	0.38	0.14	0.20	1.02	0.30	0.38	0.06	2.42	1.56	51.41
10 L Sto In ave5	0.59	0.30	0.53	0.22	0.17	1.27	0.21	0.41	0.06	2.30	1.52	48.93
1 D Gi La ave5	0.59	0.51	0.29	0.19	0.39	0.46	0.36	0.64	0.13	0.66	0.81	14.06
5 D Gi La ave5	0.59	0.62	0.36	0.28	0.45	0.47	0.30	0.78	0.16	-0.24	0.49	-5.05
10 D Gi La ave5	0.59	0.63	0.36	0.29	0.46	0.45	0.31	0.80	0.16	-0.32	0.56	-6.72
1 L Gi La ave5	0.59	0.48	0.32	0.20	0.37	0.53	0.33	0.61	0.12	0.85	0.92	18.06
5 L Gi La ave5	0.59	0.60	0.37	0.28	0.44	0.49	0.30	0.75	0.16	-0.08	0.29	-1.75
10 L Gi La ave5	0.59	0.61	0.34	0.26	0.45	0.44	0.32	0.78	0.15	-0.17	0.41	-3.54
1 D Sto La ave5	0.59	0.38	0.23	0.11	0.31	0.48	0.41	0.49	0.09	1.66	1.29	35.19
5 D Sto La ave5	0.59	0.50	0.27	0.17	0.40	0.42	0.38	0.64	0.13	0.69	0.83	14.69
10 D Sto La ave5	0.59	0.57	0.34	0.24	0.42	0.48	0.32	0.72	0.15	0.16	0.39	3.30
1 L Sto La ave5	0.59	0.35	0.23	0.10	0.29	0.52	0.41	0.45	0.09	1.92	1.39	40.83
5 L Sto La ave5	0.59	0.47	0.28	0.17	0.37	0.46	0.37	0.60	0.12	0.93	0.96	19.67
10 L Sto La ave5	0.59	0.54	0.35	0.24	0.40	0.51	0.31	0.68	0.14	0.35	0.59	7.45

Table A.23: Calibration statistics for modelled and observed interstitial deposition in S2Q30D48-2, velocity deposition model

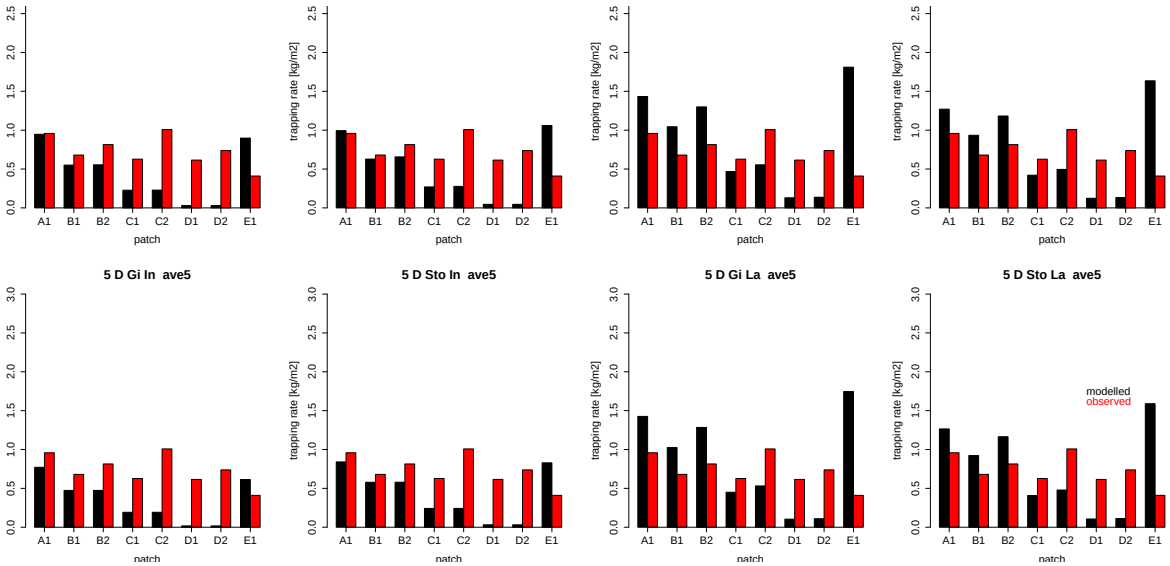

Figure A.22: Modelled and observed interstitial deposition in S2Q30D37, velocity deposition model for eight selected value set combinations

	TR		r^2	LM_{mo}		LM_{om}		RMA		Error		
	obs	mod		a	b	a	b	a	b	MSE	SMSE	PBIAS
1 D Gi In mean	0.73	0.53	0.13	-0.27	0.72	-0.06	0.76	2.13	-1.03	1.65	1.28	28.19
5 D Gi In mean	0.73	0.43	0.04	-0.07	0.49	-0.02	0.74	1.86	-0.93	2.38	1.54	40.73
10 D Gi In mean	0.73	0.43	0.14	0.26	0.24	0.07	0.70	1.88	-0.95	2.41	1.55	41.15
1 L Gi In mean	0.73	0.47	0.13	-0.24	0.65	-0.07	0.76	1.92	-0.93	2.06	1.43	35.18
5 L Gi In mean	0.73	0.38	0.04	-0.07	0.43	-0.03	0.74	1.64	-0.82	2.82	1.68	48.18
10 L Gi In mean	0.73	0.38	0.13	0.21	0.22	0.08	0.70	1.65	-0.83	2.84	1.69	48.54
1 D Sto In mean	0.73	0.47	0.17	-0.32	0.70	-0.09	0.77	1.87	-0.90	2.10	1.45	35.88
5 D Sto In mean	0.73	0.50	0.09	-0.19	0.63	-0.04	0.75	2.05	-1.00	1.87	1.37	32.03
10 D Sto In mean	0.73	0.43	0.09	-0.18	0.56	-0.05	0.75	1.85	-0.93	2.41	1.55	41.15
1 L Sto In mean	0.73	0.42	0.17	-0.29	0.63	-0.10	0.77	1.69	-0.81	2.46	1.57	42.12
5 L Sto In mean	0.73	0.45	0.08	-0.14	0.56	-0.04	0.75	1.86	-0.91	2.22	1.49	38.02
10 L Sto In mean	0.73	0.38	0.10	-0.16	0.49	-0.06	0.75	1.63	-0.82	2.84	1.69	48.58
1 D Gi La mean	0.73	0.76	0.16	-0.44	1.08	-0.06	0.77	2.84	-1.32	-0.22	0.46	-3.69
5 D Gi La mean	0.73	0.86	0.13	-0.42	1.17	-0.04	0.77	3.23	-1.50	-1.03	1.01	-17.55
10 D Gi La mean	0.73	0.95	0.06	-0.21	1.10	-0.02	0.75	3.55	-1.65	-1.72	1.31	-29.35
1 L Gi La mean	0.73	0.70	0.15	-0.40	1.00	-0.06	0.77	2.63	-1.22	0.22	0.47	3.77
5 L Gi La mean	0.73	0.82	0.13	-0.42	1.13	-0.04	0.77	3.10	-1.45	-0.73	0.85	-12.45
10 L Gi La mean	0.73	0.92	0.08	-0.27	1.12	-0.02	0.75	3.46	-1.61	-1.50	1.23	-25.69
1 D Sto La mean	0.73	0.60	0.17	-0.38	0.88	-0.08	0.78	2.24	-1.04	1.07	1.04	18.34
5 D Sto La mean	0.73	0.77	0.14	-0.41	1.07	-0.05	0.77	2.89	-1.34	-0.34	0.59	-5.90
10 D Sto La mean	0.73	0.79	0.15	-0.46	1.13	-0.05	0.77	2.97	-1.39	-0.47	0.68	-7.96
1 L Sto La mean	0.73	0.55	0.17	-0.35	0.80	-0.08	0.78	2.05	-0.95	1.48	1.22	25.38
5 L Sto La mean	0.73	0.73	0.13	-0.34	0.98	-0.05	0.77	2.72	-1.26	0.01	0.07	0.09
10 L Sto La mean	0.73	0.74	0.15	-0.43	1.06	-0.05	0.77	2.81	-1.31	-0.10	0.32	-1.79
1 D Gi In ave5	0.73	0.46	0.09	-0.17	0.59	-0.05	0.75	1.84	-0.88	2.17	1.47	37.01
5 D Gi In ave5	0.73	0.34	0.06	0.09	0.28	0.04	0.72	1.44	-0.71	3.10	1.76	52.99
10 D Gi In ave5	0.73	0.34	0.27	0.42	0.04	0.17	0.67	1.54	-0.79	3.11	1.76	53.15
1 L Gi In ave5	0.73	0.42	0.09	-0.16	0.53	-0.06	0.75	1.65	-0.79	2.53	1.59	43.19
5 L Gi In ave5	0.73	0.30	0.06	0.08	0.24	0.05	0.72	1.25	-0.62	3.47	1.86	59.32
10 L Gi In ave5	0.73	0.30	0.26	0.35	0.04	0.20	0.67	1.34	-0.68	3.48	1.86	59.44
1 D Sto In ave5	0.73	0.43	0.15	-0.25	0.61	-0.08	0.77	1.71	-0.82	2.42	1.56	41.35
5 D Sto In ave5	0.73	0.42	0.04	-0.07	0.47	-0.02	0.74	1.69	-0.82	2.48	1.57	42.33
10 D Sto In ave5	0.73	0.34	0.02	-0.03	0.36	-0.01	0.74	1.42	-0.70	3.11	1.76	53.12
1 L Sto In ave5	0.73	0.39	0.15	-0.23	0.55	-0.10	0.77	1.54	-0.74	2.75	1.66	47.05
5 L Sto In ave5	0.73	0.38	0.02	-0.04	0.41	-0.02	0.74	1.54	-0.74	2.77	1.66	47.38
10 L Sto In ave5	0.73	0.30	0.02	-0.02	0.31	-0.01	0.74	1.23	-0.61	3.48	1.87	59.46
1 D Gi La ave5	0.73	0.74	0.14	-0.41	1.04	-0.05	0.77	2.82	-1.32	-0.08	0.29	-1.45
5 D Gi La ave5	0.73	0.83	0.11	-0.36	1.10	-0.03	0.76	3.20	-1.51	-0.83	0.91	-14.12
10 D Gi La ave5	0.73	0.92	0.04	-0.13	1.02	-0.01	0.74	3.54	-1.67	-1.52	1.23	-25.92
1 L Gi La ave5	0.73	0.69	0.14	-0.37	0.95	-0.05	0.77	2.61	-1.22	0.35	0.59	6.03
5 L Gi La ave5	0.73	0.80	0.11	-0.35	1.05	-0.04	0.76	3.07	-1.45	-0.52	0.72	-8.82
10 L Gi La ave5	0.73	0.89	0.06	-0.19	1.03	-0.02	0.75	3.45	-1.63	-1.29	1.14	-22.04
1 D Sto La ave5	0.73	0.59	0.16	-0.36	0.85	-0.07	0.77	2.22	-1.04	1.16	1.08	19.83
5 D Sto La ave5	0.73	0.76	0.13	-0.36	1.02	-0.04	0.76	2.87	-1.34	-0.20	0.44	-3.34
10 D Sto La ave5	0.73	0.77	0.14	-0.41	1.06	-0.05	0.77	2.95	-1.39	-0.28	0.53	-4.86
1 L Sto La ave5	0.73	0.54	0.16	-0.33	0.78	-0.08	0.77	2.03	-0.95	1.57	1.25	26.81
5 L Sto La ave5	0.73	0.71	0.11	-0.30	0.93	-0.04	0.76	2.70	-1.26	0.16	0.40	2.72
10 L Sto La ave5	0.73	0.72	0.13	-0.37	0.99	-0.05	0.77	2.78	-1.31	0.09	0.29	1.47

Table A.24: Calibration statistics for modelled and observed interstitial deposition in S2Q30D37, velocity deposition model

Figure A.23: Modelled and observed interstitial deposition in S2Q100D48-1, velocity deposition model for eight selected value set combinations

./pics_flumo_Step3_obsTR/CalStep3v_S2Q100D48_1_TRobs.pdf

	TR		r^2	LM_{mo}		LM_{om}		RMA		Error		
	obs	mod		a	b	a	b	a	b	MSE	SMSE	PBIAS
1 D Gi In mean	1.47	0.33	0.21	0.15	0.10	0.28	1.37	0.74	-0.75	9.10	3.02	77.66
5 D Gi In mean	1.47	0.33	0.40	0.24	-0.03	0.66	1.25	0.60	-0.56	9.12	3.02	77.79
10 D Gi In mean	1.47	0.30	0.47	0.25	-0.06	0.90	1.20	0.52	-0.47	9.33	3.05	79.57
1 L Gi In mean	1.47	0.31	0.21	0.14	0.10	0.31	1.37	0.68	-0.70	9.26	3.04	78.99
5 L Gi In mean	1.47	0.29	0.40	0.22	-0.03	0.74	1.25	0.54	-0.50	9.37	3.06	79.95
10 L Gi In mean	1.47	0.27	0.48	0.23	-0.06	1.03	1.19	0.47	-0.42	9.54	3.09	81.38
1 D Sto In mean	1.47	0.30	0.13	0.09	0.16	0.18	1.41	0.70	-0.74	9.36	3.06	79.84
5 D Sto In mean	1.47	0.32	0.26	0.17	0.06	0.40	1.34	0.66	-0.65	9.18	3.03	78.31
10 D Sto In mean	1.47	0.30	0.33	0.20	0.01	0.55	1.30	0.60	-0.58	9.32	3.05	79.53
1 L Sto In mean	1.47	0.28	0.14	0.09	0.15	0.21	1.41	0.65	-0.68	9.49	3.08	80.96
5 L Sto In mean	1.47	0.29	0.26	0.16	0.06	0.44	1.34	0.60	-0.59	9.43	3.07	80.42
10 L Sto In mean	1.47	0.27	0.33	0.18	0.01	0.62	1.30	0.54	-0.52	9.53	3.09	81.34
1 D Gi La mean	1.47	0.47	0.07	0.09	0.35	0.06	1.44	1.19	-1.27	7.93	2.82	67.63
5 D Gi La mean	1.47	0.59	0.10	0.15	0.38	0.07	1.42	1.42	-1.48	6.96	2.64	59.39
10 D Gi La mean	1.47	0.62	0.13	0.19	0.34	0.09	1.41	1.49	-1.56	6.73	2.59	57.40
1 L Gi La mean	1.47	0.45	0.07	0.08	0.33	0.06	1.44	1.12	-1.19	8.11	2.85	69.18
5 L Gi La mean	1.47	0.57	0.09	0.13	0.38	0.07	1.43	1.36	-1.42	7.15	2.67	60.98
10 L Gi La mean	1.47	0.61	0.12	0.18	0.35	0.08	1.41	1.46	-1.53	6.82	2.61	58.21
1 D Sto La mean	1.47	0.37	0.05	0.05	0.30	0.06	1.44	0.94	-1.00	8.72	2.95	74.42
5 D Sto La mean	1.47	0.49	0.08	0.10	0.34	0.07	1.43	1.21	-1.28	7.77	2.79	66.30
10 D Sto La mean	1.47	0.53	0.08	0.11	0.37	0.06	1.43	1.30	-1.38	7.49	2.74	63.94
1 L Sto La mean	1.47	0.35	0.06	0.05	0.28	0.07	1.44	0.87	-0.92	8.89	2.98	75.82
5 L Sto La mean	1.47	0.46	0.07	0.08	0.34	0.07	1.43	1.13	-1.19	8.03	2.83	68.51
10 L Sto La mean	1.47	0.51	0.07	0.09	0.37	0.06	1.43	1.23	-1.30	7.68	2.77	65.50
1 D Gi In ave5	1.47	0.19	0.12	0.06	0.10	0.21	1.42	0.55	-0.61	10.17	3.19	86.78
5 D Gi In ave5	1.47	0.17	0.18	0.08	0.06	0.43	1.39	0.43	-0.45	10.33	3.21	88.11
10 D Gi In ave5	1.47	0.15	0.20	0.07	0.04	0.58	1.38	0.35	-0.36	10.54	3.25	89.95
1 L Gi In ave5	1.47	0.19	0.13	0.07	0.09	0.25	1.42	0.51	-0.57	10.22	3.20	87.16
5 L Gi In ave5	1.47	0.16	0.19	0.07	0.05	0.48	1.39	0.38	-0.40	10.46	3.23	89.21
10 L Gi In ave5	1.47	0.14	0.22	0.07	0.03	0.70	1.37	0.31	-0.32	10.63	3.26	90.71
1 D Sto In ave5	1.47	0.19	0.11	0.06	0.11	0.19	1.43	0.55	-0.62	10.18	3.19	86.81
5 D Sto In ave5	1.47	0.18	0.14	0.07	0.08	0.29	1.41	0.47	-0.52	10.30	3.21	87.90
10 D Sto In ave5	1.47	0.15	0.13	0.05	0.07	0.32	1.42	0.42	-0.46	10.51	3.24	89.64
1 L Sto In ave5	1.47	0.19	0.12	0.06	0.10	0.23	1.42	0.52	-0.57	10.22	3.20	87.19
5 L Sto In ave5	1.47	0.16	0.14	0.06	0.07	0.32	1.41	0.43	-0.47	10.43	3.23	89.02
10 L Sto In ave5	1.47	0.14	0.14	0.05	0.06	0.38	1.41	0.37	-0.41	10.60	3.26	90.41
1 D Gi La ave5	1.47	0.39	0.06	0.07	0.28	0.05	1.45	1.24	-1.43	8.64	2.94	73.67
5 D Gi La ave5	1.47	0.46	0.07	0.11	0.29	0.04	1.45	1.65	-1.95	8.07	2.84	68.85
10 D Gi La ave5	1.47	0.46	0.06	0.11	0.30	0.03	1.45	1.83	-2.21	8.02	2.83	68.43
1 L Gi La ave5	1.47	0.36	0.06	0.07	0.26	0.05	1.45	1.15	-1.32	8.83	2.97	75.30
5 L Gi La ave5	1.47	0.42	0.06	0.10	0.27	0.04	1.45	1.54	-1.84	8.37	2.89	71.45
10 L Gi La ave5	1.47	0.43	0.06	0.10	0.28	0.03	1.45	1.74	-2.12	8.27	2.88	70.53
1 D Sto La ave5	1.47	0.32	0.05	0.05	0.25	0.05	1.45	0.93	-1.05	9.20	3.03	78.47
5 D Sto La ave5	1.47	0.39	0.06	0.08	0.28	0.05	1.45	1.30	-1.51	8.57	2.93	73.09
10 D Sto La ave5	1.47	0.41	0.05	0.08	0.29	0.04	1.45	1.48	-1.77	8.45	2.91	72.11
1 L Sto La ave5	1.47	0.30	0.06	0.05	0.23	0.07	1.45	0.86	-0.96	9.34	3.06	79.70
5 L Sto La ave5	1.47	0.36	0.06	0.07	0.26	0.05	1.45	1.19	-1.38	8.86	2.98	75.57
10 L Sto La ave5	1.47	0.38	0.05	0.07	0.27	0.04	1.45	1.37	-1.64	8.72	2.95	74.37

Table A.25: Calibration statistics for modelled and observed interstitial deposition in S2Q100D48-1, velocity deposition model

Figure A.24: Modelled and observed interstitial deposition in S2Q100D48-2, velocity deposition model for eight selected value set combinations

./pics_flumo_Step3_obsTR/CalStep3v_S2Q100D48_2_TRobs.pdf

	TR		r^2	LM_{mo}		LM_{om}		RMA		Error		
	obs	mod		a	b	a	b	a	b	MSE	SMSE	PBIAS
1 D Gi In mean	2.08	0.33	0.22	-0.08	0.49	-0.63	2.28	0.35	-0.40	13.99	3.74	84.23
5 D Gi In mean	2.08	0.33	0.08	-0.02	0.37	-0.27	2.16	0.29	-0.27	14.00	3.74	84.32
10 D Gi In mean	2.08	0.30	0.02	-0.00	0.31	-0.07	2.10	0.25	-0.22	14.21	3.77	85.58
1 L Gi In mean	2.08	0.31	0.22	-0.07	0.46	-0.68	2.28	0.33	-0.37	14.14	3.76	85.17
5 L Gi In mean	2.08	0.29	0.08	-0.02	0.33	-0.29	2.16	0.26	-0.24	14.25	3.78	85.85
10 L Gi In mean	2.08	0.27	0.01	-0.00	0.28	-0.02	2.08	0.22	-0.19	14.42	3.80	86.86
1 D Sto In mean	2.08	0.30	0.28	-0.10	0.49	-0.85	2.33	0.34	-0.40	14.24	3.77	85.77
5 D Sto In mean	2.08	0.32	0.17	-0.05	0.43	-0.55	2.25	0.31	-0.34	14.06	3.75	84.69
10 D Sto In mean	2.08	0.30	0.12	-0.03	0.37	-0.41	2.20	0.29	-0.29	14.21	3.77	85.55
1 L Sto In mean	2.08	0.28	0.28	-0.09	0.46	-0.90	2.33	0.31	-0.37	14.37	3.79	86.56
5 L Sto In mean	2.08	0.29	0.17	-0.05	0.39	-0.61	2.25	0.28	-0.30	14.31	3.78	86.18
10 L Sto In mean	2.08	0.27	0.11	-0.03	0.33	-0.44	2.20	0.26	-0.26	14.42	3.80	86.83
1 D Gi La mean	2.08	0.47	0.34	-0.19	0.87	-0.59	2.36	0.57	-0.70	12.81	3.58	77.15
5 D Gi La mean	2.08	0.59	0.32	-0.22	1.05	-0.48	2.36	0.67	-0.80	11.84	3.44	71.33
10 D Gi La mean	2.08	0.62	0.31	-0.22	1.08	-0.44	2.35	0.71	-0.85	11.61	3.41	69.93
1 L Gi La mean	2.08	0.45	0.34	-0.18	0.83	-0.64	2.36	0.53	-0.66	12.99	3.60	78.24
5 L Gi La mean	2.08	0.57	0.33	-0.21	1.01	-0.51	2.37	0.65	-0.77	12.03	3.47	72.46
10 L Gi La mean	2.08	0.61	0.31	-0.22	1.06	-0.45	2.35	0.69	-0.83	11.71	3.42	70.50
1 D Sto La mean	2.08	0.37	0.34	-0.15	0.69	-0.77	2.36	0.45	-0.55	13.61	3.69	81.94
5 D Sto La mean	2.08	0.49	0.33	-0.19	0.90	-0.58	2.36	0.58	-0.70	12.65	3.56	76.21
10 D Sto La mean	2.08	0.53	0.34	-0.21	0.96	-0.55	2.36	0.62	-0.76	12.38	3.52	74.55
1 L Sto La mean	2.08	0.35	0.34	-0.14	0.65	-0.83	2.37	0.42	-0.51	13.77	3.71	82.93
5 L Sto La mean	2.08	0.46	0.34	-0.18	0.84	-0.63	2.37	0.54	-0.66	12.91	3.59	77.77
10 L Sto La mean	2.08	0.51	0.34	-0.20	0.92	-0.58	2.37	0.59	-0.71	12.56	3.54	75.65
1 D Gi In ave5	2.08	0.19	0.30	-0.08	0.35	-1.14	2.30	0.26	-0.35	15.06	3.88	90.67
5 D Gi In ave5	2.08	0.17	0.26	-0.05	0.28	-1.26	2.30	0.20	-0.25	15.21	3.90	91.60
10 D Gi In ave5	2.08	0.15	0.24	-0.04	0.23	-1.42	2.29	0.17	-0.20	15.43	3.93	92.91
1 L Gi In ave5	2.08	0.19	0.30	-0.07	0.34	-1.21	2.30	0.24	-0.32	15.10	3.89	90.94
5 L Gi In ave5	2.08	0.16	0.26	-0.05	0.25	-1.40	2.30	0.18	-0.22	15.34	3.92	92.39
10 L Gi In ave5	2.08	0.14	0.22	-0.03	0.21	-1.49	2.28	0.15	-0.17	15.52	3.94	93.44
1 D Sto In ave5	2.08	0.19	0.30	-0.08	0.36	-1.14	2.30	0.26	-0.35	15.06	3.88	90.69
5 D Sto In ave5	2.08	0.18	0.29	-0.06	0.31	-1.27	2.30	0.23	-0.29	15.19	3.90	91.46
10 D Sto In ave5	2.08	0.15	0.29	-0.06	0.27	-1.45	2.30	0.20	-0.26	15.39	3.92	92.69
1 L Sto In ave5	2.08	0.19	0.30	-0.07	0.34	-1.21	2.30	0.25	-0.32	15.10	3.89	90.96
5 L Sto In ave5	2.08	0.16	0.29	-0.06	0.28	-1.41	2.30	0.20	-0.26	15.32	3.91	92.25
10 L Sto In ave5	2.08	0.14	0.28	-0.05	0.25	-1.59	2.30	0.18	-0.23	15.48	3.93	93.23
1 D Gi La ave5	2.08	0.39	0.31	-0.18	0.76	-0.52	2.28	0.59	-0.84	13.52	3.68	81.42
5 D Gi La ave5	2.08	0.46	0.29	-0.23	0.93	-0.37	2.24	0.78	-1.17	12.95	3.60	78.01
10 D Gi La ave5	2.08	0.46	0.29	-0.25	0.99	-0.33	2.23	0.87	-1.34	12.90	3.59	77.72
1 L Gi La ave5	2.08	0.36	0.31	-0.17	0.71	-0.56	2.28	0.55	-0.78	13.71	3.70	82.56
5 L Gi La ave5	2.08	0.42	0.29	-0.21	0.86	-0.40	2.24	0.73	-1.10	13.26	3.64	79.85
10 L Gi La ave5	2.08	0.43	0.29	-0.24	0.93	-0.35	2.23	0.83	-1.29	13.15	3.63	79.20
1 D Sto La ave5	2.08	0.32	0.32	-0.14	0.61	-0.72	2.30	0.44	-0.60	14.08	3.75	84.80
5 D Sto La ave5	2.08	0.39	0.30	-0.19	0.78	-0.49	2.27	0.62	-0.89	13.45	3.67	81.01
10 D Sto La ave5	2.08	0.41	0.30	-0.21	0.84	-0.42	2.25	0.71	-1.06	13.34	3.65	80.31
1 L Sto La ave5	2.08	0.30	0.32	-0.13	0.57	-0.78	2.31	0.41	-0.55	14.23	3.77	85.67
5 L Sto La ave5	2.08	0.36	0.30	-0.17	0.71	-0.53	2.27	0.57	-0.82	13.74	3.71	82.75
10 L Sto La ave5	2.08	0.38	0.30	-0.19	0.78	-0.45	2.25	0.65	-0.98	13.60	3.69	81.90

Table A.26: Calibration statistics for modelled and observed interstitial deposition in S2Q100D48-2, velocity deposition model

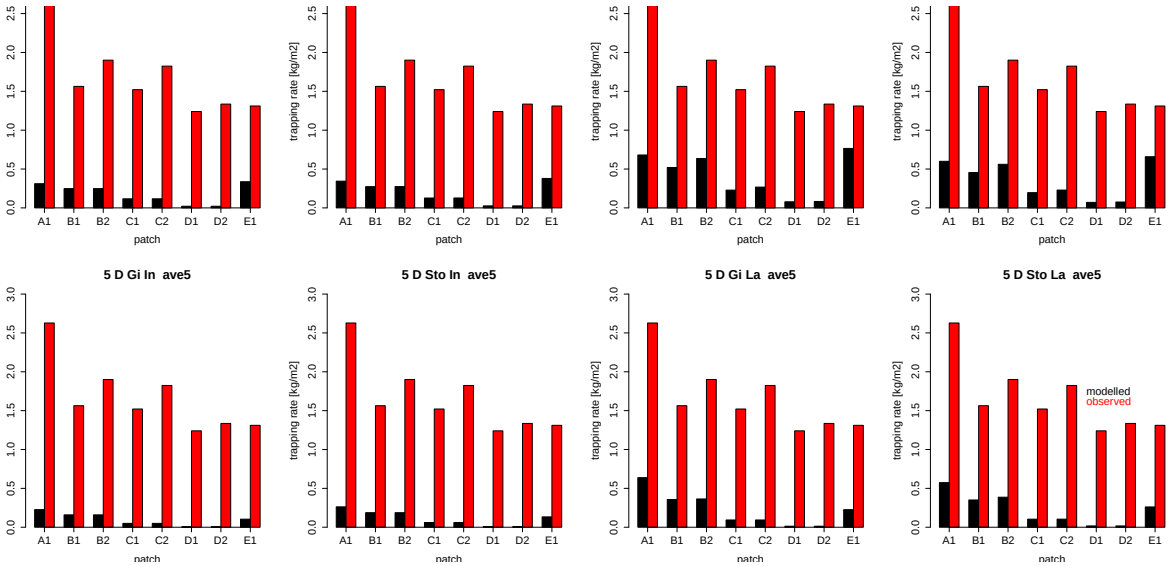

Figure A.25: Modelled and observed interstitial deposition in S2Q100D37, velocity deposition model for eight selected value set combinations

	TR		r^2	LM_{mo}		LM_{om}		RMA		Error		
	obs	mod		a	b	a	b	a	b	MSE	SMSE	PBIAS
1 D Gi In mean	1.67	0.21	0.43	0.14	-0.02	1.35	1.39	0.32	-0.33	11.67	3.42	87.58
5 D Gi In mean	1.67	0.18	0.50	0.14	-0.05	1.82	1.34	0.27	-0.28	11.90	3.45	89.34
10 D Gi In mean	1.67	0.18	0.64	0.18	-0.12	2.27	1.26	0.28	-0.29	11.91	3.45	89.36
1 L Gi In mean	1.67	0.20	0.46	0.14	-0.03	1.51	1.37	0.30	-0.31	11.75	3.43	88.21
5 L Gi In mean	1.67	0.16	0.51	0.13	-0.05	2.05	1.33	0.25	-0.26	12.02	3.47	90.24
10 L Gi In mean	1.67	0.16	0.66	0.17	-0.12	2.55	1.25	0.26	-0.27	12.03	3.47	90.25
1 D Sto In mean	1.67	0.19	0.45	0.13	-0.03	1.51	1.37	0.30	-0.30	11.79	3.43	88.46
5 D Sto In mean	1.67	0.20	0.49	0.15	-0.05	1.60	1.35	0.30	-0.31	11.75	3.43	88.17
10 D Sto In mean	1.67	0.18	0.47	0.13	-0.04	1.72	1.36	0.28	-0.28	11.90	3.45	89.32
1 L Sto In mean	1.67	0.18	0.48	0.13	-0.04	1.71	1.35	0.28	-0.28	11.86	3.44	88.99
5 L Sto In mean	1.67	0.18	0.49	0.13	-0.04	1.77	1.35	0.27	-0.28	11.90	3.45	89.32
10 L Sto In mean	1.67	0.16	0.49	0.12	-0.04	1.95	1.35	0.25	-0.26	12.02	3.47	90.23
1 D Gi La mean	1.67	0.34	0.47	0.24	-0.05	0.93	1.35	0.51	-0.50	10.59	3.25	79.46
5 D Gi La mean	1.67	0.41	0.49	0.30	-0.08	0.81	1.34	0.61	-0.60	10.07	3.17	75.55
10 D Gi La mean	1.67	0.45	0.54	0.36	-0.16	0.80	1.31	0.67	-0.67	9.75	3.12	73.14
1 L Gi La mean	1.67	0.33	0.48	0.23	-0.06	1.00	1.34	0.48	-0.48	10.72	3.27	80.45
5 L Gi La mean	1.67	0.39	0.49	0.29	-0.08	0.84	1.34	0.58	-0.58	10.18	3.19	76.42
10 L Gi La mean	1.67	0.44	0.54	0.36	-0.16	0.82	1.31	0.66	-0.66	9.83	3.13	73.74
1 D Sto La mean	1.67	0.27	0.48	0.19	-0.05	1.20	1.34	0.40	-0.40	11.14	3.34	83.59
5 D Sto La mean	1.67	0.36	0.50	0.26	-0.08	0.95	1.33	0.53	-0.52	10.48	3.24	78.64
10 D Sto La mean	1.67	0.38	0.48	0.27	-0.07	0.86	1.34	0.56	-0.55	10.31	3.21	77.35
1 L Sto La mean	1.67	0.26	0.50	0.19	-0.06	1.32	1.32	0.38	-0.38	11.25	3.35	84.46
5 L Sto La mean	1.67	0.33	0.50	0.24	-0.07	1.01	1.33	0.49	-0.49	10.67	3.27	80.11
10 L Sto La mean	1.67	0.36	0.49	0.26	-0.07	0.91	1.34	0.53	-0.53	10.45	3.23	78.40
1 D Gi In ave5	1.67	0.12	0.69	0.15	-0.12	3.29	1.26	0.21	-0.23	12.33	3.51	92.57
5 D Gi In ave5	1.67	0.09	0.77	0.14	-0.13	4.34	1.25	0.18	-0.20	12.57	3.55	94.32
10 D Gi In ave5	1.67	0.10	0.83	0.17	-0.19	4.08	1.27	0.20	-0.24	12.56	3.54	94.25
1 L Gi In ave5	1.67	0.12	0.69	0.14	-0.12	3.34	1.25	0.21	-0.22	12.34	3.51	92.61
5 L Gi In ave5	1.67	0.09	0.77	0.13	-0.12	4.64	1.25	0.17	-0.19	12.61	3.55	94.63
10 L Gi In ave5	1.67	0.09	0.83	0.16	-0.18	4.32	1.27	0.19	-0.23	12.60	3.55	94.56
1 D Sto In ave5	1.67	0.12	0.69	0.14	-0.12	3.29	1.26	0.21	-0.23	12.34	3.51	92.59
5 D Sto In ave5	1.67	0.11	0.75	0.16	-0.15	3.67	1.25	0.21	-0.23	12.42	3.52	93.21
10 D Sto In ave5	1.67	0.09	0.76	0.13	-0.13	4.35	1.25	0.18	-0.20	12.57	3.55	94.33
1 L Sto In ave5	1.67	0.12	0.69	0.14	-0.12	3.35	1.25	0.21	-0.22	12.34	3.51	92.62
5 L Sto In ave5	1.67	0.10	0.74	0.14	-0.13	4.01	1.25	0.19	-0.20	12.49	3.53	93.76
10 L Sto In ave5	1.67	0.09	0.76	0.12	-0.12	4.65	1.25	0.16	-0.18	12.61	3.55	94.64
1 D Gi La ave5	1.67	0.23	0.75	0.31	-0.29	1.78	1.26	0.42	-0.47	11.49	3.39	86.23
5 D Gi La ave5	1.67	0.22	0.83	0.40	-0.43	1.73	1.28	0.48	-0.57	11.53	3.40	86.51
10 D Gi La ave5	1.67	0.23	0.86	0.47	-0.54	1.59	1.29	0.54	-0.67	11.46	3.39	86.03
1 L Gi La ave5	1.67	0.22	0.75	0.30	-0.28	1.89	1.25	0.40	-0.44	11.59	3.40	86.96
5 L Gi La ave5	1.67	0.21	0.83	0.37	-0.41	1.88	1.28	0.44	-0.53	11.67	3.42	87.57
10 L Gi La ave5	1.67	0.22	0.87	0.44	-0.52	1.70	1.30	0.51	-0.64	11.60	3.41	87.05
1 D Sto La ave5	1.67	0.20	0.70	0.24	-0.20	2.04	1.26	0.34	-0.37	11.73	3.42	88.00
5 D Sto La ave5	1.67	0.23	0.79	0.35	-0.35	1.79	1.26	0.44	-0.51	11.51	3.39	86.39
10 D Sto La ave5	1.67	0.22	0.81	0.37	-0.39	1.81	1.27	0.45	-0.53	11.58	3.40	86.87
1 L Sto La ave5	1.67	0.19	0.71	0.23	-0.20	2.16	1.25	0.33	-0.36	11.80	3.44	88.56
5 L Sto La ave5	1.67	0.21	0.79	0.31	-0.32	1.98	1.26	0.40	-0.46	11.68	3.42	87.66
10 L Sto La ave5	1.67	0.20	0.82	0.34	-0.37	1.97	1.27	0.42	-0.49	11.72	3.42	87.93

Table A.27: Calibration statistics for modelled and observed interstitial deposition in S2Q100D37, velocity deposition model

A.1.5 Calibration sandy experimental runs

	r^2	LM_{mo}		LM_{om}		RMA		Error		
		a	b	a	b	a	b	MSE	SMSE	PBIAS
1-Ri -Shi-er-Txyz	0.97	0.97	0.07	0.97	-0.05	1.00	0.06	-0.59	0.77	-20.95
5-Ri -Shi-er-Txyz	1.00	1.01	-0.03	0.99	0.03	1.01	-0.03	0.23	0.48	8.17
10-Ri -Shi-er-Txyz	1.00	1.01	-0.03	0.99	0.03	1.01	-0.03	0.30	0.55	10.66
1-Gi -Shi-er-Txyz	0.97	0.98	0.06	0.97	-0.04	1.00	0.05	-0.50	0.71	-17.88
5-Gi -Shi-er-Txyz	1.00	1.01	-0.03	0.99	0.03	1.01	-0.03	0.25	0.50	8.75
10-Gi -Shi-er-Txyz	1.00	1.01	-0.03	0.99	0.03	1.01	-0.03	0.31	0.55	10.88
1-Ri -La -Txyz	0.96	0.95	0.13	0.96	-0.10	0.99	0.12	-1.15	1.07	-40.83
5-Ri -La -Txyz	1.00	1.00	-0.00	0.99	0.01	1.00	-0.00	0.03	0.17	1.08
10-Ri -La -Txyz	1.00	1.01	-0.02	0.99	0.02	1.01	-0.02	0.20	0.45	7.18
1-Gi -La -Txyz	0.96	0.95	0.12	0.97	-0.09	0.99	0.11	-1.05	1.03	-37.35
5-Gi -La -Txyz	1.00	1.00	-0.01	0.99	0.01	1.01	-0.01	0.06	0.25	2.29
10-Gi -La -Txyz	1.00	1.01	-0.02	0.99	0.02	1.01	-0.03	0.22	0.47	7.83
1-Ri -Shi-er-Tz	0.97	0.98	0.06	0.97	-0.04	1.00	0.05	-0.55	0.74	-19.33
5-Ri -Shi-er-Tz	1.00	1.01	-0.03	0.99	0.03	1.01	-0.03	0.24	0.49	8.59
10-Ri -Shi-er-Tz	1.00	1.01	-0.03	0.99	0.03	1.01	-0.03	0.30	0.55	10.81
1-Gi -Shi-er-Tz	0.98	0.98	0.05	0.97	-0.04	1.00	0.04	-0.46	0.68	-16.29
5-Gi -Shi-er-Tz	1.00	1.01	-0.03	0.99	0.03	1.01	-0.03	0.26	0.51	9.12
10-Gi -Shi-er-Tz	1.00	1.01	-0.03	0.99	0.03	1.01	-0.03	0.31	0.56	10.99
1-Ri -La -Tz	1.00	1.00	-0.00	0.99	0.00	1.00	-0.00	0.01	0.10	0.35
5-Ri -La -Tz	1.00	1.01	-0.02	0.99	0.02	1.01	-0.02	0.17	0.41	5.93
10-Ri -La -Tz	1.00	1.01	-0.03	0.99	0.03	1.01	-0.03	0.27	0.52	9.57
1-Gi -La -Tz	0.97	0.97	0.08	0.97	-0.06	1.00	0.07	-0.69	0.83	-24.62
5-Gi -La -Tz	1.00	1.01	-0.02	0.99	0.02	1.01	-0.02	0.19	0.44	6.72
10-Gi -La -Tz	1.00	1.01	-0.03	0.99	0.03	1.01	-0.03	0.28	0.53	9.97

Table A.28: Graphical representaiton of statisitcal evaluation of modeled and observed suspended sediment concentration loss in S2Q100D48-s1, shear stress deposition model

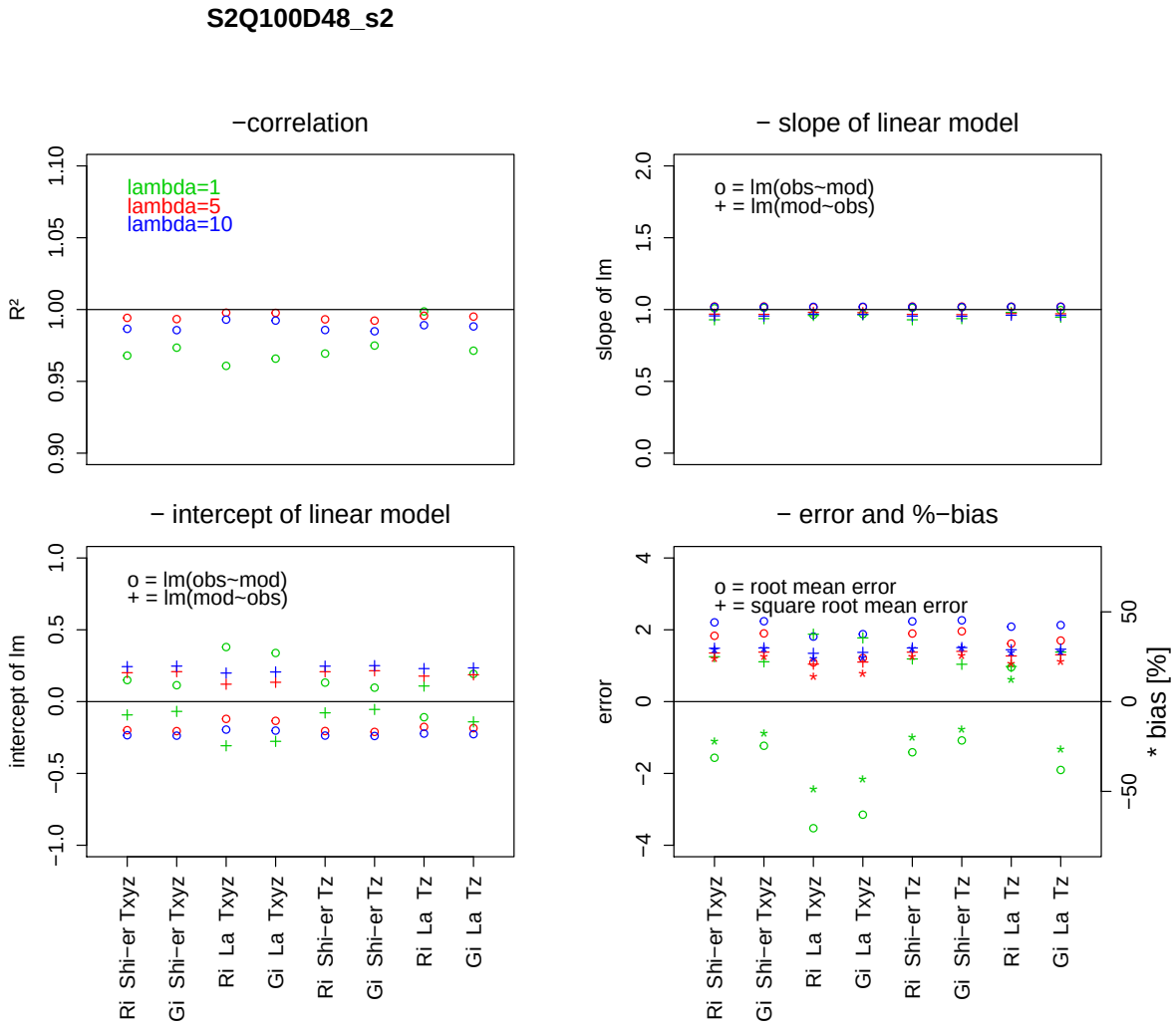

Figure A.26: Graphical representaiton of statisitcal evaluation of modeled and observed suspended sediment concentration loss in S1Q100D48-s2, shear stress deposition model

	r^2	LM_{mo}		LM_{om}		RMA		Error		
		a	b	a	b	a	b	MSE	SMSE	PBIAS
1-Ri -Shi-er-Txyz	0.97	1.01	0.15	0.93	-0.09	1.04	0.13	-1.56	1.25	-21.19
5-Ri -Shi-er-Txyz	0.99	1.02	-0.20	0.97	0.20	1.03	-0.20	1.83	1.35	24.84
10-Ri -Shi-er-Txyz	0.99	1.02	-0.23	0.96	0.24	1.03	-0.24	2.21	1.49	29.90
1-Gi -Shi-er-Txyz	0.97	1.01	0.11	0.94	-0.07	1.04	0.09	-1.23	1.11	-16.67
5-Gi -Shi-er-Txyz	0.99	1.02	-0.21	0.97	0.21	1.03	-0.21	1.90	1.38	25.74
10-Gi -Shi-er-Txyz	0.99	1.02	-0.24	0.95	0.25	1.03	-0.25	2.24	1.50	30.33
1-Ri -La -Txyz	0.96	0.96	0.38	0.96	-0.31	1.00	0.35	-3.53	1.88	-47.77
5-Ri -La -Txyz	1.00	1.02	-0.12	0.98	0.12	1.02	-0.12	1.09	1.04	14.76
10-Ri -La -Txyz	0.99	1.02	-0.19	0.97	0.20	1.03	-0.20	1.81	1.35	24.53
1-Gi -La -Txyz	0.97	0.97	0.34	0.96	-0.28	1.00	0.31	-3.15	1.77	-42.68
5-Gi -La -Txyz	1.00	1.02	-0.13	0.98	0.13	1.02	-0.14	1.21	1.10	16.44
10-Gi -La -Txyz	0.99	1.02	-0.20	0.97	0.21	1.03	-0.21	1.88	1.37	25.45
1-Ri -Shi-er-Tz	0.97	1.01	0.13	0.93	-0.08	1.04	0.11	-1.41	1.19	-19.12
5-Ri -Shi-er-Tz	0.99	1.02	-0.20	0.97	0.21	1.03	-0.21	1.90	1.38	25.69
10-Ri -Shi-er-Tz	0.99	1.02	-0.24	0.95	0.25	1.03	-0.25	2.23	1.49	30.28
1-Gi -Shi-er-Tz	0.97	1.01	0.10	0.94	-0.05	1.04	0.08	-1.08	1.04	-14.65
5-Gi -Shi-er-Tz	0.99	1.02	-0.21	0.96	0.21	1.03	-0.22	1.96	1.40	26.53
10-Gi -Shi-er-Tz	0.98	1.02	-0.24	0.95	0.25	1.03	-0.25	2.26	1.50	30.68
1-Ri -La -Tz	1.00	1.02	-0.11	0.98	0.11	1.02	-0.11	0.96	0.98	12.97
5-Ri -La -Tz	1.00	1.02	-0.18	0.97	0.18	1.02	-0.18	1.62	1.27	21.89
10-Ri -La -Tz	0.99	1.02	-0.22	0.96	0.23	1.03	-0.23	2.09	1.44	28.28
1-Gi -La -Tz	0.97	1.00	0.19	0.95	-0.14	1.03	0.17	-1.90	1.38	-25.79
5-Gi -La -Tz	1.00	1.02	-0.18	0.97	0.19	1.03	-0.19	1.70	1.30	23.03
10-Gi -La -Tz	0.99	1.02	-0.23	0.96	0.23	1.03	-0.24	2.13	1.46	28.88

Table A.29: Graphical representaiton of statisitcal evaluation of modeled and observed suspended sediment concentration loss in S2Q100D48-s2, shear stress deposition model

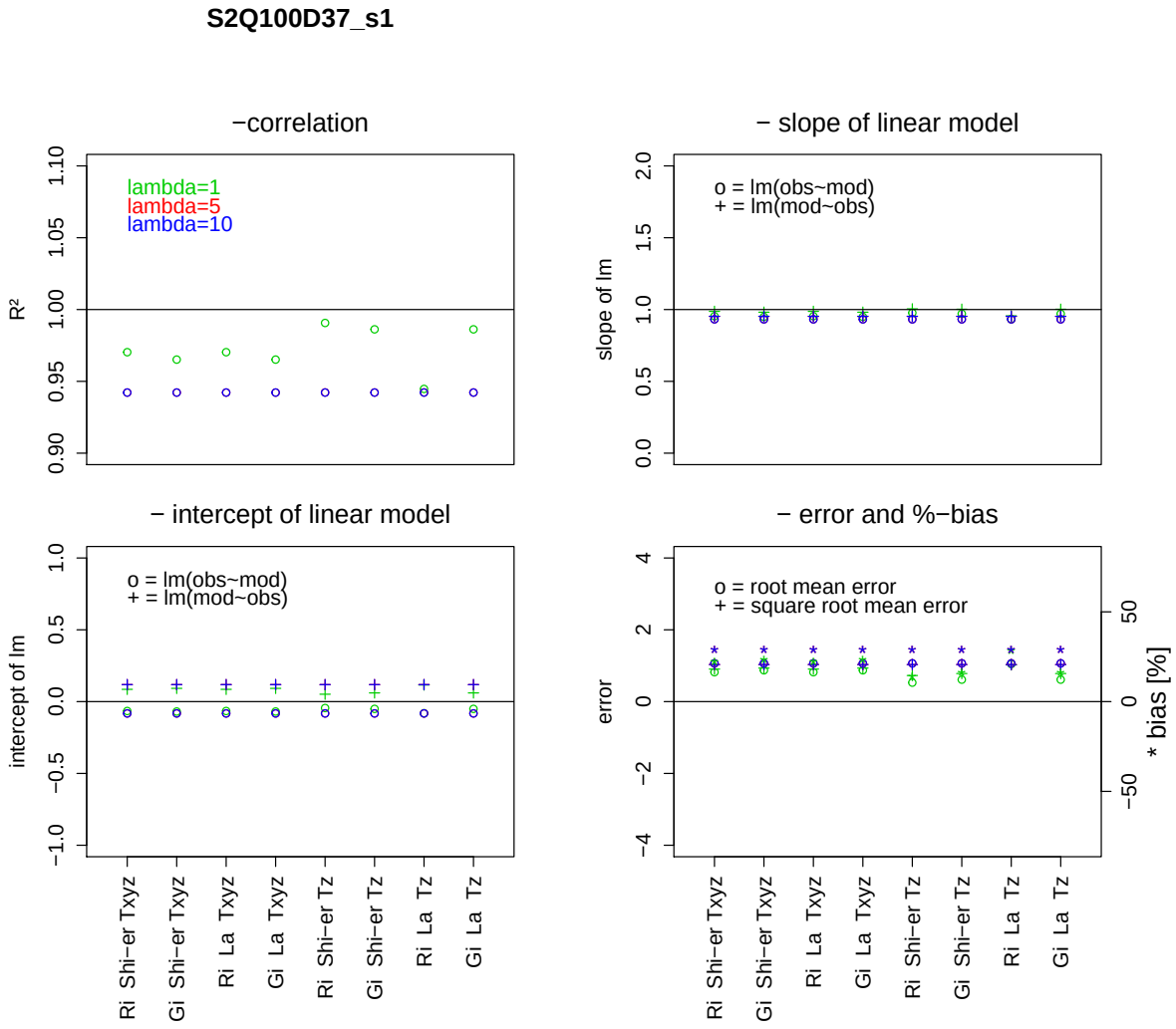

Figure A.27: Graphical representaiton of statisitcal evaluation of modeled and observed suspended sediment concentration loss in S1Q100D37-s1, shear stress deposition model

	r^2	LM_{mo}		LM_{om}		RMA		Error		
		a	b	a	b	a	b	MSE	SMSE	PBIAS
1-Ri -Shi-er-Txyz	0.97	0.95	-0.07	0.99	0.09	0.98	-0.08	0.82	0.91	22.98
5-Ri -Shi-er-Txyz	0.94	0.93	-0.08	0.95	0.12	0.99	-0.10	1.07	1.03	29.88
10-Ri -Shi-er-Txyz	0.94	0.93	-0.08	0.95	0.12	0.99	-0.10	1.07	1.03	29.88
1-Gi -Shi-er-Txyz	0.97	0.95	-0.07	0.98	0.09	0.98	-0.08	0.87	0.93	24.45
5-Gi -Shi-er-Txyz	0.94	0.93	-0.08	0.95	0.12	0.99	-0.10	1.07	1.03	29.88
10-Gi -Shi-er-Txyz	0.94	0.93	-0.08	0.95	0.12	0.99	-0.10	1.07	1.03	29.88
1-Ri -La -Txyz	0.97	0.95	-0.07	0.99	0.09	0.98	-0.08	0.82	0.91	22.98
5-Ri -La -Txyz	0.94	0.93	-0.08	0.95	0.12	0.99	-0.10	1.07	1.03	29.88
10-Ri -La -Txyz	0.94	0.93	-0.08	0.95	0.12	0.99	-0.10	1.07	1.03	29.88
1-Gi -La -Txyz	0.97	0.95	-0.07	0.98	0.09	0.98	-0.08	0.87	0.93	24.45
5-Gi -La -Txyz	0.94	0.93	-0.08	0.95	0.12	0.99	-0.10	1.07	1.03	29.88
10-Gi -La -Txyz	0.94	0.93	-0.08	0.95	0.12	0.99	-0.10	1.07	1.03	29.88
1-Ri -Shi-er-Tz	0.99	0.98	-0.04	1.00	0.05	0.99	-0.05	0.53	0.73	14.82
5-Ri -Shi-er-Tz	0.94	0.93	-0.08	0.95	0.12	0.99	-0.10	1.06	1.03	29.87
10-Ri -Shi-er-Tz	0.94	0.93	-0.08	0.95	0.12	0.99	-0.10	1.07	1.03	29.88
1-Gi -Shi-er-Tz	0.99	0.97	-0.05	1.00	0.06	0.98	-0.06	0.61	0.78	17.16
5-Gi -Shi-er-Tz	0.94	0.93	-0.08	0.95	0.12	0.99	-0.10	1.07	1.03	29.88
10-Gi -Shi-er-Tz	0.94	0.93	-0.08	0.95	0.12	0.99	-0.10	1.07	1.03	29.88
1-Ri -La -Tz	0.94	0.93	-0.08	0.96	0.12	0.99	-0.10	1.05	1.02	29.35
5-Ri -La -Tz	0.94	0.93	-0.08	0.95	0.12	0.99	-0.10	1.06	1.03	29.87
10-Ri -La -Tz	0.94	0.93	-0.08	0.95	0.12	0.99	-0.10	1.07	1.03	29.88
1-Gi -La -Tz	0.99	0.97	-0.05	1.00	0.06	0.98	-0.06	0.61	0.78	17.16
5-Gi -La -Tz	0.94	0.93	-0.08	0.95	0.12	0.99	-0.10	1.07	1.03	29.88
10-Gi -La -Tz	0.94	0.93	-0.08	0.95	0.12	0.99	-0.10	1.07	1.03	29.88

Table A.30: Graphical representaiton of statisitcal evaluation of modeled and observed suspended sediment concentration loss in S2Q100D37-s1, shear stress deposition model

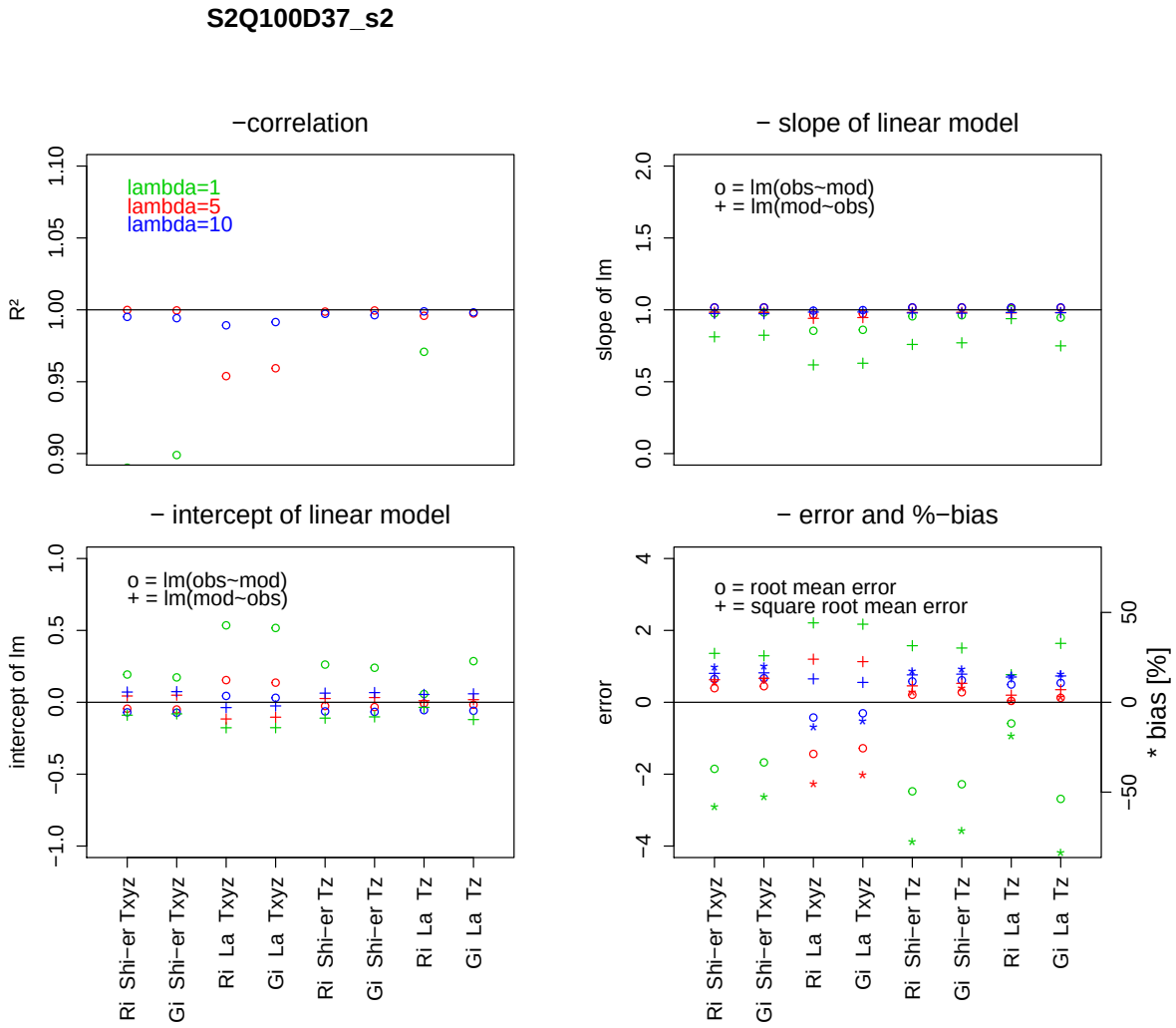

Figure A.28: Graphical representaiton of statisitcal evaluation of modeled and observed suspended sediment concentration loss in S1Q100D37-s2, shear stress deposition model

	r^2	LM_{mo}		LM_{om}		RMA		Error		
		a	b	a	b	a	b	MSE	SMSE	PBIAS
1-Ri -Shi-er-Txyz	0.89	0.98	0.19	0.81	-0.09	1.10	0.15	-1.85	1.36	-57.24
5-Ri -Shi-er-Txyz	1.00	1.02	-0.04	0.98	0.04	1.02	-0.04	0.39	0.63	12.14
10-Ri -Shi-er-Txyz	1.00	1.02	-0.07	0.97	0.07	1.02	-0.07	0.65	0.80	20.02
1-Gi -Shi-er-Txyz	0.90	0.98	0.17	0.82	-0.08	1.09	0.14	-1.67	1.29	-51.71
5-Gi -Shi-er-Txyz	1.00	1.02	-0.05	0.98	0.05	1.02	-0.05	0.45	0.67	13.81
10-Gi -Shi-er-Txyz	0.99	1.02	-0.07	0.97	0.07	1.02	-0.07	0.67	0.82	20.72
1-Ri -La -Txyz	0.73	0.85	0.54	0.62	-0.18	1.18	0.43	-4.88	2.21	-150.86
5-Ri -La -Txyz	0.95	0.97	0.15	0.94	-0.12	1.01	0.14	-1.44	1.20	-44.41
10-Ri -La -Txyz	0.99	0.99	0.04	0.98	-0.04	1.00	0.04	-0.42	0.65	-13.11
1-Gi -La -Txyz	0.74	0.86	0.52	0.63	-0.18	1.17	0.42	-4.72	2.17	-145.88
5-Gi -La -Txyz	0.96	0.97	0.14	0.95	-0.10	1.01	0.12	-1.28	1.13	-39.52
10-Gi -La -Txyz	0.99	1.00	0.03	0.98	-0.03	1.01	0.03	-0.31	0.55	-9.45
1-Ri -Shi-er-Tz	0.85	0.95	0.26	0.76	-0.11	1.12	0.21	-2.48	1.57	-76.55
5-Ri -Shi-er-Tz	1.00	1.02	-0.03	0.98	0.03	1.02	-0.03	0.21	0.46	6.45
10-Ri -Shi-er-Tz	1.00	1.02	-0.06	0.98	0.06	1.02	-0.06	0.58	0.76	17.96
1-Gi -Shi-er-Tz	0.86	0.96	0.24	0.77	-0.10	1.12	0.19	-2.28	1.51	-70.48
5-Gi -Shi-er-Tz	1.00	1.02	-0.03	0.98	0.03	1.02	-0.03	0.28	0.53	8.62
10-Gi -Shi-er-Tz	1.00	1.02	-0.07	0.98	0.07	1.02	-0.07	0.61	0.78	18.96
1-Ri -La -Tz	0.97	1.00	0.06	0.94	-0.04	1.03	0.05	-0.59	0.77	-18.21
5-Ri -La -Tz	1.00	1.01	-0.01	0.98	0.01	1.02	-0.01	0.04	0.20	1.21
10-Ri -La -Tz	1.00	1.02	-0.05	0.98	0.05	1.02	-0.06	0.49	0.70	15.28
1-Gi -La -Tz	0.84	0.95	0.29	0.75	-0.12	1.12	0.23	-2.69	1.64	-83.07
5-Gi -La -Tz	1.00	1.01	-0.02	0.98	0.02	1.02	-0.02	0.12	0.35	3.80
10-Gi -La -Tz	1.00	1.02	-0.06	0.98	0.06	1.02	-0.06	0.54	0.73	16.59

Table A.31: Graphical representaiton of statisitcal evaluation of modeled and observed suspended sediment concentration loss in S2Q100D37-s2, shear stress deposition model

	TR		r^2	LM_{mo}		LM_{om}		RMA		Error		
	obs	mod		a	b	a	b	a	b	MSE	SMSE	PBIAS
1-Ri -Shi-er-Txyz	2.57	2.57	0.22	0.17	2.12	0.28	1.85	0.78	0.55	0.03	0.18	0.15
5-Ri -Shi-er-Txyz	2.57	2.45	0.46	0.31	1.66	0.70	0.85	0.66	0.75	1.01	1.00	4.89
10-Ri -Shi-er-Txyz	2.57	2.33	0.80	0.51	1.03	1.28	-0.41	0.63	0.71	1.95	1.39	9.45
1-Gi -Shi-er-Txyz	2.57	2.57	0.23	0.18	2.11	0.29	1.83	0.78	0.56	0.03	0.18	0.16
5-Gi -Shi-er-Txyz	2.57	2.43	0.50	0.32	1.60	0.76	0.71	0.65	0.76	1.11	1.05	5.39
10-Gi -Shi-er-Txyz	2.57	2.32	0.85	0.55	0.91	1.32	-0.49	0.64	0.66	2.04	1.43	9.94
1-Ri -La -Txyz	2.57	2.78	0.17	0.17	2.33	0.17	2.11	1.03	0.14	-1.66	1.29	-8.05
5-Ri -La -Txyz	2.57	2.78	0.32	0.30	2.00	0.34	1.64	0.95	0.33	-1.68	1.30	-8.15
10-Ri -La -Txyz	2.57	2.67	0.58	0.50	1.39	0.68	0.76	0.86	0.47	-0.80	0.89	-3.88
1-Gi -La -Txyz	2.57	2.80	0.17	0.18	2.34	0.17	2.11	1.03	0.14	-1.80	1.34	-8.76
5-Gi -La -Txyz	2.57	2.77	0.34	0.32	1.94	0.36	1.57	0.94	0.35	-1.58	1.26	-7.68
10-Gi -La -Txyz	2.57	2.66	0.63	0.54	1.28	0.74	0.61	0.85	0.47	-0.71	0.84	-3.44
1-Ri -Shi-er-Tz	2.57	2.01	0.36	0.22	1.46	0.59	1.38	0.60	0.46	4.48	2.12	21.75
5-Ri -Shi-er-Tz	2.57	2.10	0.41	0.28	1.38	0.60	1.31	0.68	0.35	3.77	1.94	18.32
10-Ri -Shi-er-Tz	2.57	0.78	0.35	0.10	0.54	1.30	1.56	0.27	0.08	14.30	3.78	69.50
1-Gi -Shi-er-Tz	2.57	2.02	0.36	0.22	1.45	0.59	1.37	0.61	0.46	4.45	2.11	21.63
5-Gi -Shi-er-Tz	2.57	2.11	0.42	0.29	1.37	0.60	1.30	0.69	0.33	3.67	1.92	17.85
10-Gi -Shi-er-Tz	2.57	0.79	0.35	0.10	0.54	1.30	1.55	0.27	0.08	14.28	3.78	69.37
1-Ri -La -Tz	2.57	2.10	0.28	0.20	1.60	0.40	1.73	0.70	0.31	3.76	1.94	18.26
5-Ri -La -Tz	2.57	2.15	0.31	0.23	1.57	0.42	1.67	0.74	0.26	3.37	1.84	16.37
10-Ri -La -Tz	2.57	0.84	0.11	0.04	0.74	0.34	2.29	0.34	-0.03	13.88	3.72	67.42
1-Gi -La -Tz	2.57	2.05	0.26	0.17	1.61	0.39	1.77	0.66	0.36	4.19	2.05	20.35
5-Gi -La -Tz	2.57	2.16	0.31	0.23	1.56	0.42	1.66	0.75	0.25	3.27	1.81	15.90
10-Gi -La -Tz	2.57	0.84	0.12	0.04	0.74	0.34	2.29	0.34	-0.03	13.85	3.72	67.27

Table A.32: Calibration statistics for modelled and observed interstitial deposition in S2Q30D48-s1, shear stress deposition model

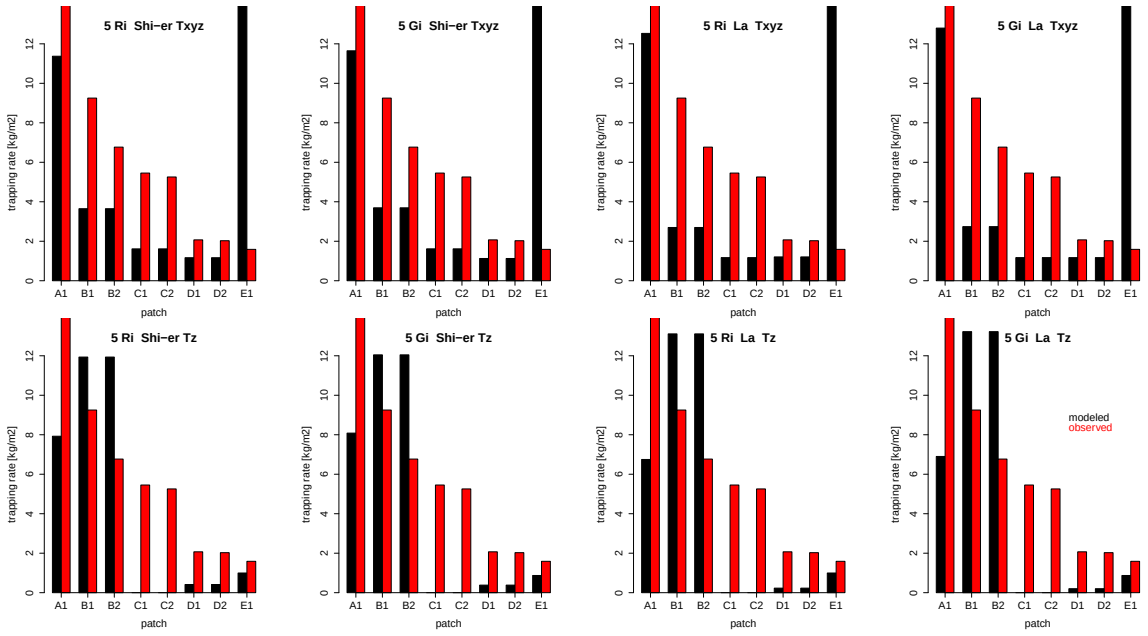

Figure A.29: Modelled and observed interstitial deposition in S2Q100D48-s2, shear stress deposition model for eight selected value set combinations

	TR		r^2	LM_{mo}		LM_{om}		RMA		Error		
	obs	mod		a	b	a	b	a	b	MSE	SMSE	PBIAS
1-Ri -Shi-er-Txyz	8.65	5.14	0.18	0.10	4.31	0.33	6.94	0.54	0.50	28.11	5.30	40.62
5-Ri -Shi-er-Txyz	8.65	4.89	0.43	0.19	3.23	0.94	4.03	0.45	0.98	30.06	5.48	43.44
10-Ri -Shi-er-Txyz	8.65	4.66	0.78	0.34	1.76	1.81	0.20	0.43	0.94	31.94	5.65	46.15
1-Gi -Shi-er-Txyz	8.65	5.14	0.18	0.10	4.29	0.34	6.89	0.53	0.51	28.11	5.30	40.62
5-Gi -Shi-er-Txyz	8.65	4.87	0.46	0.20	3.10	1.03	3.62	0.45	1.02	30.27	5.50	43.73
10-Gi -Shi-er-Txyz	8.65	4.63	0.83	0.36	1.48	1.88	-0.07	0.44	0.83	32.14	5.67	46.44
1-Ri -La -Txyz	8.65	5.56	0.12	0.09	4.81	0.18	7.67	0.70	-0.51	24.73	4.97	35.74
5-Ri -La -Txyz	8.65	5.56	0.27	0.18	4.01	0.42	6.31	0.65	-0.08	24.69	4.97	35.68
10-Ri -La -Txyz	8.65	5.34	0.54	0.32	2.60	0.92	3.71	0.59	0.28	26.45	5.14	38.22
1-Gi -La -Txyz	8.65	5.60	0.13	0.09	4.83	0.18	7.66	0.71	-0.52	24.44	4.94	35.32
5-Gi -La -Txyz	8.65	5.54	0.30	0.19	3.89	0.46	6.09	0.64	-0.02	24.89	4.99	35.96
10-Gi -La -Txyz	8.65	5.32	0.59	0.35	2.33	1.01	3.25	0.58	0.27	26.63	5.16	38.48
1-Ri -Shi-er-Tz	8.65	4.03	0.38	0.16	2.65	0.93	4.91	0.41	0.45	37.00	6.08	53.46
5-Ri -Shi-er-Tz	8.65	4.20	0.44	0.20	2.43	0.94	4.70	0.47	0.17	35.59	5.97	51.42
10-Ri -Shi-er-Tz	8.65	1.57	0.39	0.07	0.95	2.07	5.41	0.19	-0.04	56.66	7.53	81.86
1-Gi -Shi-er-Tz	8.65	4.03	0.39	0.16	2.65	0.93	4.91	0.41	0.44	36.95	6.08	53.39
5-Gi -Shi-er-Tz	8.65	4.23	0.44	0.21	2.41	0.94	4.68	0.47	0.13	35.40	5.95	51.14
10-Gi -Shi-er-Tz	8.65	1.58	0.39	0.07	0.95	2.06	5.40	0.19	-0.05	56.60	7.52	81.79
1-Ri -La -Tz	8.65	4.21	0.31	0.15	2.92	0.65	5.92	0.48	0.07	35.56	5.96	51.39
5-Ri -La -Tz	8.65	4.30	0.34	0.17	2.83	0.67	5.76	0.50	-0.05	34.79	5.90	50.26
10-Ri -La -Tz	8.65	1.68	0.15	0.04	1.37	0.66	7.55	0.23	-0.32	55.80	7.47	80.62
1-Gi -La -Tz	8.65	4.10	0.29	0.13	2.98	0.64	6.05	0.45	0.21	36.43	6.04	52.63
5-Gi -La -Tz	8.65	4.33	0.35	0.18	2.80	0.68	5.72	0.51	-0.08	34.59	5.88	49.98
10-Gi -La -Tz	8.65	1.68	0.15	0.04	1.38	0.66	7.54	0.23	-0.32	55.74	7.47	80.54

Table A.33: Calibration statistics for modelled and observed interstitial deposition in S2Q30D48-2, shear stress deposition model

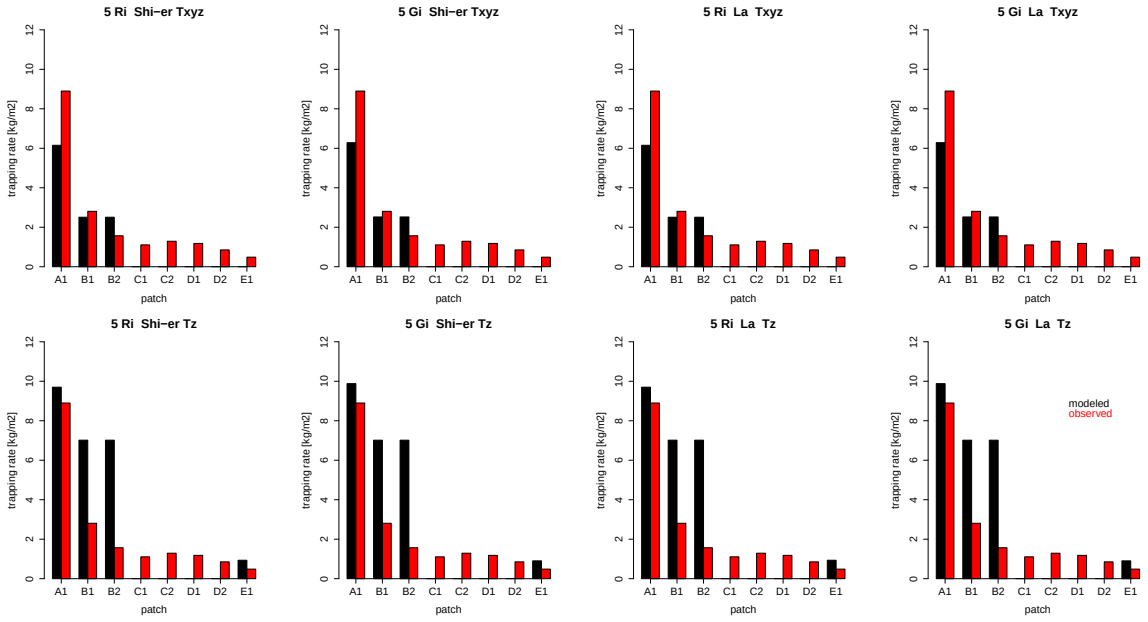

Figure A.30: Modelled and observed interstitial deposition in S2Q100D37-s1, shear stress deposition model for eight selected value set combinations

	TR		r^2	LM_{mo}		LM_{om}		RMA		Error		
	obs	mod		a	b	a	b	a	b	MSE	SMSE	PBIAS
1-Ri -Shi-er-Txyz	2.27	1.25	0.91	0.64	-0.20	1.31	0.64	0.70	-0.34	8.22	2.87	45.21
5-Ri -Shi-er-Txyz	2.27	1.40	0.93	0.75	-0.32	1.16	0.66	0.81	-0.44	7.02	2.65	38.60
10-Ri -Shi-er-Txyz	2.27	1.61	0.96	0.94	-0.53	0.97	0.70	0.98	-0.62	5.29	2.30	29.06
1-Gi -Shi-er-Txyz	2.27	1.25	0.91	0.64	-0.20	1.31	0.64	0.70	-0.34	8.20	2.86	45.05
5-Gi -Shi-er-Txyz	2.27	1.42	0.94	0.77	-0.34	1.14	0.66	0.82	-0.46	6.86	2.62	37.73
10-Gi -Shi-er-Txyz	2.27	1.66	0.96	0.99	-0.58	0.94	0.72	1.02	-0.67	4.91	2.22	27.01
1-Ri -La -Txyz	2.27	1.25	0.91	0.64	-0.20	1.31	0.64	0.70	-0.34	8.22	2.87	45.21
5-Ri -La -Txyz	2.27	1.40	0.93	0.75	-0.32	1.16	0.66	0.81	-0.44	7.02	2.65	38.60
10-Ri -La -Txyz	2.27	1.61	0.96	0.94	-0.53	0.97	0.70	0.98	-0.62	5.29	2.30	29.06
1-Gi -La -Txyz	2.27	1.25	0.91	0.64	-0.20	1.31	0.64	0.70	-0.34	8.20	2.86	45.05
5-Gi -La -Txyz	2.27	1.42	0.94	0.77	-0.34	1.14	0.66	0.82	-0.46	6.86	2.62	37.73
10-Gi -La -Txyz	2.27	1.66	0.96	0.99	-0.58	0.94	0.72	1.02	-0.67	4.91	2.22	27.01
1-Ri -Shi-er-Tz	2.27	2.93	0.72	0.97	0.72	0.53	0.73	1.36	-0.16	-5.27	2.29	-28.95
5-Ri -Shi-er-Tz	2.27	3.08	0.78	1.15	0.47	0.52	0.66	1.48	-0.29	-6.48	2.54	-35.60
10-Ri -Shi-er-Tz	2.27	3.26	0.85	1.41	0.06	0.51	0.60	1.66	-0.51	-7.90	2.81	-43.41
1-Gi -Shi-er-Tz	2.27	2.94	0.72	0.98	0.71	0.53	0.73	1.36	-0.17	-5.30	2.30	-29.11
5-Gi -Shi-er-Tz	2.27	3.10	0.78	1.17	0.44	0.52	0.65	1.50	-0.31	-6.62	2.57	-36.40
10-Gi -Shi-er-Tz	2.27	3.29	0.86	1.46	-0.03	0.51	0.60	1.70	-0.56	-8.15	2.85	-44.79
1-Ri -La -Tz	2.27	3.01	0.75	1.06	0.60	0.52	0.70	1.42	-0.22	-5.87	2.42	-32.29
5-Ri -La -Tz	2.27	3.08	0.78	1.15	0.47	0.52	0.66	1.48	-0.29	-6.48	2.54	-35.60
10-Ri -La -Tz	2.27	3.26	0.85	1.41	0.06	0.51	0.60	1.66	-0.51	-7.90	2.81	-43.41
1-Gi -La -Tz	2.27	2.94	0.72	0.98	0.71	0.53	0.73	1.36	-0.17	-5.30	2.30	-29.11
5-Gi -La -Tz	2.27	3.10	0.78	1.17	0.44	0.52	0.65	1.50	-0.31	-6.62	2.57	-36.40
10-Gi -La -Tz	2.27	3.29	0.86	1.46	-0.03	0.51	0.60	1.70	-0.56	-8.15	2.85	-44.79

Table A.34: Calibration statistics for modelled and observed interstitial deposition in S2Q30D37-s1, shear stress deposition model

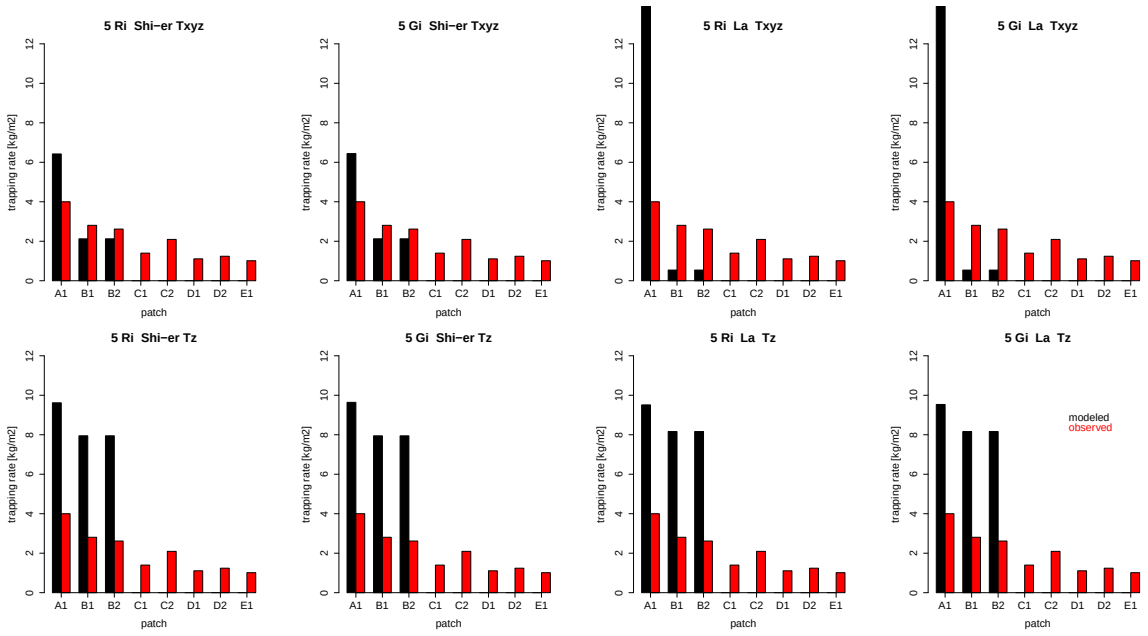

Figure A.31: Modelled and observed interstitial deposition in S2Q100D37-s2, shear stress deposition model for eight selected value set combinations

	TR		r^2	LM_{mo}		LM_{om}		RMA		Error		
	obs	mod		a	b	a	b	a	b	MSE	SMSE	PBIAS
1-Ri -Shi-er-Txyz	2.03	1.27	0.93	1.89	-2.58	0.46	1.45	2.04	-2.87	6.11	2.47	37.56
5-Ri -Shi-er-Txyz	2.03	1.33	0.93	2.00	-2.74	0.43	1.46	2.16	-3.06	5.61	2.37	34.47
10-Ri -Shi-er-Txyz	2.03	1.38	0.92	2.09	-2.87	0.41	1.47	2.26	-3.22	5.25	2.29	32.27
1-Gi -Shi-er-Txyz	2.03	1.28	0.93	1.91	-2.60	0.45	1.45	2.05	-2.89	6.04	2.46	37.13
5-Gi -Shi-er-Txyz	2.03	1.34	0.93	2.01	-2.75	0.43	1.46	2.16	-3.07	5.59	2.36	34.35
10-Gi -Shi-er-Txyz	2.03	1.38	0.92	2.10	-2.89	0.41	1.47	2.27	-3.24	5.21	2.28	32.01
1-Ri -La -Txyz	2.03	1.41	0.79	2.68	-4.05	0.23	1.71	3.38	-5.48	5.02	2.24	30.82
5-Ri -La -Txyz	2.03	1.92	0.78	3.71	-5.64	0.16	1.72	4.74	-7.74	0.95	0.98	5.85
10-Ri -La -Txyz	2.03	2.07	0.78	4.04	-6.14	0.15	1.72	5.17	-8.45	-0.31	0.56	-1.91
1-Gi -La -Txyz	2.03	1.44	0.79	2.75	-4.15	0.23	1.71	3.47	-5.62	4.76	2.18	29.22
5-Gi -La -Txyz	2.03	1.95	0.78	3.78	-5.74	0.16	1.72	4.83	-7.89	0.68	0.83	4.18
10-Gi -La -Txyz	2.03	2.09	0.78	4.06	-6.18	0.15	1.72	5.21	-8.52	-0.42	0.65	-2.57
1-Ri -Shi-er-Tz	2.03	3.03	0.90	3.60	-4.30	0.23	1.35	3.99	-5.09	-7.93	2.82	-48.73
5-Ri -Shi-er-Tz	2.03	3.19	0.91	3.83	-4.61	0.22	1.35	4.21	-5.39	-9.23	3.04	-56.71
10-Ri -Shi-er-Tz	2.03	3.23	0.92	3.94	-4.78	0.21	1.34	4.29	-5.50	-9.59	3.10	-58.89
1-Gi -Shi-er-Tz	2.03	3.06	0.90	3.64	-4.35	0.22	1.35	4.03	-5.14	-8.17	2.86	-50.20
5-Gi -Shi-er-Tz	2.03	3.19	0.91	3.84	-4.62	0.22	1.35	4.22	-5.39	-9.25	3.04	-56.83
10-Gi -Shi-er-Tz	2.03	3.24	0.92	3.95	-4.80	0.21	1.34	4.30	-5.51	-9.63	3.10	-59.14
1-Ri -La -Tz	2.03	3.20	0.90	3.80	-4.52	0.21	1.35	4.22	-5.38	-9.35	3.06	-57.44
5-Ri -La -Tz	2.03	3.23	0.90	3.84	-4.59	0.21	1.35	4.26	-5.43	-9.56	3.09	-58.72
10-Ri -La -Tz	2.03	3.27	0.91	3.94	-4.74	0.21	1.35	4.32	-5.53	-9.88	3.14	-60.71
1-Gi -La -Tz	2.03	3.03	0.90	3.57	-4.24	0.23	1.35	3.98	-5.08	-7.94	2.82	-48.75
5-Gi -La -Tz	2.03	3.23	0.90	3.85	-4.60	0.21	1.35	4.26	-5.44	-9.58	3.10	-58.85
10-Gi -La -Tz	2.03	3.27	0.91	3.95	-4.76	0.21	1.35	4.33	-5.54	-9.92	3.15	-60.93

Table A.35: Calibration statistics for modelled and observed interstitial deposition in S2Q30D37-s2, shear stress deposition model

A.1.6 Step 2, sandy experimental runs with adapted critical shear stress

Figure A.32: Calibration statistics for modelled and observed concentration loss in S2Q100D48-s1, shear stress deposition model

	r^2	LM_{mo}		LM_{om}		RMA		Error		
		a	b	a	b	a	b	MSE	SMSE	PBIAS
1 D Ri ad1 Txyz	0.99	0.96	0.10	1.01	-0.08	0.98	0.09	-0.48	0.69	-17.83
5 D Ri ad1 Txyz	1.00	1.01	-0.03	0.99	0.03	1.01	-0.03	0.13	0.35	4.67
10 D Ri ad1 Txyz	1.00	1.01	-0.04	0.99	0.03	1.01	-0.04	0.17	0.42	6.50
1 L Ri ad1 Txyz	0.99	0.96	0.10	1.01	-0.08	0.98	0.09	-0.48	0.69	-17.83
5 L Ri ad1 Txyz	1.00	1.01	-0.03	0.99	0.03	1.01	-0.03	0.13	0.35	4.67
10 L Ri ad1 Txyz	1.00	1.01	-0.04	0.99	0.03	1.01	-0.04	0.17	0.42	6.50
1 D Gi ad1 Txyz	0.99	0.97	0.08	1.01	-0.07	0.98	0.08	-0.41	0.64	-15.28
5 D Gi ad1 Txyz	1.00	1.01	-0.03	0.99	0.03	1.01	-0.03	0.14	0.37	5.13
10 D Gi ad1 Txyz	1.00	1.01	-0.04	0.99	0.04	1.01	-0.04	0.18	0.42	6.64
1 L Gi ad1 Txyz	0.99	0.97	0.08	1.01	-0.07	0.98	0.08	-0.41	0.64	-15.28
5 L Gi ad1 Txyz	1.00	1.01	-0.03	0.99	0.03	1.01	-0.03	0.14	0.37	5.13
10 L Gi ad1 Txyz	1.00	1.01	-0.04	0.99	0.04	1.01	-0.04	0.18	0.42	6.64
1 D Ri ad2 Txyz	0.99	0.97	0.08	1.01	-0.07	0.98	0.07	-0.39	0.63	-14.67
5 D Ri ad2 Txyz	1.00	1.01	-0.03	0.99	0.03	1.01	-0.03	0.13	0.37	4.99
10 D Ri ad2 Txyz	1.00	1.01	-0.04	0.99	0.04	1.01	-0.04	0.18	0.42	6.59
1 L Ri ad2 Txyz	0.99	0.97	0.08	1.01	-0.07	0.98	0.07	-0.39	0.63	-14.67
5 L Ri ad2 Txyz	1.00	1.01	-0.03	0.99	0.03	1.01	-0.03	0.13	0.37	4.99
10 L Ri ad2 Txyz	1.00	1.01	-0.04	0.99	0.04	1.01	-0.04	0.18	0.42	6.59
1 D Gi ad2 Txyz	0.99	0.97	0.07	1.01	-0.06	0.98	0.06	-0.33	0.58	-12.39
5 D Gi ad2 Txyz	1.00	1.01	-0.03	0.99	0.03	1.01	-0.03	0.15	0.38	5.41
10 D Gi ad2 Txyz	1.00	1.01	-0.04	0.99	0.04	1.01	-0.04	0.18	0.42	6.71
1 L Gi ad2 Txyz	0.99	0.97	0.07	1.01	-0.06	0.98	0.06	-0.33	0.58	-12.39
5 L Gi ad2 Txyz	1.00	1.01	-0.03	0.99	0.03	1.01	-0.03	0.15	0.38	5.41
10 L Gi ad2 Txyz	1.00	1.01	-0.04	0.99	0.04	1.01	-0.04	0.18	0.42	6.71
1 D Ri ad1 Tz	0.97	0.94	0.16	1.01	-0.14	0.96	0.15	-0.81	0.90	-30.21
5 D Ri ad1 Tz	1.00	1.01	-0.02	0.99	0.02	1.01	-0.02	0.08	0.28	2.96
10 D Ri ad1 Tz	1.00	1.01	-0.03	0.99	0.03	1.01	-0.03	0.16	0.40	5.88
1 L Ri ad1 Tz	0.97	0.94	0.16	1.01	-0.14	0.96	0.15	-0.81	0.90	-30.21
5 L Ri ad1 Tz	1.00	1.01	-0.02	0.99	0.02	1.01	-0.02	0.08	0.28	2.96
10 L Ri ad1 Tz	1.00	1.01	-0.03	0.99	0.03	1.01	-0.03	0.16	0.40	5.88
1 D Gi ad1 Tz	0.97	0.94	0.14	1.01	-0.12	0.97	0.13	-0.72	0.85	-26.66
5 D Gi ad1 Tz	1.00	1.01	-0.02	0.99	0.02	1.01	-0.02	0.10	0.31	3.63
10 D Gi ad1 Tz	1.00	1.01	-0.03	0.99	0.03	1.01	-0.03	0.17	0.41	6.17
1 L Gi ad1 Tz	0.97	0.94	0.14	1.01	-0.12	0.97	0.13	-0.72	0.85	-26.66
5 L Gi ad1 Tz	1.00	1.01	-0.02	0.99	0.02	1.01	-0.02	0.10	0.31	3.63
10 L Gi ad1 Tz	1.00	1.01	-0.03	0.99	0.03	1.01	-0.03	0.17	0.41	6.17
1 D Ri ad2 Tz	1.00	1.00	0.00	1.00	-0.00	1.00	0.00	-0.01	0.12	-0.55
5 D Ri ad2 Tz	1.00	1.01	-0.02	0.99	0.02	1.01	-0.02	0.09	0.31	3.53
10 D Ri ad2 Tz	1.00	1.01	-0.03	0.99	0.03	1.01	-0.03	0.16	0.40	6.07
1 L Ri ad2 Tz	0.98	0.95	0.13	1.01	-0.12	0.97	0.12	-0.65	0.81	-24.35
5 L Ri ad2 Tz	1.00	1.01	-0.02	0.99	0.02	1.01	-0.02	0.09	0.31	3.53
10 L Ri ad2 Tz	1.00	1.01	-0.03	0.99	0.03	1.01	-0.03	0.16	0.40	6.07
1 D Gi ad2 Tz	0.98	0.95	0.12	1.01	-0.10	0.97	0.11	-0.57	0.76	-21.31
5 D Gi ad2 Tz	1.00	1.01	-0.02	0.99	0.02	1.01	-0.02	0.11	0.33	4.13
10 D Gi ad2 Tz	1.00	1.01	-0.03	0.99	0.03	1.01	-0.03	0.17	0.41	6.32
1 L Gi ad2 Tz	0.98	0.95	0.12	1.01	-0.10	0.97	0.11	-0.57	0.76	-21.31
5 L Gi ad2 Tz	1.00	1.01	-0.02	0.99	0.02	1.01	-0.02	0.11	0.33	4.13
10 L Gi ad2 Tz	1.00	1.01	-0.03	0.99	0.03	1.01	-0.03	0.17	0.41	6.32

Table A.36: a Calibration statistics for modelled and observed concentration loss in S2Q100D48-s1, shear stress deposition model

	r^2	LM_{mo}		LM_{om}		RMA		Error		
		a	b	a	b	a	b	MSE	SMSE	PBIAS
1 D Ri ad3 Txyz	0.99	0.97	0.07	1.01	-0.06	0.98	0.07	-0.35	0.59	-12.89
5 D Ri ad3 Txyz	1.00	1.01	-0.03	0.99	0.03	1.01	-0.03	0.14	0.37	5.23
10 D Ri ad3 Txyz	1.00	1.01	-0.04	0.99	0.04	1.01	-0.04	0.18	0.42	6.66
1 L Ri ad3 Txyz	0.99	0.97	0.07	1.01	-0.06	0.98	0.07	-0.35	0.59	-12.89
5 L Ri ad3 Txyz	1.00	1.01	-0.03	0.99	0.03	1.01	-0.03	0.14	0.37	5.23
10 L Ri ad3 Txyz	1.00	1.01	-0.04	0.99	0.04	1.01	-0.04	0.18	0.42	6.66
1 D Gi ad3 Txyz	0.99	0.98	0.06	1.01	-0.05	0.99	0.05	-0.29	0.54	-10.77
5 D Gi ad3 Txyz	1.00	1.01	-0.03	0.99	0.03	1.01	-0.03	0.15	0.39	5.62
10 D Gi ad3 Txyz	1.00	1.01	-0.04	0.99	0.04	1.01	-0.04	0.18	0.43	6.76
1 L Gi ad3 Txyz	0.99	0.98	0.06	1.01	-0.05	0.99	0.05	-0.29	0.54	-10.77
5 L Gi ad3 Txyz	1.00	1.01	-0.03	0.99	0.03	1.01	-0.03	0.15	0.39	5.62
10 L Gi ad3 Txyz	1.00	1.01	-0.04	0.99	0.04	1.01	-0.04	0.18	0.43	6.76
1 D Ri ad4 Txyz	0.99	0.98	0.06	1.01	-0.06	0.98	0.06	-0.31	0.56	-11.66
5 D Ri ad4 Txyz	1.00	1.01	-0.03	0.99	0.03	1.01	-0.03	0.15	0.38	5.42
10 D Ri ad4 Txyz	1.00	1.01	-0.04	0.99	0.04	1.01	-0.04	0.18	0.42	6.71
1 L Ri ad4 Txyz	0.99	0.98	0.06	1.01	-0.06	0.98	0.06	-0.31	0.56	-11.66
5 L Ri ad4 Txyz	1.00	1.01	-0.03	0.99	0.03	1.01	-0.03	0.15	0.38	5.42
10 L Ri ad4 Txyz	1.00	1.01	-0.04	0.99	0.04	1.01	-0.04	0.18	0.42	6.71
1 D Gi ad4 Txyz	0.99	0.98	0.05	1.01	-0.05	0.99	0.05	-0.26	0.51	-9.65
5 D Gi ad4 Txyz	1.00	1.01	-0.03	0.99	0.03	1.01	-0.03	0.16	0.39	5.78
10 D Gi ad4 Txyz	1.00	1.01	-0.04	0.99	0.04	1.01	-0.04	0.18	0.43	6.79
1 L Gi ad4 Txyz	0.99	0.98	0.05	1.01	-0.05	0.99	0.05	-0.26	0.51	-9.65
5 L Gi ad4 Txyz	1.00	1.01	-0.03	0.99	0.03	1.01	-0.03	0.16	0.39	5.78
10 L Gi ad4 Txyz	1.00	1.01	-0.04	0.99	0.04	1.01	-0.04	0.18	0.43	6.79
1 D Ri ad3 Tz	0.98	0.96	0.11	1.01	-0.10	0.97	0.11	-0.56	0.75	-20.67
5 D Ri ad3 Tz	1.00	1.01	-0.02	0.99	0.02	1.01	-0.02	0.10	0.32	3.87
10 D Ri ad3 Tz	1.00	1.01	-0.03	0.99	0.03	1.01	-0.03	0.17	0.41	6.18
1 L Ri ad3 Tz	0.98	0.96	0.11	1.01	-0.10	0.97	0.11	-0.56	0.75	-20.67
5 L Ri ad3 Tz	1.00	1.01	-0.02	0.99	0.02	1.01	-0.02	0.10	0.32	3.87
10 L Ri ad3 Tz	1.00	1.01	-0.03	0.99	0.03	1.01	-0.03	0.17	0.41	6.18
1 D Gi ad3 Tz	0.99	0.96	0.10	1.01	-0.09	0.98	0.09	-0.48	0.69	-17.95
5 D Gi ad3 Tz	1.00	1.01	-0.02	0.99	0.02	1.01	-0.02	0.12	0.34	4.42
10 D Gi ad3 Tz	1.00	1.01	-0.03	0.99	0.03	1.01	-0.03	0.17	0.41	6.41
1 L Gi ad3 Tz	0.99	0.96	0.10	1.01	-0.09	0.98	0.09	-0.48	0.69	-17.95
5 L Gi ad3 Tz	1.00	1.01	-0.02	0.99	0.02	1.01	-0.02	0.12	0.34	4.42
10 L Gi ad3 Tz	1.00	1.01	-0.03	0.99	0.03	1.01	-0.03	0.17	0.41	6.41
1 D Ri ad4 Tz	1.00	1.00	-0.00	1.00	0.01	1.00	-0.01	0.02	0.15	0.86
5 D Ri ad4 Tz	1.00	1.01	-0.02	0.99	0.02	1.01	-0.02	0.11	0.33	4.10
10 D Ri ad4 Tz	1.00	1.01	-0.03	0.99	0.03	1.01	-0.03	0.17	0.41	6.27
1 L Ri ad4 Tz	0.99	0.96	0.10	1.01	-0.09	0.97	0.09	-0.49	0.70	-18.39
5 L Ri ad4 Tz	1.00	1.01	-0.02	0.99	0.02	1.01	-0.02	0.11	0.33	4.10
10 L Ri ad4 Tz	1.00	1.01	-0.03	0.99	0.03	1.01	-0.03	0.17	0.41	6.27
1 D Gi ad4 Tz	0.99	0.97	0.09	1.01	-0.08	0.98	0.08	-0.43	0.65	-15.85
5 D Gi ad4 Tz	1.00	1.01	-0.03	0.99	0.03	1.01	-0.03	0.12	0.35	4.63
10 D Gi ad4 Tz	1.00	1.01	-0.04	0.99	0.03	1.01	-0.04	0.17	0.42	6.48
1 L Gi ad4 Tz	0.99	0.97	0.09	1.01	-0.08	0.98	0.08	-0.43	0.65	-15.85
5 L Gi ad4 Tz	1.00	1.01	-0.03	0.99	0.03	1.01	-0.03	0.12	0.35	4.63
10 L Gi ad4 Tz	1.00	1.01	-0.04	0.99	0.03	1.01	-0.04	0.17	0.42	6.48

Table A.37: b Calibration statistics for modelled and observed concentration loss in S2Q100D48-s1, shear stress deposition model

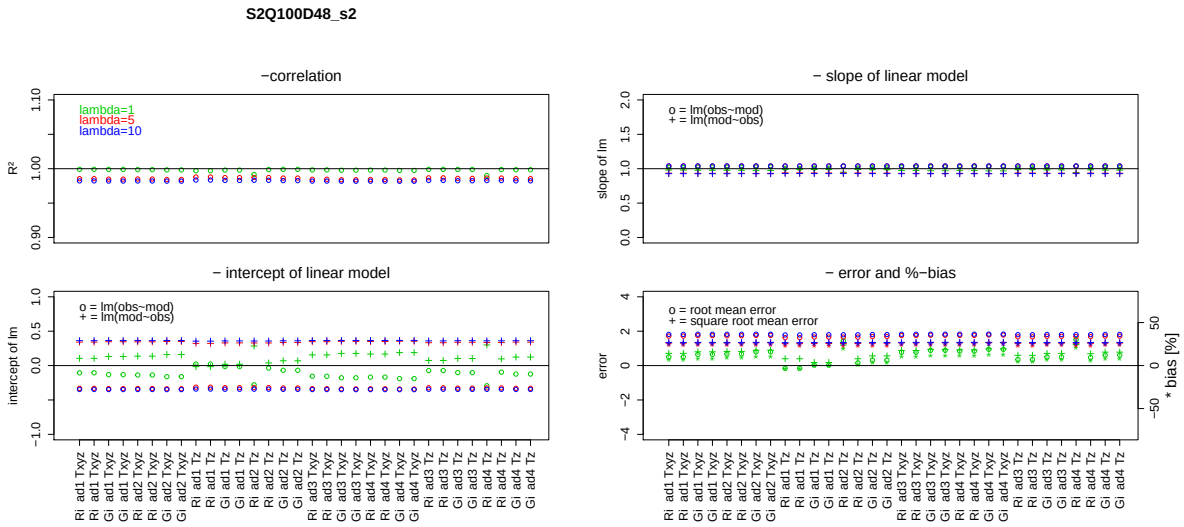

Figure A.33: Calibration statistics for modelled and observed concentration loss in S2Q100D48-s2, shear stress deposition model

	r^2	LM_{mo}		LM_{om}		RMA		Error		
		a	b	a	b	a	b	MSE	SMSE	PBIAS
1 D Ri ad1 Txyz	1.00	1.02	-0.11	0.98	0.11	1.02	-0.11	0.51	0.71	7.42
5 D Ri ad1 Txyz	0.99	1.04	-0.33	0.93	0.34	1.05	-0.35	1.72	1.31	25.10
10 D Ri ad1 Txyz	0.98	1.04	-0.35	0.93	0.36	1.06	-0.37	1.81	1.35	26.53
1 L Ri ad1 Txyz	1.00	1.02	-0.11	0.98	0.11	1.02	-0.11	0.51	0.71	7.42
5 L Ri ad1 Txyz	0.99	1.04	-0.33	0.93	0.34	1.05	-0.35	1.72	1.31	25.10
10 L Ri ad1 Txyz	0.98	1.04	-0.35	0.93	0.36	1.06	-0.37	1.81	1.35	26.53
1 D Gi ad1 Txyz	1.00	1.02	-0.13	0.98	0.13	1.02	-0.13	0.64	0.80	9.42
5 D Gi ad1 Txyz	0.98	1.04	-0.33	0.93	0.35	1.06	-0.35	1.74	1.32	25.46
10 D Gi ad1 Txyz	0.98	1.04	-0.35	0.93	0.36	1.06	-0.37	1.82	1.35	26.65
1 L Gi ad1 Txyz	1.00	1.02	-0.13	0.98	0.13	1.02	-0.13	0.64	0.80	9.42
5 L Gi ad1 Txyz	0.98	1.04	-0.33	0.93	0.35	1.06	-0.35	1.74	1.32	25.46
10 L Gi ad1 Txyz	0.98	1.04	-0.35	0.93	0.36	1.06	-0.37	1.82	1.35	26.65
1 D Ri ad2 Txyz	1.00	1.02	-0.14	0.98	0.14	1.02	-0.14	0.68	0.82	9.90
5 D Ri ad2 Txyz	0.99	1.04	-0.33	0.93	0.35	1.06	-0.35	1.73	1.32	25.35
10 D Ri ad2 Txyz	0.98	1.04	-0.35	0.93	0.36	1.06	-0.37	1.82	1.35	26.61
1 L Ri ad2 Txyz	1.00	1.02	-0.14	0.98	0.14	1.02	-0.14	0.68	0.82	9.90
5 L Ri ad2 Txyz	0.99	1.04	-0.33	0.93	0.35	1.06	-0.35	1.73	1.32	25.35
10 L Ri ad2 Txyz	0.98	1.04	-0.35	0.93	0.36	1.06	-0.37	1.82	1.35	26.61
1 D Gi ad2 Txyz	1.00	1.02	-0.16	0.97	0.16	1.03	-0.16	0.80	0.89	11.69
5 D Gi ad2 Txyz	0.98	1.04	-0.34	0.93	0.35	1.06	-0.36	1.76	1.32	25.68
10 D Gi ad2 Txyz	0.98	1.04	-0.35	0.93	0.36	1.06	-0.37	1.82	1.35	26.70
1 L Gi ad2 Txyz	1.00	1.02	-0.16	0.97	0.16	1.03	-0.16	0.80	0.89	11.69
5 L Gi ad2 Txyz	0.98	1.04	-0.34	0.93	0.35	1.06	-0.36	1.76	1.32	25.68
10 L Gi ad2 Txyz	0.98	1.04	-0.35	0.93	0.36	1.06	-0.37	1.82	1.35	26.70
1 D Ri ad1 Tz	1.00	1.00	0.02	0.99	-0.02	1.01	0.02	-0.16	0.40	-2.31
5 D Ri ad1 Tz	0.99	1.04	-0.31	0.94	0.32	1.05	-0.33	1.62	1.27	23.75
10 D Ri ad1 Tz	0.98	1.04	-0.34	0.93	0.36	1.06	-0.36	1.78	1.33	26.05
1 L Ri ad1 Tz	1.00	1.00	0.02	0.99	-0.02	1.01	0.02	-0.16	0.40	-2.31
5 L Ri ad1 Tz	0.99	1.04	-0.31	0.94	0.32	1.05	-0.33	1.62	1.27	23.75
10 L Ri ad1 Tz	0.98	1.04	-0.34	0.93	0.36	1.06	-0.36	1.78	1.33	26.05
1 D Gi ad1 Tz	1.00	1.01	-0.01	0.99	0.02	1.01	-0.02	0.03	0.18	0.48
5 D Gi ad1 Tz	0.99	1.04	-0.32	0.94	0.33	1.05	-0.34	1.66	1.29	24.28
10 D Gi ad1 Tz	0.98	1.04	-0.34	0.93	0.36	1.06	-0.36	1.80	1.34	26.27
1 L Gi ad1 Tz	1.00	1.01	-0.01	0.99	0.02	1.01	-0.02	0.03	0.18	0.48
5 L Gi ad1 Tz	0.99	1.04	-0.32	0.94	0.33	1.05	-0.34	1.66	1.29	24.28
10 L Gi ad1 Tz	0.98	1.04	-0.34	0.93	0.36	1.06	-0.36	1.80	1.34	26.27
1 D Ri ad2 Tz	0.99	1.04	-0.28	0.95	0.28	1.04	-0.29	1.43	1.20	20.99
5 D Ri ad2 Tz	0.99	1.04	-0.32	0.94	0.33	1.05	-0.34	1.65	1.29	24.21
10 D Ri ad2 Tz	0.98	1.04	-0.34	0.93	0.36	1.06	-0.36	1.79	1.34	26.20
1 L Ri ad2 Tz	1.00	1.01	-0.04	0.99	0.04	1.01	-0.04	0.16	0.40	2.30
5 L Ri ad2 Tz	0.99	1.04	-0.32	0.94	0.33	1.05	-0.34	1.65	1.29	24.21
10 L Ri ad2 Tz	0.98	1.04	-0.34	0.93	0.36	1.06	-0.36	1.79	1.34	26.20
1 D Gi ad2 Tz	1.00	1.01	-0.07	0.98	0.07	1.01	-0.07	0.32	0.57	4.68
5 D Gi ad2 Tz	0.99	1.04	-0.33	0.94	0.34	1.05	-0.34	1.69	1.30	24.68
10 D Gi ad2 Tz	0.98	1.04	-0.35	0.93	0.36	1.06	-0.37	1.80	1.34	26.39
1 L Gi ad2 Tz	1.00	1.01	-0.07	0.98	0.07	1.01	-0.07	0.32	0.57	4.68
5 L Gi ad2 Tz	0.99	1.04	-0.33	0.94	0.34	1.05	-0.34	1.69	1.30	24.68
10 L Gi ad2 Tz	0.98	1.04	-0.35	0.93	0.36	1.06	-0.37	1.80	1.34	26.39

Table A.38: a Calibration statistics for modelled and observed concentration loss in S2Q100D48-s2, shear stress deposition model

	r^2	LM_{mo}		LM_{om}		RMA		Error		
		a	b	a	b	a	b	MSE	SMSE	PBIAS
1 D Ri ad3 Txyz	1.00	1.02	-0.16	0.97	0.16	1.03	-0.16	0.77	0.88	11.30
5 D Ri ad3 Txyz	0.98	1.04	-0.34	0.93	0.35	1.06	-0.35	1.75	1.32	25.54
10 D Ri ad3 Txyz	0.98	1.04	-0.35	0.93	0.36	1.06	-0.37	1.82	1.35	26.66
1 L Ri ad3 Txyz	1.00	1.02	-0.16	0.97	0.16	1.03	-0.16	0.77	0.88	11.30
5 L Ri ad3 Txyz	0.98	1.04	-0.34	0.93	0.35	1.06	-0.35	1.75	1.32	25.54
10 L Ri ad3 Txyz	0.98	1.04	-0.35	0.93	0.36	1.06	-0.37	1.82	1.35	26.66
1 D Gi ad3 Txyz	1.00	1.03	-0.18	0.97	0.18	1.03	-0.18	0.89	0.94	12.96
5 D Gi ad3 Txyz	0.98	1.04	-0.34	0.93	0.35	1.06	-0.36	1.77	1.33	25.84
10 D Gi ad3 Txyz	0.98	1.04	-0.35	0.93	0.37	1.06	-0.37	1.83	1.35	26.74
1 L Gi ad3 Txyz	1.00	1.03	-0.18	0.97	0.18	1.03	-0.18	0.89	0.94	12.96
5 L Gi ad3 Txyz	0.98	1.04	-0.34	0.93	0.35	1.06	-0.36	1.77	1.33	25.84
10 L Gi ad3 Txyz	0.98	1.04	-0.35	0.93	0.37	1.06	-0.37	1.83	1.35	26.74
1 D Ri ad4 Txyz	1.00	1.02	-0.17	0.97	0.17	1.03	-0.17	0.84	0.92	12.26
5 D Ri ad4 Txyz	0.98	1.04	-0.34	0.93	0.35	1.06	-0.36	1.76	1.33	25.69
10 D Ri ad4 Txyz	0.98	1.04	-0.35	0.93	0.36	1.06	-0.37	1.82	1.35	26.70
1 L Ri ad4 Txyz	1.00	1.02	-0.17	0.97	0.17	1.03	-0.17	0.84	0.92	12.26
5 L Ri ad4 Txyz	0.98	1.04	-0.34	0.93	0.35	1.06	-0.36	1.76	1.33	25.69
10 L Ri ad4 Txyz	0.98	1.04	-0.35	0.93	0.36	1.06	-0.37	1.82	1.35	26.70
1 D Gi ad4 Txyz	1.00	1.03	-0.19	0.97	0.19	1.03	-0.19	0.95	0.97	13.85
5 D Gi ad4 Txyz	0.98	1.04	-0.34	0.93	0.35	1.06	-0.36	1.77	1.33	25.97
10 D Gi ad4 Txyz	0.98	1.04	-0.35	0.93	0.37	1.06	-0.37	1.83	1.35	26.76
1 L Gi ad4 Txyz	1.00	1.03	-0.19	0.97	0.19	1.03	-0.19	0.95	0.97	13.85
5 L Gi ad4 Txyz	0.98	1.04	-0.34	0.93	0.35	1.06	-0.36	1.77	1.33	25.97
10 L Gi ad4 Txyz	0.98	1.04	-0.35	0.93	0.37	1.06	-0.37	1.83	1.35	26.76
1 D Ri ad3 Tz	1.00	1.01	-0.07	0.99	0.07	1.01	-0.07	0.35	0.60	5.19
5 D Ri ad3 Tz	0.99	1.04	-0.32	0.94	0.33	1.05	-0.34	1.67	1.29	24.47
10 D Ri ad3 Tz	0.98	1.04	-0.34	0.93	0.36	1.06	-0.37	1.80	1.34	26.29
1 L Ri ad3 Tz	1.00	1.01	-0.07	0.99	0.07	1.01	-0.07	0.35	0.60	5.19
5 L Ri ad3 Tz	0.99	1.04	-0.32	0.94	0.33	1.05	-0.34	1.67	1.29	24.47
10 L Ri ad3 Tz	0.98	1.04	-0.34	0.93	0.36	1.06	-0.37	1.80	1.34	26.29
1 D Gi ad3 Tz	1.00	1.02	-0.10	0.98	0.10	1.02	-0.10	0.50	0.71	7.33
5 D Gi ad3 Tz	0.99	1.04	-0.33	0.94	0.34	1.05	-0.35	1.70	1.30	24.90
10 D Gi ad3 Tz	0.98	1.04	-0.35	0.93	0.36	1.06	-0.37	1.81	1.34	26.46
1 L Gi ad3 Tz	1.00	1.02	-0.10	0.98	0.10	1.02	-0.10	0.50	0.71	7.33
5 L Gi ad3 Tz	0.99	1.04	-0.33	0.94	0.34	1.05	-0.35	1.70	1.30	24.90
10 L Gi ad3 Tz	0.98	1.04	-0.35	0.93	0.36	1.06	-0.37	1.81	1.34	26.46
1 D Ri ad4 Tz	0.99	1.04	-0.29	0.95	0.30	1.05	-0.31	1.51	1.23	22.10
5 D Ri ad4 Tz	0.99	1.04	-0.33	0.94	0.34	1.05	-0.34	1.68	1.30	24.65
10 D Ri ad4 Tz	0.98	1.04	-0.35	0.93	0.36	1.06	-0.37	1.80	1.34	26.36
1 L Ri ad4 Tz	1.00	1.01	-0.10	0.98	0.10	1.02	-0.10	0.48	0.69	6.97
5 L Ri ad4 Tz	0.99	1.04	-0.33	0.94	0.34	1.05	-0.34	1.68	1.30	24.65
10 L Ri ad4 Tz	0.98	1.04	-0.35	0.93	0.36	1.06	-0.37	1.80	1.34	26.36
1 D Gi ad4 Tz	1.00	1.02	-0.12	0.98	0.12	1.02	-0.12	0.61	0.78	8.97
5 D Gi ad4 Tz	0.99	1.04	-0.33	0.93	0.34	1.05	-0.35	1.71	1.31	25.06
10 D Gi ad4 Tz	0.98	1.04	-0.35	0.93	0.36	1.06	-0.37	1.81	1.35	26.52
1 L Gi ad4 Tz	1.00	1.02	-0.12	0.98	0.12	1.02	-0.12	0.61	0.78	8.97
5 L Gi ad4 Tz	0.99	1.04	-0.33	0.93	0.34	1.05	-0.35	1.71	1.31	25.06
10 L Gi ad4 Tz	0.98	1.04	-0.35	0.93	0.36	1.06	-0.37	1.81	1.35	26.52

Table A.39: b Calibration statistics for modelled and observed concentration loss in S2Q100D48-s2, shear stress deposition model

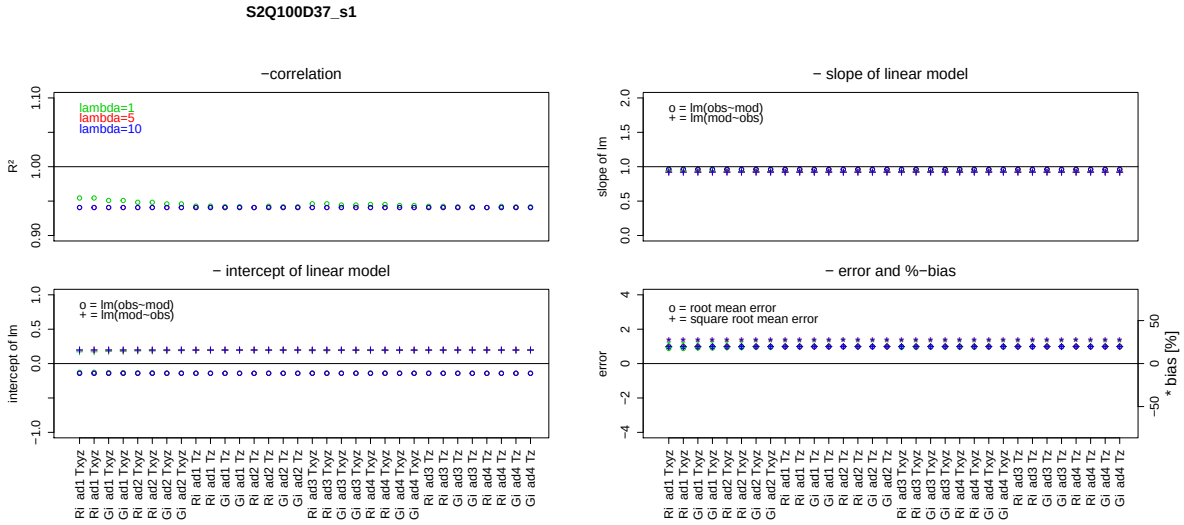

Figure A.34: Calibration statistics for modelled and observed concentration loss in S1Q100D37-s1, shear stress deposition model

	r^2	LM_{mo}		LM_{om}		RMA		Error		
		a	b	a	b	a	b	MSE	SMSE	PBIAS
1 D Ri ad1 Txyz	0.95	0.97	-0.13	0.94	0.17	1.01	-0.15	0.88	0.94	25.15
5 D Ri ad1 Txyz	0.94	0.96	-0.14	0.92	0.20	1.02	-0.18	0.99	0.99	28.31
10 D Ri ad1 Txyz	0.94	0.96	-0.14	0.92	0.20	1.02	-0.18	0.99	0.99	28.31
1 L Ri ad1 Txyz	0.95	0.97	-0.13	0.94	0.17	1.01	-0.15	0.88	0.94	25.15
5 L Ri ad1 Txyz	0.94	0.96	-0.14	0.92	0.20	1.02	-0.18	0.99	0.99	28.31
10 L Ri ad1 Txyz	0.94	0.96	-0.14	0.92	0.20	1.02	-0.18	0.99	0.99	28.31
1 D Gi ad1 Txyz	0.95	0.97	-0.13	0.94	0.18	1.02	-0.16	0.91	0.95	26.00
5 D Gi ad1 Txyz	0.94	0.96	-0.14	0.92	0.20	1.02	-0.18	0.99	0.99	28.31
10 D Gi ad1 Txyz	0.94	0.96	-0.14	0.92	0.20	1.02	-0.18	0.99	0.99	28.31
1 L Gi ad1 Txyz	0.95	0.97	-0.13	0.94	0.18	1.02	-0.16	0.91	0.95	26.00
5 L Gi ad1 Txyz	0.94	0.96	-0.14	0.92	0.20	1.02	-0.18	0.99	0.99	28.31
10 L Gi ad1 Txyz	0.94	0.96	-0.14	0.92	0.20	1.02	-0.18	0.99	0.99	28.31
1 D Ri ad2 Txyz	0.95	0.96	-0.13	0.93	0.18	1.02	-0.16	0.93	0.96	26.61
5 D Ri ad2 Txyz	0.94	0.96	-0.14	0.92	0.20	1.02	-0.18	0.99	0.99	28.31
10 D Ri ad2 Txyz	0.94	0.96	-0.14	0.92	0.20	1.02	-0.18	0.99	0.99	28.31
1 L Ri ad2 Txyz	0.95	0.96	-0.13	0.93	0.18	1.02	-0.16	0.93	0.96	26.61
5 L Ri ad2 Txyz	0.94	0.96	-0.14	0.92	0.20	1.02	-0.18	0.99	0.99	28.31
10 L Ri ad2 Txyz	0.94	0.96	-0.14	0.92	0.20	1.02	-0.18	0.99	0.99	28.31
1 D Gi ad2 Txyz	0.95	0.96	-0.14	0.93	0.19	1.02	-0.17	0.95	0.97	27.15
5 D Gi ad2 Txyz	0.94	0.96	-0.14	0.92	0.20	1.02	-0.18	0.99	0.99	28.31
10 D Gi ad2 Txyz	0.94	0.96	-0.14	0.92	0.20	1.02	-0.18	0.99	0.99	28.31
1 L Gi ad2 Txyz	0.95	0.96	-0.14	0.93	0.19	1.02	-0.17	0.95	0.97	27.15
5 L Gi ad2 Txyz	0.94	0.96	-0.14	0.92	0.20	1.02	-0.18	0.99	0.99	28.31
10 L Gi ad2 Txyz	0.94	0.96	-0.14	0.92	0.20	1.02	-0.18	0.99	0.99	28.31
1 D Ri ad1 Tz	0.94	0.96	-0.14	0.92	0.19	1.02	-0.17	0.97	0.99	27.86
5 D Ri ad1 Tz	0.94	0.96	-0.14	0.92	0.20	1.02	-0.18	0.99	0.99	28.31
10 D Ri ad1 Tz	0.94	0.96	-0.14	0.92	0.20	1.02	-0.18	0.99	0.99	28.31
1 L Ri ad1 Tz	0.94	0.96	-0.14	0.92	0.19	1.02	-0.17	0.97	0.99	27.86
5 L Ri ad1 Tz	0.94	0.96	-0.14	0.92	0.20	1.02	-0.18	0.99	0.99	28.31
10 L Ri ad1 Tz	0.94	0.96	-0.14	0.92	0.20	1.02	-0.18	0.99	0.99	28.31
1 D Gi ad1 Tz	0.94	0.96	-0.14	0.92	0.20	1.02	-0.17	0.98	0.99	28.05
5 D Gi ad1 Tz	0.94	0.96	-0.14	0.92	0.20	1.02	-0.18	0.99	0.99	28.31
10 D Gi ad1 Tz	0.94	0.96	-0.14	0.92	0.20	1.02	-0.18	0.99	0.99	28.31
1 L Gi ad1 Tz	0.94	0.96	-0.14	0.92	0.20	1.02	-0.17	0.98	0.99	28.05
5 L Gi ad1 Tz	0.94	0.96	-0.14	0.92	0.20	1.02	-0.18	0.99	0.99	28.31
10 L Gi ad1 Tz	0.94	0.96	-0.14	0.92	0.20	1.02	-0.18	0.99	0.99	28.31
1 D Ri ad2 Tz	0.94	0.96	-0.14	0.92	0.20	1.02	-0.18	0.99	0.99	28.31
5 D Ri ad2 Tz	0.94	0.96	-0.14	0.92	0.20	1.02	-0.18	0.99	0.99	28.31
10 D Ri ad2 Tz	0.94	0.96	-0.14	0.92	0.20	1.02	-0.18	0.99	0.99	28.31
1 L Ri ad2 Tz	0.94	0.96	-0.14	0.92	0.19	1.02	-0.17	0.97	0.99	27.90
5 L Ri ad2 Tz	0.94	0.96	-0.14	0.92	0.20	1.02	-0.18	0.99	0.99	28.31
10 L Ri ad2 Tz	0.94	0.96	-0.14	0.92	0.20	1.02	-0.18	0.99	0.99	28.31
1 D Gi ad2 Tz	0.94	0.96	-0.14	0.92	0.20	1.02	-0.18	0.98	0.99	28.07
5 D Gi ad2 Tz	0.94	0.96	-0.14	0.92	0.20	1.02	-0.18	0.99	0.99	28.31
10 D Gi ad2 Tz	0.94	0.96	-0.14	0.92	0.20	1.02	-0.18	0.99	0.99	28.31
1 L Gi ad2 Tz	0.94	0.96	-0.14	0.92	0.20	1.02	-0.18	0.98	0.99	28.07
5 L Gi ad2 Tz	0.94	0.96	-0.14	0.92	0.20	1.02	-0.18	0.99	0.99	28.31
10 L Gi ad2 Tz	0.94	0.96	-0.14	0.92	0.20	1.02	-0.18	0.99	0.99	28.31

Table A.40: a Calibration statistics for modelled and observed concentration loss in S2Q100D37-s1, shear stress deposition model

	r^2	LM_{mo}		LM_{om}		RMA		Error		
		a	b	a	b	a	b	MSE	SMSE	PBIAS
1 D Ri ad3 Txyz	0.95	0.96	-0.14	0.93	0.19	1.02	-0.17	0.94	0.97	27.10
5 D Ri ad3 Txyz	0.94	0.96	-0.14	0.92	0.20	1.02	-0.18	0.99	0.99	28.31
10 D Ri ad3 Txyz	0.94	0.96	-0.14	0.92	0.20	1.02	-0.18	0.99	0.99	28.31
1 L Ri ad3 Txyz	0.95	0.96	-0.14	0.93	0.19	1.02	-0.17	0.94	0.97	27.10
5 L Ri ad3 Txyz	0.94	0.96	-0.14	0.92	0.20	1.02	-0.18	0.99	0.99	28.31
10 L Ri ad3 Txyz	0.94	0.96	-0.14	0.92	0.20	1.02	-0.18	0.99	0.99	28.31
1 D Gi ad3 Txyz	0.94	0.96	-0.14	0.93	0.19	1.02	-0.17	0.96	0.98	27.51
5 D Gi ad3 Txyz	0.94	0.96	-0.14	0.92	0.20	1.02	-0.18	0.99	0.99	28.31
10 D Gi ad3 Txyz	0.94	0.96	-0.14	0.92	0.20	1.02	-0.18	0.99	0.99	28.31
1 L Gi ad3 Txyz	0.94	0.96	-0.14	0.93	0.19	1.02	-0.17	0.96	0.98	27.51
5 L Gi ad3 Txyz	0.94	0.96	-0.14	0.92	0.20	1.02	-0.18	0.99	0.99	28.31
10 L Gi ad3 Txyz	0.94	0.96	-0.14	0.92	0.20	1.02	-0.18	0.99	0.99	28.31
1 D Ri ad4 Txyz	0.95	0.96	-0.14	0.93	0.19	1.02	-0.17	0.95	0.98	27.33
5 D Ri ad4 Txyz	0.94	0.96	-0.14	0.92	0.20	1.02	-0.18	0.99	0.99	28.31
10 D Ri ad4 Txyz	0.94	0.96	-0.14	0.92	0.20	1.02	-0.18	0.99	0.99	28.31
1 L Ri ad4 Txyz	0.95	0.96	-0.14	0.93	0.19	1.02	-0.17	0.95	0.98	27.33
5 L Ri ad4 Txyz	0.94	0.96	-0.14	0.92	0.20	1.02	-0.18	0.99	0.99	28.31
10 L Ri ad4 Txyz	0.94	0.96	-0.14	0.92	0.20	1.02	-0.18	0.99	0.99	28.31
1 D Gi ad4 Txyz	0.94	0.96	-0.14	0.93	0.19	1.02	-0.17	0.97	0.98	27.68
5 D Gi ad4 Txyz	0.94	0.96	-0.14	0.92	0.20	1.02	-0.18	0.99	0.99	28.31
10 D Gi ad4 Txyz	0.94	0.96	-0.14	0.92	0.20	1.02	-0.18	0.99	0.99	28.31
1 L Gi ad4 Txyz	0.94	0.96	-0.14	0.93	0.19	1.02	-0.17	0.97	0.98	27.68
5 L Gi ad4 Txyz	0.94	0.96	-0.14	0.92	0.20	1.02	-0.18	0.99	0.99	28.31
10 L Gi ad4 Txyz	0.94	0.96	-0.14	0.92	0.20	1.02	-0.18	0.99	0.99	28.31
1 D Ri ad3 Tz	0.94	0.96	-0.14	0.92	0.19	1.02	-0.17	0.97	0.99	27.92
5 D Ri ad3 Tz	0.94	0.96	-0.14	0.92	0.20	1.02	-0.18	0.99	0.99	28.31
10 D Ri ad3 Tz	0.94	0.96	-0.14	0.92	0.20	1.02	-0.18	0.99	0.99	28.31
1 L Ri ad3 Tz	0.94	0.96	-0.14	0.92	0.19	1.02	-0.17	0.97	0.99	27.92
5 L Ri ad3 Tz	0.94	0.96	-0.14	0.92	0.20	1.02	-0.18	0.99	0.99	28.31
10 L Ri ad3 Tz	0.94	0.96	-0.14	0.92	0.20	1.02	-0.18	0.99	0.99	28.31
1 D Gi ad3 Tz	0.94	0.96	-0.14	0.92	0.20	1.02	-0.18	0.98	0.99	28.09
5 D Gi ad3 Tz	0.94	0.96	-0.14	0.92	0.20	1.02	-0.18	0.99	0.99	28.31
10 D Gi ad3 Tz	0.94	0.96	-0.14	0.92	0.20	1.02	-0.18	0.99	0.99	28.31
1 L Gi ad3 Tz	0.94	0.96	-0.14	0.92	0.20	1.02	-0.18	0.98	0.99	28.09
5 L Gi ad3 Tz	0.94	0.96	-0.14	0.92	0.20	1.02	-0.18	0.99	0.99	28.31
10 L Gi ad3 Tz	0.94	0.96	-0.14	0.92	0.20	1.02	-0.18	0.99	0.99	28.31
1 D Ri ad4 Tz	0.94	0.96	-0.14	0.92	0.20	1.02	-0.18	0.99	0.99	28.31
5 D Ri ad4 Tz	0.94	0.96	-0.14	0.92	0.20	1.02	-0.18	0.99	0.99	28.31
10 D Ri ad4 Tz	0.94	0.96	-0.14	0.92	0.20	1.02	-0.18	0.99	0.99	28.31
1 L Ri ad4 Tz	0.94	0.96	-0.14	0.92	0.19	1.02	-0.17	0.97	0.99	27.93
5 L Ri ad4 Tz	0.94	0.96	-0.14	0.92	0.20	1.02	-0.18	0.99	0.99	28.31
10 L Ri ad4 Tz	0.94	0.96	-0.14	0.92	0.20	1.02	-0.18	0.99	0.99	28.31
1 D Gi ad4 Tz	0.94	0.96	-0.14	0.92	0.20	1.02	-0.18	0.98	0.99	28.09
5 D Gi ad4 Tz	0.94	0.96	-0.14	0.92	0.20	1.02	-0.18	0.99	0.99	28.31
10 D Gi ad4 Tz	0.94	0.96	-0.14	0.92	0.20	1.02	-0.18	0.99	0.99	28.31
1 L Gi ad4 Tz	0.94	0.96	-0.14	0.92	0.20	1.02	-0.18	0.98	0.99	28.09
5 L Gi ad4 Tz	0.94	0.96	-0.14	0.92	0.20	1.02	-0.18	0.99	0.99	28.31
10 L Gi ad4 Tz	0.94	0.96	-0.14	0.92	0.20	1.02	-0.18	0.99	0.99	28.31

Table A.41: b Calibration statistics for modelled and observed concentration loss in S2Q100D37-s1, shear stress deposition model

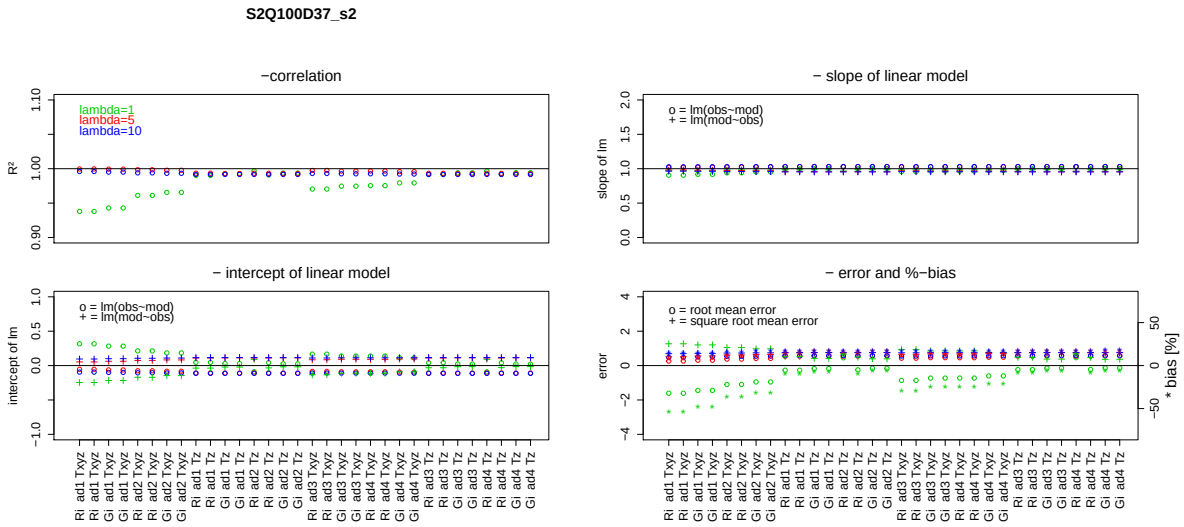

Figure A.35: Calibration statistics for modelled and observed concentration loss in S2Q100D37-s2, shear stress deposition model

	r^2	LM_{mo}		LM_{om}		RMA		Error		
		a	b	a	b	a	b	MSE	SMSE	PBIAS
1 D Ri ad1 Txyz	0.94	0.91	0.32	0.97	-0.25	0.97	0.29	-1.61	1.27	-52.17
5 D Ri ad1 Txyz	1.00	1.02	-0.05	0.98	0.05	1.02	-0.05	0.26	0.51	8.54
10 D Ri ad1 Txyz	1.00	1.03	-0.09	0.96	0.10	1.03	-0.10	0.48	0.69	15.61
1 L Ri ad1 Txyz	0.94	0.91	0.32	0.97	-0.25	0.97	0.29	-1.61	1.27	-52.17
5 L Ri ad1 Txyz	1.00	1.02	-0.05	0.98	0.05	1.02	-0.05	0.26	0.51	8.54
10 L Ri ad1 Txyz	1.00	1.03	-0.09	0.96	0.10	1.03	-0.10	0.48	0.69	15.61
1 D Gi ad1 Txyz	0.94	0.92	0.28	0.97	-0.22	0.97	0.25	-1.44	1.20	-46.79
5 D Gi ad1 Txyz	1.00	1.02	-0.06	0.98	0.06	1.02	-0.06	0.31	0.56	10.14
10 D Gi ad1 Txyz	1.00	1.03	-0.10	0.96	0.10	1.03	-0.10	0.51	0.71	16.41
1 L Gi ad1 Txyz	0.94	0.92	0.28	0.97	-0.22	0.97	0.25	-1.44	1.20	-46.79
5 L Gi ad1 Txyz	1.00	1.02	-0.06	0.98	0.06	1.02	-0.06	0.31	0.56	10.14
10 L Gi ad1 Txyz	1.00	1.03	-0.10	0.96	0.10	1.03	-0.10	0.51	0.71	16.41
1 D Ri ad2 Txyz	0.96	0.94	0.21	0.98	-0.17	0.98	0.19	-1.10	1.05	-35.58
5 D Ri ad2 Txyz	1.00	1.02	-0.08	0.97	0.08	1.03	-0.08	0.38	0.61	12.25
10 D Ri ad2 Txyz	0.99	1.03	-0.10	0.96	0.11	1.04	-0.11	0.53	0.73	17.30
1 L Ri ad2 Txyz	0.96	0.94	0.21	0.98	-0.17	0.98	0.19	-1.10	1.05	-35.58
5 L Ri ad2 Txyz	1.00	1.02	-0.08	0.97	0.08	1.03	-0.08	0.38	0.61	12.25
10 L Ri ad2 Txyz	0.99	1.03	-0.10	0.96	0.11	1.04	-0.11	0.53	0.73	17.30
1 D Gi ad2 Txyz	0.97	0.95	0.18	0.98	-0.15	0.99	0.17	-0.95	0.98	-30.85
5 D Gi ad2 Txyz	1.00	1.03	-0.08	0.97	0.08	1.03	-0.08	0.42	0.64	13.46
10 D Gi ad2 Txyz	0.99	1.03	-0.11	0.96	0.11	1.04	-0.11	0.55	0.74	17.80
1 L Gi ad2 Txyz	0.97	0.95	0.18	0.98	-0.15	0.99	0.17	-0.95	0.98	-30.85
5 L Gi ad2 Txyz	1.00	1.03	-0.08	0.97	0.08	1.03	-0.08	0.42	0.64	13.46
10 L Gi ad2 Txyz	0.99	1.03	-0.11	0.96	0.11	1.04	-0.11	0.55	0.74	17.80
1 D Ri ad1 Tz	0.99	0.99	0.05	0.99	-0.04	1.00	0.04	-0.27	0.52	-8.71
5 D Ri ad1 Tz	0.99	1.03	-0.11	0.96	0.11	1.04	-0.11	0.55	0.74	17.68
10 D Ri ad1 Tz	0.99	1.03	-0.11	0.95	0.12	1.04	-0.12	0.58	0.76	18.90
1 L Ri ad1 Tz	0.99	0.99	0.05	0.99	-0.04	1.00	0.04	-0.27	0.52	-8.71
5 L Ri ad1 Tz	0.99	1.03	-0.11	0.96	0.11	1.04	-0.11	0.55	0.74	17.68
10 L Ri ad1 Tz	0.99	1.03	-0.11	0.95	0.12	1.04	-0.12	0.58	0.76	18.90
1 D Gi ad1 Tz	0.99	1.00	0.03	0.99	-0.02	1.01	0.03	-0.17	0.42	-5.66
5 D Gi ad1 Tz	0.99	1.03	-0.11	0.96	0.11	1.04	-0.11	0.56	0.75	18.10
10 D Gi ad1 Tz	0.99	1.03	-0.11	0.95	0.12	1.04	-0.12	0.58	0.76	18.93
1 L Gi ad1 Tz	0.99	1.00	0.03	0.99	-0.02	1.01	0.03	-0.17	0.42	-5.66
5 L Gi ad1 Tz	0.99	1.03	-0.11	0.96	0.11	1.04	-0.11	0.56	0.75	18.10
10 L Gi ad1 Tz	0.99	1.03	-0.11	0.95	0.12	1.04	-0.12	0.58	0.76	18.93
1 D Ri ad2 Tz	1.00	1.03	-0.09	0.97	0.09	1.03	-0.09	0.45	0.67	14.70
5 D Ri ad2 Tz	0.99	1.03	-0.11	0.96	0.11	1.04	-0.11	0.55	0.74	17.74
10 D Ri ad2 Tz	0.99	1.03	-0.11	0.95	0.12	1.04	-0.12	0.58	0.76	18.90
1 L Ri ad2 Tz	0.99	1.00	0.04	0.99	-0.03	1.01	0.04	-0.25	0.50	-8.01
5 L Ri ad2 Tz	0.99	1.03	-0.11	0.96	0.11	1.04	-0.11	0.55	0.74	17.74
10 L Ri ad2 Tz	0.99	1.03	-0.11	0.95	0.12	1.04	-0.12	0.58	0.76	18.90
1 D Gi ad2 Tz	0.99	1.00	0.03	0.99	-0.02	1.01	0.02	-0.15	0.39	-5.01
5 D Gi ad2 Tz	0.99	1.03	-0.11	0.96	0.11	1.04	-0.11	0.56	0.75	18.15
10 D Gi ad2 Tz	0.99	1.03	-0.11	0.95	0.12	1.04	-0.12	0.58	0.76	18.93
1 L Gi ad2 Tz	0.99	1.00	0.03	0.99	-0.02	1.01	0.02	-0.15	0.39	-5.01
5 L Gi ad2 Tz	0.99	1.03	-0.11	0.96	0.11	1.04	-0.11	0.56	0.75	18.15
10 L Gi ad2 Tz	0.99	1.03	-0.11	0.95	0.12	1.04	-0.12	0.58	0.76	18.93

Table A.42: a Calibration statistics for modelled and observed concentration loss in S2Q100D37-s2, shear stress deposition model

	r^2	LM_{mo}		LM_{om}		RMA		Error		
		a	b	a	b	a	b	MSE	SMSE	PBIAS
10 D Ri ad3 Txyz	0.99	1.03	-0.11	0.96	0.11	1.04	-0.11	0.55	0.74	17.96
1 L Ri ad3 Txyz	0.97	0.96	0.17	0.98	-0.13	0.99	0.15	-0.86	0.93	-27.95
5 L Ri ad3 Txyz	1.00	1.03	-0.08	0.97	0.09	1.03	-0.09	0.43	0.65	13.89
10 L Ri ad3 Txyz	0.99	1.03	-0.11	0.96	0.11	1.04	-0.11	0.55	0.74	17.96
1 D Gi ad3 Txyz	0.97	0.97	0.14	0.98	-0.11	0.99	0.13	-0.73	0.85	-23.62
5 D Gi ad3 Txyz	1.00	1.03	-0.09	0.97	0.09	1.03	-0.09	0.46	0.68	14.92
10 D Gi ad3 Txyz	0.99	1.03	-0.11	0.96	0.11	1.04	-0.11	0.56	0.75	18.31
1 L Gi ad3 Txyz	0.97	0.97	0.14	0.98	-0.11	0.99	0.13	-0.73	0.85	-23.62
5 L Gi ad3 Txyz	1.00	1.03	-0.09	0.97	0.09	1.03	-0.09	0.46	0.68	14.92
10 L Gi ad3 Txyz	0.99	1.03	-0.11	0.96	0.11	1.04	-0.11	0.56	0.75	18.31
1 D Ri ad4 Txyz	0.98	0.97	0.14	0.99	-0.11	0.99	0.13	-0.73	0.85	-23.54
5 D Ri ad4 Txyz	1.00	1.03	-0.09	0.97	0.09	1.03	-0.09	0.46	0.68	14.82
10 D Ri ad4 Txyz	0.99	1.03	-0.11	0.96	0.11	1.04	-0.11	0.56	0.75	18.28
1 L Ri ad4 Txyz	0.98	0.97	0.14	0.99	-0.11	0.99	0.13	-0.73	0.85	-23.54
5 L Ri ad4 Txyz	1.00	1.03	-0.09	0.97	0.09	1.03	-0.09	0.46	0.68	14.82
10 L Ri ad4 Txyz	0.99	1.03	-0.11	0.96	0.11	1.04	-0.11	0.56	0.75	18.28
1 D Gi ad4 Txyz	0.98	0.97	0.11	0.98	-0.09	0.99	0.10	-0.60	0.78	-19.48
5 D Gi ad4 Txyz	1.00	1.03	-0.10	0.96	0.10	1.03	-0.10	0.49	0.70	15.73
10 D Gi ad4 Txyz	0.99	1.03	-0.11	0.95	0.11	1.04	-0.12	0.57	0.76	18.54
1 L Gi ad4 Txyz	0.98	0.97	0.11	0.98	-0.09	0.99	0.10	-0.60	0.78	-19.48
5 L Gi ad4 Txyz	1.00	1.03	-0.10	0.96	0.10	1.03	-0.10	0.49	0.70	15.73
10 L Gi ad4 Txyz	0.99	1.03	-0.11	0.95	0.11	1.04	-0.12	0.57	0.76	18.54
1 D Ri ad3 Tz	0.99	1.00	0.04	0.99	-0.03	1.01	0.04	-0.23	0.48	-7.59
5 D Ri ad3 Tz	0.99	1.03	-0.11	0.96	0.11	1.04	-0.11	0.55	0.74	17.79
10 D Ri ad3 Tz	0.99	1.03	-0.11	0.95	0.12	1.04	-0.12	0.58	0.76	18.91
1 L Ri ad3 Tz	0.99	1.00	0.04	0.99	-0.03	1.01	0.04	-0.23	0.48	-7.59
5 L Ri ad3 Tz	0.99	1.03	-0.11	0.96	0.11	1.04	-0.11	0.55	0.74	17.79
10 L Ri ad3 Tz	0.99	1.03	-0.11	0.95	0.12	1.04	-0.12	0.58	0.76	18.91
1 D Gi ad3 Tz	0.99	1.00	0.02	0.99	-0.02	1.01	0.02	-0.14	0.38	-4.62
5 D Gi ad3 Tz	0.99	1.03	-0.11	0.96	0.11	1.04	-0.11	0.56	0.75	18.18
10 D Gi ad3 Tz	0.99	1.03	-0.11	0.95	0.12	1.04	-0.12	0.58	0.76	18.94
1 L Gi ad3 Tz	0.99	1.00	0.02	0.99	-0.02	1.01	0.02	-0.14	0.38	-4.62
5 L Gi ad3 Tz	0.99	1.03	-0.11	0.96	0.11	1.04	-0.11	0.56	0.75	18.18
10 L Gi ad3 Tz	0.99	1.03	-0.11	0.95	0.12	1.04	-0.12	0.58	0.76	18.94
1 D Ri ad4 Tz	1.00	1.03	-0.09	0.97	0.09	1.03	-0.09	0.46	0.68	14.87
5 D Ri ad4 Tz	0.99	1.03	-0.11	0.96	0.11	1.04	-0.11	0.55	0.74	17.82
10 D Ri ad4 Tz	0.99	1.03	-0.11	0.95	0.12	1.04	-0.12	0.58	0.76	18.91
1 L Ri ad4 Tz	0.99	1.00	0.04	0.99	-0.03	1.01	0.03	-0.23	0.47	-7.31
5 L Ri ad4 Tz	0.99	1.03	-0.11	0.96	0.11	1.04	-0.11	0.55	0.74	17.82
10 L Ri ad4 Tz	0.99	1.03	-0.11	0.95	0.12	1.04	-0.12	0.58	0.76	18.91
1 D Gi ad4 Tz	0.99	1.00	0.02	0.99	-0.01	1.01	0.02	-0.13	0.37	-4.35
5 D Gi ad4 Tz	0.99	1.03	-0.11	0.96	0.11	1.04	-0.11	0.56	0.75	18.21
10 D Gi ad4 Tz	0.99	1.03	-0.11	0.95	0.12	1.04	-0.12	0.58	0.76	18.94
1 L Gi ad4 Tz	0.99	1.00	0.02	0.99	-0.01	1.01	0.02	-0.13	0.37	-4.35
5 L Gi ad4 Tz	0.99	1.03	-0.11	0.96	0.11	1.04	-0.11	0.56	0.75	18.21
10 L Gi ad4 Tz	0.99	1.03	-0.11	0.95	0.12	1.04	-0.12	0.58	0.76	18.94

Table A.43: b Calibration statistics for modelled and observed concentration loss in S2Q100D37-s2, shear stress deposition model

A.1.7 Step 3, sandy experimental runs with adapted critical shear stress

	TR		r^2	LM_{mo}		LM_{om}		RMA		Error		
	obs	mod		a	b	a	b	a	b	MSE	SMSE	PBIAS
1 Ri ad1 Txyz	2.57	2.12	0.39	0.20	1.61	0.77	0.95	0.51	0.81	3.64	1.91	17.68
5 Ri ad1 Txyz	2.57	2.14	0.53	0.31	1.33	0.90	0.65	0.59	0.62	3.48	1.87	16.92
10 Ri ad1 Txyz	2.57	0.82	0.47	0.11	0.54	2.08	0.86	0.23	0.24	14.02	3.74	68.14
1 Ri ad1 Txyz	2.57	2.12	0.39	0.20	1.61	0.77	0.95	0.51	0.81	3.64	1.91	17.68
5 Ri ad1 Txyz	2.57	2.14	0.53	0.31	1.33	0.90	0.65	0.59	0.62	3.48	1.87	16.92
10 Ri ad1 Txyz	2.57	0.82	0.47	0.11	0.54	2.08	0.86	0.23	0.24	14.02	3.74	68.14
1 Gi ad1 Txyz	2.57	2.12	0.39	0.20	1.60	0.77	0.94	0.51	0.81	3.63	1.91	17.65
5 Gi ad1 Txyz	2.57	2.14	0.54	0.33	1.30	0.90	0.64	0.60	0.60	3.43	1.85	16.66
10 Gi ad1 Txyz	2.57	0.82	0.48	0.11	0.54	2.09	0.86	0.23	0.23	14.02	3.74	68.10
1 Gi ad1 Txyz	2.57	2.12	0.39	0.20	1.60	0.77	0.94	0.51	0.81	3.63	1.91	17.65
5 Gi ad1 Txyz	2.57	2.14	0.54	0.33	1.30	0.90	0.64	0.60	0.60	3.43	1.85	16.66
10 Gi ad1 Txyz	2.57	0.82	0.48	0.11	0.54	2.09	0.86	0.23	0.23	14.02	3.74	68.10
1 Ri ad2 Txyz	2.57	2.11	0.38	0.19	1.63	0.79	0.91	0.49	0.86	3.69	1.92	17.93
5 Ri ad2 Txyz	2.57	2.12	0.57	0.32	1.30	1.03	0.39	0.56	0.68	3.59	1.89	17.44
10 Ri ad2 Txyz	2.57	0.81	0.52	0.11	0.53	2.41	0.61	0.21	0.26	14.08	3.75	68.41
1 Ri ad2 Txyz	2.57	2.11	0.38	0.19	1.63	0.79	0.91	0.49	0.86	3.69	1.92	17.93
5 Ri ad2 Txyz	2.57	2.12	0.57	0.32	1.30	1.03	0.39	0.56	0.68	3.59	1.89	17.44
10 Ri ad2 Txyz	2.57	0.81	0.52	0.11	0.53	2.41	0.61	0.21	0.26	14.08	3.75	68.41
1 Gi ad2 Txyz	2.57	2.11	0.39	0.19	1.62	0.80	0.89	0.49	0.86	3.69	1.92	17.91
5 Gi ad2 Txyz	2.57	2.13	0.59	0.34	1.26	1.03	0.38	0.58	0.65	3.53	1.88	17.14
10 Gi ad2 Txyz	2.57	0.81	0.52	0.11	0.52	2.42	0.60	0.22	0.26	14.07	3.75	68.39
1 Gi ad2 Txyz	2.57	2.11	0.39	0.19	1.62	0.80	0.89	0.49	0.86	3.69	1.92	17.91
5 Gi ad2 Txyz	2.57	2.13	0.59	0.34	1.26	1.03	0.38	0.58	0.65	3.53	1.88	17.14
10 Gi ad2 Txyz	2.57	0.81	0.52	0.11	0.52	2.42	0.60	0.22	0.26	14.07	3.75	68.39
1 Ri ad1 Tz	2.57	2.18	0.20	-0.13	2.51	-0.31	3.26	0.63	0.55	3.13	1.77	15.19
5 Ri ad1 Tz	2.57	2.27	0.15	-0.12	2.56	-0.21	3.04	0.75	0.34	2.45	1.56	11.90
10 Ri ad1 Tz	2.57	0.86	0.14	-0.04	0.97	-0.46	2.97	0.30	0.08	13.68	3.70	66.46
1 Ri ad1 Tz	2.57	2.18	0.20	-0.13	2.51	-0.31	3.26	0.63	0.55	3.13	1.77	15.19
5 Ri ad1 Tz	2.57	2.27	0.15	-0.12	2.56	-0.21	3.04	0.75	0.34	2.45	1.56	11.90
10 Ri ad1 Tz	2.57	0.86	0.14	-0.04	0.97	-0.46	2.97	0.30	0.08	13.68	3.70	66.46
1 Gi ad1 Tz	2.57	2.19	0.20	-0.13	2.51	-0.31	3.25	0.64	0.55	3.09	1.76	15.01
5 Gi ad1 Tz	2.57	2.28	0.15	-0.11	2.57	-0.20	3.02	0.76	0.32	2.36	1.54	11.45
10 Gi ad1 Tz	2.57	0.87	0.14	-0.04	0.97	-0.45	2.96	0.30	0.08	13.65	3.70	66.35
1 Gi ad1 Tz	2.57	2.19	0.20	-0.13	2.51	-0.31	3.25	0.64	0.55	3.09	1.76	15.01
5 Gi ad1 Tz	2.57	2.28	0.15	-0.11	2.57	-0.20	3.02	0.76	0.32	2.36	1.54	11.45
10 Gi ad1 Tz	2.57	0.87	0.14	-0.04	0.97	-0.45	2.96	0.30	0.08	13.65	3.70	66.35
1 Ri ad2 Tz	2.57	2.31	0.04	-0.02	2.36	-0.07	2.74	0.53	0.95	2.10	1.45	10.19
5 Ri ad2 Tz	2.57	2.32	0.01	0.01	2.31	0.02	2.53	0.59	0.81	1.99	1.41	9.65
10 Ri ad2 Tz	2.57	0.88	0.12	-0.03	0.95	-0.46	2.98	0.25	0.22	13.58	3.68	65.98
1 Ri ad2 Tz	2.57	2.30	0.09	-0.04	2.42	-0.19	3.02	0.48	1.07	2.17	1.47	10.52
5 Ri ad2 Tz	2.57	2.32	0.01	0.01	2.31	0.02	2.53	0.59	0.81	1.99	1.41	9.65
10 Ri ad2 Tz	2.57	0.88	0.12	-0.03	0.95	-0.46	2.98	0.25	0.22	13.58	3.68	65.98
1 Gi ad2 Tz	2.57	2.30	0.09	-0.04	2.42	-0.19	3.00	0.48	1.07	2.14	1.46	10.42
5 Gi ad2 Tz	2.57	2.33	0.02	0.01	2.30	0.04	2.49	0.60	0.78	1.94	1.39	9.44
10 Gi ad2 Tz	2.57	0.88	0.11	-0.03	0.95	-0.45	2.96	0.26	0.21	13.57	3.68	65.92
1 Gi ad2 Tz	2.57	2.30	0.09	-0.04	2.42	-0.19	3.00	0.48	1.07	2.14	1.46	10.42
5 Gi ad2 Tz	2.57	2.33	0.02	0.01	2.30	0.04	2.49	0.60	0.78	1.94	1.39	9.44
10 Gi ad2 Tz	2.57	0.88	0.11	-0.03	0.95	-0.45	2.96	0.26	0.21	13.57	3.68	65.92

Table A.44: a Calibration statistics for modelled and observed trapping rates in S2Q100D48-s1, shear stress deposition model

	TR		r^2	LM_{mo}		LM_{om}		RMA		Error		
	obs	mod		a	b	a	b	a	b	MSE	SMSE	PBIAS
1 Ri ad3 Txyz	2.57	2.14	0.38	0.18	1.69	0.81	0.83	0.47	0.94	3.44	1.85	16.72
5 Ri ad3 Txyz	2.57	2.15	0.60	0.32	1.32	1.12	0.16	0.54	0.77	3.37	1.83	16.35
10 Ri ad3 Txyz	2.57	0.81	0.54	0.11	0.52	2.62	0.44	0.21	0.28	14.08	3.75	68.42
1 Ri ad3 Txyz	2.57	2.14	0.38	0.18	1.69	0.81	0.83	0.47	0.94	3.44	1.85	16.72
5 Ri ad3 Txyz	2.57	2.15	0.60	0.32	1.32	1.12	0.16	0.54	0.77	3.37	1.83	16.35
10 Ri ad3 Txyz	2.57	0.81	0.54	0.11	0.52	2.62	0.44	0.21	0.28	14.08	3.75	68.42
1 Gi ad3 Txyz	2.57	2.14	0.39	0.18	1.68	0.82	0.81	0.47	0.94	3.44	1.86	16.72
5 Gi ad3 Txyz	2.57	2.16	0.62	0.34	1.28	1.12	0.16	0.55	0.74	3.30	1.82	16.04
10 Gi ad3 Txyz	2.57	0.81	0.55	0.11	0.52	2.64	0.43	0.21	0.28	14.08	3.75	68.39
1 Gi ad3 Txyz	2.57	2.14	0.39	0.18	1.68	0.82	0.81	0.47	0.94	3.44	1.86	16.72
5 Gi ad3 Txyz	2.57	2.16	0.62	0.34	1.28	1.12	0.16	0.55	0.74	3.30	1.82	16.04
10 Gi ad3 Txyz	2.57	0.81	0.55	0.11	0.52	2.64	0.43	0.21	0.28	14.08	3.75	68.39
1 Ri ad4 Txyz	2.57	2.17	0.38	0.17	1.73	0.83	0.78	0.45	1.00	3.24	1.80	15.75
5 Ri ad4 Txyz	2.57	2.17	0.62	0.32	1.34	1.19	-0.01	0.52	0.83	3.18	1.78	15.46
10 Ri ad4 Txyz	2.57	0.82	0.56	0.11	0.53	2.82	0.26	0.20	0.31	14.02	3.74	68.13
1 Ri ad4 Txyz	2.57	2.17	0.38	0.17	1.73	0.83	0.78	0.45	1.00	3.24	1.80	15.75
5 Ri ad4 Txyz	2.57	2.17	0.62	0.32	1.34	1.19	-0.01	0.52	0.83	3.18	1.78	15.46
10 Ri ad4 Txyz	2.57	0.82	0.56	0.11	0.53	2.82	0.26	0.20	0.31	14.02	3.74	68.13
1 Gi ad4 Txyz	2.57	2.17	0.38	0.17	1.72	0.84	0.74	0.45	1.00	3.24	1.80	15.77
5 Gi ad4 Txyz	2.57	2.18	0.64	0.34	1.30	1.19	-0.02	0.54	0.80	3.12	1.76	15.14
10 Gi ad4 Txyz	2.57	0.82	0.57	0.11	0.53	2.84	0.25	0.20	0.30	14.02	3.74	68.10
1 Gi ad4 Txyz	2.57	2.17	0.38	0.17	1.72	0.84	0.74	0.45	1.00	3.24	1.80	15.77
5 Gi ad4 Txyz	2.57	2.18	0.64	0.34	1.30	1.19	-0.02	0.54	0.80	3.12	1.76	15.14
10 Gi ad4 Txyz	2.57	0.82	0.57	0.11	0.53	2.84	0.25	0.20	0.30	14.02	3.74	68.10
1 Ri ad3 Tz	2.57	2.31	0.02	0.01	2.29	0.04	2.48	0.42	1.22	2.13	1.46	10.33
5 Ri ad3 Tz	2.57	2.32	0.16	0.09	2.10	0.31	1.84	0.52	0.98	2.03	1.42	9.86
10 Ri ad3 Tz	2.57	0.88	0.00	-0.00	0.88	-0.00	2.58	0.22	0.32	13.54	3.68	65.80
1 Ri ad3 Tz	2.57	2.31	0.02	0.01	2.29	0.04	2.48	0.42	1.22	2.13	1.46	10.33
5 Ri ad3 Tz	2.57	2.32	0.16	0.09	2.10	0.31	1.84	0.52	0.98	2.03	1.42	9.86
10 Ri ad3 Tz	2.57	0.88	0.00	-0.00	0.88	-0.00	2.58	0.22	0.32	13.54	3.68	65.80
1 Gi ad3 Tz	2.57	2.31	0.02	0.01	2.29	0.05	2.46	0.42	1.22	2.11	1.45	10.26
5 Gi ad3 Tz	2.57	2.32	0.18	0.10	2.08	0.33	1.80	0.54	0.94	1.98	1.41	9.64
10 Gi ad3 Tz	2.57	0.88	0.00	0.00	0.88	0.02	2.56	0.22	0.31	13.53	3.68	65.76
1 Gi ad3 Tz	2.57	2.31	0.02	0.01	2.29	0.05	2.46	0.42	1.22	2.11	1.45	10.26
5 Gi ad3 Tz	2.57	2.32	0.18	0.10	2.08	0.33	1.80	0.54	0.94	1.98	1.41	9.64
10 Gi ad3 Tz	2.57	0.88	0.00	0.00	0.88	0.02	2.56	0.22	0.31	13.53	3.68	65.76
1 Ri ad4 Tz	2.57	2.29	0.18	0.08	2.09	0.42	1.60	0.43	1.18	2.22	1.49	10.81
5 Ri ad4 Tz	2.57	2.31	0.26	0.13	1.97	0.54	1.33	0.49	1.04	2.14	1.46	10.38
10 Ri ad4 Tz	2.57	0.87	0.08	0.02	0.83	0.40	2.22	0.20	0.36	13.58	3.69	66.01
1 Ri ad4 Tz	2.57	2.30	0.08	0.03	2.21	0.21	2.10	0.40	1.27	2.21	1.49	10.72
5 Ri ad4 Tz	2.57	2.31	0.26	0.13	1.97	0.54	1.33	0.49	1.04	2.14	1.46	10.38
10 Ri ad4 Tz	2.57	0.87	0.08	0.02	0.83	0.40	2.22	0.20	0.36	13.58	3.69	66.01
1 Gi ad4 Tz	2.57	2.30	0.09	0.03	2.21	0.22	2.07	0.40	1.27	2.19	1.48	10.66
5 Gi ad4 Tz	2.57	2.31	0.28	0.14	1.95	0.55	1.30	0.51	1.01	2.09	1.44	10.14
10 Gi ad4 Tz	2.57	0.88	0.09	0.02	0.83	0.42	2.20	0.20	0.35	13.58	3.68	65.97
1 Gi ad4 Tz	2.57	2.30	0.09	0.03	2.21	0.22	2.07	0.40	1.27	2.19	1.48	10.66
5 Gi ad4 Tz	2.57	2.31	0.28	0.14	1.95	0.55	1.30	0.51	1.01	2.09	1.44	10.14
10 Gi ad4 Tz	2.57	0.88	0.09	0.02	0.83	0.42	2.20	0.20	0.35	13.58	3.68	65.97

Table A.45: b Calibration statistics for modelled and observed trapping rates in S2Q100D48-s1, shear stress deposition model

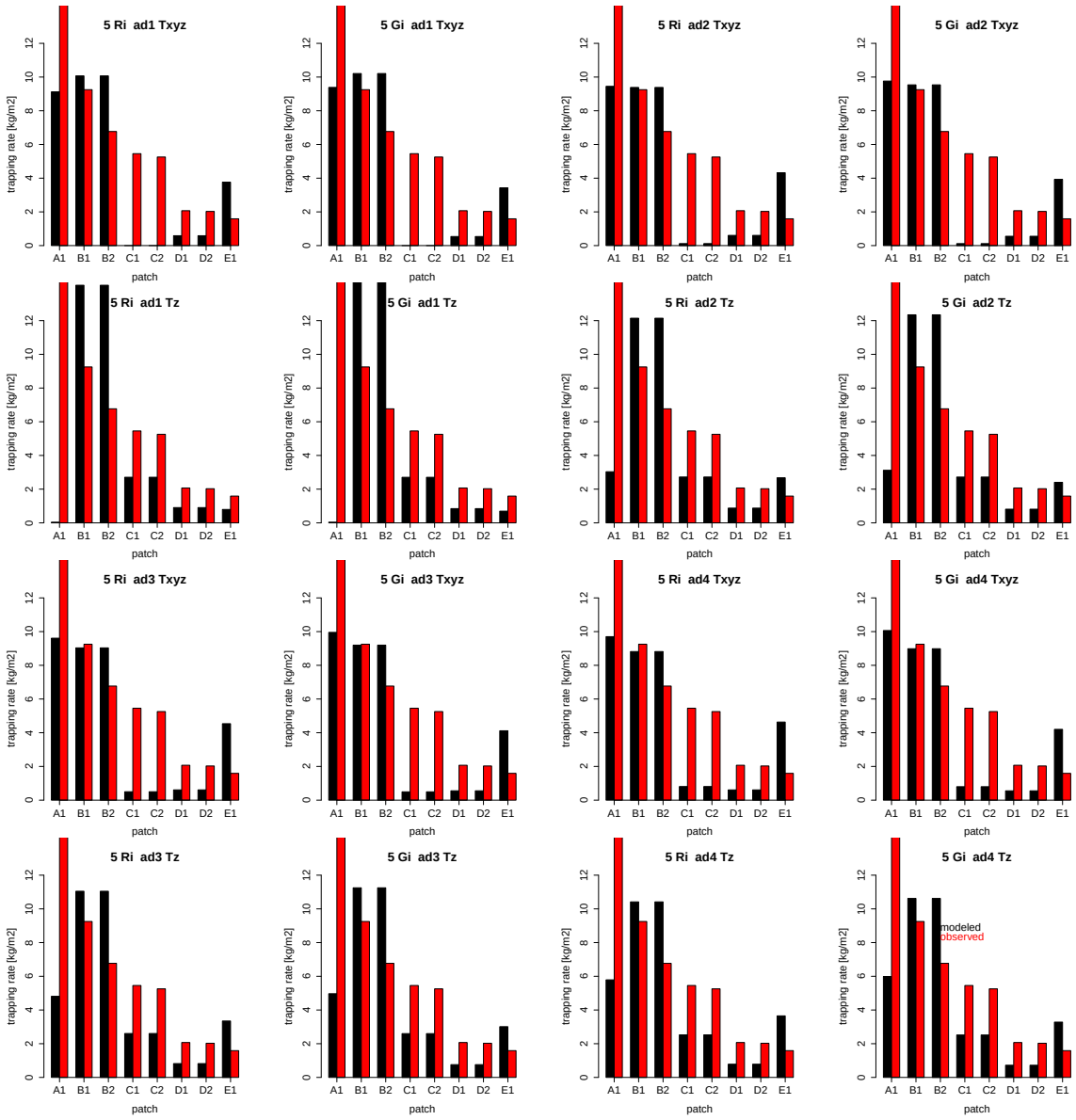

Figure A.36: Calibration statistics for modelled and observed trapping rates in S2Q100D48-s2, shear stress deposition model

	TR		r^2	LM_{mo}		LM_{om}		RMA		Error		
	obs	mod		a	b	a	b	a	b	MSE	SMSE	PBIAS
1 Ri ad1 Txyz	8.65	4.24	0.39	0.14	3.06	1.12	3.92	0.35	1.23	35.33	5.94	51.04
5 Ri ad1 Txyz	8.65	4.27	0.55	0.22	2.38	1.35	2.86	0.40	0.79	35.01	5.92	50.59
10 Ri ad1 Txyz	8.65	1.64	0.49	0.08	0.98	3.15	3.48	0.16	0.30	56.10	7.49	81.05
1 Ri ad1 Txyz	8.65	4.24	0.39	0.14	3.06	1.12	3.92	0.35	1.23	35.33	5.94	51.04
5 Ri ad1 Txyz	8.65	4.27	0.55	0.22	2.38	1.35	2.86	0.40	0.79	35.01	5.92	50.59
10 Ri ad1 Txyz	8.65	1.64	0.49	0.08	0.98	3.15	3.48	0.16	0.30	56.10	7.49	81.05
1 Gi ad1 Txyz	8.65	4.24	0.39	0.14	3.05	1.13	3.87	0.35	1.22	35.31	5.94	51.02
5 Gi ad1 Txyz	8.65	4.29	0.56	0.23	2.30	1.36	2.83	0.41	0.73	34.90	5.91	50.43
10 Gi ad1 Txyz	8.65	1.64	0.50	0.08	0.97	3.16	3.46	0.16	0.29	56.08	7.49	81.03
1 Gi ad1 Txyz	8.65	4.24	0.39	0.14	3.05	1.13	3.87	0.35	1.22	35.31	5.94	51.02
5 Gi ad1 Txyz	8.65	4.29	0.56	0.23	2.30	1.36	2.83	0.41	0.73	34.90	5.91	50.43
10 Gi ad1 Txyz	8.65	1.64	0.50	0.08	0.97	3.16	3.46	0.16	0.29	56.08	7.49	81.03
1 Ri ad2 Txyz	8.65	4.22	0.38	0.13	3.14	1.13	3.90	0.33	1.34	35.43	5.95	51.19
5 Ri ad2 Txyz	8.65	4.25	0.59	0.22	2.30	1.53	2.16	0.38	0.93	35.23	5.94	50.90
10 Ri ad2 Txyz	8.65	1.63	0.53	0.08	0.96	3.60	2.80	0.15	0.36	56.21	7.50	81.21
1 Ri ad2 Txyz	8.65	4.22	0.38	0.13	3.14	1.13	3.90	0.33	1.34	35.43	5.95	51.19
5 Ri ad2 Txyz	8.65	4.25	0.59	0.22	2.30	1.53	2.16	0.38	0.93	35.23	5.94	50.90
10 Ri ad2 Txyz	8.65	1.63	0.53	0.08	0.96	3.60	2.80	0.15	0.36	56.21	7.50	81.21
1 Gi ad2 Txyz	8.65	4.22	0.38	0.13	3.12	1.14	3.83	0.33	1.33	35.42	5.95	51.18
5 Gi ad2 Txyz	8.65	4.26	0.60	0.24	2.21	1.53	2.12	0.39	0.86	35.10	5.92	50.72
10 Gi ad2 Txyz	8.65	1.63	0.54	0.08	0.94	3.62	2.77	0.15	0.35	56.20	7.50	81.20
1 Gi ad2 Txyz	8.65	4.22	0.38	0.13	3.12	1.14	3.83	0.33	1.33	35.42	5.95	51.18
5 Gi ad2 Txyz	8.65	4.26	0.60	0.24	2.21	1.53	2.12	0.39	0.86	35.10	5.92	50.72
10 Gi ad2 Txyz	8.65	1.63	0.54	0.08	0.94	3.62	2.77	0.15	0.35	56.20	7.50	81.20
1 Ri ad1 Tz	8.65	4.36	0.15	-0.07	4.94	-0.35	10.20	0.43	0.61	34.30	5.86	49.56
5 Ri ad1 Tz	8.65	4.53	0.11	-0.05	5.01	-0.21	9.60	0.51	0.10	32.95	5.74	47.60
10 Ri ad1 Tz	8.65	1.73	0.09	-0.02	1.89	-0.44	9.42	0.21	-0.07	55.40	7.44	80.05
1 Ri ad1 Tz	8.65	4.36	0.15	-0.07	4.94	-0.35	10.20	0.43	0.61	34.30	5.86	49.56
5 Ri ad1 Tz	8.65	4.53	0.11	-0.05	5.01	-0.21	9.60	0.51	0.10	32.95	5.74	47.60
10 Ri ad1 Tz	8.65	1.73	0.09	-0.02	1.89	-0.44	9.42	0.21	-0.07	55.40	7.44	80.05
1 Gi ad1 Tz	8.65	4.37	0.15	-0.07	4.95	-0.35	10.18	0.44	0.60	34.23	5.85	49.45
5 Gi ad1 Tz	8.65	4.56	0.10	-0.05	5.02	-0.20	9.55	0.52	0.04	32.76	5.72	47.34
10 Gi ad1 Tz	8.65	1.73	0.09	-0.02	1.90	-0.43	9.40	0.21	-0.07	55.36	7.44	79.98
1 Gi ad1 Tz	8.65	4.37	0.15	-0.07	4.95	-0.35	10.18	0.44	0.60	34.23	5.85	49.45
5 Gi ad1 Tz	8.65	4.56	0.10	-0.05	5.02	-0.20	9.55	0.52	0.04	32.76	5.72	47.34
10 Gi ad1 Tz	8.65	1.73	0.09	-0.02	1.90	-0.43	9.40	0.21	-0.07	55.36	7.44	79.98
1 Ri ad2 Tz	8.65	4.62	0.00	0.00	4.61	0.01	8.61	0.36	1.49	32.24	5.68	46.59
5 Ri ad2 Tz	8.65	4.65	0.06	0.02	4.45	0.14	8.01	0.40	1.17	32.02	5.66	46.27
10 Ri ad2 Tz	8.65	1.75	0.07	-0.01	1.86	-0.41	9.37	0.17	0.24	55.20	7.43	79.77
1 Ri ad2 Tz	8.65	4.60	0.06	-0.02	4.77	-0.18	9.47	0.33	1.77	32.38	5.69	46.78
5 Ri ad2 Tz	8.65	4.65	0.06	0.02	4.45	0.14	8.01	0.40	1.17	32.02	5.66	46.27
10 Ri ad2 Tz	8.65	1.75	0.07	-0.01	1.86	-0.41	9.37	0.17	0.24	55.20	7.43	79.77
1 Gi ad2 Tz	8.65	4.61	0.06	-0.02	4.77	-0.17	9.42	0.33	1.76	32.34	5.69	46.72
5 Gi ad2 Tz	8.65	4.66	0.07	0.03	4.42	0.16	7.90	0.41	1.09	31.93	5.65	46.14
10 Gi ad2 Tz	8.65	1.75	0.07	-0.01	1.86	-0.39	9.34	0.18	0.23	55.18	7.43	79.73
1 Gi ad2 Tz	8.65	4.61	0.06	-0.02	4.77	-0.17	9.42	0.33	1.76	32.34	5.69	46.72
5 Gi ad2 Tz	8.65	4.66	0.07	0.03	4.42	0.16	7.90	0.41	1.09	31.93	5.65	46.14
10 Gi ad2 Tz	8.65	1.75	0.07	-0.01	1.86	-0.39	9.34	0.18	0.23	55.18	7.43	79.73

Table A.46: a Calibration statistics for modelled and observed trapping rates in S2Q100D48-s2, shear stress deposition model

	TR		r^2	LM_{mo}		LM_{om}		RMA		Error		
	obs	mod		a	b	a	b	a	b	MSE	SMSE	PBIAS
1 Ri ad3 Txyz	8.65	4.28	0.37	0.12	3.26	1.15	3.70	0.32	1.52	34.93	5.91	50.47
5 Ri ad3 Txyz	8.65	4.30	0.61	0.23	2.35	1.67	1.47	0.37	1.12	34.78	5.90	50.25
10 Ri ad3 Txyz	8.65	1.62	0.55	0.08	0.95	3.89	2.32	0.14	0.40	56.21	7.50	81.22
1 Ri ad3 Txyz	8.65	4.28	0.37	0.12	3.26	1.15	3.70	0.32	1.52	34.93	5.91	50.47
5 Ri ad3 Txyz	8.65	4.30	0.61	0.23	2.35	1.67	1.47	0.37	1.12	34.78	5.90	50.25
10 Ri ad3 Txyz	8.65	1.62	0.55	0.08	0.95	3.89	2.32	0.14	0.40	56.21	7.50	81.22
1 Gi ad3 Txyz	8.65	4.28	0.38	0.12	3.24	1.18	3.61	0.32	1.52	34.93	5.91	50.47
5 Gi ad3 Txyz	8.65	4.32	0.63	0.24	2.25	1.67	1.44	0.38	1.04	34.65	5.89	50.07
10 Gi ad3 Txyz	8.65	1.63	0.56	0.08	0.93	3.92	2.28	0.14	0.39	56.20	7.50	81.20
1 Gi ad3 Txyz	8.65	4.28	0.38	0.12	3.24	1.18	3.61	0.32	1.52	34.93	5.91	50.47
5 Gi ad3 Txyz	8.65	4.32	0.63	0.24	2.25	1.67	1.44	0.38	1.04	34.65	5.89	50.07
10 Gi ad3 Txyz	8.65	1.63	0.56	0.08	0.93	3.92	2.28	0.14	0.39	56.20	7.50	81.20
1 Ri ad4 Txyz	8.65	4.33	0.36	0.11	3.36	1.18	3.55	0.31	1.65	34.53	5.88	49.89
5 Ri ad4 Txyz	8.65	4.35	0.63	0.23	2.40	1.77	0.95	0.36	1.26	34.41	5.87	49.72
10 Ri ad4 Txyz	8.65	1.64	0.57	0.08	0.97	4.19	1.78	0.14	0.46	56.09	7.49	81.04
1 Ri ad4 Txyz	8.65	4.33	0.36	0.11	3.36	1.18	3.55	0.31	1.65	34.53	5.88	49.89
5 Ri ad4 Txyz	8.65	4.35	0.63	0.23	2.40	1.77	0.95	0.36	1.26	34.41	5.87	49.72
10 Ri ad4 Txyz	8.65	1.64	0.57	0.08	0.97	4.19	1.78	0.14	0.46	56.09	7.49	81.04
1 Gi ad4 Txyz	8.65	4.33	0.37	0.12	3.34	1.20	3.44	0.31	1.65	34.54	5.88	49.90
5 Gi ad4 Txyz	8.65	4.37	0.65	0.24	2.29	1.77	0.93	0.37	1.18	34.28	5.85	49.53
10 Gi ad4 Txyz	8.65	1.64	0.58	0.08	0.95	4.21	1.74	0.14	0.45	56.08	7.49	81.03
1 Gi ad4 Txyz	8.65	4.33	0.37	0.12	3.34	1.20	3.44	0.31	1.65	34.54	5.88	49.90
5 Gi ad4 Txyz	8.65	4.37	0.65	0.24	2.29	1.77	0.93	0.37	1.18	34.28	5.85	49.53
10 Gi ad4 Txyz	8.65	1.64	0.58	0.08	0.95	4.21	1.74	0.14	0.45	56.08	7.49	81.03
1 Ri ad3 Tz	8.65	4.61	0.04	0.01	4.51	0.15	7.98	0.29	2.12	32.30	5.68	46.67
5 Ri ad3 Tz	8.65	4.64	0.20	0.07	4.01	0.57	5.99	0.36	1.55	32.11	5.67	46.39
10 Ri ad3 Tz	8.65	1.76	0.04	0.01	1.70	0.29	8.14	0.15	0.46	55.13	7.43	79.66
1 Ri ad3 Tz	8.65	4.61	0.04	0.01	4.51	0.15	7.98	0.29	2.12	32.30	5.68	46.67
5 Ri ad3 Tz	8.65	4.64	0.20	0.07	4.01	0.57	5.99	0.36	1.55	32.11	5.67	46.39
10 Ri ad3 Tz	8.65	1.76	0.04	0.01	1.70	0.29	8.14	0.15	0.46	55.13	7.43	79.66
1 Gi ad3 Tz	8.65	4.62	0.05	0.01	4.50	0.16	7.92	0.29	2.12	32.27	5.68	46.63
5 Gi ad3 Tz	8.65	4.65	0.22	0.08	3.95	0.60	5.87	0.37	1.47	32.02	5.66	46.26
10 Gi ad3 Tz	8.65	1.76	0.05	0.01	1.70	0.32	8.09	0.15	0.45	55.12	7.42	79.64
1 Gi ad3 Tz	8.65	4.62	0.05	0.01	4.50	0.16	7.92	0.29	2.12	32.27	5.68	46.63
5 Gi ad3 Tz	8.65	4.65	0.22	0.08	3.95	0.60	5.87	0.37	1.47	32.02	5.66	46.26
10 Gi ad3 Tz	8.65	1.76	0.05	0.01	1.70	0.32	8.09	0.15	0.45	55.12	7.42	79.64
1 Ri ad4 Tz	8.65	4.59	0.21	0.06	4.04	0.72	5.35	0.30	2.03	32.50	5.70	46.95
5 Ri ad4 Tz	8.65	4.61	0.30	0.10	3.73	0.90	4.51	0.34	1.71	32.32	5.69	46.70
10 Ri ad4 Tz	8.65	1.75	0.12	0.02	1.60	0.89	7.09	0.14	0.56	55.22	7.43	79.78
1 Ri ad4 Tz	8.65	4.59	0.10	0.03	4.35	0.37	6.94	0.27	2.24	32.46	5.70	46.90
5 Ri ad4 Tz	8.65	4.61	0.30	0.10	3.73	0.90	4.51	0.34	1.71	32.32	5.69	46.70
10 Ri ad4 Tz	8.65	1.75	0.12	0.02	1.60	0.89	7.09	0.14	0.56	55.22	7.43	79.78
1 Gi ad4 Tz	8.65	4.60	0.11	0.03	4.34	0.39	6.86	0.27	2.23	32.44	5.70	46.87
5 Gi ad4 Tz	8.65	4.62	0.32	0.11	3.67	0.92	4.40	0.35	1.62	32.22	5.68	46.56
10 Gi ad4 Tz	8.65	1.75	0.13	0.02	1.60	0.93	7.03	0.14	0.55	55.20	7.43	79.76
1 Gi ad4 Tz	8.65	4.60	0.11	0.03	4.34	0.39	6.86	0.27	2.23	32.44	5.70	46.87
5 Gi ad4 Tz	8.65	4.62	0.32	0.11	3.67	0.92	4.40	0.35	1.62	32.22	5.68	46.56
10 Gi ad4 Tz	8.65	1.75	0.13	0.02	1.60	0.93	7.03	0.14	0.55	55.20	7.43	79.76

Table A.47: b Calibration statistics for modelled and observed trapping rates in S2Q100D48-s2, shear stress deposition model

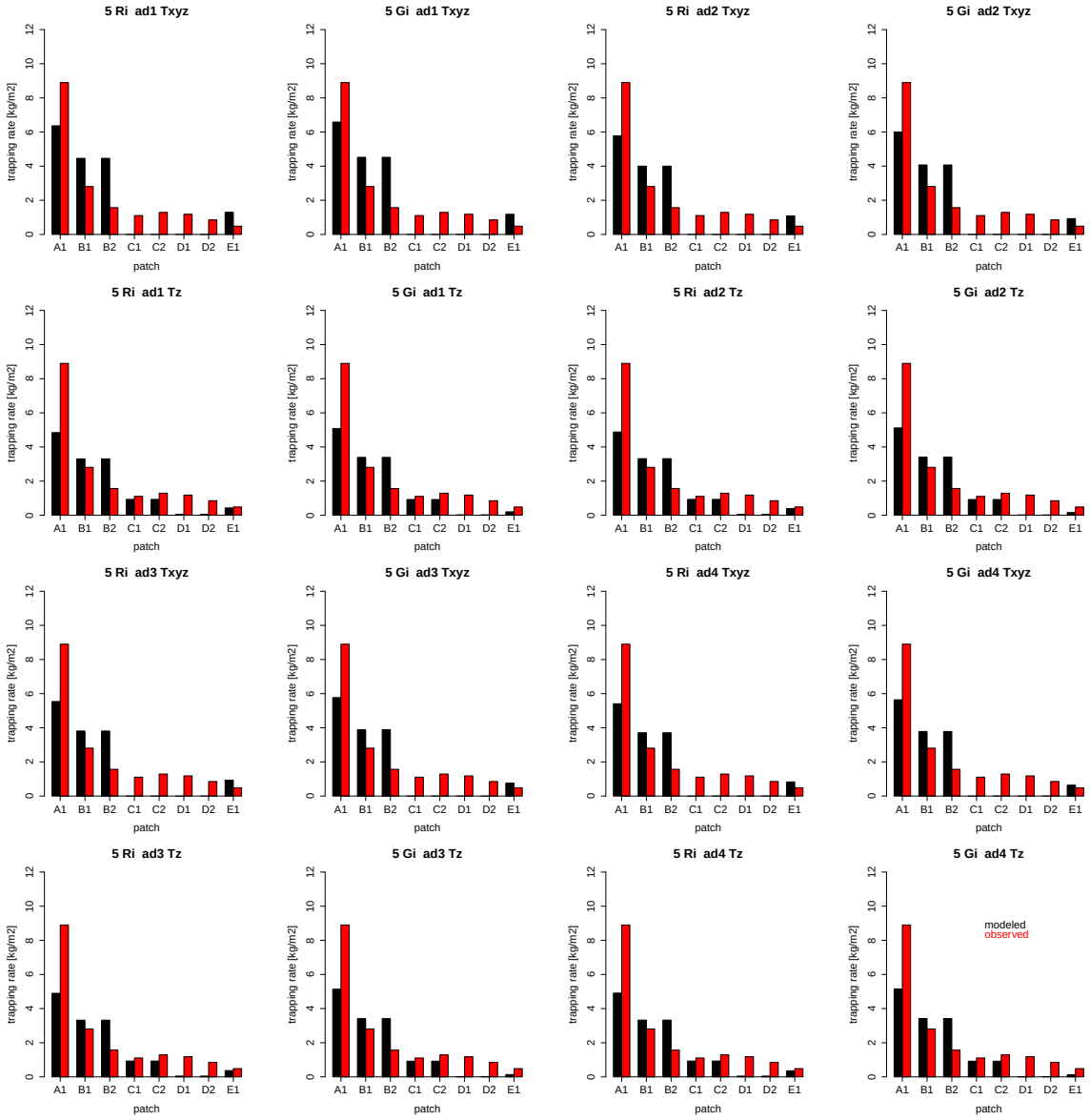

Figure A.37: Calibration statistics for modelled and observed trapping rates in S1Q100D37-s1, shear stress deposition model

	TR		r^2	LM_{mo}		LM_{om}		RMA		Error		
	obs	mod		a	b	a	b	a	b	MSE	SMSE	PBIAS
1 Ri ad1 Txyz	2.27	1.88	0.66	0.51	0.73	0.86	0.66	0.77	0.14	3.15	1.78	17.33
5 Ri ad1 Txyz	2.27	2.07	0.78	0.73	0.41	0.82	0.57	0.94	-0.07	1.61	1.27	8.86
10 Ri ad1 Txyz	2.27	2.40	0.87	1.09	-0.07	0.69	0.62	1.25	-0.45	-1.03	1.01	-5.64
1 Ri ad1 Txyz	2.27	1.88	0.66	0.51	0.73	0.86	0.66	0.77	0.14	3.15	1.78	17.33
5 Ri ad1 Txyz	2.27	2.07	0.78	0.73	0.41	0.82	0.57	0.94	-0.07	1.61	1.27	8.86
10 Ri ad1 Txyz	2.27	2.40	0.87	1.09	-0.07	0.69	0.62	1.25	-0.45	-1.03	1.01	-5.64
1 Gi ad1 Txyz	2.27	1.88	0.66	0.51	0.72	0.86	0.65	0.77	0.13	3.12	1.77	17.16
5 Gi ad1 Txyz	2.27	2.10	0.79	0.76	0.37	0.81	0.57	0.97	-0.11	1.39	1.18	7.63
10 Gi ad1 Txyz	2.27	2.48	0.88	1.17	-0.18	0.66	0.63	1.32	-0.54	-1.61	1.27	-8.88
1 Gi ad1 Txyz	2.27	1.88	0.66	0.51	0.72	0.86	0.65	0.77	0.13	3.12	1.77	17.16
5 Gi ad1 Txyz	2.27	2.10	0.79	0.76	0.37	0.81	0.57	0.97	-0.11	1.39	1.18	7.63
10 Gi ad1 Txyz	2.27	2.48	0.88	1.17	-0.18	0.66	0.63	1.32	-0.54	-1.61	1.27	-8.88
1 Ri ad2 Txyz	2.27	1.69	0.63	0.43	0.72	0.94	0.69	0.68	0.16	4.64	2.15	25.50
5 Ri ad2 Txyz	2.27	1.86	0.78	0.67	0.34	0.92	0.57	0.85	-0.08	3.33	1.82	18.30
10 Ri ad2 Txyz	2.27	0.00		0.00	-0.00		2.27	0.00	0.00	18.19	4.27	100.00
1 Ri ad2 Txyz	2.27	1.69	0.63	0.43	0.72	0.94	0.69	0.68	0.16	4.64	2.15	25.50
5 Ri ad2 Txyz	2.27	1.86	0.78	0.67	0.34	0.92	0.57	0.85	-0.08	3.33	1.82	18.30
10 Ri ad2 Txyz	2.27	0.00		0.00	-0.00		2.27	0.00	0.00	18.19	4.27	100.00
1 Gi ad2 Txyz	2.27	1.70	0.64	0.43	0.71	0.94	0.68	0.68	0.15	4.62	2.15	25.37
5 Gi ad2 Txyz	2.27	1.88	0.79	0.70	0.29	0.90	0.58	0.88	-0.12	3.12	1.77	17.14
10 Gi ad2 Txyz	2.27	0.00		0.00	-0.00		2.27	0.00	0.00	18.19	4.27	100.00
1 Gi ad2 Txyz	2.27	1.70	0.64	0.43	0.71	0.94	0.68	0.68	0.15	4.62	2.15	25.37
5 Gi ad2 Txyz	2.27	1.88	0.79	0.70	0.29	0.90	0.58	0.88	-0.12	3.12	1.77	17.14
10 Gi ad2 Txyz	2.27	0.00		0.00	-0.00		2.27	0.00	0.00	18.19	4.27	100.00
1 Ri ad1 Tz	2.27	1.70	0.61	0.26	1.10	1.42	-0.13	0.43	0.72	4.62	2.15	25.39
5 Ri ad1 Tz	2.27	1.73	0.81	0.54	0.51	1.23	0.14	0.66	0.23	4.35	2.09	23.91
10 Ri ad1 Tz	2.27	0.00		0.00	-0.00		2.27	0.00	0.00	18.19	4.27	100.00
1 Ri ad1 Tz	2.27	1.70	0.61	0.26	1.10	1.42	-0.13	0.43	0.72	4.62	2.15	25.39
5 Ri ad1 Tz	2.27	1.73	0.81	0.54	0.51	1.23	0.14	0.66	0.23	4.35	2.09	23.91
10 Ri ad1 Tz	2.27	0.00		0.00	-0.00		2.27	0.00	0.00	18.19	4.27	100.00
1 Gi ad1 Tz	2.27	1.70	0.62	0.27	1.09	1.44	-0.16	0.43	0.71	4.62	2.15	25.41
5 Gi ad1 Tz	2.27	1.74	0.82	0.57	0.44	1.17	0.23	0.70	0.15	4.24	2.06	23.33
10 Gi ad1 Tz	2.27	0.00		0.00	-0.00		2.27	0.00	0.00	18.19	4.27	100.00
1 Gi ad1 Tz	2.27	1.70	0.62	0.27	1.09	1.44	-0.16	0.43	0.71	4.62	2.15	25.41
5 Gi ad1 Tz	2.27	1.74	0.82	0.57	0.44	1.17	0.23	0.70	0.15	4.24	2.06	23.33
10 Gi ad1 Tz	2.27	0.00		0.00	-0.00		2.27	0.00	0.00	18.19	4.27	100.00
1 Ri ad2 Tz	2.27	1.70	0.76	0.39	0.80	1.46	-0.21	0.52	0.52	4.61	2.15	25.32
5 Ri ad2 Tz	2.27	1.73	0.81	0.54	0.50	1.22	0.16	0.67	0.22	4.34	2.08	23.84
10 Ri ad2 Tz	2.27	0.00		0.00	-0.00		2.27	0.00	0.00	18.19	4.27	100.00
1 Ri ad2 Tz	2.27	1.70	0.61	0.26	1.10	1.42	-0.14	0.43	0.72	4.62	2.15	25.40
5 Ri ad2 Tz	2.27	1.73	0.81	0.54	0.50	1.22	0.16	0.67	0.22	4.34	2.08	23.84
10 Ri ad2 Tz	2.27	0.00		0.00	-0.00		2.27	0.00	0.00	18.19	4.27	100.00
1 Gi ad2 Tz	2.27	1.70	0.62	0.27	1.09	1.44	-0.16	0.43	0.71	4.62	2.15	25.42
5 Gi ad2 Tz	2.27	1.75	0.82	0.58	0.43	1.16	0.25	0.71	0.14	4.23	2.06	23.25
10 Gi ad2 Tz	2.27	0.00		0.00	-0.00		2.27	0.00	0.00	18.19	4.27	100.00
1 Gi ad2 Tz	2.27	1.70	0.62	0.27	1.09	1.44	-0.16	0.43	0.71	4.62	2.15	25.42
5 Gi ad2 Tz	2.27	1.75	0.82	0.58	0.43	1.16	0.25	0.71	0.14	4.23	2.06	23.25
10 Gi ad2 Tz	2.27	0.00		0.00	-0.00		2.27	0.00	0.00	18.19	4.27	100.00

Table A.48: a Calibration statistics for modelled and observed trapping rates in S2Q100D37-s1, shear stress deposition model

	TR		r^2	LM_{mo}		LM_{om}		RMA		Error		
	obs	mod		a	b	a	b	a	b	MSE	SMSE	PBIAS
1 Ri ad3 Txyz	2.27	1.62	0.62	0.40	0.71	0.97	0.71	0.64	0.16	5.27	2.29	28.94
5 Ri ad3 Txyz	2.27	1.76	0.79	0.64	0.30	0.96	0.58	0.82	-0.10	4.10	2.02	22.54
10 Ri ad3 Txyz	2.27	0.00		0.00	-0.00		2.27	0.00	0.00	18.19	4.27	100.00
1 Ri ad3 Txyz	2.27	1.62	0.62	0.40	0.71	0.97	0.71	0.64	0.16	5.27	2.29	28.94
5 Ri ad3 Txyz	2.27	1.76	0.79	0.64	0.30	0.96	0.58	0.82	-0.10	4.10	2.02	22.54
10 Ri ad3 Txyz	2.27	0.00		0.00	-0.00		2.27	0.00	0.00	18.19	4.27	100.00
1 Gi ad3 Txyz	2.27	1.62	0.63	0.40	0.70	0.97	0.70	0.64	0.16	5.25	2.29	28.84
5 Gi ad3 Txyz	2.27	1.79	0.80	0.68	0.25	0.94	0.59	0.85	-0.14	3.90	1.97	21.44
10 Gi ad3 Txyz	2.27	0.00		0.00	-0.00		2.27	0.00	0.00	18.19	4.27	100.00
1 Gi ad3 Txyz	2.27	1.62	0.63	0.40	0.70	0.97	0.70	0.64	0.16	5.25	2.29	28.84
5 Gi ad3 Txyz	2.27	1.79	0.80	0.68	0.25	0.94	0.59	0.85	-0.14	3.90	1.97	21.44
10 Gi ad3 Txyz	2.27	0.00		0.00	-0.00		2.27	0.00	0.00	18.19	4.27	100.00
1 Ri ad4 Txyz	2.27	1.57	0.61	0.38	0.71	0.99	0.72	0.62	0.16	5.61	2.37	30.85
5 Ri ad4 Txyz	2.27	1.71	0.79	0.63	0.27	0.99	0.59	0.80	-0.11	4.54	2.13	24.96
10 Ri ad4 Txyz	2.27	0.00		0.00	-0.00		2.27	0.00	0.00	18.19	4.27	100.00
1 Ri ad4 Txyz	2.27	1.57	0.61	0.38	0.71	0.99	0.72	0.62	0.16	5.61	2.37	30.85
5 Ri ad4 Txyz	2.27	1.71	0.79	0.63	0.27	0.99	0.59	0.80	-0.11	4.54	2.13	24.96
10 Ri ad4 Txyz	2.27	0.00		0.00	-0.00		2.27	0.00	0.00	18.19	4.27	100.00
1 Gi ad4 Txyz	2.27	1.57	0.62	0.39	0.70	0.99	0.71	0.62	0.16	5.59	2.37	30.76
5 Gi ad4 Txyz	2.27	1.73	0.80	0.67	0.22	0.96	0.60	0.83	-0.16	4.35	2.09	23.91
10 Gi ad4 Txyz	2.27	0.00		0.00	-0.00		2.27	0.00	0.00	18.19	4.27	100.00
1 Gi ad4 Txyz	2.27	1.57	0.62	0.39	0.70	0.99	0.71	0.62	0.16	5.59	2.37	30.76
5 Gi ad4 Txyz	2.27	1.73	0.80	0.67	0.22	0.96	0.60	0.83	-0.16	4.35	2.09	23.91
10 Gi ad4 Txyz	2.27	0.00		0.00	-0.00		2.27	0.00	0.00	18.19	4.27	100.00
1 Ri ad3 Tz	2.27	1.70	0.61	0.26	1.10	1.42	-0.14	0.43	0.72	4.62	2.15	25.40
5 Ri ad3 Tz	2.27	1.73	0.81	0.54	0.49	1.22	0.17	0.67	0.21	4.33	2.08	23.81
10 Ri ad3 Tz	2.27	0.00		0.00	-0.00		2.27	0.00	0.00	18.19	4.27	100.00
1 Ri ad3 Tz	2.27	1.70	0.61	0.26	1.10	1.42	-0.14	0.43	0.72	4.62	2.15	25.40
5 Ri ad3 Tz	2.27	1.73	0.81	0.54	0.49	1.22	0.17	0.67	0.21	4.33	2.08	23.81
10 Ri ad3 Tz	2.27	0.00		0.00	-0.00		2.27	0.00	0.00	18.19	4.27	100.00
1 Gi ad3 Tz	2.27	1.70	0.62	0.27	1.09	1.44	-0.17	0.43	0.71	4.63	2.15	25.43
5 Gi ad3 Tz	2.27	1.75	0.82	0.58	0.42	1.16	0.26	0.71	0.13	4.22	2.05	23.20
10 Gi ad3 Tz	2.27	0.00		0.00	-0.00		2.27	0.00	0.00	18.19	4.27	100.00
1 Gi ad3 Tz	2.27	1.70	0.62	0.27	1.09	1.44	-0.17	0.43	0.71	4.63	2.15	25.43
5 Gi ad3 Tz	2.27	1.75	0.82	0.58	0.42	1.16	0.26	0.71	0.13	4.22	2.05	23.20
10 Gi ad3 Tz	2.27	0.00		0.00	-0.00		2.27	0.00	0.00	18.19	4.27	100.00
1 Ri ad4 Tz	2.27	1.70	0.76	0.40	0.80	1.46	-0.21	0.52	0.51	4.61	2.15	25.32
5 Ri ad4 Tz	2.27	1.73	0.81	0.55	0.49	1.21	0.17	0.67	0.21	4.33	2.08	23.79
10 Ri ad4 Tz	2.27	0.00		0.00	-0.00		2.27	0.00	0.00	18.19	4.27	100.00
1 Ri ad4 Tz	2.27	1.70	0.61	0.26	1.10	1.42	-0.14	0.43	0.72	4.62	2.15	25.41
5 Ri ad4 Tz	2.27	1.73	0.81	0.55	0.49	1.21	0.17	0.67	0.21	4.33	2.08	23.79
10 Ri ad4 Tz	2.27	0.00		0.00	-0.00		2.27	0.00	0.00	18.19	4.27	100.00
1 Gi ad4 Tz	2.27	1.70	0.62	0.27	1.08	1.44	-0.17	0.43	0.71	4.63	2.15	25.43
5 Gi ad4 Tz	2.27	1.75	0.82	0.59	0.41	1.15	0.26	0.71	0.13	4.21	2.05	23.17
10 Gi ad4 Tz	2.27	0.00		0.00	-0.00		2.27	0.00	0.00	18.19	4.27	100.00
1 Gi ad4 Tz	2.27	1.70	0.62	0.27	1.08	1.44	-0.17	0.43	0.71	4.63	2.15	25.43
5 Gi ad4 Tz	2.27	1.75	0.82	0.59	0.41	1.15	0.26	0.71	0.13	4.21	2.05	23.17
10 Gi ad4 Tz	2.27	0.00		0.00	-0.00		2.27	0.00	0.00	18.19	4.27	100.00

Table A.49: b Calibration statistics for modelled and observed trapping rates in S2Q100D37-s1, shear stress deposition model

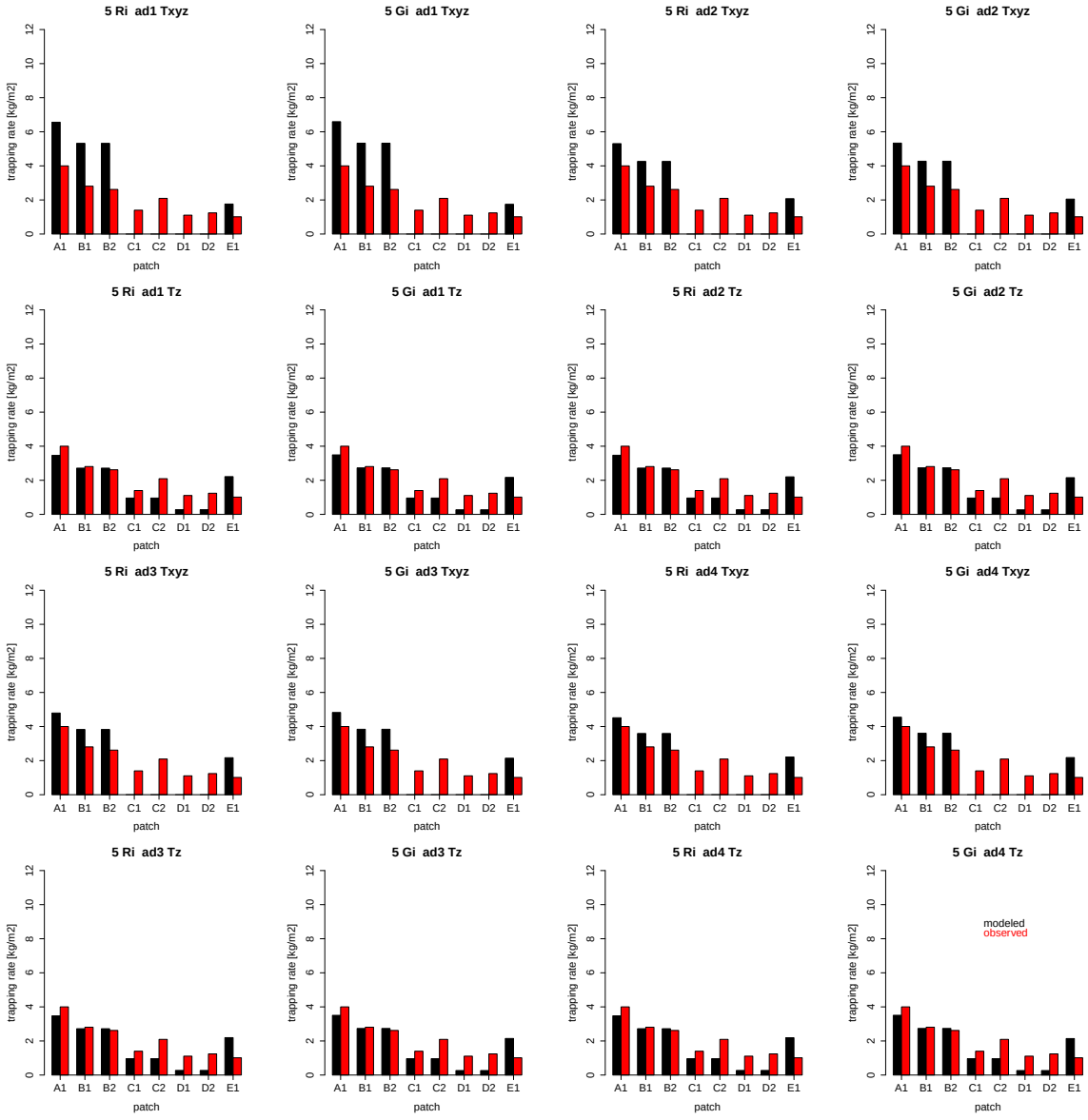

Figure A.38: Calibration statistics for modelled and observed trapping rates in S2Q100D37-s2, shear stress deposition model

	TR		r^2	LM_{mo}		LM_{om}		RMA		Error		
	obs	mod		a	b	a	b	a	b	MSE	SMSE	PBIAS
1 Ri ad1 Txyz	2.03	2.24	0.84	2.12	-2.08	0.33	1.29	2.52	-2.89	-1.63	1.28	-9.99
5 Ri ad1 Txyz	2.03	2.37	0.87	2.36	-2.44	0.32	1.28	2.73	-3.19	-2.69	1.64	-16.50
10 Ri ad1 Txyz	2.03	2.45	0.89	2.58	-2.79	0.31	1.29	2.91	-3.46	-3.31	1.82	-20.33
1 Ri ad1 Txyz	2.03	2.24	0.84	2.12	-2.08	0.33	1.29	2.52	-2.89	-1.63	1.28	-9.99
5 Ri ad1 Txyz	2.03	2.37	0.87	2.36	-2.44	0.32	1.28	2.73	-3.19	-2.69	1.64	-16.50
10 Ri ad1 Txyz	2.03	2.45	0.89	2.58	-2.79	0.31	1.29	2.91	-3.46	-3.31	1.82	-20.33
1 Gi ad1 Txyz	2.03	2.26	0.84	2.15	-2.11	0.33	1.29	2.54	-2.92	-1.80	1.34	-11.03
5 Gi ad1 Txyz	2.03	2.37	0.87	2.38	-2.46	0.32	1.28	2.74	-3.21	-2.72	1.65	-16.70
10 Gi ad1 Txyz	2.03	2.46	0.89	2.60	-2.83	0.30	1.29	2.92	-3.49	-3.38	1.84	-20.77
1 Gi ad1 Txyz	2.03	2.26	0.84	2.15	-2.11	0.33	1.29	2.54	-2.92	-1.80	1.34	-11.03
5 Gi ad1 Txyz	2.03	2.37	0.87	2.38	-2.46	0.32	1.28	2.74	-3.21	-2.72	1.65	-16.70
10 Gi ad1 Txyz	2.03	2.46	0.89	2.60	-2.83	0.30	1.29	2.92	-3.49	-3.38	1.84	-20.77
1 Ri ad2 Txyz	2.03	1.91	0.79	1.61	-1.36	0.39	1.30	2.04	-2.25	0.97	0.99	5.98
5 Ri ad2 Txyz	2.03	1.99	0.83	1.82	-1.71	0.38	1.28	2.19	-2.47	0.38	0.62	2.33
10 Ri ad2 Txyz	2.03	2.06	0.87	2.06	-2.13	0.37	1.28	2.37	-2.76	-0.19	0.43	-1.15
1 Ri ad2 Txyz	2.03	1.91	0.79	1.61	-1.36	0.39	1.30	2.04	-2.25	0.97	0.99	5.98
5 Ri ad2 Txyz	2.03	1.99	0.83	1.82	-1.71	0.38	1.28	2.19	-2.47	0.38	0.62	2.33
10 Ri ad2 Txyz	2.03	2.06	0.87	2.06	-2.13	0.37	1.28	2.37	-2.76	-0.19	0.43	-1.15
1 Gi ad2 Txyz	2.03	1.92	0.79	1.62	-1.38	0.38	1.30	2.06	-2.26	0.90	0.95	5.50
5 Gi ad2 Txyz	2.03	1.99	0.83	1.83	-1.74	0.38	1.28	2.20	-2.48	0.35	0.59	2.15
10 Gi ad2 Txyz	2.03	2.07	0.87	2.09	-2.18	0.37	1.28	2.39	-2.80	-0.26	0.51	-1.58
1 Gi ad2 Txyz	2.03	1.92	0.79	1.62	-1.38	0.38	1.30	2.06	-2.26	0.90	0.95	5.50
5 Gi ad2 Txyz	2.03	1.99	0.83	1.83	-1.74	0.38	1.28	2.20	-2.48	0.35	0.59	2.15
10 Gi ad2 Txyz	2.03	2.07	0.87	2.09	-2.18	0.37	1.28	2.39	-2.80	-0.26	0.51	-1.58
1 Ri ad1 Tz	2.03	1.70	0.63	0.69	0.30	0.57	1.06	1.10	-0.53	2.66	1.63	16.36
5 Ri ad1 Tz	2.03	1.70	0.79	0.93	-0.19	0.68	0.88	1.17	-0.68	2.71	1.65	16.67
10 Ri ad1 Tz	2.03	1.70	0.91	1.25	-0.83	0.66	0.90	1.37	-1.08	2.65	1.63	16.26
1 Ri ad1 Tz	2.03	1.70	0.63	0.69	0.30	0.57	1.06	1.10	-0.53	2.66	1.63	16.36
5 Ri ad1 Tz	2.03	1.70	0.79	0.93	-0.19	0.68	0.88	1.17	-0.68	2.71	1.65	16.67
10 Ri ad1 Tz	2.03	1.70	0.91	1.25	-0.83	0.66	0.90	1.37	-1.08	2.65	1.63	16.26
1 Gi ad1 Tz	2.03	1.70	0.63	0.69	0.29	0.57	1.06	1.10	-0.54	2.66	1.63	16.35
5 Gi ad1 Tz	2.03	1.70	0.80	0.95	-0.23	0.68	0.88	1.18	-0.70	2.71	1.65	16.68
10 Gi ad1 Tz	2.03	1.71	0.92	1.28	-0.91	0.66	0.91	1.40	-1.14	2.63	1.62	16.18
1 Gi ad1 Tz	2.03	1.70	0.63	0.69	0.29	0.57	1.06	1.10	-0.54	2.66	1.63	16.35
5 Gi ad1 Tz	2.03	1.70	0.80	0.95	-0.23	0.68	0.88	1.18	-0.70	2.71	1.65	16.68
10 Gi ad1 Tz	2.03	1.71	0.92	1.28	-0.91	0.66	0.91	1.40	-1.14	2.63	1.62	16.18
1 Ri ad2 Tz	2.03	1.70	0.72	0.81	0.05	0.64	0.95	1.12	-0.59	2.70	1.64	16.58
5 Ri ad2 Tz	2.03	1.70	0.80	0.93	-0.20	0.68	0.88	1.17	-0.69	2.72	1.65	16.68
10 Ri ad2 Tz	2.03	1.70	0.91	1.26	-0.86	0.66	0.91	1.38	-1.10	2.64	1.63	16.25
1 Ri ad2 Tz	2.03	1.70	0.63	0.69	0.30	0.57	1.06	1.10	-0.53	2.66	1.63	16.36
5 Ri ad2 Tz	2.03	1.70	0.80	0.93	-0.20	0.68	0.88	1.17	-0.69	2.72	1.65	16.68
10 Ri ad2 Tz	2.03	1.70	0.91	1.26	-0.86	0.66	0.91	1.38	-1.10	2.64	1.63	16.25
1 Gi ad2 Tz	2.03	1.70	0.63	0.69	0.29	0.57	1.06	1.10	-0.54	2.66	1.63	16.36
5 Gi ad2 Tz	2.03	1.70	0.81	0.95	-0.24	0.68	0.88	1.18	-0.71	2.72	1.65	16.69
10 Gi ad2 Tz	2.03	1.71	0.92	1.30	-0.93	0.65	0.92	1.41	-1.16	2.63	1.62	16.15
1 Gi ad2 Tz	2.03	1.70	0.63	0.69	0.29	0.57	1.06	1.10	-0.54	2.66	1.63	16.36
5 Gi ad2 Tz	2.03	1.70	0.81	0.95	-0.24	0.68	0.88	1.18	-0.71	2.72	1.65	16.69
10 Gi ad2 Tz	2.03	1.71	0.92	1.30	-0.93	0.65	0.92	1.41	-1.16	2.63	1.62	16.15

Table A.50: a Calibration statistics for modelled and observed trapping rates in S2Q100D37-s2, shear stress deposition model

	TR		r^2	LM_{mo}		LM_{om}		RMA		Error		
	obs	mod		a	b	a	b	a	b	MSE	SMSE	PBIAS
1 Ri ad3 Txyz	2.03	1.77	0.75	1.39	-1.06	0.40	1.32	1.86	-2.01	2.08	1.44	12.80
5 Ri ad3 Txyz	2.03	1.83	0.81	1.60	-1.43	0.41	1.29	1.98	-2.20	1.66	1.29	10.19
10 Ri ad3 Txyz	2.03	1.89	0.86	1.86	-1.89	0.40	1.28	2.15	-2.49	1.15	1.07	7.09
1 Ri ad3 Txyz	2.03	1.77	0.75	1.39	-1.06	0.40	1.32	1.86	-2.01	2.08	1.44	12.80
5 Ri ad3 Txyz	2.03	1.83	0.81	1.60	-1.43	0.41	1.29	1.98	-2.20	1.66	1.29	10.19
10 Ri ad3 Txyz	2.03	1.89	0.86	1.86	-1.89	0.40	1.28	2.15	-2.49	1.15	1.07	7.09
1 Gi ad3 Txyz	2.03	1.78	0.75	1.40	-1.07	0.40	1.32	1.87	-2.02	2.04	1.43	12.52
5 Gi ad3 Txyz	2.03	1.83	0.81	1.61	-1.45	0.41	1.29	1.99	-2.21	1.63	1.28	10.03
10 Gi ad3 Txyz	2.03	1.90	0.87	1.89	-1.94	0.40	1.28	2.17	-2.53	1.09	1.04	6.68
1 Gi ad3 Txyz	2.03	1.78	0.75	1.40	-1.07	0.40	1.32	1.87	-2.02	2.04	1.43	12.52
5 Gi ad3 Txyz	2.03	1.83	0.81	1.61	-1.45	0.41	1.29	1.99	-2.21	1.63	1.28	10.03
10 Gi ad3 Txyz	2.03	1.90	0.87	1.89	-1.94	0.40	1.28	2.17	-2.53	1.09	1.04	6.68
1 Ri ad4 Txyz	2.03	1.70	0.72	1.28	-0.90	0.41	1.34	1.76	-1.89	2.71	1.64	16.62
5 Ri ad4 Txyz	2.03	1.74	0.80	1.48	-1.28	0.43	1.29	1.86	-2.05	2.37	1.54	14.54
10 Ri ad4 Txyz	2.03	1.80	0.86	1.75	-1.76	0.42	1.28	2.04	-2.35	1.91	1.38	11.72
1 Ri ad4 Txyz	2.03	1.70	0.72	1.28	-0.90	0.41	1.34	1.76	-1.89	2.71	1.64	16.62
5 Ri ad4 Txyz	2.03	1.74	0.80	1.48	-1.28	0.43	1.29	1.86	-2.05	2.37	1.54	14.54
10 Ri ad4 Txyz	2.03	1.80	0.86	1.75	-1.76	0.42	1.28	2.04	-2.35	1.91	1.38	11.72
1 Gi ad4 Txyz	2.03	1.70	0.73	1.28	-0.91	0.41	1.34	1.77	-1.89	2.68	1.64	16.43
5 Gi ad4 Txyz	2.03	1.74	0.80	1.50	-1.31	0.43	1.29	1.87	-2.07	2.34	1.53	14.39
10 Gi ad4 Txyz	2.03	1.80	0.87	1.78	-1.82	0.42	1.28	2.06	-2.38	1.85	1.36	11.34
1 Gi ad4 Txyz	2.03	1.70	0.73	1.28	-0.91	0.41	1.34	1.77	-1.89	2.68	1.64	16.43
5 Gi ad4 Txyz	2.03	1.74	0.80	1.50	-1.31	0.43	1.29	1.87	-2.07	2.34	1.53	14.39
10 Gi ad4 Txyz	2.03	1.80	0.87	1.78	-1.82	0.42	1.28	2.06	-2.38	1.85	1.36	11.34
1 Ri ad3 Tz	2.03	1.70	0.63	0.69	0.30	0.57	1.06	1.10	-0.53	2.66	1.63	16.36
5 Ri ad3 Tz	2.03	1.70	0.80	0.94	-0.21	0.68	0.88	1.17	-0.69	2.72	1.65	16.69
10 Ri ad3 Tz	2.03	1.70	0.91	1.27	-0.87	0.66	0.91	1.38	-1.11	2.64	1.63	16.24
1 Ri ad3 Tz	2.03	1.70	0.63	0.69	0.30	0.57	1.06	1.10	-0.53	2.66	1.63	16.36
5 Ri ad3 Tz	2.03	1.70	0.80	0.94	-0.21	0.68	0.88	1.17	-0.69	2.72	1.65	16.69
10 Ri ad3 Tz	2.03	1.70	0.91	1.27	-0.87	0.66	0.91	1.38	-1.11	2.64	1.63	16.24
1 Gi ad3 Tz	2.03	1.70	0.63	0.69	0.29	0.57	1.06	1.10	-0.54	2.66	1.63	16.36
5 Gi ad3 Tz	2.03	1.70	0.81	0.95	-0.25	0.68	0.88	1.18	-0.71	2.72	1.65	16.69
10 Gi ad3 Tz	2.03	1.71	0.92	1.30	-0.95	0.65	0.92	1.41	-1.17	2.63	1.62	16.14
1 Gi ad3 Tz	2.03	1.70	0.63	0.69	0.29	0.57	1.06	1.10	-0.54	2.66	1.63	16.36
5 Gi ad3 Tz	2.03	1.70	0.81	0.95	-0.25	0.68	0.88	1.18	-0.71	2.72	1.65	16.69
10 Gi ad3 Tz	2.03	1.71	0.92	1.30	-0.95	0.65	0.92	1.41	-1.17	2.63	1.62	16.14
1 Ri ad4 Tz	2.03	1.70	0.72	0.81	0.05	0.64	0.95	1.12	-0.59	2.70	1.64	16.59
5 Ri ad4 Tz	2.03	1.70	0.80	0.94	-0.21	0.68	0.88	1.17	-0.69	2.72	1.65	16.69
10 Ri ad4 Tz	2.03	1.70	0.92	1.27	-0.88	0.66	0.91	1.39	-1.12	2.64	1.63	16.23
1 Ri ad4 Tz	2.03	1.70	0.63	0.69	0.30	0.57	1.07	1.10	-0.53	2.66	1.63	16.36
5 Ri ad4 Tz	2.03	1.70	0.80	0.94	-0.21	0.68	0.88	1.17	-0.69	2.72	1.65	16.69
10 Ri ad4 Tz	2.03	1.70	0.92	1.27	-0.88	0.66	0.91	1.39	-1.12	2.64	1.63	16.23
1 Gi ad4 Tz	2.03	1.70	0.63	0.69	0.29	0.57	1.06	1.10	-0.54	2.66	1.63	16.36
5 Gi ad4 Tz	2.03	1.69	0.81	0.96	-0.25	0.68	0.88	1.18	-0.71	2.72	1.65	16.70
10 Gi ad4 Tz	2.03	1.71	0.92	1.31	-0.96	0.65	0.92	1.42	-1.18	2.63	1.62	16.13
1 Gi ad4 Tz	2.03	1.70	0.63	0.69	0.29	0.57	1.06	1.10	-0.54	2.66	1.63	16.36
5 Gi ad4 Tz	2.03	1.69	0.81	0.96	-0.25	0.68	0.88	1.18	-0.71	2.72	1.65	16.70
10 Gi ad4 Tz	2.03	1.71	0.92	1.31	-0.96	0.65	0.92	1.42	-1.18	2.63	1.62	16.13

Table A.51: b Calibration statistics for modelled and observed trapping rates in S2Q100D37-s2, shear stress deposition model

	r^2	LM_{mo}		LM_{om}		RMA		Error		
		a	b	a	b	a	b	MSE	SMSE	PBIAS
1-Gi-In -mean	0.99	0.99	0.03	1.00	-0.02	0.99	0.03	-0.15	0.38	-5.42
5-Gi-In -mean	1.00	1.01	-0.03	0.99	0.03	1.01	-0.03	0.17	0.41	6.40
10-Gi-In -mean	1.00	1.01	-0.04	0.99	0.04	1.01	-0.04	0.18	0.43	6.88
1-Sto-In -mean	0.98	0.94	0.15	1.02	-0.13	0.96	0.14	-0.72	0.85	-26.86
5-Sto-In -mean	1.00	1.01	-0.01	0.99	0.01	1.01	-0.01	0.07	0.26	2.54
10-Sto-In -mean	1.00	1.01	-0.03	0.99	0.03	1.01	-0.03	0.15	0.39	5.62
1-Gi-La -mean	1.00	0.99	0.03	1.00	-0.02	0.99	0.03	-0.14	0.38	-5.33
5-Gi-La -mean	1.00	1.01	-0.03	0.99	0.03	1.01	-0.04	0.17	0.42	6.43
10-Gi-La -mean	1.00	1.01	-0.04	0.99	0.04	1.01	-0.04	0.18	0.43	6.88
1-Sto-La -mean	0.98	0.94	0.14	1.02	-0.13	0.96	0.14	-0.72	0.85	-26.70
5-Sto-La -mean	1.00	1.01	-0.01	0.99	0.01	1.01	-0.01	0.07	0.26	2.62
10-Sto-La -mean	1.00	1.01	-0.03	0.99	0.03	1.01	-0.03	0.15	0.39	5.66
1-Gi-In -ave5	0.99	0.98	0.05	1.01	-0.04	0.99	0.05	-0.24	0.49	-9.04
5-Gi-In -ave5	1.00	1.01	-0.03	0.99	0.03	1.01	-0.03	0.15	0.39	5.58
10-Gi-In -ave5	1.00	1.01	-0.04	0.99	0.04	1.01	-0.04	0.18	0.43	6.74
1-Sto-In -ave5	0.98	0.93	0.18	1.03	-0.17	0.95	0.17	-0.88	0.94	-32.92
5-Sto-In -ave5	1.00	1.00	-0.00	1.00	0.00	1.00	-0.00	0.01	0.08	0.24
10-Sto-In -ave5	1.00	1.01	-0.02	0.99	0.02	1.01	-0.02	0.12	0.34	4.32
1-Gi-La -ave5	0.99	0.98	0.04	1.00	-0.03	0.99	0.04	-0.20	0.44	-7.29
5-Gi-La -ave5	1.00	1.01	-0.03	0.99	0.03	1.01	-0.03	0.16	0.41	6.13
10-Gi-La -ave5	1.00	1.01	-0.04	0.99	0.04	1.01	-0.04	0.18	0.43	6.85
1-Sto-La -ave5	0.98	0.94	0.16	1.02	-0.15	0.96	0.15	-0.81	0.90	-30.22
5-Sto-La -ave5	1.00	1.00	-0.01	0.99	0.01	1.00	-0.01	0.04	0.21	1.60
10-Sto-La -ave5	1.00	1.01	-0.03	0.99	0.03	1.01	-0.03	0.14	0.37	5.16

Table A.52: Graphical representaiton of statisitcal evaluation of modeled and observed suspended sediment concentration loss in S2Q100D48-s1, velocity deposition model

Calibration sandy experimental runs velocity deposition model

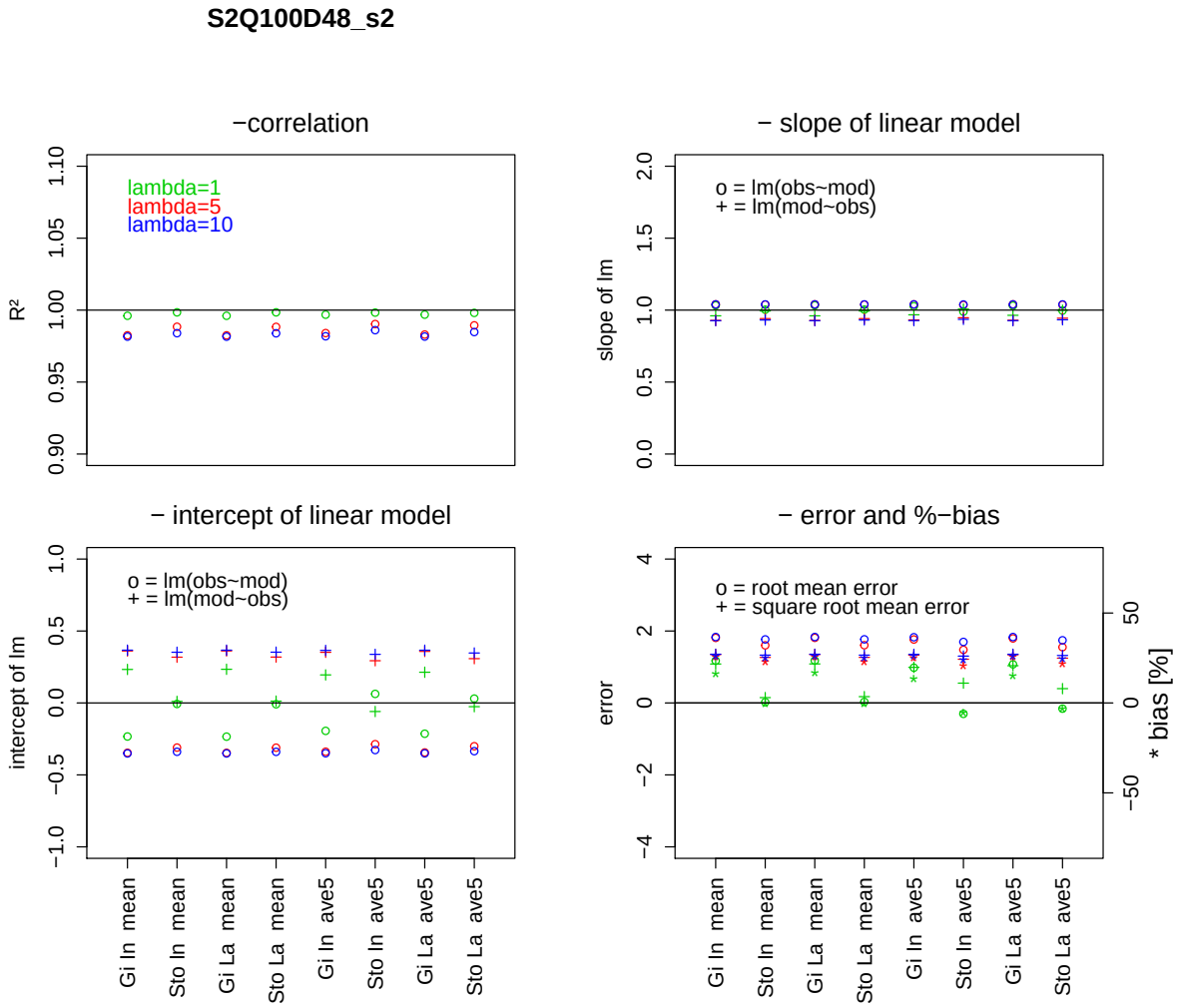

Figure A.39: Graphical representaiton of statisitcal evaluation of modeled and observed suspended sediment concentration loss in S1Q100D48-s2, velocity deposition model

	r^2	LM_{mo}		LM_{om}		RMA		Error		
		a	b	a	b	a	b	MSE	SMSE	PBIAS
1-Gi-In -mean	1.00	1.03	-0.23	0.96	0.23	1.04	-0.24	1.17	1.08	17.17
5-Gi-In -mean	0.98	1.04	-0.35	0.93	0.36	1.06	-0.37	1.81	1.34	26.46
10-Gi-In -mean	0.98	1.04	-0.35	0.93	0.37	1.06	-0.37	1.83	1.35	26.83
1-Sto-In -mean	1.00	1.00	-0.01	0.99	0.01	1.00	-0.01	0.02	0.15	0.32
5-Sto-In -mean	0.99	1.04	-0.31	0.94	0.32	1.05	-0.32	1.60	1.27	23.42
10-Sto-In -mean	0.98	1.04	-0.34	0.93	0.35	1.06	-0.36	1.77	1.33	25.84
1-Gi-La -mean	1.00	1.03	-0.23	0.96	0.23	1.04	-0.24	1.18	1.09	17.24
5-Gi-La -mean	0.98	1.04	-0.35	0.93	0.36	1.06	-0.37	1.81	1.35	26.48
10-Gi-La -mean	0.98	1.04	-0.35	0.93	0.37	1.06	-0.37	1.83	1.35	26.83
1-Sto-La -mean	1.00	1.00	-0.01	0.99	0.01	1.01	-0.01	0.03	0.18	0.45
5-Sto-La -mean	0.99	1.04	-0.31	0.94	0.32	1.05	-0.32	1.61	1.27	23.48
10-Sto-La -mean	0.98	1.04	-0.34	0.93	0.35	1.06	-0.36	1.77	1.33	25.88
1-Gi-In -ave5	1.00	1.03	-0.19	0.97	0.19	1.03	-0.20	0.98	0.99	14.33
5-Gi-In -ave5	0.98	1.04	-0.34	0.93	0.35	1.06	-0.36	1.76	1.33	25.81
10-Gi-In -ave5	0.98	1.04	-0.35	0.93	0.37	1.06	-0.37	1.83	1.35	26.73
1-Sto-In -ave5	1.00	0.99	0.06	1.01	-0.06	0.99	0.06	-0.30	0.55	-4.44
5-Sto-In -ave5	0.99	1.04	-0.29	0.95	0.29	1.05	-0.30	1.48	1.22	21.61
10-Sto-In -ave5	0.99	1.04	-0.33	0.94	0.34	1.05	-0.34	1.70	1.30	24.82
1-Gi-La -ave5	1.00	1.03	-0.21	0.96	0.21	1.03	-0.22	1.07	1.04	15.70
5-Gi-La -ave5	0.98	1.04	-0.34	0.93	0.36	1.06	-0.36	1.79	1.34	26.25
10-Gi-La -ave5	0.98	1.04	-0.35	0.93	0.37	1.06	-0.37	1.83	1.35	26.81
1-Sto-La -ave5	1.00	1.00	0.03	1.00	-0.03	1.00	0.03	-0.16	0.40	-2.32
5-Sto-La -ave5	0.99	1.04	-0.30	0.94	0.31	1.05	-0.31	1.55	1.25	22.68
10-Sto-La -ave5	0.98	1.04	-0.34	0.93	0.35	1.06	-0.35	1.74	1.32	25.48

Table A.53: Graphical representaiton of statisitcal evaluation of modeled and observed suspended sediment concentration loss in S2Q100D48-s2, velocity deposition model

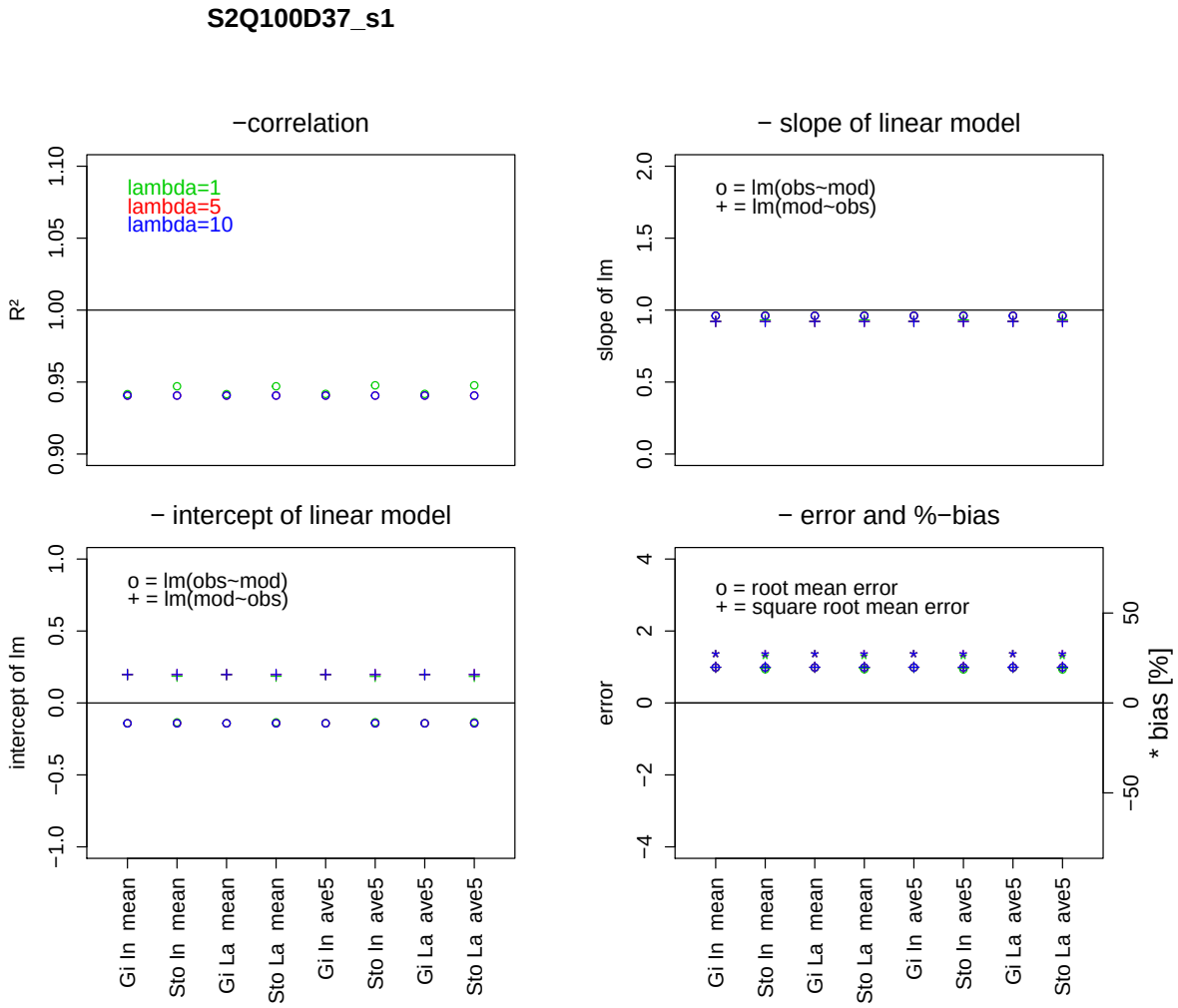

Figure A.40: Graphical representaiton of statisitcal evaluation of modeled and observed suspended sediment concentration loss in S1Q100D37-s1, velocity deposition model

	r^2	LM_{mo}		LM_{om}		RMA		Error		
		a	b	a	b	a	b	MSE	SMSE	PBIAS
1-Gi-In -mean	0.94	0.96	-0.14	0.92	0.20	1.02	-0.18	0.98	0.99	28.10
5-Gi-In -mean	0.94	0.96	-0.14	0.92	0.20	1.02	-0.18	0.99	0.99	28.31
10-Gi-In -mean	0.94	0.96	-0.14	0.92	0.20	1.02	-0.18	0.99	0.99	28.31
1-Sto-In -mean	0.95	0.96	-0.14	0.93	0.19	1.02	-0.17	0.94	0.97	26.89
5-Sto-In -mean	0.94	0.96	-0.14	0.92	0.20	1.02	-0.18	0.99	0.99	28.31
10-Sto-In -mean	0.94	0.96	-0.14	0.92	0.20	1.02	-0.18	0.99	0.99	28.31
1-Gi-La -mean	0.94	0.96	-0.14	0.92	0.20	1.02	-0.18	0.98	0.99	28.10
5-Gi-La -mean	0.94	0.96	-0.14	0.92	0.20	1.02	-0.18	0.99	0.99	28.31
10-Gi-La -mean	0.94	0.96	-0.14	0.92	0.20	1.02	-0.18	0.99	0.99	28.31
1-Sto-La -mean	0.95	0.96	-0.14	0.93	0.19	1.02	-0.17	0.94	0.97	26.89
5-Sto-La -mean	0.94	0.96	-0.14	0.92	0.20	1.02	-0.18	0.99	0.99	28.31
10-Sto-La -mean	0.94	0.96	-0.14	0.92	0.20	1.02	-0.18	0.99	0.99	28.31
1-Gi-In -ave5	0.94	0.96	-0.14	0.92	0.20	1.02	-0.18	0.98	0.99	28.06
5-Gi-In -ave5	0.94	0.96	-0.14	0.92	0.20	1.02	-0.18	0.99	0.99	28.31
10-Gi-In -ave5	0.94	0.96	-0.14	0.92	0.20	1.02	-0.18	0.99	0.99	28.31
1-Sto-In -ave5	0.95	0.96	-0.13	0.93	0.18	1.02	-0.17	0.93	0.97	26.74
5-Sto-In -ave5	0.94	0.96	-0.14	0.92	0.20	1.02	-0.18	0.99	0.99	28.31
10-Sto-In -ave5	0.94	0.96	-0.14	0.92	0.20	1.02	-0.18	0.99	0.99	28.31
1-Gi-La -ave5	0.94	0.96	-0.14	0.92	0.20	1.02	-0.18	0.98	0.99	28.06
5-Gi-La -ave5	0.94	0.96	-0.14	0.92	0.20	1.02	-0.18	0.99	0.99	28.31
10-Gi-La -ave5	0.94	0.96	-0.14	0.92	0.20	1.02	-0.18	0.99	0.99	28.31
1-Sto-La -ave5	0.95	0.96	-0.13	0.93	0.18	1.02	-0.17	0.93	0.97	26.74
5-Sto-La -ave5	0.94	0.96	-0.14	0.92	0.20	1.02	-0.18	0.99	0.99	28.31
10-Sto-La -ave5	0.94	0.96	-0.14	0.92	0.20	1.02	-0.18	0.99	0.99	28.31

Table A.54: Graphical representaiton of statisitcal evaluation of modeled and observed suspended sediment concentration loss in S2Q100D37-s1, velocity deposition model

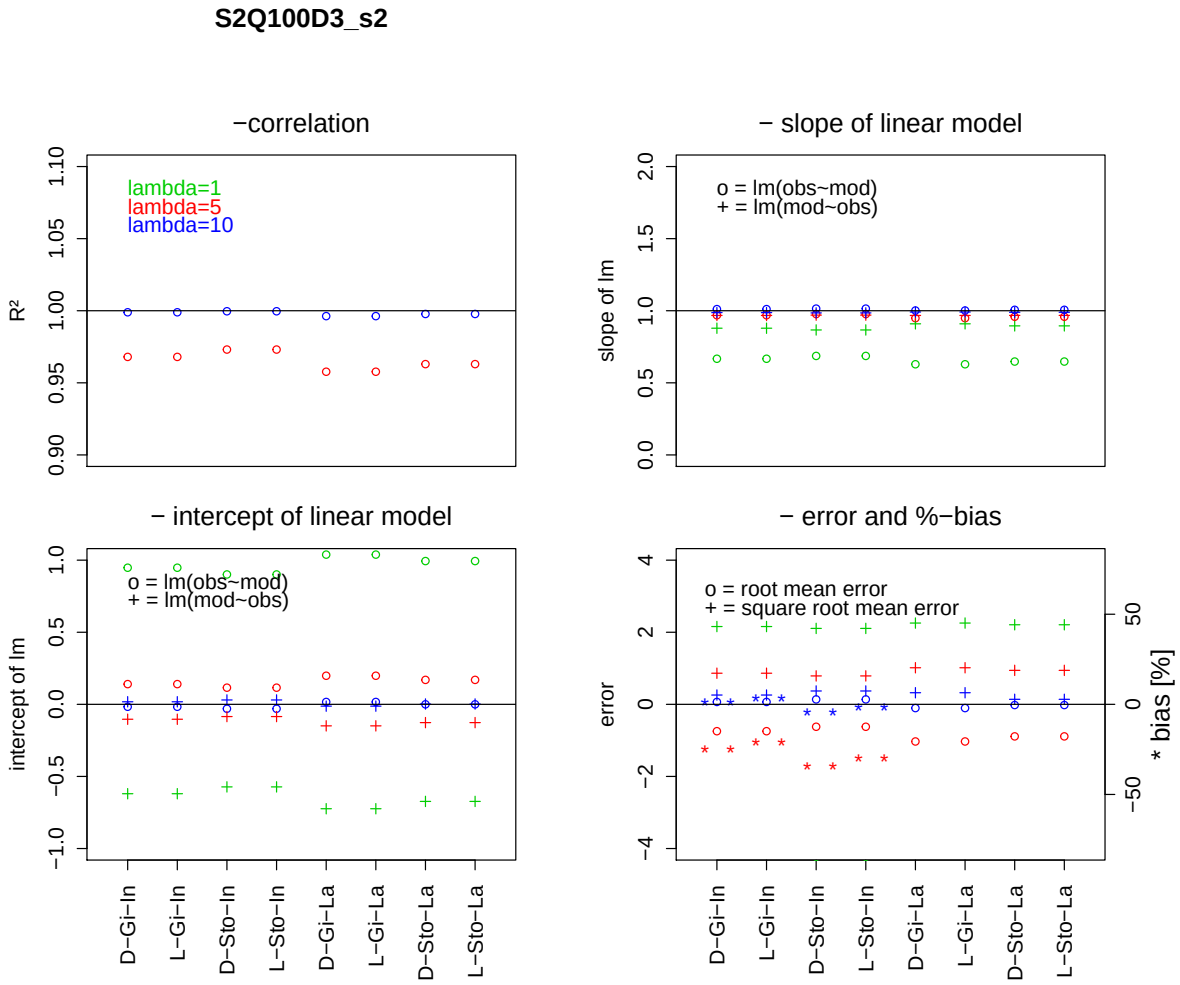

Figure A.41: Graphical representaiton of statisitcal evaluation of modeled and observed suspended sediment concentration loss in S1Q100D37-s2, velocity deposition model

	r^2	LM_{mo}		LM_{om}		RMA		Error		
		a	b	a	b	a	b	MSE	SMSE	PBIAS
1-Gi-In -mean	0.99	1.00	0.02	0.99	-0.01	1.01	0.02	-0.13	0.36	-4.16
5-Gi-In -mean	0.99	1.03	-0.11	0.96	0.11	1.04	-0.11	0.56	0.75	18.24
10-Gi-In -mean	0.99	1.03	-0.11	0.95	0.12	1.04	-0.12	0.58	0.76	18.94
1-Sto-In -mean	0.94	0.92	0.28	0.95	-0.21	0.98	0.25	-1.45	1.20	-46.93
5-Sto-In -mean	1.00	1.02	-0.07	0.98	0.07	1.02	-0.07	0.33	0.58	10.82
10-Sto-In -mean	0.99	1.03	-0.10	0.96	0.10	1.04	-0.10	0.52	0.72	16.83
1-Gi-La -mean	0.99	1.00	0.02	0.99	-0.01	1.01	0.02	-0.12	0.35	-3.98
5-Gi-La -mean	0.99	1.03	-0.11	0.96	0.11	1.04	-0.11	0.56	0.75	18.28
10-Gi-La -mean	0.99	1.03	-0.11	0.95	0.12	1.04	-0.12	0.58	0.76	18.94
1-Sto-La -mean	0.94	0.92	0.28	0.95	-0.20	0.98	0.25	-1.44	1.20	-46.60
5-Sto-La -mean	1.00	1.02	-0.07	0.98	0.07	1.02	-0.07	0.34	0.58	10.97
10-Sto-La -mean	0.99	1.03	-0.10	0.96	0.10	1.04	-0.11	0.52	0.72	16.90
1-Gi-In -ave5	0.99	0.99	0.07	0.99	-0.06	1.00	0.06	-0.37	0.61	-11.99
5-Gi-In -ave5	0.99	1.03	-0.10	0.96	0.10	1.03	-0.10	0.52	0.72	16.70
10-Gi-In -ave5	0.99	1.03	-0.11	0.95	0.12	1.04	-0.12	0.58	0.76	18.77
1-Sto-In -ave5	0.93	0.89	0.37	0.98	-0.29	0.95	0.34	-1.86	1.36	-60.32
5-Sto-In -ave5	1.00	1.01	-0.04	0.99	0.04	1.01	-0.04	0.18	0.42	5.80
10-Sto-In -ave5	1.00	1.03	-0.09	0.97	0.09	1.03	-0.09	0.44	0.66	14.16
1-Gi-La -ave5	0.99	1.00	0.04	0.99	-0.03	1.01	0.04	-0.25	0.50	-8.12
5-Gi-La -ave5	0.99	1.03	-0.11	0.96	0.11	1.04	-0.11	0.55	0.74	17.76
10-Gi-La -ave5	0.99	1.03	-0.11	0.95	0.12	1.04	-0.12	0.58	0.76	18.91
1-Sto-La -ave5	0.93	0.90	0.33	0.95	-0.24	0.97	0.29	-1.67	1.29	-54.17
5-Sto-La -ave5	1.00	1.02	-0.06	0.98	0.05	1.02	-0.06	0.27	0.52	8.83
10-Sto-La -ave5	1.00	1.03	-0.10	0.96	0.10	1.03	-0.10	0.49	0.70	15.91

Table A.55: Graphical representaiton of statisitcal evaluation of modeled and observed suspended sediment concentration loss in S2Q100D37-s2, velocity deposition model

	TR		r^2	LM_{mo}		LM_{om}		RMA		Error		
	obs	mod		a	b	a	b	a	b	MSE	SMSE	PBIAS
1 Gi In mean	2.57	2.22	0.18	0.07	2.03	0.45	1.57	0.40	1.18	2.82	1.68	13.72
5 Gi In mean	2.57	2.10	0.72	0.29	1.37	1.79	-1.19	0.40	1.07	3.76	1.94	18.26
10 Gi In mean	2.57	0.80	0.64	0.09	0.58	4.68	-1.19	0.14	0.45	14.15	3.76	68.75
1 Sto In mean	2.57	2.23	0.14	0.06	2.08	0.33	1.84	0.42	1.14	2.75	1.66	13.36
5 Sto In mean	2.57	2.14	0.55	0.19	1.65	1.58	-0.80	0.35	1.25	3.50	1.87	17.00
10 Sto In mean	2.57	0.83	0.31	0.04	0.72	2.25	0.70	0.14	0.48	13.92	3.73	67.65
1 Gi La mean	2.57	2.22	0.18	0.07	2.03	0.45	1.56	0.40	1.18	2.81	1.68	13.67
5 Gi La mean	2.57	2.10	0.72	0.29	1.37	1.79	-1.19	0.40	1.07	3.75	1.94	18.22
10 Gi La mean	2.57	0.81	0.64	0.09	0.58	4.67	-1.19	0.14	0.45	14.14	3.76	68.71
1 Sto La mean	2.57	2.23	0.14	0.06	2.08	0.33	1.84	0.42	1.14	2.74	1.65	13.30
5 Sto La mean	2.57	2.14	0.55	0.19	1.65	1.58	-0.80	0.35	1.25	3.49	1.87	16.95
10 Sto La mean	2.57	0.83	0.31	0.04	0.72	2.25	0.70	0.14	0.48	13.91	3.73	67.61
1 Gi In ave5	2.57	2.23	0.17	0.07	2.04	0.40	1.68	0.42	1.15	2.77	1.66	13.46
5 Gi In ave5	2.57	2.10	0.71	0.28	1.39	1.82	-1.25	0.39	1.10	3.75	1.94	18.22
10 Gi In ave5	2.57	0.81	0.59	0.08	0.60	4.39	-0.97	0.14	0.46	14.12	3.76	68.61
1 Sto In ave5	2.57	2.22	0.13	0.06	2.08	0.30	1.92	0.43	1.10	2.82	1.68	13.72
5 Sto In ave5	2.57	2.14	0.52	0.18	1.67	1.49	-0.62	0.35	1.24	3.46	1.86	16.81
10 Sto In ave5	2.57	0.84	0.27	0.04	0.73	1.78	1.09	0.15	0.45	13.88	3.73	67.46
1 Gi La ave5	2.57	2.23	0.17	0.07	2.04	0.42	1.65	0.42	1.16	2.77	1.66	13.44
5 Gi La ave5	2.57	2.10	0.71	0.28	1.39	1.82	-1.25	0.39	1.10	3.75	1.94	18.22
10 Gi La ave5	2.57	0.81	0.60	0.08	0.60	4.49	-1.05	0.13	0.46	14.13	3.76	68.66
1 Sto La ave5	2.57	2.23	0.13	0.06	2.08	0.30	1.90	0.43	1.12	2.74	1.65	13.29
5 Sto La ave5	2.57	2.14	0.53	0.18	1.67	1.51	-0.66	0.35	1.24	3.46	1.86	16.80
10 Sto La ave5	2.57	0.84	0.28	0.04	0.73	1.88	1.00	0.15	0.46	13.88	3.73	67.46

Table A.56: Calibration statistics for modelled and observed trapping rates in S2Q100D48-s1, velocity deposition model

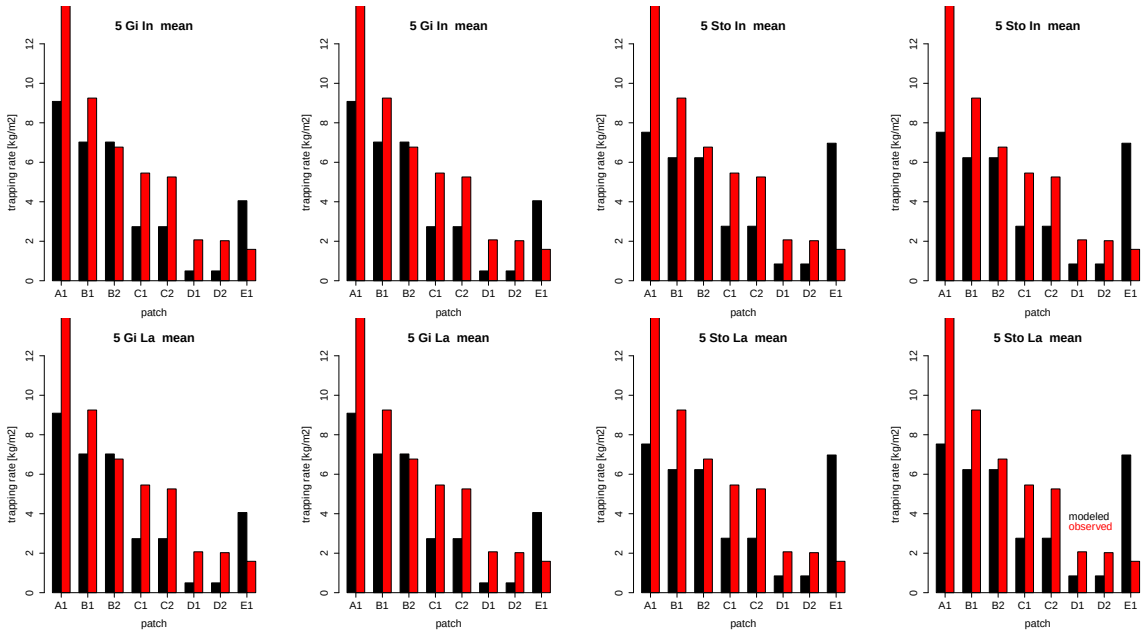

Figure A.42: Modelled and observed interstitial deposition in S2Q100D48-s1, velocity deposition model for eight selected value set combinations

	TR		r^2	LM_{mo}		LM_{om}		RMA		Error		
	obs	mod		a	b	a	b	a	b	MSE	SMSE	PBIAS
1 Gi In mean	8.65	4.44	0.16	0.04	4.05	0.59	6.03	0.28	2.05	33.69	5.80	48.69
5 Gi In mean	8.65	4.21	0.74	0.20	2.45	2.70	-2.72	0.27	1.84	35.57	5.96	51.39
10 Gi In mean	8.65	1.61	0.65	0.06	1.08	7.02	-2.64	0.09	0.80	56.34	7.51	81.41
1 Sto In mean	8.65	4.46	0.11	0.03	4.17	0.40	6.88	0.29	1.96	33.55	5.79	48.47
5 Sto In mean	8.65	4.27	0.55	0.13	3.14	2.34	-1.34	0.24	2.22	35.04	5.92	50.63
10 Sto In mean	8.65	1.66	0.30	0.03	1.42	3.17	3.38	0.09	0.84	55.89	7.48	80.76
1 Gi La mean	8.65	4.44	0.16	0.05	4.05	0.59	6.03	0.28	2.05	33.68	5.80	48.66
5 Gi La mean	8.65	4.21	0.74	0.20	2.45	2.70	-2.72	0.27	1.84	35.55	5.96	51.36
10 Gi La mean	8.65	1.61	0.65	0.06	1.08	7.01	-2.63	0.09	0.80	56.33	7.51	81.39
1 Sto La mean	8.65	4.46	0.12	0.03	4.17	0.40	6.87	0.29	1.96	33.52	5.79	48.44
5 Sto La mean	8.65	4.27	0.55	0.13	3.14	2.34	-1.33	0.24	2.22	35.03	5.92	50.61
10 Sto La mean	8.65	1.67	0.30	0.03	1.42	3.17	3.38	0.10	0.84	55.88	7.48	80.74
1 Gi In ave5	8.65	4.45	0.15	0.04	4.09	0.51	6.38	0.29	1.97	33.59	5.80	48.53
5 Gi In ave5	8.65	4.21	0.73	0.20	2.52	2.73	-2.86	0.27	1.90	35.55	5.96	51.36
10 Gi In ave5	8.65	1.62	0.60	0.06	1.13	6.50	-1.85	0.09	0.82	56.29	7.50	81.33
1 Sto In ave5	8.65	4.44	0.10	0.03	4.17	0.35	7.11	0.30	1.87	33.70	5.80	48.69
5 Sto In ave5	8.65	4.28	0.53	0.13	3.19	2.19	-0.72	0.24	2.21	34.97	5.91	50.52
10 Sto In ave5	8.65	1.67	0.25	0.03	1.45	2.43	4.58	0.10	0.79	55.81	7.47	80.65
1 Gi La ave5	8.65	4.45	0.15	0.04	4.08	0.53	6.29	0.28	1.99	33.58	5.79	48.52
5 Gi La ave5	8.65	4.21	0.73	0.20	2.51	2.74	-2.87	0.27	1.89	35.55	5.96	51.36
10 Gi La ave5	8.65	1.61	0.61	0.06	1.13	6.67	-2.10	0.09	0.82	56.31	7.50	81.36
1 Sto La ave5	8.65	4.46	0.11	0.03	4.19	0.36	7.05	0.30	1.90	33.52	5.79	48.43
5 Sto La ave5	8.65	4.28	0.53	0.13	3.18	2.22	-0.85	0.24	2.21	34.96	5.91	50.52
10 Sto La ave5	8.65	1.67	0.26	0.03	1.45	2.59	4.32	0.10	0.81	55.81	7.47	80.65

Table A.57: Modelled and observed interstitial deposition in S2Q100D48-s2, velocity deposition model for eight selected value set combinations

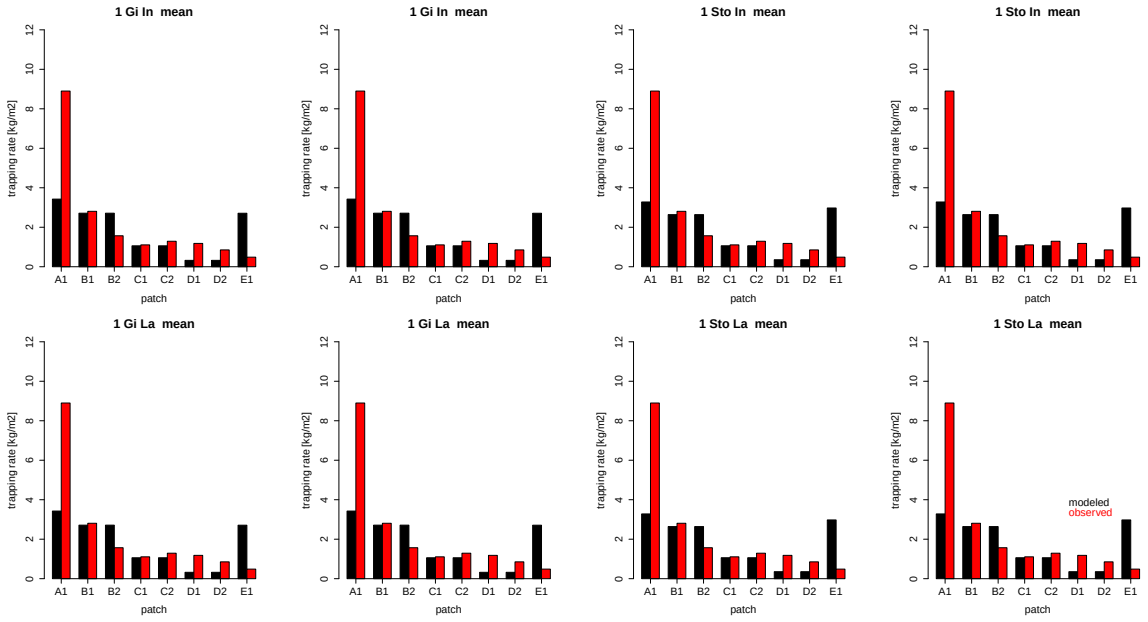

Figure A.43: Modelled and observed trapping rates for selected value set combintaitons in S2Q100D37-s1, velocity deposition model

	TR		r^2	LM_{mo}		LM_{om}		RMA		Error		
	obs	mod		a	b	a	b	a	b	MSE	SMSE	PBIAS
1 Gi In mean	2.27	1.79	0.60	0.27	1.18	1.35	-0.14	0.45	0.78	3.87	1.97	21.25
5 Gi In mean	2.27	0.00		0.00	-0.00		2.27	0.00	0.00	18.19	4.27	100.00
10 Gi In mean	2.27	0.00		0.00	-0.00		2.27	0.00	0.00	18.19	4.27	100.00
1 Sto In mean	2.27	1.80	0.55	0.24	1.25	1.25	0.04	0.44	0.80	3.83	1.96	21.05
5 Sto In mean	2.27	1.80	0.81	0.52	0.63	1.26	0.01	0.64	0.35	3.75	1.94	20.64
10 Sto In mean	2.27	0.00		0.00	-0.00		2.27	0.00	0.00	18.19	4.27	100.00
1 Gi La mean	2.27	1.79	0.60	0.27	1.18	1.35	-0.14	0.45	0.78	3.87	1.97	21.25
5 Gi La mean	2.27	0.00		0.00	-0.00		2.27	0.00	0.00	18.19	4.27	100.00
10 Gi La mean	2.27	0.00		0.00	-0.00		2.27	0.00	0.00	18.19	4.27	100.00
1 Sto La mean	2.27	1.80	0.55	0.24	1.25	1.25	0.04	0.44	0.80	3.83	1.96	21.05
5 Sto La mean	2.27	1.80	0.81	0.52	0.63	1.26	0.01	0.64	0.35	3.75	1.94	20.64
10 Sto La mean	2.27	0.00		0.00	-0.00		2.27	0.00	0.00	18.19	4.27	100.00
1 Gi In ave5	2.27	1.79	0.60	0.27	1.19	1.34	-0.12	0.45	0.78	3.87	1.97	21.27
5 Gi In ave5	2.27	0.00		0.00	-0.00		2.27	0.00	0.00	18.19	4.27	100.00
10 Gi In ave5	2.27	0.00		0.00	-0.00		2.27	0.00	0.00	18.19	4.27	100.00
1 Sto In ave5	2.27	1.80	0.54	0.24	1.25	1.23	0.06	0.44	0.80	3.83	1.96	21.05
5 Sto In ave5	2.27	1.80	0.81	0.51	0.64	1.28	-0.03	0.63	0.36	3.81	1.95	20.93
10 Sto In ave5	2.27	0.00		0.00	-0.00		2.27	0.00	0.00	18.19	4.27	100.00
1 Gi La ave5	2.27	1.79	0.60	0.27	1.19	1.34	-0.12	0.45	0.78	3.87	1.97	21.27
5 Gi La ave5	2.27	0.00		0.00	-0.00		2.27	0.00	0.00	18.19	4.27	100.00
10 Gi La ave5	2.27	0.00		0.00	-0.00		2.27	0.00	0.00	18.19	4.27	100.00
1 Sto La ave5	2.27	1.80	0.54	0.24	1.25	1.23	0.06	0.44	0.80	3.83	1.96	21.05
5 Sto La ave5	2.27	1.80	0.81	0.51	0.64	1.28	-0.03	0.63	0.36	3.81	1.95	20.93
10 Sto La ave5	2.27	0.00		0.00	-0.00		2.27	0.00	0.00	18.19	4.27	100.00

Table A.58: Modelled and observed interstitial deposition in S2Q100D37-s1, velocity deposition model for eight selected value set combinations

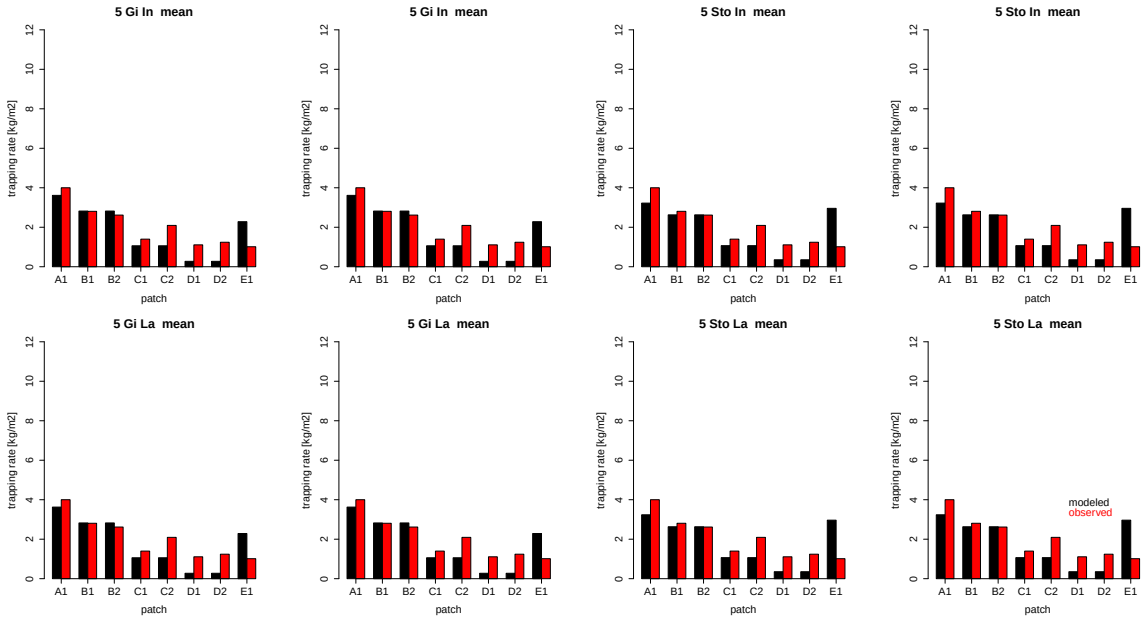

Figure A.44: Modelled and observed trapping rates for selected value set combintaitons in S2Q100D37-s2, velocity deposition model

	TR		r^2	LM_{mo}		LM_{om}		RMA		Error		
	obs	mod		a	b	a	b	a	b	MSE	SMSE	PBIAS
1 Gi In mean	2.03	1.79	0.54	0.62	0.54	0.48	1.17	1.13	-0.51	1.94	1.39	11.95
5 Gi In mean	2.03	1.78	0.80	0.97	-0.20	0.66	0.86	1.21	-0.69	2.07	1.44	12.72
10 Gi In mean	2.03	1.79	0.94	1.45	-1.15	0.61	0.94	1.54	-1.34	1.95	1.40	11.97
1 Sto In mean	2.03	1.78	0.50	0.57	0.63	0.45	1.24	1.13	-0.51	2.03	1.43	12.48
5 Sto In mean	2.03	1.78	0.64	0.73	0.30	0.56	1.03	1.14	-0.53	2.00	1.42	12.31
10 Sto In mean	2.03	1.78	0.78	0.94	-0.13	0.65	0.87	1.20	-0.66	2.06	1.44	12.66
1 Gi La mean	2.03	1.79	0.55	0.62	0.53	0.48	1.17	1.14	-0.52	1.92	1.39	11.80
5 Gi La mean	2.03	1.78	0.80	0.97	-0.20	0.66	0.86	1.21	-0.69	2.05	1.43	12.59
10 Gi La mean	2.03	1.79	0.94	1.45	-1.15	0.61	0.94	1.54	-1.34	1.93	1.39	11.86
1 Sto La mean	2.03	1.78	0.50	0.57	0.62	0.45	1.24	1.13	-0.52	2.00	1.42	12.30
5 Sto La mean	2.03	1.79	0.64	0.73	0.30	0.56	1.03	1.14	-0.53	1.98	1.41	12.17
10 Sto La mean	2.03	1.78	0.78	0.94	-0.13	0.65	0.87	1.20	-0.66	2.04	1.43	12.53
1 Gi In ave5	2.03	1.79	0.49	0.57	0.63	0.42	1.29	1.17	-0.59	1.96	1.40	12.07
5 Gi In ave5	2.03	1.77	0.75	0.90	-0.06	0.63	0.93	1.20	-0.67	2.12	1.46	13.02
10 Gi In ave5	2.03	1.78	0.92	1.35	-0.96	0.63	0.92	1.46	-1.20	2.07	1.44	12.70
1 Sto In ave5	2.03	1.75	0.45	0.52	0.70	0.39	1.34	1.15	-0.58	2.29	1.51	14.06
5 Sto In ave5	2.03	1.78	0.58	0.68	0.40	0.50	1.14	1.16	-0.58	2.03	1.42	12.45
10 Sto In ave5	2.03	1.77	0.73	0.87	-0.00	0.61	0.94	1.19	-0.65	2.10	1.45	12.91
1 Gi La ave5	2.03	1.79	0.51	0.59	0.60	0.44	1.25	1.16	-0.57	1.92	1.38	11.78
5 Gi La ave5	2.03	1.77	0.76	0.92	-0.09	0.64	0.90	1.20	-0.67	2.09	1.44	12.81
10 Gi La ave5	2.03	1.78	0.93	1.36	-0.98	0.63	0.91	1.47	-1.21	2.06	1.44	12.68
1 Sto La ave5	2.03	1.77	0.47	0.54	0.68	0.41	1.31	1.15	-0.57	2.08	1.44	12.77
5 Sto La ave5	2.03	1.79	0.60	0.69	0.37	0.52	1.10	1.15	-0.56	1.99	1.41	12.21
10 Sto La ave5	2.03	1.78	0.74	0.89	-0.03	0.63	0.92	1.19	-0.64	2.07	1.44	12.72

Table A.59: Modelled and observed interstitial deposition in S2Q100D37-s2, velocity deposition model for eight selected value set combinations

A.1.8 Step 4 λ calibration

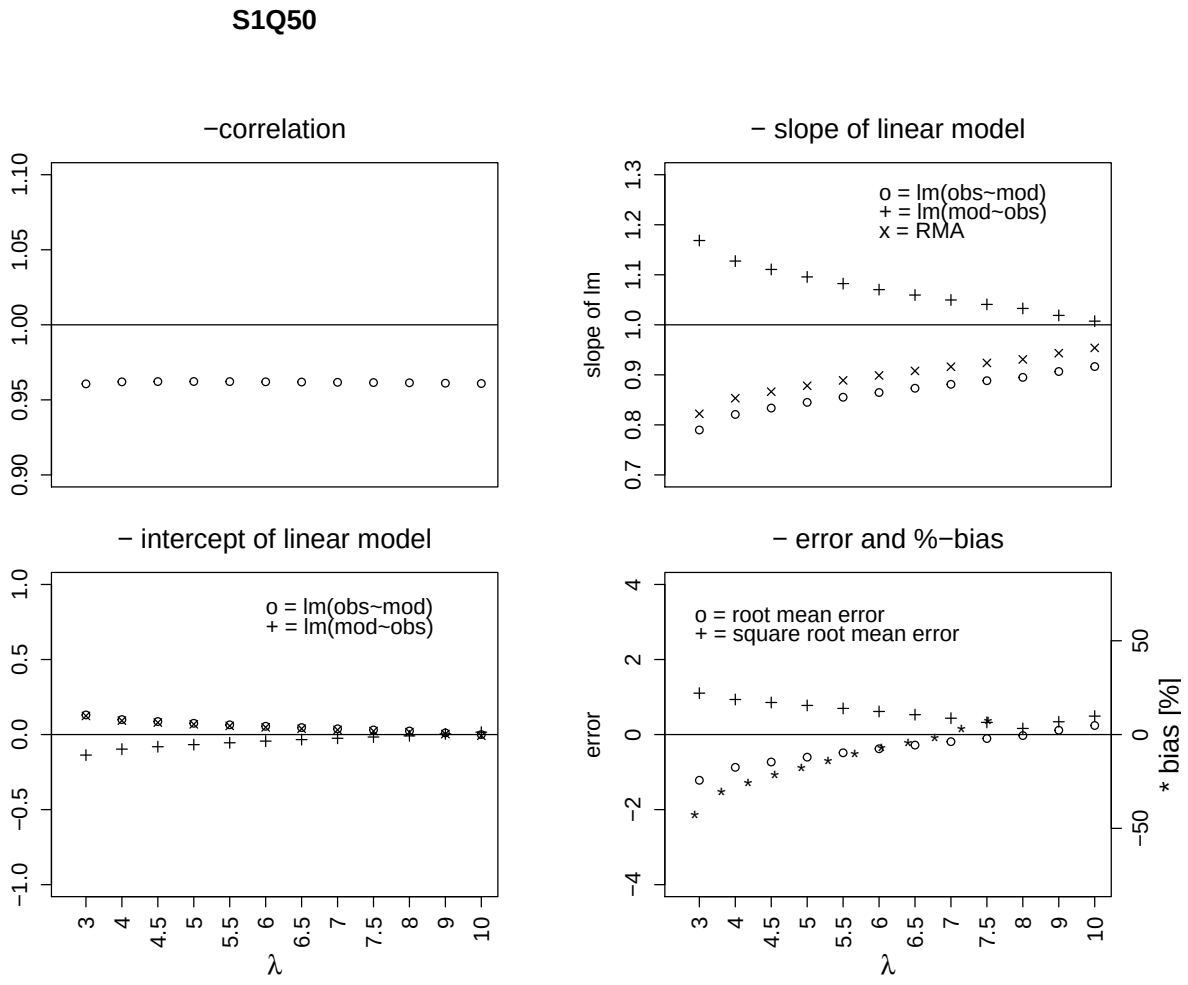

Figure A.45: Step 4, λ calibration statistics for modeled and observed concentration loss in S1Q50, shear stress deposition model

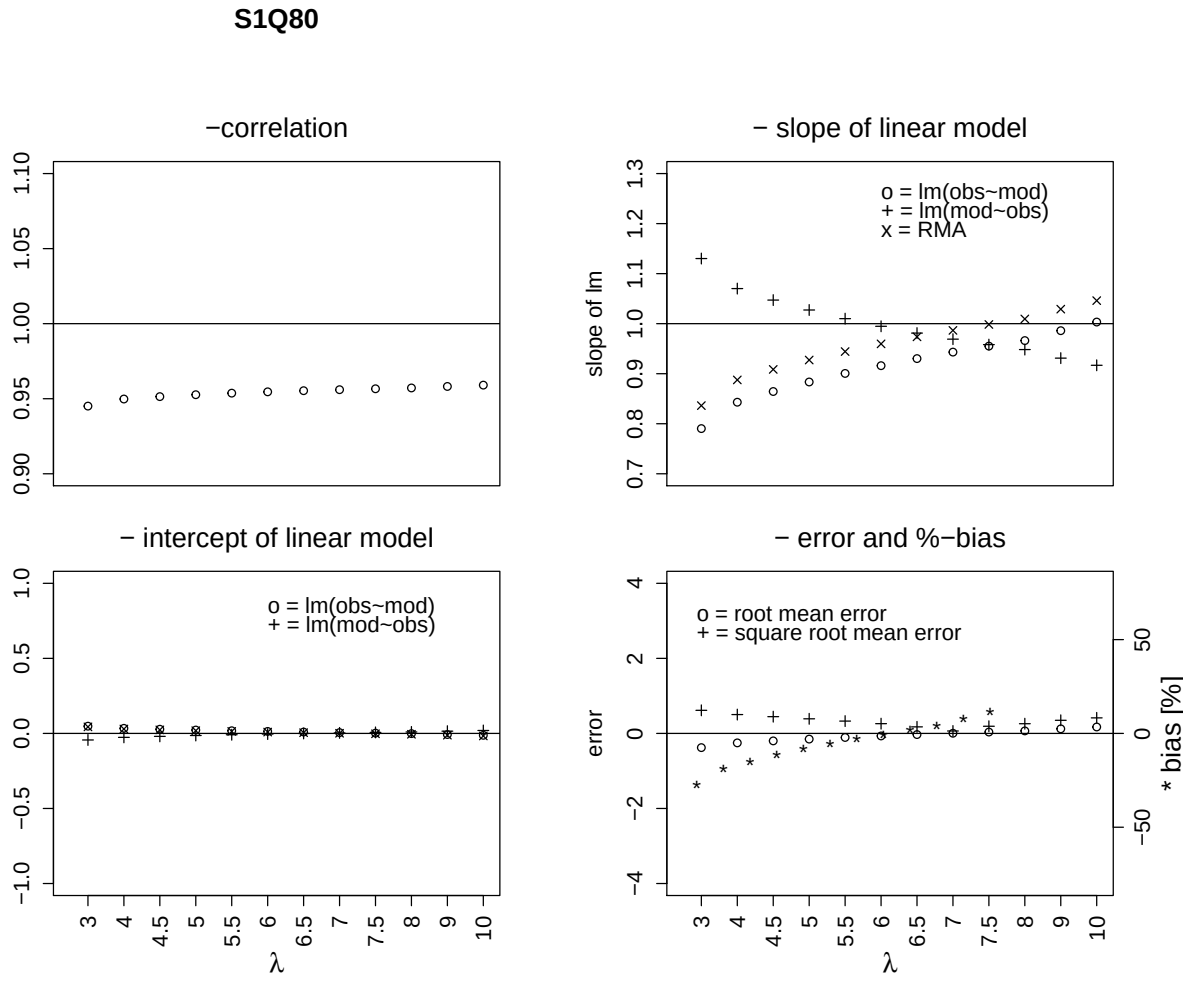

Figure A.46: Step 4, λ calibration statistics for modeled and observed concentration loss in S1Q80, shear stress deposition model

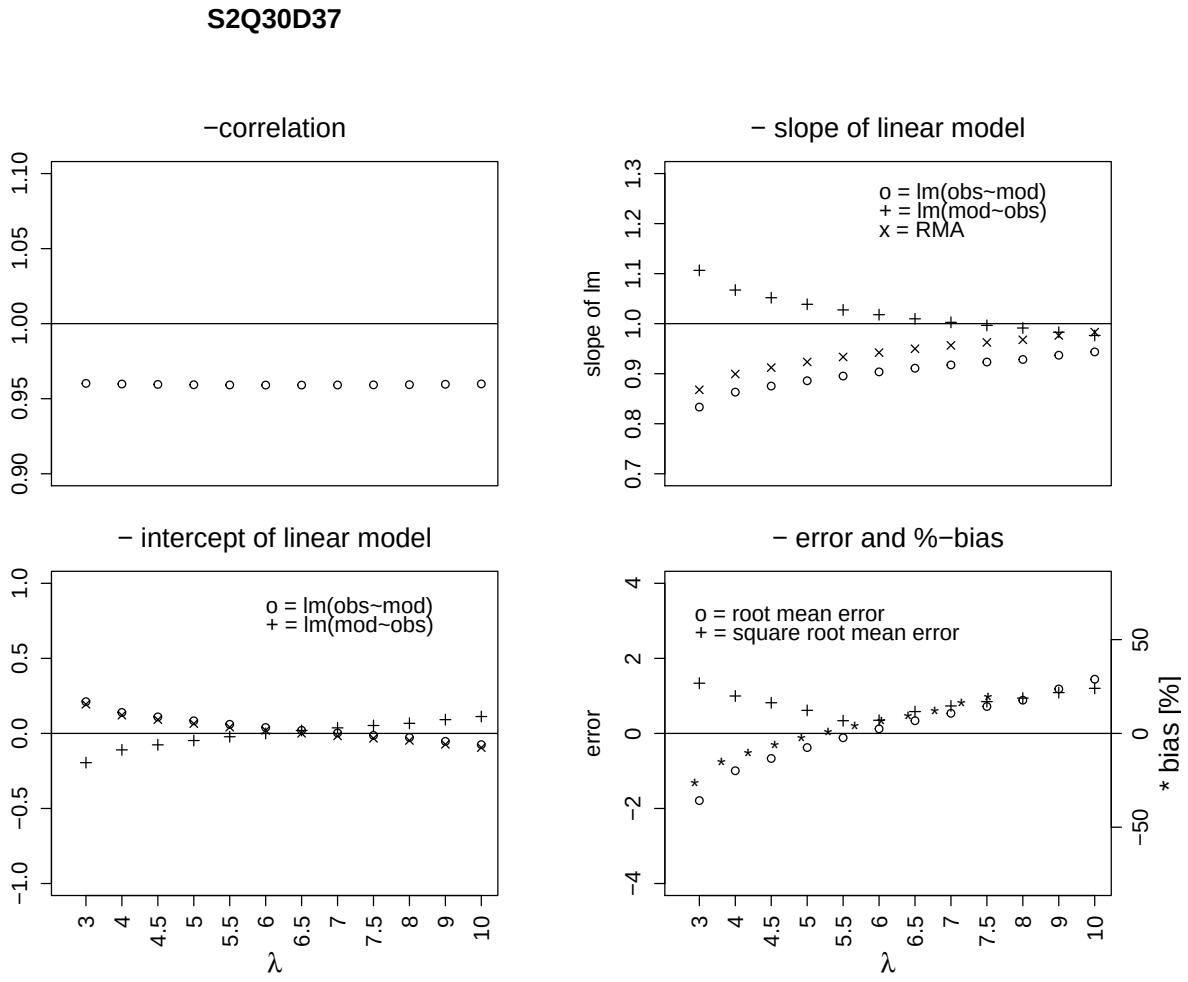

Figure A.47: Step 4, λ calibration statistics for modeled and observed concentration loss in S2Q30D37, shear stress deposition model

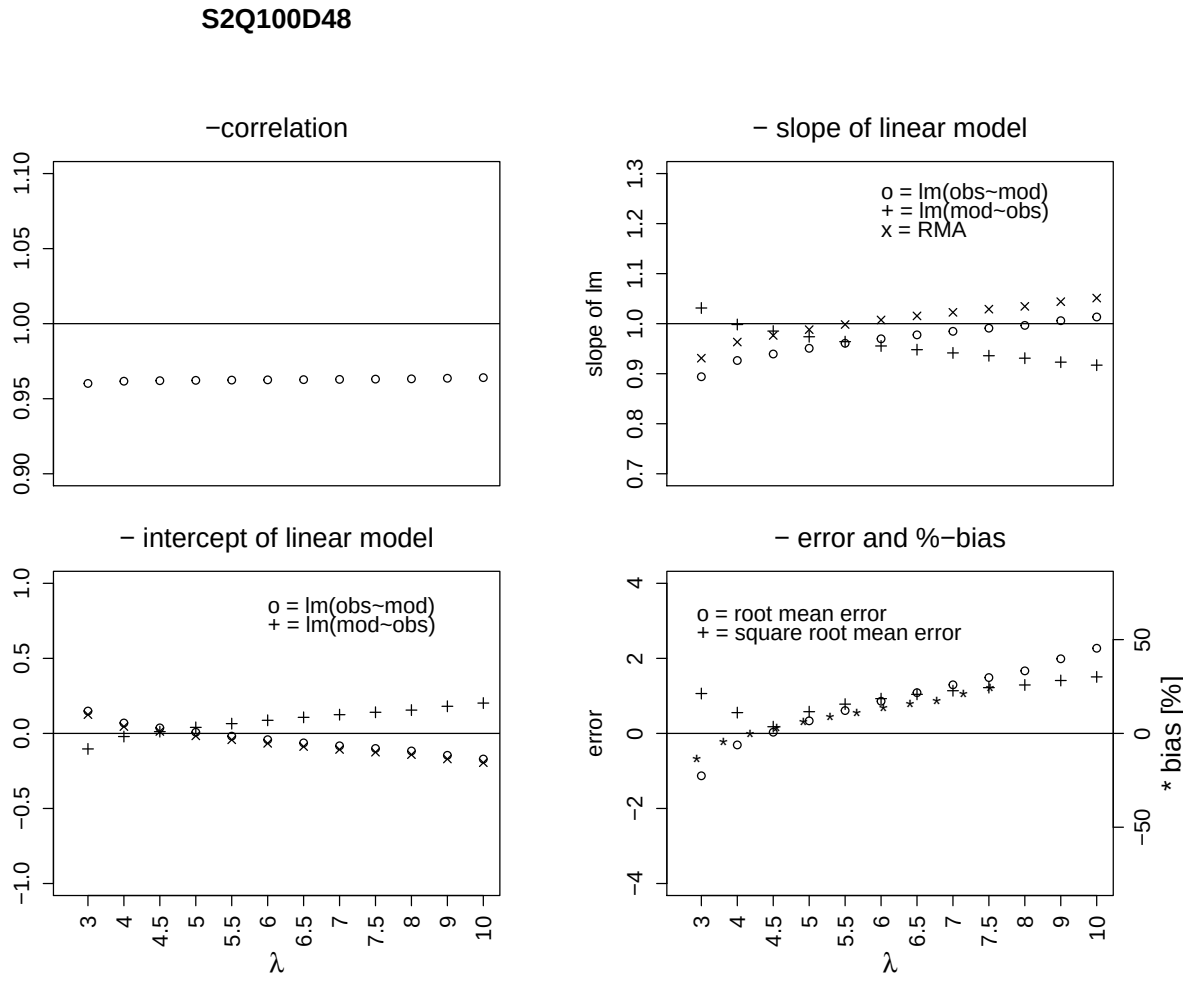

Figure A.48: Step 4, λ calibration statistics for modeled and observed concentration loss in S2Q100D48, shear stress deposition model

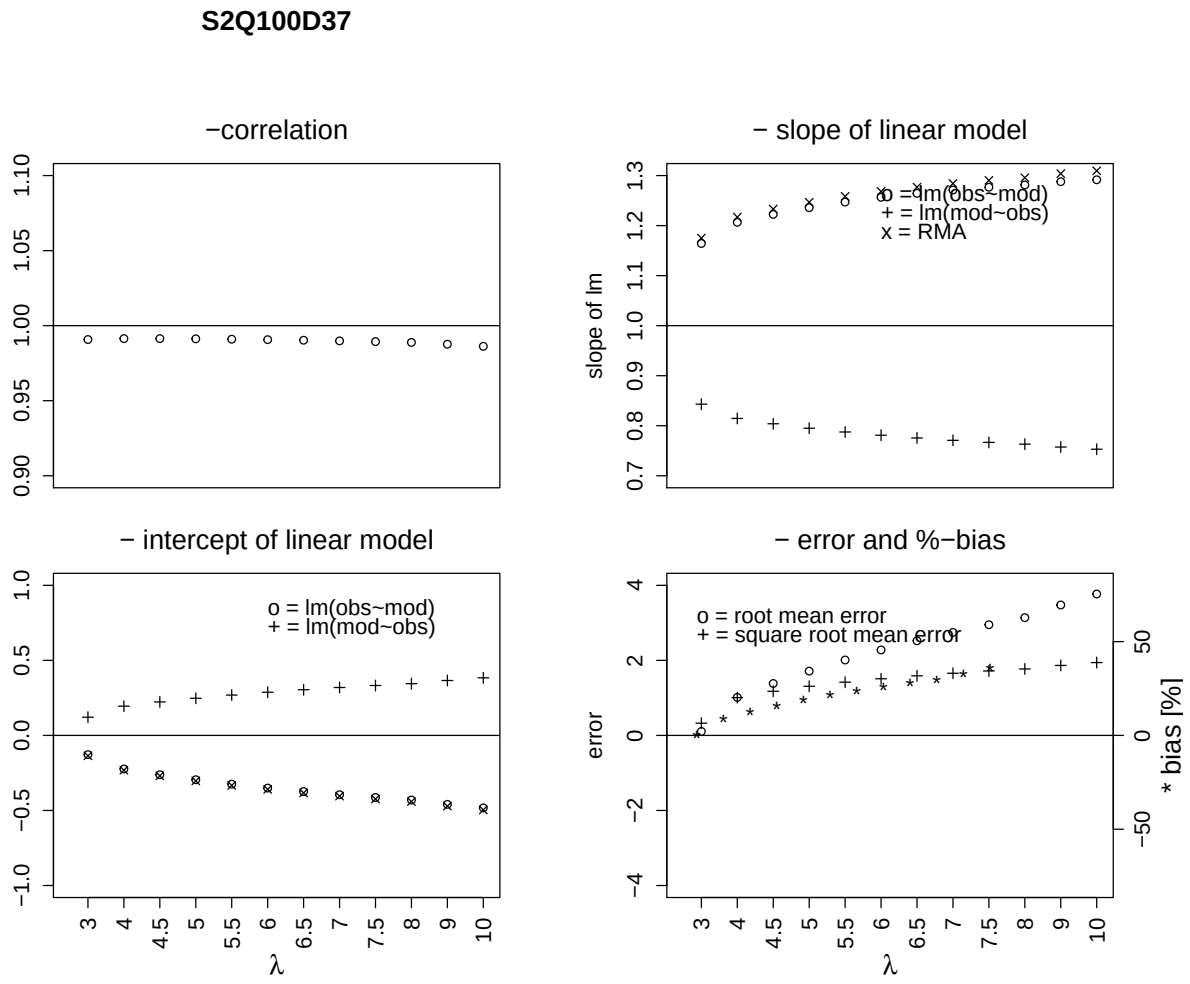

Figure A.49: Step 4, λ calibration statistics for modeled and observed concentration loss in S2Q100D37, shear stress deposition model

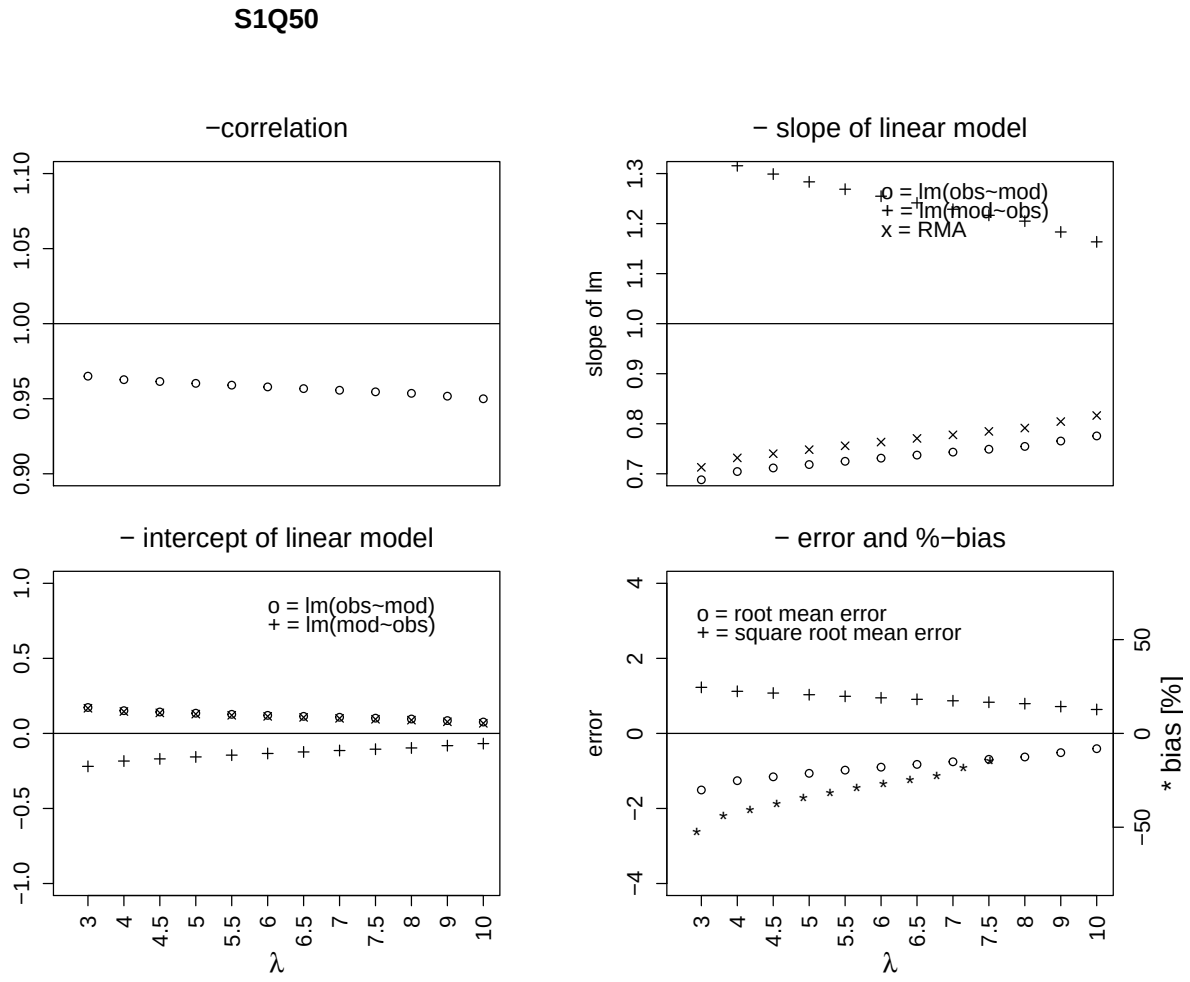

Figure A.50: Step 4, λ calibration statistics for modeled and observed concentration loss in S1Q50, velocity deposition model

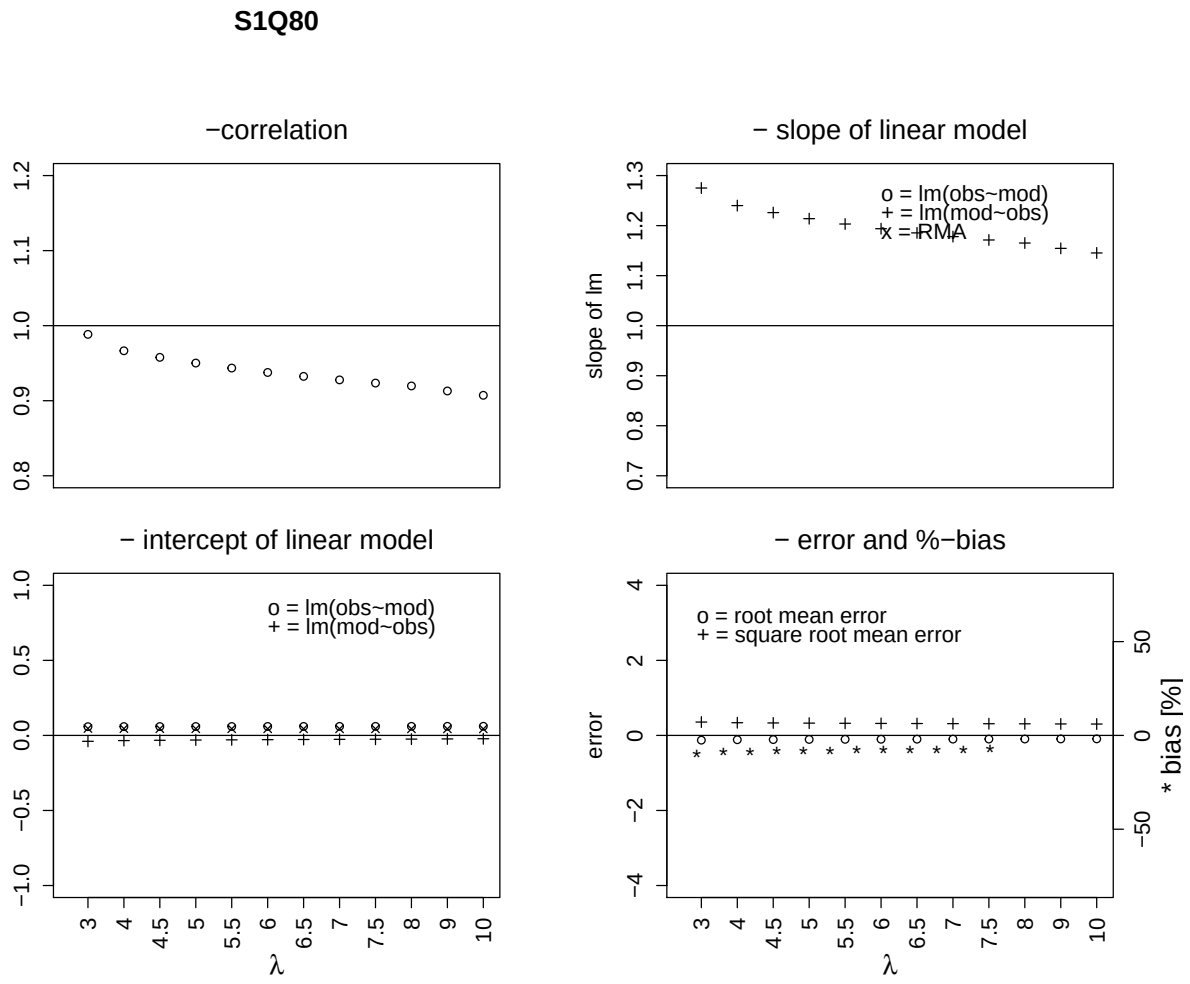

Figure A.51: Step 4, λ calibration statistics for modeled and observed concentration loss in S1Q80, velocity deposition model

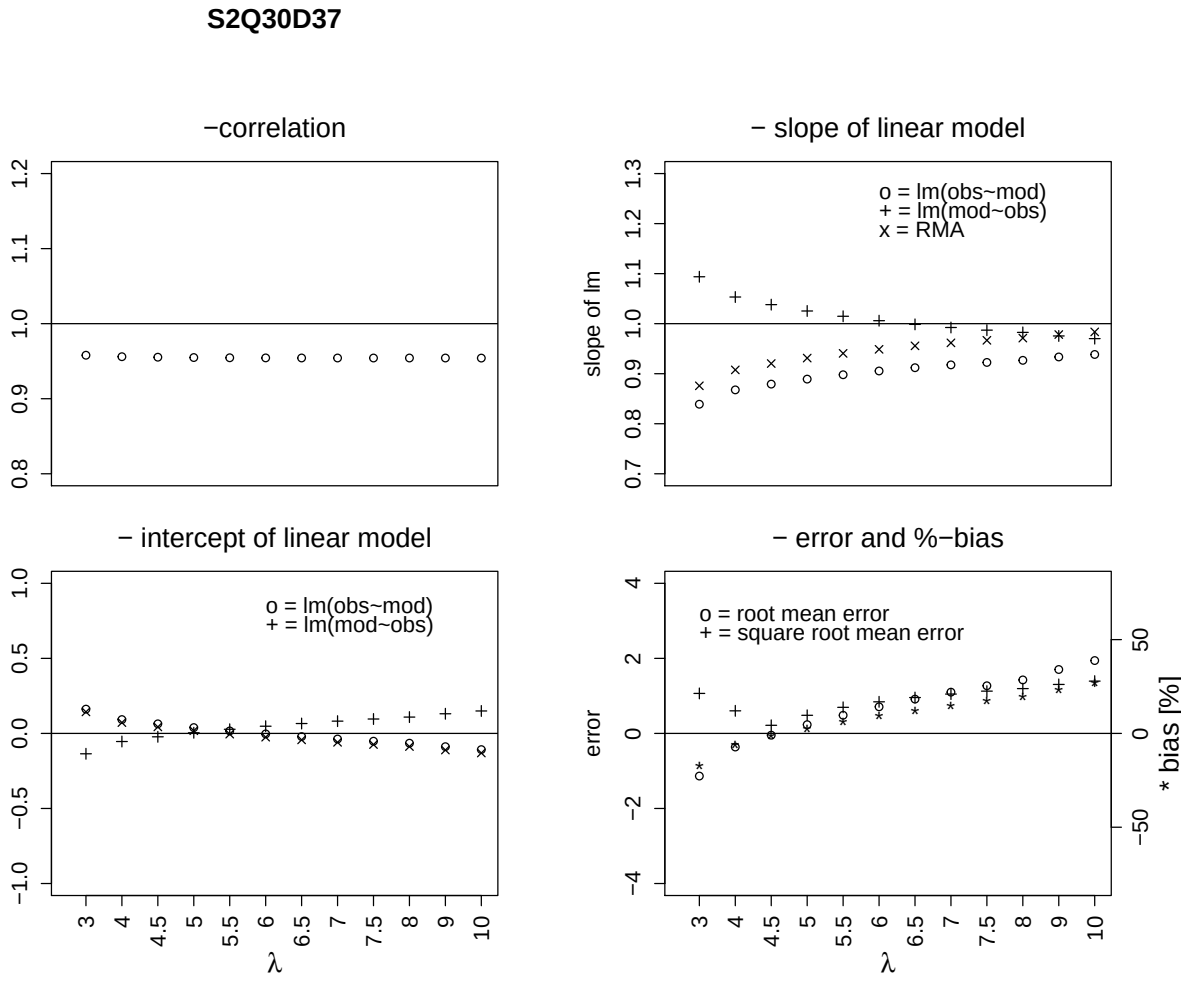

Figure A.52: Step 4, λ calibration statistics for modeled and observed concentration loss in S2Q30D37, velocity deposition model

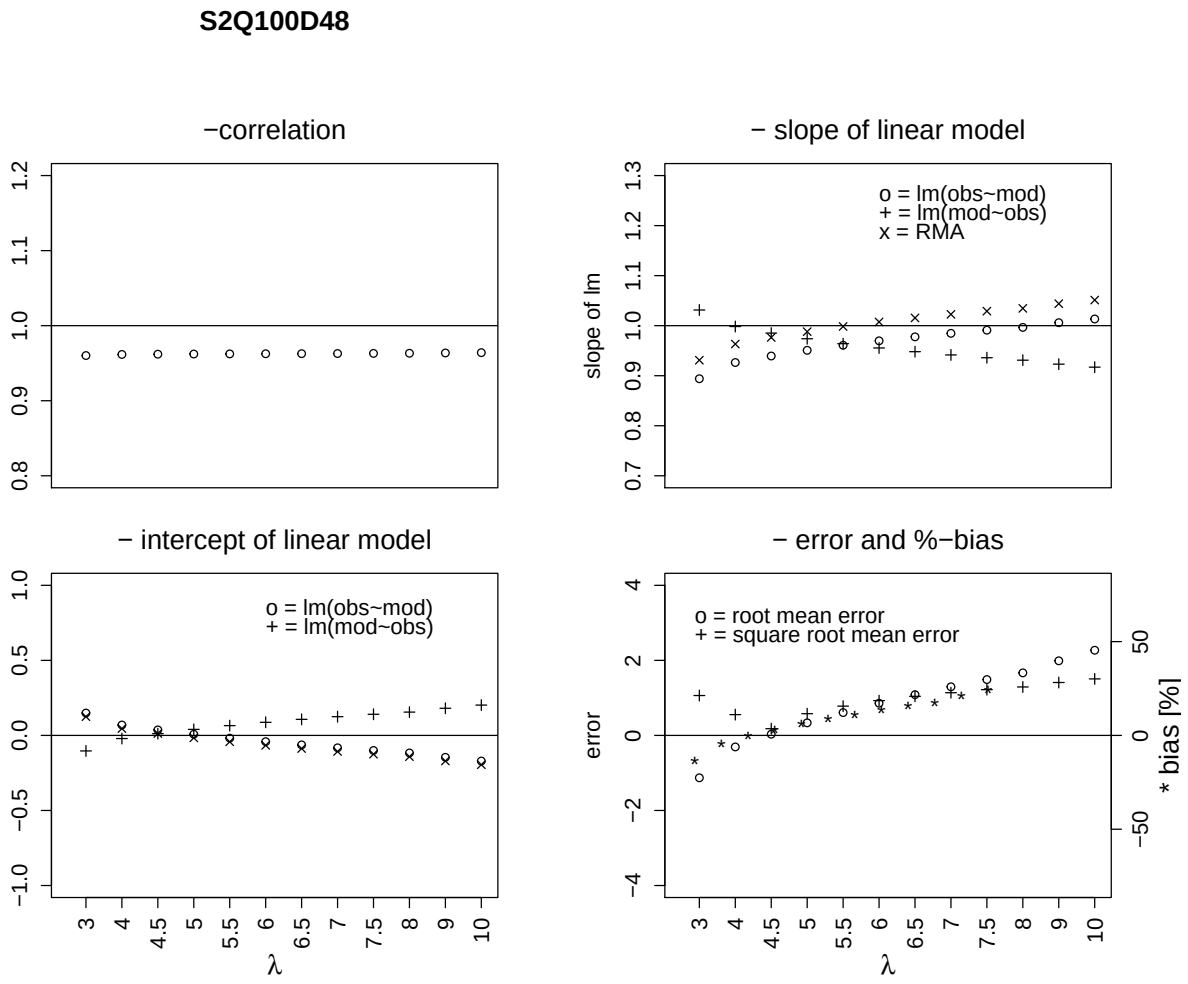

Figure A.53: Step 4, λ calibration statistics for modeled and observed concentration loss in S2Q100D48, velocity deposition model

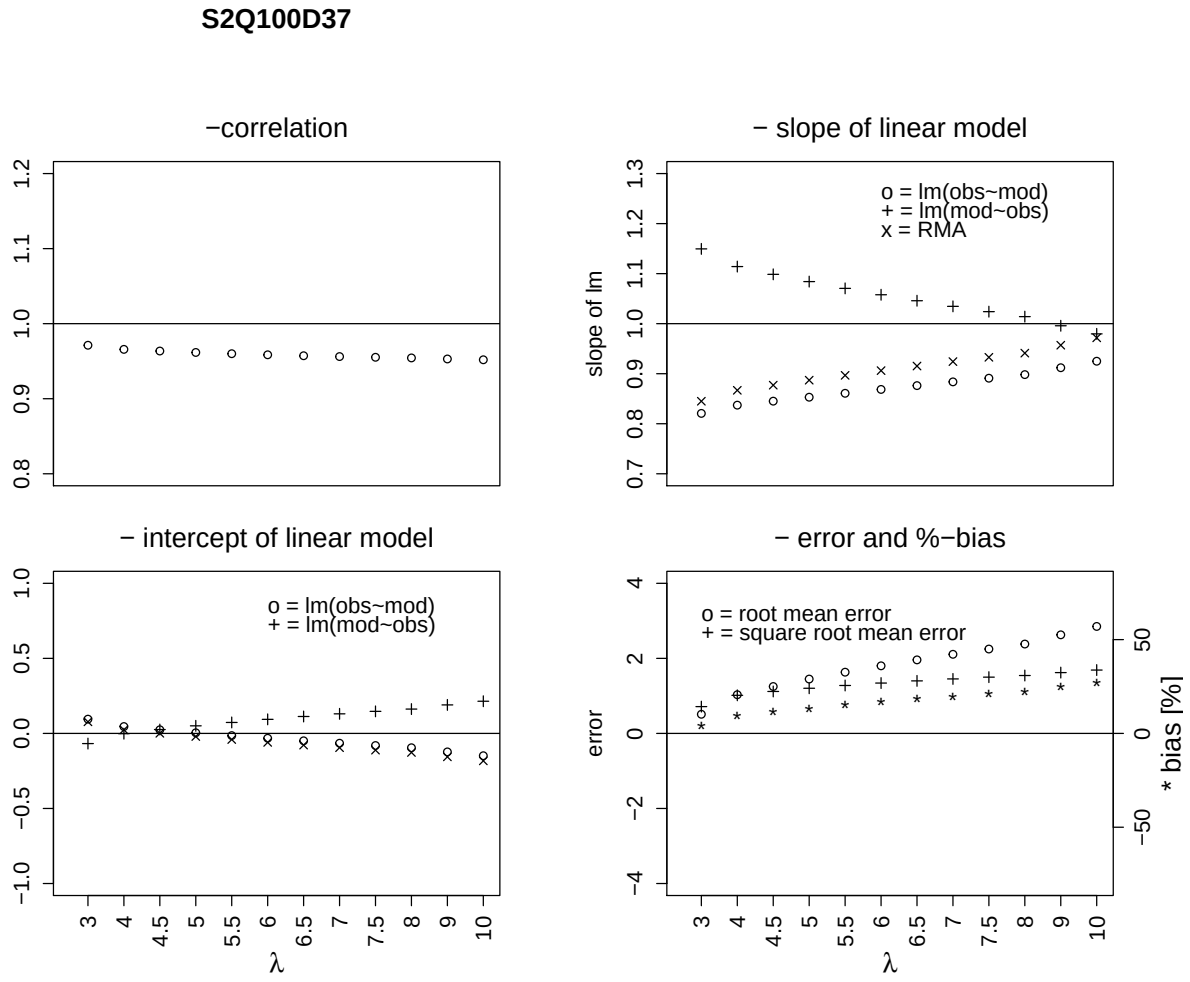

Figure A.54: Step 4, λ calibration statistics for modeled and observed concentration loss in S2Q100D37, velocity deposition model

A.2 Hydrodynamic models

A.2.1 Roughness coefficients

	run	r	r2	mosl	moint	omsl	omint	mona	omna	RMAsl	RMAint	RME	SRME	PBIAS	mean.mod.
1	c5	0.960	0.921	1.531	0.188	0.602	-0.083	-2.543	-2.028	1.595	0.164	-0.394	0.628	-101.815	0.781
2	c10	0.968	0.937	1.253	0.079	0.747	-0.035	0.099	0.212	1.295	0.063	-0.177	0.421	-45.809	0.564
3	c12	0.970	0.942	1.187	0.054	0.793	-0.020	0.499	0.564	1.224	0.040	-0.126	0.355	-32.633	0.513
4	c15	0.971	0.943	1.139	0.035	0.828	-0.007	0.716	0.754	1.173	0.022	-0.089	0.299	-23.078	0.476
5	c20	0.973	0.946	1.085	0.011	0.872	0.011	0.887	0.905	1.116	-0.000	-0.044	0.210	-11.455	0.431
6	c30	0.972	0.944	1.035	-0.016	0.912	0.037	0.929	0.942	1.065	-0.028	0.003	0.055	0.774	0.384
7	c40	0.972	0.945	1.011	-0.028	0.934	0.048	0.893	0.916	1.040	-0.040	0.024	0.155	6.211	0.363
8	c80	0.962	0.925	1.004	-0.049	0.922	0.074	0.715	0.804	1.044	-0.064	0.047	0.217	12.181	0.340
9	c100	0.963	0.926	1.004	-0.052	0.923	0.076	0.687	0.790	1.043	-0.067	0.050	0.224	13.000	0.337
10	c10_32	0.964	0.930	1.147	0.194	0.811	-0.130	-0.758	-1.510	1.189	0.177	-0.251	0.501	-64.802	0.637
11	c15_32	0.965	0.932	0.982	0.167	0.948	-0.132	0.101	-0.549	1.018	0.153	-0.160	0.400	-41.326	0.547
12	c20_32	0.964	0.929	0.886	0.156	1.049	-0.136	0.425	-0.133	0.919	0.143	-0.112	0.334	-28.895	0.499
13	w1	0.972	0.944	1.017	-0.034	0.928	0.053	0.877	0.907	1.047	-0.046	0.027	0.165	7.071	0.359
14	w5	0.973	0.948	1.032	-0.019	0.918	0.038	0.928	0.943	1.060	-0.030	0.006	0.081	1.678	0.380
15	w10	0.974	0.949	1.042	-0.008	0.910	0.027	0.938	0.949	1.070	-0.019	-0.008	0.092	-2.167	0.395
16	w15	0.974	0.949	1.055	-0.000	0.899	0.020	0.933	0.944	1.083	-0.011	-0.021	0.146	-5.492	0.408
17	w30	0.975	0.950	1.081	0.015	0.879	0.006	0.886	0.902	1.109	0.005	-0.047	0.216	-12.090	0.434
18	w100	0.973	0.947	1.154	0.062	0.821	-0.030	0.532	0.566	1.186	0.050	-0.121	0.348	-31.392	0.508
19	w150	0.972	0.944	1.189	0.085	0.794	-0.046	0.258	0.293	1.224	0.072	-0.158	0.398	-40.875	0.545

Table A.61: Stonyford, calibration, water level

	run	r	r2	mosl	moint	omsl	omint	mona	omna	RMAsl	RMAint	RME	SRME	PBIAS
1	c5	0.791	0.625	0.955	0.386	0.654	-0.080	-1.570	-1.703	1.208	0.269	-0.366	0.605	-79.184
2	c10	0.821	0.674	0.850	0.224	0.794	-0.028	0.097	0.013	1.035	0.139	-0.155	0.393	-33.496
3	c12	0.824	0.680	0.823	0.187	0.826	-0.007	0.320	0.271	0.998	0.106	-0.106	0.325	-22.888
4	c15	0.825	0.680	0.804	0.161	0.846	0.012	0.425	0.400	0.975	0.082	-0.070	0.265	-15.262
5	c20	0.829	0.688	0.785	0.127	0.875	0.033	0.518	0.508	0.947	0.052	-0.027	0.166	-5.950
6	c30	0.829	0.686	0.759	0.096	0.904	0.058	0.544	0.536	0.916	0.023	0.016	0.125	3.366
7	c40	0.833	0.694	0.759	0.075	0.915	0.073	0.534	0.548	0.911	0.004	0.037	0.192	7.980
8	c80	0.832	0.692	0.766	0.049	0.903	0.098	0.461	0.519	0.921	-0.023	0.059	0.244	12.883
9	c100	0.834	0.695	0.770	0.044	0.903	0.101	0.449	0.523	0.923	-0.027	0.063	0.250	13.580
10	c10_32	0.820	0.672	0.818	0.317	0.822	-0.109	-0.392	-0.835	0.998	0.234	-0.233	0.482	-50.397
11	c15_32	0.805	0.649	0.760	0.255	0.854	-0.056	0.113	-0.103	0.943	0.171	-0.145	0.380	-31.311
12	c20_32	0.791	0.625	0.729	0.223	0.858	-0.018	0.285	0.152	0.922	0.134	-0.098	0.313	-21.207
13	w1	0.834	0.695	0.761	0.070	0.913	0.076	0.528	0.547	0.913	0.000	0.040	0.200	8.625
14	w5	0.833	0.694	0.762	0.090	0.911	0.059	0.555	0.549	0.915	0.019	0.020	0.141	4.312
15	w10	0.830	0.689	0.765	0.102	0.901	0.051	0.550	0.540	0.922	0.030	0.006	0.077	1.289
16	w15	0.831	0.690	0.772	0.111	0.893	0.044	0.547	0.535	0.930	0.038	-0.006	0.076	-1.258
17	w30	0.828	0.686	0.783	0.129	0.876	0.032	0.514	0.503	0.946	0.054	-0.029	0.172	-6.386
18	w100	0.828	0.686	0.783	0.129	0.876	0.032	0.514	0.503	0.946	0.054	-0.029	0.172	-6.386
19	w150	0.828	0.686	0.783	0.129	0.876	0.032	0.514	0.503	0.946	0.054	-0.029	0.172	-6.386

Table A.62: Stonyford, calibration, water depth

A.2.2 Calibration tables

A.2.3 Grid

run	LM					RMA					NS	
	r^2	mo sl	int	om sl	int	sl	int	MSE	RMSE	PBIAS	mo	om
c1	0.933	1.186	-14.45	0.734	20.03	1.271	-20.64	0.889	0.943	1.22	-5.52	-2.98
c2.4	0.951	1.051	-4.93	0.860	11.22	1.106	-8.88	1.177	1.085	1.61	-10.12	-7.93
c5	0.962	0.991	-0.69	0.934	6.07	1.030	-3.54	1.320	1.149	1.81	-12.94	-11.87
c10	0.969	0.969	0.89	0.970	3.55	0.999	-1.35	1.397	1.182	1.92	-14.59	-14.30
c14	0.971	0.969	0.86	0.974	3.28	0.997	-1.22	1.421	1.192	1.95	-15.80	-15.61
c20	0.972	0.973	0.56	0.972	3.41	1.000	-1.45	1.435	1.198	1.97	-15.43	-15.10
c40	0.972	0.967	0.93	0.976	3.17	0.996	-1.13	1.450	1.204	1.99	-15.80	-15.61
c80	0.972	0.972	0.60	0.972	3.48	1.000	-1.46	1.457	1.207	2.00	-15.96	-15.61
c200	0.972	0.971	0.63	0.972	3.44	1.000	-1.43	1.459	1.208	2.00	-16.00	-15.67
w1	0.972	0.970	0.75	0.974	3.28	0.998	-1.28	1.450	1.204	1.99	-15.80	-15.54
w5	0.972	0.971	0.70	0.974	3.31	0.998	-1.32	1.446	1.202	1.98	-15.69	-15.41
w10	0.972	0.971	0.66	0.973	3.36	0.999	-1.37	1.440	1.200	1.97	-15.55	-15.25
w15	0.973	0.974	0.44	0.971	3.51	1.002	-1.56	1.435	1.198	1.97	-15.45	-15.07
w30	0.972	0.971	0.70	0.973	3.33	0.999	-1.33	1.427	1.194	1.96	-15.25	-14.97
w100	0.971	0.979	0.12	0.962	4.12	1.009	-2.05	1.390	1.179	1.91	-14.43	-13.86
w150	0.969	0.986	-0.35	0.953	4.72	1.017	-2.62	1.372	1.171	1.88	-14.03	-13.25
w200	0.968	0.991	-0.68	0.947	5.17	1.023	-3.03	1.357	1.165	1.86	-13.71	-12.78

Table A.63: Smithincott, calibration, water level

run	LM					RMA					NS	
	r^2	mo sl	int	om sl	int	sl	int	MSE	RMSE	PBIAS	mo	om
c1	0.876	0.898	0.61	0.854	-0.44	1.025	0.563	-0.572	0.756	-164.43	-1.82	-5.31
c2.4	0.914	0.851	0.33	0.982	-0.27	0.931	0.306	-0.282	0.531	-81.04	-0.19	-1.41
c5	0.943	0.838	0.19	1.060	-0.17	0.889	0.176	-0.137	0.371	-39.51	0.44	-0.03
c10	0.959	0.837	0.12	1.098	-0.10	0.874	0.104	-0.060	0.246	-17.34	0.69	0.49
c14	0.963	0.848	0.09	1.094	-0.07	0.881	0.078	-0.036	0.190	-10.42	0.76	0.62
c20	0.966	0.857	0.07	1.088	-0.06	0.888	0.062	-0.023	0.150	-6.47	0.79	0.68
c40	0.966	0.864	0.05	1.081	-0.04	0.894	0.044	-0.007	0.083	-1.97	0.81	0.73
c80	0.967	0.867	0.05	1.078	-0.03	0.897	0.036	-0.000	0.007	-0.02	0.82	0.75
c200	0.966	0.868	0.04	1.075	-0.02	0.899	0.034	0.002	0.041	0.48	0.82	0.75
w1	0.967	0.864	0.05	1.082	-0.04	0.893	0.044	-0.007	0.082	-1.95	0.81	0.73
w5	0.966	0.861	0.06	1.084	-0.04	0.891	0.049	-0.012	0.108	-3.35	0.81	0.71
w10	0.967	0.861	0.07	1.085	-0.05	0.891	0.055	-0.017	0.132	-5.01	0.80	0.70
w15	0.966	0.859	0.07	1.087	-0.05	0.889	0.060	-0.022	0.147	-6.23	0.79	0.69
w30	0.965	0.851	0.08	1.094	-0.07	0.882	0.072	-0.031	0.175	-8.80	0.77	0.64
w100	0.960	0.844	0.12	1.092	-0.11	0.879	0.109	-0.067	0.259	-19.32	0.68	0.46
w150	0.957	0.844	0.14	1.085	-0.12	0.882	0.126	-0.068	0.261	-24.56	0.63	0.36
w200	0.954	0.844	0.15	1.079	-0.14	0.884	0.141	-0.070	0.265	-28.91	0.58	0.26

Table A.64: Smithincott, calibration, water depth

run	LM					RMA					NS	
	r^2	m-o slope	Int	o-m slope	Int	slope	Int	RME	SRME	PBIAS	m-o	o-m
c5	0.977	1.53	-13.35	0.624	9.49	1.56	-14.26	-0.068	0.2615	-0.3615	-2.341	-0.368
c10	0.977	1.36	-9.05	0.703	7.53	1.39	-9.88	-0.025	0.1585	-0.1328	0.385	0.681
c15	0.973	1.27	-6.93	0.742	6.50	1.31	-7.83	-0.043	0.2073	-0.2273	-0.335	0.221
c20	0.975	1.27	-6.88	0.747	6.41	1.30	-7.72	-0.009	0.0945	-0.0472	0.792	0.878
c30	0.975	1.23	-5.87	0.772	5.79	1.26	-6.67	-0.005	0.0708	-0.0265	0.852	0.907
c10n	0.973	1.27	-6.93	0.742	6.50	1.31	-7.83	-0.043	0.2073	-0.2273	-0.335	0.221
c30n	0.975	1.23	-5.87	0.772	5.79	1.26	-6.67	-0.005	0.0708	-0.0265	0.852	0.907
w10n	0.975	1.25	-6.30	0.761	6.06	1.28	-7.12	-0.005	0.0740	-0.0289	0.838	0.901
w1	0.975	1.21	-5.27	0.787	5.42	1.24	-6.07	-0.002	0.045	-0.011	0.877	0.920
w5	0.975	1.23	-5.85	0.772	5.79	1.26	-6.66	-0.004	0.062	-0.020	0.858	0.911
w10	0.975	1.25	-6.46	0.758	6.15	1.29	-7.28	-0.007	0.082	-0.036	0.825	0.895
w15	0.975	1.26	-6.69	0.752	6.29	1.30	-7.52	-0.007	0.086	-0.039	0.812	0.888
w30	0.975	1.29	-7.23	0.739	6.61	1.32	-8.08	-0.012	0.110	-0.064	0.740	0.851
w100	0.977	1.35	-8.82	0.707	7.41	1.38	-9.64	-0.030	0.173	-0.159	0.222	0.592
w150	0.977	1.38	-9.48	0.694	7.75	1.41	-10.32	-0.041	0.203	-0.218	-0.310	0.338
w200	0.977	1.40	-10.22	0.679	8.11	1.44	-11.07	-0.051	0.227	-0.271	-0.923	0.069

Table A.65: Rewe, calibration, water level

run	LM					RMA					NS	
	r^2	m-o slope	Int	o-m slope	Int	slope	Int	RME	SRME	PBIAS	m-o	o-m
c5	0.684	0.864	0.1624	0.541	0.211	1.26	-0.0618	-7.39e-02	0.27183	-15.3936	-0.19059	0.258
c10	0.688	0.835	0.1262	0.567	0.224	1.21	-0.0860	-2.87e-02	0.16927	-5.9694	-0.01862	0.349
c15	0.630	0.765	0.2106	0.518	0.230	1.21	-0.0419	-6.72e-02	0.25916	-13.9923	-0.25974	0.190
c20	0.690	0.824	0.1111	0.578	0.230	1.19	-0.0966	-1.08e-02	0.10371	-2.2407	0.00990	0.363
c30	0.690	0.822	0.1071	0.580	0.232	1.19	-0.0999	-6.06e-03	0.07785	-1.2626	0.01196	0.364
c15n	0.630	0.765	0.2106	0.518	0.230	1.21	-0.0419	-6.72e-02	0.25916	-13.9923	-0.25974	0.190
c30n	0.690	0.822	0.1071	0.580	0.232	1.19	-0.0999	-6.06e-03	0.07785	-1.2626	0.01196	0.364
w10n	0.690	0.822	0.1071	0.580	0.232	1.19	-0.0999	-6.06e-03	0.07785	-1.2626	0.01196	0.364
w1	0.681	0.824	0.0985	0.563	0.245	1.21	-0.1179	8.04e-05	0.00897	0.0168	-0.10807	0.344
w5	0.689	0.818	0.1090	0.580	0.231	1.19	-0.0981	-6.04e-03	0.07773	-1.2586	0.01174	0.361
w10	0.682	0.806	0.1237	0.577	0.229	1.18	-0.0873	-1.27e-02	0.11275	-2.6486	-0.00110	0.347
w15	0.682	0.807	0.1242	0.576	0.229	1.18	-0.0870	-1.35e-02	0.11631	-2.8181	-0.00186	0.347
w30	0.682	0.811	0.1274	0.574	0.227	1.19	-0.0846	-1.82e-02	0.13488	-3.7899	-0.00670	0.345
w100	0.650	0.788	0.159	0.536	0.239	1.21	-0.0786	-3.45e-02	0.18567	-7.1818	-0.1173	0.280
w150	0.640	0.797	0.166	0.514	0.246	1.24	-0.0855	-4.44e-02	0.21077	-9.2550	-0.2415	0.256
w200	0.637	0.803	0.175	0.506	0.245	1.26	-0.0818	-5.49e-02	0.23440	-11.4464	-0.3104	0.234

Table A.66: Rewe, calibration, water depth

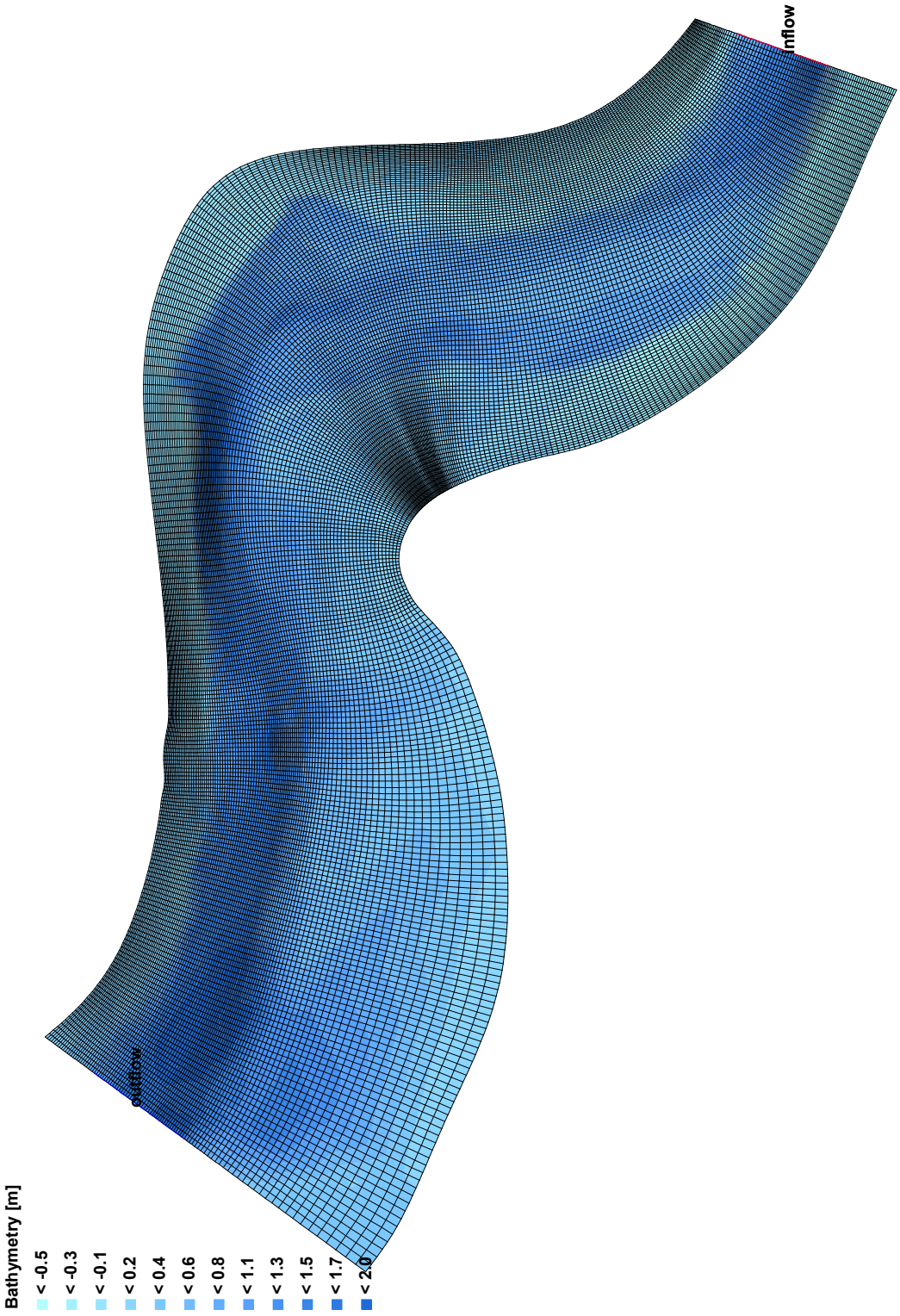

Figure A.55: Grid and bathimetry for Smithincott reach

Figure A.56: Grid and bathimetry for Stonyford reach

A.3 Reach scale deposition model

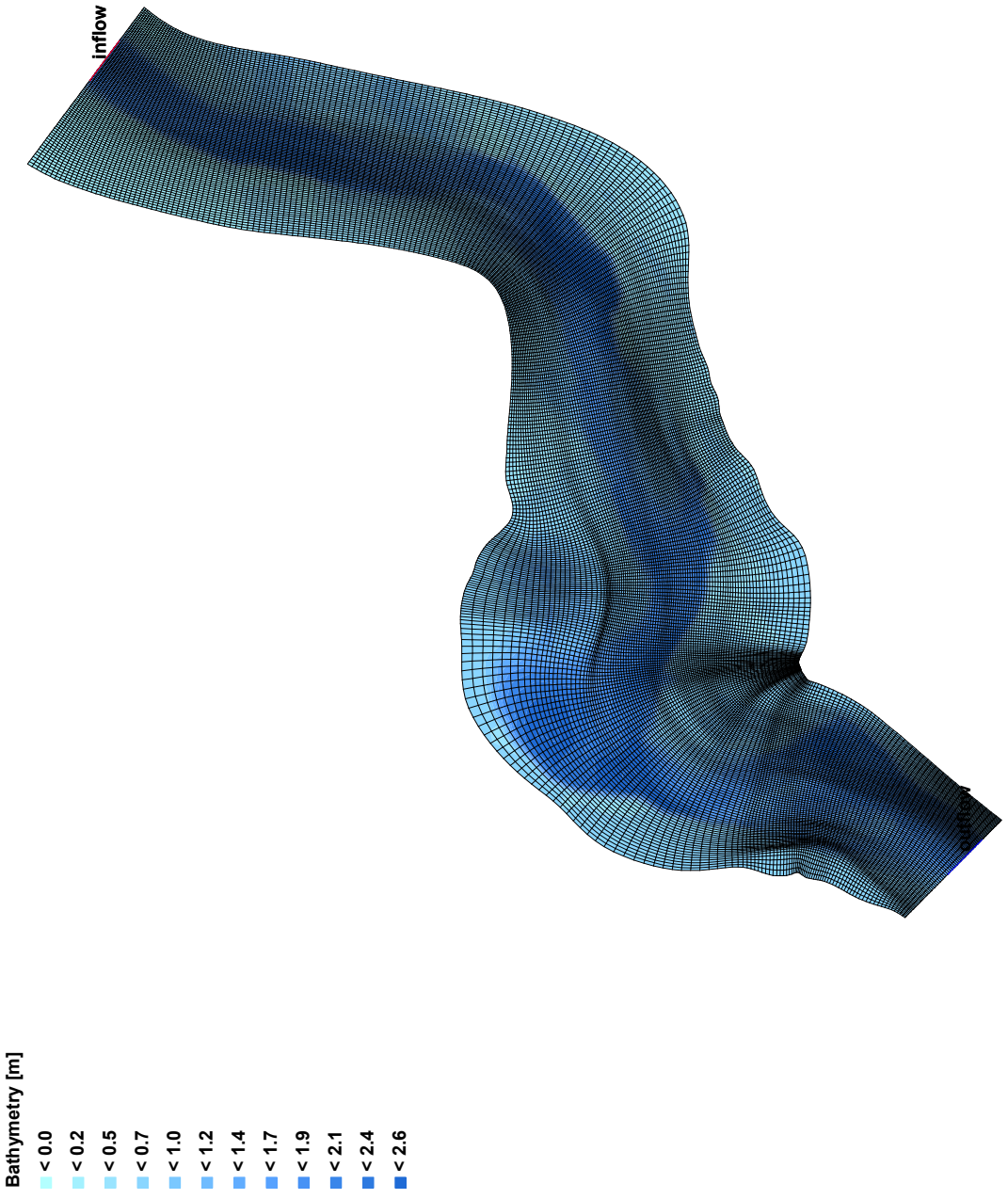

Figure A.57: Grid and bathimetry for Rewe reach

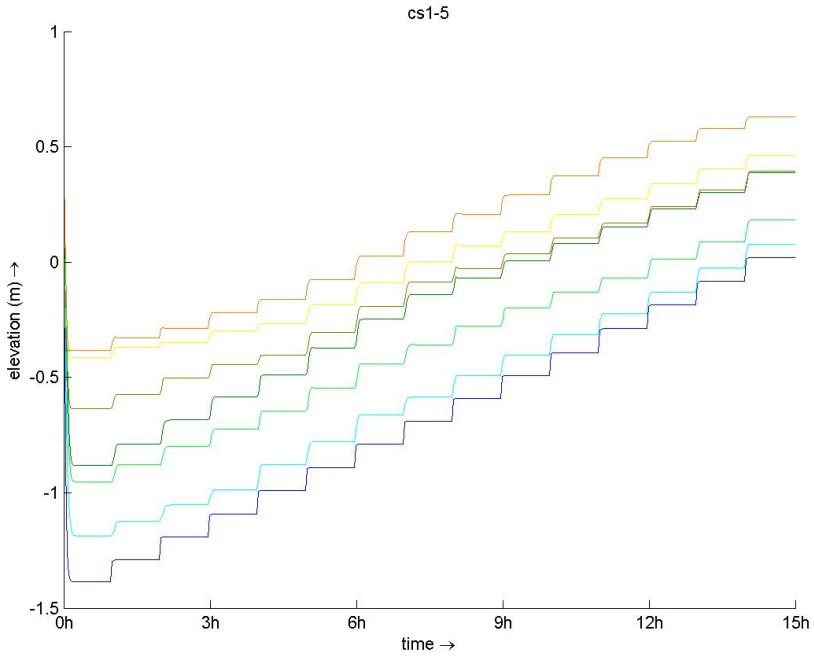

(a) Local water level

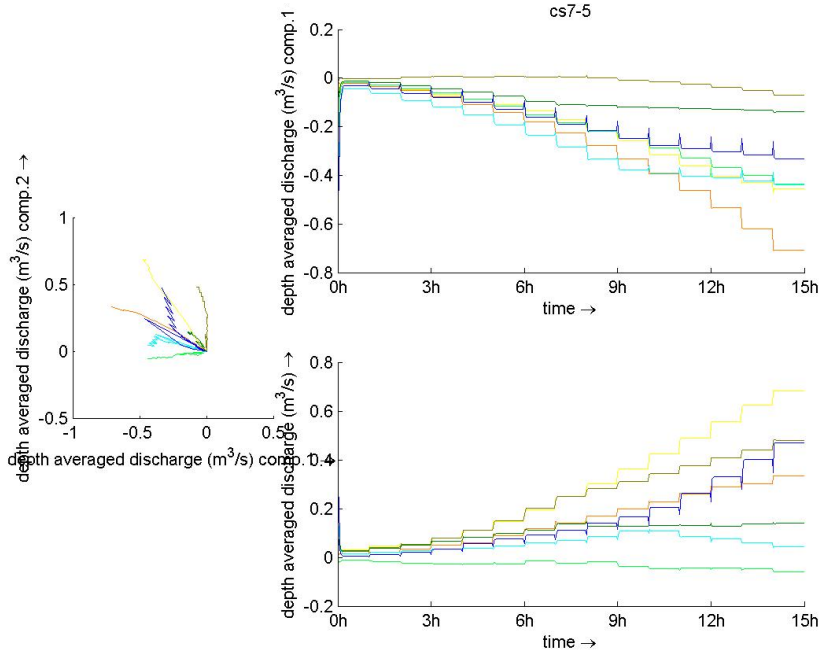

(b) Local depth averaged discharge in east (comp 1) and north (comp 2) direction

Figure A.58: Delft3D hydrodynamic model output parameter development at seven midstream observation points in the Smithincott study reach showing the quality of the single simulation steps

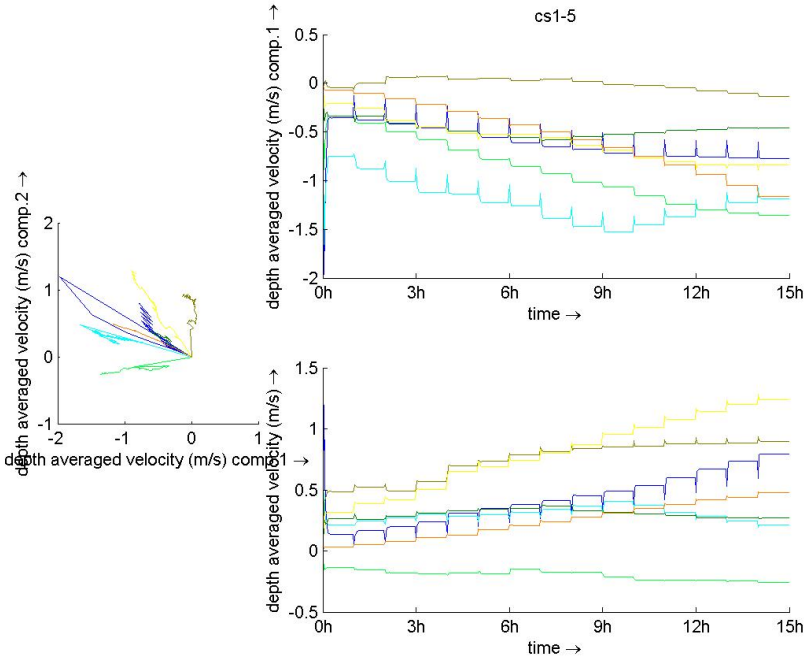

(a) Depth averaged velocity

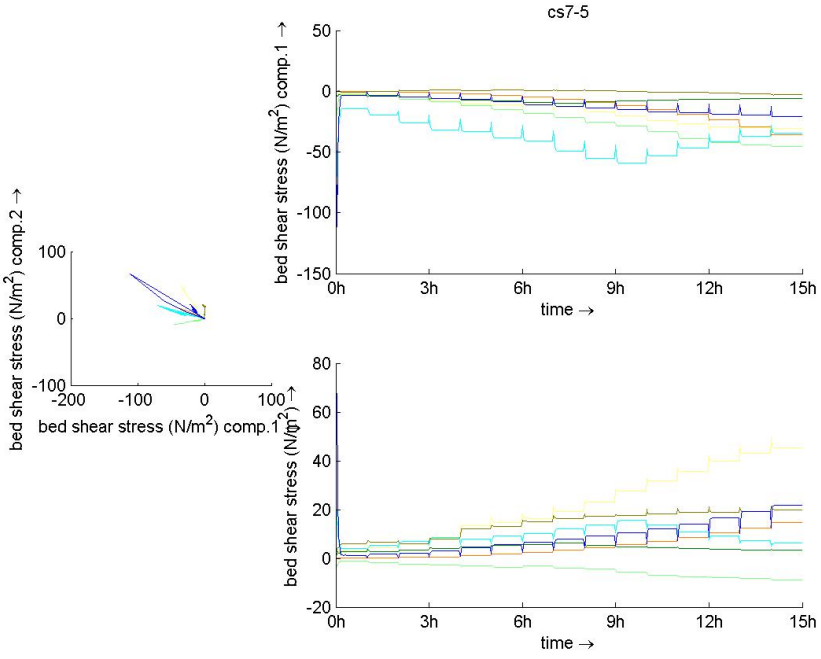

(b) Bed shear stress

Figure A.59: Output parameter development at seven observation points in the hydrodynamic model of the Smithincott study reach

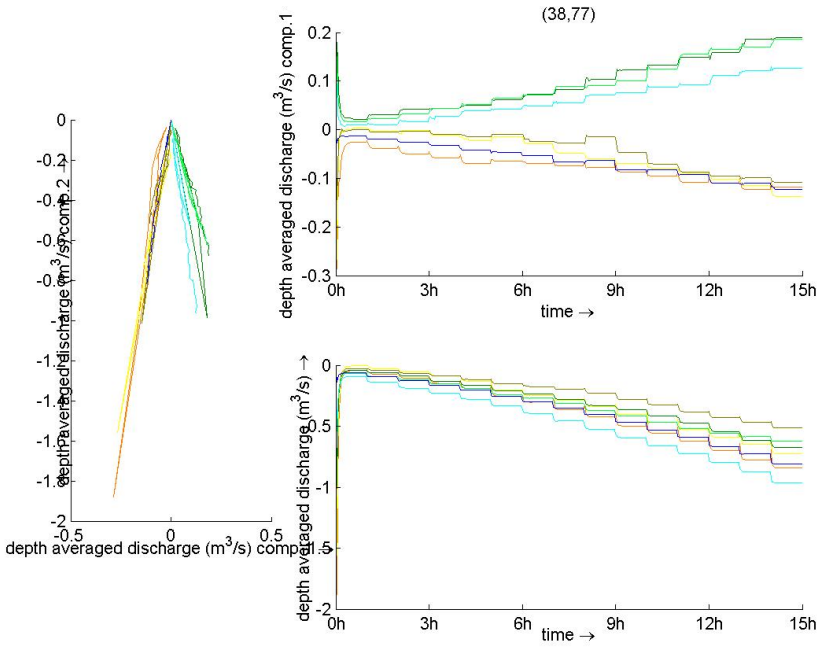

(a) Local depth averaged discharge

Figure A.60: Delft3D hydrodynamic model output parameter development at 7 midstream observation points in the Stonyford study reach showing the quality of the single simulation steps

A.4 Bibliography

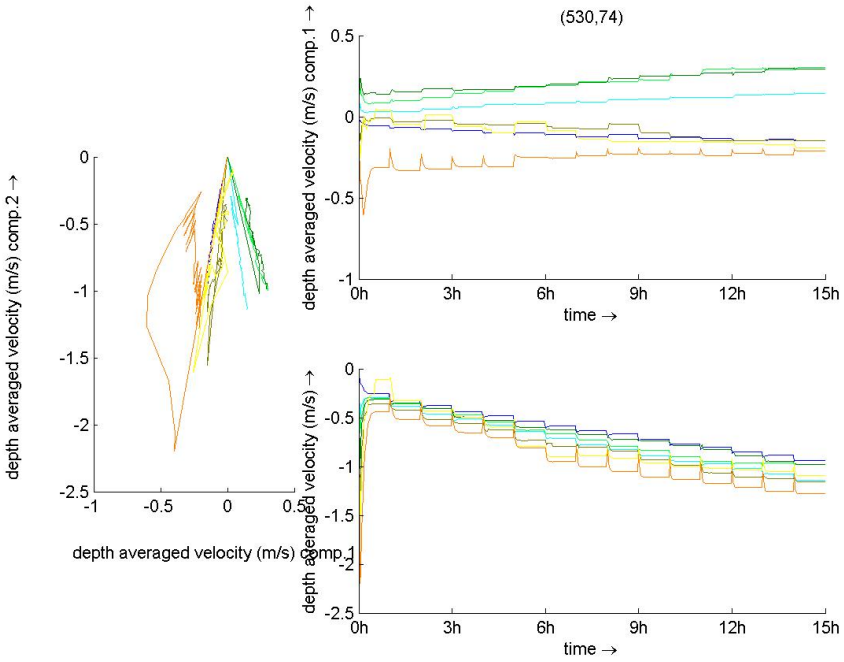

(a) Depth averaged velocity

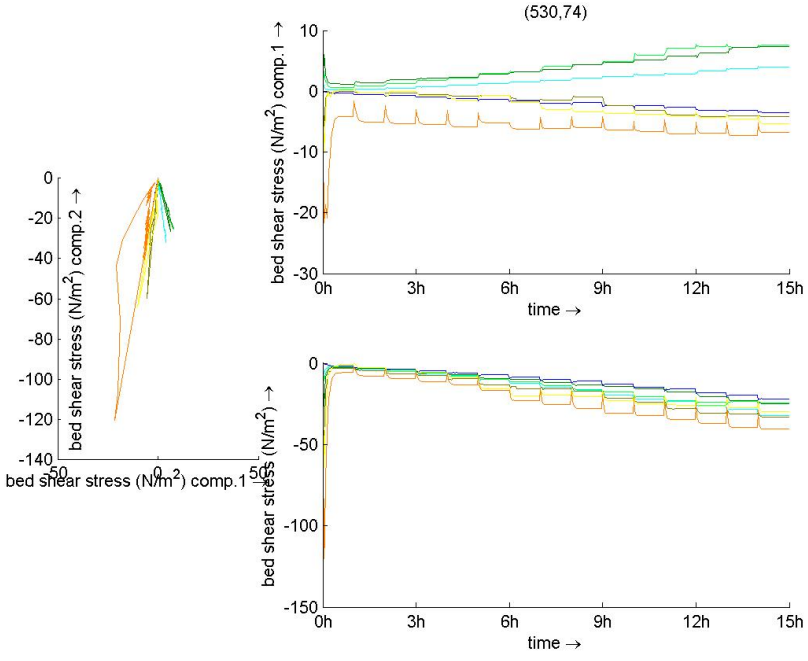

(b) Bed shear stress

Figure A.61: Output parameter development at 7 observation points in the hydrodynamic model of the Stonyford study reach

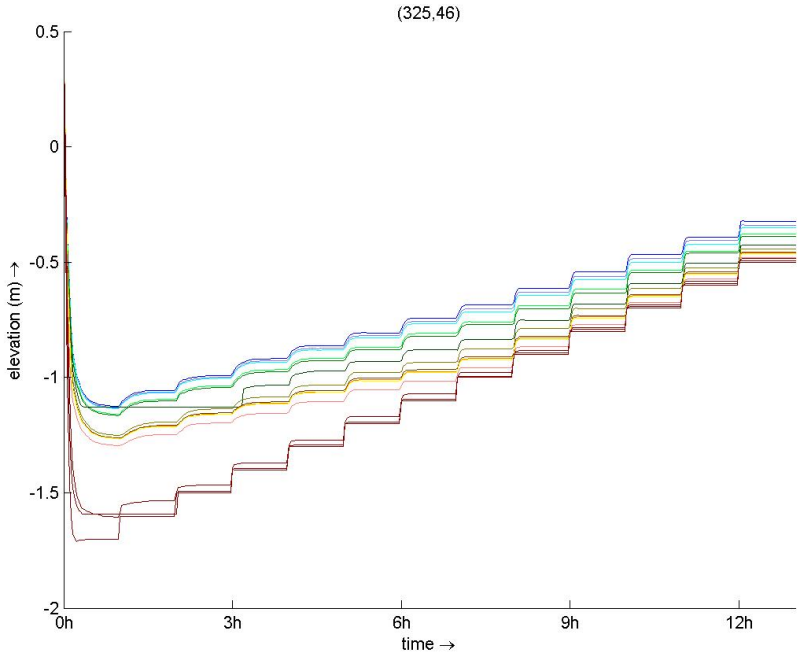

(a) Local water level

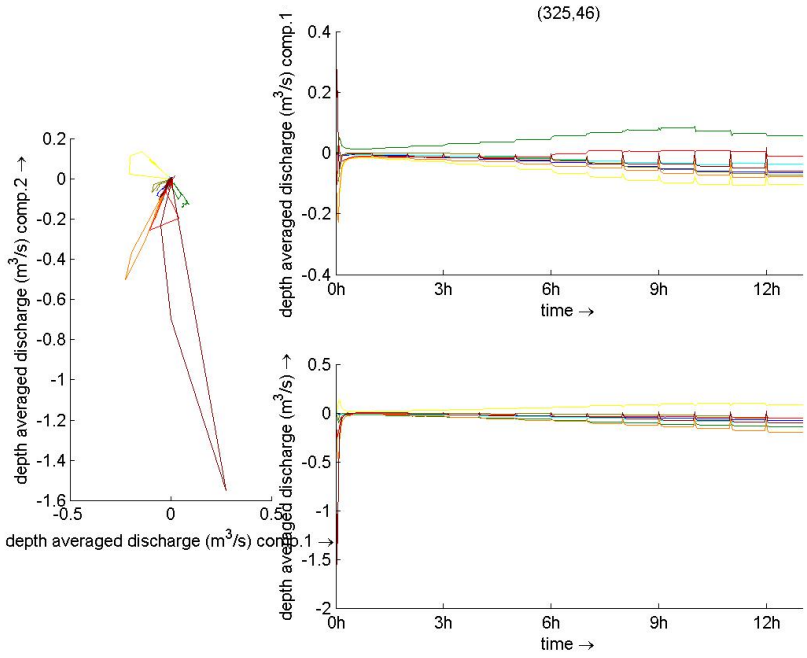

(b) Local depth averaged discharge in east (comp 1) and north (comp 2) direction

Figure A.62: Delft3D hydrodynamic model output parameter development at 8 mid-stream observation points in the Rewe study reach showing the quality of the single simulation steps

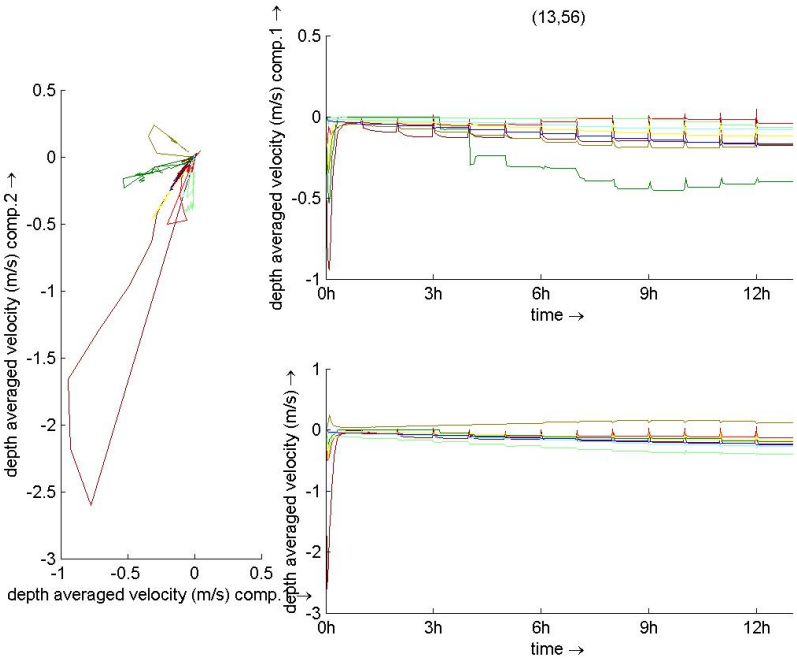

(a) Depth averaged velocity

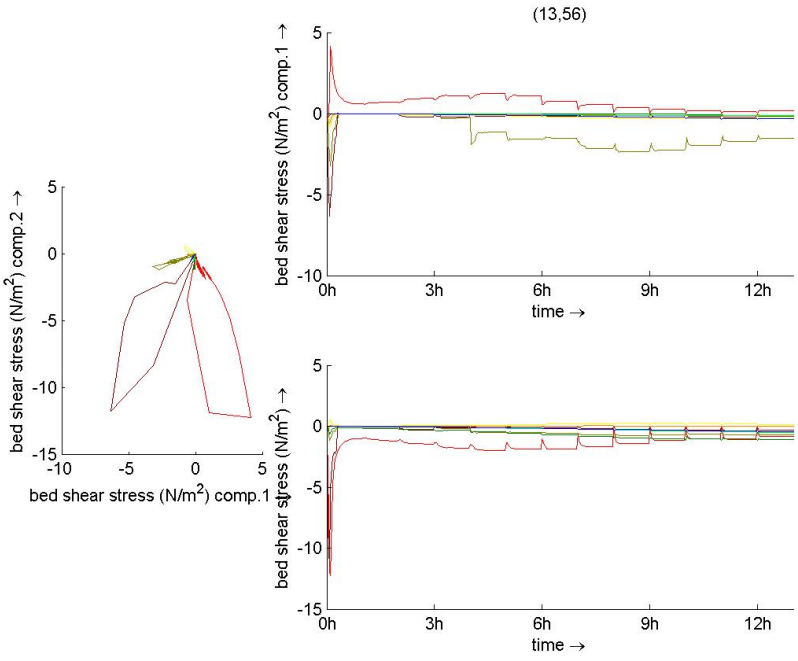

(b) Bed shear stress

Figure A.63: Output parameter development at 8 observation points in the hydrodynamic model of the Rewe study reach

Bibliography

Abbaspour, K. C., Vejdani, M., and Haghighat, S. (2007). SWAT-CUP calibration and uncertainty programs for SWAT. In *MODSIM 2007 International Congress on Modelling and Simulation, Modelling and Simulation Society of Australia and New Zealand*.

Acornley, R. M. and Sear, D. A. (1999). Sediment transport and siltation of brown trout spawning gravels in chalk streams. *Hydrological Processes*, 13(3):447–458.

Agrawal, Y. C. and Pottsmith, H. C. (2000). Instruments for particle size and settling velocity observations in sediment transport. *Marine Geology*, 168(1-4):89–114.

Ali, M., Sterk, G., Seeger, M., Boersema, M. P., and Peters, P. (2011). Effect of hydraulic parameters on sediment transport capacity in overland flow over erodible beds. *Hydrology & Earth System Sciences Discussions*, 8(4).

Allan, A. F. and Frostick, L. (1999). Framework dilation, winnowing, and matrix particle size: The behavior of some sand-gravel mixtures in a laboratory flume. *Journal of Sedimentary Research*, 69(1).

Alonso, C. V., Theurer, F. D., and Zachmann, D. W. (1988). Tucannon River offsite study: Sediment intrusion and dissolved-oxygen transport model. USDA. *Agricul. Res. Serv., Hydro-Ecosystems Res. Group, Fort Collins, CO*.

Arcement, G. J., Schneider, V. R., and Division, U. G. S. W. R. (1984). *Guide for selecting manning's roughness coefficients for natural channels and flood plains*. National Technical Information Service.

Ashworth, P. J. and Ferguson, R. I. (1989). Size-selective entrainment of bed load in gravel bed streams. *Water Resources Research*, 25(4):P. 627.

Bagnold, R. A. (1966). The shearing and dilatation of dry sand and the 'singing' mechanism. *Proceedings of the Royal Society of London. Series A. Mathematical and Physical Sciences*, pages 219–232.

Barr, D. and White, C. (1975). Technical note. Two additional methods of direct solution of the Colebrook-White function. In *ICE Proceedings*, volume 59, pages 827–835.

Baugh, J. V. and Manning, A. J. (2007). An assessment of a new settling velocity parameterisation for cohesive sediment transport modeling. *Continental Shelf Research*, 27(13):1835–1855.

Benda, L. and Dunne, T. (1997). Stochastic forcing of sediment routing and storage in channel networks. *Water Resources Research*, 33(12):2865–2880.

Berlamont, J., Ockenden, M., Toorman, E., and Winterwerp, J. (1993). The characterisation of cohesive sediment properties. *Coastal Engineering*, 21(1-3):105–128.

Beschta, R. L. and Jackson, W. L. (1979). The intrusion of fine sediments into a stable gravel bed. *Journal of the Fisheries Research Board of Canada*, 36(2).

Bettess, R. (1999). Flow resistance equations for gravel bed rivers. *Proceedings of the 28th Congress of the IAHR, Graz, Austria, August 22 27*.

Beven, K. (2007). Towards integrated environmental models of everywhere: uncertainty, data and modelling as a learning process. *Hydrology and Earth System Sciences Discussions*, 11(1):460–467.

Beven, K. (2010). *Environmental Modelling: An Uncertain Future?* CRC Press.

Beven, K. and Binley, A. (1992). The future of distributed models: Model calibration and uncertainty prediction. *Hydrological Processes*, 6(3):279–298.

Beven, K. and Freer, J. (2001). Equifinality, data assimilation, and uncertainty estimation in mechanistic modelling of complex environmental systems using the GLUE methodology. *Journal of hydrology*, 249(1):11–29.

Bilotta, G. and Brazier, R. (2008). Understanding the influence of suspended solids on water quality and aquatic biota. *Water Research*, 42(12):2849–2861.

Biron, P. M., Robson, C., Lapointe, M. F., and Gaskin, S. J. (2004). Comparing different methods of bed shear stress estimates in simple and complex flow fields. *Earth Surface Processes and Landforms*, 29(11):1403–1415.

Blott, S. J. and Pye, K. (2001). GRADISTAT: a grain size distribution and statistics package for the analysis of unconsolidated sediments. *Earth Surface Processes and Landforms*, 26(11):1237–1248.

Bouma, T., van Duren, L., Temmerman, S., Claverie, T., Blanco-Garcia, A., Ysebaert, T., and Herman, P. (2007). Spatial flow and sedimentation patterns within patches of epibenthic structures: Combining field, flume and modelling experiments. *Continental Shelf Research*, 27(8):1020–1045.

Boyle, D. P., Gupta, H. V., Sorooshian, S., et al. (2000). Toward improved calibration of hydrologic models: Combining the strengths of manual and automatic methods. *Water Resour. Res*, 36(12):36633674.

Brasington, J., Middleton, R., Frostick, L. E., and Murphy, B. J. (2000). Detecting significant sediment motion in a laboratory flume using digital video image analysis. *Earth Surface Processes and Landforms*, 25(2):191–196.

Brenning, A. (2011). *RSAGA: SAGA Geoprocessing and Terrain Analysis in R*.

Brkic, D. (2011). Review of explicit approximations to the Colebrook relation for flow friction. *Journal of Petroleum Science and Engineering*, 77(1):34–48.

Buffington, J. and Montgomery, D. (1997). A systematic analysis of eight decades of incipient motion studies, with special reference to gravel-bedded rivers. *Water Resources Research*, 33(8):1993–2029.

Bunte, K. and Abt, S. R. (2001). Sampling surface and subsurface particle-size distributions in wadable gravel-and cobble-bed streams for analyses in sediment transport, hydraulics, and streambed monitoring. *Gen. Tech. Rep. RMRS-GTR-74. Fort Collins,CO: U.S. Department of Agriculture, Forest Service, Rocky Mountain Research Station. 428 pp*.

Burt, T. P. and Walling, D. E. (1984). Catchment experiments in fluvial geomorphology: A review of objectives and methodology. In Burt, T. P. and Walling, D., editors, *Catchment Experiments in Fluvial Geomorphology*, pages 301—332. Geo Books, Norwich.

Campbell, A. J. and Sidle, R. C. (1985). Bedload transport in a pool-riffle sequence of a Coastal Alaska. *JAWRA Journal of the American Water Resources Association*, 21(4):579590.

Carling, P. A. (1984a). Deposition of fine and coarse sand in an open-work gravel bed. *Canadian Journal of Fisheries and Aquatic Sciences*, 41(2):263–270.

Carling, P. A. (1984b). Deposition of fine and coarse sand in an open-work gravel bed. *Canadian Journal of Fisheries and Aquatic Sciences*, 41(2).

Carling, P. A. (2009). Use and misuse of the reduced major axis for line-fitting. *American Journal of Physical Anthropology*, 140(3):476–486.

Carling, P. A., Irvine, B. J., Hill, A., and Wood, M. (2001). Reducing sediment inputs to Scottish streams: A review of the efficacy of soil conservation practices in upland forestry. *The Science of The Total Environment*, 265(1-3):209–227.

Carling, P. A. and Reader, N. A. (1982). Structure, composition and bulk properties of

upland stream gravels. *EARTH SURF. PROCESS. AND LANDFORMS.*, 7(4):349–365.

Chan, W., Wai, O. W., and Li, Y. (2006). Critical shear stress for deposition of cohesive sediments in Mai Po. *Journal of Hydrodynamics, Ser. B*, 18(3, Supplement 1):300–305.

Chanson, H. (2004). *Hydraulics of Open Channel Flow*. Butterworth-Heinemann, Oxford.

Chapman, D. W. (1988). Critical review of variables used to define effects of fines in redds of large salmonids. *Transactions of the American Fisheries Society*, 117(1):1–21.

Cheng, C. T., Ou, C. P., and Chau, K. W. (2002). Combining a fuzzy optimal model with a genetic algorithm to solve multi-objective rainfallrunoff model calibration. *Journal of Hydrology*, 268(14):72–86.

Cheng, N. S. (1997). Simplified settling velocity formula for sediment particle. *Journal of hydraulic engineering*, 123:149–152.

Chow, V. T. (1964). *Handbook of Applied Hydrology*. McGraw-Hill Book, New York.

Church, M. (1984). On experimental method in geomorphology. In Burt, T. P. and Walling, D., editors, *Catchment Experiments in Fluvial Geomorphology*, pages 563–581. Geo Books, Norwich.

Clifford, N. J., Richards, K. S., Brown, R. A., and Lane, S. N. (1995). Laboratory and field assessment of an infrared turbidity probe and its response to particle size and variation in suspended sediment concentration. *Hydrological Sciences Journal*, 40(6):771–791.

Clift, R., Grace, J. R., and Weber, M. E. (1978). *Bubbles, Drops, and Particles*. Academic Press, New York.

Collins, A. and Walling, D. (2007a). Sources of fine sediment recovered from the channel bed of lowland groundwater-fed catchments in the UK. *Geomorphology*, 88(1-2):120–138.

Collins, A. L., Anthony, S. G., Hawley, J., and Turner, T. (2009a). The potential impact of projected change in farming by 2015 on the importance of the agricultural sector as a sediment source in England and Wales. *Catena*, 79(3):243250.

Collins, A. L., Anthony, S. G., Hawley, J., and Turner, T. (2009b). Predicting potential change in agricultural sediment inputs to rivers across england and wales by 2015. *Marine and Freshwater Research*, 60(7):626–637.

Collins, A. L., Strmqvist, J., Davison, P. S., and Lord, E. I. (2007). Appraisal of phosphorus and sediment transfer in three pilot areas identified for the catchment sensitive farming initiative in England: Application of the prototype PSYCHIC model. *Soil Use and Management*, 23:117–132.

Collins, A. L. and Walling, D. E. (2004). Documenting catchment suspended sediment sources: problems, approaches and prospects. *Progress in Physical Geography*, 28(2):159–196.

Collins, A. L. and Walling, D. E. (2006). Investigating the remobilization of fine sediment stored on the channel bed of lowland permeable catchments in the UK. *IAHS Publication no. 306, , Wallingford*, pages 471–479.

Collins, A. L. and Walling, D. E. (2007b). Fine-grained bed sediment storage within the main channel systems of the frome and piddle catchments, Dorset, UK. *Hydrological Processes*, 21(11):1448–1459.

Collins, M. B. and Rigler, J. K. (1982). The use of settling velocity in defining the initiation of motion of heavy mineral grains, under unidirectional flow. *Sedimentology*, 29(3):419–426.

Cowan, W. L. (1956). Estimating hydraulic roughnes coefficients. *Agricultural Engineering*, 37(7):473–475.

Cui, Y., Wooster, J. K., Baker, P. F., Dusterhoff, S. R., Sklar, L. S., and Dietrich, W. E. (2008). Theory of fine sediment infiltration into immobile gravel bed. *Journal of Hydraulic Engineering*, 134(10):1421–1429.

Curran, J. C. (2007). The decrease in shear stress and increase in transport rates subsequent to an increase in sand supply to a gravel-bed channel. *Sedimentary Geology*, 202(3):572–580.

Davies, A. and Fearn, T. (2006). Back to basics: calibration statistics. *Spectroscopy Europe*, 18(2):31–32.

Davison, P. S., Withers, P. J. A., Lord, E. I., Betson, M. J., and Strmqvist, J. (2008). PSYCHIC a process-based model of phosphorus and sediment mobilisation and delivery within agricultural catchments. Part 1: Model description and parameterisation. *Journal of Hydrology*, 350(34):290–302.

Deltares, S. (2010). Delft3d suite.

Digimap (2012). Digimap home page. `http://digimap.edina.ac.uk/digimap/home#`.

Dinehart, R. L. (2012). Evolution of coarse gravel bed forms: Field measurements at flood stage. *Water Resources Research*, 28(10):2667–2689.

Diplas, P. (1994). Modelling of fine and coarse sediment interaction over alternate bars. *Journal of Hydrology*, 159(1-4):335–351.

Diplas, P. and Parker, G. (1985). Pollution of gravel spawning grounds due to fine sediment. st. anthony falls hydraulic lab. project report 240. *University of Minnesota, Minneapolis*, pages 238–247.

Diplas, P. and Parker, G. (1992). Deposition and removal of fines in gravel-bed streams. In P. Billi, R.D. Hey, C. T. and Tacconi., P., editors, *Dynamics of gravel-bed rivers*, pages 313–329. John Wiley and Sons, Chichester.

Dittrich, A. (1998). *Wechselwirkung Morphologie und Strömung naturnaher Fließgewässer*. Inst. f. Wasserwirtschaft u. Kulturtechnik, Karlsruhe,Germany.

Douillet, P., Ouillon, S., and Cordier, E. (2001). A numerical model for fine suspended sediment transport in the southwest lagoon of New Caledonia. *Coral Reefs*, 20(4):361–372.

Droppo, I. G. and Ongley, E. (1998). Suspended sediment structure: implications for sediment and contaminant transport modelling. In *Modelling soil erosion, sediment transport and closely related hydrological processes: proceedings of an International Symposium held at Vienna from 13 to 17 July 1998... organized by the International Commission on Continental Erosion of the International Association of Hydrological Sciences...*, page 437.

Dyck, S. and Peschke, G. (1989). *Grundlagen der Hydrologie*. Ernst und Sohn Verlag fuer Architektur und technische Wissenschaften, Berlin.

Efstratiadis, A. and Koutsoyiannis, D. (2010). One decade of multi-objective calibration approaches in hydrological modelling: a review. *Hydrological Sciences Journal*, 55(1):58–78.

Einstein, H. A. (1968). Deposition of suspended particles in a gravel bed. In *Journal of the Hydraulics Division, American Society of Civil Engineers*, volume 94, pages 1197–1205.

Einstein, H. A. and Krone, R. B. (1962). Experiments to determine modes of cohesive sediment transport in salt water. *Journal of Geophysical Research*, 67(4):1451–1461.

Einstein, H. A. and Shen, H. W. (1964). A study on meandering in straight alluvial channels. *Journal of Geophysical Research*, 69(24):5239–5247.

Ferguson, R. (2003a). The missing dimension: effects of lateral variation on 1-d calculations of fluvial bedload transport. *Geomorphology*, 56(1-2):1–14.

Ferguson, R. and Church, M. (2004). A simple universal equation for grain settling velocity. *Journal of Sedimentary Research*, 74(6):933–937.

Ferguson, R. I. (2003b). Flow in meander bends with recirculation at the inner bank. *Water Resources Research*, 39(11).

Fetter, C. W. and Fetter Jr, C. W. (1999). *Contaminant hydrogeology*. Macmillan, New York.

Fettweis, M. (2008). Uncertainty of excess density and settling velocity of mud flocs derived from in situ measurements. *Estuarine, Coastal and Shelf Science*, 78(2):426–436.

Folk, R. L. and Ward, W. C. (1957). Brazos River Bar [Texas]: A study in the significance of grain size parameters. *Journal of Sedimentary Research*, 27(1):3–26.

Foster, I., Gurnell, A. M., and Webb, B. (1995). *Sediment and water quality in river catchments*. John Wiley and Sons, Chichester.

Frostick, L. E., Lucas, P. M., and Reid, I. (1984a). The infiltration of fine matrices into coarse-grained alluvial sediments and its implications for stratigraphical interpretation. *Journal of the Geological Society*, 141(6):955–965.

Frostick, L. E., Lucas, P. M., and Reid, I. (1984b). The infiltration of fine matrices into coarse-grained alluvial sediments and its implications for stratigraphical interpretation. *Journal of the Geological Society*, 141(6):955–965.

Gailani, J., Lick, W., Kirk Ziegler, C., and Endicott, D. (1996). Development and calibration of a fine-grained sediment transport model for the Buffalo River. *Journal of Great Lakes Research*, 22(3):765–778.

Gailani, J., Ziegler, C. K., and Lick, W. (1991). Transport of suspended solids in the Lower Fox River. *Journal of Great Lakes Research*, 17(4):479–494.

Garde, R. J. and Raju, K. G. R. (2000). *Mechanics of Sediment Transportation and Alluvial Stream Problems*. Taylor & Francis, Abingdon.

Ghoshal, K., Mazumder, B., and Purkait, B. (2010). Grain-size distributions of bed load: Inferences from flume experiments using heterogeneous sediment beds. *Sedimentary Geology*, 223(1-2):1–14.

Gibbs, R. J., Matthews, M. D., and Link, D. A. (1971). The relationship between sphere size and settling velocity. *JOURNAL OF SEDIMENTARY RESEARCH*, 41(1):7–18.

Golosov, V., Belyaev, V., Walling, D. E., Lomonosova, M. g. u. i. M., and Sciences, I. A. o. H. (2004). *Sediment Transfer Through the Fluvial System: Proceedings of the International Symposium Held at Moscow, Russia, from 2 to 6 August, 2004*. IAHS.

Gordon, N. D., McMahon, T. A., Finlayson, B. L., Gippel, C. J., and Nathan, R. J. (2004). *Stream Hydrology: An Introduction for Ecologists*. John Wiley & Sons, Chichester.

Grams, P. E. and Wilcock, P. R. (2007). Equilibrium entrainment of fine sediment over a coarse immobile bed. *Water Resources Research*, 43(10):W10420.

Greig, S., Sear, D., and Carling, P. (2005). The impact of fine sediment accumulation on the survival of incubating salmon progeny: Implications for sediment management. *Science of The Total Environment*, 344(1-3):241–258.

Greig, S. M., Sear, D. A., and Carling, P. A. (2007). A review of factors influencing the availability of dissolved oxygen to incubating salmonid embryos. *Hydrological Processes*, 21(3):323–334.

Grost, R., Hubert, W., and Wesche, T. (1991). Field comparison of three devices used to sample substrate in small streams. *North American Journal of Fisheries Management*, 11(3):347–351.

Guilln, J., Palanques, A., Puig, P., Durrieu de Madron, X., and Nyffeler, F. (2008). Field calibration of optical sensors for measuring suspended sediment concentration in the Western Mediterranean. *Scientia Marina*, 64(4).

Guo, L., Zhang, D., Xu, D., and Chen, Y. (2009). An experimental study of low concentration sludge settling velocity under turbulent condition. *Water Research*, 43(9):2383–2390.

Haralampides, K., McCorquodale, J. A., and Krishnappan, B. G. (2003). Deposition properties of fine sediment. *Journal of Hydraulic Engineering*, 129(3):230–234.

Hardy, R. J., Bates, P. D., and Anderson, M. G. (2000). Modelling suspended sediment deposition on a fluvial floodplain using a two-dimensional dynamic finite element model. *Journal of Hydrology*, 229(3-4):202–218.

Harnischmacher, S. (2007). Thresholds in small rivers? hypotheses developed from fluvial morphological research in western Germany. *Geomorphology*, 92(3-4):119–133.

Haschenburger, J. K. and Roest, P. (2009). Substrate indices as indicators of interstitial pore space in gravel-bed channels. *River Research and Applications*, 25(1):98–105.

Hassan, M. A. and Reid, I. (1990). The influence of microform bed roughness elements on flow and sediment transport in gravel bed rivers. *Earth Surface Processes and Landforms*, 15(8):739–750.

Havis, R. N., Alonso, C. V., King, J. G., and Thurow, R. F. (1993). A mathematical model of salmonid spawning habitat. *Journal of the American Water Resources Association*, 29(3):435–444.

Haygarth, P. M., Bilotta, G. S., Bol, R., Brazier, R. E., Butler, P. J., Freer, J., Gimbert, L. J., Granger, S. J., Krueger, T., and Macleod, C. J. A. (2006). Processes affecting transfer of sediment and colloids, with associated phosphorus, from intensively farmed grasslands: an overview of key issues. *Hydrological Processes*, 20(20):4407–4413.

Hendriks, I. E., van Duren, L. A., and Herman, P. M. (2006). Turbulence levels in a flume compared to the field: Implications for larval settlement studies. *Journal of Sea Research*, 55(1):15–29.

Herschy, R. W. (1995). *Streamflow measurement*. CRC Press, Boca Raton, Florida.

Heywood, M. J. T. and Walling, D. E. (2007). The sedimentation of salmonid spawning gravels in the Hampshire Avon catchment, UK: implications for the dissolved oxygen content of intragravel water and embryo survival. *Hydrological Processes*, 21(6):770–788.

Hjulstrom, F. (1935). *Studies of the morphological activity of rivers as illustrated by the River Fyris*. Almqvist & Wiksells, Uppsala.

Hjulstrom, F. (1939). Transportation of detritus by moving water.

Holmes, N., Boon, P., and Rowell, T. (1998). A revised classification system for british rivers based on their aquatic plant communities. *Aquatic Conservation: Marine and Freshwater Ecosystems*, 8(4):555–578.

Horowitz, A. J. (2005a). 61. monitoring suspended sediment and associated trace element and nutrient fluxes in large river basins in the USA. *Water and Energy Abstracts*, 15(2):22.

Horowitz, A. J. (2005b). Monitoring suspended sediment and associated trace element and nutrient fluxes in large river basins in the USA. *Water and Energy Abstracts*, 15(2):22.

Horowitz, A. J., Rinella, F. A., Lamothe, P., Miller, T. L., Edwards, T. K., Roche, R. L., and Rickert, D. A. (1990). Variations in suspended sediment and associated trace element concentrations in selected riverine cross sections. *Environ. Sci. Technol*, 24(9):1313–1320.

Hosseini, S., Shamsai, A., and Ataie-Ashtiani, B. (2006). Synchronous measurements of the velocity and concentration in low density turbidity currents using an Acoustic Doppler Velocimeter. *Flow Measurement and Instrumentation*, 17(1):59–68.

Hostache, R., Matgen, P., Schumann, G., Puech, C., Hoffmann, L., and Pfister, L. (2009). Water level estimation and reduction of hydraulic model calibration uncertainties using satellite SAR images of floods. *IEEE Transactions on Geoscience and Remote Sensing*, 47(2):431 –441.

Inman, D. L. (1952). Measures for describing the size distribution of sediments. *Journal of Sedimentary Research*, 22(3):125–145.

Jain, S. K. and Sudheer, K. P. (2008). Fitting of hydrologic models: A close look at the NashSutcliffe index. *Journal of Hydrologic Engineering*, 13(10):981–986.

Ji, Z.-G., Hamrick, J. H., and Pagenkopf, J. (2002). Sediment and metals modeling in shallow river. *Journal of Environmental Engineering*, 128(2):105–119.

Keller, E. A. (1971). Areal sorting of bed-load material: The hypothesis of velocity reversal. *Geological Society of America Bulletin*, 82(3):753–756.

Kersten, M. and Smedes, F. (2002). Normalization procedures for sediment contaminants in spatial and temporal trend monitoring. *Journal of Environmental Monitoring*, 4(1):109–115.

Kim, S. C., Friedrichs, C. T., Maa, J. P. Y., and Wright, L. D. (2000). Estimating bottom stress in tidal boundary layer from acoustic doppler velocimeter data. *Journal of Hydraulic Engineering*, 126(6):399–406.

Kineke, G. C. and Sternberg, R. W. (1992). Measurements of high concentration suspended sediments using the optical backscatterance sensor. *Marine Geology*, 108(34):253–258.

Kirchner, J. W. (2006). Getting the right answers for the right reasons: Linking measurements, analyses, and models to advance the science of hydrology. *Water Resources Research*, 42(3):W03S04.

Kirchner, J. W., Dietrich, W. E., Iseya, F., and Ikeda, H. (1990). The variability of critical shear stress, friction angle, and grain protrusion in water-worked sediments. *Sedimentology*, 37(4):647–672.

Kleinhans, M. G. and van Rijn, L. C. (2002). Stochastic prediction of sediment transport in sand-gravel bed rivers. *Journal of hydraulic engineering*, 128(4):412–425.

Klingeman, P. C. (1998). *Gravel-bed Rivers in the Environment*. Water Resources Publication, Highlands Ranch, USA.

Knighton, D. (1998). *Fluvial Forms and Processes: A New Perspective*. Hodder Arnold, London, 2nd ed edition.

Kondolf, G. M. and Wolman, M. G. (1993). The sizes of salmonid spawning gravels. *Water Resources Research*, 29(7):2275–2285.

Kozerski, H.-P. (2002). Determination of areal sedimentation rates in rivers by using plate sediment trap measurements and flow velocity–settling flux relationship. *Water Research*, 36(12):2983–2990.

Kranck, K. (1975). Sediment deposition from flocculated suspensions. *Sedimentology*, 22(1):111–123.

Krishnappan, B. (1994). Critical shear stress for erosion and deposition of fine suspended sediment in the fraser river. Technical report, Environment Canada: Environmental Conservation Branch Science Division.

Krishnappan, B. G. (2006). Cohesive sediment transport in a rotating circular flume. In *Proceedings of the 7th International Conference on Hydro Science and Engineering*, Philadelphia, USA.

Krone, R. B. (1962). Flume studies of the transport of sediment in estuarial shoaling processes : final report. Prepared for san francisco district corps of engineers, U.S. army, University of California, Berkeley. Hydraulic Engineering Laboratory.

Lambert, C. and Walling, D. (1988). Measurement of channel storage of suspended sediment in a gravel-bed river. *CATENA*, 15(1):65–80.

Lambert, C. P. and Walling, D. E. (1987). Floodplain sedimentation: A preliminary investigation of contemporary deposition within the lower reaches of the River Culm, Devon, UK. *Geografiska Annaler. Series A, Physical Geography*, 69(3/4):393–404.

Landrum, P. F. and Robbins, J. A. (1990). Bioavailability of sediment-associated contaminants to benthic invertebrates. In Baudo, R., Giesy, J., and Muntau, H., editors, *Sediments: chemistry and toxicity of in-place pollutants.*, pages 237–263. CRC Press, Boca Raton, USA.

Lau, Y. L., Droppo, I. G., and Krishnappan, B. G. (2001). Sequential erosion/deposition experiments–demonstrating the effects of depositional history on sediment erosion. *Water Research*, 35(11):2767–2773.

Lau, Y. L. and Krishnappan, B. G. (1992). Size distribution and settling velocity of cohesive sediments during settling. *Journal of Hydraulic Research*, 30(5):673.

Lauck, T., Lamberson, R., Lisle, T. E., and others (1993). A simulation model for the infiltration of heterogeneous sediment into a stream bed. *Advances in Hydro-Science and-Engineering*, 1:229–236.

Lawless, M. and Robert, A. (2001). Three-dimensional flow structure around small-scale bedforms in a simulated gravel-bed environment. *Earth Surface Processes and Landforms*, 26(5):507–522.

Le Roux, J. (2005). Grains in motion: A review. *Sedimentary Geology*, 178(3-4):285–313.

Le Roux, J. P. (1991). A rapid method to determine the critical shear stress for sphere entrainment under unidirectional fluid flow. *Sedimentary Geology*, 75(1-2):13.

Leduc, D. J. (1987). A comparative analysis of the reduced major axis technique of fitting lines to bivariate data. *Canadian Journal of Forest Research*, 17(7):654659.

Leeks, G., Walling, D. E., and Collins, A. L. (2005). Storage of fine-grained sediment and associated contaminants within the channels of lowland permeable catchments in the UK. In *IAHS publication 291*, pages 259–268, Foz do Iguacu, Brazil.

Legates, D. R. and McCabe, G. J. (1999). Evaluating the use of goodness-of-fit measures in hydrologic and hydroclimatic model validation. *Water resources research*, 35(1):233–241.

Linsley Jr, R. K., Kohler, M. A., and Paulhus, J. L. (1975). *Hydrology for engineers*. McGraw-Hill, New York.

Lisle, T. E. (1979). A sorting mechanism for a riffle-pool sequence. *Geological Society of America Bulletin*, 90(2):1142–1157.

Lisle, T. E. (1989). Sediment transport and resulting deposition in spawning gravels, north coastal california. *Water Resources Research*, 25(6):1303–1319.

Lisle, T. E. and Church, M. (2002). Sediment transport-storage relations for degrading, gravel bed channels. *Water Resources Research*, 38:14 PP.

Lisle, T. E. and Hilton, S. (1992). Volume of fine sediment in pools. an index of sediment supply in gravel-bed streams. *Water Resources Bulletin*, 28(2):371–383.

Lisle, T. E. and Madej, M. A. (1992). Spatial variation in armouring in a channel with high sediment supply. *P. Billi, RDHey, CR Thorne, and P. Tacconi (ed.), Dynamics of Gravel-bed Rivers. John Wiley and Sons, London. p. 277-293*.

Liu, W. C., Hsu, M. H., and Kuo, A. Y. (2002). Modelling of hydrodynamics and cohesive sediment transport in Tanshui River estuarine system, Taiwan. *Marine Pollution Bulletin*, 44(10):10761088.

Loch, R. J. (2001). Settling velocity - a new approach to assessing soil and sediment properties. *Computers and Electronics in Agriculture*, 31(3):305–316.

Lopes, V. L. and Lane, L. J. (1988). Modeling sedimentation processes in small watersheds. In Bordas, M. and Walling, D. E., editors, *In Sediment Budgets, IAHS Publication no 174*, page 497508. IAHS.

Lumborg, U. and Pejrup, M. (2005). Modelling of cohesive sediment transport in a tidal lagoonan annual budget. *Marine Geology*, 218(14):1–16.

Maa, J.-Y., Kwon, J.-I., and Ha, H.-K. (2008). Critical bed-shear stress for cohesive sediment deposition under steady flows. *Journal of Hydraulic Engineering*, 134(12):1767–1771.

Mahoney, D. and Erman, D. C. (1984). An index of stored fine sediment in gravel bedded streams. *American Water Resources Association*, 20(3):343–348.

Marquis, G. A. and Roy, A. G. (2012). Using multiple bed load measurements: Toward the identification of bed dilation and contraction in gravel-bed rivers. *Journal of Geophysical Research: Earth Surface*, 117(F1):F01014.

McCuen, R. H., Knight, Z., and Cutter, A. G. (2006). Evaluation of the NashSutcliffe efficiency index. *Journal of Hydrologic Engineering*, 11(6):597–602.

McGahey, C. and Samuels, P. (2004). River roughness. The integration of diverse

knowledge. In *River Flow. Proceedings of the Second International Conference on Fluvial Hydraulics, Balkema, Napoli, Italy*, Balkema, Napoli, Italy.

McVan Instruments (2007). Analite nep9000 and nep9500 series turbidity probe user manual. http://www.observatormeteohydro.com/cms/uploads/documenten/licentie_1/document_159.pdf.

Meade, R. H. (1988). Movement and storage of sediment in river systems. *Physical and chemical weathering in geochemical cycles*, page 165179.

Mehta, A. J. and Partheniades, E. (1975). An investigation of the depositional properties of flocculated fine sediments. *Journal of Hydraulic Research*, 13(4):361.

Merritt, W. S., Letcher, R. A., and Jakeman, A. J. (2003). A review of erosion and sediment transport models. *Environmental Modelling & Software*, 18(8):761–799.

Metoffice, U. (2014). Cullompton climate. http://www.metoffice.gov.uk/public/weather/climate/cullompton-devon#?tab=climateTables&fcTime=1398031200.

Meyer-Peter, E. and Mueller, R. (1948). Formulas for bed-load transport. In *IAHSR 2nd meeting, Stockholm*, pages 38–65.

Middleton, R., Brasington, J., Murphy, B. J., and Frostick, L. E. (2000). Monitoring gravel framework dilation using a new digital particle tracking method. *Computers & Geosciences*, 26(3):329–340.

Miller, M. C., McCave, I. N., and Komar, P. D. (1977). Threshold of sediment motion under unidirectional currents. *Sedimentology*, 24(4):507–527.

Milne, J. A. (1982). Bed-material size and the riffle-pool sequence. *Sedimentology*, 29(2):267–278.

Minella, J. P., Merten, G. H., Reichert, J. M., and Clarke, R. T. (2008). Estimating suspended sediment concentrations from turbidity measurements and the calibration problem. *Hydrological Processes*, 22(12):1819–1830.

Montanari, M., Hostache, R., Matgen, P., Schumann, G., Pfister, L., Hoffmann, L., et al. (2009). Calibration and sequential updating of a coupled hydrologic-hydraulic model using remote sensing-derived water stages. *Hydrology and Earth System Sciences*, 13(3):367–380.

Moriasi, D., Arnold, J., Van Liew, M., Bingner, R., Harmel, R., and Veith, T. (2007). Model evaluation guidelines for systematic quantification of accuracy in watershed simulations. *Transaktions of the ASABE*, 50(3):885–900.

Moustakidis, I., Papanicolaou, A., and Tsakiris, A. (2012). The Effect of Boulder Spacing on Flow Patterns Around Boulders Under Partial Submergence.

Nelson, E. J. and Booth, D. B. (2002). Sediment sources in an urbanizing, mixed land-use watershed. *Journal of Hydrology*, 264(1):51–68.

Nicholas, A. P. and Walling, D. E. (1998). Numerical modelling of floodplain hydraulics and suspended sediment transport and deposition. *Hydrological Processes*, 12(8):13391355.

Orghidan, T. (1959). Ein neuer lebensraum des unterirdischen wassers, das hyporheische biotop. *Archiv fr Hydrobiologie*, page 392ff.

Orghidan, T. (2010). A new habitat of subsurface waters: the hyporheic biotope. *Fundamental and applied limnology*, 176(4):291.

Owen, M. W. (1976). Determination of the settling velocities of cohesive muds. Technical Report IT 161, Hydraulics Research Station, Wallingford.

Owens, P., Walling, D., and Leeks, G. (1999). Deposition and storage of fine-grained sediment within the main channel system of the River Tweed, Scotland. *Earth Surface Processes and Landforms*, 24(12):1061–1076.

Owens, P. N., Batalla, R. J., Collins, A. J., Gomez, B., Hicks, D. M., Horowitz, A. J., Kondolf, G. M., Marden, M., Page, M. J., and Peacock, D. H. (2005). Fine-grained

sediment in river systems: environmental significance and management issues. *River Research and Applications*, 21(7).

Owens, P. N. and Collins, A. J. (2006). *Soil Erosion and Sediment Redistribution in River Catchments: Measurement, Modelling and Management*. CABI.

Padmore, C. L., Newson, M. D., and Charlton, M. E. (1998). Instream habitat in gravel bed rivers: identification and characterisation of biotopes. *Gravel Bed Rivers in the Environment. Water Resources Publications, Highlands Ranch, CO*, pages 345–364.

Papanicolaou, A. N., Tsakiris, A. G., and Kramer, C. M. (2010). Effects of relative submergence on flow and sediment patterns around clasts. *River Flow 2010*, pages 793–799.

Pattison, I., Sear, D., Carling, P., Collins, A. L. and Jones, J., and Naden, P. (2012). Assessing the effect of fine sediment upon salmonid egg incubation using a modelling approach: SIDO-UK. *BHS Eleventh National Symposium, Hydrology for a changing world, Dundee 2012*.

Pattison, I., Sear, D., Collins, A., Jones, I., and Naden, P. (2013). Modelling the effect of fine sediment on salmonid spawning habitat. In *EGU General Assembly 2013, held 7-12 April, 2013 in Vienna*, volume 15.

Peckham, S. D. (2003). Fluvial landscape models and catchment-scale sediment transport. *Global and Planetary Change*, 39(1-2):31–51.

Petit, F. (1994). Dimensionless critical shear stress evaluation from flume experiments using different gravel beds. *Earth Surface Processes and Landforms*, 19(6):565–576.

Petrie, J., Diplas, P., and Nam, S. (2010). Local boundary shear stress estimates from velocity profiles measured with ADCP. In Dittrich, A., Koll, K., Aberle, J., and

Geisenhainer, P., editors, *River Flow 2010*. Bundesanstalt fr Wasserbau, Braunschweig.

Phillips, J. M. and Walling, D. E. (1999). The particle size characteristics of fine-grained channel deposits in the River Exe Basin, Devon, UK. *Hydrological Processes*, 13(1):1–19.

Piedra, M. M. (2010). *Flume investigation of the effects of sub-threshold rising flows on the entrainment of gravel beds*. Ph.D., University of Glasgow.

Pope, N., Widdows, J., and Brinsley, M. (2006). Estimation of bed shear stress using the turbulent kinetic energy approach. A comparison of annular flume and field data. *Continental Shelf Research*, 26(8):959–970.

Prosser, I., Rustomji, P., Young, B., Moran, C., and Hughes, A. (2001). Constructing river basin sediment budgets for the national land and water resources audit. *CSIRO Land and Water Technical Report*, 15(1):01–34.

R Core Team (2012). *R: A Language and Environment for Statistical Computing*. R Foundation for Statistical Computing, Vienna, Austria. ISBN 3-900051-07-0.

Rathburn, S. and Wohl, E. (2003). Predicting fine sediment dynamics along a pool-riffle mountain channel. *Geomorphology*, 55(1-4):111–124.

Ratto, M., Tarantola, S., and Saltelli, A. (2001). Sensitivity analysis in model calibration: GSA-GLUE approach. *Computer Physics Communications*, 136(3):212–224.

Reid, I. and Frostick, L. E. (1986). Dynamics of bedload transport in turkey brook, a coarse-grained alluvial channel. *Earth Surface Processes and Landforms*, 11(2):143–155.

Reidenbach, M. A. and Koehl, M. a. R. (2011). The spatial and temporal patterns of odors sampled by lobsters and crabs in a turbulent plume. *The Journal of Experimental Biology*, 214(18):3138–3153.

Relyea, C. D., Minshall, G. W., and Danehy, R. J. (2000). Stream insects as bioindicators of fine sediment. *Proceedings of the Water Environment Federation*, 2000:663–686.

Rempel, L. L., Richardson, J. S., Healey, M. C., Rempel, L. L., Richardson, J. S., and Healey, M. C. (2000). Macroinvertebrate community structure along gradients of hydraulic and sedimentary conditions in a large gravelbed river, macroinvertebrate community structure along gradients of hydraulic and sedimentary conditions in a large gravelbed river. *Freshwater Biology, Freshwater Biology*, 45(1):57–73.

Reynoldson, T. B. (1987). Interactions between sediment contaminants and benthic organisms. In Thomas, R. L., Evans, R., Hamilton, A. L., Munawar, M., Reynoldson, T. B., and Sadar, M. H., editors, *Ecological Effects of In Situ Sediment Contaminants*, number 39 in Developments in Hydrobiology, pages 53–66. Springer, Heidelberg.

Robinson, R. A. and Sutherland, W. J. (2002). Post-war changes in arable farming and biodiversity in great britain. *Journal of Applied Ecology*, 39(1):157–176. ArticleType: primary_article / Full publication date: Feb., 2002 / Copyright 2002 British Ecological Society.

Rosgen, D. L. (1994). A classification of natural rivers. *Catena*, 22(3):169–199.

Sakthivadivel, R. and Einstein, H. A. (1970). Clogging of Porous Column of Spheres by Sediment. *Journal of the Hydraulics Division*, 96(2):461–472.

Salehin, M., Packman, A. I., and Paradis, M. (2004). Hyporheic exchange with heterogeneous streambeds: Laboratory experiments and modeling. *Water Resources Research*, 40(11):W11504.

Saltelli, A. (2002). Making best use of model evaluations to compute sensitivity indices. *Computer Physics Communications*, 145(2):280–297.

Sambrook Smith, G. H. and Ferguson, R. I. (1996). The gravel-sand transition: flume study of channel response to reduced slope. *Geomorphology*, 16(2):147–159.

Sawyer, A. M., Pasternack, G. B., Moir, H. J., and Fulton, A. A. (2010). Riffle-pool maintenance and flow convergence routing observed on a large gravel-bed river. *Geomorphology*, 114(3):143–160.

Schlichting, H., Gersten, K., and Gersten, K. (2000). *Boundary-layer theory*. Springer, Heidelberg.

Schlchli, U. (1992). The clogging of coarse gravel river beds by fine sediment. *Hydrobiologia*, 235-236(1):189–197.

Sear, D. A. (1993). Fine sediment infiltration into gravel spawning beds within a regulated river experiencing floods: Ecological implications for salmonids. *Regulated Rivers: Research & Management*, 8(4):373–390.

Sear, D. A. (1996). Sediment transport processes in Pool - Riffle sequences. *Earth Surface Processes and Landforms*, 21(3):241–262.

Sear, D. A., Frostick, L. B., Rollinson, G., and Lisle, T. E. (2008). The significance and mechanics of fine-sediment infiltration and accumulation in gravel spawning beds. In Sear, D. A. and DeVries, P., editors, *Salmonid Spawning Habitat in Rivers: Physical Controls, Biological Responses, and Approaches to Remediation*, pages 149–174. American Fisheries Society, Bethesda, USA.

Sear, D. A., Pattison, I., Collins, A. L., Newson, M. D., Jones, J. I., Naden, P. S., and Carling, P. A. (2014). Factors controlling the temporal variability in dissolved oxygen regime of salmon spawning gravels. *Hydrological Processes*, 28(1):86–103.

Self, R. F., Nowell, A. R., and Jumars, P. A. (1989). Factors controlling critical shears for deposition and erosion of individual grains. *Marine Geology*, 86(2-3):181–199.

Shams, M., Ahmadi, G., and Smith, D. H. (2002). Computational modeling of flow and sediment transport and deposition in meandering rivers. *Advances in Water Resources*, 25(6):689–699.

Shields, A., Ott, W. P., and van Uchelen, J. C. (1936). Application of similarity principles and turbulence research to bed-load movement. Technical report, California Institute of Technology.

Shvidchenko, A. B. (2000). *Incipient motion of streambeds*. Ph.D., University of Glasgow.

Skalak, K. and Pizzuto, J. (2010). The distribution and residence time of suspended sediment stored within the channel margins of a gravel-bed bedrock river. *Earth Surface Processes and Landforms*, 35(4):435–446.

Soulsby, C., Youngson, A. F., Moir, H. J., and Malcolm, I. A. (2001). Fine sediment influence on salmonid spawning habitat in a lowland agricultural stream: a preliminary assessment. *The Science of The Total Environment*, 265(1-3):295–307.

Soulsby, R. (1983). Chapter 5 the bottom boundary layer of shelf seas. In Johns, B., editor, *Physical Oceanography of Coastal and Shelf Seas*, volume Volume 35, pages 189–266. Elsevier, Amsterdam.

Stokes, G. G. (1851). On the effect of the internal friction of fluids on the motion of pendulums. *Transactions of the Cambridge Philosophical Society*, 9.

Stone, M. and Droppo, I. G. (1994). Flocculation of fine-grained suspended solids in the river continuum. *IAHS Publications-Series of Proceedings and Reports-Intern Assoc Hydrological Sciences*, 224:479–490.

Strom (2004). Microforms in Gravel Bed Rivers: Formation, Disintegration, and Effects on Bedload Transport. *Journal of Hydraulic Engineering*, 130(6):554–567.

Summer, W., Klaghofer, E., and Zhang, W., editors (1998). *Modelling soil erosion, sediment transport and closely related hydrological*. IHAS Publication no. 249. IAHS Press, Wallingford.

Thompson, D. M., Wohl, E. E., and Jarrett, R. D. (1999). Velocity reversals and sediment sorting in pools and riffles controlled by channel constrictions. *Geomorphology*, 27(3-4):229–241.

Tonina, D. (2005). *Interaction between river morphology and intra-gravel flow path within the hypotheic zone*. PhD thesis, Collage of Graduate Studies University of Idaho.

Tsakiris, A. G. and Papanicolaou, A. N. (2008). A fractal approach for characterizing microroughness in gravel streams. *Archives of Hydro-Engineering and Environmental Mechanics*, 55(1-2):29–43.

Van Rijn, L. C. (1984a). Sediment pick-up functions. *Journal of Hydraulic Engineering*, 110(10):1494–1502.

Van Rijn, L. C. (1984b). Sediment transport, part i: bed load transport. *Journal of hydraulic engineering*, 110(10):14311456.

Van Rijn, L. C. (1984c). Sediment transport, part II: suspended load transport. *Journal of Hydraulic Engineering*, 110(11):1613–1641.

van Rijn, L. C. (1984). Sediment transport, part III: bed forms and alluvial roughness. *Journal of Hydraulic Engineering*, 110(12):17331754.

Vanoni, V. A., Hydraulics, W. K. L. o., and Resources, W. (1964). Measurements of critical shear stress for entraining fine sediments in a boundary layer. final report to the US public health service. Technical Report Research Grant RG 6915, California Institute of Technology.

Villanueva, I., Pender, G., Lin, B., Mason, D. C., Falconer, R. A., Neelz, S., Crossley, A. J., Bates, P. D., Liang, D., Hunter, N. M., Wright, N. G., and Waller, S. (2008). Benchmarking 2d hydraulic models for urban flooding. *Proceedings of the ICE - Water Management*, 161(1):13–30.

Walling, D., Bradley, S., and Lambert, C. (1986). Conveyance losses of suspended sediment within a flood plain system. In Hadley, R., editor, *IAHS-AISH publication*, 159, pages 119–131. IAHS Press, Wallingford.

Walling, D. and Ongley, E. (1998). Suspended sediment structure: implications for sediment and contaminant transport modelling. *Modelling soil erosion, sediment transport and closely related hydrological processes*, page 437.

Walling, D. E. and Amos, C. M. (1999). Source, storage and mobilisation of fine sediment in a chalk stream system. *Hydrological Processes*, 13(3):323–340.

Walling, D. E. and Bradley, S. B. (1989). Rates and patterns of contemporary floodplain sedimentation: A case study of the River Culm, Devon, UK. *GeoJournal*, 19(1):53–62.

Walling, D. E. and Moorehead, P. W. (1987). Spatial and temporal variation of the particle-size characteristics of fluvial suspended sediment. *Geografiska Annaler. Series A, Physical Geography*, 69(1):47–59.

Walling, D. E. and Moorehead, P. W. (1989). The particle size characteristics of fluvial suspended sediment: an overview. *Hydrobiologia*, 176-177(1):125–149.

Walling, D. E., Owens, P. N., Carter, J., Leeks, G. J. L., Lewis, S., Meharg, A. A., and Wright, J. (2003). Storage of sediment-associated nutrients and contaminants in river channel and floodplain systems. *Applied Geochemistry*, 18(2):195–220.

Walling, D. E., Owens, P. N., and Leeks, G. J. L. (1998). The role of channel and floodplain storage in the suspended sediment budget of the River Ouse, Yorkshire, UK. *Geomorphology*, 22(3-4):225–242.

Wathen, S. J., Hoey, T. B., and Werritty, A. (1997). Quantitative determination of the activity of within-reach sediment storage in a small gravel-bed river using transit time and response time. *Geomorphology*, 20(1-2):113–134.

Wentworth, C. (1928). Studies of coarse sediments, 1923-1927. In Twenhofel, W., editor, *Report of the Committee on Sedimentation, 1923-1927*, 85, pages 23–35. Reprint and Circular Series of the National Research Council, Washington.

Wilcock, P. R. (1988). Methods for estimating the critical shear stress. *Water Resources Research*, 24(7):1127–1135.

Wilcock, P. R. (1998). Two-fraction model of initial sediment motion in gravel-bed rivers. *Science*, 280(5362):410–412.

Wilkinson, S. N., Prosser, I. P., Rustomji, P., and Read, A. M. (2009). Modelling and testing spatially distributed sediment budgets to relate erosion processes to sediment yields. *Environmental Modelling & Software*, 24(4):489–501.

Wilson, A. J., Walling, D. E., and Leeks, G. J. L. (2005). In-channel, storage of fine sediment in rivers of Southwest England. *Water and Energy Abstracts*, 15(2):23.

Wood, P. and Armitage, P. (1999). Sediment deposition in a small lowland stream-management implications. *Regulated Rivers: Research & Management*, 15(1-3):199–210.

Wood, P. J. and Armitage, P. D. (1997). Biological effects of fine sediment in the lotic environment. *Environmental Management*, 21(2):203–217.

Woodruff, J. D., Geyer, W. R., Sommerfield, C. K., and Driscoll, N. W. (2001). Seasonal variation of sediment deposition in the Hudson River estuary. *Marine Geology*, 179(12):105–119.

Wooster, J. K., Dusterhoff, S. R., Cui, Y., Sklar, L. S., Dietrich, W. E., and Malko,

M. (2008). Sediment supply and relative size distribution effects on fine sediment infiltration into immobile gravels. *Water Resources Research*, 44(3):1–18.

Zanke, U. (1977). Berechnung der Sinkgeschwindigkeiten von Sedimenten. Technical Report 46, Mitteilung des Franzius-Instituts fr Wasserbau, No 46, Technical University of Hannover, Hannover.

Zimmermann, A. E. and Lapointe, M. (2005). Sediment infiltration traps: their use to monitor salmonid spawning habitat in headwater tributaries of the Cascapedia River, Quebec. *Hydrological Processes*, 19(20):4161–4177.